Volume 68 • Number 2 • April 2020

Acta Geophysica

PAN

POLISH ACADEMY OF SCIENCES

Institute of Geophysics
Polish Academy of Sciences

Springer

Acta Geophysica (2020) 68:289–302
https://doi.org/10.1007/s11600-020-00406-3

REVIEW ARTICLE - SOLID EARTH SCIENCES

Analysis of the characteristics of magnetic properties change in the rock failure process

He Zhang[1,2] · Qiang Sun[2,3,4] · Zhenlong Ge[1]

Received: 14 June 2019 / Accepted: 28 January 2020 / Published online: 4 February 2020

Abstract

It is difficult to observe changes in the internal structure of natural rocks when under certain pressure ranges. However, such rocks have specific magnetic properties that are established during their formation process. Through studying changes in their magnetic properties while under pressure, which are readily observed and analyzed, as combined and contrasted with their associated structural changes, the relationship between the stress–strain and the magnetic field intensity can be established. Based on the stress–strain and magnetic field strength data obtained from the relevant literature, the process of rock and rock-like mechanical failure can be divided into three stages: elastic, plastic, and rupture. The performances of different rocks during these stages were analyzed, and there was an obvious transition point between any two adjacent stages. Thus, this study provides theoretical support to establish the relationship between structure and magnetic variations of rocks and rock-like bodies.

Keywords Failure · Stress–strain · Structure · Magnetic change · Stability

Introduction

Many researchers have used different methods to study changes in the magnetic properties of rocks under various pressures. When a rock or rock-like body is under an external pressure, a series of changes occur in its internal structure, which introduce variations in its physical properties, such as their magnetic response, acoustic emission rate, and electrical signals (Martin and Wyss 1975; Revol et al. 1977; Byerlee 1978; Bolyachkin et al. 2015; Sun et al. 2015; Saltas et al. 2019). Some scholars have studied magnetic properties, such as the initial magnetization of rocks (Kean et al. 1976), residual magnetization (Ohnaka and Kinoshita 2010; Lanham and Fuller 2013), and piezomagnetic curve determination (Li et al. 1985). In addition, the relationships between the strain, stress, and magnetic properties during the entire rock failure process while under compression have been the research content of many researchers (Cress et al. 1987; Borradaile 1988; Hao et al. 1993). Yu (2011), Chen et al. (2012), and Sun (2014) measured and discussed the stress magnetic induction intensity for different rock types during extrusion failure. The Pressure Stimulated Current (PSC) is generated during rock stress failure (Anastasiadis et al. 2007; Triantis et al. 2012), which can be applied to rock damage monitoring (Triantis et al. 2015; Xue et al. 2013, 2014). Erber et al. (1999) and Guralnick et al. (2008) studied the relationship between magnetic fields and material damage. When considering material fatigue limits, Lazreg and Hubert (2010) compared the results of magnetomagnetic pressure measurements with those of autothermal methods. Huang et al. (1990) studied magnetic characteristics and their changes in rock samples around the seismic center. He et al. (2015) and Sun et al. (2016) monitored microfracture events and their associated deformation and failure processes. It was shown that during rock failure, changes in the acoustic emission rate are similar to those of the magnetic field. Lockner (1993) comprehensively discussed the success and failure for acoustic emissions in rock failure research

✉ Qiang Sun
sunqiang04@cumt.edu.cn

1 College of Geology and Environment, Xi'an University of Science and Technology, Xi'an 710054, Shaanxi, China

2 Shaanxi Provincial Key Laboratory of Geological Support for Coal Green Exploitation, Xi'an 710054, China

3 Geological Research Institute for Coal Green Mining, Xi'an University of Science and Technology, Xi'an 710054, China

4 Key Laboratory of Coal Resources Exploration and Comprehensive Utilization, Ministry of Land and Resources, Xi'an, China

and divided acoustic emission for seismic reverse research into three categories. Subsequently, Mansurov (1994) further studied the acoustic emission phenomenon of rocks during failure. Frid (1997) studied changes in the acoustic and electrical properties of rocks at the region where the stress was concentrated to determine a method that predicts rock failure more quickly. Stavrakas et al. (2019) enhanced PSC signal strength by applying the integrated grid of sensors and proved with a new method that the relationship of PSC, sound emission technology, and monitor rock damage. Lavrov (2001) studied the Kaiser effect of brittle rocks under different cyclic times and loading rates. In addition, according to the researches of Triantis et al. (2012), the PSC of rocks also has a Kaiser effect.

In the field of civil engineering, many studies have considered changes in the magnetic properties of concrete after undergoing compression (Jin et al. 2016). One example is to determine concrete damage after a fire has been detected using the magnetic method (Miao et al. 2004). Zhang et al. (2014) observed changes in the magnetic field of concrete with magnetic cores from the beginning of the loading until failure.

By collecting and sorting experimental data and research results from previous studies, it was discovered that many works considered the influence of a single or only a few factors that impact the magnetic properties of natural rocks, such as the uniaxial pressure, microfractures, and temperature. Since the existing body of research has had varying foci, it is inevitable that some of the more valuable phenomena have been overlooked. In this paper, we comprehensively discuss previous research to provide theoretical support and guidance for future investigations.

Study of the magnetic change in rock after loading

Rocks are composed of a series of mineral particles and crystals. When these components include a small amount of magnetic minerals, the rock is considered to be magnetic. The magnetization of rocks is determined by the type, size, and amount of magnetic minerals, as well as the temperature and pressure of the external environment. Magnetic rocks can be considered as paramagnetic, diamagnetic, and ferromagnetic. In general, among the three types of magnetic rocks, igneous rocks have the strongest magnetic properties followed by metamorphic rocks and sedimentary rocks. The corresponding primary magnetic sources for these rock types are the thermal, chemical, and sedimentary remanences, respectively.

The structure, morphology, porosity, and other physical properties of rocks change when under pressure. The best feature to measure the magnetic properties of rock is from cracks and voids, which are often proportional to the density of the magnetic induction line. Therefore, we can monitor changes in the magnetic induction line, while the rock is under stress to analyze the pore development. This method is practical when studying rock and rock-like piezomagnetism. The rest of this paper discusses the experimental research data from relevant researchers with references to their figures and tables. The data and methods referenced in this paper are given in Table 1. Reinforced concrete requires a built-in magnetic core to enhance the effects of experiments.

Analysis

Figure 1a shows changes in the magnetic properties and stress of concrete (Zhang et al. 2014) with an increased strain after compression. The experimental data can be divided into three stages: During the first stage, the concrete retained its original shape and, at greater stress, the magnetic field strength briefly decreased. During the second stage, the magnetic field strength increased steadily and slowly, and the elastic deformation occurred primarily at its interior with stresses concentrated around the cracks. During the third stage, the stress decreased sharply when the concrete broke down and the magnetic field around the sample increased significantly. Figure 1b shows the position of the sample during the experiments.

Fatigue damage will occur when concrete is repeatedly pressurized, which is difficult to observe directly. However, we can indirectly obtain the degree of fatigue damage by considering changes in the magnetic field of concrete during repeated compressions. When both loading and unloading pressures occur, the magnetic induction intensity curves intersect, and the corresponding loading and unloading forces remain within a certain range. The load at the beginning of the sample rupture remains within this range, as shown in Fig. 2a. Figure 2b, c shows changes in the magnetic properties of reinforced concrete beams under repeated compressions (Jin et al. 2016). Figure 2b shows that during the initial loading cycle for concrete under compression, the magnetic properties were quite different at the beginning than at the end of the first cycle. The magnetic curve gradually increased and then maintained a similar position, and the law of variation did not change significantly, as shown in Fig. 2c. Figure 2d shows a diagram of the sample placement during testing.

After compression, changes in the magnetic properties of rocks can be divided into three stages: elastic, plastic, and rupture (Chen et al. 2012). Figure 3a, b describes the strain and magnetic changes for marble under stress, respectively, and Fig. 3c, d shows the same for limestone. The strain curves for both rock types changed at the first transition point of the magnetic field strength curve when the rock

Table 1 Characteristics of the reviewed

Parameter type	Rock type	References	Site	Main mineral	Sample size (mm) h–d	Test equipment	Test process
Remanent magnetization	Granodiorite (FFHS2-3)	Hao et al. (1993)	Fangshan, Beijing, China	Plagioclase 46%; orthoclase and microclinite 18%; quartz 20%; hornblende 12%; biotite 2%; magnetite 1%	100 × 50	MiniSpin Magnetizer; MiniSep Magnetizer	–
Remanent magnetization	Magnetite quartzite (MCS4-2)	Hao et al. (1993)	Miyun, Beijing, China	Quartz 62%; magnetite 31%; actinolite 6%; few limonite	100 × 50	MiniSpin Magnetizer; MiniSep Magnetizer	–
Remanent magnetization	Pyroxenite (MGHC1-5)	Hao et al. (1993)	Miyun, Beijing, China	Pyroxene 80%; magnetite 8%; hornblende 1%; spinel 5%; peridot 4%; carbonatite 2%	100 × 50	MiniSpin Magnetizer; MiniSep Magnetizer	–
Remanent magnetization	Biotite hornblende monzonite granite (MRH1-3)	Hao et al. (1993)	Miyun, Beijing, China	Plagioclase 60%; hornblende 11%; orthoclase and microclinite 10%; quartz 12%; pyroxene 3%; biotite 2%; magnetite 2%	100 × 50	MiniSpin Magnetizer; MiniSep Magnetizer	–
Magnetic susceptibility	Basalt	Li et al. (1985)	Pinggu, Beijing, China	Magnetite 15%	100 × 60	–	a
Magnetic susceptibility	Lamprophyre	Li et al. (1985)	Yanqing, Beijing, China	Magnetite 5%	100 × 60	–	a
Magnetic susceptibility	Granite gneiss	Li et al. (1985)	Qianan, Hebei, China	Magnetite 8%	100 × 60	–	a
Magnetic susceptibility	Amphibolite	Li et al. (1985)	Miyun, Beijing, China	Magnetite 3%	100 × 60	–	a
Magnetic susceptibility	Magnetite quartzite	Li et al. (1985)	Miyun, Beijing, China	Magnetite 30%	100 × 60	–	a
Magnetic susceptibility	Monzonite	He et al. (2015)	Jiaocheng, Shanxi, China	Plagioclase; hornblende; orthoclase; small amount of other minerals	22 × 22	Kappabridge MFK1-FA;	b
Magnetic intensity	Quartz magnetite	Sun (2014)	Liaoyang, Liaoning, China	Magnetite 55–100%; quartz 40–45%; tremolite (about 3%)	100 × 50	Weak magnetic detector of NT-10	c
Magnetic intensity	Granite with magnetic core	Yu (2011)	Zhuanghe, Liaoning, China	–	110 × 55	Weak magnetic detector of NT-10	d
Magnetic induction intensity	Limestone with magnetic core	Chen et al. (2012)	–	–	105 × 55	Weak magnetic detector of NT-10	e
Magnetic induction intensity	Marble with magnetic core	Chen et al. (2012)	–	–	105 × 55	Weak magnetic detector of NT-10	e
Magnetic flux density	Reinforced concrete	Jin et al. (2016)	–	–	150 × 200 × 1500	Fluxgate magnetometer of APS 428 D	–

Table 1 (continued)

Parameter type	Rock type	References	Site	Main mineral	Sample size (mm) h–d	Test equipment	Test process
Magnetic flux density	Concrete with magnetic core	Zhang et al. (2014)	–	–	100 × 100 × 100	YJ-3000t press machine, Ultrasonic transmission Reflection method (UTRM)	f
Magnetic induction intensity	–	Byerlee (1978)	–	–	–	–	–

(a) Increase pressure gradually until it breaks down
(b) 0.1 kN/s, pressurize in 10 steps. The target loads for each step are 20, 40, 50, 60, 70, 75, 80, 85, 90, 95 kN
(c) 2 kN/min, the experimental force reached 20 kN, changed to 10 kN/min, keep
(d) Step one: 2 kN/min, keep and then tune to 5 kN/min. Step two: load reaches 20 kN and increased to 10 kN/min. Load reaches 30 kN and increased to 20 kN/min. Load reaches 50 kN and increases to 30 kN/min, keep
(e) 20 °C/min, keep 20 min, 1 GPa
(f) 1 GPa

was under pressure, which is the transition from the elastic to the plastic stage. Before this point, the elastic formation of rock after compression altered the cracks and voids in the rock, and as the pressure increased, the rock underwent plastic deformation. This varied the structure while the magnetic field intensity remained relatively constant, giving a nearly flat curve.

When the pressure is gradually increased, the stable structure inside the rock is finally destroyed, which decimates the entire structure, and the relative magnetoresistance of the rock mass decreases to its lowest level. Then, the magnetic field intensity curve jumps upward again in a more intense and obvious way than before, which signifies the transition from the plastic to the rupture stage. The corresponding pressure and strain at this point is the ultimate bearing capacity and maximum deformation of the rock.

Figure 4 shows the relationship between the stress, strain, and magnetic properties under the brittle failure mode (Yu 2011). It can be seen from Fig. 4a that the abrupt change in the magnetic field was delayed relative to the maximum stress point. This is because cracks in the rock developed during the period from the maximum stress point to the abrupt change of the magnetic field until fracturing occurred. Granite has a hard texture and the plastic stage is not obvious, as shown in Fig. 4b. When the stress reaches its maximum value, the magnetic properties also begin to mutate and the rock produces macro-cracks before finally breaking down.

When studying the brittle fracture of granite, the curves based on the data can be divided into two types. The first is that as the stress and strain change, sensors placed on the front and back sides of the granite collect similar data. When the stress increases, the magnetic field intensity grows slowly. However, when the stress reaches a maximum and begins to decrease, the magnetic field intensity increases sharply, and the increasing trend becomes less obvious, as illustrated in Fig. 4c. In the other curve type, the data on the front side of the rock rupture are the same as for the first type, but the magnetic field intensity on the back side decreases slowly with increased stress. The field then decreases sharply after the maximum stress point before decreasing more gradually, as illustrated in Fig. 4d. Figure 4e shows the position of the sample and sensor during data collection.

Figure 5 shows the relationship between the stress–strain and magnetic field strength of ferromagnetic rocks (Sun 2014). In the first stage after the rock is stressed, the strain is proportional to the stress but inversely proportional to the magnetic field strength. When the stress reaches its maximum value, the stress does not increase with the strain, but remains within a certain range. At this time, the magnetic field intensity curve of ferromagnetic rocks changes with three distinct behaviors: (1) slow increase; (2) nearly

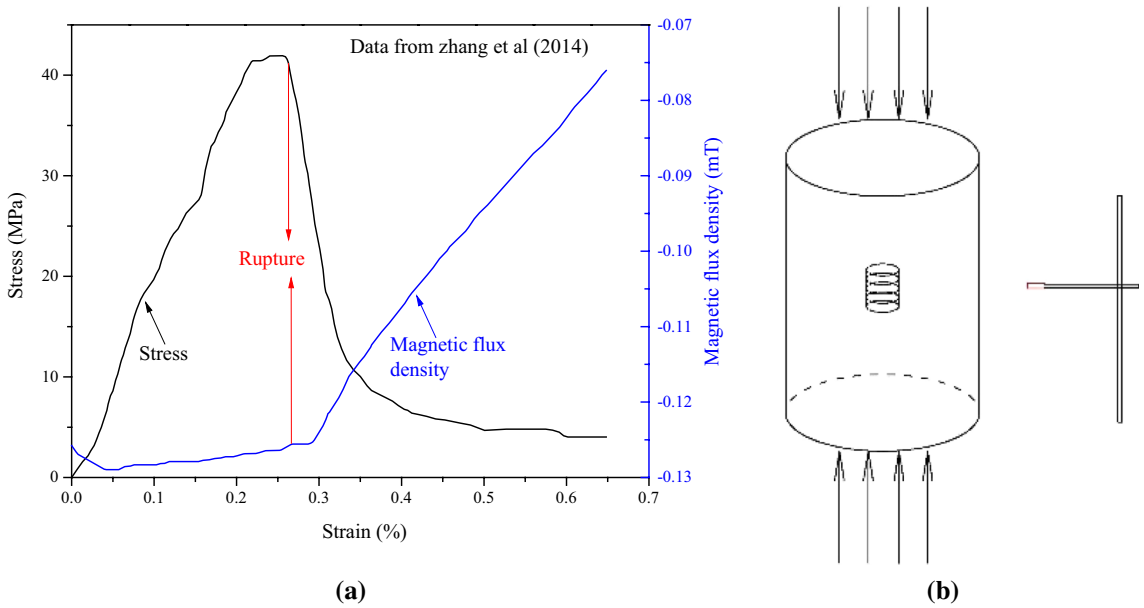

Fig. 1 Relationship between stress–strain and magnetism during uniaxial compression: **a** strain–stress–magnetic curve, **b** concrete with built-in magnetic core

unchanged; and (3) rapid decrease. When the strain in the rock reaches a certain value, the stress–strain curve begins to decrease rapidly. The magnetic field strength curve is divided into the following two cases: (1) slow increase and (2) nearly unchanged with a slight decrease. Thus, Fig. 5 shows that the stress–strain curves are nearly the same, and the overall trend of the strain–magnetic field intensity curves decreases. However, there are some differences in the middle region of these changes. The positional relationship between the sample and the sensor is shown in Fig. 1b.

The properties of rocks vary along different directions, which is called anisotropy. While under stress, rock shapes change non-symmetrically due to their anisotropy. He et al. (2015) introduced a relative shape factor as a parameter to evaluate these deformations. Figure 6a shows the anisotropic change for rocks under compression. As the anisotropic change gradually accelerates, the rock structures, such as cracks, develop more rapidly. The rock eventually ruptures once the pressure reaches a certain limit. As shown in Fig. 6b, changes in the relative shape factor gradually accelerate and are nearly consistent with the anisotropy. Therefore, the relative shape factor can be used as an important parameter to study the stress and strain of rocks.

The concept of wall-shift magnetization was introduced based on a study of the piezomagnetic properties of magnetite–quartzite and lamprophyre (Li et al. 1985). In theory, the magnetization of rocks should be proportional to the pressure, but Fig. 7a, b shows that the magnetization increases in part during the initial pressure, which is from the effect of wall-shifting magnetization. Comparing Fig. 7 with Fig. 2b, c, similar variation rules are caused from fatigue damage of the rock or rock-like body. Figure 7c, d shows that when the volume of an amphibole rock expands, the magnetic susceptibility does not change abnormally, indicating that the volume change of the rock structure does not affect its magnetic susceptibility. The magnetic properties for this rock type are mainly from the ferromagnetic mineral inside. An expanded volume maintains the mineral composition, but will increase the crack distribution and magnetic induction line. Therefore, changes in the magnetic field intensity detected after rocks are under stress are independent of its magnetic susceptibility, because the change rule for magnetic susceptibility remains nearly unchanged during this process.

The responses of the magnetic susceptibilities for different rock types to pressure can vary. However, for andesite, changes in the magnetic susceptibility under uniaxial pressure are nearly the same (Huang et al. 1990), as shown in Fig. 8a. Figure 8b shows the susceptibility of seven rock samples at different temperatures after heating. Although the magnetic susceptibility of each rock varies widely, the basic trend remains the same. At 580 °C, the magnetic susceptibility of the rocks decreased sharply to zero, and the natural remanence disappeared. This temperature is considered as the magnetic transition temperature or Curie temperature of the rock.

Figure 9 shows the changes in the strain, magnetic properties, acoustic emission, and other properties for different rocks after being loaded (Hao et al. 1993). Figure 9a shows the variations in the residual magnetic properties of granodiorite under different uniaxial pressures. When the

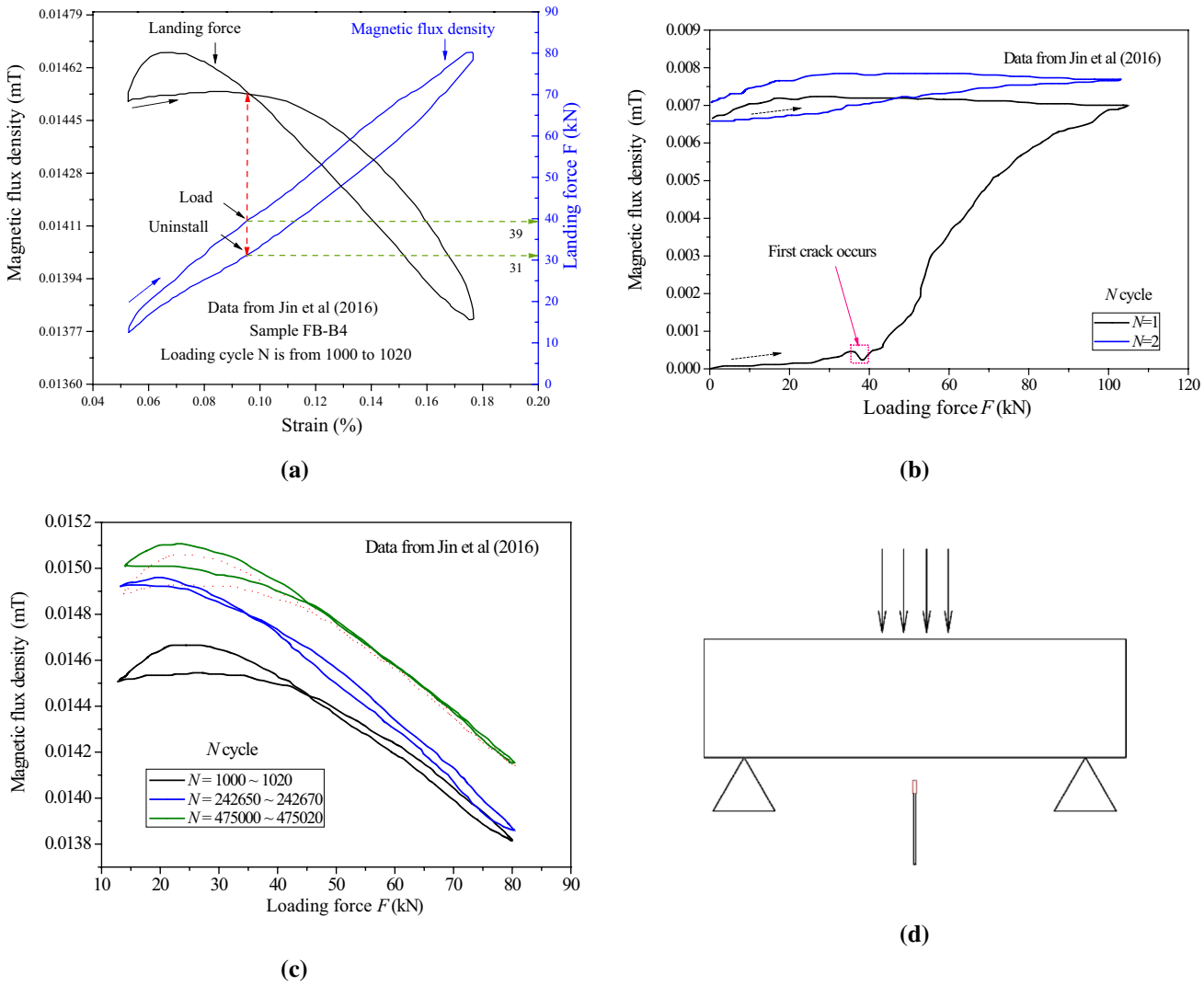

Fig. 2 Strain–stress–magnetic curve of reinforced concrete beams. **a** Single-cycle strain–stress–magnetic variation, **b** magnetic variations under the first and second stress cycles, **c** stress–magnetic variation with different cycles, **d** experimental diagram

pressure is lower than 25 MPa, the residual magnetic properties and acoustic emissivity remain nearly unchanged, making the curve smooth. When the pressure is higher than 25 MPa, the acoustic emissivity and residual magnetization change abnormally and simultaneously, and this difference is present until the pressure reaches 50 MPa. This indicates that the residual magnetization and acoustic emissivity are directly related. Figure 9b reflects the relationship between the remanence and both the volume of the pyroxenite and the stress. With increased stress, the volume strain increases and the remanence decreases, but after reaching the maximum strain, the volume strain decreases and the remanence increases. In this process, tiny cracks develop inside the rock, and a region of concentrated stress appears around the cracks and acoustic emission occurs, as shown in Fig. 9a. When the stress increases to its limit in the concentrated area, it develops into a macroscopic crack, and the curve suddenly decreases, as shown in Fig. 9b. The entire change process is shown in Fig. 9c. When the rock is about to rupture, its remanence characteristics change unsteadily, as shown in Fig. 9d, where the magnetic change is used as a precursor of rock rupture.

Discussion

When rocks or rock-like bodies are subjected to a certain pressure, changes in their magnetic properties show a certain regularity, as illustrated in Figs. 1a and 10a. When the strain versus magnetic field curve changes, the stress curve also changes, and the change points of the two correspond to each other. However, variations in these curves are dependent on

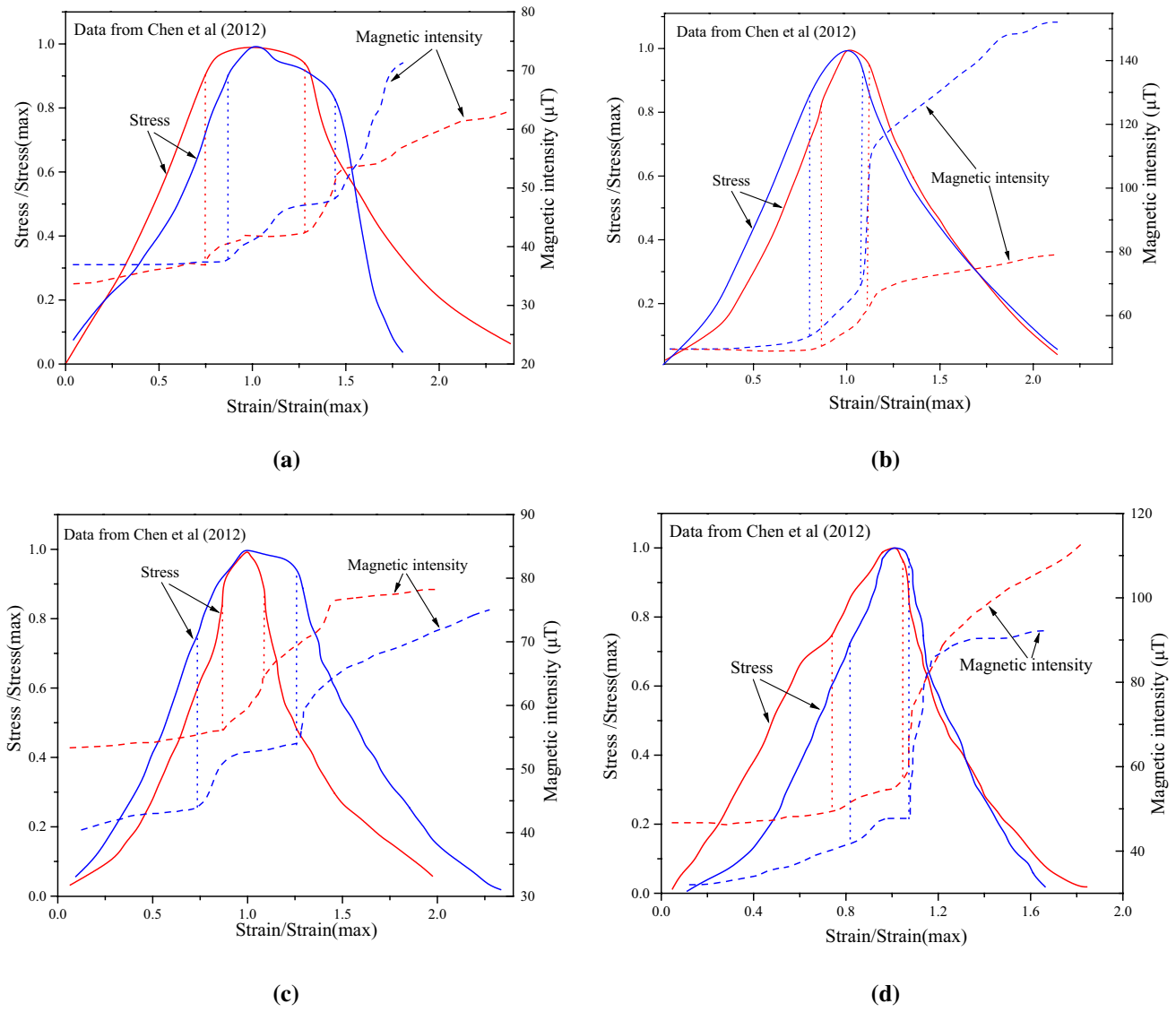

Fig. 3 Relationship curves of strain, pressure and magnetism in marble and limestone. **a** Marble, **b** marble, **c** limestone, **d** limestone

the exact situations. Combined with Fig. 11, we summarize the changes observed as categorized into three stages below.

1. Elastic stage (A–B): Depending on the rock type, two difference versions of this stage exist. (1) In brittle rock, tiny cracks are developed that cause the magnetoresistance to decrease, the permeability to increase, and the magnetic field strength to increase, as shown in Figs. 3 and 4. (2) In ferromagnetic rock, the cracks in the rock develop into macro-cracks, which cause the magnetoresistance to increase, permeability to decrease, and magnetic field intensity to decrease sharply, as shown in Fig. 5. After the brittle rock is stressed, the internal voids evolve, the magnetic path shifts, and the magnetic field intensity around the rock increases. Ferromagnetic rocks are compacted after being stressed, which causes the porosity to decrease, the magnetic resistance to increase, and the magnetic field intensity to decrease.
2. Plastic stage (B–C): When the rock deformation reaches a certain value, the stress no longer increases, but the deformation will continue until rupture. The time till rupture for rocks differs for different lithologies at this stage. However, the plastic deformation of the rocks suggests the magnetic field strength remains nearly unchanged.
3. Rupture stage (C–D): After the strain reaches its maximum value, theoretically, the variation rule of the magnetic field intensity of ferromagnetic rocks should be nearly the same as that of brittle rocks. In fact, the curves for this third stage differ significantly. There is no

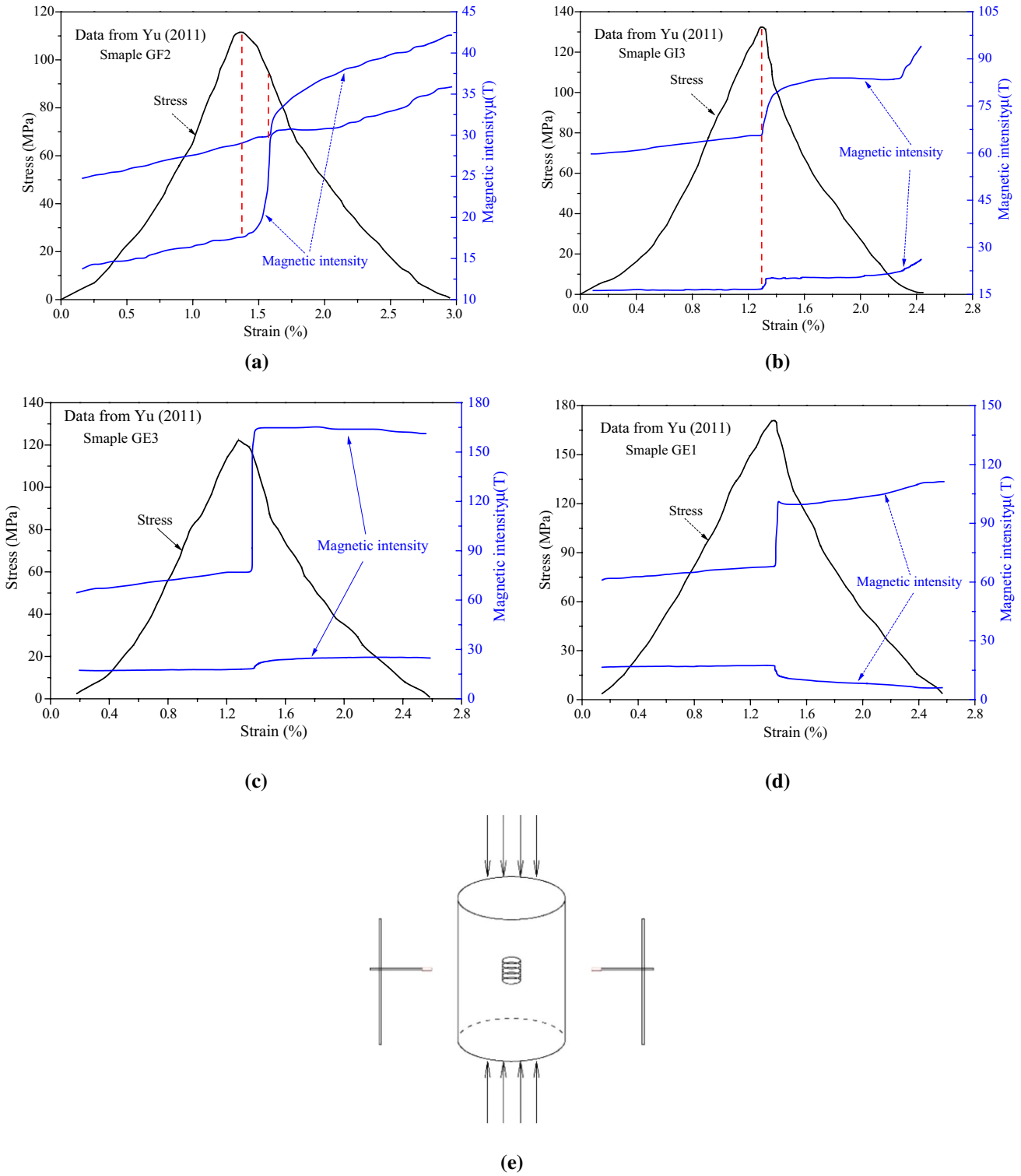

Fig. 4 Relationship between stress–strain and magnetic field intensity of three kinds of granite. **a** First granite, **b** first granite, **c** second granite, **d** third granite, **e** experimental diagram

sharp increase in the magnetic field intensity after breaking and the curves are nearly vertical. This result is not due to a decreased magnetic field intensity or a nearly constant magnetic field after fracture, but is primarily due to the relative position of the lateral fracture of the rock being different from that of the sensor, as shown

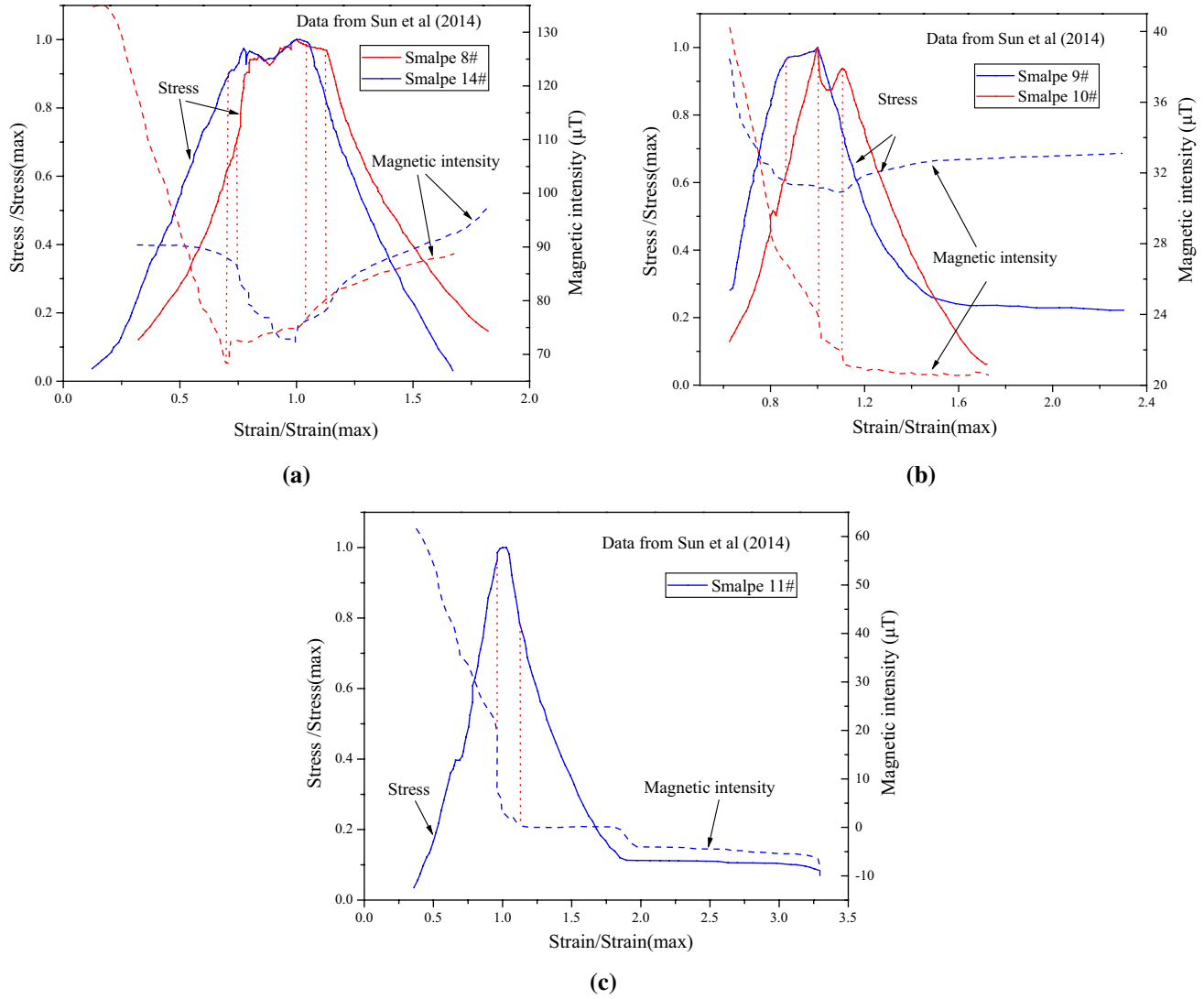

Fig. 5 Three relationship curves of strain–stress–magnetic field intensity of ferromagnetic rocks. **a** First type, **b** second type, **c** third type

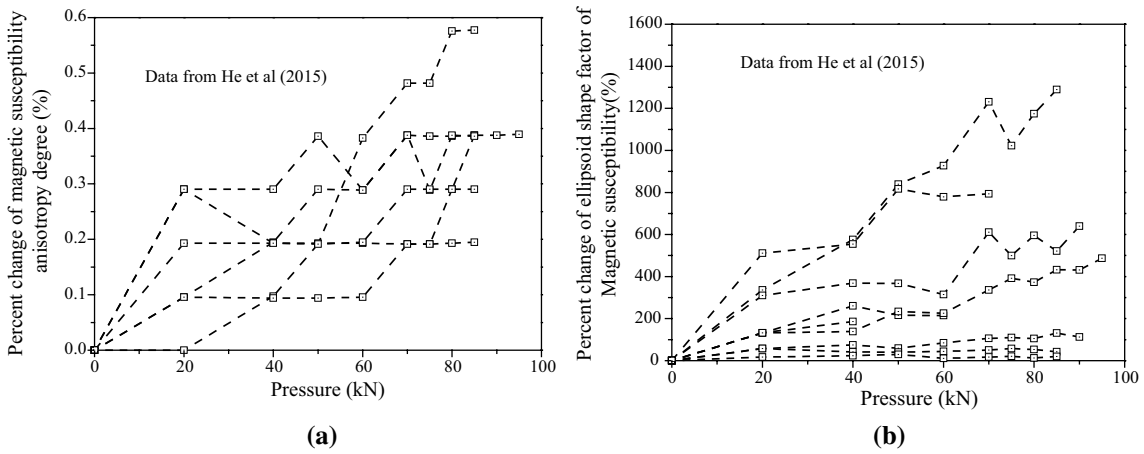

Fig. 6 Changes in two properties during rock compression. **a** Anisotropy of susceptibility, **b** relative shape factor

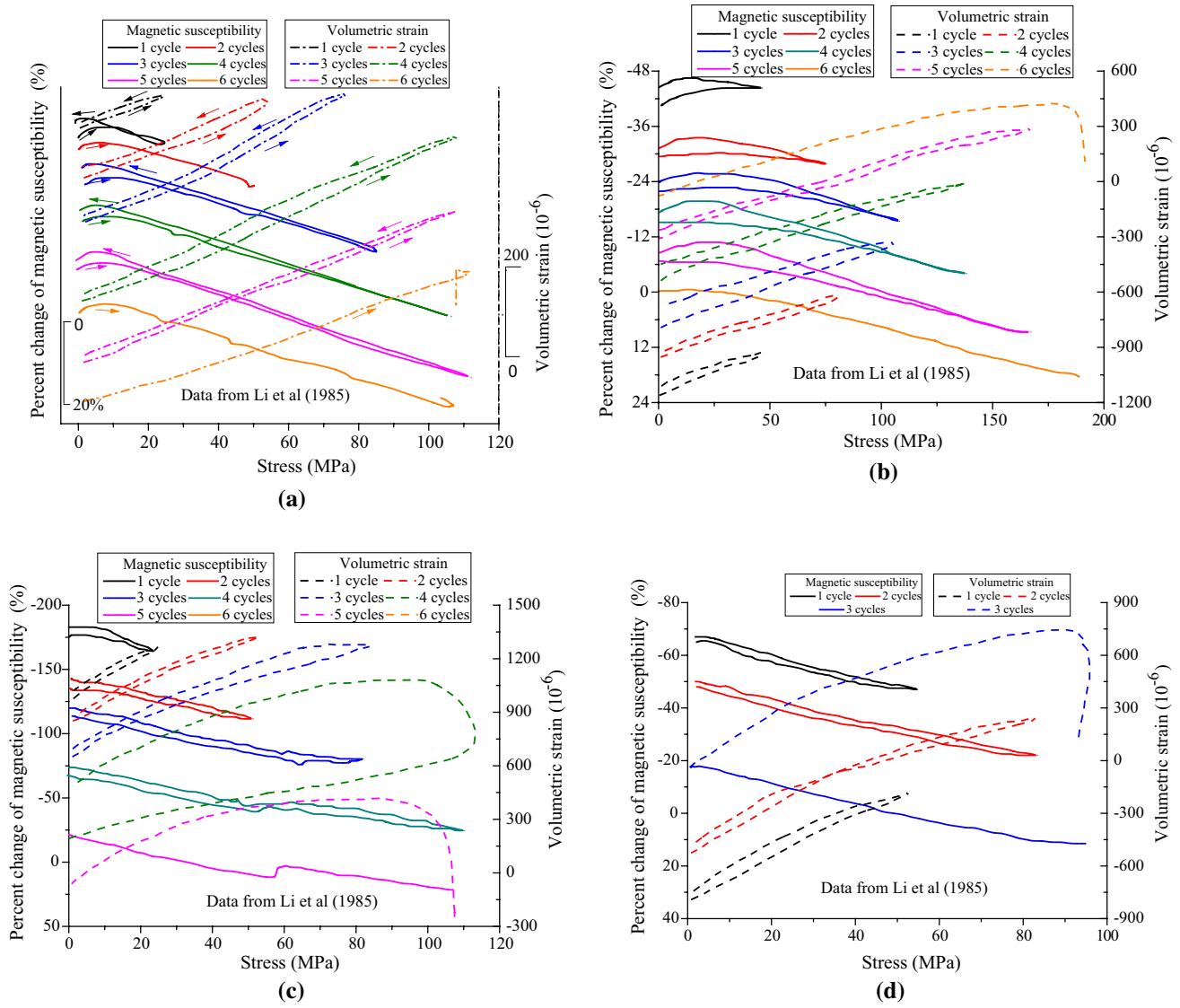

Fig. 7 Relationship between volume and susceptibility of different rock. **a** Magnetite quartzite, **b** lamprophyre, **c** amphibolite, **d** amphibolite

in Fig. 10b. In general, regardless of how the magnetic field changes, there is always a point in the curve that represents a transition in the magnetic field intensity.

Studies of rocks and rock-like bodies under repeated pressurizations have shown an increased number of internal cracks. When the stress increases gradually, fissures develop, and the magnetic field intensity increases. As the fissure development is irreversible in this process, when the stress is released, the existing fissures remain in their new state, while the magnetoresistance remains nearly unchanged. Therefore, the magnetic field intensity will remain at a higher value and will not return to its initial state. During the second compression cycle, under the same stress change conditions, there are less new cracks that appear in the rock or rock-like body. Thus, changes in the magnetic field intensity are smaller, but any new cracks will still increase the magnetic field intensity for the second cycle. After several compression cycles, changes in the magnetic field intensity tend to converge. The magnetic properties of rock or rock-like bodies then only change appreciably during a compression cycle. The experimental data show that the magnetic properties of rocks and rock-like bodies are nearly the same at the beginning and ending of the same compression cycle and that the curves of intermediate compressions and decompressions do not coincide and have opposing associated change trends. When the magnetic field intensity remains in a stable range, the development of cracks in the rock has reached a maximum, as shown in Figs. 2b, c and 7.

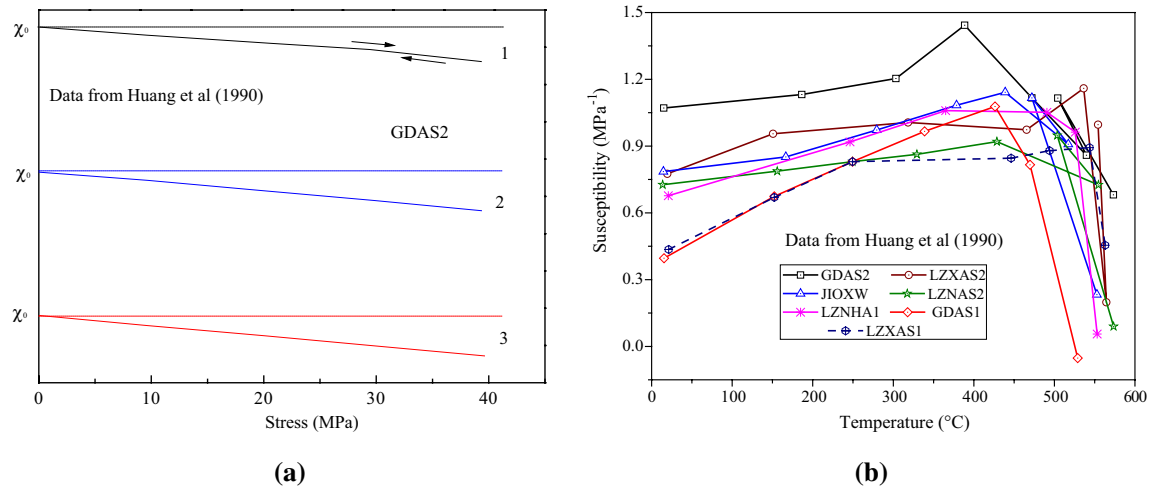

Fig. 8 Magnetic susceptibility of different rocks varies with pressure and temperature. **a** The susceptibility of andesite varies with pressure, **b** the magnetization of andesite and other seven kinds of rocks varies with temperature

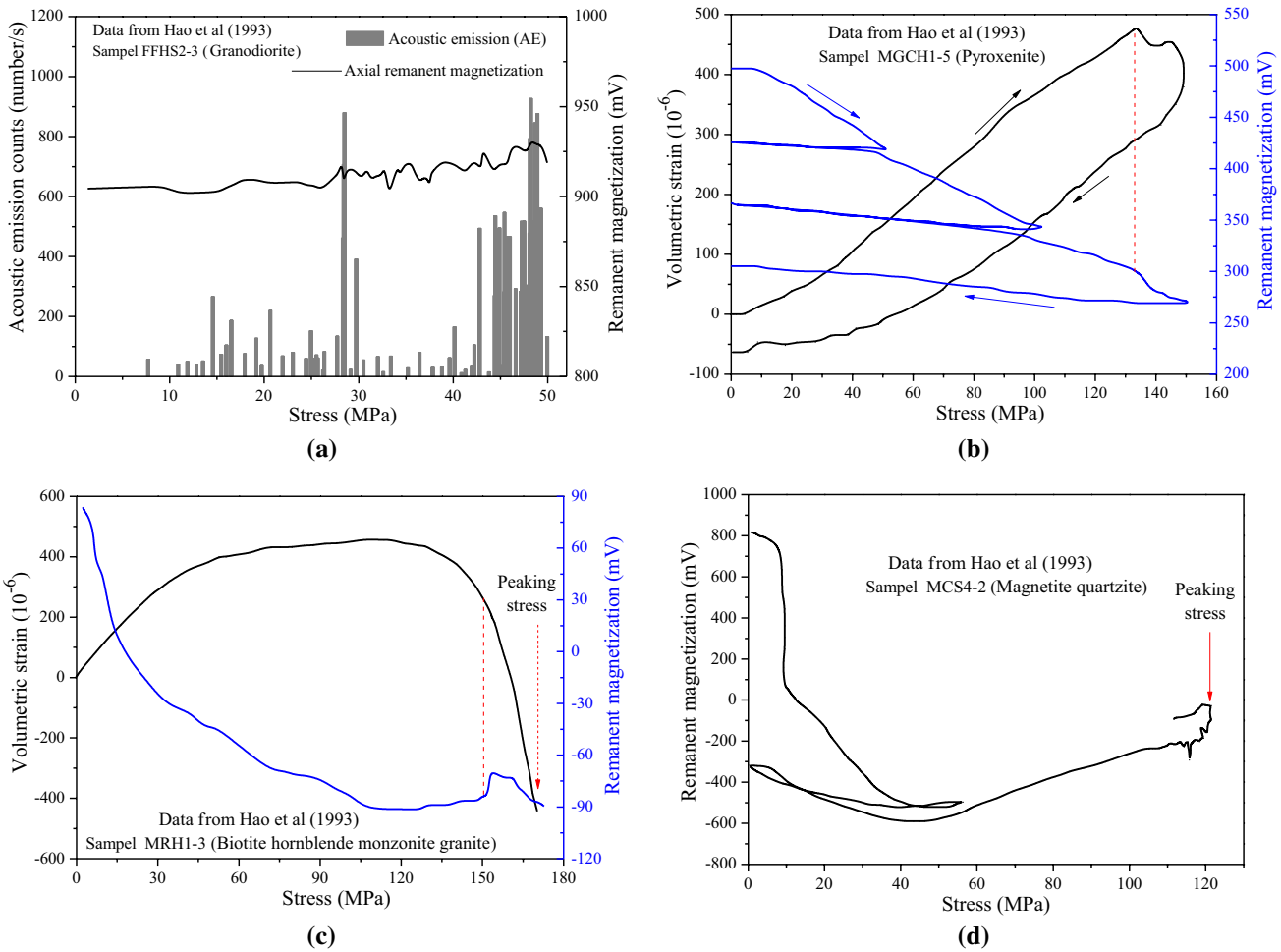

Fig. 9 Changes of different rocks after compression. **a** Granodiorite, **b** pyroxenite, **c** hornbeam black cloud monzonite, **d** magnetite quartzite

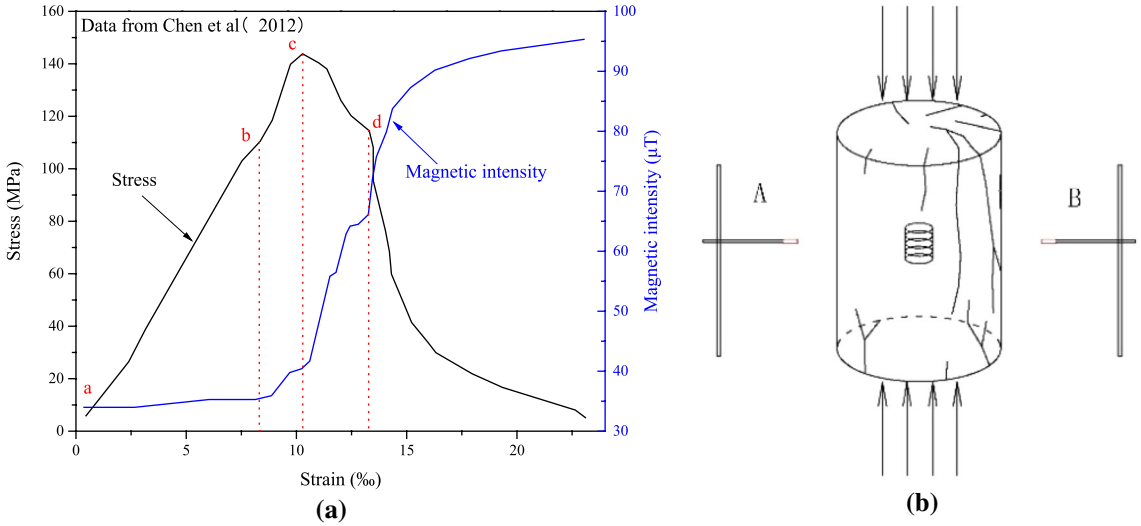

Fig. 10 Changes in the data image of the rock under compression and one of the fracture conditions. **a** General relationship of strain–stress–magnetic field strength of rocks or similar rocks, **b** unilateral failure of samples

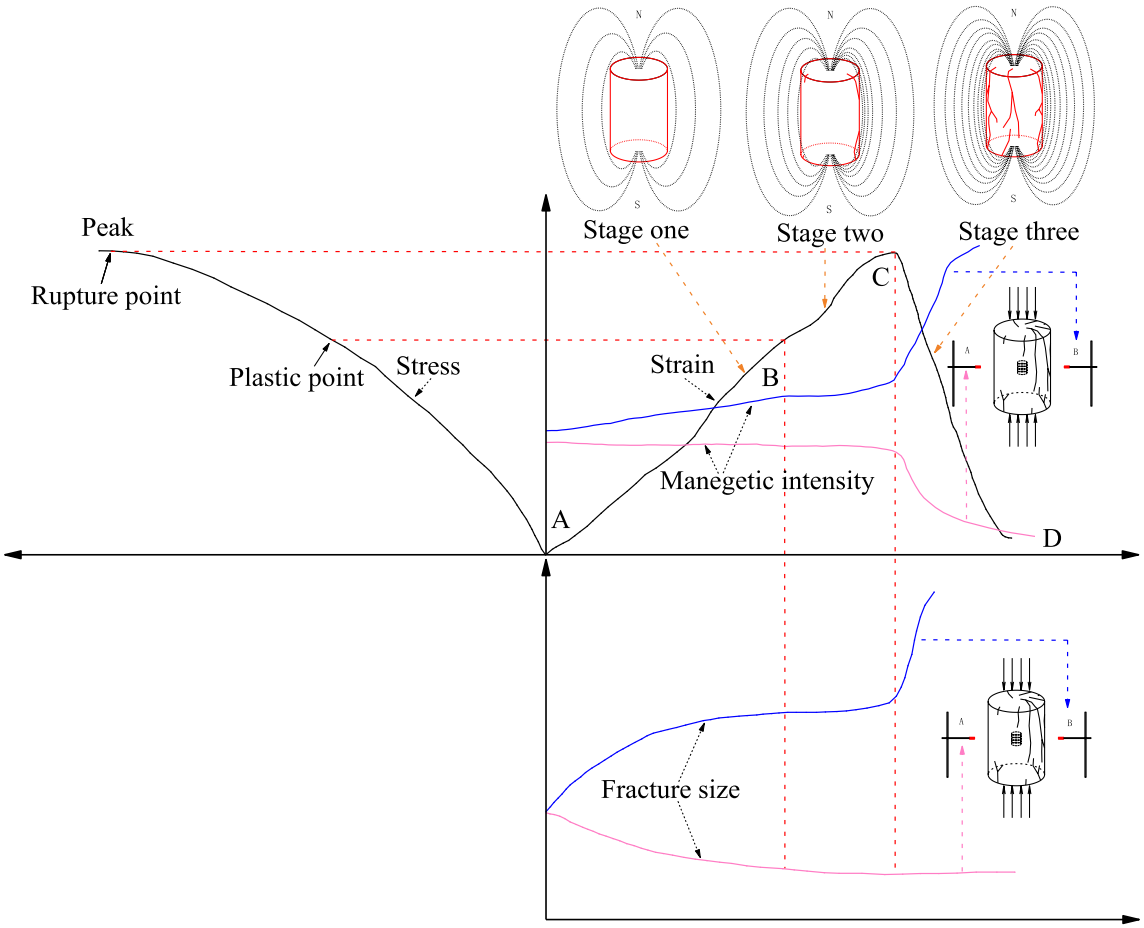

Fig. 11 A comprehensive change in the properties of a rock or rock-like fracture

Conclusions

By analyzing and summarizing the changes in the magnetic properties of various rocks and rock-like bodies while under pressure, we found that there was a close relationship between the strain and magnetic properties of rocks and reinforced concrete after loading.

1. After loading, the three stages of rock or rock-like bodies were observed that there are exhibited and different changes. During each transition stage, the magnetic data changed significantly, which affected the magnetic curve trends.
2. Different rocks have different durations and change trends during the three observed stages. Among which, differences between brittle rocks and ferromagnetic rocks were the most obvious, which provides a method to classify rock types.
3. Fatigue reactions occur in rocks or rock-like bodies during cyclic compression. Through comparative image analyses, it was concluded that the initial cyclic magnetic changes are obvious. However, once internal cracks have been fully developed and the material is in a balanced damage regime, the magnetic properties remain nearly the same for a given region.

While this work focused on the magnetic properties of rocks after compression, negative pressures are more common in nature. In this way, the original load should be removed and the resulting changes that occur inside the rock, whether these are on the internal structure or stability, can be explained by studying the associated magnetic changes.

Acknowledgements This research was supported by the National Natural Science Foundation of China (Grant Nos. 41672279, 41972288).

References

Anastasiadis C, Stavrakas I, Triantis D, Vallianatos F (2007) Correlation of pressure stimulated currents in rocks with the damage parameter. Ann Geophys 50:1–6. https://doi.org/10.4401/ag-3083

Bolyachkin AS, Neznakhin DS, Bartashevich MI (2015) The effect of magnetization anisotropy and paramagnetic susceptibility on the magnetization process. J Appl Phys 118(21):213902. https://doi.org/10.1063/1.4936604

Borradaile GJ (1988) Magnetic susceptibility. Petrofabrics and strain. Tectonophysics 156(1):1–20. https://doi.org/10.1016/0040-1951(88)90279-x

Byerlee J (1978) A review of rock mechanics studies in the United States pertinent to earthquake prediction. Pure Appl Geophys 116(4–5):586–602. https://doi.org/10.1007/bf00876526

Chen G, Xia D, Yu Y, Mao C (2012) Experimental research on stress-strain-magnetic induction intensity effect in the process of rock compression. J Exp Mech 27(6):669–676 **(in Chinese)**

Cress G, Brady B, Rowell G (1987) Sources of electromagnetic radiation from fracture of rock samples in laboratory. Geophys Res Lett 14(4):331–334. https://doi.org/10.1029/gl014i004p00331

Erber T, Guralnick SA, Desai RD, Kwok W (1999) Piezomagnetism and Fatigue. J Phys D Appl Phys 30(20):2818. https://doi.org/10.1088/0022-3727/30/20/008

Frid V (1997) Rockburst hazard forecast by electromagnetic radiation excited by rock fracture. Rock Mech Rock Eng 30(4):229–236. https://doi.org/10.1007/bf01045719

Guralnick SA, Bao S, Erber T (2008) Piezomagnetism and Fatigue: II. J Phys D Appl Phys 41(11):115006. https://doi.org/10.1088/0022-3727/41/11/115006

Hao J, Huang P, Zhou J (1993) The effect of cracking on remanent magnetization of rocks—it's implication to earthquake prediction. Acta Geophys Sin 36(2):203–211 **(in Chinese)**

He Y, Song X, Li B, Li Z, Liu L (2015) A laboratory research on magnetic fabric response of natural rock samples in the process of uniaxial compression to rupture. Journal of Taiyuan Univ Technol 46(6):672–679. https://doi.org/10.16355/j.cnki.issn1007-9432tyut.2015.06.008 **(in Chinese)**

Huang P, Hao J, Zhou J (1990) The effect pressure and temperature on magnetic of rocks from the area near the epicenter of the Liyang earthquake. Earthq Res China 6(1):14–22 **(in Chinese)**

Jin W, Zhang J, Chen C, Mao J, Cui L (2016) A new method for fatigue study of reinforced concrete structures based on piezomagnetism. J Build Struct 37(4):133–142. https://doi.org/10.14006/j.jzjgxb.2016.04.018 **(in Chinese)**

Kean WF, Day R, Fuller M, Schmidt VA (1976) The effect of uniaxial compression on the initial susceptibility of rocks as a function of grain size and composition of their constituent titanomagnetites. J Geophys Res 81(5):861–872. https://doi.org/10.1029/jb081i005p00861

Lanham M, Fuller M (2013) Weak field control of remanent magnetization changes produced by uniaxial stress cycling. Geophys Res Lett 15(5):511–513. https://doi.org/10.1029/gl015i005p00511

Lavrov A (2001) Kaiser effect observation in brittle rock cyclically loaded with different loading rates. Mech Mater 33(11):669–677. https://doi.org/10.1016/s0167-6636(01)00081-3

Lazreg S, Hubert O (2010) Detection of fatigue limit thanks to piezomagnetic measurements. IEEE Trans Magn 46(2):556–559. https://doi.org/10.1109/tmag.2009.2033126

Li S, Huang P, Liu X (1985) The variation of rock susceptibility with uniaxial pressure. Northwest Seismol J 7(2):14–22 **(in Chinese)**

Lockner DA (1993) The role of acoustic emission in the study of rock fracture. Int J Rock Mech Min Sci Geomech Abstr 30(7):883–899. https://doi.org/10.1016/0148-9062(93)90041-b

Mansurov VA (1994) Acoustic emission from failing rock behaviour. Rock Mech Rock Eng 27(3):173–182. https://doi.org/10.1007/bf01020309

Martin RJ, Wyss M (1975) Magnetic properties of rocks and volumetric strain in uniaxial failure tests. Pure Appl Geophys 113(1):107–118. https://doi.org/10.1007/bf01592903

Miao C, Zhang X, Du HX (2004) New fire concrete damage assessment technology. In: Proceedings of the eighth national conference on nondestructive testing technology for construction projects (**in Chinese**)

Ohnaka M, Kinoshita H (2010) Effects of uniaxial compression on remanent magnetization. J Geomagn Geoelectr 20(2):93–99. https://doi.org/10.5636/jgg.20.93

Revol J, Day R, Fuller MD (1977) Magnetic behavior of magnetite and rocks stressed to failure—relation to earthquake prediction. Earth Planet Sci Lett 37(2):296–306. https://doi.org/10.1016/0012-821x(77)90175-3

Saltas V, Vallianatos F, Triantis D, Koumoudeli T, Stavrakas I (2019) Non-extensive statistical analysis of acoustic emissions series

recorded during the uniaxial compression of brittle rocks. Phys A 528(2019):121498. https://doi.org/10.1016/j.physa.2019.121498

Stavrakas I, Kourkoulis S, Triantis D (2019) Damage evolution in marble under uniaxial compression monitored by pressure stimulated currents and acoustic emissions. Fract Struct Integr 13(50):573–583. https://doi.org/10.3221/igf-esis.50.48

Sun X (2014) Experimental research of magnetic induction abnormality of compression failure process. Master thesis of Northeastern University (**in Chinese**)

Sun Q, Zhu S, Xue L (2015) Electrical resistivity variation in uniaxial rock compression. Arab J Geosci 8(4):1869–1880. https://doi.org/10.1007/s12517-014-1381-3

Sun Q, Zhao CH, Lv HJ (2016) Radon emission evolution and rock failure. Acta Geodaetica Et Geophysica 51(3):583–595. https://doi.org/10.1007/s40328-015-0147-z

Triantis D, Vallianatos F, Stavrakas I, Hloupis G (2012) Relaxation phenomena of electric signal emissions from rocks following to abrupt mechanical stress application. Ann Geophys 55:207–212. https://doi.org/10.4401/ag-5316

Triantis D, Stavrakas I, Pasiou ED, Hloupis G, Kourkoulis SK (2015) Innovative experimental techniques in the service of restoration of stone monuments—part II: marble epistyles under shear. Procedia Eng 109:276–284. https://doi.org/10.1016/j.proeng.2015.06.233

Xue L, Qin S, Sun Q, Wang Y (2013) A study on crack damage stress thresholds of different rock types based on uniaxial compression tests. Rock Mech Rock Eng 47:1183–1195. https://doi.org/10.1007/s00603-013-0479-3

Xue L, Qin S, Sun Q, Wang Y, Qian H (2014) A quantitative criterion to describe the deformation process of rock sample subjected to uniaxial compression: from criticality to final failure. Physica A 410(12):470–482. https://doi.org/10.1016/j.physa.2014.05.062

Yu Y (2011) Research on stress-magnetic strength experimental of compression process for brittle rock. Master thesis of Northeastern University. https://doi.org/10.7666/d.j0123352 (**in Chinese**)

Zhang G, Zhang J, Jin L, Chen J (2014) Research progress on mechanics and fatigue of magnetic materials based on magnetostatic effect. Mater Introd 36(5):1–3. https://doi.org/10.3969/j.issn.1005-023x.2014.09.002 **(in Chinese)**

Acta Geophysica (2020) 68:303–324
https://doi.org/10.1007/s11600-019-00395-y

RESEARCH ARTICLE - SOLID EARTH SCIENCES

Neural network-based hybrid ground motion prediction equations for Western Himalayas and North-Eastern India

J. Dhanya[1] · S. T. G. Raghukanth[1]

Received: 2 September 2019 / Accepted: 23 December 2019 / Published online: 24 January 2020

Abstract

This work aims at developing a hybrid ground motion prediction equation (GMPE) for spectral acceleration in Western Himalayas and North-Eastern India. The GMPE is derived using an efficient nonparametric modelling based on neural network algorithm. In this study, owing to sparsity in the recorded ground motions (498 recordings) for the region, the available information is combined with 13,294 records from the well-tested NGA-West 2 database. For the methodology adopted in the study, regional flags are assigned to the records. Thus, given a magnitude, distance, shear wave velocity, fault type and region, the model is able to predict the possible spectral acceleration. The developed GMPE is observed to be unbiased with respect to region. Further, the inter- and intra-event standard deviations are also in acceptable ranges. It is observed that developed GMPE for Western Himalayas and North-Eastern India is able to capture all the known ground motion characteristics. Additionally, the GMPE is compared with the existing GMPE for rock-type soil condition available for the Western Himalayas and North-Eastern India. Furthermore, applicability of the developed GMPE model in estimating hazard is analysed by obtaining the uniform hazard response spectra for Delhi and Guwahati.

Keywords Western Himalayas · North-Eastern India · GMPE · Hybrid ANN

Introduction

Ground motion prediction equations (GMPEs) are essential in understanding the regional characteristic of seismic wave and resultant hazard. However, it is challenging to estimate reliable GMPE especially in regions with sparse recorded data. Many researchers utilize the available recorded data itself to develop GMPEs (Douglas 2018). But reliability and applicability of these GMPEs are limited to the data used in the modelling. Additionally, most commonly adopted methods for such regions with sparse recorded data are by resorting to synthetic database (Iyengar and Raghukanth 2004). In that case also, the results will be biased towards the input parameters used in the simulations as well as on the other computational limitations of the methodology used in generating database. Furthermore, it is well known that accounting for all the inhomogeneities exhibited in the process of generation and propagation of seismic wave is computationally very expensive. Thus, the best representatives of the region ground motion characteristics are the recorded ground motion databases. Taking this into consideration, Campbell (2003) proposed a hybrid empirical technique, where modifications factors for Western North American records are estimated, so as to scale the records to Eastern North America which is having relatively less records. These factors are estimated using the regional seismological model parameters reported in the literature. Similar studies have been reported in Tavakoli and Pezeshk (2005), Pezeshk et al. (2011). One can observe that the modification factors are obtained using stochastic seismological model approach, and hence, the estimates are affected by the uncertainty regarding the parameters chosen in estimating the ground motion transfer function. Recently, there are numerous researches pointing to the efficiency of artificial neural network in handling the complex ground motion characteristics (Derras et al.

Electronic supplementary material The online version of this article (https://doi.org/10.1007/s11600-019-00395-y) contains supplementary material, which is available to authorized users.

✉ J. Dhanya
dhanyaj17@gmail.com

[1] Indian Institute of Technology Madras Chennai, Chennai, Tamil Nadu, India

2014; Dhanya and Raghukanth 2018). It is observed that the neural network-based ground motion prediction is able to adapt all the features of ground motion with minimum number of unknowns and lesser standard deviation. However, effectiveness of neural network-based approaches in handling regions with sparse records is not discussed in the literature.

In India, Himalayan mountain ranges which is formed from the Indo-Eurasian subduction is seismically very active due to the continuous tectonic movements. The vulnerability in the region is also high due to the proximity of several mega cities including the capital city Delhi to these seismically active faults. However, the seismic instrumentation got commissioned for the region only in the recent decades, and hence, there is only limited recorded information. Owing to the sparsity in recorded data, Sharma et al. (2009) combined the available ground motion record for Himalayas with Zagros region of Iran having similar geological regime and utilized the data for prediction of spectral acceleration. The results are only based on 6 Indian and 10 Iranian events. Moreover, as all the ground motions records are considered together, one cannot avoid the possibility of results getting biased to the data from Zagros used in developing the model. In another direction, Natural Disaster Management Agency (NDMA 2010), Raghukanth and Kavitha (2014) used simulation-based approaches to predict GMPE for spectral accelerations for India. It should be noted that these GMPEs are valid for only at rock-type soil condition. Hence, the application of the model to Himalayas and adjoined regions constituting a wide range of geological characteristics is limited. To address local site condition typically, modification factor and scaling are proposed in the literature (IBC 2015). However, the methodology adopted is based on equivalent linear site responses, and hence, the 3D scattering of wave is not accounted in models.

Thus, the present study aims at developing reliable GMPE for Western Himalayas and North-Eastern India implementing hybrid algorithm utilizing the efficiencies for artificial neural network (ANN)-based methodologies. Here, the available records for Indian conditions are combined with the well-tested NGA West2 database separated by regional flags. In the proposed GMPE, the network learns the prominent ground motion features from the NGA West2 database and combines that with the regional recorded data features. The developed network thus becomes efficient for applicability to a wide range of magnitude and distances. The efficiency of the model in capturing the data is tested by estimating region specific inter- and intra-event residuals. The model is also compared with the existing relations for the region. Further, the region specific GMPE developed form

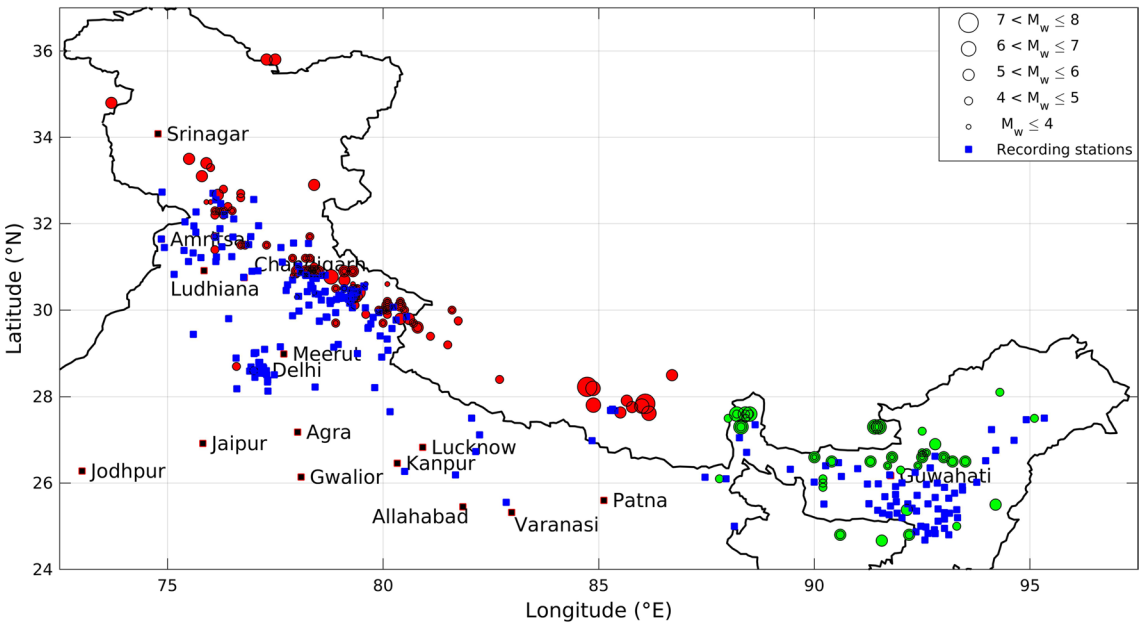

Fig. 1 Spatial distribution of the events along with recording stations (blue squares) for Western Himalayas and North-Eastern India in the period 1986–2017 considered for the analysis performed in this work along with the location of some major cities in the region (note: circles filled with red colour indicate the Western Himalayan events and those filled with green colour indicate North-Eastern Indian events)

the study is applied to estimate uniform hazard response spectra for Delhi and Guwahati for varied soil conditions

Ground motion database

The database for Western Himalayas and North-Eastern India is obtained from records available in COSMOS (Consortium of Organizations for Strong-Motion Observation Systems, https://strongmotioncenter.org/) and PESMOS (Program for Excellence in Strong-Motion Studies) networks. Additionally, ground motions records provided by CESMD (Center for Engineering Strong Motion Data) for the 2015 Mw 7.8 Nepal earthquake and its aftershocks and records from 14 stations in IG-Basin during main-event recorded by the CIGN (Central Indo-Gangetic Plains network) (Chadha et al. 2015; Raghucharan and Somala 2017) are included in the database. The recorded data are segregated into Western Himalayas and North-Eastern India owing to the variabilities associated with the geological and tectonic conditions in both regimes. The distribution of events along with the recording stations is illustrated in Fig. 1. The distribution consists of 108 events in the magnitude range Mw 3–7.8 in the Western Himalayan region and 38 events with Mw 4–6.8 in North-Eastern India during the period 1986–2017. It is clear from the figure that the recording stations are spread over a larger domain, which constitute the Indo-Gangetic basin. It should be noted that the hypocentral depths of Western-Himalayan events range from 2–80 km, whereas that of North-Eastern Indian events vary between 5 and 56 km. It should also be noted here that the events from the Indo-Burmese region are not considered in the present study owing to the variability associated with the tectonic characteristic attributed from deep subduction events. Thus, there are a total of 374 records for Western Himalayas and 124 records for North-Eastern India. Among the events in Western Himalayas, 8 (45 records) are strike-slip event, 98 (322 records) are with reverse mechanism and 1 (1 record) with normal faulting mechanism. For North-Eastern India, the corresponding tally is 21 (67 records), 16 (56 records) and 1(1 record), respectively. Note that the events are sorted into different faulting mechanisms based on the rake angle. The available records for Western Himalayas are for the sites with V_{s30} between 167 and 828 m/s and for North-Eastern India between 150 and 840 m/s. It should be noted that the processing of the recorded data is performed as per the study of Gupta (2018). Furthermore, 5% damped rotd50 horizontal spectra, which correspond to the median values for response spectra of a ground motion when rotated over all horizontal orientations between 0° and 180°, are taken for analysis in this work. The distribution of the database with respect to magnitude and distance is illustrated in Fig. 3. It is clear from the figure that the available data for the region are not comprehensive having considerable gap between the records. A suitable way to

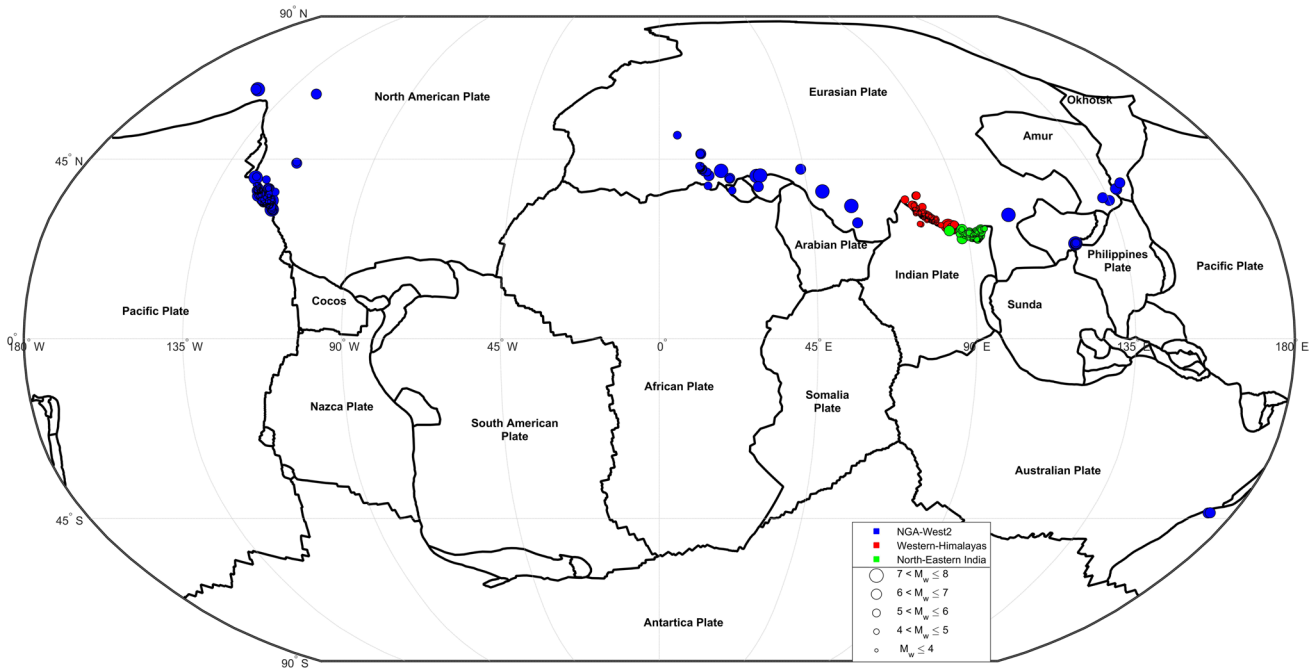

Fig. 2 Spatial distribution of the events considered for developing artificial neural network-based ground motion prediction equations (note: colour is given to differentiate the events in different regions)

Table 1 Weights and bias between the input and the hidden layer

Weights	Input parameter (i)	Number of hidden neurons (k)					
		1	2	3	4	5	6
$W_{ik,1}$	M_w	0.022	0.685	0.111	1.942	– 1.190	– 1.119
	$\log_{10}(V_{s30})$	0.282	– 0.139	0.077	– 0.082	– 0.110	– 0.016
	R_{epi}	0.376	0.058	0.267	0.736	– 0.923	– 0.112
	$\log_{10}(R_{epi})$	1.152	– 0.381	– 0.232	– 0.789	0.497	0.906
	F_{mech}	0.064	– 0.005	– 0.013	– 0.096	0.115	0.025
	F_{loc}	– 0.391	0.814	– 1.383	– 0.351	– 1.029	– 1.135
$Bias_{k,1}$		– 1.768	1.131	– 1.697	1.293	– 1.919	– 1.736

Table 2 Weights and bias values between the hidden and output layer

Weights	Output parameter (j), $\log_{10}(.)$	Number of hidden neurons (k)						$Bias_{j,2}$
		1	2	3	4	5	6	
$W_{jk,2}$	PGA	– 0.468	0.599	0.679	0.117	0.328	– 0.297	0.083
	$Sa_{0.01s}$	– 0.475	0.572	0.670	0.116	0.319	– 0.308	0.075
	$Sa_{0.02s}$	– 0.464	0.589	0.675	0.114	0.329	– 0.307	0.085
	$Sa_{0.03s}$	– 0.477	0.494	0.658	0.102	0.303	– 0.354	0.065
	$Sa_{0.04s}$	– 0.468	0.459	0.658	0.086	0.305	– 0.389	0.076
	$Sa_{0.05s}$	– 0.477	0.405	0.651	0.076	0.297	– 0.425	0.077
	$Sa_{0.06s}$	– 0.489	0.346	0.634	0.071	0.285	– 0.454	0.067
	$Sa_{0.075s}$	– 0.502	0.328	0.634	0.066	0.282	– 0.464	0.072
	$Sa_{0.09s}$	– 0.500	0.349	0.620	0.072	0.287	– 0.443	0.067
	$Sa_{0.10s}$	– 0.490	0.376	0.601	0.080	0.291	– 0.410	0.045
	$Sa_{0.15s}$	– 0.507	0.504	0.580	0.123	0.310	– 0.307	0.037
	$Sa_{0.20s}$	– 0.542	0.637	0.614	0.159	0.308	– 0.193	– 0.018
	$Sa_{0.30s}$	– 0.521	0.891	0.680	0.212	0.337	– 0.016	– 0.026
	$Sa_{0.40s}$	– 0.531	1.086	0.782	0.249	0.351	0.110	– 0.003
	$Sa_{0.50s}$	– 0.521	1.158	0.830	0.269	0.342	0.179	0.009
	$Sa_{0.60s}$	– 0.514	1.229	0.886	0.283	0.339	0.226	0.000
	$Sa_{0.70s}$	– 0.505	1.257	0.919	0.288	0.325	0.260	– 0.019
	$Sa_{0.75s}$	– 0.500	1.348	0.967	0.300	0.346	0.297	0.005
	$Sa_{0.80s}$	– 0.526	1.324	0.970	0.310	0.326	0.297	0.000
	$Sa_{0.90s}$	– 0.516	1.394	1.008	0.320	0.334	0.338	0.002
	$Sa_{1.00s}$	– 0.525	1.409	1.031	0.328	0.323	0.355	0.007
	$Sa_{1.20s}$	– 0.502	1.428	1.063	0.325	0.305	0.379	0.026
	$Sa_{1.50s}$	– 0.490	1.508	1.148	0.332	0.299	0.416	0.089
	$Sa_{2.00s}$	– 0.462	1.508	1.206	0.310	0.267	0.423	0.123
	$Sa_{2.50s}$	– 0.475	1.466	1.234	0.294	0.230	0.413	0.102
	$Sa_{3.00s}$	– 0.472	1.451	1.270	0.268	0.204	0.410	0.134
	$Sa_{4.00s}$	– 0.488	1.482	1.398	0.232	0.164	0.411	0.214

address this issue is to combine the available data with a more comprehensive database. In this study, we chose to combine the available data for the region with well-tested NGA West2 database. The choice is judicial as NGA-West2 also comprises of data from active regions similar to the region under consideration. We sorted out 13,294 records from the reported 21,540 records in the database based on data quality analysis as reported in Dhanya and Raghukanth (2018). Thus, the database considered in the model is from 286 events; the distribution of these events along with that for Western Himalayas and North-Eastern India is shown in Fig. 2. Among the events considered,

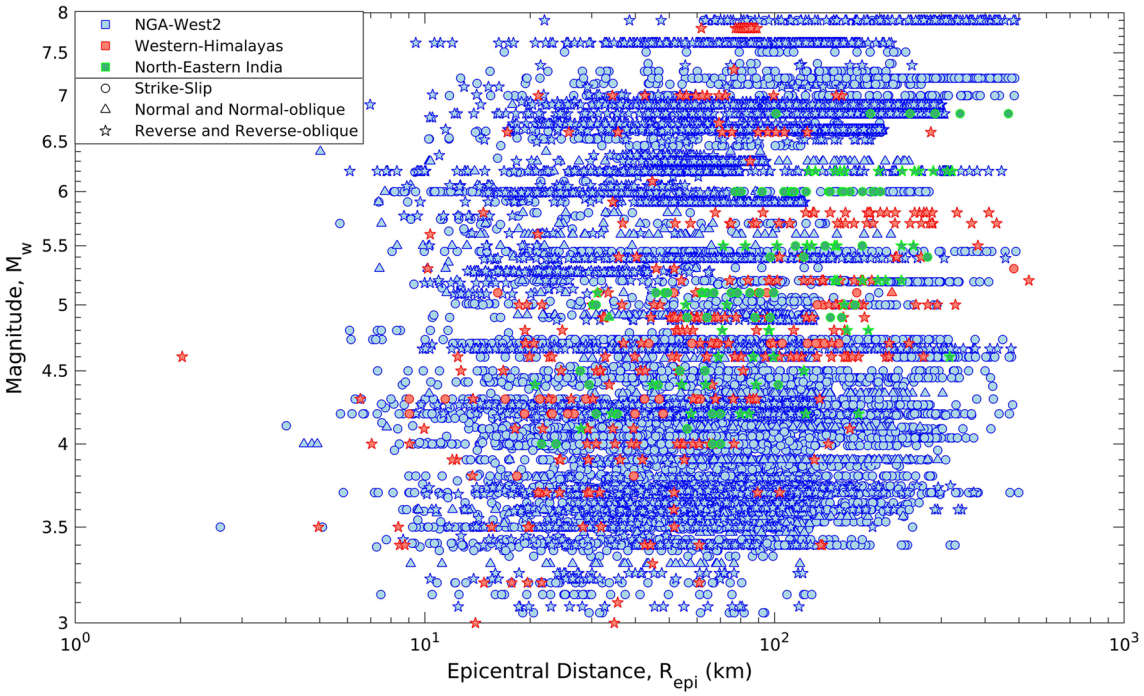

Fig. 3 Distribution of ground motion records with respect to magnitude (M_w) and epicentre distance (R_{epi}) corresponding data available form NGA West2 database and that form PESMOS and COSMOS for Western Himalayas and North-Eastern India

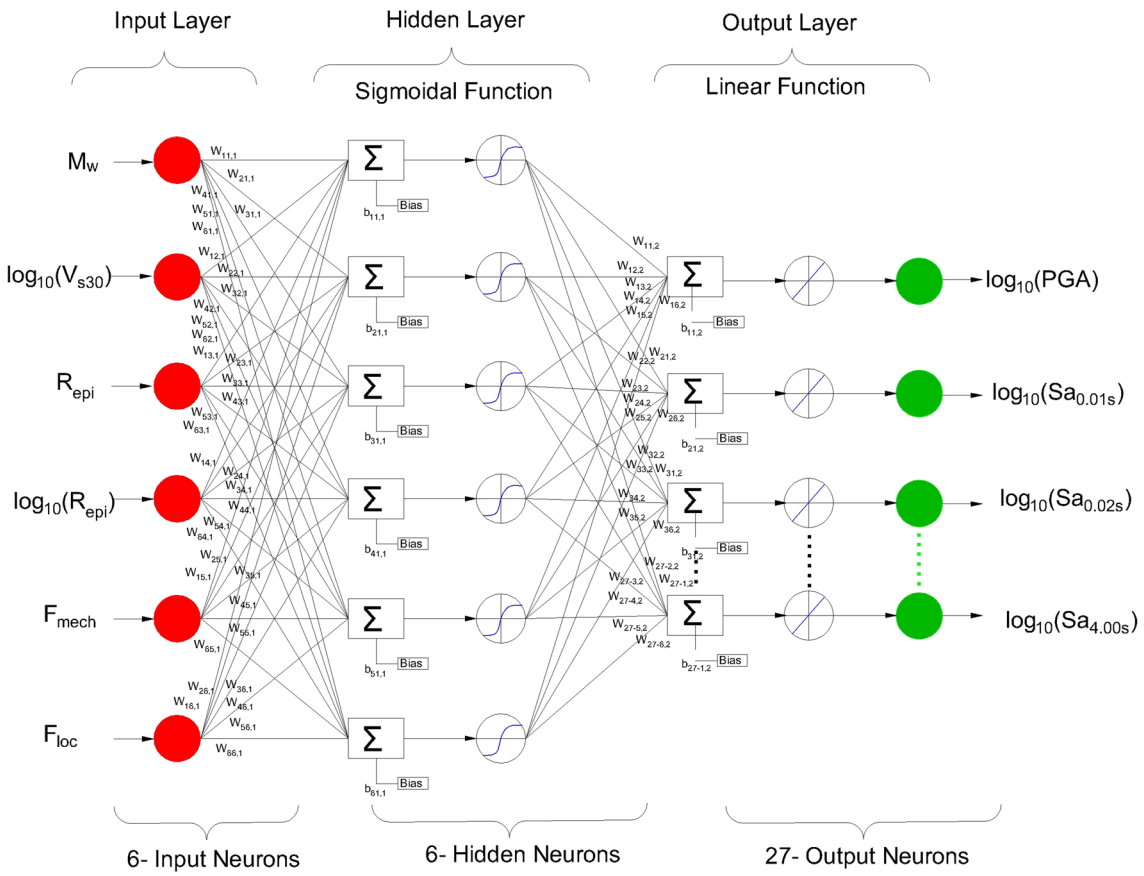

Fig. 4 Artificial neural network (ANN) architecture considered for developing the ground motion prediction equations (GMPEs) for the region

179 (7851 records) are from strike-slip, 69 (3100 records) are from reverse and 38 (318 records) are from normal faulting mechanisms. From the distribution shown in Fig. 3, it is evident that the NGA West2 database covers a broader and comprehensive range of records in comparison with that available for regions under study. Thus, it can be seen that NGA-West 2 is a suitable candidate especially in models based on data-driven methods for ascertain the ground motion features. These information can be suitably combined with regions with sparse records to arrive a more efficient GMPE as discussed further.

Development of hybrid ground motion prediction equation

The hybrid ground motion prediction equation idea postulated from this study is to combine the records from regions with sparse data along with that from the more comprehensive database and segregate with regional flags. The formulation chosen for the ground motion prediction can be represented as follows:

$$\begin{bmatrix} \log_{10}(\mathrm{PGA}) \\ \log_{10}(\mathrm{Sa}_{0.01s}) \\ \log_{10}(\mathrm{Sa}_{0.02s}) \\ \vdots \\ \log_{10}(\mathrm{Sa}_{4.00s}) \end{bmatrix} = f(M_w, \log_{10}(V_{s30}), R_{\mathrm{epi}}, \log_{10}(R_{\mathrm{epi}}), F_{\mathrm{mech}}, F_{\mathrm{loc}}) \tag{1}$$

where *PGA* represents peak ground acceleration, *Sa* denotes spectral acceleration, M_w the moment magnitude, V_{s30} the shear wave velocity from top 30 m of the soil, R_{epi} the epicentral distance, F_{mech} represents the flag for faulting mechanism (1 for strike-slip, 2-normal and 3-reverse mechanisms) and F_{loc} represents the regional flag. It should be noted that $F_{\mathrm{loc}} = 1$ is given for records from NGA-West2 database, 2 for those from Western Himalayas and 3 for those from North-Eastern India. The network architecture considered for the modelling is shown in Fig. 4. The number of hidden nodes is taken after proper trial and error between the size of input and output layers and less than twice the size of input nodes as suggested by Berry and Linoff (1997). A minimum of six hidden nodes is found ideal for the data under consideration. Here, tanh function is used between the input and hidden nodes and linear function between the

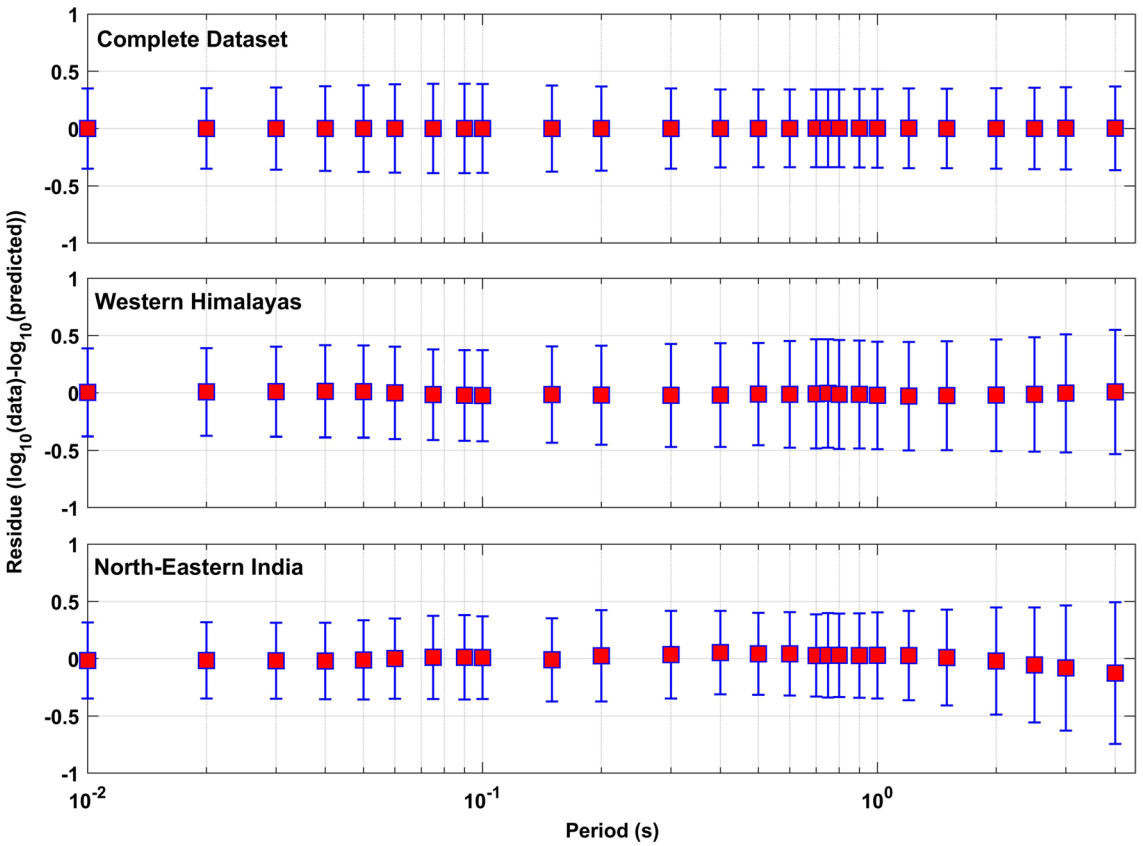

Fig. 5 Mean and standard deviation of residue with respect to period for complete dataset used in the modelling along with that obtained separately for records from Western-Himalayas and North-Eastern India

hidden and output nodes. The resultant functional form for ground motion prediction can be represented as

$$Y_j = \text{bias}_{j,2} + \sum_{k=1}^{m} W_{jk,2}\left(\frac{1-\exp\left(-2\left(\text{bias}_{k,1}+\sum_{i=1}^{n} W_{ik,1}X_i\right)\right)}{1+\exp\left(-2\left(\text{bias}_{k,1}+\sum_{i=1}^{n} W_{ik,1}X_i\right)\right)}\right) \quad (2)$$

where Y_j represents the values for output parameter, X_i represents the input parameters, $W_{ik,1}$ and $\text{bias}_{k,1}$ represents the weights and biases between the input and hidden nodes and $W_{jk,2}$ and $\text{bias}_{j,2}$ are the connection weight and biases between hidden and output nodes, n is the number of input nodes, and m is the number of hidden nodes, respectively. In the network architecture chosen for the study, n=m=6. It should be noted that the choice of tanh function for the model is because the problem belongs to regression analysis. Further, the input and output parameters are scaled between −1 and +1 such that

$$Y = a\left(Y - y_{\min}\right) + x_{\min} \quad \text{where} \quad a = \frac{x_{\max} - x_{\min}}{y_{\max} - y_{\min}} \quad (3)$$

where $x_{\min} = -1$ and $x_{\max} = +1$, and $y_{\min}$ and $y_{\max}$ correspond to the minimum and maximum value of the parameter that needs to be mapped. In total, there are 231 unknowns to predict spectral accelerations at 27 periods for 3 regions taken for the study. The network is trained using Ga-ANN methodology as proposed by Dhanya and Raghukanth (2018). Thus, Ga algorithm is used for initializing the weights and further training is performed based on Levenberg–Marquardt (LM) technique. To ensure the predictive capacity of the model, the data are divided as 70% for training 15% for validation 15% for testing. The corresponding random distribution is done such as representative sample of each region is equally distributed in all sets without overlap. Further, the residual analysis is performed following the mixed effect regression procedure as proposed by Abrahamson and Youngs (1992). The resultant weights and biased

Table 3 Performance of the developed ANN model with respect to correlation coefficient (R) and mean squared error (MSE) for complete dataset and that obtained separately for records from Western Himalayas and North-Eastern India

Parameter	Complete data		Western Himalayas		North-Eastern India	
	R	MSE	*R*	MSE	*R*	MSE
PGA	0.945	0.122	0.675	0.144	0.564	0.110
$Sa_{0.01s}$	0.944	0.123	0.665	0.146	0.567	0.110
$Sa_{0.02s}$	0.944	0.124	0.664	0.146	0.561	0.110
$Sa_{0.03s}$	0.942	0.129	0.646	0.154	0.554	0.110
$Sa_{0.04s}$	0.938	0.136	0.632	0.161	0.549	0.111
$Sa_{0.05s}$	0.935	0.143	0.631	0.162	0.538	0.119
$Sa_{0.06s}$	0.932	0.149	0.636	0.161	0.544	0.122
$Sa_{0.075s}$	0.931	0.152	0.637	0.155	0.566	0.131
$Sa_{0.09s}$	0.931	0.152	0.632	0.156	0.552	0.135
$Sa_{0.10s}$	0.931	0.151	0.633	0.157	0.566	0.129
$Sa_{0.15s}$	0.935	0.141	0.627	0.176	0.543	0.131
$Sa_{0.20s}$	0.938	0.134	0.669	0.186	0.526	0.159
$Sa_{0.30s}$	0.947	0.123	0.735	0.201	0.622	0.146
$Sa_{0.40s}$	0.952	0.117	0.772	0.204	0.684	0.134
$Sa_{0.50s}$	0.956	0.115	0.804	0.197	0.716	0.129
$Sa_{0.60s}$	0.958	0.115	0.811	0.215	0.745	0.133
$Sa_{0.70s}$	0.960	0.116	0.815	0.226	0.757	0.129
$Sa_{0.75s}$	0.960	0.116	0.823	0.222	0.759	0.135
$Sa_{0.80s}$	0.961	0.116	0.827	0.224	0.774	0.132
$Sa_{0.90s}$	0.962	0.117	0.838	0.221	0.783	0.135
$Sa_{1.00s}$	0.963	0.118	0.846	0.219	0.788	0.141
$Sa_{1.20s}$	0.964	0.121	0.853	0.223	0.799	0.151
$Sa_{1.50s}$	0.966	0.120	0.862	0.225	0.791	0.174
$Sa_{2.00s}$	0.968	0.123	0.864	0.237	0.771	0.217
$Sa_{2.50s}$	0.969	0.127	0.866	0.248	0.754	0.253
$Sa_{3.00s}$	0.970	0.128	0.866	0.263	0.731	0.303
$Sa_{4.00s}$	0.971	0.133	0.864	0.292	0.706	0.396

obtained after the training process for the database under consideration is summarized in Table 1 for that between input and hidden nodes and that between hidden and output nodes are summarized in Table 2. The next step in modelling is to ascertain how good is the prediction. The details of performance analysis are summarized in the following section.

Performance analysis

The first step in performance analysis is the estimation of correlation coefficient and mean squared error between the predicted and actual data. Here, the correlation coefficient (R) can be obtained as

$$R = \frac{\sum_{i=1}^{N}(T_i - \overline{T_i})(Y_i - \overline{Y_i})}{\sqrt{\sum_{i=1}^{N}(Y_i - \overline{Y_i})^2 \sum_{i=1}^{N}(T_i - \overline{T_i})^2}} \quad (4)$$

and mean squared error (MSE) is estimated using

$$\mathrm{MSE} = \frac{1}{N}\sum_{i=1}^{N}(T_i - Y_i)^2) \quad (5)$$

where Y represents the predicted data, T represents the target or recorded data and N represents the total number of data points. The corresponding values obtained for the complete dataset and that for the Western Himalayas and North-Eastern India separately are summarized in Table 3. It can be inferred from the table that there is significant correlation between the observed and predicted data as $R \geq 2/\sqrt{N}$ for the region considered for all 27 periods. Furthermore, the MSE < 0.4 which is within the acceptable limits. It should also be noted that, the correlation coefficient R value obtained for the model is < 1 and MSE > 0 which signifies that the model is not over-fitted with respect to data.

Furthermore, it is important to estimate the standard deviation of the residues. The corresponding values are important in quantifying the uncertainties in hazard estimations. Figure 5 illustrates the variation of standard deviation of residues with period. It is observed that the data are not showing any bias or trend with the data. However, it is known that the earthquake records show variability between events and within events.

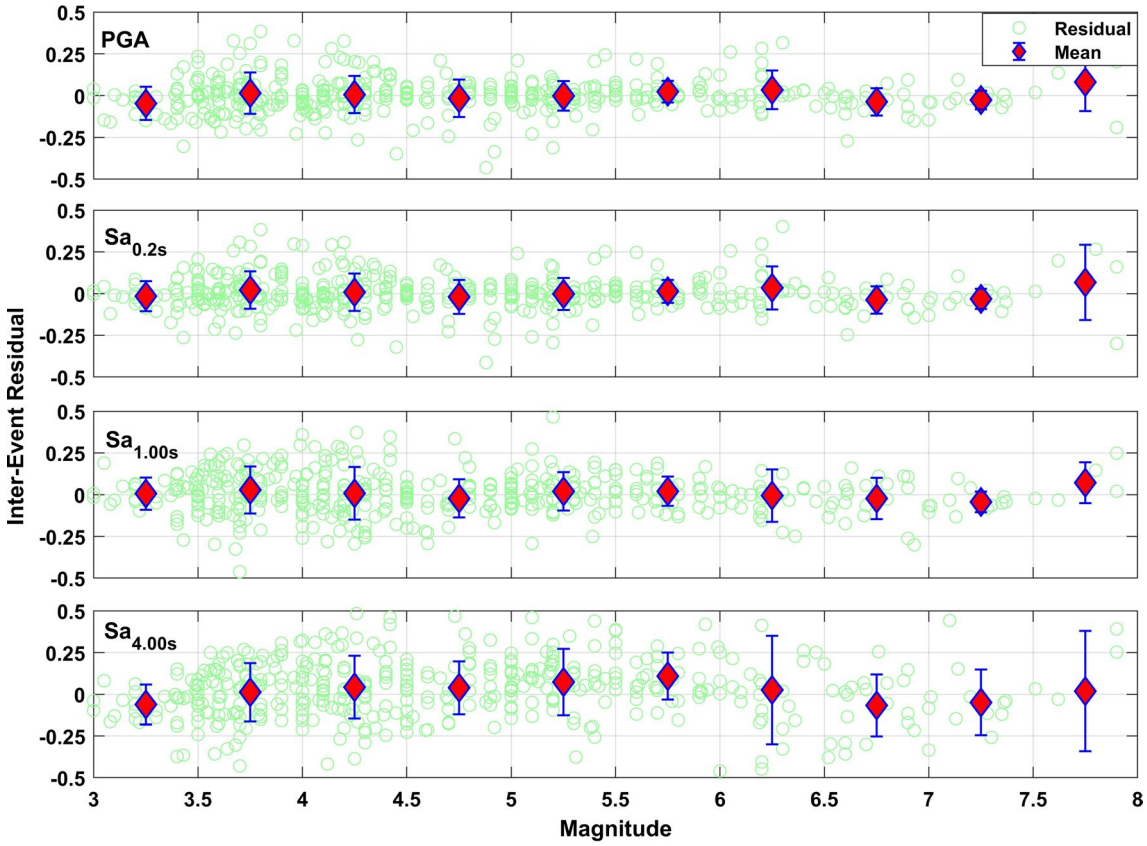

Fig. 6 Inter-event residual with respect to moment magnitude (M_w) corresponding to PGA ($T = 0$ s), Sa at $T = 0.20$ s, 1.00 s and 4.00 s considering all events together

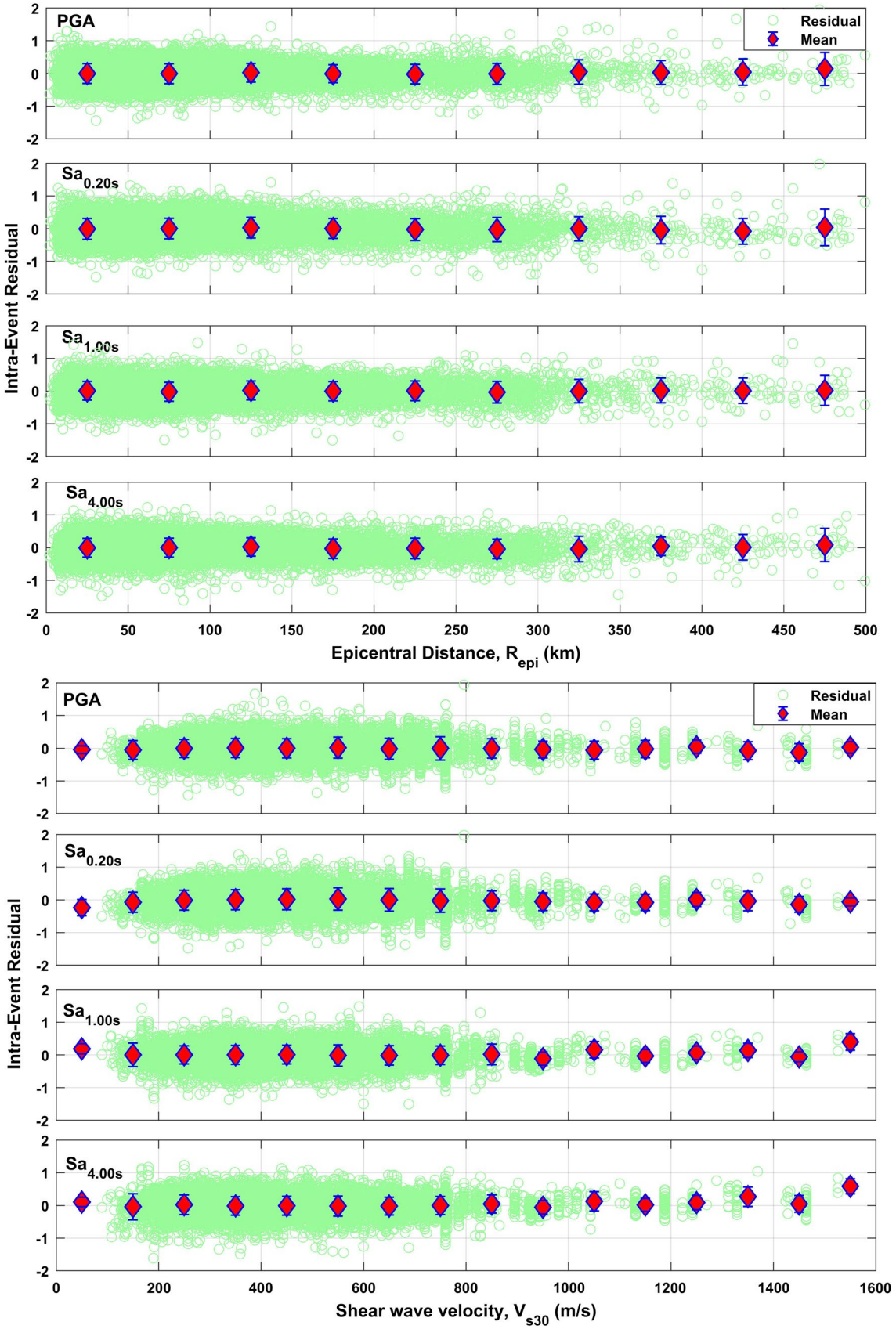

Fig. 7 Intra-event residual with respect to epicentral distance (R_{epi}) and shear wave velocity (V_{s30}) corresponding to PGA ($T = 0$ s), Sa at $T = 0.20$ s, 1.00 s and 4.00 s considering all events together

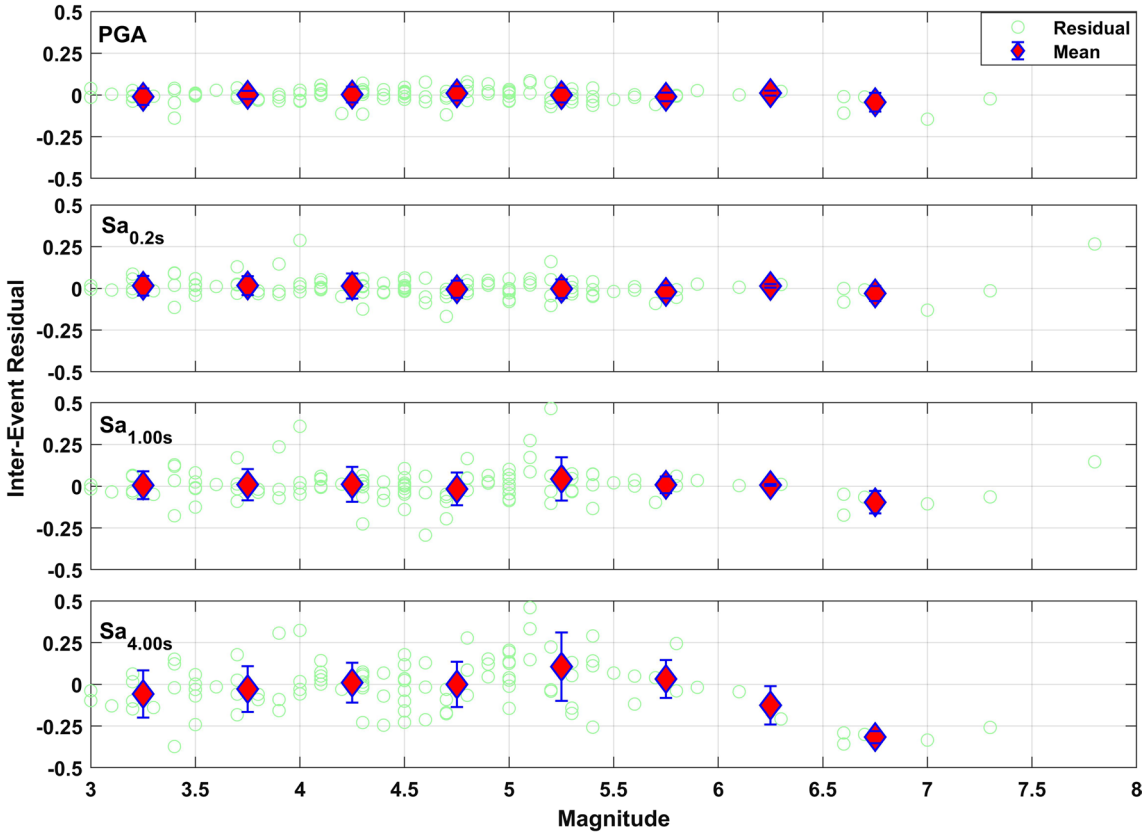

Fig. 8 Inter-event residual with respect to moment magnitude (M_w) corresponding to PGA (T = 0 s), Sa at $T = 0.20$ s, 1.00 s and 4.00 s considering events at Western Himalayas

Hence, it is more acceptable to split the obtained residues into inter (η_i) and intra (ε_{ij}) event residuals. The corresponding functional form can be expressed as:

$$\log_{10}\hat{\mathbf{Y}} = f(M_w, V_{s30}, R_{\text{epi}}, F_{\text{mech}}, F_{\text{loc}}, W, b) + \eta_i + \varepsilon_{ij} \quad (6)$$

where i indicate the event and j represent the recording at jth station for the ith event, and $f(.)$ is the mean prediction. As the proposed GMPE has interconnected nodes, the best way to estimate residuals is through mixed effect algorithm proposed by Abrahamson and Youngs (1992). The algorithm is applied similar to that explained in Dhanya and Raghukanth (2018). The corresponding procedure is briefed for better clarity. Here, first estimate the initial weights and biases using the fixed effect regression technique for the data and functional form under consideration. Then, estimate τ^2 and ϕ^2 using the weights and biases employing maximizing the likelihood using equation (7) of Abrahamson and Youngs (1992). Further, estimate the random inter-event term η_i using equation (10) in Abrahamson and Youngs (1992). Estimate new weights and biases for $(\log 10(\hat{\mathbf{Y}} - \eta_i))$. Repeat the procedure till the likelihood in the second step is maximized. Following this procedure, inter- and intra-event residuals are extracted for the developed model and the corresponding values are summarized in Table 4 for complete database and in Table 5 for Western Himalayas and North-Eastern India separately. It can be observed that the regional level standard deviations is in range of 0.302–0.498, which are less or almost of same order in comparison with that available in the literature (Sharma et al. 2009; Raghukanth and Kavitha 2014). Furthermore, to check for any bias with the input variables, the variation of inter-event residue with magnitude and intra-event residue with epicentral distance and shear wave velocity is illustrated in Figs. 6 and 7, respectively. Furthermore, the corresponding plots for Western Himalayan region are shown in Figs. 8 and 9 and that corresponding to records from North-Eastern India is Illustrated in Figs. 10 and 11. It is evident from the all these illustrations that the residual distribution patten that the developed ANN model is not only unbiased for the complete dataset, but also for the regional records.

Table 4 Standard deviations of the residuals (aleatory uncertainty) in the developed ANN model

Parameter	Inter-event τ ($\log_{10}$ units)	Intra-event ϕ ($\log_{10}$ units)	Total σ ($\log_{10}$ units)
PGA	0.107	0.301	0.319
$Sa_{0.01s}$	0.107	0.301	0.320
$Sa_{0.02s}$	0.188	0.299	0.353
$Sa_{0.03s}$	0.115	0.306	0.327
$Sa_{0.04s}$	0.124	0.312	0.335
$Sa_{0.05s}$	0.131	0.316	0.342
$Sa_{0.06s}$	0.136	0.321	0.349
$Sa_{0.075s}$	0.137	0.323	0.351
$Sa_{0.09s}$	0.135	0.323	0.350
$Sa_{0.10s}$	0.133	0.323	0.350
$Sa_{0.15s}$	0.116	0.322	0.342
$Sa_{0.20s}$	0.105	0.320	0.337
$Sa_{0.30s}$	0.095	0.310	0.324
$Sa_{0.40s}$	0.093	0.303	0.317
$Sa_{0.50s}$	0.098	0.300	0.315
$Sa_{0.60s}$	0.105	0.296	0.314
$Sa_{0.70s}$	0.114	0.296	0.317
$Sa_{0.75s}$	0.117	0.293	0.316
$Sa_{0.80s}$	0.119	0.294	0.317
$Sa_{0.90s}$	0.125	0.294	0.319
$Sa_{1.00s}$	0.130	0.294	0.321
$Sa_{1.20s}$	0.141	0.293	0.325
$Sa_{1.50s}$	0.150	0.289	0.325
$Sa_{2.00s}$	0.162	0.288	0.331
$Sa_{2.50s}$	0.171	0.291	0.337
$Sa_{3.00s}$	0.177	0.290	0.339
$Sa_{4.00s}$	0.194	0.292	0.351

Now, it will be interesting to check the sensitivity of input parameters towards output. Here, the estimation procedure based on weights in the network, proposed by Garson (1991), is utilized to understand sensitivity. According to this method, relative importance (**RI**) of each input variable i for a particular output variable j is obtained as

$$\mathbf{RI}_i\% = \frac{\sum_{k=1}^{m} \frac{|W_{ik} \times W_{jk}|}{\sum_{i=1}^{n} |W_{ik} \times W_{jk}|}}{\sum_{i=1}^{n} \sum_{k=1}^{m} \frac{|W_{ik} \times W_{jk}|}{\sum_{i=1}^{n} |W_{ik} \times W_{jk}|}} \times 100 \tag{7}$$

The corresponding estimates for the developed model are shown in Fig. 12. From the figure, it can be noted that the outputs are more sensitive towards moment magnitude, epicentral distance and fault location. Furthermore, it would be interesting to check whether the regional level ground motion prediction equation is able to capture all known attenuation features of seismic wave. Hence, spectral acceleration is estimated for varying magnitude, distance, shear wave velocity and fault mechanisms as shown in Fig. 13 for Western-Himalayas and in Fig. 14 for North-Eastern India. It can be noted by comparing the figures that the amplitudes are different for both the regions. However, both regions are able to exhibit the general ground motion patterns. Whereby, with distance the amplitudes are reducing and the peak period is shifting towards longer periods. Additionally, as shear wave velocity reduces, the amplitudes are increasing and the peak period is shifting towards long period. Thus, from the illustrations, it is can be seen that the developed ANN model is unbiased and capable of capturing the known ground motion patterns. It will be interesting now to check how is the prediction compared with the existing relations as discussed in the following section.

Comparison with the existing relations

As first step, the spectral acceleration predictions for NGA West 2 ($F_{\text{loc}} = 1$) from the developed model are compared with the GMPEs from same database. Here, the predictions are compared with that reported by Abrahamson et al. (2014), Boore et al. (2014), Campbell and Bozorgnia (2014), Chiou and Youngs (2014) and Dhanya and Raghukanth (2018). The corresponding comparison is

Table 5 Standard deviations of the residuals (aleatory uncertainty) in the developed ANN model considering separately the records at Western Himalayas and North-Eastern India

Parameter	Western Himalaya			North-Eastern India		
	Inter-event τ ($\log_{10}$ units)	Intra-event ϕ ($\log_{10}$ units)	Total σ ($\log_{10}$ units)	Inter-event τ ($\log_{10}$ units)	Intra-event ϕ ($\log_{10}$ units)	Total σ ($\log_{10}$ units)
PGA	0.049	0.363	0.367	0.055	0.297	0.302
$Sa_{0.01s}$	0.050	0.369	0.373	0.055	0.300	0.305
$Sa_{0.02s}$	0.105	0.332	0.348	0.116	0.249	0.274
$Sa_{0.03s}$	0.054	0.380	0.384	0.056	0.289	0.294
$Sa_{0.04s}$	0.060	0.389	0.393	0.059	0.282	0.288
$Sa_{0.05s}$	0.063	0.364	0.370	0.064	0.295	0.302
$Sa_{0.06s}$	0.064	0.383	0.388	0.067	0.280	0.288
$Sa_{0.075s}$	0.061	0.358	0.363	0.069	0.308	0.316
$Sa_{0.09s}$	0.061	0.371	0.376	0.068	0.306	0.314
$Sa_{0.10s}$	0.062	0.367	0.372	0.066	0.304	0.311
$Sa_{0.15s}$	0.064	0.375	0.380	0.060	0.334	0.339
$Sa_{0.20s}$	0.064	0.383	0.388	0.061	0.381	0.386
$Sa_{0.30s}$	0.067	0.396	0.402	0.052	0.394	0.397
$Sa_{0.40s}$	0.070	0.400	0.406	0.047	0.401	0.404
$Sa_{0.50s}$	0.073	0.397	0.404	0.056	0.386	0.390
$Sa_{0.60s}$	0.082	0.403	0.411	0.058	0.333	0.338
$Sa_{0.70s}$	0.092	0.414	0.424	0.066	0.383	0.389
$Sa_{0.75s}$	0.094	0.404	0.415	0.071	0.322	0.330
$Sa_{0.80s}$	0.097	0.410	0.421	0.073	0.380	0.387
$Sa_{0.90s}$	0.100	0.409	0.421	0.078	0.385	0.393
$Sa_{1.00s}$	0.103	0.408	0.421	0.084	0.392	0.401
$Sa_{1.20s}$	0.112	0.408	0.423	0.097	0.394	0.406
$Sa_{1.50s}$	0.120	0.412	0.430	0.113	0.397	0.413
$Sa_{2.00s}$	0.135	0.417	0.438	0.141	0.356	0.382
$Sa_{2.50s}$	0.145	0.423	0.447	0.160	0.385	0.417
$Sa_{3.00s}$	0.154	0.430	0.457	0.178	0.363	0.404
$Sa_{4.00s}$	0.176	0.466	0.498	0.211	0.410	0.461

shown in Fig. 15. From the figure, it can be observed that the predicted spectral acceleration from the present model is comparing well with the pattern exhibited by the already existing relations. Now, it will be interesting to compare the spectral acceleration predictions from the developed model for Western-Himalayas and North-Eastern India with the existing relations. Sharma et al. (2009) developed ground motion prediction equation for spectral acceleration at 13 periods between 0.04 and 2.5 s. The results are arrived from combining together 58 records from Himalayas with 143 records From Zagros. Later, NDMA (2010) and Raghukanth and Kavitha (2014) developed GMPE for the geological regions in India using synthetic database generated using regional seismological model. However, the results are valid for only rock-type soil condition. Recently, Singh et al. (2017) developed GMPE for response spectra in Indo-Gangetic plain region based on only the records from 2015 Nepal earthquakes and its four aftershocks. The spectral acceleration predictions from these studies are compared with the respective predictions from the present study; the patterns are illustrated in Fig. 16. It should be noted that the comparison is done for rock level ground motion with V_{s30} 760 m/s considering the validity of the existing GMPEs. From the figure, it can be noted that the variable with magnitude for the GMPE by Sharma et al. (2009) is less and the pattern is also different from that exhibited by other GMPE. The limited information used in developing the model might have attributed to this observation. Further, the existing GMPEs from synthetic database are observed to over predict when compared to the prediction from the present model. The choice of the parameters in developing the synthetic database and the corresponding limitations in the prediction might have attributed to these differences observed for the regional ground motion predictions. It is also observed that the predictions from Singh et al. (2017) are also on the upper bound. The limited amount of data and the difference attributed from site conditions could be a possible reason for such a variation. In North-Eastern India,

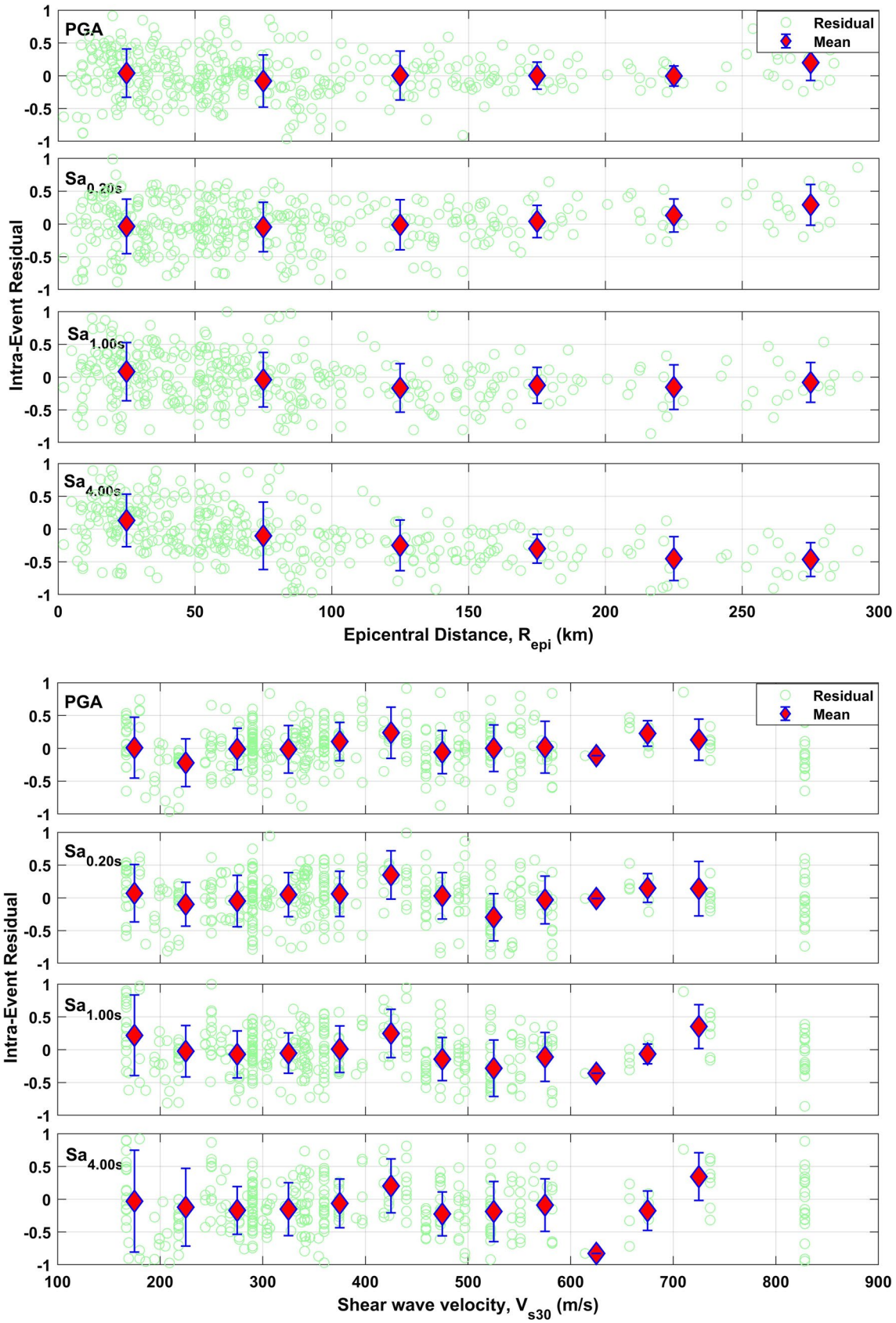

Fig. 9 Intra-event residual with respect to epicentral distance (R_{epi}) and shear wave velocity (V_{s30}) corresponding to PGA ($T = 0$ s), Sa at $T = 0.20$ s, 1.00 s and 4.00 s considering events at Western Himalayas

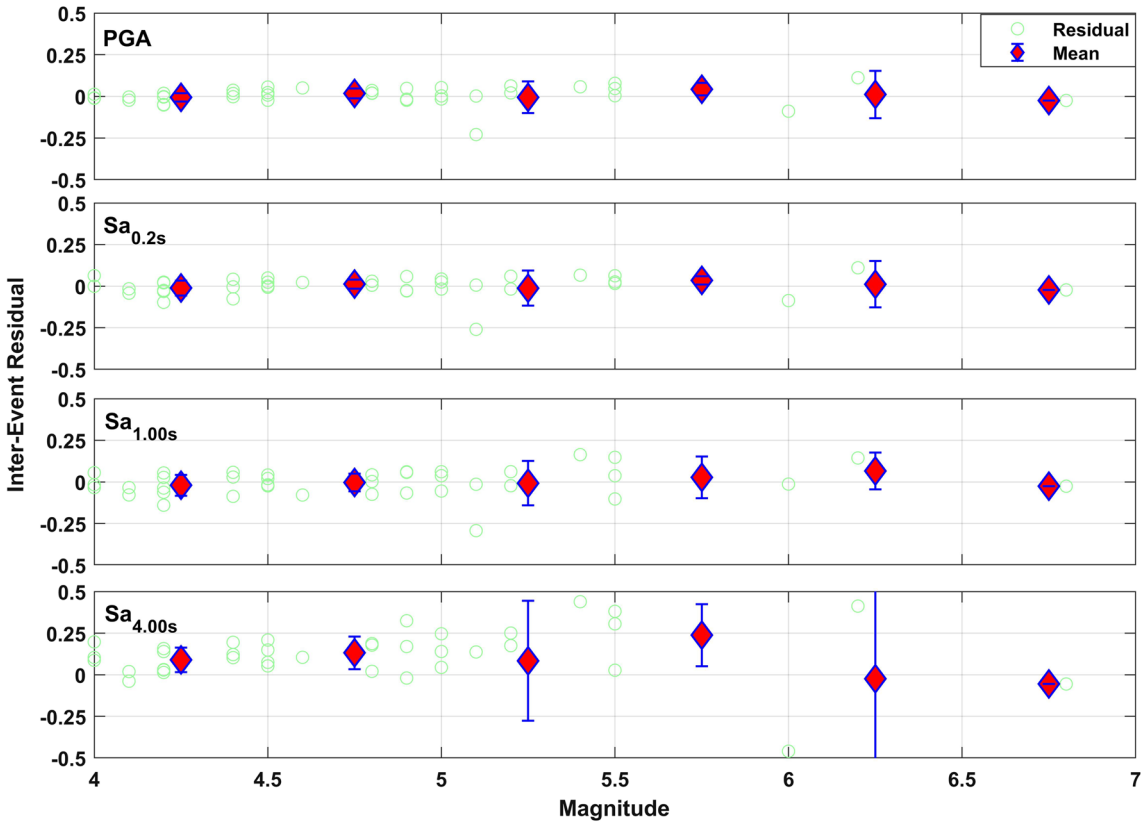

Fig. 10 Inter-event residual with respect to moment magnitude (M_w) corresponding to PGA ($T = 0$ s), Sa at $T = 0.20$ s, 1.00 s and 4.00 s considering events at North-Eastern India

predictions from Raghukanth and Kavitha (2014) are lower when compared to other relations because the particular GMPE considered deeper events from Indo-burmese arc region. It should however be noted that most of the GMPE for available for the region is based on synthetic database or by just using the available limited number of records. Whereas the model developed from this study understands the possible ground motion pattern from a comprehensive dataset and scales the same based on the recorded data information available for the region. Thus, the variance of error is nominal and the predictions are exhibiting all the known ground motion patterns. Now it will interesting to explore the application of the developed GMPE in hazard estimations as discussed further.

Application to hazard estimations

To demonstrate one of the widely used applications of GMPE, uniform hazard response spectra (UHRS) are obtained for two major cities. Here, first NGA West2 expressions are used in estimation of UHRS at Delhi (77.1025° E, 28.7041° N) and Guwahati (91.736° E, 26.145° N). Then, The Western Himalayas GMPE is used to estimate hazard for Delhi (77.1025° E, 28.7041° N) and North-Eastern India GMPE is used in the estimation of hazard for Guwahati (91.736° E, 26.145° N). The tectonic setting of Delhi, Guwahati and adjoining areas is illustrated in Fig. 17. The faults lines shown in the figure are identified from the seismotectonic atlas of India GSI (2000). The region is seismically very active with numerous thrust faults like Main Frontal Thrust (MFT), Main Central Thrust (MCT), Main Boundary Thrust (MBT), etc. passing through the region. It can be seen that the selected cities belong to the category of mega-cities, and hence, there are numerous constructional activities happening in the region. The proximity to the seismically active faults has attributed to the risk in the region. Hence, it is essential to determine the probable seismic hazard values for the region. The seismic hazard estimation procedure adopted in the study is that proposed by Cornell (1968) and modified by Kiureghian and Ang (1977) which is explained in detail by Kramer (1996). Accordingly, assuming that the earthquake follows a Poisson process, the probability

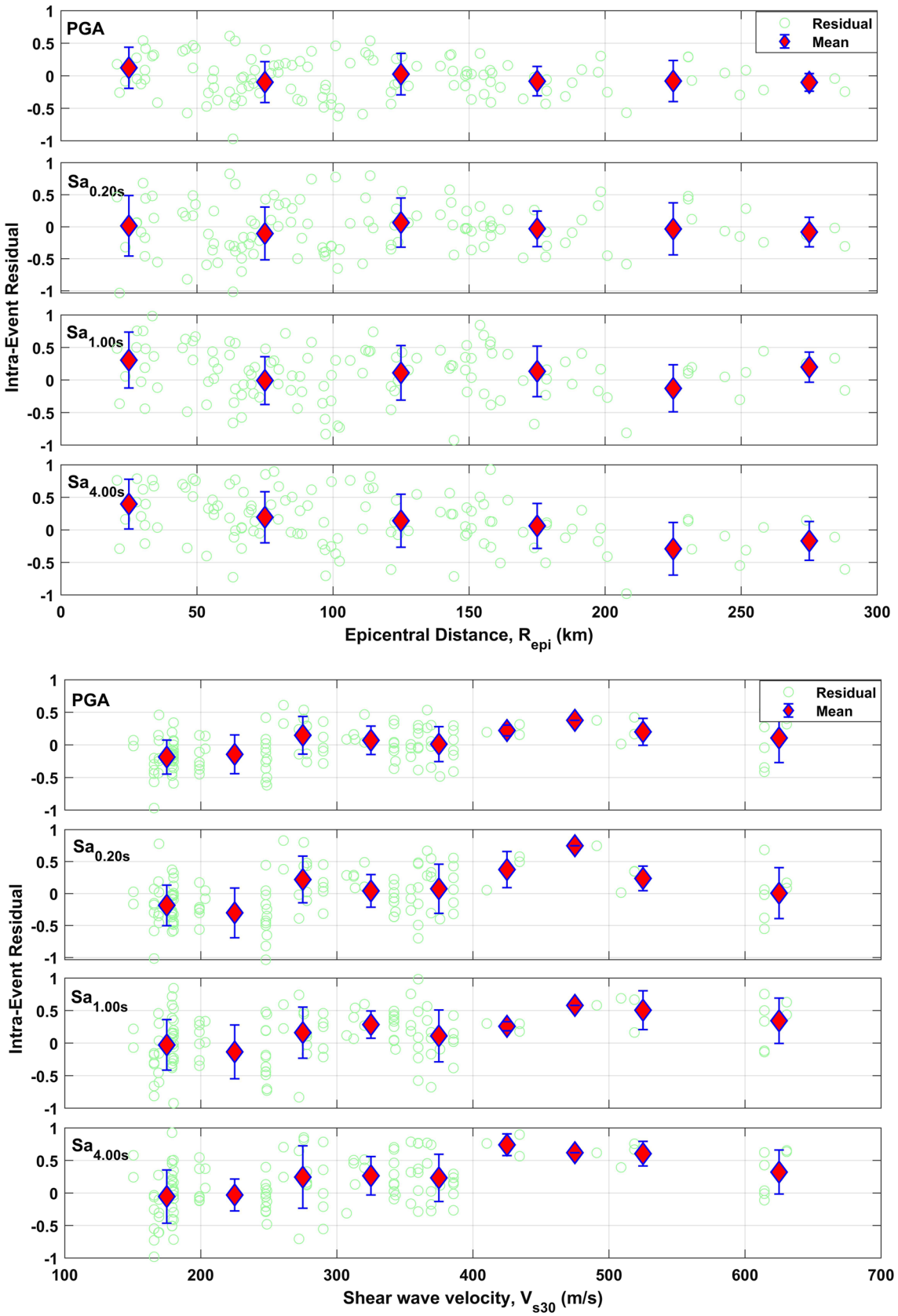

Fig. 11 Intra-event residual with respect to epicentral distance (R_{epi}) and shear wave velocity (V_{s30}) corresponding to PGA ($T = 0$ s), Sa at $T = 0.20$ s, 1.00 s and 4.00 s considering events at North-Eastern India

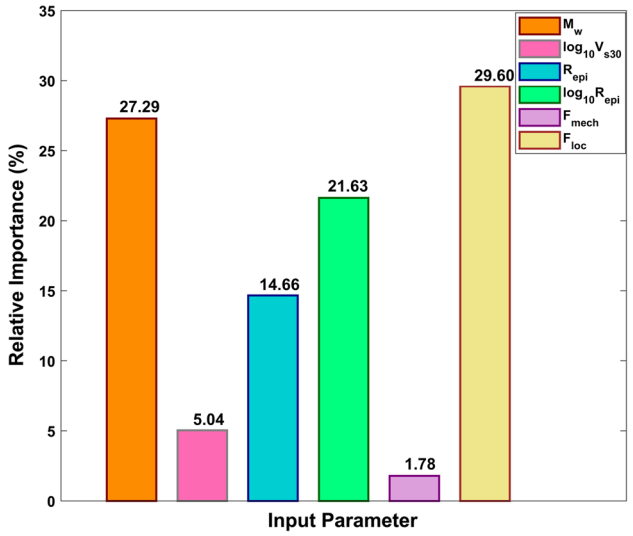

Fig. 12 Sensitivity of the input parameters of the developed ANN model towards output based on Garson's algorithm

that the control variable Y exceeds level y^*, in a time window of T years is given by

$$P(Y > y^* \text{ in } T \text{ years}) = 1 - \exp(-\mu_{y^*} T). \tag{8}$$

The rate of exceedance, μ_{y^*} is computed from the expression

$$\mu_{y^*} = \sum_{i=1}^{K} N_i(m_0) \int_m \int_r P(Y > y^*|m, r) P_{R|m}(r|m) P_M(m)\, \partial r\, \partial m \tag{9}$$

Here, K is indicates the in the region, $P_M(m)$ and $P_{R|m}(r|m))$ are the probability density functions (pdf) of magnitude and distance, respectively, $P(Y > y^*|m, r)$ is the conditional probability of exceedance of the ground motion parameter Y. $P(Y > y^*|m, r)$ is taken as a log-normal random variable, conditioned on particular values of m and r, with mean value provided by the GMPE. The reciprocal of the annual probability of exceedance gives the return period for the corresponding variable. The mean annual rate of exceedance of y^* is obtained by summing over the individual probabilities from each fault line. The procedure is repeated for various ground motion values y^* to obtain the seismic hazard curves. These hazard curves are first obtained individually for all the faults located in the region and then combined to estimate the aggregated hazard at the site. The uniform hazard response spectra (UHRS) are the spectra having the same mean recurrence interval (return period) at all frequencies.

In the present study, this method is adopted to determine the UHRS for Delhi and Guwahati. The recurrence parameter of each fault line is taken as per that reported by Muthuganeisan (2017). GMPEs for the respective regions are used in hazard estimations. Further, from Satyam and Rao (2010) and Kumar et al. (2018), the site conditions in Delhi and Guwahati are heterogeneous with varied soil conditions ranging from B to D type soil classes. Moreover, to have an understanding on how the hazard values from ANN-based methodology compare with the existing relations, first UHRS are obtained for both the sites using the NGA West2 relations available in the literature (Abrahamson et al. 2014; Boore et al. 2014; Campbell and Bozorgnia 2014; Chiou and Youngs 2014; Dhanya and Raghukanth 2018) and that from the present study with regional flag $F_{loc} = 1$ corresponding to C Type soil class($V_{s30} = 560$ m/s). Figure 18 (top layer) illustrates the corresponding UHRS for 2500 years return period (2% probability in 50 years). It can be seen that the UHRS from the present model is well in range with that obtained using the existing relations. Furthermore, hazard values for Guwahati are observed to be slightly higher than that obtained for delhi owing to the corresponding recurrence characteristics. Now, it will be intering to see how the hazard values look when regional GMPEs are used for the respective sites. Here, hazard estimations are obtained corresponding to B ($V_{s30} = 1130$ m/s) , C ($V_{s30} = 560$ m/s) and D ($V_{s30} = 270$ m/s) type soil class for the cities considering the material property variations reported in the literature. It should be noted that the other GMPEs available at the regional level are not considered here as they are mostly valid for rock-type soil class and were also showing considerable variabilities (Fig. 16). The UHRS corresponding to 2500 years return period, obtained for Delhi and Guwahati using respective regional level GMPEs developed from present work and performing hazard analysis are shown in Fig. 18 (bottom layer). It can be noted that the regional level estimates are different from that obtained by using NGA-West2 relations. Furthermore, the hazard values of Delhi are observed to be less than that for Guwahati. Additionally, the UHRS showed visible variations and period shift with soil type at each location. This exercise thus demonstrated the applicability of the developed GMPE in hazard estimations for sites in the region.

Summary and conclusion

The present works develop a hybrid ANN model for region with sparse recorded data like Western-Himalayas and North-Eastern India. The methodology adopted is to develop a network combining the dataset of a region with comprehensive database with those having sparse data segregated by flags.

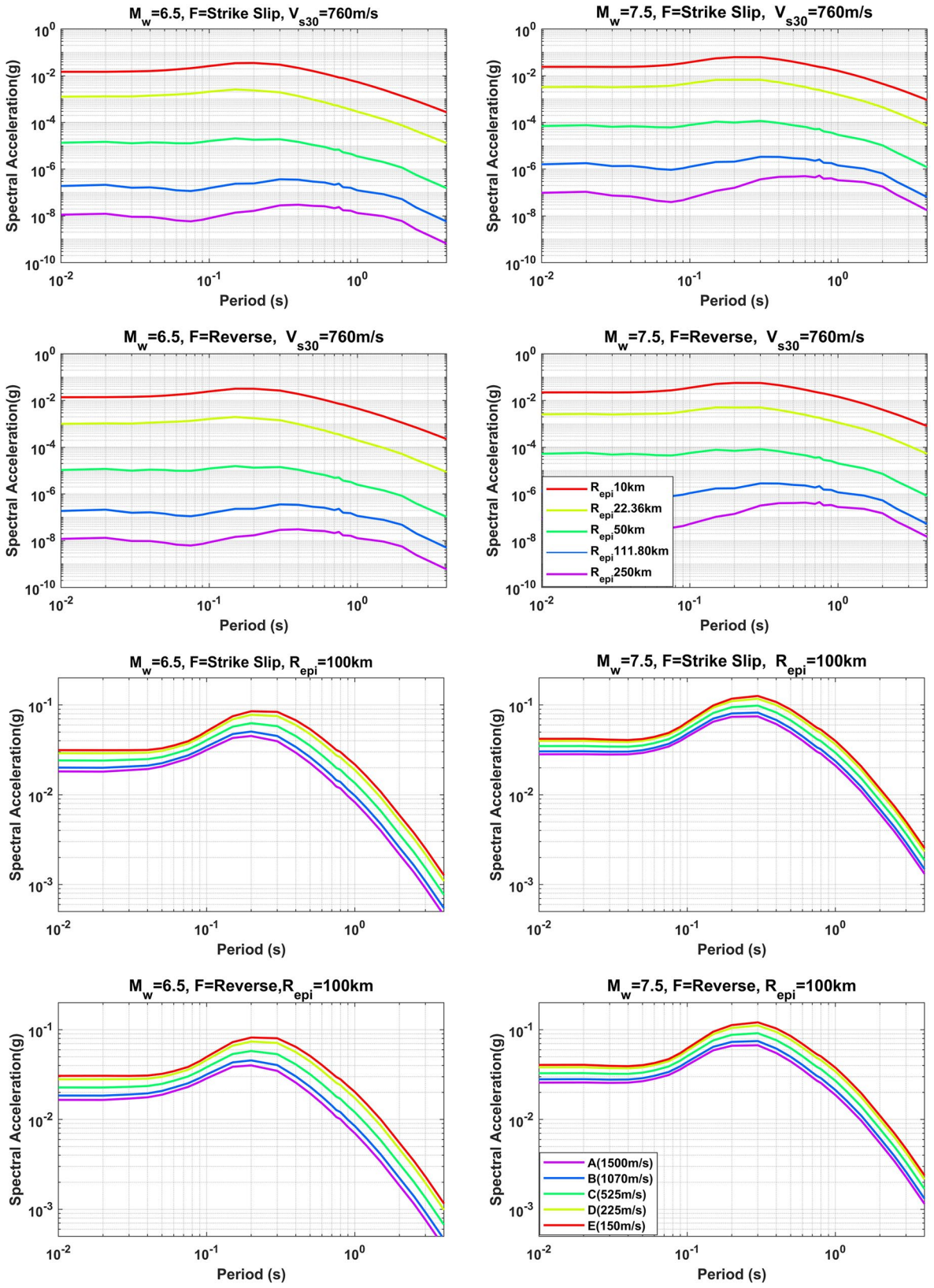

Fig. 13 Variation of spectral acceleration (top) with respect to epicentral distance (R_{epi}) (bottom) with respect to shear wave velocity (V_{s30}) corresponding to GMPE developed for Western Himalayas

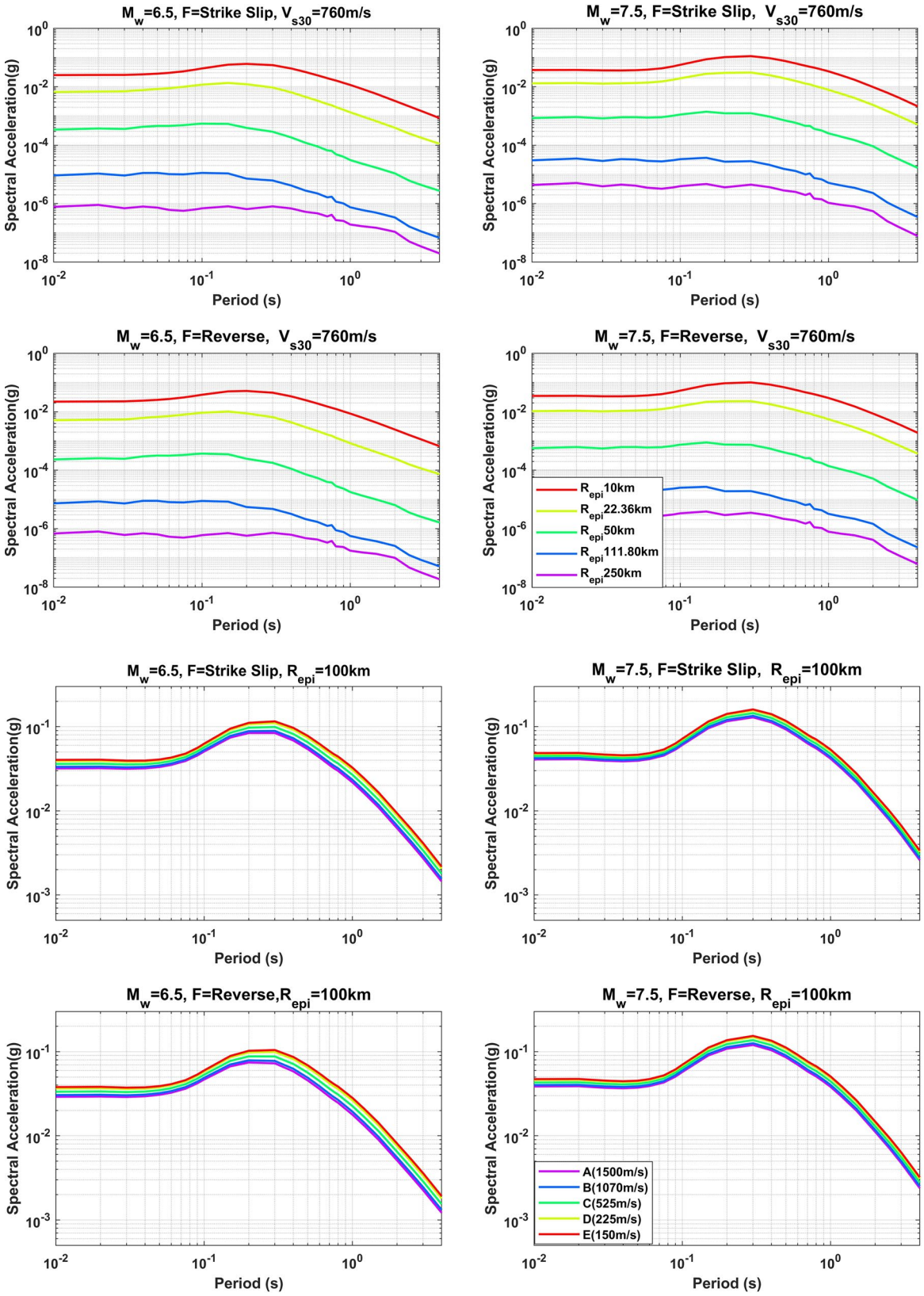

Fig. 14 Variation of spectral acceleration (top) with respect to epicentral distance (R_{epi}) (bottom) with respect to Shear wave velocity (V_{s30}) corresponding to GMPE developed for North-Eastern India

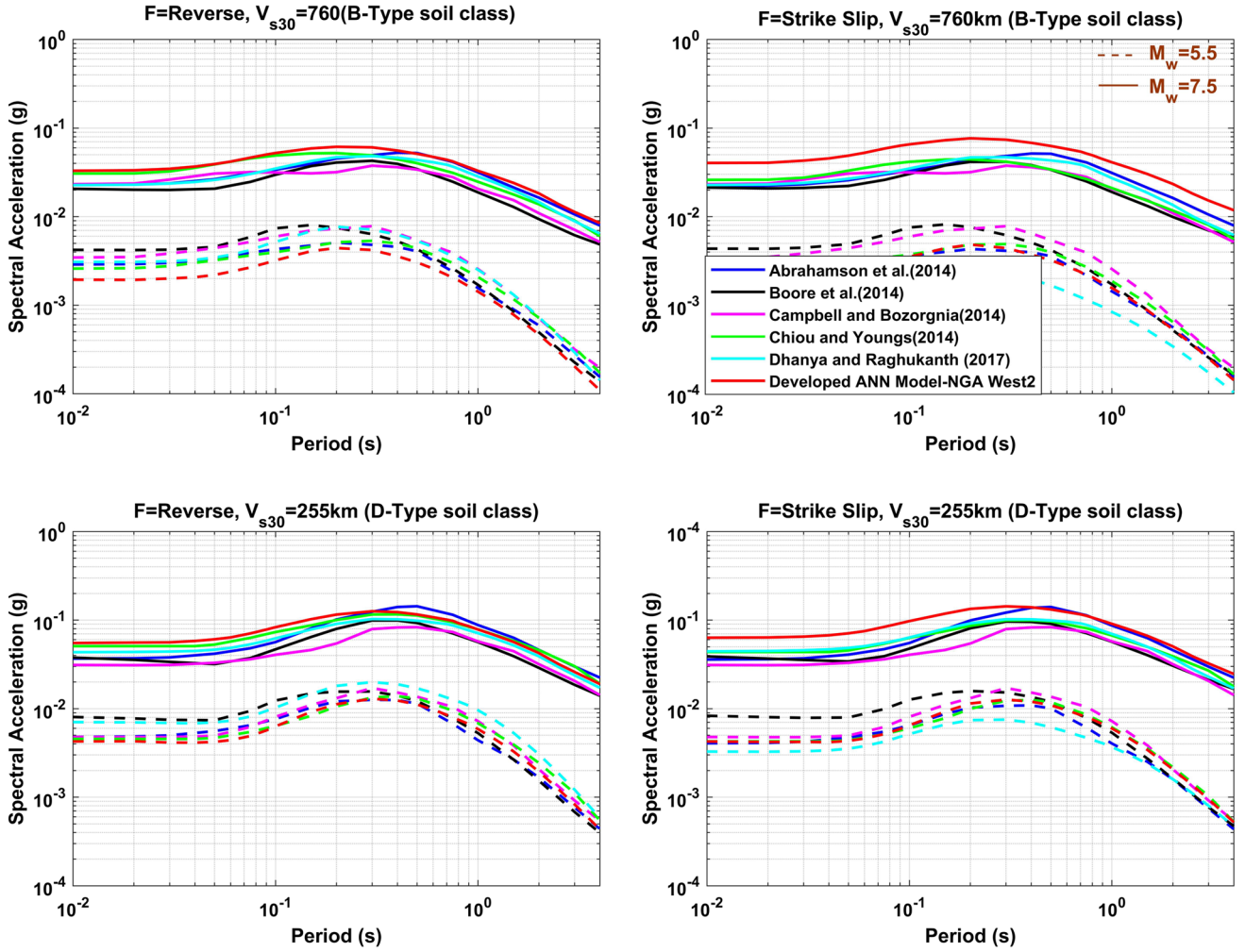

Fig. 15 Comparison of the spectral acceleration from developed ANN model for NGA West2 (F_{loc} = 1) with the other GMPEs developed from NGA-West2 database at R_{epi} = 150km

The ANN model developed for the study is shown in Fig. 4, and the corresponding weights are summarized in Tables 1 and 2. The inter-event and intra-event variability is estimated for the model for complete database as well as for the regional level records (Figs. 6, 7, 8, 9, 10, 11). The developed model is observed to be unbiased, and the variance is also less compared to the existing relations. Furthermore, performance analysis of the developed GMPE showed that the model is able to capture all known ground motion features (Figs. 13, 14). Furthermore, the model is also compared with the existing GMPE for the region (Fig. 16) and noted that the GMPEs developed from synthetic database show variable pattern compared to the present model. The application of the developed regional GMPE is demonstrated by estimating uniform hazard response spectra for Delhi and Guwahati (Fig. 18). The study thus shows that the GMPE for regions with sparse data can be suitably developed by combining the data with a more comprehensive database and implementing them in an efficient machine learning algorithm. It should however be noted that even though the network learns the predominant pattern from the whole data, the regional level scaling is performed based on the characteristics of the available records. Thus, the developed model utilizes the amplitudes of the recorded data in estimating the regional GMPE. Similar studies can be done for other regions lacking a comprehensive database.

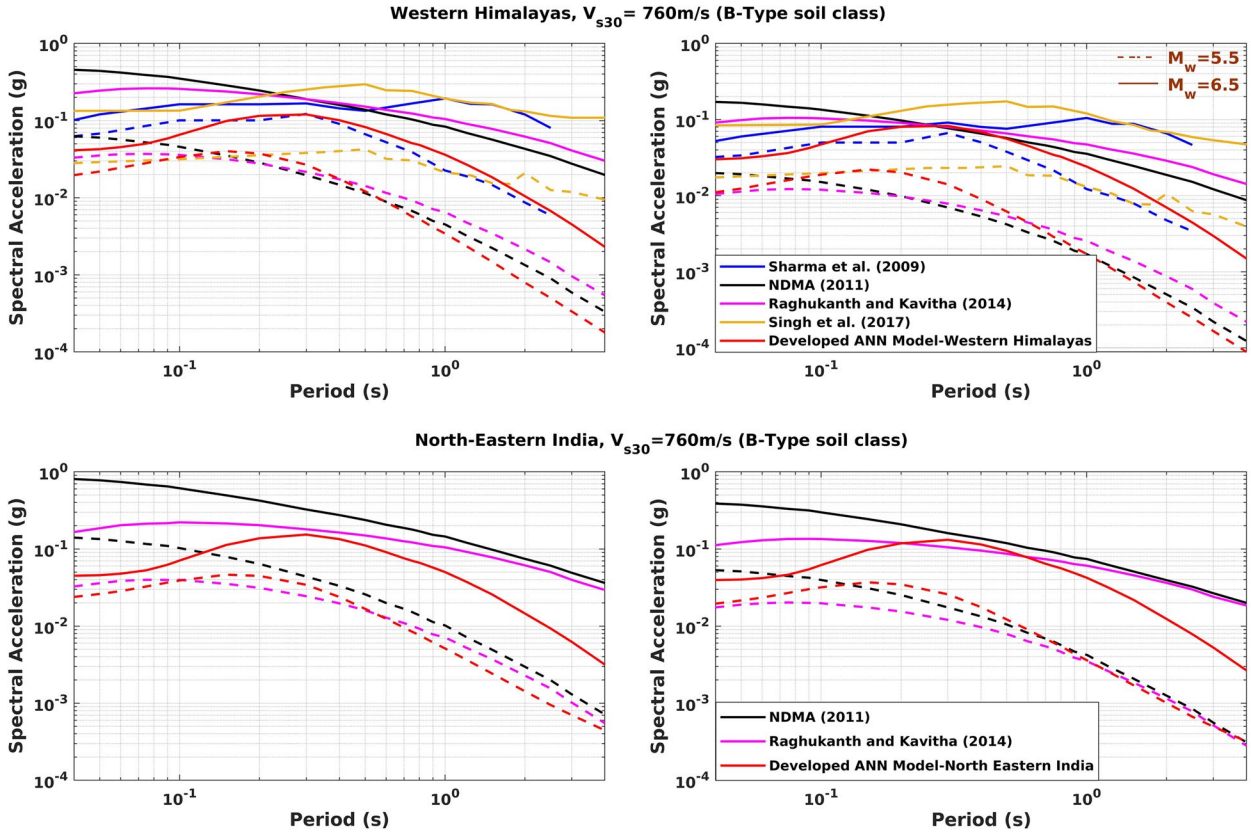

Fig. 16 Comparison of the spectral acceleration from developed ANN model for Western Himalayas ($F_{loc} = 2$) and North-Eastern India ($F_{loc} = 3$) with the other GMPEs developed for the region (rock site, reverse mechanism, $V_{s30} = 760$ m/s)

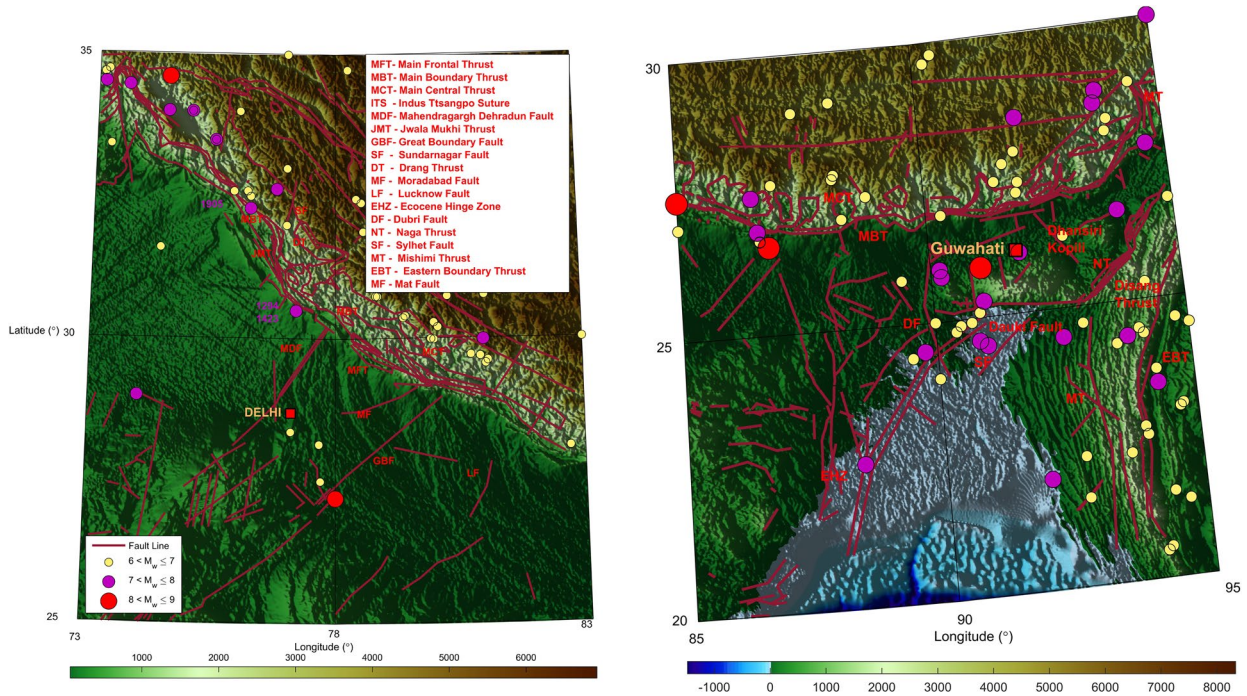

Fig. 17 Tectonic and Seismicity characteristics in (left) Delhi and adjoined regions (right) Guwahati and adjoined regions

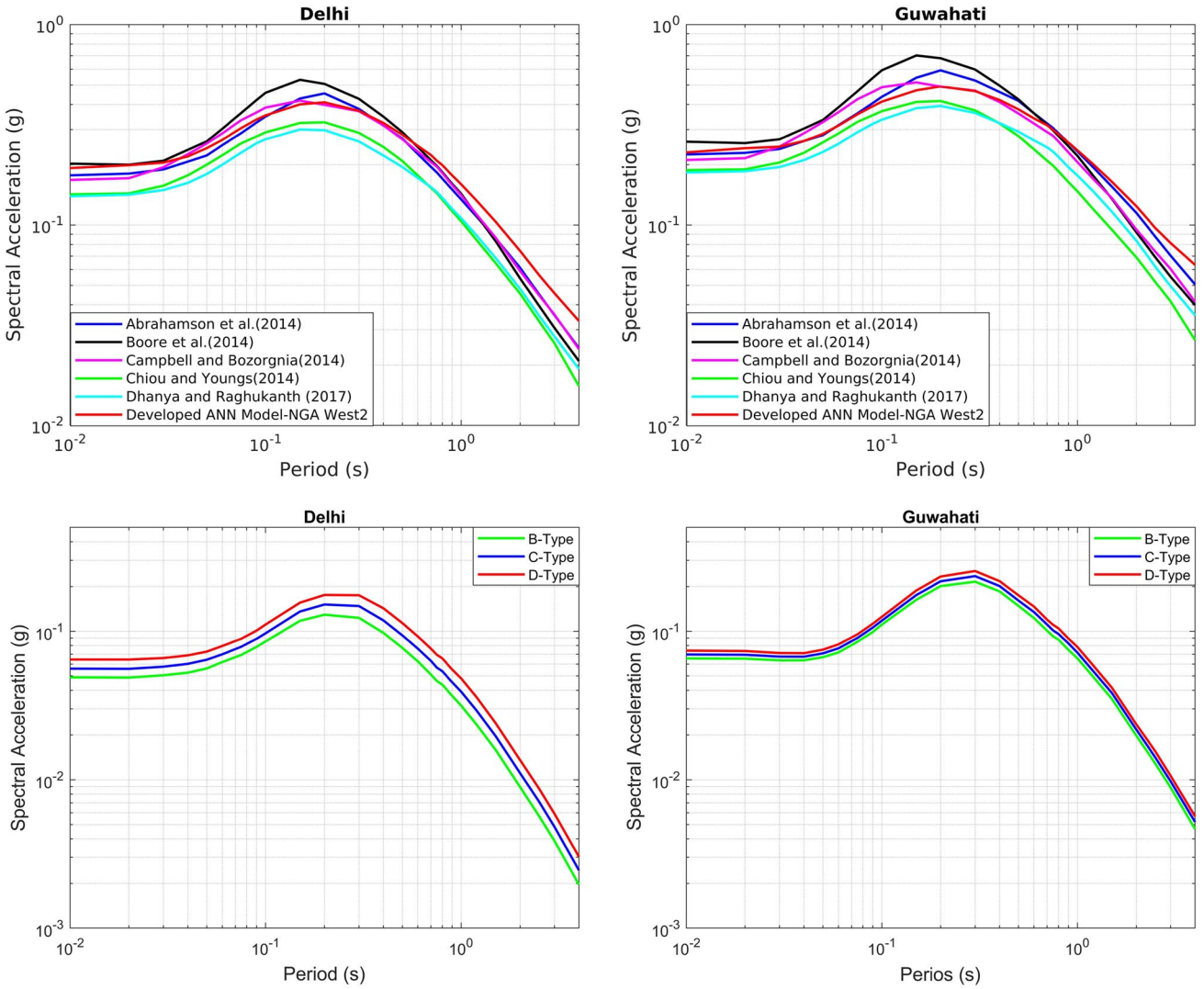

Fig. 18 Uniform hazard response spectra corresponding to 2500 years return period: [top left] Delhi using developed NGA-West2 relation along with other relations existing in the literature corresponding to C-Type soil class [top left] Guwahati using developed NGA-West2 relation along with other relations existing in the literature corresponding to C-Type soil class [bottom left] Delhi using GMPE model developed for Western Himalayas corresponding to varied soil conditions and [bottom right] Guwahati using GMPE model developed for North-Eastern India corresponding to varied soil conditions

Acknowledgements I would like to acknowledge Dr. D. Srinagesh, Chief Scientist, National Geophysical Research Institute, (NGRI), Hyderabad, for providing the data of 2015 Nepal Earthquake recorded by CIGN network. This research has been supported by National Disaster Management Authority (NDMA) for the development of "Probabilistic seismic hazard map of India" under project no:RB1920CE465NDMA008344.

Compliances with ethical standard

Conflict of interest The authors declare that they have no conflict of interest.

References

Abrahamson NA, Youngs R (1992) A stable algorithm for regression analyses using the random effects model. B Seismol Soc Am 82(1):505–510

Abrahamson NA, Silva WJ, Kamai R (2014) Summary of the ASK14 ground motion relation for active crustal regions. Earthq Spectra 30(3):1025–1055

Berry M, Linoff G (1997) Data mining techniques: for marketing, sales and marketing support. Wiley, Hoboken

Boore DM, Stewart JP, Seyhan E, Atkinson GM (2014) NGA-West2 equations for predicting PGA, PGV, and 5% damped PSA for shallow crustal earthquakes. Earthq Spectra 30(3):1057–1085

Campbell KW (2003) Prediction of strong ground motion using the hybrid empirical method and its use in the development of ground-motion (attenuation) relations in eastern north america. B Seismol Soc Am 93(3):1012–1033

Campbell KW, Bozorgnia Y (2014) NGA-West2 ground motion model for the average horizontal components of PGA, PGV, and 5% damped linear acceleration response spectra. Earthq Spectra 30(3):1087–1115

Chadha R, Srinagesh D, Srinivas D, Suresh G, Sateesh A, Singh S, Pérez-Campos X, Suresh G, Koketsu K, Masuda T et al (2015) CIGN, a strong-motion seismic network in central indo-gangetic plains, foothills of himalayas: first results. Seismol Res Lett 87(1):37–46

Chiou BSJ, Youngs RR (2014) Update of the chiou and youngs nga model for the average horizontal component of peak ground motion and response spectra. Earthq Spectra 30(3):1117–1153

Cornell CA (1968) Engineering seismic risk analysis. B Seismol Soc Am 58(5):1583–1606

Derras B, Bard PY, Cotton F (2014) Towards fully data driven ground-motion prediction models for europe. B Earthq Eng 12(1):495–516

Dhanya J, Raghukanth STG (2018) Ground motion prediction model using artificial neural network. Pure Appl Geophys 175(3):1035–1064

Douglas J (2018) Ground motion prediction equations 1964–2018. University of Strathclyde, Glasgow

Garson GD (1991) Interpreting neural-network connection weights. AI Expert 6(4):46–51

GSI (2000) Seismotectonic atlas of India and its environs. Geological Survey of India

Gupta I (2018) Uniformly processed strong motion database for himalaya and northeast region of india. Pure Appl Geophys 175(3):829–863

IBC I (2015) International building code. International Code Council, Inc (formerly BOCA, ICBO and SBCCI)

Iyengar R, Raghukanth STG (2004) Attenuation of strong ground motion in Peninsular India. Seismol Res Lett 75(4):530–540

Kiureghian AD, Ang AH (1977) A fault-rupture model for seismic risk analysis. B Seismol Soc Am 67(4):1173–1194

Kramer SL (1996) Geotechnical earthquake engineering. In: Hall WJ (ed) Prentice-hall international series in civil engineering and engineering mechanics. Prentice-Hall, Upper Saddle River

Kumar A, Harinarayan N, Verma V, Anand S, Borah U, Bania M (2018) Seismic site classification and empirical correlation between standard penetration test n value and shear wave velocity for guwahati based on thorough subsoil investigation data. Pure Appl Geophys 175(8):2721–2738

Muthuganeisan P (2017) Development of seismic displacement and velocity hazard maps of India. Ph.D. thesis, Indian Institute of Technology Madras

NDMA (2010) Development of probabilistic seismic hazard map of India. The National Disater Management Authority, p 86

Pezeshk S, Zandieh A, Tavakoli B (2011) Hybrid empirical ground-motion prediction equations for eastern north america using nga models and updated seismological parameters. B Seismol Soc Am 101(4):1859–1870

Raghucharan M, Somala SN (2017) Simulation of strong ground motion for the 25 April 2015 Nepal (Gorkha) Mw 7.8 earthquake using the SCEC broadband platform. J Seismol 21(4):777–808

Raghukanth STG, Kavitha B (2014) Ground motion relations for active regions in india. Pure Appl Geophys 171(9):2241–2275

Satyam DN, Rao K (2010) Multi channel analysis of surface wave (MASW) testing for dynamic site characterization of Delhi region. In: Fifth international conference on recent advances on geotechnical earthquake engineering and soil dynamics and symposium in honor of Professor I. M. Idriss. 24–29 May 2010, San Diago, CA

Sharma ML, Douglas J, Bungum H, Kotadia J (2009) Ground-motion prediction equations based on data from the Himalayan and Zagros regions. J Earthq Eng 13(8):1191–1210

Singh S, Srinagesh D, Srinivas D, Arroyo D, Pérez-Campos X, Chadha R, Suresh G, Suresh G (2017) Strong ground motion in the indo-gangetic plains during the 2015 Gorkha, Nepal, earthquake sequence and its prediction during future earthquakes. B Seismol Soc Am 107(3):1293–1306

Tavakoli B, Pezeshk S (2005) Empirical-stochastic ground-motion prediction for eastern North America. B Seismol Soc Am 95(6):2283–2296

Acta Geophysica (2020) 68:325–336
https://doi.org/10.1007/s11600-019-00396-x

RESEARCH ARTICLE - SOLID EARTH SCIENCES

A comparative study of empirical and ensemble machine learning algorithms in predicting air over-pressure in open-pit coal mine

Hoang Nguyen[1,2] · Xuan-Nam Bui[1,2] · Quang-Hieu Tran[1] · Pham Van Hoa[1] · Dinh-An Nguyen[1] · Le Thi Thu Hoa[1] · Qui-Thao Le[1,2] · Ngoc-Hoan Do[1,3] · Tran Dinh Bao[1] · Hoang-Bac Bui[4,5] · Hossein Moayedi[6,7]

Received: 9 April 2019 / Accepted: 26 December 2019 / Published online: 30 January 2020

Abstract

This study aims to take into account the feasibility of three ensemble machine learning algorithms for predicting blast-induced air over-pressure (AOp) in open-pit mine, including gradient boosting machine (GBM), random forest (RF), and Cubist. An empirical technique was also applied to predict AOp and compared with those of the ensemble models. To employ this study, 146 events of blast were investigated with 80% of the total database (approximately 118 blasting events) being used for developing the models, whereas the rest (20% ~ 28 blasts) were used to validate the models' accuracy. RMSE, MAE, and R^2 were used as performance indices for evaluating the reliability of the models. The findings revealed that the ensemble models yielded more precise accuracy than those of the empirical model. Of the ensemble models, the Cubist model provided better performance than those of RF and GBM models with RMSE, MAE, and R^2 of 2.483, 0.976, and 0.956, respectively, whereas the RF and GBM models provided poorer accuracy with an RMSE of 2.579, 2.721; R^2 of 0.953, 0.950, and MAE of 1.103, 1.498, respectively. In contrast, the empirical model was interpreted as the poorest model with an RMSE of 4.448, R^2 of 0.872, and MAE of 3.719. In addition, other findings indicated that explosive charge capacity, spacing, stemming, monitoring distance, and air humidity were the most important inputs for the AOp predictive models using artificial intelligence.

Keywords Air over-pressure · Open-pit mine · Ensemble algorithm · Random forest · Gradient boosting machine · Cubist

Introduction

One of the most effective techniques for fragmenting rock in open-pit mines is blasting because of its advantages from technical and economical points of view. It can generate a large amount of rock for the subsequent operations (e.g., loading, transporting) with low cost (Jhanwar et al. 1999). However, its ill side influences are not negligible, including air over-pressure (AOp), flyrock, ground vibration, dust, and fumes (Nguyen et al. 2018; Zhang et al. 2019; Shang et al. 2019) (Fig. 1). Of those, AOp is considered as a dangerous phenomenon, which is needed to control (Alel et al. 2018; Armaghani et al. 2015; Khandelwal and Kankar 2011;

✉ Xuan-Nam Bui
buixuannam@humg.edu.vn

[1] Department of Surface Mining, Hanoi University of Mining and Geology, 18 Vien St., Duc Thang ward, Bac Tu Liem Dist., Hanoi, Vietnam

[2] Center for Mining, Electro-Mechanical Research, Hanoi University of Mining and Geology, 18 Vien St., Duc Thang Ward, Bac Tu Liem Dist., Hanoi, Vietnam

[3] Faculty of Mining, Saint-Petersburg Mining University, Saint Petersburg, Russia

[4] Faculty of Geosciences and Geoengineering, Hanoi University of Mining and Geology, 18 Vien St., Duc Thang ward, Bac Tu Liem Dist., Hanoi, Vietnam

[5] Center for Excellence in Analysis and Experiment, Hanoi University of Mining and Geology, 18 Vien St., Duc Thang ward, Bac Tu Liem Dist., Hanoi, Vietnam

[6] Department for Management of Science and Technology Development, Ton Duc Thang University, Ho Chi Minh City, Vietnam

[7] Faculty of Civil Engineering, Ton Duc Thang University, Ho Chi Minh City, Vietnam

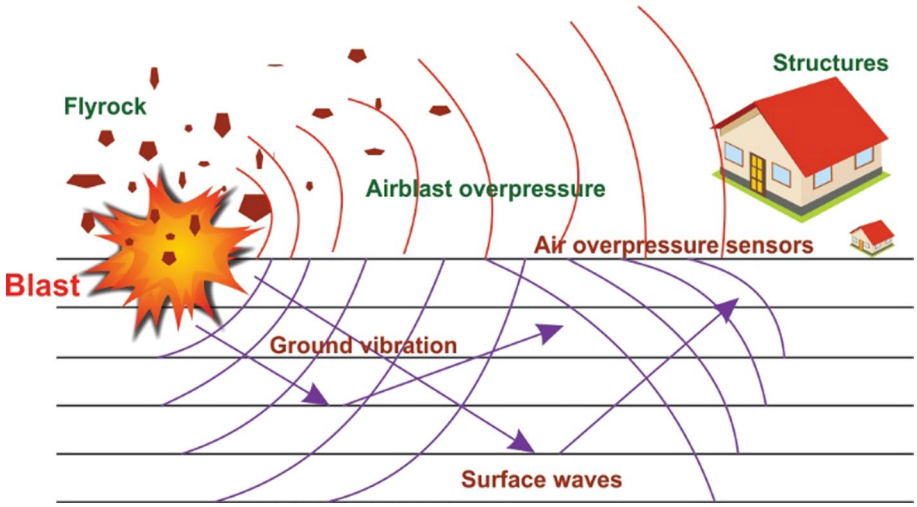

Fig. 1 Illustration of the undesirable effects of blasting operations

Table 1 Several empirical equations for predicting blast-induced AOp

No.	References	Empirical model
1	Siskind et al. (1980)	$\mathrm{AOp} = k(\mathrm{SD})^{-\beta}$
2	Loder (1985)	$\mathrm{AOp} = \frac{140\sqrt[3]{\frac{W}{200}}}{D}$
3	McKenzie (1990)	$\mathrm{AOp} = 165 - 24\log\left(R/D^{1/3}\right)$

k and β are the coefficients of the study site; SD denotes the scaled distance (m $\mathrm{kg}^{0.33}$)

Khandelwal and Singh 2005; Nguyen and Bui 2018; Nguyen et al. 2017, 2018).

For predicting blast-induced AOp, several scholars proposed empirical equations, as listed in Table 1. Accordingly, the relationship between monitoring distance (D) and explosive charge per delay/maximum explosive charge capacity (W) was established through empirical equations.

Of the empirical equations in Table 1, the equation No.1 (USBM empirical equation) has been widely used to predict blast-induced AOp (Siskind et al. 1980; Hustrulid 1999; Walter 1990; Kuzu et al. 2009; Hasanipanah et al. 2016; Mahdiyar et al. 2018). However, the accuracy of empirical models was often not high due to some drawbacks of them, as discussed by Hasanipanah et al. (Hasanipanah et al. 2016), Mahdiyar et al. (Mahdiyar et al. 2018).

Recently, artificial intelligence (AI) became more appropriate and highly used in different fields, especially mining technology (Pierini et al. 2013; Rahmani and Farnood Ahmadi 2018; Montahaei and Oskooi 2014; Wiszniowski 2016; Naganna and Deka 2019; Piasecki et al. 2018; Nguyen et al. 2019a, b, c, d; Zhou et al. 2019; Asteris et al. 2016; Asteris and Nikoo 2019). In order to estimate blast-induced AOp, Hajihassani et al. (Hajihassani et al. 2014) trained an artificial neural network (ANN) by an evolutionary algorithm (Particle Swarm Optimization—PSO), namely ANN-based PSO model, using 62 AOp datasets. Their results showed that the ANN-based PSO model performed properly in forecasting blast-caused AOp with the correlation coefficient (CC) of 0.94. In another study, Mohamad et al. (Mohamad et al. 2016) predicted blast-induced AOp by an ANN-based genetic algorithm (GA), abbreviated as GA-ANN, using 76 blasting events. Empirical and ANN models were also provided to predict AOp and compared them to those of the GA-ANN model. Their results interpreted that the GA-ANN model performed better than those of empirical and ANN models. Hasanipanah et al. (2016) used ANFIS, ANN, fuzzy system (FS) techniques, and an empirical equation for estimating blast-induced AOp. For developing these models, a group of 77 blasting events was used in their study. Their findings revealed that the ANFIS system was the most superior approach in forecasting AOp. Amiri et al. (2016) also introduced a new combination of k-nearest neighbors (KNN) and ANN models to predict AOp using 75 blasting events. Their results indicated that the KNN-ANN model predicted better than those of ANN and empirical models. Mahdiyar et al. (2018) also proposed three AI models to estimate AOp based on PSO algorithm and 80 blasting events. The results indicated that the PSO model estimated AOp very well with a promising result. Nguyen et al. (2019) also discovered a hybrid model based on clustering technique and backpropagation neural networks. In another study, Nguyen et al. (2018) performed a comparative study of MLP neural nets, BRNN, and HYFIS in estimating AOp. Their results showed that the MLP neural nets were the most superior model than those of the other models. They also developed another AI model based on ensemble of ANN and RF (i.e., ANNs-RF) for predicting AOp with an excellent result (Nguyen and Bui 2018). By the use of optimization algorithm, AminShokravi et al. (2018) demonstrated the potential of the PSO algorithm in predicting AOp with high accuracy. Bui et al. (2019) also evaluated the

performance of different AI techniques for estimating AOp in an open-pit coal mine, including RF, boosted regression trees, KNN, SVR, GP (Gaussian process), BART (Bayesian additive regression trees), and ANN. They claimed the feasibility of the mentioned AI techniques. ANN model was recommended as the best model in their study for estimating AOp. Zhou et al. (2019) also developed a novel AI model for forecasting AOp based on FS and firefly algorithm (FA), namely FS-FA model. A high prediction level was confirmed in their study for the proposed FS-FA model. Gao et al. (2019) also took into account the performance of the GA and group method of data handling (GMDH) for forecasting AOp. Eventually, their GA-GMDH model was proposed as a robust technique with an excellent agreement.

A review of the literature shows that blast-induced AOp predictive models were developed and proposed quite well. Nevertheless, they cannot apply and represent other locations/regions, whereas the effects of blast-induced AOp are different from country to country. In this study, blast-induced AOp was assessed and predicted by three ensemble machine learning algorithms, including RF, GBM (gradient boosting machine), and Cubist. An empirical model was also developed to predict and compare with those of ensemble models herein.

The rest of the present work is arranged as follows: "Study area and data used" section presents the study site and characteristics of the dataset; "Methods" section provides the principle of the approaches used; the preparation of the dataset is introduced in "Preparing the dataset" section; the development of the models is shown in "Establishing the AOp predictive models" section; some performance indices are presented in "Performance indices" section; and "Results and discussion" section reports the results and discussion. Finally, "Conclusions and remarks" section presents our conclusions of this work.

Study area and data used

Study area

Herein, the Deo Nai open-pit coal mine, which is located in Quang Ninh Province, Vietnam, was selected as a special study area. It lies within latitudes 21°001′00″N and 21°020′00″N and between longitudes 107°018′15″E and 107°019′20″E (Fig. 2). The coal store is 42.5 Mt, and production capacity is 2.5 Mt/year; overburden is 20–30 Mt/year. (Vinacomin 2015). With a large amount of overburden per year and the hardness of rock being high (from 10 to 14 according to Protodiakonov's classification (Bach et al. 2012)), blasting was selected as a proper technique for fragmenting rock in the mine. ANFO is the main explosive used in this mine, with the amount being up to 20 tons. The non-electric delay blasting method was applied to fragment rock with the diameter of borehole of 105 mm. The nearest distance from blasts to the residential area is about 400–500 m. Hence, the ill side effects of blasts are substantial.

Data collection and its characteristics

In this study, 146 events of blasting were investigated, with ten parameters being measured. Of the ten parameters, nine first variables were used as the inputs to predict the outcome of AOp, including powder factor (q), maximum explosive charge capacity (W), burden (B), length of stemming (T), spacing (S), number of rows per blast (N),

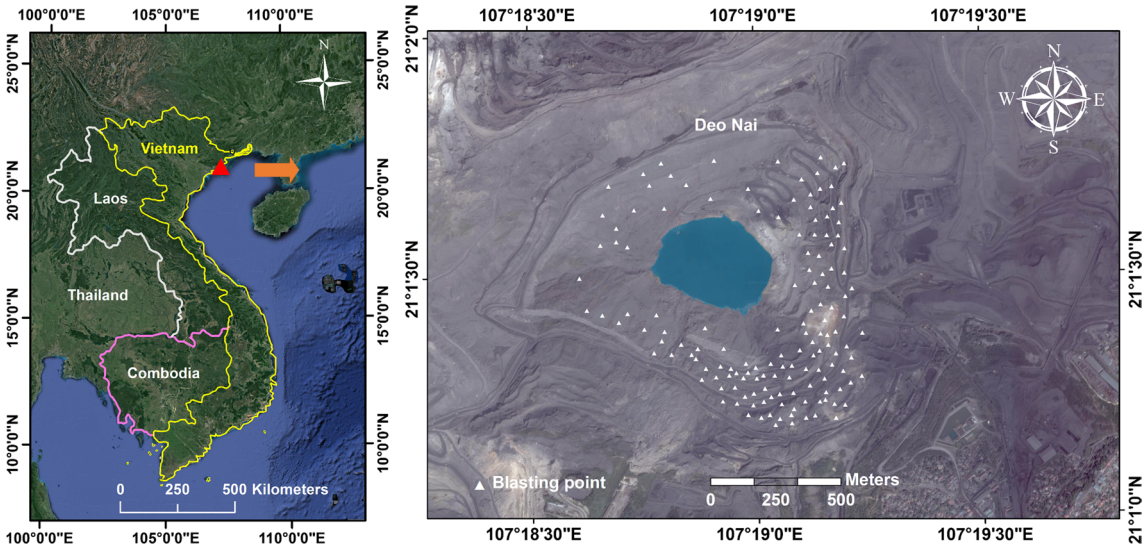

Fig. 2 Location of the study site

monitoring distance (D), bench height (H), and air humidity (RH) (Fig. 3). For monitoring blast-induced AOp, an instrument of Instantel (Canada) was utilized with a microphone. According to the guideline of the producer, the microphone should be placed at the sensitive locations and straightforward with the direction of blasts (Fig. 4). Also, a handheld GPS was used to define D. RH was measured by Kanomax 2212 air quality meter (Japan). It is one of the most influential parameters for estimating AOp, which was recommended by Nguyen et al. (2018). The remaining inputs were extracted from the design of blasts. Table 2 shows the characteristics of inputs and output in this work.

Methods

Empirical

Empirical is one of the methods which is utilized to predict blast-produced AOp in open-cast mine. Of the empirical methods (as shown in Table 1), USBM empirical formula was widely applied to predict AOp in open-pit mines (Hajihassani et al. 2014; Armaghani et al. 2016). For example, Kuzu et al. (2009) used the empirical equation of the USBM to forecast AOp with a promising result. In the USBM equation, the scaled distance was illustrated through W and D as follows:

$$SD = DW^{-0.33} \tag{1}$$

Subsequently, the USBM empirical equation can be computed according to Eq. 2:

$$\mathrm{AOp} = \gamma(SD)^{-\alpha} \tag{2}$$

where γ and α are the site factors.

Random forest

Decision tree (DT) is one of the branches of AI, and RF belongs to the DT branch, which was developed by Breiman (2001). As a robust DT model, RF can solve both classification and regression cases. Based on the different results of the trees, this method has been suggested as a suitable method for achieving predictive precision (Vigneau et al. 2018). In addition, this method used the results of the exclusive tree in the forest to present the best outcome. As a voter, each tree contributes its predictions for the final decision of RF (Gao et al. 2018). On the other hand, RF ensembles the predictions of the tree and making a final decision based on the obtained results. The key of

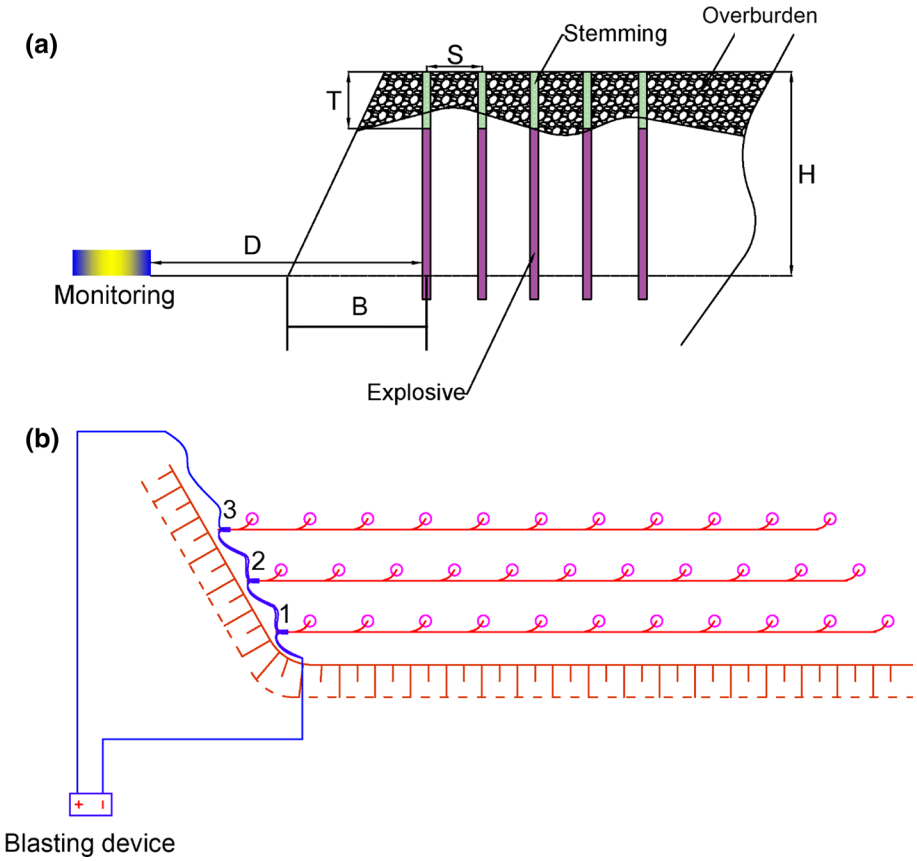

Fig. 3 Structure of the borehole and its parameters. **a** Parameters of blast design and **b** a combination plan of blasting

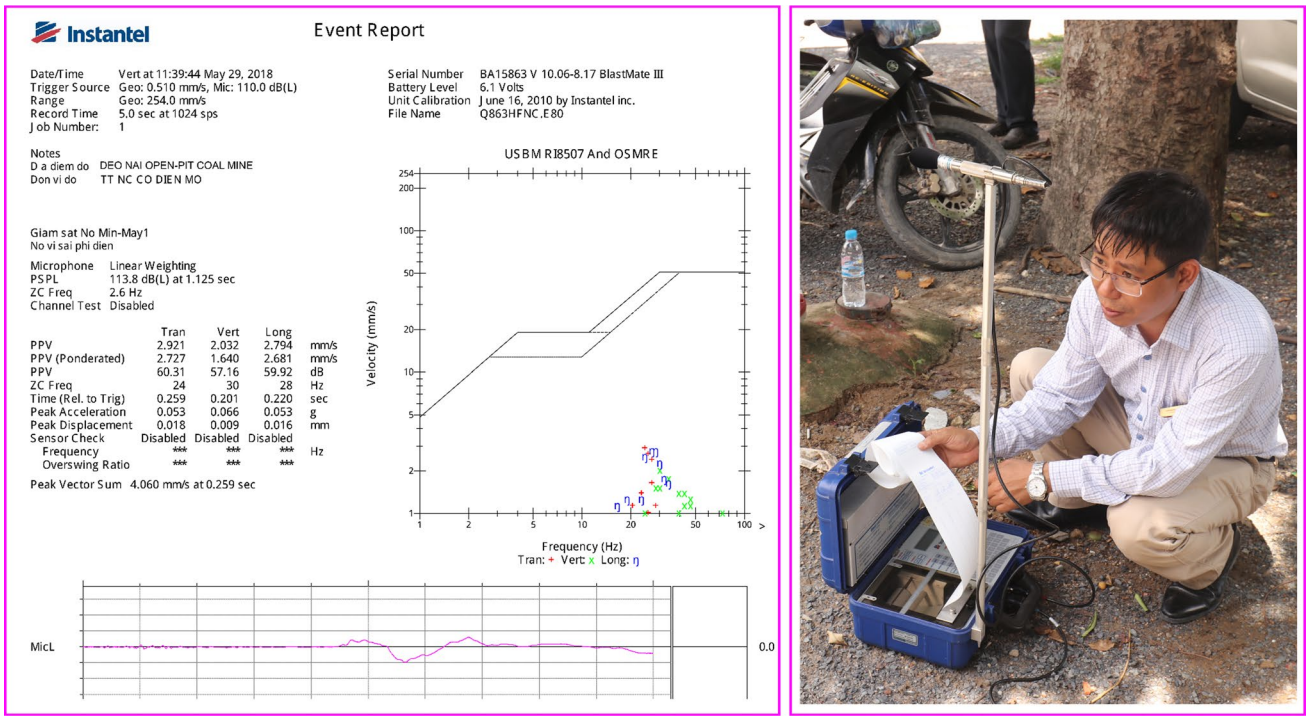

Fig. 4 Data collection for predicting AOp in this work

Table 2 Inputs, output, and their properties

Categories	*W*	*H*	*B*	*S*	*T*
Minimum	1376	13.00	7.500	7.400	6.200
Mean	13183	14.37	8.064	7.814	6.879
Maximum	24171	16.00	8.500	8.200	7.500
Standard deviation	4685.73	0.937	0.332	0.213	0.362
Categories	*q*	*N*	RH	*D*	AOp
Minimum	0.3500	2.000	76.00	180	92.26
Mean	0.4178	3.486	85.16	469	123.19
Maximum	0.4800	5.000	94.00	726	147.00
Standard deviation	0.035	1.216	4.817	159.896	11.912

the RF for regression is presented in three steps: (i) producing bootstrap instances as the tree number in the forest (n_{tree}) according to the database, (ii) expand a suitable regression tree for any bootstrap instance using random sampling of the estimators (m_{try}) (Dou et al. 2019). Of those variables, choose the most appropriate split and (iii) estimate recent perception using ensemble the estimated amounts of the trees (n_{tree}). For the regression issue (i.e., estimating AOp), the mean amount of the estimated values in the single tree is applied.

According to the training dataset, a prediction of the error rate may be calculated according to the two following steps:

1 At any iteration of bootstrap, estimate the non-information in the instance of bootstrap using the tree grown with the bootstrap instance, named "out-of-bag" (OOB).
2 Collect the OOB estimations and predict the error.

More details of the RF algorithm can be explained in (Nguyen and Bui 2018; Breiman 2001; Bui et al. 2019).

Gradient boosting machine

GBM is an ensemble approach that is suggested by Friedman (2002). It is an improved boosting algorithm and can be applied for regression, as well as classification problems (Friedman 2001). The boosting algorithm can be described according to the pseudocode in Fig. 5 (Friedman 2002).

Subsequently, Friedman (Friedman 1999) provided a particular algorithm based on the platform of boosting algorithm for various loss criteria like least squares:

$$\psi(y_{\text{AOp}}, T) = (y_{\text{AOp}} - T)^2 \tag{3}$$

Least absolute deviation:

Boosting algorithm

1 $F_0(x) = \arg\min_{\gamma} \sum_{i=1}^{N} \psi(y_i, \gamma)$

2 For m=1 to M do:

3 $\tilde{y}_{im} = -\left[\frac{\partial \psi(y_i, F(x_i))}{\partial F(x_i)}\right]_{F(x)=F_{m-1}(x)}, i = 1, N$

4 $\{R_{lm}\}_1^L = L - \text{terminal node tree}(\{\tilde{y}_{im}, x_i\}_1^N)$

5 $\gamma_{lm} = \arg\min_{\gamma} \sum_{x_i \in R_{lm}} \psi(y_i, F_{m-1}(x_i) + \gamma)$

6 $F_m(x) = F_{m-1}(x) + \nu \cdot \gamma_{lm} 1(x \in R_{lm})$

7 endFor.

Fig. 5 Pseudocode of the boosting algorithm

Gradient boosting machine

1 $F_0(x) = \arg\min_{\gamma} \sum_{i=1}^{N} \psi(y_i, \gamma)$

2 For m=1 to M do:

3 $\{\pi(i)\}_1^N = \text{rand\_perm}\{i\}_1^N$

4 $\tilde{y}_{\pi(i)m} = -\left[\frac{\partial \psi(y_{\pi(i)}, F(x_{\pi(i)}))}{\partial F(x_{\pi(i)})}\right]_{F(x)=F_{m-1}(x)}, i = 1, \tilde{N}$

5 $\{R_{lm}\}_1^L = L - \text{terminal node tree}(\{\tilde{y}_{\pi(i)m}, x_{\pi(i)}\}_1^{\tilde{N}})$

6 $\gamma_{lm} = \arg\min_{\gamma} \sum_{x_{\pi(i)} \in R_{lm}} \psi(y_{\pi(i)}, F_{m-1}(x_{\pi(i)}) + \gamma)$

7 $F_m(x) = F_{m-1}(x) + \nu \cdot \gamma_{lm} 1(x \in R_{lm})$

8 endFor.

Fig. 6 Pseudocode of the GBM algorithm

$$\psi(y_{\text{AOp}}, T) = \left|y_{\text{AOp}} - T\right| \tag{4}$$

Huber M:

$$\psi(y_{\text{AOp}}, T) = (y_{\text{AOp}} - T)^2 1(\left|y_{\text{AOp}} - T\right| \le \delta) + 2\delta(\left|y_{\text{AOp}} - T\right| - \delta/2) 1(\left|y_{\text{AOp}} - T\right| > \delta) \tag{5}$$

Let $\{y_{i.\text{AOp}}, x_{i.\text{AOp}}\}_1^N$ as the entire training information instance and $\{\pi(i)\}_i^N$ stands for random permutation for integers $\{1, \ldots, N\}$. Then, a random subsample of size $\tilde{N} < N$ is predicted by $\{y_{\pi(i.\text{AOp})}, x_{\pi(i.\text{AOp})}\}_1^{\tilde{N}}$. The pseudocode of the GBM algorithm is described in Fig. 6 (Friedman 2002).

Cubist

Cubist algorithm (Rulequest 2016a, b) is one of the rule-based algorithms, which is utilized to make predictive models according to the input information analysis, whereas the See5/C5.0 method that is able to solve classification problems (Quinlan 2004), the Cubist can solve regression issues very well. The outcomes from the Cubist model are more priority than those of linear regression models. In addition, it is simpler than the ANN model (Rulequest 2016a, b).

The Cubist model is expanded based on Quinlan's M5 model tree (Quinlan 1992) with the capability to apply for thousands of input characteristics (Rulequest 2016a, b). In the Cubist model, the targets depend on the inputs, and it is computed based on the rule(s). A combination of different conditions with a linear function is conducted for these rules. The related linear function is used to estimate the output properly if a rule takes into consideration the whole requirements. The Cubist algorithm can perform multiple situations at the same time and then detect various distinct linear functions for estimating output. Therefore, Cubist can generate various models and mixes them based on the rules which are determined before. Developing multiple models with different rules and their combinations can assist Cubist model in attaining much higher levels of precision. More details of Cubist can be found in Refs. (Nguyen et al. 2019; Kuhn et al. 2012; Drzewiecki 2016; Kuhn et al. 2018; Bernat and Drzewiecki 2015).

Preparing the dataset

In this section, the AOp dataset is prepared as a geospatial database by the ArcGIS software; 146 records of blast were divided into two sections according to the recommendations of previous researchers (Nguyen et al. 2019a, b); 80% of the total datasets (approximate 118 events of blast) are selected by randomly and applied as the training dataset to build the AOp predictive models. The rest (28 records of the blast) were utilized as the testing dataset for evaluating the AOp models' performance. Summary of training and testing datasets is shown in Tables 3 and 4, respectively.

Table 3 Summary of the training dataset

Categories	*W*	*H*	*B*	*S*	*T*
Minimum	1376	13.00	7.500	7.400	6.200
Mean	13036	14.36	8.054	7.807	6.877
Maximum	24171	16.00	8.500	8.200	7.500
Standard deviation	4735.744	0.949	0.332	0.209	0.367
Categories	*q*	*N*	RH	*D*	AOp
Minimum	0.350	2.000	76.00	180	92.26
Mean	0.417	3.466	85.22	473.4	122.98
Maximum	0.480	5.000	94.00	726	147.00
Standard deviation	0.035	1.217	4.665	158.747	11.999

Table 4 Summary of the testing dataset

Categories	*W*	*H*	*B*	*S*	*T*
Minimum	1376	13.00	7.500	7.400	6.200
Mean	13183	14.37	8.064	7.814	6.879
Maximum	24171	16.00	8.500	8.200	7.500
Standard deviation	4497.849	0.903	0.330	0.233	0.349
Categories	*q*	*N*	RH	*D*	AOp
Minimum	0.3500	2.000	76.00	180	92.26
Mean	0.4178	3.486	85.16	469	123.19
Maximum	0.4800	5.000	94.00	726	147.00
Standard deviation	0.034	1.230	5.497	166.333	11.712

Establishing the AOp predictive models

For the empirical model, 118 blasting events (training dataset) were used to compute the site factors k and β. Microsoft Excel 2016 was used to define k and β by the use of a multivariate regression analysis technique. As a result, $k = 208.26$ and $\beta = 0.183$ are the optimal values of the USBM model for predicting AOp. The USBM model (in this case) can be described as:

$$\mathrm{AOp} = 208.026(SD)^{-0.183} \quad (6)$$

For the development of the ensemble models, the ten-fold cross-validation method, along with three repetitions, is utilized to avoid overfitting. Furthermore, the ensemble models used the same training as those used for the development of the USBM model. To develop the RF model, the number of trees was set equal to 2000 to meet the diversity of the forest (Nguyen et al. 2017). Then, the random predictor (m_{try}) was tuned to get the optimal performance of the RF model. Herein, m_{try} was set in the range of 1–50 as a trial and error procedure. Ultimately, an optimal value of m_{try} was determined for the RF model with $m_{\mathrm{try}} = 41$. Figure 7 shows the efficiency of the RF model for estimating AOp.

Unlike the RF model, the GBM model used four parameters to control the model's performance, such as the *number of trees*, *max tree depth*, *shrinkage,* and *n.minobsinnode*. A grid search method was also applied to define the optimal parameters for the GBM model. As a result, *number of trees* =500, *max tree depth* =4, *shrinkage* =0.1, and *n.minobsinnode* =5 were the best values for the GBM model in this case. GBM's performance is illustrated in Fig. 8.

To develop the Cubist model, *committees* and *neighbors* were used as the key parameters. The results indicated that the Cubist model reached optimal performance with *committees* of 80 and *neighbors* of 0, as shown in Fig. 9.

Performance indices

For evaluating the efficiency of the AOp predictive models, three performance indices were computed, including mean absolute error (MAE), coefficient of determination (R^2), and root mean square error (RMSE).

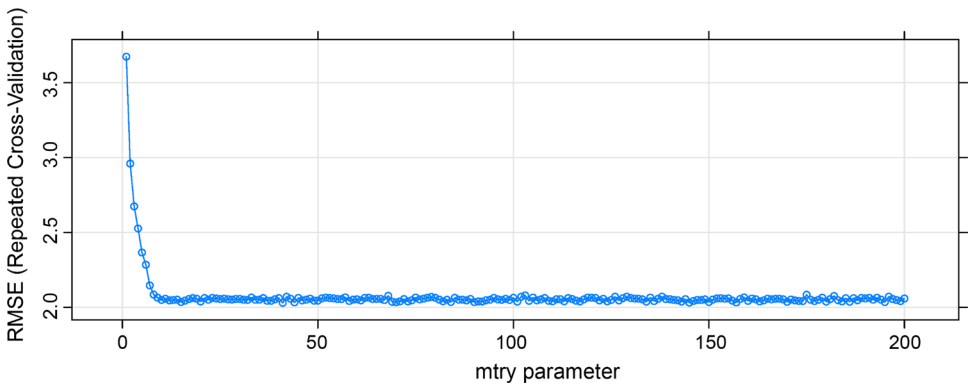

Fig. 7 RF modeling for prediction of AOp

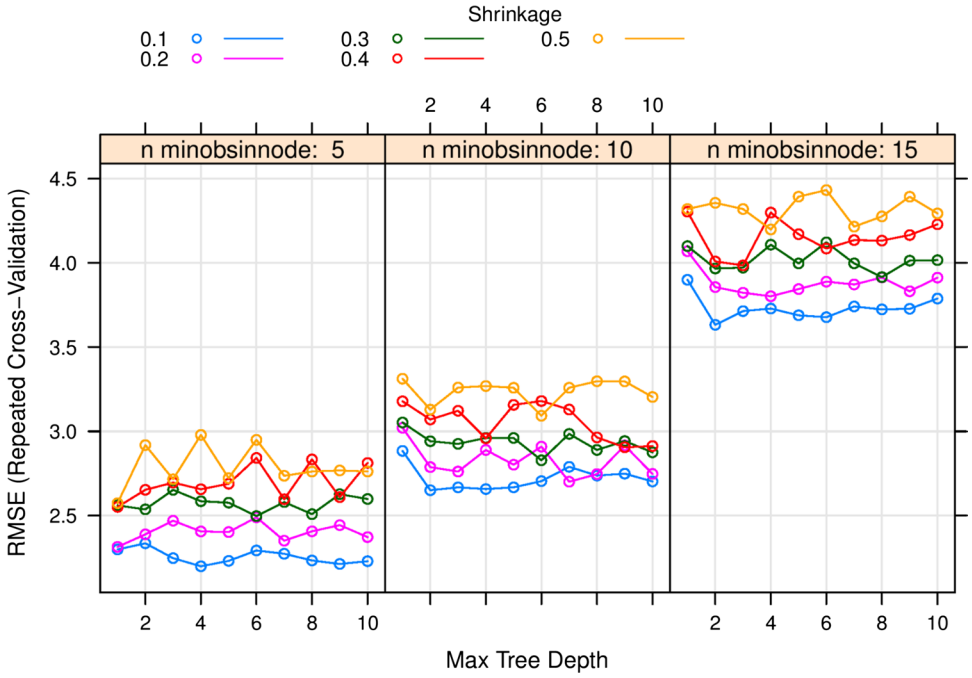

Fig. 8 GBM modeling for prediction of AOp

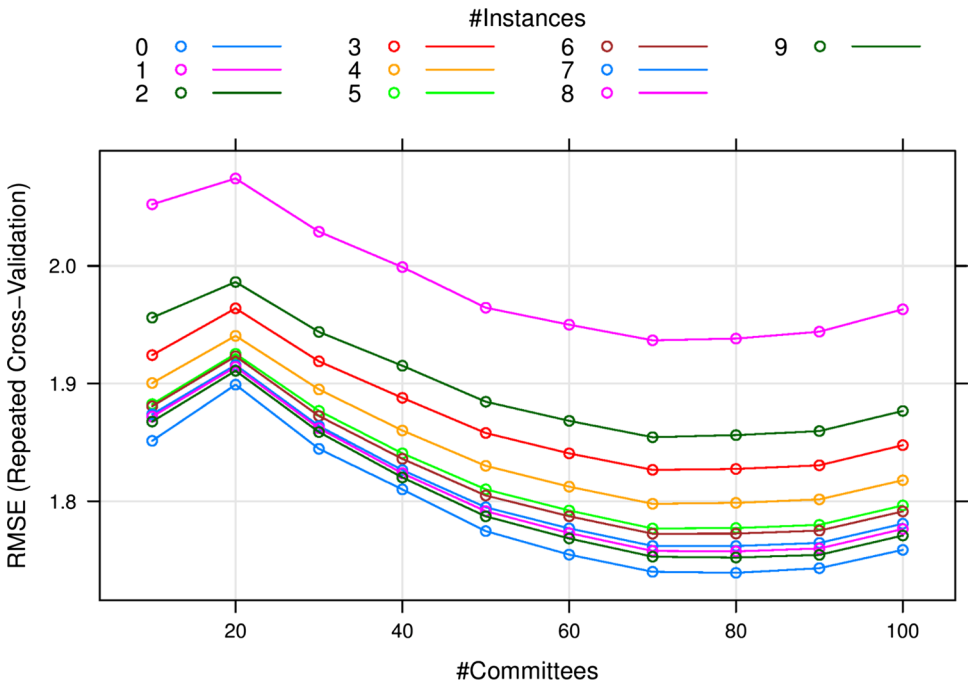

Fig. 9 Cubist modeling for prediction of AOp

Table 5 Performance indices of the ensemble and empirical models

Method	Training dataset			Testing dataset		
	RMSE	R^2	MAE	RMSE	R^2	MAE
Empirical	4.838	0.871	4.101	4.448	0.872	3.719
RF	2.030	0.968	1.143	2.592	0.953	1.103
GBM	2.199	0.970	1.451	2.721	0.950	1.498
Cubist	1.739	0.969	0.980	2.483	0.956	0.976

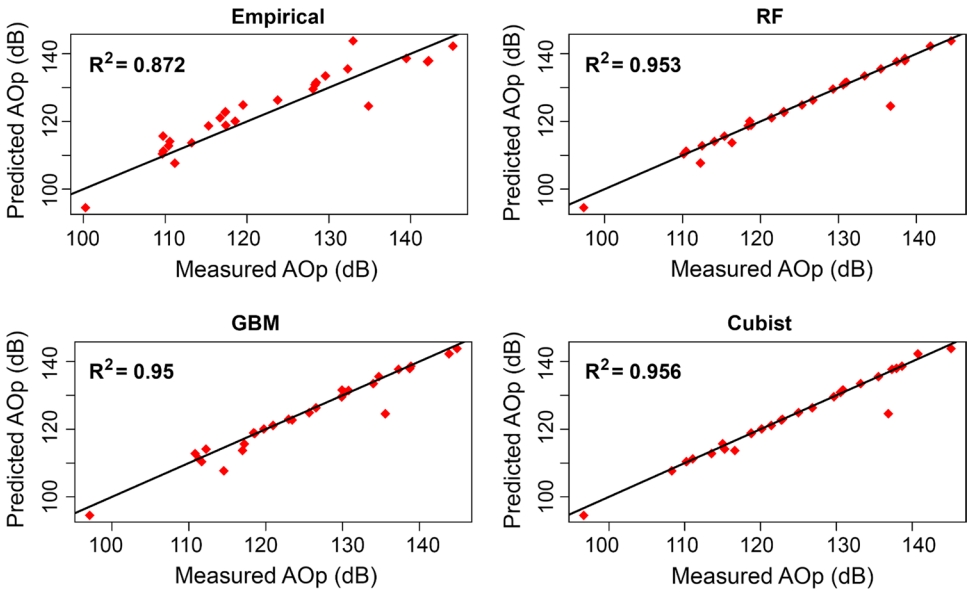

Fig. 10 Relationship of measured and predicted AOp on the ensemble and empirical models

$$\mathrm{RMSE} = \sqrt{\frac{1}{n}\sum_{i=1}^{n}(y_{\mathrm{AOp}} - \hat{y}_{\mathrm{AOp}})^2} \tag{7}$$

$$R^2 = 1 - \frac{\sum_i (y_{\mathrm{AOp}} - \hat{y}_{\mathrm{AOp}})^2}{\sum_i (y_{\mathrm{AOp}} - \bar{y}_{\mathrm{AOp}})^2} \tag{8}$$

$$MAE = \frac{1}{n}\sum_{i=1}^{n}\left|y_{\mathrm{AOp}} - \hat{y}_{\mathrm{AOp}}\right| \tag{9}$$

n is the total number of observations. y_{AOp} is recorded values, $\hat{y}_{\mathrm{AOp}}$ is predicted values, and $\bar{y}_{\mathrm{AOp}}$ is the average of recorded values.

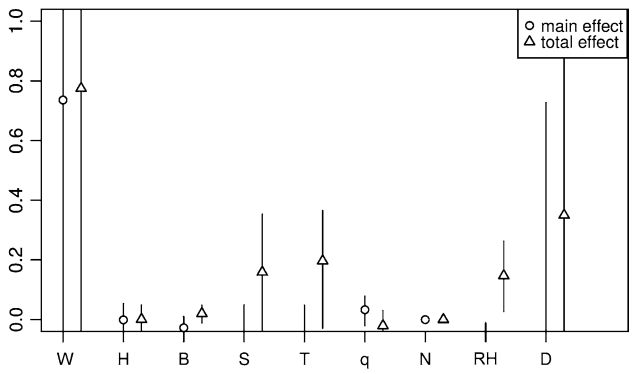

Fig. 11 Sensitivity analysis of the parameters

Results and discussion

Once the models were well established, their performance is evaluated and checked through the performance indices according to Eqs. (7–9). Table 5 shows the results, as well as the performance of the ensemble and empirical models on training/testing datasets.

It can be easy to recognize that the ensemble models performed very well in this study. On the training dataset, the ensemble models obtained high performance with RMSE of 1.739–2.199; R^2 of 0.968–0.970; and MAE of 0.980–1.451. The similar results were also observed on the testing dataset for the ensemble models with RMSE of 2.483–2.721, R^2 of 0.950–0.956, and MAE of 0.976–1.498. In contrast to the ensemble models, the empirical model provided the poorest efficiency (i.e., RMSE = 4.838, 4.448;

$R^2 = 0.871, 0.872$; and MAE = 4.101, 3.719, on the training and testing datasets, respectively). Among three ensemble models (RF, GBM, Cubist), the Cubist model was the most dominant model with an RMSE of 2.483, R^2 of 0.956, and MAE of 0.976 on the testing database. Figure 10 shows the efficiency of the AOp predictive models in testing process.

Although the efficiency of the ensemble models is better than the empirical model in this study, however, the practical technique used only two input parameters (W and D) to estimate blast-induced AOp, whereas the ensemble models used nine input parameters for predicting the same objective. Therefore, a sensitivity analysis procedure was conducted to assess the effect of the inputs on the AOp predictive model (Tarantola et al. 2007; Saltelli et al. 2010). The results showed that W, S, T, RH, and D were the most influential parameters on the AOp predictive model, as illustrated in Fig. 11.

Conclusions and remarks

Based on the obtained results of this study, some conclusions and remarks are withdrawn as follows:

- Ensemble machine learning algorithms are good candidates for predicting blast-induced AOp than those of empirical methods, especially RF, GBM, and Cubist models. They should be considered to control the undesirable effects of blasting in practical engineering.
- Cubist is a robust ensemble AI model for predicting AOp in this study. Its accuracy can ensure safety for the surrounding environment. However, it should be reconsidered in other locations/areas.
- RF and GBM are also good AI techniques for predicting AOp. However, its performance seems not to satisfy. Therefore, they need to improve and further research.
- For predicting AOp, it is not only W and D, but also S, T, and RH are the important inputs for the development of the AOp predictive models. They should be carefully collected to ensure the accuracy level of the models.

Acknowledgements This research was supported by Hanoi University of Mining and Geology (HUMG), Hanoi, Vietnam; Duy Tan University, Da Nang, Vietnam; and the Center for Mining, Electro-Mechanical research of HUMG.

Compliance with ethical standards

Conflict of interest Authors declare that they have no conflict of interest

References

Alel MNA, Upom MRA, Abdullah RA, Abidin MHZ (2018) Optimizing blasting's air overpressure prediction model using swarm intelligence. In: Journal of Physics: Conference Series, vol 1. IOP Publishing, p 012046

AminShokravi A, Eskandar H, Derakhsh AM, Rad HN, Ghanadi A (2018) The potential application of particle swarm optimization algorithm for forecasting the air-overpressure induced by mine blasting. Eng Comput 34(2):277–285. https://doi.org/10.1007/s00366-017-0539-5

Amiri M, Amnieh HB, Hasanipanah M, Khanli LM (2016) A new combination of artificial neural network and K-nearest neighbors models to predict blast-induced ground vibration and air-overpressure. Eng Comput 32(4):631–644

Armaghani DJ, Hajihassani M, Marto A, Faradonbeh RS, Mohamad ET (2015) Prediction of blast-induced air overpressure: a hybrid AI-based predictive model. Environ Monit Assess 187(11):666

Armaghani DJ, Hasanipanah M, Mohamad ET (2016) A combination of the ICA-ANN model to predict air-overpressure resulting from blasting. Eng Comput 32(1):155–171

Asteris PG, Nikoo M (2019) Artificial bee colony-based neural network for the prediction of the fundamental period of infilled frame structures. Neural Comput Appl. https://doi.org/10.1007/s00521-018-03965-1

Asteris P, Kolovos K, Douvika M, Roinos K (2016) Prediction of self-compacting concrete strength using artificial neural networks. Eur J Environ Civ Eng 20(sup1):s102–s122

Bach NV, Nam BX, An ND, Hung TK (2012) Determination of blast-induced ground vibration for non-electric delay blasting (in Vietnamse). J SciTechnol Hanoi Univ Min Geol 38(02):25–28

Bernat K, Drzewiecki W (2015) A study of selected textural features usefulness for impervious surface coverage estimation using Landsat images. In: Image and signal processing for remote sensing XXI, 2015. International society for optics and photonics, p 964327

Breiman L (2001) Random for Mach Learn 45(1):5–32

Bui XN, Nguyen H, Le HA, Bui HB, Do NH (2019a) Prediction of blast-induced air over-pressure in open-pit mine: assessment of different artificial intelligence techniques. Nat Resour Res. https://doi.org/10.1007/s11053-019-09461-0

Bui X-N, Nguyen H, Le H-A, Bui H-B, Do N-H (2019b) Prediction of blast-induced air over-pressure in open-pit mine: assessment of different artificial intelligence techniques. Nat Res Res. https://doi.org/10.1007/s11053-019-09461-0

Dou J, Yunus AP, Bui DT, Merghadi A, Sahana M, Zhu Z, Chen C-W, Khosravi K, Yang Y, Pham BT (2019) Assessment of advanced random forest and decision tree algorithms for modeling rainfall-induced landslide susceptibility in the Izu-Oshima Volcanic Island, Japan. Sci Total Environ 662:332–346

Drzewiecki W (2016) Comparison of selected machine learning algorithms for sub-pixel imperviousness change assessment. In: Geodetic Congress (Geomatics), Baltic, 2016. IEEE, pp 67–72

Friedman J (1999) Greedy function approximation: A stochastic boosting machine. Department of Statistics Stanford University

Friedman JH (2001) Greedy function approximation: a gradient boosting machine. Ann Stat 29:1189–1232

Friedman JH (2002) Stochastic gradient boosting. Comput Stat Data Anal 38(4):367–378

Gao W, Guirao JL, Basavanagoud B, Wu J (2018) Partial multi-dividing ontology learning algorithm. Inf Sci 467:35–58

Gao W, Alqahtani AS, Mubarakali A, Mavaluru D, Khalafi S (2019) Developing an innovative soft computing scheme for prediction of air overpressure resulting from mine blasting using GMDH

optimized by GA. Eng Comput. https://doi.org/10.1007/s00366-019-00720-5
Hajihassani M, Armaghani DJ, Sohaei H, Mohamad ET, Marto A (2014) Prediction of airblast-overpressure induced by blasting using a hybrid artificial neural network and particle swarm optimization. Appl Acoust 80:57–67
Hasanipanah M, Armaghani DJ, Khamesi H, Amnieh HB, Ghoraba S (2016) Several non-linear models in estimating air-overpressure resulting from mine blasting. Eng Comput 32(3):441–455
Hustrulid W (1999) Blasting principles for open-pit blasting: theoretical foundations. Balkema, Rotterdam
Jhanwar J, Cakraborty A, Anireddy H, Jethwa J (1999) Application of air decks in production blasting to improve fragmentation and economics of an open pit mine. Geotech Geol Eng 17(1):37–57
Khandelwal M, Kankar P (2011) Prediction of blast-induced air overpressure using support vector machine. Arab J Geosci 4(3–4):427–433
Khandelwal M, Singh T (2005) Prediction of blast induced air overpressure in opencast mine. Noise Vib Worldw 36(2):7–16
Kuhn M, Weston S, Keefer C, Coulter N (2012) Cubist models for regression. R package Vignette R package version 00 18
Kuhn M, Weston S, Keefer C, Kuhn MM (2018) Package 'Cubist'
Kuzu C, Fisne A, Ercelebi S (2009) Operational and geological parameters in the assessing blast induced airblast-overpressure in quarries. Appl Acoust 70(3):404–411
Loder B (1985) National Association of Australian State Road Authorities. In: Australian Workshop for Senior ASEAN Transport Officials, 1985, Canberra, 1987
Mahdiyar A, Marto A, Mirhosseinei SA (2018) Probabilistic air-overpressure simulation resulting from blasting operations. Environ Earth Sci 77(4):123
McKenzie C (1990) Quarry blast monitoring: technical and environmental perspectives. Quarry Manag 17:23–24
Mohamad ET, Armaghani DJ, Hasanipanah M, Murlidhar BR, Alel MNA (2016) Estimation of air-overpressure produced by blasting operation through a neuro-genetic technique. Environ Earth Sci 75(2):174
Montahaei M, Oskooi B (2014) Magnetotelluric inversion for azimuthally anisotropic resistivities employing artificial neural networks. Acta Geophys 62(1):12–43. https://doi.org/10.2478/s11600-013-0164-7
Naganna SR, Deka PC (2019) Artificial intelligence approaches for spatial modeling of streambed hydraulic conductivity. Acta Geophys. https://doi.org/10.1007/s11600-019-00283-5
Nguyen H, Bui X-N (2018a) Feasibility of artificial neural network in predicting blast-induced air overpressure in open-pit mine. J Min Ind 01:60–66
Nguyen H, Bui X-N (2018b) Predicting blast-induced air overpressure: a robust artificial intelligence system based on artificial neural networks and random forest. Nat Resour Res. https://doi.org/10.1007/s11053-018-9424-1
Nguyen H, Bui X-N, Tran Q-H (2017) Prediction of blast-induced air overpressure in Deo Nai open-pit coal mine using Random Forest algorithm. J Min Ind 06:47–53
Nguyen H, Bui X-N, Tran Q-H, Le T-Q, Do N-H, Hoa LTT (2018a) Evaluating and predicting blast-induced ground vibration in opencast mine using ANN: a case study in Vietnam. SN Appl Sci 1(1):125. https://doi.org/10.1007/s42452-018-0136-2
Nguyen H, Bui XN, Bui HB, Mai NL (2018b) A comparative study of artificial neural networks in predicting blast-induced air-blast overpressure at Deo Nai open-pit coal mine, Vietnam. Neural Comput Appl. https://doi.org/10.1007/s00521-018-3717-5
Nguyen H, Bui X-N, Tran Q-H, Moayedi H (2019a) Predicting blast-induced peak particle velocity using BGAMs, ANN and SVM: a case study at the Nui Beo open-pit coal mine in Vietnam. Environ Earth Sci 78(15):479. https://doi.org/10.1007/s12665-019-8491-x
Nguyen H, Bui X-N, Tran Q-H, Mai N-L (2019b) A new soft computing model for estimating and controlling blast-produced ground vibration based on hierarchical K-means clustering and cubist algorithms. Appl Soft Comput 77:376–386. https://doi.org/10.1016/j.asoc.2019.01.042
Nguyen H, Moayedi H, Foong LK, Al Najjar HAH, Jusoh WAW, Rashid ASA, Jamali J (2019c) Optimizing ANN models with PSO for predicting short building seismic response. Eng Comput. https://doi.org/10.1007/s00366-019-00733-0
Nguyen H, Drebenstedt C, Bui X-N, Bui DT (2019d) Prediction of blast-induced ground vibration in an open-pit mine by a novel hybrid model based on clustering and artificial neural network. Nat Resour Res. https://doi.org/10.1007/s11053-019-09470-z
Nguyen H, Bui X-N, Bui H-B, Cuong DT (2019e) Developing an XGBoost model to predict blast-induced peak particle velocity in an open-pit mine: a case study. Acta Geophys 67(2):477–490. https://doi.org/10.1007/s11600-019-00268-4
Nguyen H, Bui X-N, Moayedi H (2019f) A comparison of advanced computational models and experimental techniques in predicting blast-induced ground vibration in open-pit coal mine. Acta Geophys. https://doi.org/10.1007/s11600-019-00304-3
Piasecki A, Jurasz J, Adamowski JF (2018) Forecasting surface water-level fluctuations of a small glacial lake in Poland using a wavelet-based artificial intelligence method. Acta Geophys 66(5):1093–1107. https://doi.org/10.1007/s11600-018-0183-5
Pierini JO, Lovallo M, Telesca L, Gómez EA (2013) Investigating prediction performance of an artificial neural network and a numerical model of the tidal signal at Puerto Belgrano, Bahia Blanca Estuary (Argentina). Acta Geophys 61(6):1522–1537. https://doi.org/10.2478/s11600-012-0093-x
Quinlan JR (1992) Learning with continuous classes. In: 5th Australian joint conference on artificial intelligence. Singapore, pp 343–348
Quinlan R (2004) Data mining tools See5 and C5. 0
Rahmani Y, Farnood Ahmadi F (2018) Application of InSAR in measuring Earth's surface deformation caused by groundwater extraction and modeling its behavior using time series analysis by artificial neural networks. Acta Geophys 66(5):1171–1184. https://doi.org/10.1007/s11600-018-0182-6
Rulequest (2016a) Data Mining with Cubist. https://www.rulequest.com/cubist-win.html. Accessed 26 Feb 2019
Rulequest (2016b) Data Mining with Cubist. https://www.rulequestcom/cubist-info.html RuleQuest Research Pty Ltd.,St. Ives, NSW, Australia
Saltelli A, Annoni P, Azzini I, Campolongo F, Ratto M, Tarantola S (2010) Variance based sensitivity analysis of model output Design and estimator for the total sensitivity index. Comput Phys Commun 181(2):259–270
Shang Y, Nguyen H, Bui X-N, Tran Q-H, Moayedi H (2019) A novel artificial intelligence approach to predict blast-induced ground vibration in open-pit mines based on the firefly algorithm and artificial neural network. Nat Resour Res. https://doi.org/10.1007/s11053-019-09503-7
Siskind DE, Stachura VJ, Stagg MS, Kopp JW (1980) Structure response and damage produced by airblast from surface mining. Citeseer
Tarantola S, Gatelli D, Kucherenko S, Mauntz W (2007) Estimating the approximation error when fixing unessential factors in global sensitivity analysis. Reliab Eng Syst Saf 92(7):957–960
Vigneau E, Courcoux P, Symoneaux R, Guérin L, Villière A (2018) Random forests: a machine learning methodology to highlight the volatile organic compounds involved in olfactory perception. Food Qual Prefer 68:135–145
Vinacomin (2015) Report on geological exploration of Coc Sau open pit coal mine, Quang Ninh, Vietnam (in Vietnamse-unpublished). VINACOMIN, Vietnam
Walter E (1990) Surface blast design. Prentice Hall, New Jersey

Wiszniowski J (2016) Applying the general regression neural network to ground motion prediction equations of induced events in the Legnica-Głogów copper district in Poland. Acta Geophys 64(6):2430–2448. https://doi.org/10.1515/acgeo-2016-0104

Zhang X, Nguyen H, Bui X-N, Tran Q-H, Nguyen D-A, Bui DT, Moayedi H (2019) Novel soft computing model for predicting blast-induced ground vibration in open-pit mines based on particle swarm optimization and XGBoost. Nat Resour Res. https://doi.org/10.1007/s11053-019-09492-7

Zhou J, Li E, Yang S, Wang M, Shi X, Yao S, Mitri HS (2019a) Slope stability prediction for circular mode failure using gradient boosting machine approach based on an updated database of case histories. Saf Sci 118:505–518

Zhou J, Nekouie A, Arslan CA, Pham BT, Hasanipanah M (2019b) Novel approach for forecasting the blast-induced AOp using a hybrid fuzzy system and firefly algorithm. Eng Comput. https://doi.org/10.1007/s00366-019-00725-0

Acta Geophysica (2020) 68:337–355
https://doi.org/10.1007/s11600-020-00418-z

RESEARCH ARTICLE - SOLID EARTH SCIENCES

Earthquake source dynamics and kinematics of the Eastern Indian Shield and adjoining regions

Rashmi Singh[1] · Prosanta Kumar Khan[1] · A. P. Singh[2,3]

Received: 22 September 2019 / Accepted: 3 March 2020 / Published online: 13 March 2020

Abstract

The Eastern Indian Shield (EIS) consists of two cratonic nuclei, namely Singhbhum craton and Chhotanagpur Granitic Gneissic terrain. This area contains several crisscross faults, lineaments, shear zones, numerous hot springs and three major rivers (e.g., Ganga, Brahmaputra and Damodar). The area is regionally covered by 7 seismic stations and jointly recorded 16 events from the study area, and less noisy waveforms of 4 events were used for focal mechanism analysis using the Cut and Paste method. The focal parameters of these 4 events were compiled with results of 8 events computed by different workers for the study area. To understand the detailed tectonics, focal mechanisms of 21 events for the Himalayan segment were taken from CMT Harvard catalog of duration 1976–2017. Spatial variations of operative stress fields for major tectonic domains were analyzed in the present study based on stress inversion of focal mechanism parameters. We observed strike-slip-dominated movements in the EIS, which changes partially into extension in the northeast part between the Ganga and Brahmaputra Rivers. Thrust-dominated movements evidenced by focal mechanisms and the pure compression in the western segment of the Himalaya in the north might be promoting shear movements in the EIS and adjoining regions. The pure strike-slip in the eastern segment of the Himalaya and its deeper level account for lateral shearing and eastward movements of different tectonic blocks. The normal faulting earthquakes in the northeast part might be indicating stretching in the basement because of convergence of Indian lithosphere beneath the Myanmar plate.

Keywords Seismicity · Focal mechanism · Cut and Paste Method · Stress inversion · Eastern Indian Shield

Introduction

Cratons are usually composed of Precambrian metamorphic basements, which exhibit variable graded crystalline rocks of ages ranging from 3.6 to 2.6 Ga and account tectonic stability over prolonged geological period (Mukhopadhyay et al. 2008; Acharyya et al. 2010a, b; Tait et al. 2011; Mazumder et al. 2012). Cratons are evidenced with folded structures of variable dimensions, occasionally interlinked by sutures or shear zones documenting mutual lateral movements of crustal blocks (Naqvi 2005). The present study region consists of two cratonic blocks, namely Singhbhum and Chhotanagpur, converged along the Singhbhum mobile belt during the Archean times (Sarkar 1982). The region is bounded by the Gondwana formations on its western side, Eastern Ghats mobile belt, Mahanadi fault and Ranipathar shear zone on its southern side, the Himalayan Frontal Thrust (HFT) in the northern side and the Bengal Basin in the eastern side (Fig. 1). Northern side of the study area comprises NE–SW striking major crustal discontinuities such as West Patna Fault (WPF), East Patna Fault (EPF) and Munger–Saharsa Ridge Fault (MSRF), orthogonally transecting the Lower Himalaya (Valdiya 1976; Dasgupta et al. 1987). These faults are apparently oriented along the operative compressive stress evolved by the north-directed migration of the Indian Plate against the Asian Plate and are evidenced with strike-slip-dominated Holocene movements (Valdiya 1976; Sahu et al. 2010). A NW–SE fast axis of anisotropy was found to the north of the study area and noted to be orthogonal to the convergence direction of

✉ Prosanta Kumar Khan
khanprosanta1966@iitism.ac.in;
khanprosanta1966@gmail.com

[1] Department of Applied Geophysics, Indian Institute of Technology (ISM), Dhanbad 826004, India

[2] Science and Technology Department, Institute of Seismological Research, Gandhinagar 382007, India

[3] National Centre for Seismology, Ministry of Earth Sciences, Lodi Road, New Delhi 110003, India

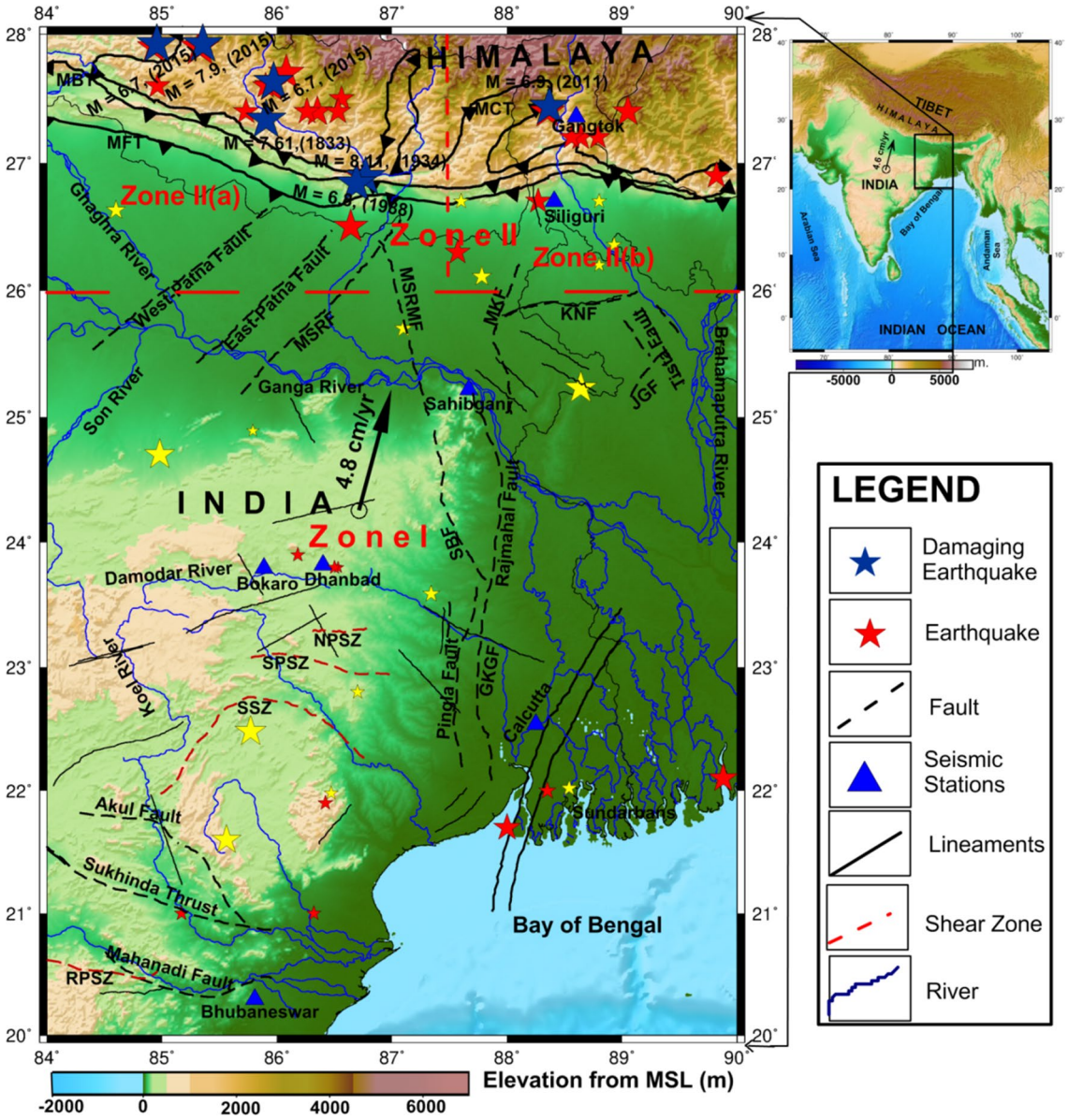

Fig. 1 Map on the left illustrates the tectonic setup and distribution of historical seismicity of the study area. Location of the study area is shown by rectangular block on the right top of the map (after Khan et al. 2015). Red and blue stars represent historical damaging earthquakes (Table 1). The size of stars varies according to the magnitude of earthquakes. Location of broadband seismic stations (blue triangles) and 16 events (yellow stars) jointly recorded by IIT(ISM) Dhanbad and IMD (Table 2). Black solid lines represent the lineaments, black dashed lines show the faults, and red dashed lines represent the shear zones. Rivers are shown by blue lines. *MSRF* Munger–Saharsa Ridge Fault, *MSRMF* Munger–Saharsa Ridge Marginal Fault, *GKGF*: Garhmayna–Khandaghosh Fault, *SBF* Sainthia Bahmani Fault, *MKF*: Malda–Kishanganj Fault, *JGF* Jangipur–Gaibandha Fault, *KNF* Katihar–Nilphamari Fault, *RPSZ* Ranipathar shear zone, *SSZ* Singhbhum shear zone, *NPSZ* North Purulia shear zone, *SPSZ* South Purulia shear zone, *MFT* Main Frontal Thrust, *MBT* Main Boundary Thrust, *MCT* Main Central Thrust

the Indian plate and accounts for diversity in the Himalayan region (Singh el al. 2007). The study region contains a large number of drainage systems along with three major rivers, namely Damodar, Ganga and Brahmaputra. Ganga River running from west to east along the Himalayan Foothills passed the 87° E, turned toward south near the Rajmahal Trap, and finally merges with the Bay of Bengal. The River Brahmaputra also meets the Bengal basin, after turning toward south around the same area happened with the Ganga River (Fig. 1). Large numbers of north–south trending strike-slip marginal faults are also identified parallel to the flow of these two great rivers (Fig. 1). The changes in natural downstream flow of these river systems are found to be guided by the tilting of different faults bound blocks

at its southward course of migration (Mohindra et al. 1992; Peakall et al. 2000; Sahu et al. 2010).

Occasional incidences of great destructive earthquakes, for example 1833 Nepal–Bihar (M_L 7.6), 1934 north Bihar–Nepal (M_W 8.1), 1988 north Bihar (M_W 6.8), 2011 Sikkim earthquake (M_W 6.9) and 2015 Nepal–Bihar earthquake (M_W 7.9), invariably account for occasional stress accumulation and subsequent amplification near the Nepal–Bihar–Sikkim border of India (Ansari and Khan 2014; Khan et al. 2017 and references therein). The Eastern Indian Shield, located to the south of this Nepal–Bihar–Sikkim border, experienced a number of moderate magnitude earthquakes such as 1811 Calcutta (5.0), 1842 Bengal (5.7), 1868 Manbhum (M 5.7), 1868 Hazaribagh (M 5.0), 1963 Singhbhum (M 5.2), 1964 Midnapore (5.5) and 1969 Bankura (M 5.7) (Kayal et al. 2009; Chandra 1977; Gupta et al. 2014; Rastogi 2016). Three moderate-size earthquakes such as 1979 (M_w 5.0), 2006 (M_w 4.7) and 2015 (M_w 5.1) were also reported from this area (Global CMT Catalog) (Fig. 1; Table 1). Incidentally, the 1979 earthquake was associated with MSRF. Normal faulting kinematics was also noted on its eastern side (Gupta et al. 2014), while on the western side of this fault, both thrust and strike-slip-dominated movements are apparent. The 1988 earthquake was located near the EPF which shows strike-slip movement (Ansari and Khan 2014; Dasgupta et al. 2013), and the 2011 Sikkim earthquake also showed similar movement along the Tista lineament (Dasgupta et al. 2013). Major damaging earthquakes (e.g., 1833 Nepal–Bihar, 1934 north Bihar–Nepal, 1988 north Bihar, 2011 Sikkim, 2015 Nepal earthquake) were found to be concentrated to the north of the study area along the Himalayan belt.

Other several strike-slip-dominated northward striking faults like Sainthia–Bahmani, Malda–Kishanganj, Pingla, Garhmayna–Khandaghosh and Rajmahal are passing along the western margin of the Ganga Basin toward its downstream, and few are likely continued up to the Himalayan Foothills (Godin and Harris 2014). The NNE-oriented gravity high identified in the study region (Chandra et al. 1993; Godin and Harris 2014), the downwarping of the basement caused by overriding of the Myanmar micro-plate (Roy and Chatterjee 2015) toward eastern margin of the study area (Sengupta 1966), the basement upliftment around the Rajmahal Trap, and the strike-slip-dominated movements along the Dauki faults facilitated the turning of the eastward moving Ganga River and the westward moving Brahmaputra River into the southward direction (Godin and Harris 2014). Anisotropic study (Singh et al. 2007) noted a distinct change in the directions of fast axes orientation at 88° E, near the area coinciding with the continuation of north–south trending marginal strike-slip fault (Fig. 1). Northward Holocene migration, accommodation of the Indian lithosphere and the concurrent intense southward thrusting along the crustal-scale discontinuities in the Himalayan Foothills facilitated backpropagation of compressive stress field right within the Indian continental interior (Aggarwal et al. 2016; Khan et al. 2014, 2016). These deformations were identified in the Central Indian Basin and genetically linked with the deformation of the Himalayas (Khan et al. 2018). The deformation in the Himalaya toward north and the basement deformation toward east beneath the lower Gangetic Basin apparently caused by the subduction dynamics along the Myanmar margin transformed the study area into spectacular one in view of tectonic setting and motivated us for its in-depth probing. The present study involves seismicity, focal mechanisms and stress parameters compiled as well as computed using broadband waveform recorded by stations located in the Eastern Indian Shield and adjoining regions. The source parameters were used for finding the predominant stress fields operative at different tectonic domains extended from the Bay of Bengal in the southern side to the Himalaya in the northern side.

Table 1 List of historical damaging earthquakes of magnitude ≥ 5.0 occurred in the Eastern Indian Shield Region

Sl. no	Date	Lat (°N)	Long (°E)	Mag	References
1	01-02-1811	22.6	88.4	5.0	OLD
2	21-05-1842	25.0	87.0	5.7	OLD
3	16-02-1861	22.6	88.4	5.7	OLD
4	23-05-1866	25.0	87.0	6.3	OLD
5	31-07-1868	24.0	85.4	5.0	OLD
6	30-09-1868	24.0	85.0	5.5	OLD
7	15-01-1934	26.84	86.75	8.1	USGS
8	08-05-1963	21.7	84.9	5.2	RO
9	03-05-1969	23.0	86.6	5.7	IMD

OLD Oldham, *USGS* United States Geological Survey, *RO* Rothe, *IMD* India Meteorological Department (after Bapat et al. 1983)

Seismotectonics of the Eastern Indian Shield

The Indian continent was evolved and restructured in the period from Late Triassic to Early Jurassic (~200 Ma), when the Gondwana Land was separated from Pangaea, subsequently the East Gondowana from West Gondowana (Dietz and Holden 1970; Biswas 1987). Indian plate started northward journey and was resisted against the southern margin of the Asian plate, causing submergence evolving the active Himalayan orogeny. Further, separation of Indo-Myanmar plate from Australian plate and the convergence of the Indian plate in the eastern part thrived the subduction of the Indian plate under the Asian plate (Biswas 2008). As a result, Bay of Bengal started to converge and the Arabian Sea started to spread. It is also reported that the Indian plate is continuously experiencing north–northeasterly ridge

push force (Biswas 2008) and easterly slab pull force causing it to move northward. Northward movement caused a compressive stress operative within all over the plate resulting tectonic activities in almost all sedimentary basins. The dynamic nature of the Indian continent can be understood by the mutual interactions of the Indian, Asian and Burma plates.

As a consequence of convergence of the Indian plate, a ~ 1000 km laterally extended Ganges foredeep basin was evolved on the downwarp Indian lithosphere during the Early to Middle Tertiary period (Dewey and Bird 1970; DeMets et al. 1994) and successive tectonic events (Gansser 1964; Lyon-Caen and Molnar 1983; Thakur 1992; Khan et al. 2010). The Ganga Basin is segmented into different tectonic domains demarcated and separated by different faults and highs. The southward extension of the Ganga Plains between the East Patna Fault (EPF) and the West Patna Fault (WPF) experienced stretching and channel migration induced by tilting of blocks (Alam et al. 2003). Ganga River has migrated in the down-tilting direction and enters into the thickened Early Cretaceous–Holocene sediment of the Bengal Basin. The Ganga River in this area is controlled by different tectonic features on all sides, except in the southern part (Roy and Chatterjee 2015). The western Archean shield plunges at ~ 87° E longitude and prolongs further toward east below the dense covers of recent sediment (Sengupta 1972). A dense outcrop of horizontal to sub-horizontal basaltic lava flow of Late Jurassic to Early Cretaceous times casing over 4000 km^2 (i.e., Rajmahal hills) is found in the western portion of the Bengal Basin (Sengupta 1966). The region has been acknowledged by numerous landforms, namely plateau, hills, uplands, plains, several regional lineaments and active drainage system in the form of rivers. Those are the Ganga, Son, Ghaghra, Tista, Brahmaputra, Damodar, Subarnarekha and Mahanadi rivers; all are dipping toward east or southeast directions. Along with them, a large number of hot springs are also found in the study area.

Data and methodology

Earthquake data

Eastern Indian Shield is covered by 7 seismic stations at Gangtok (GTK), Siliguri (SILIG), Calcutta (CAL), Sahibganj (SAHIB), Bhubaneshwar (BWNR) and Bokaro (BOKR). These are maintained by India Meteorological Department (IMD), Government of India, New Delhi, and other one by Indian Institute of Technology (ISM), Dhanbad (Fig. 1). Earthquake waveform data of 16 events (Table 2) have been collected from IMD and IIT(ISM) catalogs for the period from January 2008 to May 2017. Finally, waveforms of 4 events (Table 3) recorded at IIT(ISM) Dhanbad, GTK, SILIG, CAL, BWNR and BOKR with hypocentral distance between 144 and 380 km were found excellent quality. These waveform data were used for analysis of focal mechanisms based on correlation coefficient between synthetic and observed waveforms. The selected waveforms have more than 70% correlation coefficients for long-period body wave (Pnl) and 75% for surface waves. We follow the criteria given by Zhu and Helmberger (1996), D'Amico et al. (2011), Tan et al. (2006) and Singh et al. (2016) for determining the best focal mechanism solutions. Cut-and-paste (CAP) method (Zhao and Helmberger 1994; Zhu and Helmberger 1996)

Table 2 List of events recorded by IIT(ISM) and IMD seismic stations

Sl. no	Date	Origin time hr:min:sec	Lat. (°N)	Long. (°E)	Mag. (M_W)	Depth (km)	Recording seismic stations
1	21-06-2017	18:36:11	25.7	87.1	4.5	50	BOKR, CAL, IIT(ISM), GTK, SAHIB, BWNR
2	29-05-2017	14:43:17	26.7	88.8	3.7	30	BOKR, CAL, GTK, BWNR, SILIG
3	17-05-2016	10:12:32	26.2	88.8	3.5	08	BOKR, GTK, IIT(ISM)
4	25-04-2015	08:20:46	26.63	84.60	4.7	10	BOKR, SILIG, IIT(ISM), GTK
5	14-02-2015	17:06:51	26.7	87.6	3.8	10	BWNR, BOKR, GTK
6	01-06-2013	13:28:55.1	22.02	88.54	4.0	16.5	BOKR, GTK, IIT(ISM)
7	27-03-2012	23:40:12.6	26.11	87.78	4.9	27.8	BOKR, SILIG, GTK, IIT(ISM)
8	25-02-2012	08:45:57.7	26.36	88.93	3.8	19.2	BOKR, SHL, GTK, IIT(ISM)
9	05-11-2011	02:32:12.5	21.50	85.56	3.9	21.2	BWNR, BOKR, SILIG, GTK, IIT(ISM)
10	09-08-2011	03:33:46.8	22.80	86.70	3.5	10.0	BOKR, SHL, GTK, IIT(ISM)
11	28-07-2011	17:53:38.3	25.23	88.64	4.5	15.0	BOKR, SILIG, GTK, IIT(ISM)
12	26-12-2010	05:47:16.5	24.89	85.79	3.1	15.0	BOKR, SHL, IIT(ISM)
13	26-03-2009	04:44:13.0	22.48	85.77	4.2	10.0	BWNR, CAL, IIT(ISM)
14	08-11-2008	16:51:38.5	23.59	87.34	4.2	10.0	BWNR, CAL, IIT(ISM), BOK, SHL
15	06-10-2008	06:15:59.8	21.98	86.47	3.5	10.0	BWNR, CAL, BOKR, IIT(ISM)
16	06-06-2008	21:16:33.7	24.70	84.98	4.1	10.6	IIT(ISM), BOK, CAL

Table 3 Source parameters of earthquake events occurred in Zone I

Event no	Date	Time (hr:min:sec)	Lat. (°N)	Long. (°E)	Mag. (M_W)	Depth (km)	NP1			NP2			Source
							Strike (deg.)	Dip (deg.)	Rake (deg.)	Strike (deg.)	Dip (deg.)	Rake (deg.)	
1	12-06-1989	00:0 4:16.3	22.1	89.88	5.8	15	354	67	164	90	75	24	Global CMT
2	07-11-2007	13:21:55.5	23.8	86.53	2.4	26	102	83	− 157	9	67	− 8	Kayal et al. (2009)
3	29-11-2007	01:54:58.0	23.8	86.5	2.8	26	134	89	− 162	43	72	− 1	Kayal et al. (2009)
4	06-06-2008	21:16:33.7	24.7	84.98	4.1	10.6	130	82	− 180	40	90	− 8	Present study
5	26-03-2009	04:44:13.0	22.4	85.77	4.2	10.0	51	57	10	315	81	146	Present study
6	28-07-2011	17:53:38.3	25.2	88.64	4.5	15.0	346	35	− 90	166	55	− 90	Present study
7	05-11-2011	02:32:12.5	21.5	85.56	3.9	21.2	311	77	− 172	220	83	− 13	Present study
8	08-02-2013	10:54:44.6	21.0	86.32	3.0	16.9	35	55	15	297	78	144	Biswas and Mandal (2017)
9	20-02-2013	05:14:07.4	21.0	85.17	3.0	9.7	218	63	− 2	309	88	− 153	Biswas and Mandal (2017)
10	16-04-2013	19:42:10.20	21.9	86.42	3	23	203	20	-168	101	86	-71	Biswas and Mandal (2017)
11	01-06-2013	13:27:57.21	22.0	88.35	3.5	15	278	71	− 69	48	28	− 137	Biswas and Mandal (2017)
12	10-09-2013	17:43:51.91	23.9	86.18	2.9	14.6	225	23	− 116	73	70	− 80	Biswas and Mandal (2017)

has been applied for waveform inversion using 1D velocity model (Kayal et al. 2011). Seismograms were decomposed, and amplitude information was extracted over different time windows of body and surface waves (Fig. 2a) to increase the stability and resolution of the inversion process (Zhu and Helmberger 1996).

Focal mechanism

The CAP method has been used in the present analysis for computing focal parameters. This method is suitable for small- to large-magnitude earthquakes and accounts for errors in the location of the event vis-à-vis Green's function (D'Amico et al. 2014). Inversion of the whole waveform is difficult as it depends on various factors like velocity model, event location, azimuthal coverage of stations and the Green's function, which is affected by the strongest portion of the waveform (i.e., surface wave, Tan et al. 2006). The CAP method takes account of two decomposed segments, i.e., long-period body wave (Pnl) and surface wave (Zhu and Helmberger 1996; D'Amico et al. 2011; Tan et al. 2006). It weights differently in the misfit calculation because the surface waves are directed by shallow crustal divergence and the Pnl waves are apparently influenced by the mean crustal velocity structure, and the amplitudes decay differently with distance (Zhu and Helmberger 1996). Thus, the CAP method provides a more efficient and stable inversion when azimuthal coverage around the source is poor (D'Amico et al 2013, 2014).

Recorded waveform data have three factors: (a) source factor, (b) Green's function, and (c) instrument response. Source factor is retrieved by deconvolving the instrument response, while Green's functions are retrieved from the recorded waveform data. The instrumental response-corrected three component waveforms are cut into 5 different seismic phase windows (i.e., vertical and radial components of long-period primary wave (Pnl), vertical and radial components of Rayleigh wave and transverse component of Love wave), which help to increase the resolution and stability of the solutions. The CAP method allows a selective time shift among synthetic and observe waveforms to overcome the inaccuracy in the 1D model applied for calculation of Green's functions, locations and origin time of the earthquakes. It makes the final results of focal mechanism solutions less sensitive to the 1D velocity model, Green's functions and earthquake location errors. Positive time shift implies that the model estimation is too quick, so the synthetics are to be late to match the observed trace and vice versa. In the present computation, we have taken instrumental response-corrected SAC format waveforms, processed with the help of header information (e.g., location of events and stations, epicentral distances and azimuth). Time windows have been selected as 25 s and 60 s for Pnl and surface waves, and the cutoff band-pass frequencies of 0.05–0.3 Hz for Pnl and 0.02–0.1 Hz for surface waves (Fig. 2a) (Tan et al. 2006; Zhu and Helmberger 1996; D'Amico et al. 2011). These windows were extracted automatically according to P- and S-wave arrival times based upon the information stored in the Green's function file (Zhao et al. 2013). A weighting factor of 2 is taken for the P-wave comparative to the S-wave for the waveform matching. We have used distant scaling factors of 1–0.5 for P- and S-waves (Zhu and Helmberger 1996). There are three reasons to select the frequency ranges: First one is the removal of long-period offset generated from long-period microtremors and the integrated process used for velocity to displacement conversion; second one is to avoid small-scale effect due to inhomogeneous structures of the crust; and the third one is for computing accurate scalar moment (Lv et al. 2013).

Green's functions are computed by applying the Haskell propagator matrix (fk) method (Zhu and Rivera 2002). We have taken here an appropriate 1D velocity model for the study region (Kayal et al. 2011). We calculate the Green's function for all epicenter–station distances and depth range from 1.0 to 10.0 km, which depends on the double couple type, epicentral distance and focal depth. During computation of the source mechanism (Fig. 2b), the station location and epicenter are fixed, and a grid search is performed at a depth interval of 1 km and 6° of angle interval of strike, dip and rake to determine the finest source parameters and focal mechanism with minimum residuals between synthetic and recorded waveforms. Figure 2c shows a comparison between observed and synthetic waveforms, and a fairly good fitting is obtained. A mutual time lag is found between synthetic and recorded waveform due to error in epicentral distances vis-à-vis Green's functions, and the error is taken care using waveform cross-correlation. It is clear that the inversion variance reaches its minimal value at a focal depth of 15 km (Fig. 2d). The best focal depth and the best mechanism solution are obtained by minimizing the misfit function of the

Fig. 2 Plots in **a** indicate a complete time series of an event of magnitude M_w 4.5 occurred on July 28, 2011. Various phases are also clearly marked on the time series. The first trace for all three stations shows unfiltered time series of the event recorded on Z-components with marking of P-phase. The second trace for all the stations is filtered time series used for clear marking of Pnl, and the third trace is used for clear marking of Rayleigh phase on vertical and radial components, respectively. Tangential component is used for marking Love phase. **b** Optimal focal mechanism solution (beach ball) **c** Comparison between synthetic (red traces) and observed (black traces) waveforms for finding optimal solution. Radial and vertical components of P- and S-waves are denoted by Pr, Pz and Sr, Sz, respectively. Two numerical values are written in each component trace: The top one is the time shift in seconds and the bottom one indicates the correlation coefficient. Epicentral distances in km are written below the station name. **d** Plot for waveform misfit variation with source depth for optimal focal mechanism solution. Moment magnitude of earthquake is written on the top of each beach ball

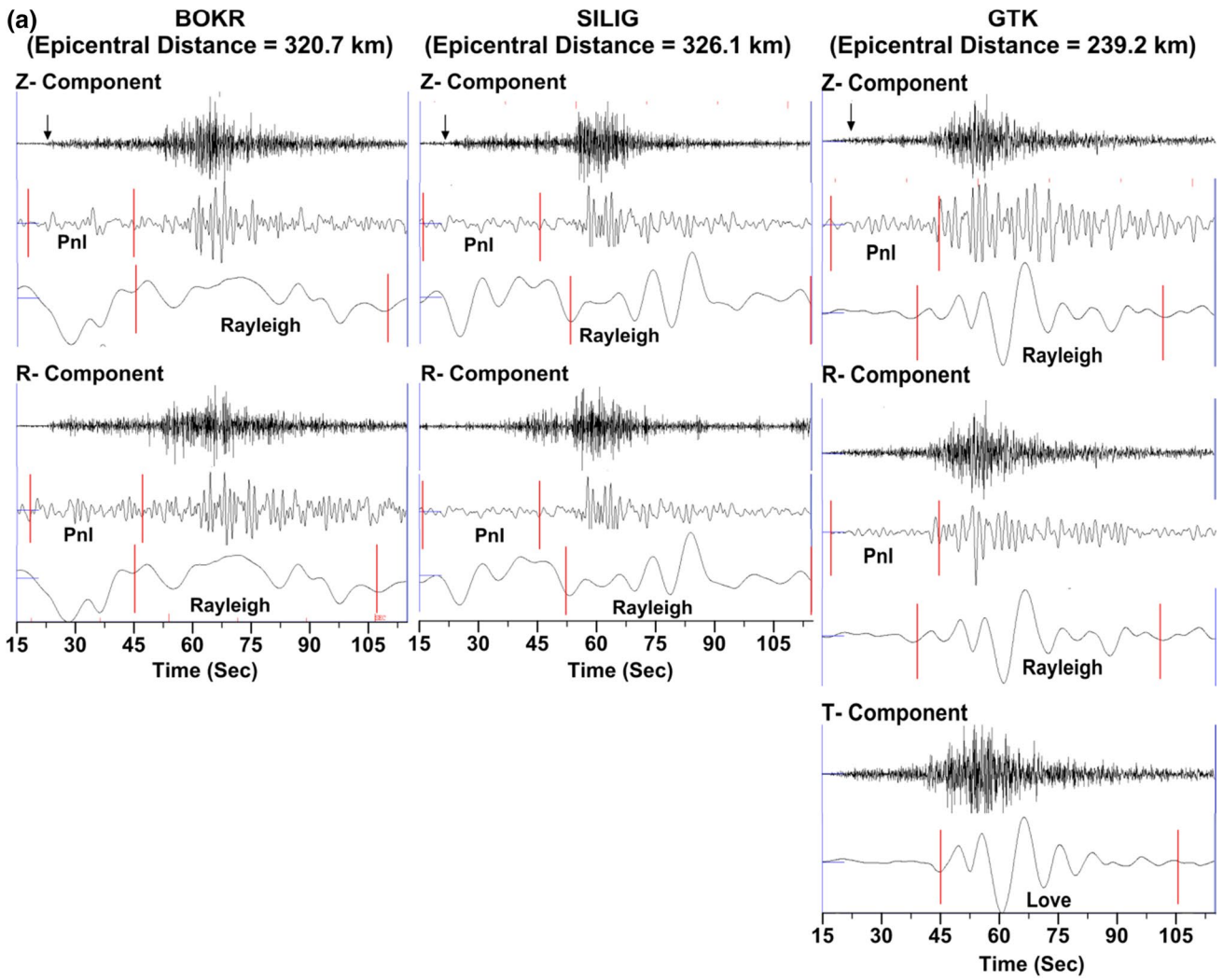
(a)
BOKR
(Epicentral Distance = 320.7 km)
SILIG
(Epicentral Distance = 326.1 km)
GTK
(Epicentral Distance = 239.2 km)
Z- Component
Pnl
Rayleigh
R- Component
T- Component
Love
15 30 45 60 75 90 105
Time (Sec)

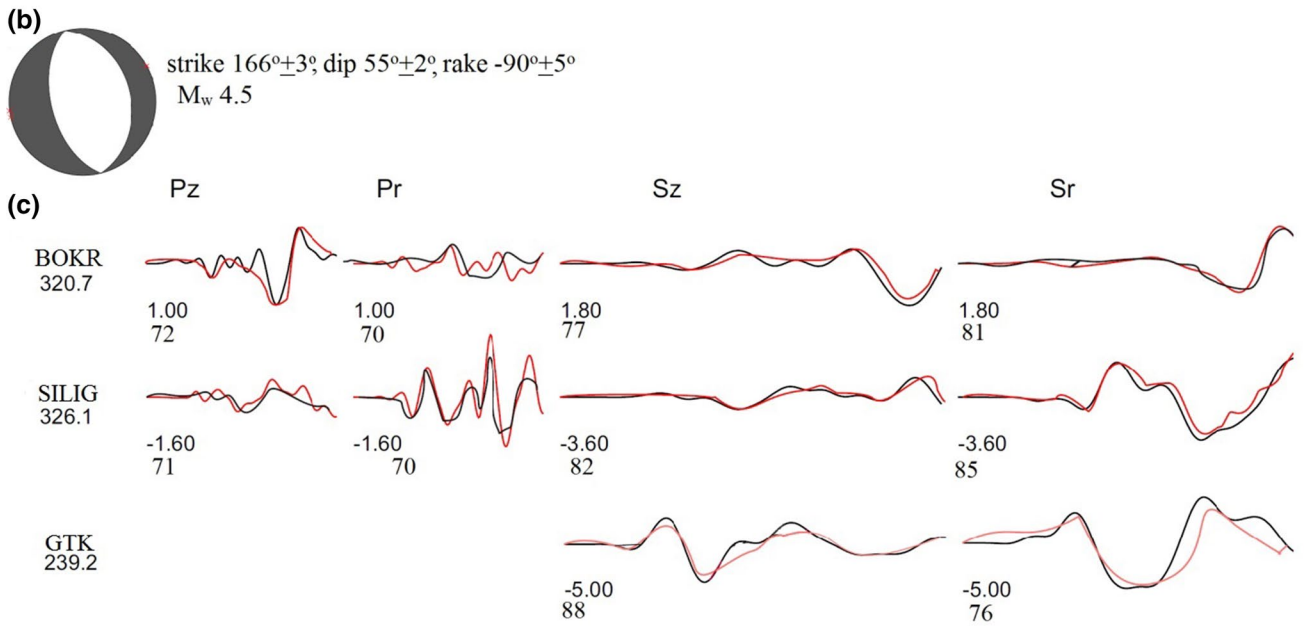
(b)
strike 166°±3°, dip 55°±2°, rake -90°±5°
Mw 4.5
(c)
Pz
Pr
Sz
Sr
BOKR
320.7
1.00
72
1.00
70
1.80
77
1.80
81
SILIG
326.1
-1.60
71
-1.60
70
-3.60
82
-3.60
85
GTK
239.2
-5.00
88
-5.00
76

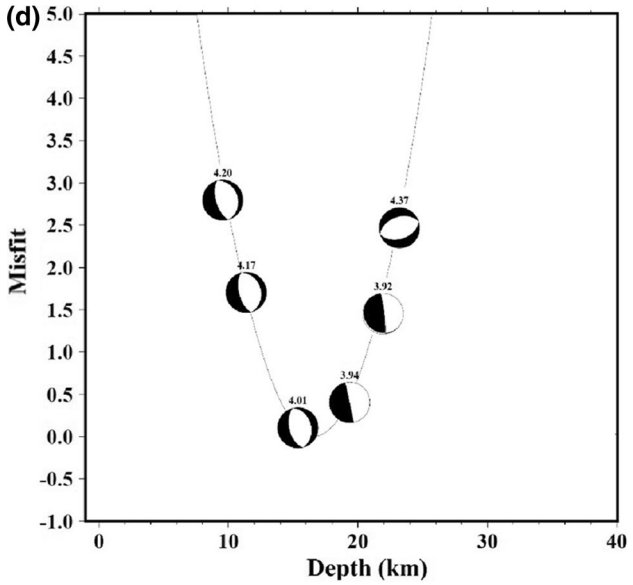

Fig. 2 (continued)

inversion (Figs. 2, 3; Table 3). Synthetic and recorded seismograms of each phase window of P- and S-waves over different frequency bands are independently evaluated for best fit. This method uses parting of P- and S-waves to enhance the impact of P-wave as well as the resolution of source parameter, mainly source depth. This method improves the result of relatively large-amplitude arrivals. After computing the focal mechanism of 4 best recorded events (Fig. 4), the scalar moment M_0 is computed using least-square fit between amplitudes of the synthetics and records of entire stations.

Stress inversion

Totally, 34 events (Fig. 5) were considered for stress inversion analysis using the STRESSINVERSE code of Václav Vavryčuk (2014). STRESSINVERSE procedure of Václav Vavryčuk (2014) is a modified method of Micheal (1984). Although Micheal method is quite fast and reasonably accurate for the computation of the principal stresses, it does not give accurate shape ratio if the nodal and auxiliary planes are not properly selected. Instead, the stress inversion method of Václav Vavryčuk (2014) takes care of the selection of the fault parameters using joint inversion of stress and nodal plane parameters.

Of the 34 events, focal mechanism solutions of 12 events of magnitude $M_W \geq 2.5$, are selected for Zone I and lie between 20° and 26° *N* (Figs. 1, 4; Table 3). Of the 12 focal mechanisms, 4 were computed under the present study using the CAP method, 1 has been taken from CMT Harvard catalog, 2 from Kayal et al. (2009), while the other 5 have been taken from Biswas and Mandal (2017). In addition, focal mechanism parameters of 8 events of Zone I, lying in the depth range of 0–20 km, were analyzed through stress inversion to find the optimum stress field prevailing in the region. Remaining 21 focal mechanism solutions of earthquakes of magnitude $M_W > 4.5$ that occurred during 1976–2017 between latitudes 26° and 28° *N* in the Himalayan foothills have been compiled from the CMT Harvard catalog (Table 5) and demarcated by Zone II (Fig. 1). Based on the diversity of focal mechanisms, Zone II has been divided over two depth ranges: 8 events for shallow part (0–20 km) and 13 events for deeper part (> 20 km). For high-resolution stress inversion analysis, Zone II has been further divided into Zones II(a) and II(b) at longitude 87.5° *E* (Fig. 1) based on the tectonics of the area (Valdiya 1976; Dasgupta et al. 1987; Singh et al. 2007; Sahu et al. 2010). Solutions of 8 events, occurred up to a depth of 30 km, were considered for Zone II(a) to compute the optimum inverted solution. To avoid scattered solution of inverted stress parameters for the deeper events, 4 events for the shallower (up to 30 km depth) part of Zone II(b) were considered for optimum stress inverted solution.

Strike of the fault planes is corrected by using the fault variability constraint, and stress is computed in each iteration giving an overall friction on the fault. We compute three principal stress variables (σ_1, σ_2 and σ_3) and shape ratio (R) with the help of stress inversion analysis (Fig. 6; Table 6). The deviations of the maximum compressive stress directions for respective zones have been computed (Fig. 6). The stress tensors were categorized into extensional strike-slip (ESS), pure strike-slip (PSS), pure compression (PC), radial compression (RC), compressional strike-slip (CSS) and semi-compressional strike-slip (SCSS) in a manner of relative magnitude of the intermediate (σ_2) axis (Table 6) and shape ratio R (Delvaux et al. 1995; Khan et al. 2019; Shamim et al. 2019).

Results

Focal mechanism

We estimate fault plane solutions of 4 best recorded events (event nos. 4, 5, 6, 7, Table 3) out of 16 events (Table 2) for understanding the seismoteconics of the area (Fig. 4). The strike, dip and rake of nodal plane 1 for event 4 of magnitude $M_w = 4.1$ were 130°, 82°, and − 180°, whereas 40°, 90° and − 8° for nodal plane 2 (Fig. 4; Table 3). It was occurred on June 6, 2008, near the Indo-Gangetic Plain and associated a throw on a vertical dipping plane and was dominated by strike-slip motion. The azimuth and plunge of P-axis were 310° and 6°, and the T-axis was oriented horizontally along

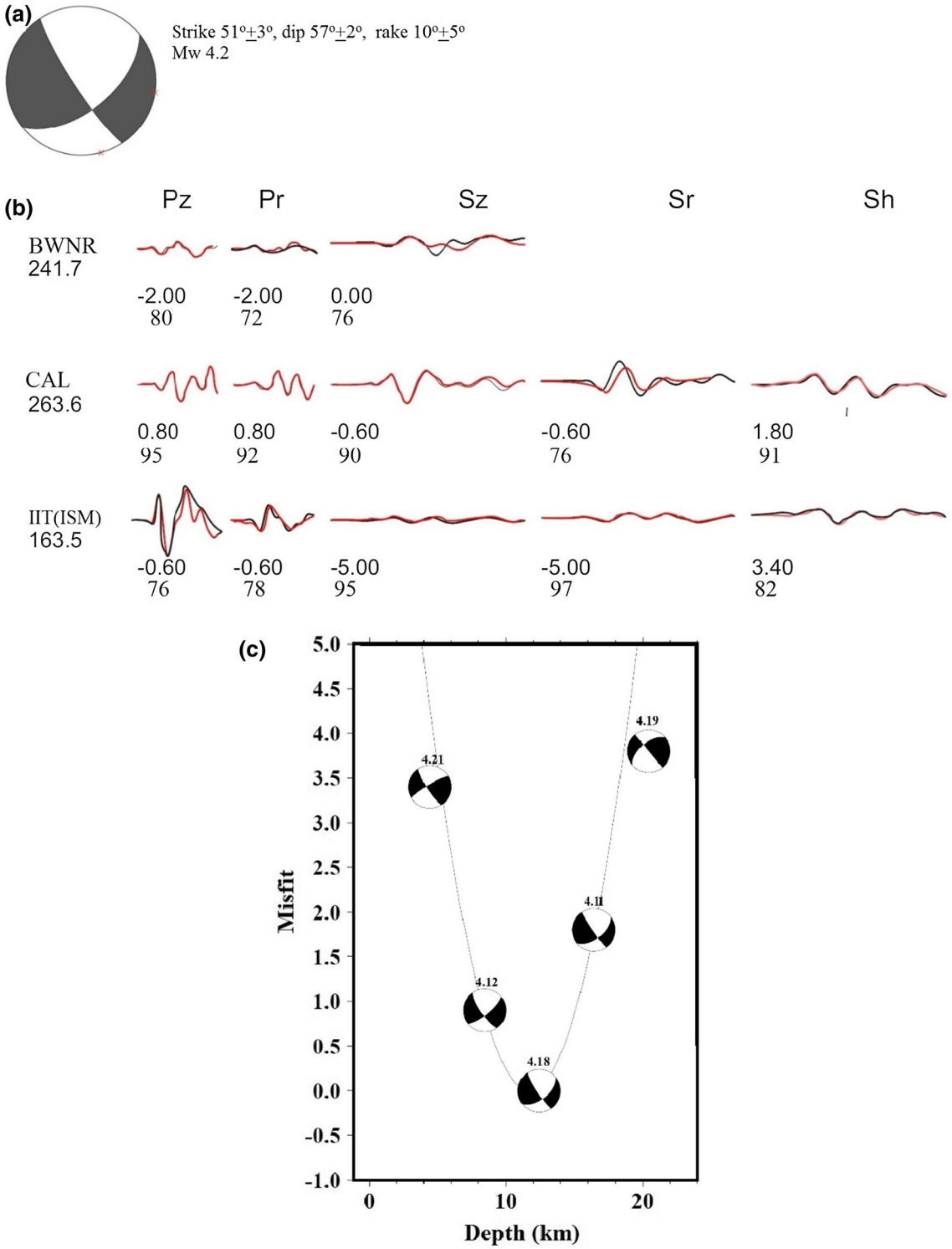

Fig. 3 Plots indicate the methodology of computation of focal mechanism. **a** Optimal focal mechanism solution (beach ball) for March 26, 2009, M_w 4.2 earthquake. **b** Comparison between synthetic (red traces) and observed (black traces) waveforms for finding optimal solution. Radial and vertical components of P- and S-waves are denoted by Pr, Pz and Sr, Sz, respectively. Two numerical values are written in each component trace: The top one is the time shift in seconds, and the bottom one shows the correlation coefficient. Epicentral distance in km is written below the station name. **c** Plot for waveform misfit variation with source depth for optimal focal mechanism solution. Moment magnitude of earthquake is written on the top of each beach ball

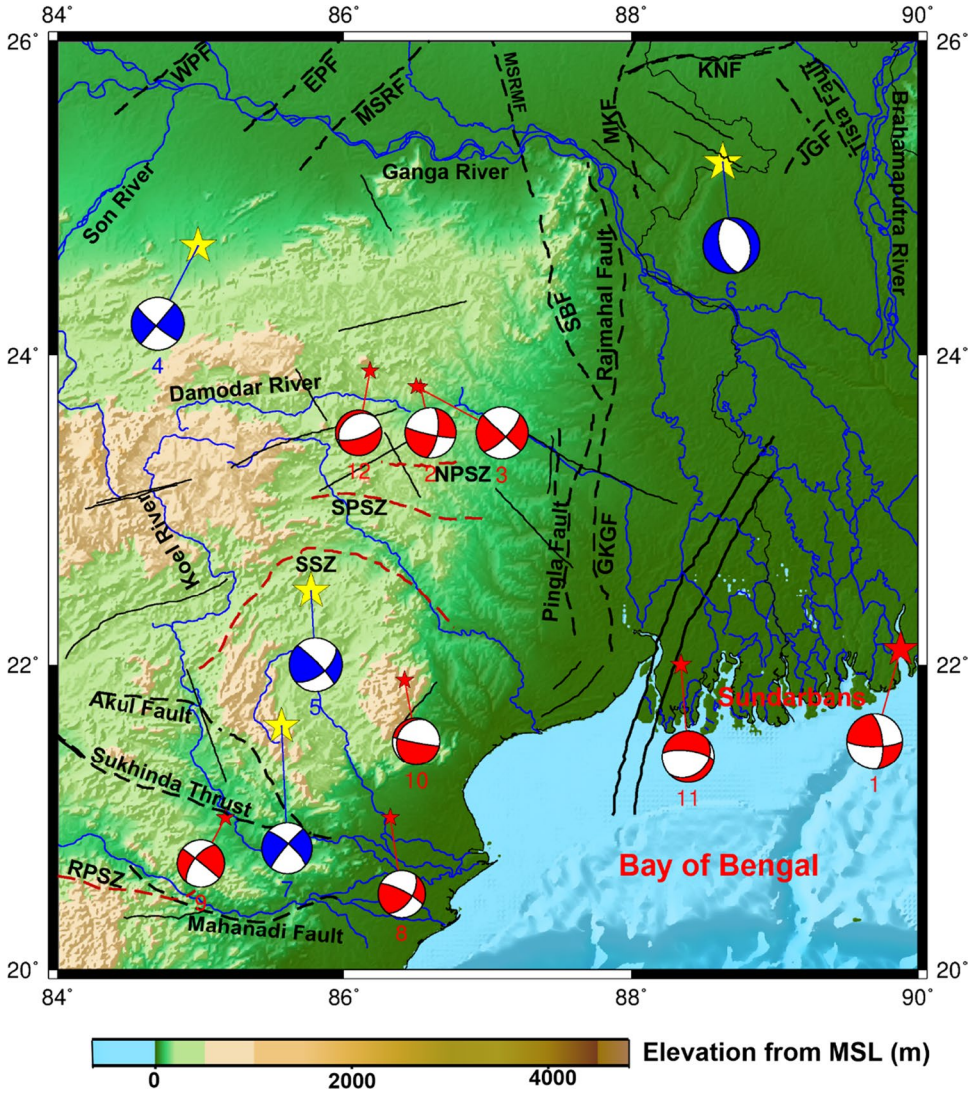

Fig. 4 Best computed focal mechanisms (blue-colored beach ball) for Eastern Indian Shield Region using the CAP method. Yellow stars represent the events precisely located by IMD and IIT(ISM) seismic stations, and red beach ball for earthquake source mechanisms that were compiled from Biswas and Mandal (2017) and Kayal et al. (2009)

E–W direction (Table 4). Event 5 of magnitude $M_w = 4.2$ occurred on March 26, 2009, in the area near Singhbhum shear zone. The strike, dip and rake of nodal planes 1 and 2 were 51°, 57° and 10° and 315°, 81° and 146°, respectively (Fig. 3; Table 3). Beach ball plot of this event shows a strike-slip-dominated movement (Fig. 4). Orientation of P-axis is found with an azimuth 220° and a plunge of 16°, while an azimuth of 268° and a plunge of 29° for T-axis. This indicates nearly horizontal compression along NE–SW direction and predominant tension along E–W direction (Table 4). Event 6 of magnitude $M_W = 4.5$ occurred on July 28, 2011, right within the zone between the southward turning of the Ganga and Brahmaputra Rivers. Strike, dip and rake are 346°, 35° and − 90° and 166°, 55° and − 90° for nodal planes 1 and 2 (Fig. 4; Table 3), and the source was dominated by normal faulting with P-axis along ~ NE–SW (azimuth = 231° and plunge = 80°) and T-axis was acting along ~ E–W directions plunging horizontally (azimuth = 256° and plunge = 10°). Event 7 of magnitude $M_W = 3.9$ occurred on November 5, 2011, at latitude 21.50°N and longitude 85.56°E. Fault plane solution of this event illustrates strike-slip-dominated movement along NW–SE direction. Strike, dip and rake are 311°, 77° and − 172° and 220°, 83° and − 13° for nodal planes 1 and 2 (Fig. 4; Table 3). P-axis was predominantly acting along SE–NW direction and plunging almost horizontally, and the T-axis was performing along E–W direction with a plunge of 31° (Table 4).

Stress inversion

Computed focal parameters of 4 events were compiled with focal parameters of other 8 events taken from Kayal et al. (2009), Biswas and Mandal (2017) and Harvard CMT catalog. Most of these events were dominated by strike-slip movements and grouped in Zone I. The maximum compressive stress axis (σ_1) was found to be aligned

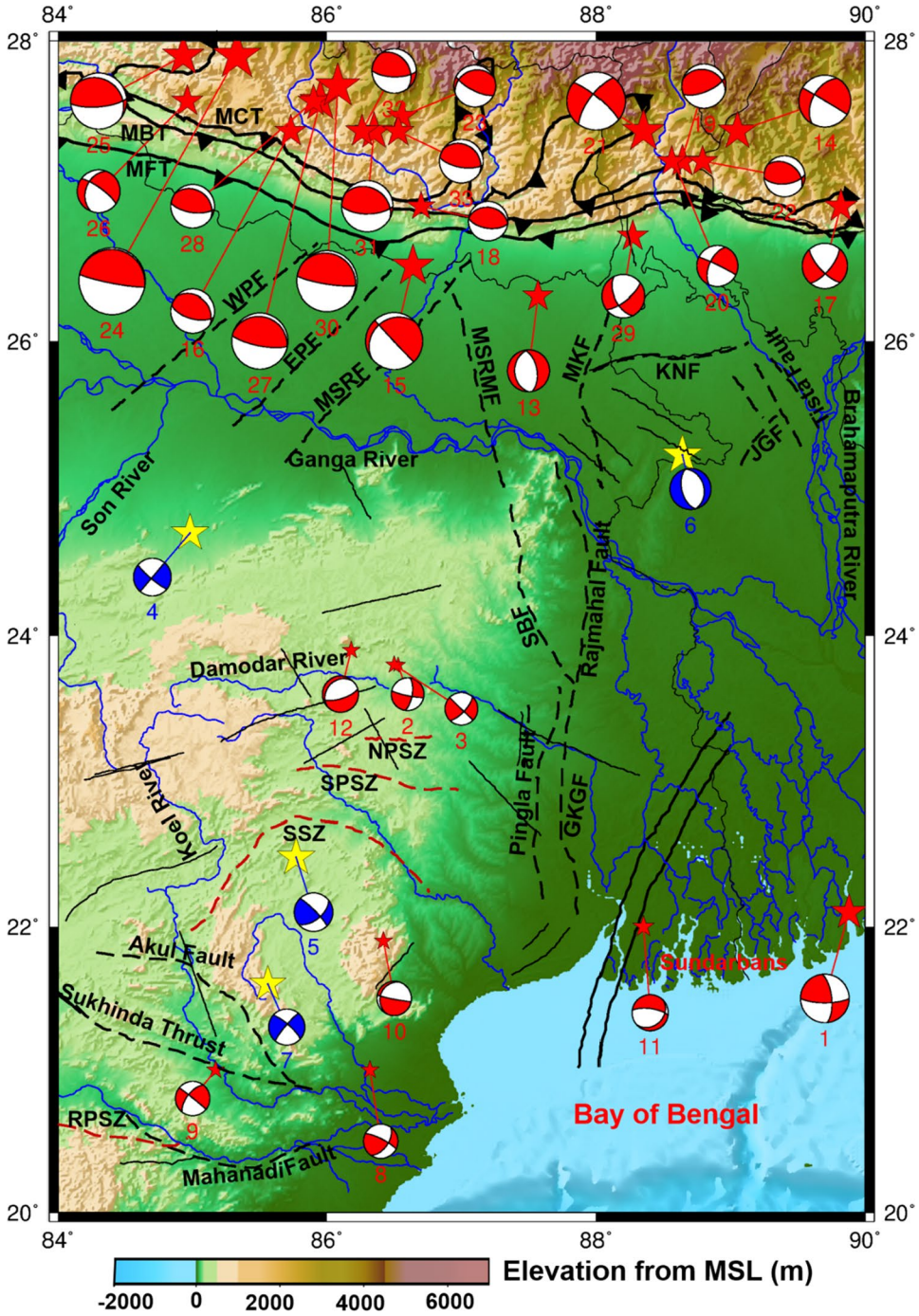

Fig. 5 Seismicity and source mechanisms illustrate the detailed tectonics of the study area and adjacent regions

almost along N–S having a plunge of 36°, whereas the minimum compressive stress axis (σ_3) was striking along E–W direction and plunging horizontally. However, the intermediate stress (σ_2) was operative along N–S having a plunge of 53°. The shape ratio and frictional coefficient were found to be 0.21 and 0.45 for the Zone I. The strike, dip and rake of the jointly derived fault plane are 155°, 76° and − 145°, respectively (Fig. 6a; Table 6). Zone I is further subdivided into shallower (depth ≤ 20 km) and deeper (depth > 20 km) parts, which contains 8 and 4 events, respectively. It was found that the σ_1 was acting along N–S direction with a plunge of 2.6°, whereas σ_3 was directing along E–W having a plunge of 5° for the shallower part, while σ_2 is dipping steeply with an azimuth of 118°. The computed shape ratio and frictional coefficient are 0.12 and 0.40, respectively (Fig. 6b; Table 6). The strike, dip and rake of the derived focal plane are 327°, 87° and 174°.

Zone II is passing across the Himalayan Foothills and Lower Himalaya. In-depth investigation has been carried out to find the genetic linkage between the strike-slip-dominated

Table 4 Stress parameters of earthquake events occurred in Zone I

Event no.	P-axis		T-axis		Sources
	Azimuth (deg.)	Plunge (deg.)	Azimuth (deg.)	Plunge (deg.)	
1	221	6	314	27	Global CMT
2	328	21	234	11	Kayal et al. (2009)
3	360	13	267	12	Kayal et al. (2009)
4	310	6	85	6	Present study
5	220	16	268	29	Present study
6	231	80	256	10	Present study
7	136	22	276	31	Present study
8	350	15	250	33	Biswas and Mandal (2017)
9	176	20	80	17	Biswas and Mandal (2017)
10	31	46	174	38	Biswas and Mandal (2017)
11	217	58	352	24	Biswas and Mandal (2017)
12	360	64	155	24	Biswas and Mandal (2017)

movement operative to the south of Zone II and the evolving tectonics of the Nepal–Bihar–Sikkim–Darjeeling segment of the Himalayan Belt. First, the stress inversion of 21 focal mechanisms of events occurring in Zone II has been carried out, and it is found that the σ_1 is oriented along an azimuth of 190° with a plunge of 29°, whereas the σ_3 is acting nearly horizontally along E–W side (Fig. 6c; Table 6), while σ_2 is operative at an azimuth of 339° with a plunge of 56°. The computed shape ratio is found to be 0.81, and the overall friction is 0.4. The derived strike, dip and rake are found to be 333°, 86° and − 146°, respectively (Fig. 6c; Table 6). Zone II is further subdivided into two depth ranges: Shallower part containing 8 events lies at ≤ 20 km, and deeper part containing 13 events lies at depth > 20 km. The azimuth of the predominant direction of σ_1 is 193° with a plunge of 32°, whereas the σ_3 is operating at an azimuth of 346° with a plunge of 54° for the shallower part. The σ_2 is acting along E–W horizontally. The shape ratio and optimum frictional coefficient are 0.88 and 0.5, respectively. The strike, dip and rake of the derived fault plane are 89°, 66° and 75°, respectively (Fig. 6d; Table 6). Joint stress inversion of 13 deeper events of Zone II shows that σ_1 is dipping at 27° and striking along NNE–SSW direction, whereas σ_2 is acting predominantly along NNW–SSE direction with a plunge of 58°. The σ_3 is almost acting along E–W direction horizontally. The computed shape ratio and friction are 0.67 and 0.45 (Fig. 6e; Table 6). The strike, dip and rake of the computed fault plane are 159°, 84° and 155°, respectively.

The thrust-dominated movements in the western segment and the strike-slip-dominated movements in the eastern segment motivated us to divide Zone II into Zones II(a) (8 events) and II(b) (4 events) (Fig. 1). The thrust-dominated 2015 Mw 7.9 Nepal earthquake and strike-slip-dominated 2011 M_w 6.9 Sikkim earthquake were also occurred in Zones II(a) and II(b), respectively. The σ_1 is found to be oriented along 200° azimuth with a plunge of 27.7°, and the σ_3 is operating at an azimuth of 349° with a plunge of 58° for Zone II(a). The intermediate σ_2 is acting at 102° azimuth and plunging at 13°. The shape ratio and overall friction are 0.61 and 0.4, respectively. The strike, dip and rake of the computed fault plane are 95°, 63° and 75° (Fig. 6f; Table 6). Joint inversion of focal parameters of 4 events in Zone II (b) shows that σ_1 is of azimuth 357.6° and plunge 3.1°, whereas σ_3 is of azimuth 267° and plunge 3.6°, while the σ_2 is acting along a direction of azimuth 128° having a plunge of 85°. The strike, dip and rake of the fault plane are 95.8°, 63.5° and 75°, respectively. The computed shape ratio and optimum friction are 0.78 and 0.9 (Fig. 6g; Table 6).

Discussions

Although the 7 seismic stations spreading over the study area recorded the 16 earthquake events, best records of 4 events were used for focal mechanism parameters computation in the present study. These 4 focal mechanism parameters are grouped with another 8 focal parameters compiled from other catalogs (discussed above) and found that 8 events (1–5, 7–9) were dominated with strike-slip movements, while 4 events (6, 10–12) were dominated by normal-type faulting (Figs. 4, 5). The hypocenters are mainly distributed in the shallower part, located in the upper crust, in this area. Stress inversion results show that the Zone I is under semi-compressive stress field with a predominant strike-slip component along the NNW–SSE direction (Table 6; Fig. 7i), while the Zone II, lying in the Himalayan Foothills and Lower Himalaya, is under extensional stress field with a strike-slip component almost along the NNW-SSE direction. Figure 7ii shows the operative stress fields at shallower (≤ 20 km) and deeper (> 20 km) parts of the lithosphere. The shallower part is dominated under radial compression (RC), whereas the deeper part is under pure strike-slip (PSS) regime (Table 6). The shallower part of Zone I (depth ≤ 20 km) is under the influence of compressive strike-slip

Table 5 Source parameters of earthquake events occurred in Zone II

Event no.	Date	Time (hr:min:sec)	Lat. (°N)	Long. (°E)	Mag. (M_W)	Depth (km)	NP1			NP2			Source
							Strike (deg.)	Dip (deg.)	Rake (deg.)	Strike (deg.)	Dip (deg.)	Rake (deg.)	
13	19-06-1979	16:29:12.4	26.3	87.57	5	24	179	34	−82	350	57	−95	Global CMT
14	19-11-1980	19: 0:55.9	27.4	89.05	6.2	44.1	209	51	−2	301	89	−141	Global CMT
15	20-08-1988	23: 9:15.9	26.5	86.64	6.8	34.7	230	23	2	137	89	113	Global CMT
16	29-10-1988	9:11: 0.8	27.4	85.73	5.2	18	309	30	109	106	62	79	Global CMT
17	25-03-2003	18:51:30.7	26.9	89.82	5.4	55.8	40	70	−21	137	71	−159	Global CMT
18	03–02-2006	1:57:51.7	26.9	86.7	4.7	30.9	279	30	91	98	60	90	Global CMT
19	14-02-2006	0:55:28.8	27.2	88.64	5.3	19.2	287	27	126	68	68	73	Global CMT
20	20-05-2007	14:18:21.6	27.2	88.56	4.9	13.6	204	58	−4	296	86	−148	Global CMT
21	18–09-2011	12:40:59.9	27.4	88.35	6.9	46	216	72	−12	310	79	−162	Global CMT
22	03-10-2013	6:12:43.8	27.2	88.79	4.9	27	304	37	123	85	59	67	Global CMT
23	18–12-2014	15:32:15.4	27.5	86.56	5	30.3	248	26	44	117	72	110	Global CMT
24	25-04-2015	6:11:58.6	27.9	85.33	7.9	12	287	6	96	101	84	89	Global CMT
25	25–04-2015	6:45:29.4	27.9	84.93	6.7	21	308	23	131	85	73	74	Global CMT
26	25-04-2015	23:16:18.1	27.6	84.96	5.1	15	201	40	−20	306	77	−129	Global CMT
27	26–04-2015	7: 9:20.1	27.6	85.95	6.7	20.6	289	14	98	101	76	88	Global CMT
28	26-04-2015	16:26: 9.6	27.6	85.9	5.2	19.8	305	26	115	98	66	78	Global CMT
29	27-04-2015	12:35:52.9	26.7	88.27	5.1	26.5	154	57	−157	52	71	−35	Global CMT
30	12–05-2015	7: 5:27.5	27.7	86.08	7.2	12	307	11	117	99	81	85	Global CMT
31	12-05-2015	7:36:59.6	27.4	86.35	6.1	20.1	299	28	116	90	65	77	Global CMT
32	16-05-2015	11:34:12.6	27.4	86.26	5.3	12	324	34	138	91	68	63	Global CMT
33	27-11-2016	23:35:26.0	27.4	86.53	5.2	35.4	305	24	113	100	67	80	Global CMT

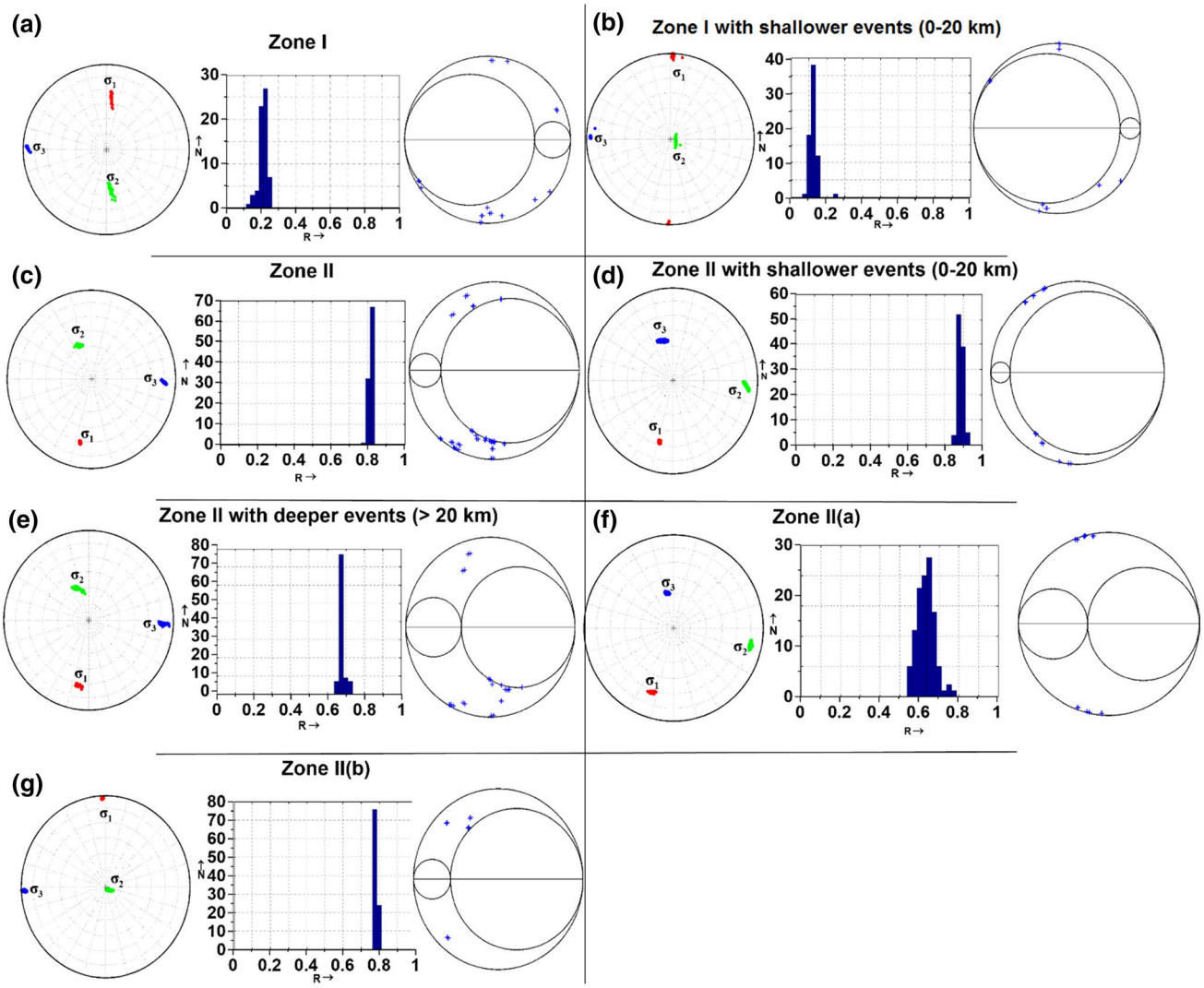

Fig. 6 Stress inversion results (after Vavryčuk 2014) for earthquakes happened in Zone I and Zone II (explained in Figs. 1 and 7, Table 6)

regime (CSS). Based on the focal mechanisms, Zone II was divided into Zone IIa (western segment) and Zone IIb (eastern segment), and the shallower levels (depth ≤ 30 km) of these two zones are dominated by pure compression (PC) and pure strike-slip (PSS), respectively (Fig. 7iii).

Although the overall tectonic processes are E–W extensive strike-slip (Fig. 7i) in this Himalayan segment (Zone II), the shallower and deeper parts of the converging lithosphere are of different tectonic domains (i.e., RC and PSS, Fig. 7ii), even the western (Zone IIa) and eastern (Zone IIb) segments are dominated differently with PC and PSS stress regimes (Fig. 7iii). Thrust faulting processes in the western segment operative under overall compressive stress field might be indicating that the Indian lithosphere is under compressional tectonics and complies with the thrust-dominated movement during incidences of 2015 M_w 7.9 and 2015 M_w 7.2 Nepal mainshocks and other major aftershocks (Fig. 2 of Khan et al. 2017). The 1934 M_w 8.11 North Bihar earthquake, which occurred at shallower level (focal depth = 20 km) in the western segment and was dominated by thrust faulting (Ansari and Khan 2014), also supports this inference. The strike-slip-dominated faulting process at deeper level during 1988 M_w 6.8 North Bihar earthquake (focal depth = 34.7 km) corroborates the PSS stress regime at deeper level in Zone II. The strike-slip-dominated movements during occurrences of 2011 M_w 6.9 Sikkim earthquake and its majority of aftershocks (Fig. 3 of Kumar et al. 2019; Paul et al. 2015) comply with the PSS stress regime operative in the eastern segment. The Monghyr–Saharsa Ridge (MSR) along with its two marginal faults (Fig. 1) is interacting through the boundary between eastern and western segments with the Himalayan trench, apparently controlling the two distinct tectonics on either sides of longitude 87.5° E. Seismic anisotropy analysis also shows the diversity in tectonics in these two

Table 6 Values of σ_1 (maximum compressive stress), σ_2 (intermediate compressive stress), σ_3 (minimum compressive stress), shape ratio (R), frictional coefficient and tensor type obtained from stress inversion and following Fig. 3 of Delvaux et al., 1995)

Various zones	Total no. of events	σ_1 (Az/Pl)(deg.)	Mean error (deg.)	σ_2 (Az/Pl) (deg.)	Mean error (deg.)	σ_3 (Az/Pl) (deg.)	Mean error (deg.)	R	F	Fault plane			Tensor type
										Strike (deg.)	Dip (deg.)	Rake (deg.)	
Zone I(20°N–26°N)	12	5/36	13.6	174/53	14.5	271/5	5.5	0.21	0.45	155	76	−145	SCSS
Zone I with shallow events (depth ≤ 20 km)	8	1.7/2.6	7.3	118/84	7.3	271/5	8.0	0.12	0.40	327	87	174	CSS
Zone II (26°N–28°N)	21	190/29	2.4	339/56	4.6	92/14	4.3	0.81	0.4	333	86	−146	ESS
Zone II with shallow events (depth ≤ 20 km)	8	193/32	2.0	95/13	6.2	346/54	6.2	0.88	0.5	89	66	75	RC
Zone II with deep events (depth ≥ 20 km)	13	191/27	5.0	338/58	8.8	93/14	9.4	0.67	0.45	159	84	155	PSS
Zone II (a) (84°E–87.5°E)	8	200/27.7	3.7	102/13	4.1	349/58	2.4	0.61	0.4	95	63	75	PC
Zone II (b) (87.5°E–90°E)	4	357.6/3.1	1.5	128/85	4.4	267/3.6	4.5	0.78	0.9	95.8	63.5	75	PSS

PSS pure strike-slip, *PC* pure compression, *ESS* extensional strike-slip, *RC* radial compression, *CSS* compressional strike-slip, *SCSS* semi-compressional strike-slip

segments (Singh et al. 2007). The sudden changes in trends of tectonic lineaments and faults toward north are found to be converging surrounding this junction. Ansari et al. (2014) found strike-slip-dominated faulting processes in the eastern Himalayan Foothills and explained to be caused by shear movements of the converging lithosphere and is principally controlled by the changes in plate obliquity. Toward south, the eastward trend of Ganga River is turning at its downstream, where the sediment thickness increases sharply (Roy and Chatterjee 2015). The PSS stress regime at the shallower part of the eastern segment as well as in the deeper part of Zone II might be accounting the eastward convergence and subduction of the Indian lithosphere beneath the floating Myanmar micro-plate (Khan 2005). The normal faulting-associated source kinematics of the earthquakes adjacent to the zone of southward migration of the Ganga River might have been affected by the eastward extension of the converging lithosphere (Curray and Moore 1974; Curray et al. 1979; Mitchell 1981) and account for rift-controlled extension in the Bengal Basin (Ismaiel et al. 2019; Khan and Chouhan 1996; Roy and Chatterjee 2015). A sudden increase in the depth of the basement passed the Eastern Indian Shield toward east, where the lithosphere begins to flexed, and the extension at the shallow level is dominant and advocates the stretching of the lithosphere (Isacks et al. 1968; Condie 1982). In Bengal basin, various crustal features along with normal and en-echelon faulting, e.g., Hing Zone (Ismaiel et al. 2019; Alam et al. 2003), indicate that the basin has been affected by extensional forces due to the outpouring of basaltic lava (i.e., Rajmahal Trap) during Cretaceous prior to tertiary deposition (Mall et al. 1999; Desikachar 1974). Kaila et al. (1992) showed by deep seismic sounding studies (DSS) that the crystalline basement of Bengal basin is dipping toward east up to a maximum depth of 14 km. The Bouguer gravity anomaly decreases from + 10 to − 12 mGal from west to east, which supports the dipping of basement toward east (Reddy et al. 1993), where the Moho varies from 26 to 36 km with a prominent domal feature of about 40 km (Reddy et al. 1993; Mall et al. 1999).

There are several factors which control faulting processes vis-à-vis stress accumulation like stress intensification adjacent to plutons (Campbell 1978; Stevenson et al. 2006), lithospheric flexure (Bilham et al. 2003; Khan 2007; Khan and Chakraborty, 2009), confined strain in middle to lower crust (Zoback et al. 1985), stress amplification near regional gravity lows (Chandrasekhar et al. 2005), stress buildup caused by lateral deviation of density (Sonder 1990), confined stress accumulation in response to plate tectonic forces in the neighborhood of crisscrossing faults (Talwani 1988; Khan et al. 2009), etc., in stable continental regions. There is a reliable pattern of a complete N–S to NNE compression indicating a shrinkage of the Indian Plate at an amount of ~ 1–10 mm/year (Bilham and Gaur 2000). Figure 7i, iii

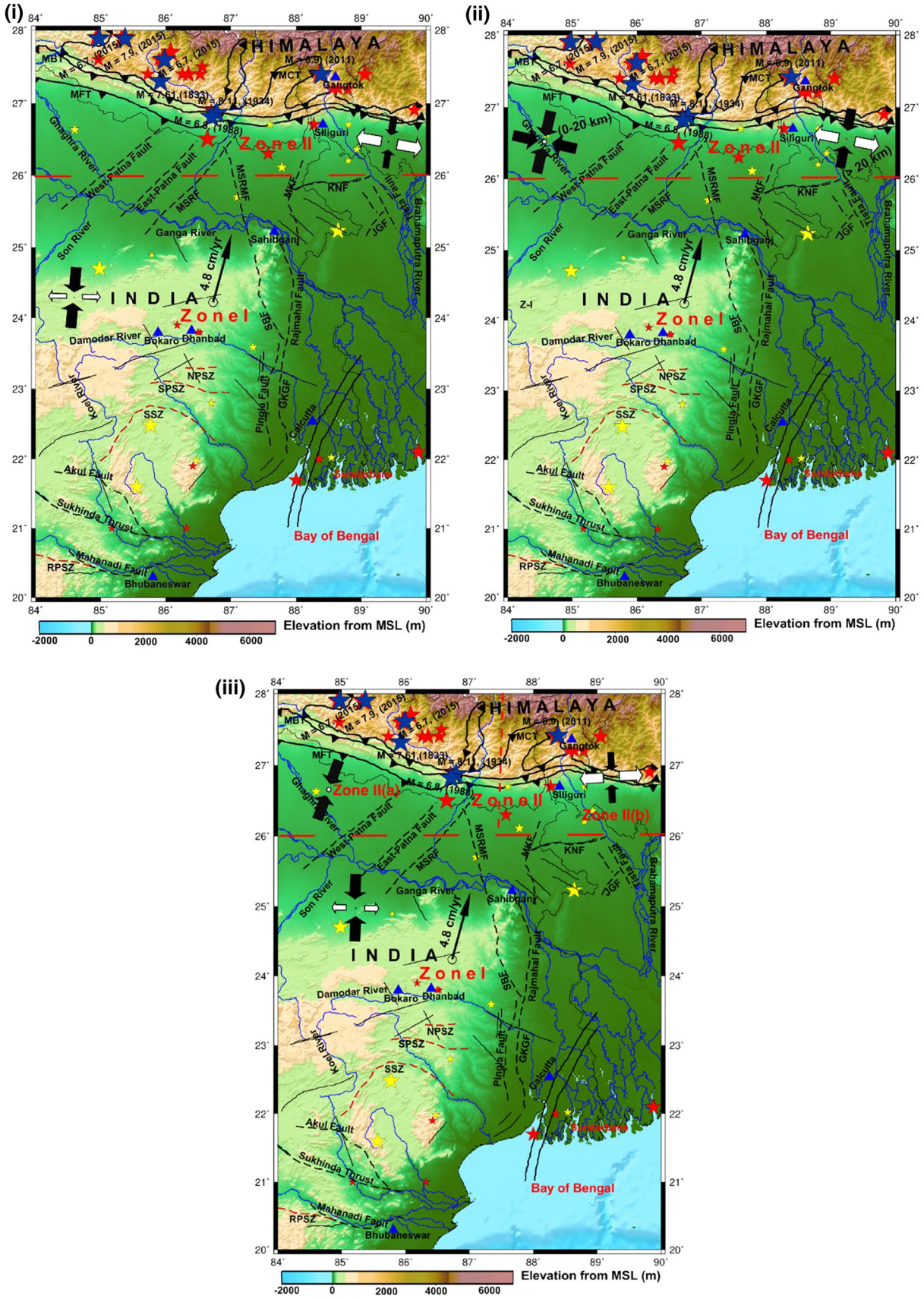
(i)
(ii)
(iii)
HIMALAYA
INDIA
Zone I
Zone II
Zone II(a)
Zone II(b)
Z-I
MBT
MCT
MFT
M = 6.7, (2015)
M = 7.9, (2015)
M = 6.9 (2011)
M = 7.61 (1833)
M = 8.11, (1934)
M = 6.8 (1988)
Gangtok
Siliguri
Ghaghra River
West Patna Fault
East Patna Fault
MSRF
MSRMF
MKF
KNF
JGF
Tista Fault
Brahamaputra River
Son River
Ganga River
Sahibganj
4.8 cm/yr
(0-20 km)
(> 20 km)
SBF
Rajmahal Fault
Damodar River
Bokaro Dhanbad
Koel River
NPSZ
SPSZ
SSZ
Pingla Fault
GKGF
Calcutta
Sundarbans
Akul Fault
Sukhinda Thrust
Mahanadi Fault
RPSZ
Bhubaneswar
Bay of Bengal
Elevation from MSL (m)
-2000
0
2000
4000
6000

◂**Fig. 7** Maps illustrate the predominant operative stress fields for different tectonic domains. Stress patterns of Zone I and Zone II (**i**), shallower (≤ 20 km) and deeper levels (≥ 20 km) of Zone II (**ii**), and Zones II(a) and II(b) and shallower level (≤ 20 km) of Zone I (**iii**)

shows an operative strike-slip-dominated stress regime in the EIS region, and about 70% events are strike-slip-dominated movements with both P- and T-axes sloping sub-horizontally (Fig. 4; Table 5). It is thus clear that multiple processes are involved under changing environment of stress field thriving co-seismic slip along the preexisting fractures, seismicity, flexible flow of subcrustal rocks and inter-seismic strain accumulation (Singh et al. 2012, 2016). The alignment of the principle stress axes obtained from the inversion of earthquake focal mechanism parameters also indicates that the whole EIS province is controlled through the CSS and SCSS (Table 6). This pure strike-slip motion in the EIS might be genetically linked with the compressive stress regime in the Himalaya. It was also proposed elsewhere that the operative stress field in the continental interior has been rightly controlled by the convergence of the Indian lithosphere and its consequent resistance by the Himalayan orogeny (Khan et al. 2016, 2019).

Summary

Several crisscross faults, lineaments and three big rivers (Ganga, Brahmaputra and Damodar) have transformed the study area into a strange tectonic setting. Basement undulation with widely variable thickness of sediments and numerous hot springs with interspaced shear zones account for shallow-level deformation of the lithosphere, while on the north, the interacting domal shape basement (MSR) and the faults (e.g., MSRF, EPF, WPF) with the Foothills of the Himalayas are apparently controlling the tectonics of this area. The eastward convergence and subsequent subduction of the Indian lithosphere under the Myanmar plate started stretching and rifting in the basement of the Bengal Basin and enhanced accommodation of sediments in the graben (Ismaiel et al. 2019; Roy and Chatterjee 2015). The strike-slip-dominated movements supported by the focal mechanisms over the study area are likely caused by the north to north–northeast convergence of the Indian plate. Holocene-activated north–south trending faults over the shield area and the transecting faults near the Foothills of this part of the Himalayas might also be accounting some parts of the convergence of the Indian lithosphere. The thrust-dominated movements in the northwestern segment of the study area account for strong deformation of the converging lithosphere to the south of the Nepal Himalaya. The pure compression (PC, Fig. 7iii) in this segment supports this inference. Focal mechanisms of two events show normal faulting, either indicating that the stretching of the basement is still continued or subsidence is quite active. The E–W strike-parallel extension is found to be quite active in the northeastern part of the study area, and the operative stress field of pure strike-slip regime (Fig. 7iii) corroborates this views. The strike-slip-dominated faulting processes in the Foothills areas of northeastern part might be operative for shear movements of the converging lithosphere and is proposed to be controlled by changes in India plate obliquity toward north (Ansari et al. 2014). We therefore may propose that the PSS stress regime at the shallower part of the eastern segment as well as in the deeper part of Zone II might be accounting the eastward convergence and subduction of the Indian lithosphere under the floating Myanmar micro-plate. Finally, we can conclude that the entire EIS region is dominated by CSS and SCSS (Table 6) and might be genetically linked with the compressive stress regime in the Himalaya.

Acknowledgements We are grateful to the Director, National Centre of Seismology (NCS), New Delhi, and J. L. Gautam, India Metrological Department (IMD), New Delhi, for providing the waveform data. Rashmi Singh is thankful to Mr. Raj Kumar Prasad for giving the earthquake waveform data recorded by the IIT(ISM) observatory. Rashmi Singh is also grateful to Ravi Kumar, Director General, Institute of Seismological Research, Gandhinagar, Gujarat, for his essential support during basic analysis of the focal mechanisms. The first author is thankful to Li Zhao for his support during computation of focal mechanism through personal communication. We are thankful to both the anonymous reviewers for suggesting modifications, which improved the quality of our manuscript significantly.

References

Acharyya SK, Gupta A, Orihashi Y (2010a) New U-Pb zircon ages from Palaeo-Mesoarchaean TTG gneisses of the Singhbhum Craton, eastern India. Geochem J 44:81–88

Acharyya SK, Gupta A, Orihashi Y (2010b) Neoarchaean-Palaeoproterozoic stratigraphy of the Dhanjori basin, Singhbhum craton, Eastern India: and recording of a few U-Pb zircon dates from its basal part. J Asian Earth Sci 39:527–536

Aggarwal SK, Khan PK, Mohanty SP, Roumeliotid Z (2016) Moment tensors, state of stress and their relation to faulting processes in Gujarat, western India. Phys Chem Earth Parts A/B/C 95:19–35

Alam M, Alam MM, Curray JR, Chowdhury MLR, Gani MR (2003) An overview of the sedimentary geology of the Bengal Basin in the regional tectonic framework and basin fill history. Sediment Geol 155:179–208

Ansari MA, Khan PK (2014) Occurrences of damaging earthquakes between the Himachal and Darjeeling Himalayas: tectonic implications. Acta Geophy 62:699–736

Ansari MA, Khan PK, Tiwari VM, Banerjee J (2014) Gravity anomalies, flexure, and deformation of the converging Indian lithosphere in Nepal and Sikkim Darjeeling Himalayas. Int J Earth Sci 103:1681–1697

Bapat A, Kulkarni RC, Guha SK (1983) Catalogue of Earthquakes in India and neighbourhood from historical period upto 1979. Indian Society of Earthquake Technology, Roorkee, India, p 211

Bilham R, Gaur VK (2000) The geodetic contribution to Indian seismotectonics. Curr Sci 79:1259–1269
Bilham R, Bendick R, Wallace K (2003) Flexure of the Indian plate and intraplate earthquakes. Proc Indian Acad Sci 112:315–329
Biswas SK (1987) Regional tectonic framework, structure and evolution of the western marginal basins of India. Tectonophysics 135:307–327
Biswas SK (2008) Geodynamics of Indian plate and evolution of the Mesozoic-Cenozoic basins. Mem J Geol Soc India 10:371–390
Biswas K, Mandal P (2017) Modeling of source parameters and moment tensors of local earthquakes occurring in the eastern Indian shield. J Geol Soc India 89:619–630
Campbell DL (1978) Investigation of the stress–concentration mechanism for intraplate earthquakes. Geophys Res Lett 5:477–479
Chandra U (1977) Earthquakes of Peninsular India - a seismotectonic study. Bull Seismol Soc Am 67:1387–1413
Chandra M, Mallik S, Das D, Thakur RK, Sinha MK (1993) Lithostatigraphy of Indian Petroliferous Basin. Document-IX. E, ONGC, Dehradun
Chandrasekhar DV, Singh B, Firozishah M, Mishra DC (2005) Analysis of gravity and magnetic anomalies of Kachchh rift basin, India and its comparison with the New Madrid seismic zone. Curr Sci 88:1601–1608
Condie KC (1982) Plate tectonics and crustal evolution, 2nd edn. Pergamon Press, Oxford, p 310
Curray JR, Moore DG (1974) Sedimentary and tectonic processes in the Bengal deep-sea fan and geosyncline. In: Burk CA, Drake CL (eds) The geology of continental margins. Springer, Berlin, pp 617–627
Curray JR, Moore DG, Lawver LA, Emmel FJ, Raitt RW, Henry M, Kieckhefe R (1979) Tectonics of the Andaman sea and Burma: convergent margins. In: Watkins JS, Montadert L, Dickerson PW (eds) Geological and geophysical investigations of continental margins, vol 29. American Association of Petroleum Geologists, Tulsa, pp 189–198
D'Amico S, Orecchio B, Presti D, Gervasi A, Guerra I, Neri G, Zhu L, Herrmann RB (2011) Testing the stability of moment tensor solutions for small moderate earthquakes in the Calabrian–Peloritan arc region. Boll Geofis Teor Appl 52:283–298
D'Amico S, Orecchio B, Presti D, Neri G, Wu W-N, Sandu I, Zhu L, Herrmann RB (2013) Source parameters of small and moderate earthquakes in the area of the 2009 L'Aquila seismic sequence (central Italy). Phys Chem Earth Parts A/B/C 63:77–91
D'Amico S, Cammarata L, Cangemi M, Cavallaro D (2014) Seismic moment tensors and regional stress in the area of the December 2013-January 2014, Matese earthquake sequence (Italy). J Geodyn 82:118–124
Dasgupta S, Mukhopadhyay M, Nandy DR (1987) Active transverse features in the central portions of the Himalaya. Tectonophysics 136:255–264
Dasgupta S, Mukhopadhyay B, Mukhopadhyay M, Nandy DR (2013) Role of transverse tectonics in the himalayan collision: further evidences from two contemporary earthquakes. J Geol Soc India 81:241–247
Desikachar SV (1974) A review of the tectonic and geological history of eastern India in terms of plate tectonic theory. J Geol Soc India 15:137–149
Delvaux D, Moeys R, Stapel G, Melnikov A, Ermikov V (1995) Palaeostress reconstruction and geodynamics of the Baikal region, Central Asia, Part I. Palaeoz Mesoz Pre-rift evol Tectonophys 252:61–101
DeMets C, Gordon RG, Argus DF, Stein S (1994) Effect of recent revisions to the geomagnetic reversal time scale on estimates of current plate motions. Geophys Res Lett 21:2191–2194
Dewey JF, Bird JM (1970) Mountain belts and the new global tectonics. J Geophys Res 75:2625–2647
Dietz RS, Holden JC (1970) Reconstruction of pangaea: breakup and dispersion of continents, permian to present. J Geophys Res 75:4939–4956
Gansser A (1964) Geology of the Himalayas. Interscience Publishers, London, p 289
Gupta S, Mohanty WK, Mandal A, Misra S (2014) Ancient terrane boundaries as probable seismic hazards: a case study from the northern boundary of the Eastern Ghats Belt. India Geosci Fron 5:17–24
Godin L, Harris BL (2014) Tracking basement cross-strike discontinuities in the Indian crust beneath the Himalayan orogen using gravity data – relationship to upper crustal faults. Geophys J Int 198:198–215
Isacks B, Oliver J, Sykes LR (1968) Seismology and the new global tectonics. J Geophys Res 73:5855–5899
Ismaiel M, Krishna KS, Srinivas K, Mishra J, Saha D (2019) Crustal architecture and Moho topography beneath the eastern Indian and Bangladesh margins—new insights on rift evolution and the continent–ocean boundary. J Geol Soc 176:553–573
Kaila KL, Reddy PR, Murty PRK, Venkateshwarlu N, Rao PK, Murty ASN, Prasad ASSSRS (1992) Structural trends of sedimentary sequence basement and Moho from DSS studies in West Bengal basin and inferred results. J Assoc Explor Geophys 3:145–151
Kayal JR, Srivastava VK, Bhattacharya SN, Khan PK, Chatterjee R (2009) Source parameters and focal mechanisms of local earthquakes: single broadband observatory at ISM Dhanbad. J Geol Soc India 4:413–419
Kayal JR, Srivastava VK, Kumar P, Chatterjee R, Khan PK (2011) Evaluation of crustal and upper mantle structures using receiver function analysis: ISM broadband observatory data. J Geol Soc India 78:76–80
Khan AA, Chouhan RKS (1996) The crustal dynamics and the tectonic trends in the Bengal Basin. J Geodyn 22:267–286
Khan PK (2005) Variation in dip-angle of the Indian plate subducting beneath the Burma plate and its tectonic implications. Geosci J 9:227–234
Khan PK (2007) Lithospheric deformation under pre- and post-seismic stress fields along the Nicobar–Sumatra subduction margin during 2004 Sumatra mega-event and its tectonic implications. Gond Res 12:468–475
Khan PK, Chakraborty PP (2009) Bearing of plate geometry and rheology on shallow-focus mega-thrust seismicity with special reference to 26 December 2004 Sumatra event. J Asian Earth Sci 34:480–491
Khan PK, Chakraborty S, Srivastava VK, Prasad R (2009) Seismicity, source parameters and scaling relationships for the eastern part of eastern Indian shield region. Indian Miner 61:65–74
Khan PK, Mohanty S, Mohanty M (2010) Geodynamic implications for the 8 October 2005 North Pakistan earthquake. Sur Geophys 31:85–106
Khan PK, Ansari MA, Mohanty S (2014) Earthquake source characteristics along the arcuate Himalayan belt: geodynamic implications. J Earth Syst Sci 123:1013–1030
Khan PK, Bhukta K, Tarafder G (2015) Coda Q in Eastern Indian shield. Acta Geod Geophys 51:333–346
Khan PK, Mohanty SP, Sinha S, Singh D (2016) Occurrences of large-magnitude earthquakes in the Kachchh region, Gujarat, western India: tectonic implications. Tectonophysics 679:102–116
Khan PK, Ansari A, Singh D (2017) Insights into the great M_w 7.9 Nepal earthquake of 25 April 2015. Curr Sci 113:2014–2020
Khan PK, Banerjee J, Shamim S, Mohanty M (2018) Long-term seismic observations along Myanmar-Sunda subduction margin: insights for 2004 Mw %3e 9.0 earthquake. Int J Earth Sci 28:1–12
Khan PK, Shamim SK, Mohanty SP, Aggarwal SK (2019) Change of stress patterns during 2004 MW 9.3 of-Sumatra mega-event:

insights from ridge–trench interaction for plate margin deformation. Geol J 55:372–389
Kumarsunil TC, Earnest A, Silpa K, Andrews R (2019) Rupture of the Indian slab in the 2011 M_w 6.9 Sikkim Himalaya earthquake and its tectonic implications. J Geophys Res 124:2623–2637
Lv J, Zheng X, Xiao J (2013) The source rupture properties and seismogenic structure of the Yiliang (China) MS5. 7 and MS5. 6 earthquakes on 7 Sept, 2012. Chin J Geophys 56:2645–2654
Lyon-Caen H, Molnar P (1983) Constraints on the structure of the Himalaya from an analysis of gravity anomalies and a flexural model of the lithosphere. J Geophys Res 88:8171–8192
Mall DM, Rao VK, Reddy PR (1999) Deep sub-crustal features in the Bengal basin: seismic signatures for plume activity. Geophys Res Lett 26:2545–2548
Mazumder R, Van Loon AJ, Mallik L, Reddy SM, Arima M, Altermann W, Eriksson PG, De S (2012) Mesoarchaean-Palaeoproterozoic stratigraphic record of the Singhbhum crustal province, eastern India: a synthesis. In: Mazumder R, Saha D (eds) Palaeoproterozoic of India, vol 365. Geological Society, London, pp 31–49
Michael AJ (1984) Determination of stress from slip data: faults and folds. J Geophys Res 89:11517–11526
Mitchell AHG (1981) Phanerozoic plate boundaries in mainland SE Asia, the Himalayas and Tibet. J Geol Soc 138:109–122
Mohindra R, Parkash B, Prasad J (1992) Historical geomorphology and pedology of the Gandakmegafan, Middle Gangetic plains, India. Earth Surf Proc Landf 17:643–662
Mukhopadhyay J, Beukes NJ, Armstrong RA, Zimmermann U, Ghosh G, Medda RA (2008) Dating the oldest Greenstone in India: a 3.51 Ga precise U-Pb SHRIMP Zircon Age for Dacitic Lava of the Southern Iron Ore Group. Singhbhum Craton J Geol 116:449–461
Naqvi SM (2005) Geology and evolution of the Indian plate. Capital Publishing Company, New Delhi, p 450
Paul H, Mitra S, Bhattacharya SN, Suresh G (2015) Active transverse faulting within underthrust Indian crust beneath the Sikkim Himalaya. Geophys J Int 201:1072–1083
Peakall J, Leeder M, Best J, Ashworth P (2000) River response to lateral ground tilting: a synthesis and some implications for the modelling of alluvial architecture in extensional basins. Basin Res 12:413–424
Rastogi BK (2016) Seismicity of Indian Stable continental region, 2016. J Earthq Sci Eng 3:57–93
Reddy PR, Venkateswarlu N, Prasad ASSSRS, Koteswara PR (1993) Crustal density model across West Bengal basin, India: An integrated interpretation of seismic and gravity data. Proc Indian Acad Sci 102:487–505
Roy AB, Chatterjee A (2015) Tectonic framework and evolutionary history of the Bengal Basin in the Indian subcontinent. Curr Sci 109:271–279
Sahu S, Raju NJ, Saha D (2010) Active tectonics and geomorphology in the Sone-Ganga alluvial tract in mid-Ganga Basin, India. Quat Int 227:116–126
Sarkar SN (1982) Precambrian tectonic evaluation of eastern India: a model of conversing microplates. Tectonophysics 86:363–397
Sengupta S (1966) Geological and geophysical studies in western part of Bengal basin, India. Am Assoc Petrol Geolog Bull 50:1001–1017
Sengupta S (1972) Geological framework of the Bhagirathi–Hooghly basin, In: Bagchi K (ed) The Bhagirathi–Hooghly basin. Proceedings of the interdisciplinary symposium, University of Calcutta, Kolkata
Shamim SK, Khan PK, Mohanty SP (2019) Stress reconstruction and lithosphere dynamics along the Sumatra subduction margin. J Asian Earth Sci 170:174–187
Singh A, Ravi Kumar M, Solomon Raju P (2007) Mantle deformation in Sikkim and adjoining Himalaya: Evidences for a complex flow pattern. Phys Earth Planet Int 64:232–241
Singh AP, Mishra OP, Yadav RBS, Kumar D (2012) A new insight into crustal heterogeneity beneath the 2001 Bhuj earthquake region of Northwest India and its implications for rupture initiations. J Asian Earth Sci 48:31–42
Singh AP, Zhao L, Kumar S, Mishra S (2016) Inversions for earthquake focal mechanisms and regional stress in the Kachchh rift basin, western India: tectonic implications. J Asian Earth Sci 117:269–283
Sonder LJ (1990) Effects of density contrasts on the orientation of stresses in the lithosphere: relation to principal stress directions in the Transverse Ranges, California. Tectonics 9:761–771
Stevenson D, Gangopadhyay A, Talwani P (2006) Booming plutons: source of micro earthquakes in South Carolina. Geophys Res Lett 33(3)
Tait J, Zimmermann U, Miyazaki T, Presnyakov S, Chang Q, Mukhopadhyay J, Sergeev S (2011) Possible juvenile Palaeoarchaean TTG magmatism in eastern India and its constraints for the evolution of the Singhbhum craton. Geol Mag 148:340–347
Tan Y, Zhu L, Helmberger D, Saikia C (2006) Locating and modeling regional earthquakes with two stations. J Geophys Res 111:B01306
Talwani P (1988) The intersection model for intraplate earthquakes. Seismol Res Lett 59(305):310
Thakur VC (1992) Geology of Western Himalaya. Pergamon Press, Oxford, p 363
Valdiya KS (1976) Himalayan transverse faults and folds and their parallelism with subsurface structures of north Indian Plains. Tectonophysics 32:353–386
Vavryčuk V (2014) Iterative joint inversion for stress and fault orientations from focal mechanism. Geophys J Int 199:69–77
Zhao LS, Helmberger DV (1994) Source estimation from broadband regional seismograms. Bull Seismol Soc Am 84:91–104
Zhao L, Luo Y, Liu TY, Luo YJ (2013) Earthquake focal mechanism in Yunnan and their inference on regional stress field. Bull Seismol Soc Am 103:2498–2507
Zhu LS, Helmberger DV (1996) Advancement in source estimation technique using broadband regional seismograms. Bull Seismol Soc Am 86:1634–1641
Zhu L, Rivera LA (2002) A note on the dynamic and static displacement from a point source in multi-layered media. Geophys J Int 148:619–627
Zoback MD, Prescott WH, Krueger SW (1985) Evidence for lower crustal ductile strain localization in southern New York. Nature 317:705–707

Acta Geophysica (2020) 68:357–364
https://doi.org/10.1007/s11600-020-00420-5

REVIEW ARTICLE - APPLIED GEOPHYSICS

An improved local phase variation attribute and its application in channels detection

Lei Shi[1] · Junzhou Liu[1] · Lanfeng Liu[1] · Tieyi Wang[2] · Yuxin Su[2]

Received: 2 December 2019 / Accepted: 7 March 2020 / Published online: 14 March 2020

Abstract

Instantaneous phase is a commonly used attribute for structural and stratigraphic feature characterization. The conventional calculation method is to construct the complex-valued seismic trace, then get the ratio of the imaginary part to the real part and finally compute the antitangent of the ratio as the instantaneous phase attribute. In this way, the phase result at one time sample point is the total phase rotation from the beginning of the trace to this point, which means the traditional instantaneous phase is cumulative. Furthermore, the phase obtained by arctangent is usually entangled, which makes it more difficult to apply to seismic interpretation. To address the two issues above, we proposed a new way to calculate the improved local phase variation attributes. Firstly, we calculate traditional instantaneous phase and unwrap it. Then we set a time window on the unwrapped phase to compute the local phase variation by using some difference methods. Finally, we slide the time window on the whole trace to obtain the final phase variation attributes. This strategy turns the whole cumulative value into local variational value, which makes the obtained local phase variation nearly zero in the continuous region but changed greatly at the interface or the abnormal structure areas. Tested by the numerical model and the real data, the proposed attributes have a good application effect in channel detection, which provides a train of thought to seismic structure interpretation with phase attributes.

Keywords Discontinuity detection · Instantaneous phase · Local phase variation · Sliding time window

Introduction

Instantaneous phase is a commonly used seismic attribute, which was defined as the phase angle of complex seismic trace (Taner et al. 1979) and can be obtained by inverse trigonometric function. At present, the existing application studies on the phase attribute mainly focused on seismic structure interpretation, thin interbeds identification and formation thickness estimation. However, these applications mainly utilize the instantaneous phase, which has a low resolution and poor reliability, especially for the deep seismic data with a low signal-to-noise ratio. To solve this problem, some scholars adopted median filtering or other effective denoising methods to remove full-band noise or high-frequency noise by integrating (e.g., Bekara and Vender 2007; Yuan et al. 2018) and then extracting the instantaneous phase attributes. These methods have reached some good application effects, but there are still some problems such as local ambiguity or illusion.

Over the past few years, some other complex seismic trace technologies were also put forward. Gabor proposed the concept of complex signals in 1946 and applied it in the field of electronic engineering for the first time. Later Taner introduced this concept to seismic signal analysis in 1979, and it has been widely used in seismic data processing and interpretation. The conventional complex seismic trace analysis is based on the Hilbert transform, through which virtual seismic records and some related instantaneous attributes can be obtained. For example, the instantaneous amplitude or envelope can characterize the subsurface lithological variations, hydrocarbon (bright spot) and gas accumulation. The instantaneous phase can be used as a continuity measurement of seismic events.

✉ Tieyi Wang
wangty_cup@163.com

[1] Exploration and Production Research Institute, Sinopec, Beijing 100083, China

[2] State Key Laboratory of Petroleum Resources and Prospecting, CNPC Key Laboratory of Geophysical Exploration, China University of Petroleum, Changping, Beijing 102249, China

The sweetness attribute (Duan et al. 2011) is defined as the ratio of the instantaneous amplitude to the root mean square of the instantaneous frequency, and it can be used to indicate hydrocarbon reservoirs. Furthermore, compared to the instantaneous amplitude and sweetness, the instantaneous phase has a great advantage in identifying features exhibiting weak reflections with poor continuity in deep formation, such as small faults and channels. In 2010, Miao et al. adopted the fast Fourier transform to obtain the complex seismic trace and realized the fast phase calculation algorithm. In 2013, Wang et al. adopted frequency division phase technology for fault interpretation and firstly tried to combine the means of phase placement with frequency division. In 2020, Yuan et al. developed six-dimensional phase attributes for wide-azimuth seismic data interpretation. In recent years, the instantaneous attributes obtained by complex seismic trace technique have been widely used in ground-penetrating radar and other cutting-edge technologies. Phase attributes are attracting more and more attention with its unique qualities and potential advantages.

However, the physical meaning of the traditional instantaneous phase attribute is the spatial rotation of the complex seismic trace from the beginning time sample point. It means that it is difficult to establish definite numerical measurement with the phase attribute, so the related studies on the phase attributes are usually only qualitative but not quantitative. Furthermore, the wrapping of the phase results makes the phase a jumping curve bounded by $\pm\pi$ rather than a continuous function. All of these make it difficult to carry out accurate seismic interpretation by using the traditional instantaneous phase attributes.

In this paper, we proposed a new way to calculate the improved local phase variation attributes based on the sliding time window and unwrapping operation. This strategy can effectively obtain the local phase variation of seismic data and avoid the local phase value being affected by the whole seismic trace. It considers the physical significance that phase is the spatial rotation of complex seismic trace, and the local real phase variation is obtained by the idea of subsection. The effective utilization of phase attributes reflects the true location of subsurface interface and can help to identify the weak reflection and subtle structure, which offers great help to fine seismic data interpretation. Firstly, we describe the basic principle and calculation steps of the proposed method to make a brief introduction. Then, we present the results of a simple numerical model and a real data to demonstrate the feasibility of this method for identifying subsurface interfaces and structures. And the comparison of the obtained results by the proposed method and the traditional instantaneous phase method further show its advantages. Finally, some related conclusions and future work are drawn.

Method

Conventional instantaneous phase attribute

In general, we can obtain the complex seismic trace $s(t)$ corresponding to the original seismic trace $x(t)$ by using the Hilbert transform (Taner et al. 1979):

$$s(t) = x(t) + ih(t) = |s(t)|e^{i\theta(t)}, \tag{1}$$

where t represents two-way traveling time, i represents the imaginary unit, $h(t)$ is the Hilbert transform result, which is orthogonal to the real seismic signal $x(t)$, $|s(t)| = \sqrt{x^2(t) + h^2(t)}$ is the instantaneous amplitude or envelope and $\theta(t)$ is the instantaneous phase attribute. The Hilbert transform has been widely applied to seismic data processing, inversion and interpretation (e.g., Bozdag et al. 2011; Alkhalifah 2014; Lian et al. 2018; Yuan et al. 2019).

As shown in Eq. (1), the instantaneous phase is the phase angle of complex seismic trace, which can be obtained by the following arctangent function:

$$\omega(t) = a\tan(\mathrm{imag}(s(t))/\mathrm{real}(s(t))), \tag{2}$$

where real (.) and imag (.) represent taking the real part and the imaginary part of $s(t)$, respectively. The denominators are usually nonzero values in most cases, but when the values in denominator are nearly zero, the phase result is sensitive to noise. The equation often produces a discontinuous instantaneous phase in the range [− 180° 180°] due to the inverse tangent calculation.

According to Eq. (2), for the whole seismic trace, the instantaneous phase at one time sample point is the total phase accumulation from the beginning point of the trace to this point, which means the instantaneous phase obtained through the whole trace has accumulativeness. Although there are no geological structures developed in some places underground, the instantaneous phase attributes will be affected by other time locations in front of the current seismic trace, so there is often a nonzero-phase value and the value is usually uncertain. Different from the instantaneous amplitude attributes with zero values in the continuous area, this will cause the difficulty to interpret some special geological structures by using the phase attributes directly.

Besides, the phase obtained by the inverse tangent function is usually wrapped, and the direct result of the phase is

a discontinuous function limited by the extremum of $\pm\pi$. To obtain real phase results, the unwrapping operation is necessary. At present, a variety of software including MATLAB can realize the phase unwrapping operation directly. The general principle is to determine whether the difference value between two adjacent points is greater than or equal to 2π. If so, add or subtract 2π to each point beyond that later target point. Here, take a zero-phase wavelet model as an example, as shown in Fig. 1a. Figure 1b, c shows the corresponding phase results before and after unwrapping operation. The phase result becomes continuous after such an operation, which shows the necessity of unwrapping operation.

Local phase variation attribute based on sliding window

To overcome the deficiency of the instantaneous phase mentioned above, we tried to utilize the sliding time window method to calculate the improved local phase variation attributes. To explain the principle of this method better, we firstly take a simple synthetic model with a single interface as an example.

Figure 2a shows the velocity profile of the numerical model with the upper layer velocity of 2000 m/s and the lower layer velocity of 3000 m/s. The designed reflecting interface was located at 60 ms. Figure 2b shows the corresponding seismic profile, which was obtained by 30 Hz Ricker wavelet convoluted with the reflectivity coefficients calculated by the velocity model. Figure 2c displays

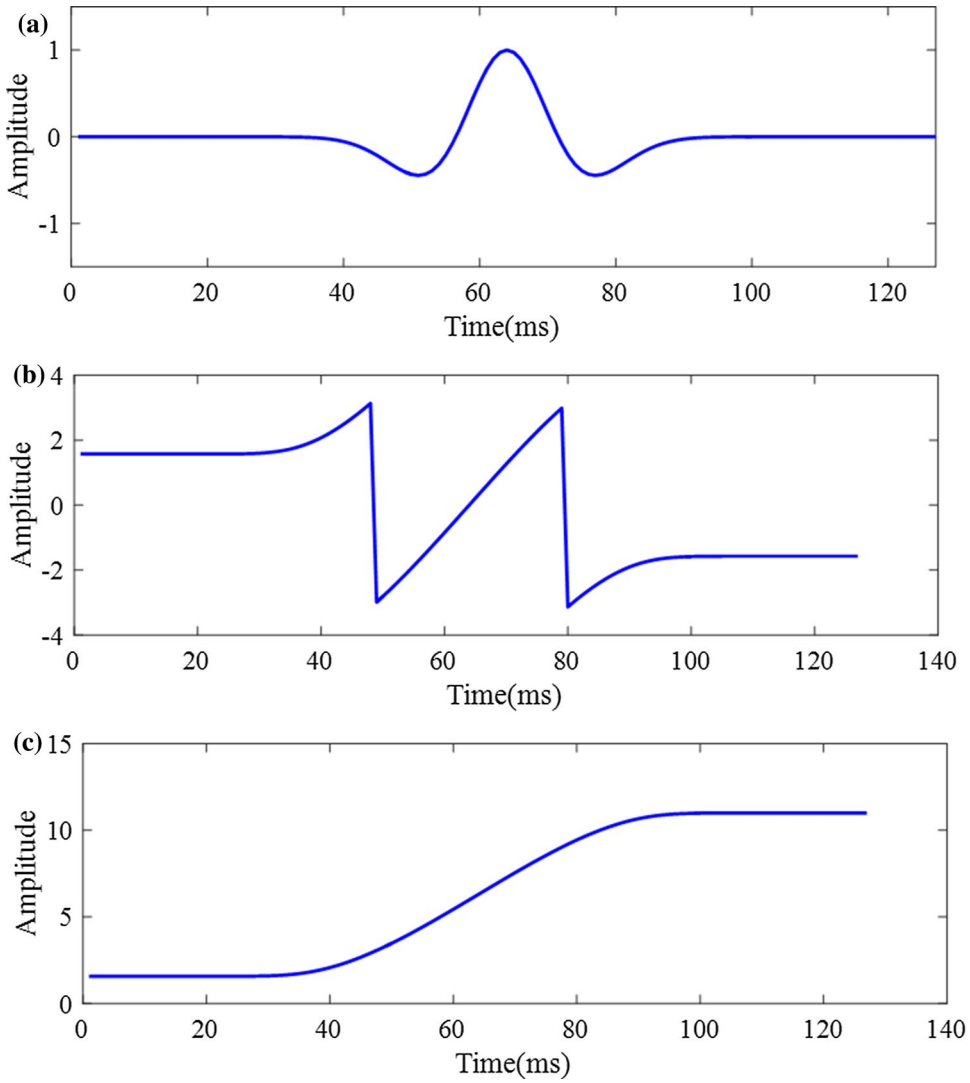

Fig. 1 **a** A zero-phase wavelet. The corresponding instantaneous phase results **b** before unwrapping operation, and **c** after unwrapping operation. The phase becomes a continuous curve after such an operation

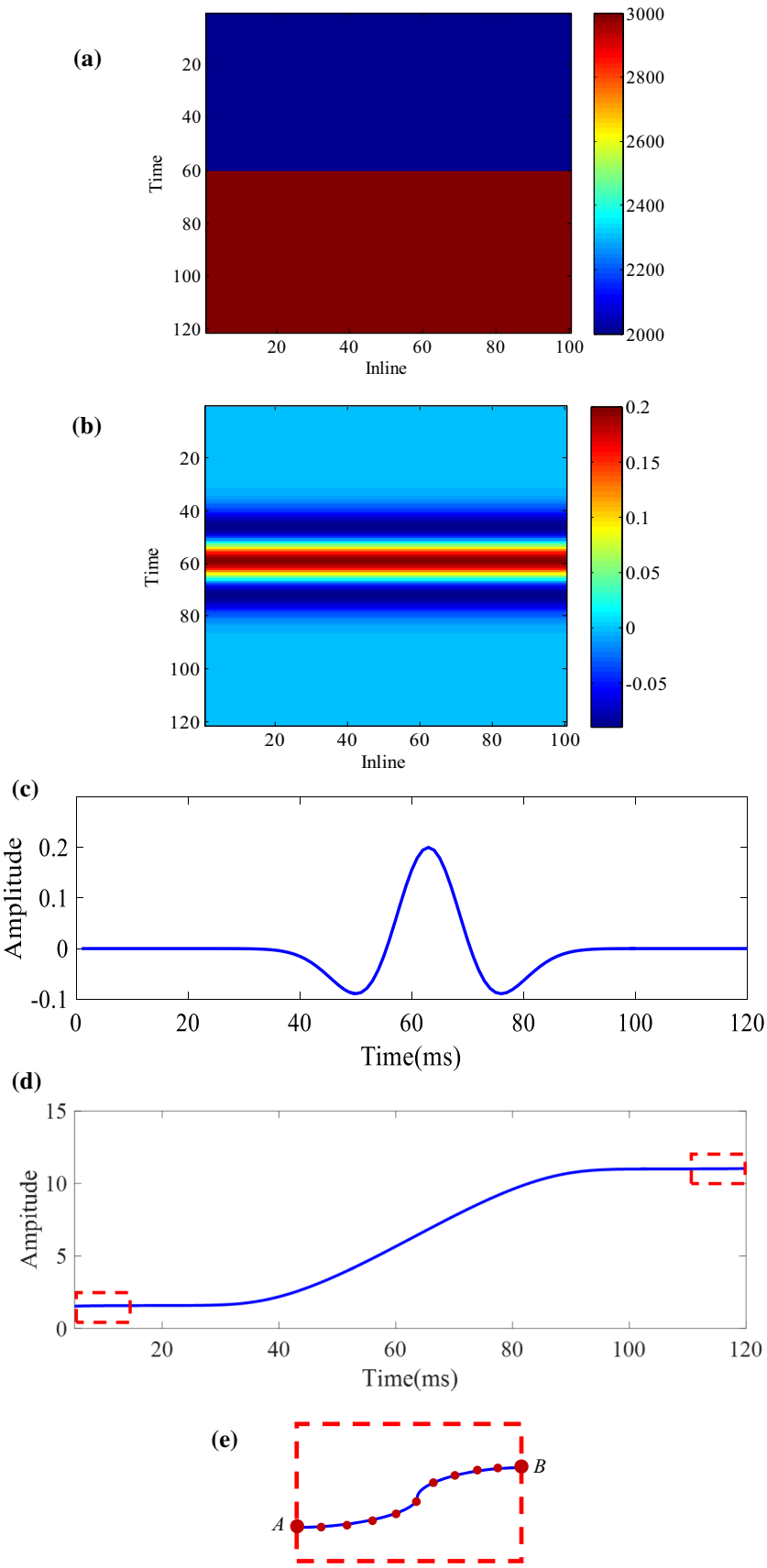

Fig. 2 **a** The velocity profile of the numerical model. The designed interface was located at 60 ms, the velocities in the upper and lower layers are 2000 m/s and 3000 m/s, respectively. **b** The obtained seismic profile by 30 Hz Ricker wavelet convolved with the calculated reflectivity coefficients. **c** A seismic trace record from **b**. **d** The corresponding phase result after unwrapping, and the red box represents the time window. Each time sample point corresponds to a sliding time window, only the first and the last windows are shown here. **e** Enlarged local time window containing 11 time sampling points, as A is the first time point and B is the last time point of the current time window

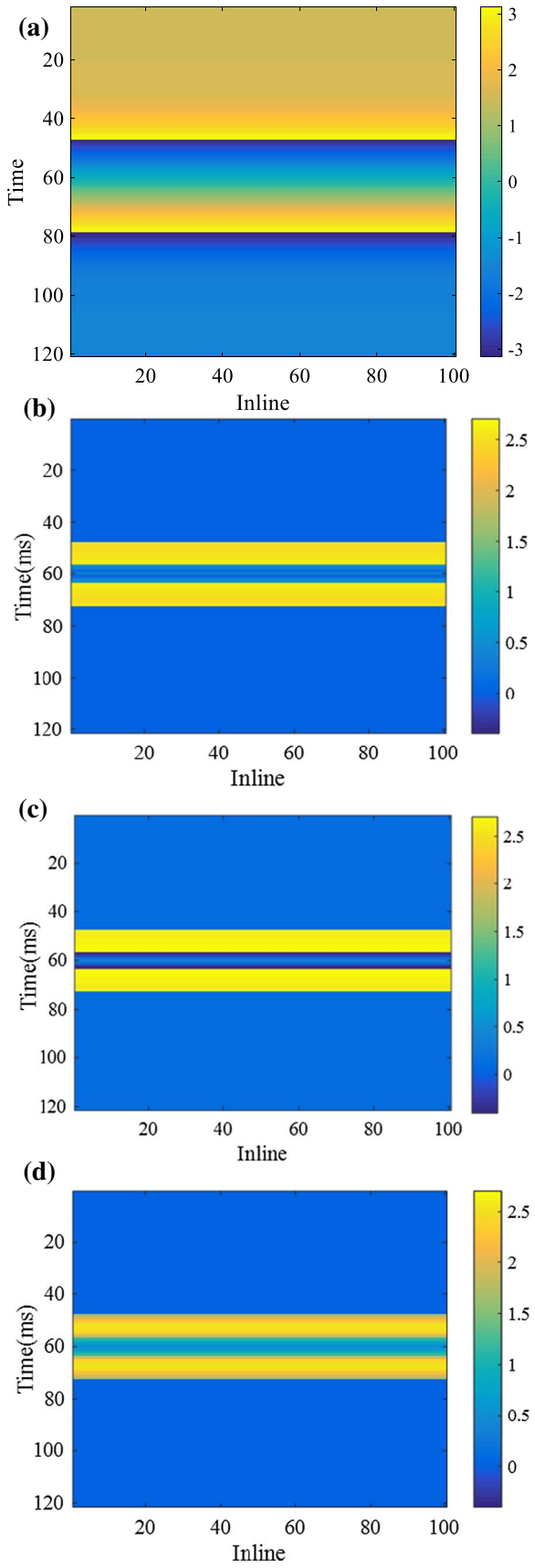

Fig. 3 **a** Conventional instantaneous phase. The local phase variation ▶ results calculated by using: **b** first point and last point difference, **c** first and last points, and middle point difference and **d** mean difference, respectively

a seismic trace record of Fig. 2b. Then, the instantaneous phase of the seismic trace was calculated and further carried out the unwrapping operation. The phase result after unwrapping is shown in Fig. 2d. We first open a time window containing several time samples at the beginning of the unwrapping phase trace, as indicated by the red box in Fig. 2d. And the enlarged local time window is shown in Fig. 2e, as A is the first time point and B is the last time point of the current time window. Then, we perform differential operations on the local phase data in the current time window to obtain the local phase variation as the improved phase attributes at the location of the center point. Here, we gave three different kinds of differential methods to calculate the local phase variation, as following:

1. First point and last point difference. We calculate the difference between the phase results at these two time points as the local phase variation of the center point in the current time window, as follows:

$$\omega_1(\Delta t+1) = \mathrm{abs}(\omega(2\Delta t+1) - \omega(1)), \tag{3}$$

where Δt represents half of the time window length but without the center point, the whole time window length can be expressed as $2\Delta t+1$,$\omega_1(\Delta t+1)$ represents the phase variation corresponding to the center point obtained by the difference between the first and last points, and *abs* represents taking the absolute value. $\omega(1)$ and $\omega(2\Delta t+1)$ represent the instantaneous phase after unwrapping corresponding to the first and last points of the current time window.

2. First and last points, and middle point difference. We calculate the difference between the phase results corresponding to the first point and middle point, and the difference between the phase results corresponding to the last point and middle point, then calculate the average value as the local phase variation of the center point in the current time window, as follows:

$$\omega_2(\Delta t+1) = [\mathrm{abs}(\omega(2\Delta t+1) - \omega(\Delta t+1)) + \mathrm{abs}(\omega(1) - \omega(\Delta t+1))]/2 \tag{4}$$

where $\omega_2(\Delta t+1)$ represents the phase variation corresponding to the center point, and the other symbols are the same as above.

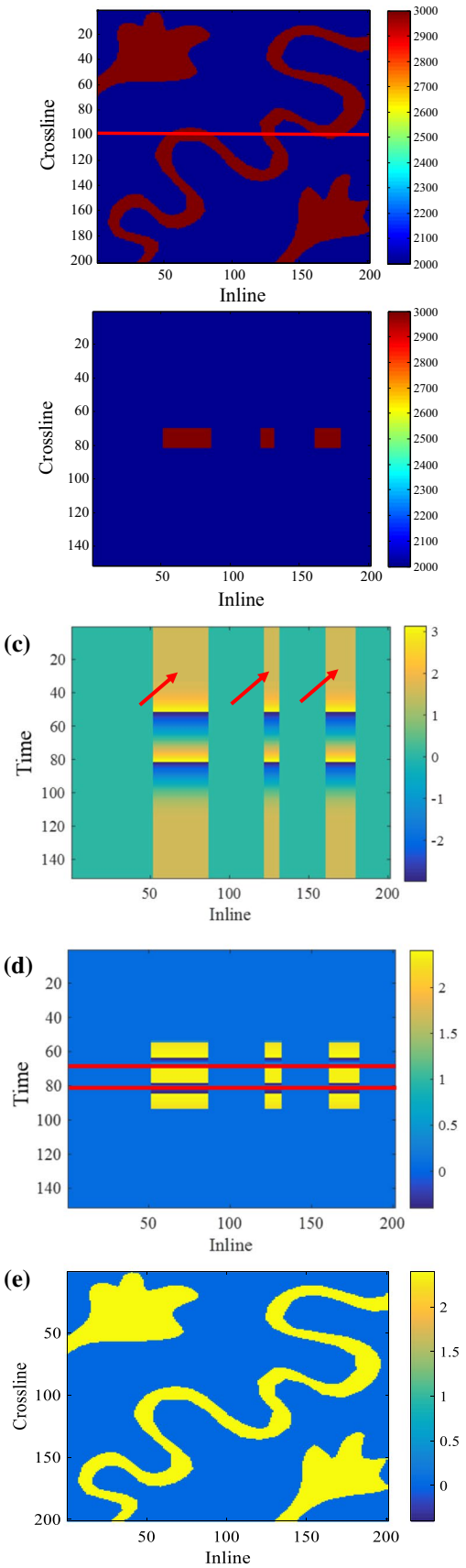

Fig. 4 **a** The horizontal slice of the numerical model at time = 100 ms. The slice position is at the center of the sand layer. **b** The velocity profile of the numerical model along the direction of crossline100 (as indicated by the red line in Figure 4a). **c** The conventional instantaneous phase attribute profile. **d** The local phase variation attribute based on the proposed method, and the red lines represent the locations of top and bottom interfaces of the target layer. **e** The time slice through the local phase variation attribute volume at time = 70 ms

3. Mean difference. After obtaining the average phase value in the time window, we calculate the difference between each time point and the average value as the phase variation of the center point in the current time the window, as follows:

$$\omega_3(\Delta t+1)=\left[\sum_{t_0=1}^{2\Delta t+1}\mathrm{abs}(\omega(t_0)-\omega_{\mathrm{aver}})\right]/(2\Delta t+1) \tag{5}$$

where $\omega_3(\Delta t+1)$ represents the phase variation corresponding to the center point by the mean difference, ω_{aver} represents the average phase value in the current time window and the other symbols are the same as above.

Among the above three different differential methods, the first method (first point and last point difference) is the simplest and highly efficient, but when the slide time window is large or the phase within the window changes in a non-monotonic way, this method will produce some wrong results. The second method (first and last points, and middle point difference) takes into account the phase change at the beginning and end points of the time window relative to the middle point. When the time window length is small and the phase change is relatively gentle, this method has a higher accuracy, but it still fails for the phase change which is more drastic. The last method (mean difference) is complex, but it ensures that all time points in the slide time window participate in the calculation, which can reflect the phase variation within the window better.

After obtaining the phase variation in the time window at one time point, we then slide the time window along the time direction and repeat the above calculation steps to obtain the final results of the whole seismic trace. Figure 3a shows the conventional instantaneous phase result corresponding to the seismic profile in Fig. 2b. Figure 3b–d shows the local phase variation results calculated by using the above three differential methods. Compared with the conventional instantaneous phase results, the obtained local phase variation results by three methods can effectively reflect the local phase changes and have a more obvious correspondence with the construction.

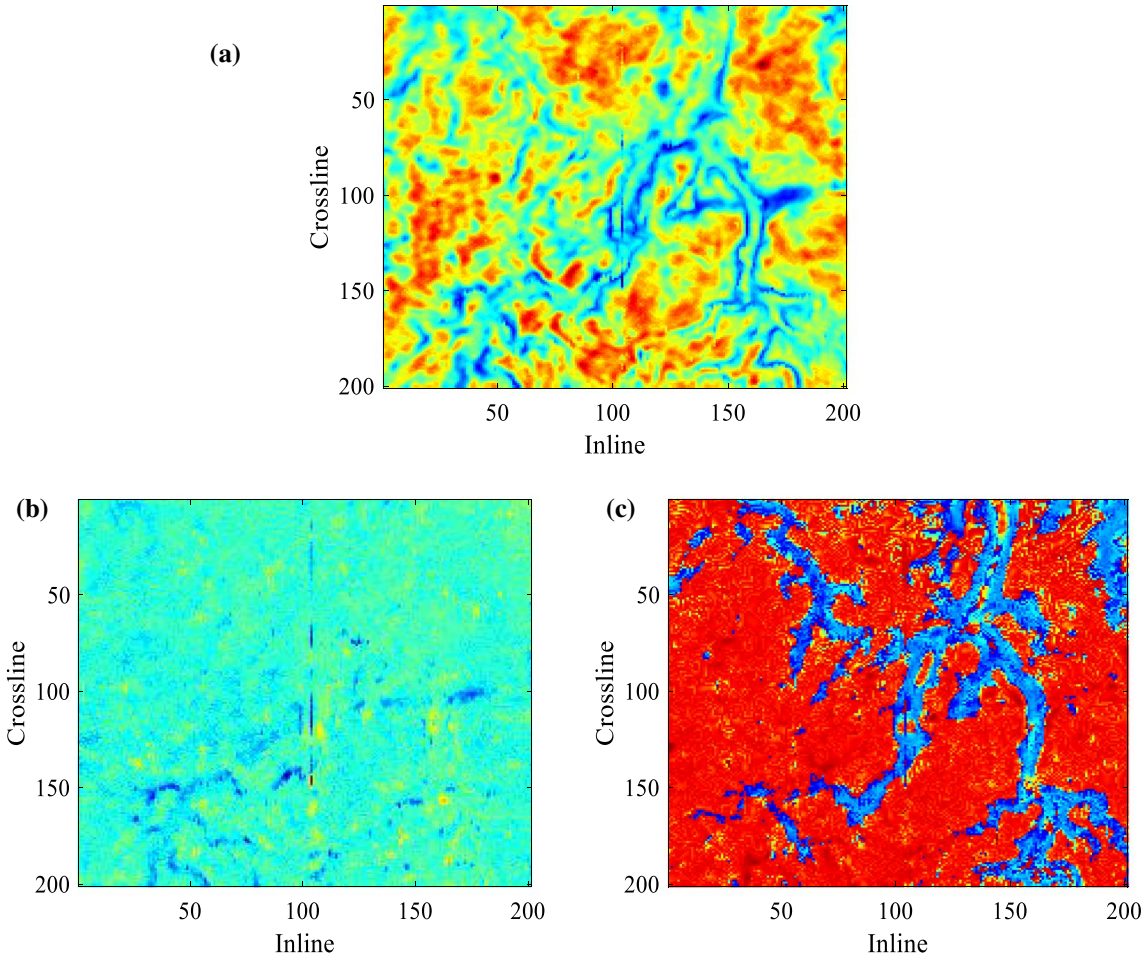

Fig. 5 **a** The horizon amplitude slice of interest. **b** The conventional instantaneous phase attribute slice. **c** The horizon slice through the improved local phase variation attribute volume

Examples

The application on the simple interface model shows the feasibility of the proposed method. In this section, we choose a 3D numerical model and a 3D real dataset to make further tests and analysis. For convenience, we use the second differential method (first and last points, and middle point difference) to obtain local phase variation attributes in this section, and the advantages of this method over the traditional instantaneous phase attribute are further illustrated.

The tested numerical model consists of surrounding rock with wave velocity of 2000 m/s and target sandstone layer with wave velocity of 3000 m/s. The total time length is 151 ms with a time–sample interval of 1 ms, and the sampling points in the inline and crossline directions are 201. The sand body with a time thickness of 12 ms ranging from 70 to 82 ms mainly consists of a channel and two alluvial fan structures. Figure 4a shows the time slice of the numerical model at time of 100 ms. It can observe the edges and spatial extension of the channel and two alluvial fan structures in the amplitude slice. Figure 4b shows the velocity profile of the numerical model along the direction of crossline 100 (as indicated by the red line in Fig. 4a), and we can see the distribution range of the target layer along the time direction and the interface location. Figure 4c, d shows the conventional instantaneous phase attribute profile and the local phase variation attribute by using the proposed method, respectively. And the red lines in Fig. 4d represent the locations of the top and bottom interfaces of the target layer. Figure 4e shows the time slice through the local phase variation attribute volume at time = 0 ms. We can see the proposed attribute that depicts the boundaries of all geological structures perfectly on the time slice, and there is also a good relationship with the interface on the profile. By comparison, it can be observed that the conventional instantaneous phase attribute has nonzero-phase value (indicated by the red arrows in Fig. 4c) even in the continuous areas, which are caused by the utilization of arctangent function. However, the local phase variation attribute by the

proposed method can effectively avoid this problem and only produce nonzero results near the interface. In this way, we can directly use the phase attribute to develop a set of interface and geological structure identification methods similar to the coherence attributes, but with much a higher calculation efficiency.

A 3D real data from Western China is used to test the applicability of the proposed method. The buried depth of the channel sand embedded in this area exceeds 4.5 km, and the reservoir has a strong lateral heterogeneity. Figure 5a shows the horizon amplitude slice of interest. The lineament and edges of the observed channels are ambiguous, which will cause great difficulties for subsequent fine structural interpretation. Figure 5b shows the conventional instantaneous phase attribute slice along the target layer. It is almost impossible to identify some geological bodies from this slice, which makes it difficult to explain. Figure 5c displays the horizon slice through the improved local phase variation attribute volume. In contrast to the conventional instantaneous phase, the result can favorably identify the edges and lineament of the channels, showing a relatively high phase change amount compared with surrounding structures. Several channel branches can be clearly identified including their widths and extension directions. The results illustrate that the proposed method in this paper has a better performance to identify subtle abnormalities in the application of real-data interpretation.

Conclusions

In this paper, we proposed a new way to calculate the improved local phase variation attributes based on the sliding time window and unwrapping operation. The examples including the numerical model and 3-D real dataset are adopted to demonstrate that the proposed method can effectively avoid the accumulation of traditional instantaneous phase attributes. Compared to conventional instantaneous phase attributes, the obtained local phase variation attributes can directly realize the identification of the geological structures and interface. The calculation method is simple and has extremely high computational efficiency. However, as the phase attributes tend to be affected by noise easily, the quality of results will be reduced when the signal-to-noise ratio is low. Furthermore, the selection of the sliding time window length also has a significant effect on the final results. It is an important content of our future work to change the window length adaptively according to the geological structure scale in subsurface.

Acknowledgments This work was financially supported by the National Key R&D Program of China (2018YFA0702504), the National Science and Technology Major Project (2016ZX05002-005-003) and the Sinopec Science and Technology Department Project (PE19008-2 and P18075-5).

References

Alkhalifah T (2014) Full-waveform inversion of the unwrapped phase of a model. Geophys Prospect 62:397–403

Bekara M, Vender BM (2007) Local singular value decomposition for signal enhancement of seismic data. Geophysics 72(2):V59–V65

Bozdag E, Trampert J, Trom J (2011) Misfit function for full waveform inversion based on instantaneous phase and envelope measurements. Geophys J Int 185:845–870

Browaeys TJ (2009) Complex-valued correlation and seismic attributes. SEG Tech Progr Expand Abstr

Brown AR (2011) Interpretation of three-dimensional seismic data. 7th edn, AAPG Memoir 42, SEG, 646

Corciulo M, Roux P, Campillo M et al (2010) Instantaneous phase estimation to measure weak velocity variations: application to noise correlation on seismic data at the exploration scale. American Geophysical Union, Washington

Das B, Chatterjee R, Singha DK et al (2017) Post-stack seismic inversion and attribute analysis in shallow offshore of Krishna-Godavari basin, India. J Geol Soc India 90(1):32–40

Duan Y, Peng Z, Zeng L, Bi M (2011) Carbonate reservoir and gas-bearing property detection using sweetness. SEG Tech Progr Expand Abstr 30(1):1197–1201

Guo H, Marfurt KJ, Liu JL (2009) Principal component spectral analysis. Geophysics 74(4):P35–P43

He M, Yang W, Chen X, Pu X (2010) Analysis and application of complex seismic trace based on FFT. J Chengdu Aeronaut Voc Tech Coll 26(1):61–65

Kaplan ST, Ulrych TJ (2007) Phase unwrapping: a review of methods and a novel technique. CSPG-CSEG Joint Conv 163:455–473

Lian SJ, Yuan SY, Wang GC, Liu T, Liu Y, Wang SX (2018) Enhancing low-wavenumber components of full-waveform inversion using an improved wavefield decomposition method in the time-space domain. J Appl Geophys 157:10–22

Lu WK, Zhang CK (2013) Robust estimation of instantaneous phase using a time-frequency adaptive filter. Geophysics 78(1):O1–O7

Marfurt KJ, Kirlin RL (2001) Narrow-band spectral analysis and thin-bed tuning. Geophysics 66:1274–1283

Oppenheim AV, Lim JS (1981) The importance of phase in signals. Proc IEEE Spec Issue Dig Image Process 69:529–541

Robertson JD, Nogami HH (1984) Complex seismic trace analysis of thin beds. Geophysics 49(4):344–352

Schimmel M, Stutzmann E, Gallart J (2011) Using instantaneous phase coherence for signal extraction from ambient noise data at a local to a global scale. Geophys J Int 184(1):494–506

Spagnolini U (1993) 2-D phase unwrapping and phase aliasing. Geophysics 58(9):1324–1334

Taner MT, Koehler F, Sheriff RR (1979) Complex seismic trace analysis. Geophysics 44:1041–1063

Ulrych TJ, Kaplan S, Sacchi MD, Galloway E (2007) The essence of phase in seismic data processing and inversion. SEG Tech Progr Expand Abstr 1765–1769

Yuan SY, Ji YZ, Shi PD, Zeng J, Gao JH, Wang SX (2019) Sparse Bayesian learning-based seismic high-resolution time-frequency analysis. IEEE Geosci Remote Sens Lett 16(4):623–627

Yuan SY, Wang SX, Luo CM, Wang TY (2018) Inversion-based 3-D seismic denoising for exploring spatial edges and spatio-temporal signal redundancy. IEEE Geosci Remote Sens Lett 15(11):1682–1686

Acta Geophysica (2020) 68:365–375
https://doi.org/10.1007/s11600-020-00399-z

RESEARCH ARTICLE - APPLIED GEOPHYSICS

3D sparse inversion of magnetic amplitude data when strong remanence exists

Zelin Li[1] · Changli Yao[2]

Received: 11 July 2019 / Accepted: 6 January 2020 / Published online: 23 January 2020

Abstract

Three-dimensional inversion for susceptibility distributions is a common approach for quantitative interpretation of magnetic data. However, this approach will fail when strong remanence exists because the total magnetization direction is unknown. Magnetic amplitude inversion can reduce remanence effects and thus improve reconstructed results. In this paper, we propose a sparse magnetic amplitude inversion method which minimizes an L_0-like-norm of model parameters subject to bound constraints. By using the iteratively reweighed least squares technique, the bound-constrained L_0-like-norm sparse inversion is transformed to a sequence of bound-constrained nonlinear least squares subproblems. To deal with the bound constraints, we use a logarithm barrier algorithm to solve each subproblem. Compared with the classical L_2-norm inversion method, the proposed sparse method utilizes the known physical property information to produce binary results characterized by sharp boundaries. This method is tested on synthetic data produced by a dipping dyke model and a field data set acquired in Australia.

Keywords Magnetic amplitude inversion · Remanence · Sparse · Binary · Sharp boundary

Introduction

Three-dimensional (3D) inversion is an important method for quantitative interpretation of magnetic data. It has been successfully applied to mineral exploration (Oldenburg et al. 1997) and in the study of geological structures (Abedi et al. 2018). The classical inversion method for susceptibility distributions (Li and Oldenburg 1996, 2003; Pilkington 1997, 2009; Portniaguine and Zhdanov 1999, 2002) assumes that there is no remanence and that the self-demagnetization effect is negligible, so that the magnetization direction is parallel to the direction of ambient field. However, when strong remanence exists, the magnetization direction can be significantly different from that of the ambient field. In this case, the classical inversion method can produce incorrect results, which poses a major challenge to quantitative interpretation of magnetic data affected by strong remanence. To overcome this problem, researchers have developed several methods that can be divided into two categories.

One category first transforms the magnetic anomalies into nonnegative quantities that are less dependent on the magnetization direction and then inverts the transformed quantities using standard magnetic inversion algorithms. Paine et al. (2001) first convert total-field data into the analytic signal of the vertical integral and the vertical integral of the analytic signal and then use these two quantities as pole-reduced anomalies for standard inversion. Shearer and Li (2004) invert the total gradient data (Nabighian 1972; Roest et al. 1992) to reduce remanence effects. Li et al. (2010), Li and Li (2014), Li et al. (2015), and Krahenbuhl and Li (2017) invert the magnetic amplitude data (Hou 1979; Stavrev and Gerovska 2000) to mitigate effects of remanence and self-demagnetization. Pilkington and Beiki (2013), Guo et al. (2014), and Zhou et al. (2015) invert the normalized source strength (Wilson 1985; Beiki et al. 2012) to alleviate effects of remanent magnetization. Such methods only exploit the amplitude information of the magnetic data.

✉ Zelin Li
lizelin@hebeu.edu.cn

Changli Yao
clyao@cugb.edu.cn

[1] Key Laboratory for Resource Exploration Research of Hebei Province, School of Earth Science and Engineering, Hebei University of Engineering, Handan 056038, China

[2] School of Geophysics and Information Technology, China University of Geosciences, Beijing 10083, China

Therefore, only the magnitude information of the magnetization is obtained.

The other category is magnetization vector inversion, which makes full use of the amplitude and phase information of the magnetic data. Wang et al. (2004) validate the feasibility of 2D magnetization vector inversion by using simple model experiments. For realistic and complicated conditions, due to the enhanced non-uniqueness introduced by the added model parameters, methods in this category require the incorporation of extra prior information to obtain geologically meaningful solutions (Lelièvre and Oldenburg 2009). One can exploit a sequential strategy to deal with the added model parameters. Li et al. (2010) first estimate the total magnetization directions and then invert the effective susceptibilities of the model, whereas Liu et al. (2013, 2015, 2017) first invert the effective susceptibilities and then recover the total magnetization directions of the model. Alternatively, one can directly recover all the parameters by explicitly introducing prior information into the objective function. Lelièvre and Oldenburg (2009) derive equations of 3D magnetization vector inversion in Cartesian and spherical coordinates and introduce some pieces of prior information that are readily incorporated into the inversion. Ellis et al. (2012) propose a similar magnetization vector inversion method. Li and Sun (2016) use fuzzy c-means clustering to incorporate magnetization direction information into the magnetization vector inversion. They also develop an algorithm to automate their clustering inversion method (Sun and Li 2018).

In this paper, we have chosen to focus on the magnetic amplitude inversion method falling into the former category for the following two reasons. First, magnetic amplitude inversion is applicable for complicated multiple-source conditions and requires minimum prior information. Second, magnetic amplitude inversion plays an important role in several magnetization vector inversion methods (Liu 2013; Li and Sun 2016). The amplitude inversion proposed by Li et al. (2010) uses the classical L_2-norm for model objective function and produces a smooth solution. An alternative choice of model objective function is the sparse norm. The sparse model norms, applied to gravity and magnetic inversion, have been used to obtain compact (Last and Kubik 1983), blocky (Farquharson and Oldenburg 1998; Farquharson 2008), and focused (Portniaguine and Zhdanov 1999; Pilkington 2009) solutions. Here, we develop a sparse magnetic amplitude inversion algorithm extended from Li et al. (2018). Similar to the approach of Li et al. (2018), this algorithm makes use of the known physical property information and produces binary results characterized by sharp boundaries in the presence of strong remanence. In the following sections, we first introduce the sparse magnetic amplitude inversion algorithm and then test this algorithm using a synthetic example and a field data example.

Method

Forward modeling

Assuming the subsurface is divided into many rectangular prisms with constant effective susceptibility defined as the ratio of magnetization magnitude over the ambient field strength, we express the forward modeling of the three orthogonal components of magnetic anomaly vector as

$$\begin{aligned} \boldsymbol{d}_x &= \boldsymbol{G}_x\boldsymbol{m} \\ \boldsymbol{d}_y &= \boldsymbol{G}_y\boldsymbol{m} \\ \boldsymbol{d}_z &= \boldsymbol{G}_z\boldsymbol{m}, \end{aligned} \tag{1}$$

where $\boldsymbol{G}_x$, $\boldsymbol{G}_y$, and $\boldsymbol{G}_z$ are the sensitivity matrices between the effective susceptibility vector $\boldsymbol{m}$ and the x, y, and z components of magnetic anomaly vector $\boldsymbol{d}_x$, $\boldsymbol{d}_y$, and $\boldsymbol{d}_z$, respectively. The amplitude vector (Hou 1979; Stavrev and Gerovska 2000) is given by

$$\boldsymbol{d} = (\boldsymbol{d}_x^2 + \boldsymbol{d}_y^2 + \boldsymbol{d}_z^2)^{1/2}. \tag{2}$$

In practice, we need to calculate the amplitude data from the measured total-field data. For plane gridded measured data in midlatitude and high latitude, we can use the wave number-domain method (Pedersen 1978) to obtain the amplitude data. For more complicated conditions, such as high topographic relief and low latitudes, using the equivalent source technique (Dampney 1969; Li and Li 2014) to calculate the amplitude data is more reasonable.

Inverse problem

First, we consider the unconstrained L_0-like-norm inversion of magnetic amplitude data. The objective function is

$$\varphi_u(\boldsymbol{m}) = \varphi_d(\boldsymbol{m}) + \mu\varphi_{um}(\boldsymbol{m}), \tag{3}$$

where μ is a regularization parameter. φ_d is a data misfit function formulated as

$$\varphi_d(\boldsymbol{m}) = \left\|\boldsymbol{W}_d[\boldsymbol{F}(\boldsymbol{m}) - \boldsymbol{d}]\right\|_2^2, \tag{4}$$

where $\boldsymbol{W}_d$ is a diagonal data-weighting matrix and $\boldsymbol{F}$ is the nonlinear forward operator. The ith diagonal element of $\boldsymbol{W}_d$ is the reciprocal of the estimated noise standard deviation of the ith datum. φ_{um} is an L_0-like-norm (Rao and Kreutz-Delgado 1999) of the model parameters and given by

$$\varphi_{um}(\boldsymbol{m}) = \sum_{j=1}^{M} \ln m_j^2. \tag{5}$$

Equation 3 is an L_0-like-norm inverse problem, which can be solved by the iteratively reweighed least squares

(IRLS) algorithm (Beaton and Tukey 1974; Holland and Welsch 1977; Chartrand and Yin 2008; Daubechies et al. 2010). By using IRLS, Eq. 3 is transformed to a sequence of L_2-norm inverse problem, where the objective function of the nth iteration is

$$\left\|\boldsymbol{W}_d[\boldsymbol{F}(\boldsymbol{m})-\boldsymbol{d}]\right\|_2^2+\mu^{(n)}\left\|\boldsymbol{R}^{(n)}\boldsymbol{m}\right\|_2^2, \tag{6}$$

where $\boldsymbol{R}^{(n)}$ is a diagonal reweighting matrix. Its diagonal element is

$$r_{jj}^{(n)}=\left(\frac{\partial\varphi_{um}(\boldsymbol{m}^{(n-1)})}{\partial m_j^{(n-1)}}\Big/ m_j^{(n-1)}\right)^{1/2}=\left|m_j^{(n-1)}\right|^{-1}. \tag{7}$$

To avoid singularity of Eq. 7 in case of $m_j=0$, Eq. 7 is modified by

$$r_{jj}^{(n)}=\left(\left|m_j^{(n-1)}\right|+\varepsilon\right)^{-1}, \tag{8}$$

where ε is a small positive number.

To obtain a geologically meaningful solution, more prior information should be incorporated into the objective function. We focus on bound-constrained sparse inversion of magnetic amplitude data. Similar as the unconstrained sparse inversion, the bound-constrained sparse inversion is formulated as a sequence of bound-constrained L_2-norm inverse problem, where the objective function of the nth iteration is defined as

$$\begin{aligned}&\min\quad \varphi_c^{(n)}(\boldsymbol{m})=\varphi_d(\boldsymbol{m})+\mu^{(n)}\varphi_{cm}^{(n)}(\boldsymbol{m})\\&\text{s.t.}\quad \boldsymbol{m}_{\min}\le\boldsymbol{m}\le\boldsymbol{m}_{\max},\end{aligned} \tag{9}$$

where φ_d is given in Eq. 4, $\mu^{(n)}$ is the regularization parameter at the nth iteration, and $\boldsymbol{m}_{\min}$ and $\boldsymbol{m}_{\max}$ are vectors of lower and upper bounds. $\varphi_{cm}^{(n)}$ is the model objective function at the nth iteration, given by

$$\varphi_{cm}^{(n)}(\boldsymbol{m})=\left\|\boldsymbol{R}^{(n)}\boldsymbol{Z}\boldsymbol{m}\right\|_2^2, \tag{10}$$

where $\boldsymbol{Z}$ is the depth weighting matrix (Li and Oldenburg, 1996). $\boldsymbol{R}^{(n)}$ is given in Eq. 8, and $\boldsymbol{R}^{(0)}$ is set to the identity matrix $\boldsymbol{I}$. Equation 9 belongs to bound-constrained nonlinear least square problems. Many algorithms, such as nonlinear mapping (Li and Oldenburg 1996; Lelièvre and Oldenburg, 2006), logarithm barrier method (Li and Oldenburg 2003), and gradient projection method (Lelièvre et al. 2009), have been successfully applied to solve these problems in gravity and magnetic inversion. In this paper, we choose to use the logarithm barrier method (Li and Oldenburg 2003) to solve Eq. 9. The detailed algorithm for solving Eq. 9 is summarized in "Appendix".

Assuming the regularization parameter at each iteration has been obtained according to Morozov's discrepancy principle, the algorithm of bound-constrained sparse inversion of magnetic amplitude data is summarized as follows:

1. Initialize $\mu^{(0)}$, $\boldsymbol{R}^{(0)}=\boldsymbol{I}$, and $n=0$.
2. Solve Eq. 9 for $\boldsymbol{m}^{(n)}$ using the algorithm in "Appendix".
3. Terminate on convergence or when n attains a specified maximum number of iterations $n_{\max}$. Otherwise, $n\leftarrow n+1$, update $\mu^{(n)}$, generate $\boldsymbol{R}^{(n)}$ from $\boldsymbol{m}^{(n-1)}$, and go to Step 2.

Synthetic example

To test the proposed sparse magnetic amplitude inversion algorithm, we invert magnetic data produced by a dipping dyke model. The dyke is buried at a depth of 100 m and extends to 1000 m depth at a dip angle of 45°. The strike length of the dyke is 1000 m in the north direction. The dyke has an effective susceptibility of 0.05 SI. The ambient field has a strength of 50,000 nT, an inclination of 65°, and a declination of −25°. The magnetization vector has an inclination of 45° and a declination of 75°. The total-field data produced by the dyke model are observed over a 21×21 grid of 100 m spacing and contaminated by uncorrelated Gaussian noise whose standard deviation is equal to 2% of the accurate datum magnitude plus 2 nT, as shown in Fig. 1a. The corresponding amplitude anomaly is shown in Fig. 1b.

Assuming an unknown magnetization direction, we invert the amplitude data in Fig. 1b using four different model norms, including the classical L_2-norm, total variation functional (Rudin et al. 1992), minimum gradient support functional (Portniaguine and Zhdanov 1999), and the proposed L_0-like-norm. The lower and upper bounds of all inversions are set to 0 and 0.05 SI, respectively. The model region is divided into $40\times40\times30$ cubes of 50 m on each side. The proposed L_0-like-norm sparse inversion is converged in 20 iterations. At each iteration, by searching for an appropriate regularization parameter, the achieved data misfit is near 441 (number of data), with 10% tolerance.

The recovered models of all inversions are shown in 3D perspective views in Fig. 2 and in 2D slice views in Fig. 3. The inversion results using the classical L_2-norm (Figs. 2a and 3a, b) are smooth and fuzzy. The model recovered from the total variation inversion (Figs. 2b and 3c, d) is blockier, but still contains smooth structures. The reconstructed model using the minimum gradient support functional (Figs. 2c and 3e, f) is piecewise constant. The results of the proposed L_0-like-norm inversion possess a binary feature. Although results of all of the four inversions are featured by a dipping slab, the model recovered from the proposed L_0-like-norm inversion has more accurate dip angle and deep structures.

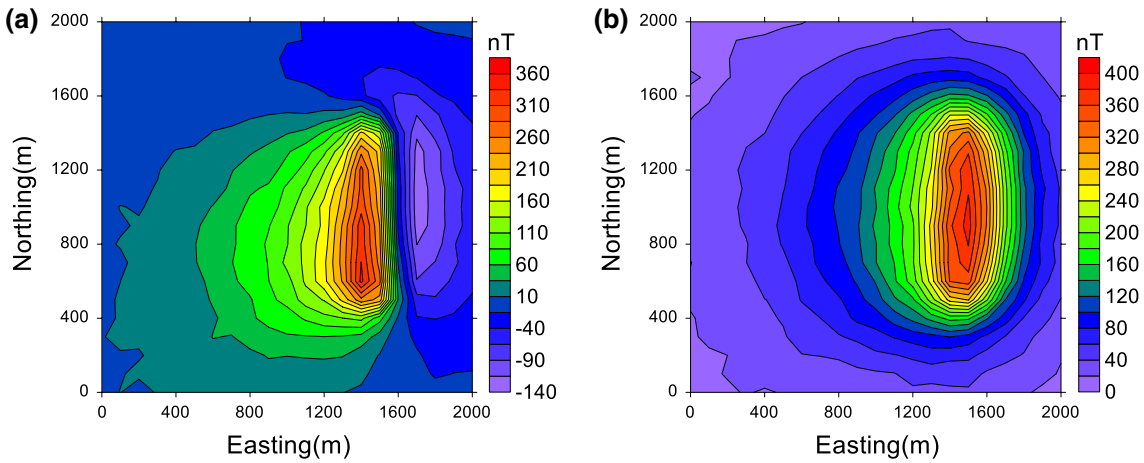

Fig. 1 **a** The total-field anomaly produced by the dipping slab model. **b** The amplitude data computed from the data in Fig. 1a

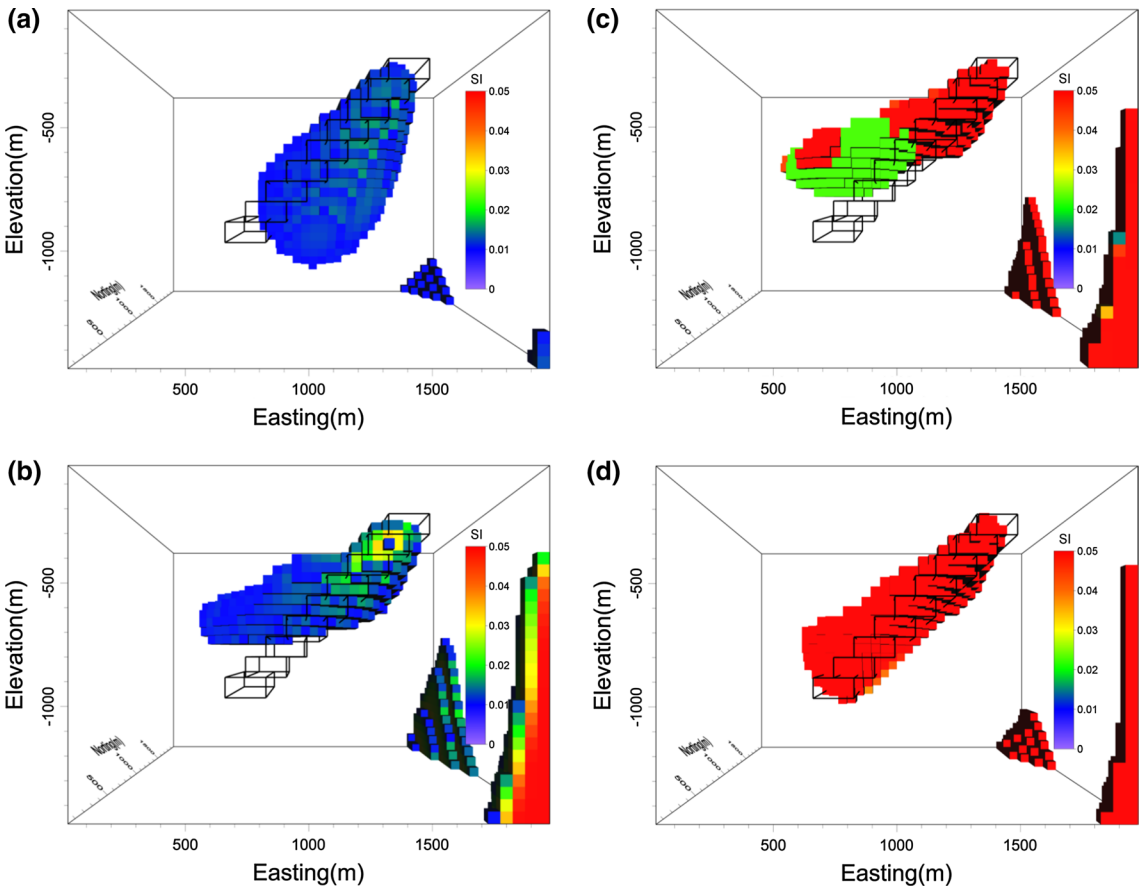

Fig. 2 Perspective views of inversion results of magnetic amplitude data in Fig. 1b using different model norms of **a** L_2-norm, **b** total variation functional, **c** minimum gradient support functional, and **d** the proposed L0-like-norm. The lower and upper bounds of all inversions are set to 0 and 0.05 SI, respectively. The cutoff values of **a** and **b** are 0.01 SI. The cutoff values of **c** and **d** are 0.001 SI. The black lines indicate the position of the true model

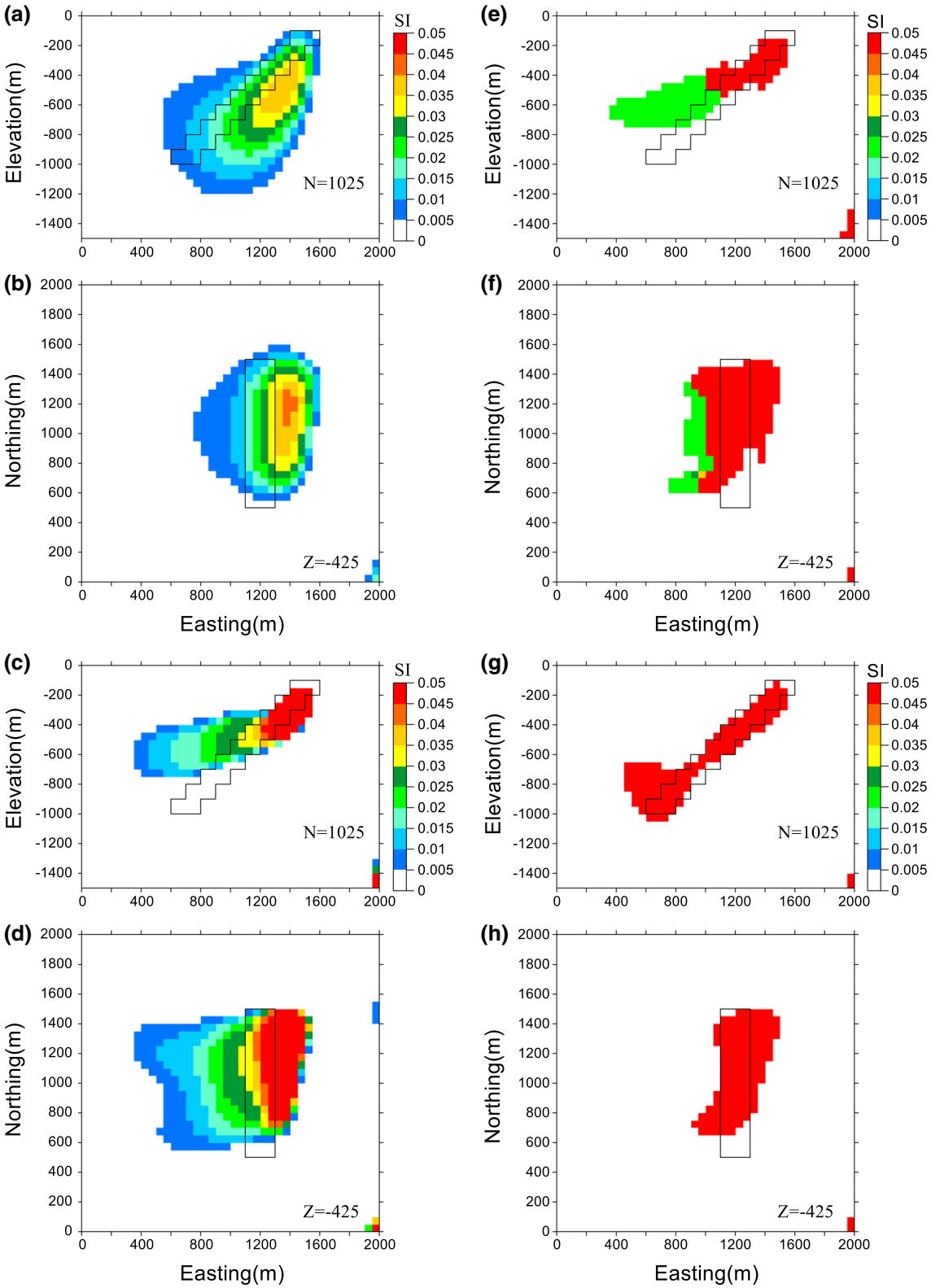

Fig. 3 Central slices of inversion results of magnetic amplitude data in Fig. 1b using different model norms of **a**–**b** L_2-norm, **c**–**d** total variation functional, **e**–**f** minimum gradient support functional, and **g**–**h** the proposed L0-like-norm. The lower and upper bounds of all inversions are set to 0 and 0.05 SI, respectively. The black lines indicate the position of the true model

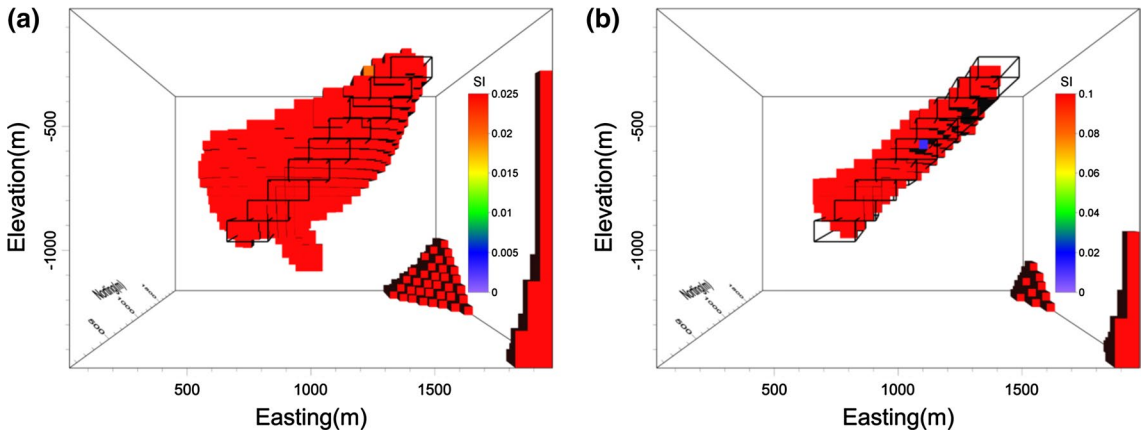

Fig. 4 Perspective views of inversion results of magnetic amplitude data in Fig. 1b using the proposed L0-like-norm with upper bounds of **a** 0.025 and **b** 0.1 SI, respectively. The cutoff values of both **a** and **b** are 0.001 SI. The black lines indicate the position of the true model

In the previous example, we invert amplitude data produced by the dyke model using the true upper bound of 0.05 SI. Here, we invert the amplitude anomaly in Fig. 1b using the proposed sparse inversion method with incorrect upper bounds of 0.025 and 0.1 SI, respectively. The recovered models are shown in 3D perspective views in Fig. 4 and 2D slice views in Fig. 5. Figures 4a and 5a, b display the model produced by using an upper bound of 0.025 SI. Figures 4b and 5c, d present results by using an upper bound of 0.1 SI. Both recovered models are still binary. However, the sizes of the recovered bodies are overestimated if a smaller upper bound is set and vice versa. Therefore, reliable physical property information

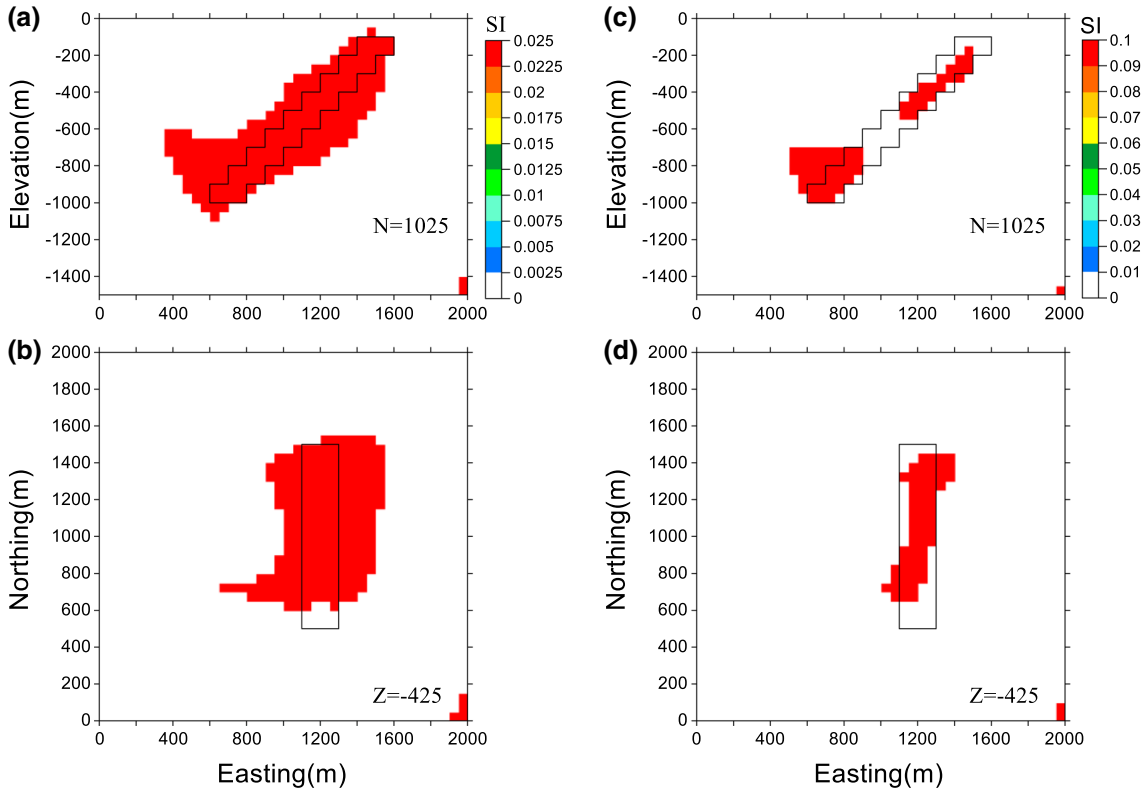

Fig. 5 Central slices of inversion results of magnetic amplitude data in Fig. 1b using upper bounds of **a**–**b** 0.025 and **c**–**d** 0.1 SI, respectively. The black lines indicate the position of the true model

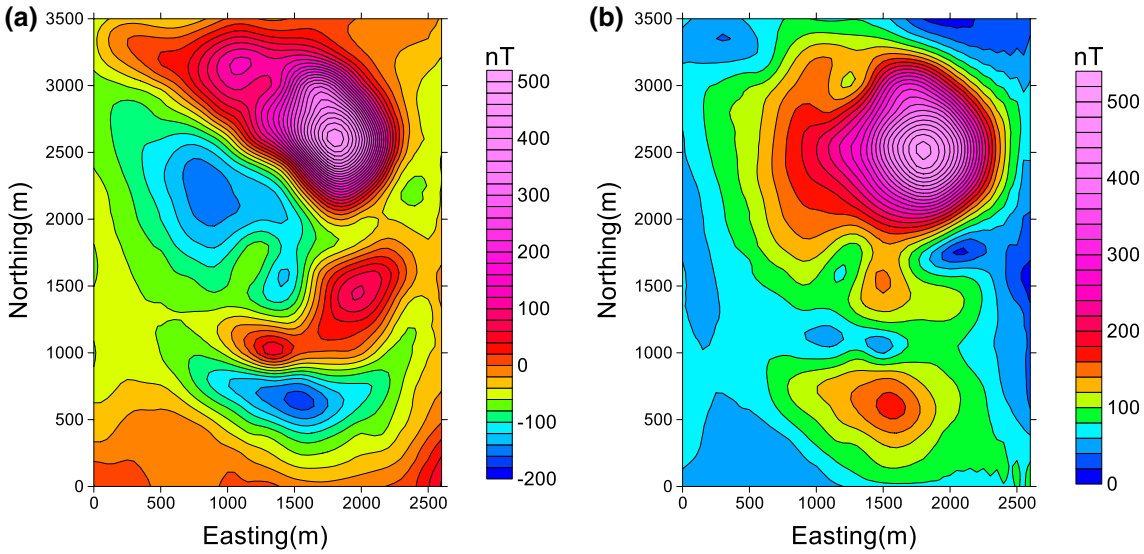

Fig. 6 **a** The total-field anomaly of the field data. **b** The amplitude data computed from the data in Fig. 6a

is crucial to precise recovery of source distribution when the proposed sparse inversion method is used.

Field example

We also apply the algorithm to a field data set acquired in Australia. The total-field anomaly is shown in Fig. 6a and gridded into a 53×71 grid of 50 m spacing. The geomagnetic field has an inclination of $-64.7°$, a declination of 2.1°, and a strength of 58240 nT. We can see that three anomalies with different orientations occur in the survey area. Using a single magnetization direction to invert these data would be clearly inappropriate. Therefore, we transform the total-field anomaly to amplitude data shown in Fig. 6b.

For the magnetic data shown in Fig. 6a, we have no available physical property information. To estimate the effective susceptibilities of causative bodies, we first perform a positivity-constrained smooth inversion of the amplitude data. The model region is divided into $52\times70\times40$ cubes of 50 m on each side. The maximum value of the smooth model (Fig. 7a) is about 0.05 SI. Considering the uncertainty of the source susceptibility, we perform three sparse inversions with different upper bounds of 0.03, 0.05, and 0.07 SI, respectively.

The models recovered from sparse inversion are shown in Fig. 7b–d. Each one possesses a binary feature. Although these models have sharp boundaries, the accuracy of boundaries depends on the upper bounds of the inversion. Figure 8 shows the inversion results in cross-sectional views. Figure 8a, b presents the results of positivity-constrained L_2-norm inversion, which are smooth and diffused. Figure 8c, d displays the results of sparse inversion with an upper bound of 0.05 SI, which are binary.

The two models (smooth and sparse) in Fig. 8 show some differences. For example, the causative bodies on the north in the two models have different dipping angles and different depth extent. Judging the reliability of the two models requires more geological information.

Conclusion

The existence of strong remanence changes magnetization directions and thereby affects inversion and interpretation of magnetic data. Magnetic amplitude inversion is an effective means for recovering subsurface source distributions in the presence of strong remanence. In this paper, we present a method for sparse inversion of magnetic amplitude data. This method minimizes a L_0-like-norm of model parameters subject to bound constraints. The IRLS technique transforms the bound-constrained sparse inversion to a sequence of bound-constrained weighted least squares subproblems, each of which is solved by the logarithm barrier algorithm. Tests on synthetic and field data examples demonstrate that the proposed method produces binary results in the presence of strong remanence.

Acknowledgements We thank Geoscience Australia for providing the field data. This work was supported by the Innovation Fund Project of Hebei University of Engineering (No. SJ010002155) and National Natural Science Foundation of China (No. 41574132). We would like to thank the associate editor T. Grabowska and two anonymous reviewers for their constructive comments that have helped improve the quality of the manuscript.

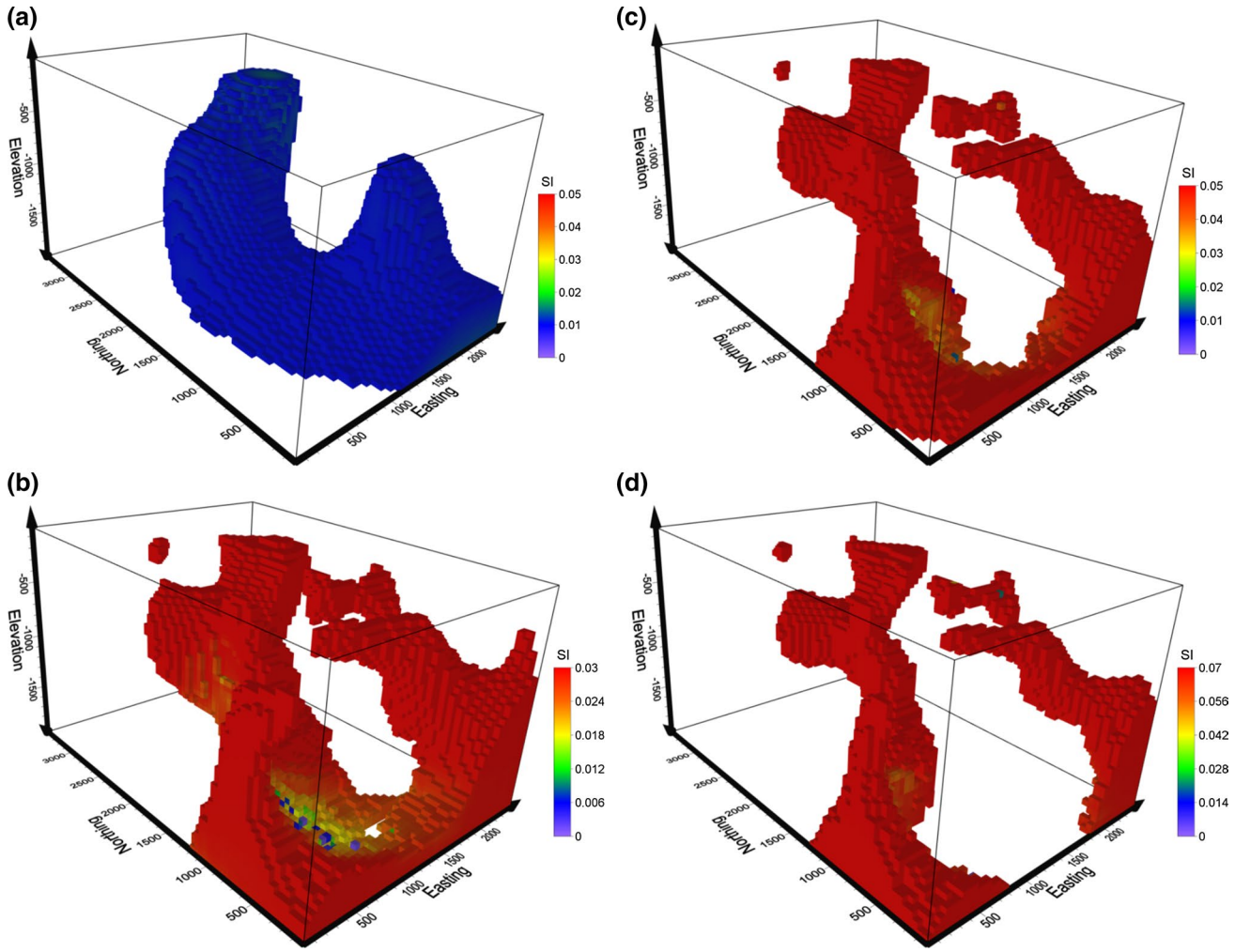

Fig. 7 Perspective views of inversion results of magnetic amplitude data in Fig. 6b. **a** Results of positivity-constrained L_2-norm inversion. **b–d** Results of sparse inversion with upper bounds of 0.03, 0.05, and 0.07 SI, respectively. Noise level is assumed to be 5% datum magnitude plus 5 nT. The cutoff value of **a** is 0.01 SI. The cutoff values of **b–d** are 0.001 SI

Compliance with ethical standards

Conflict of Interest On behalf of all authors, the corresponding author states that there is no conflict of interest.

Appendix

The logarithm barrier method for bound-constrained L_2-norm inversion of magnetic amplitude data

Li and Oldenburg (2003) and Li et al. (2010) have developed practical logarithm barrier methods for solving bound-constrained nonlinear least squares problems in magnetic inversion. We summarized their methods (Li and Oldenburg, 2003; Li et al. 2010) here. First, for simplicity, we omit the superscripts and rewrite Eq. 9 as

$$\begin{aligned} \min \quad & \varphi_c(\boldsymbol{m}) = \varphi_d(\boldsymbol{m}) + \mu\varphi_{cm}(\boldsymbol{m}) \\ \text{s.t.} \quad & \boldsymbol{m}_{\min} \le \boldsymbol{m} \le \boldsymbol{m}_{\max}. \end{aligned} \tag{11}$$

The logarithm barrier method approximates Eq. 11 as a sequence of unconstrained minimizations, making the inequality constraints implicit in the new objective function by adding a barrier term:

$$\min \quad \varphi(\boldsymbol{m}) = \varphi_c(\boldsymbol{m}) + \lambda\varphi_\lambda(\boldsymbol{m}), \tag{12}$$

where λ is a barrier parameter and will be decreased during minimization. φ_λ is a barrier function and has the form

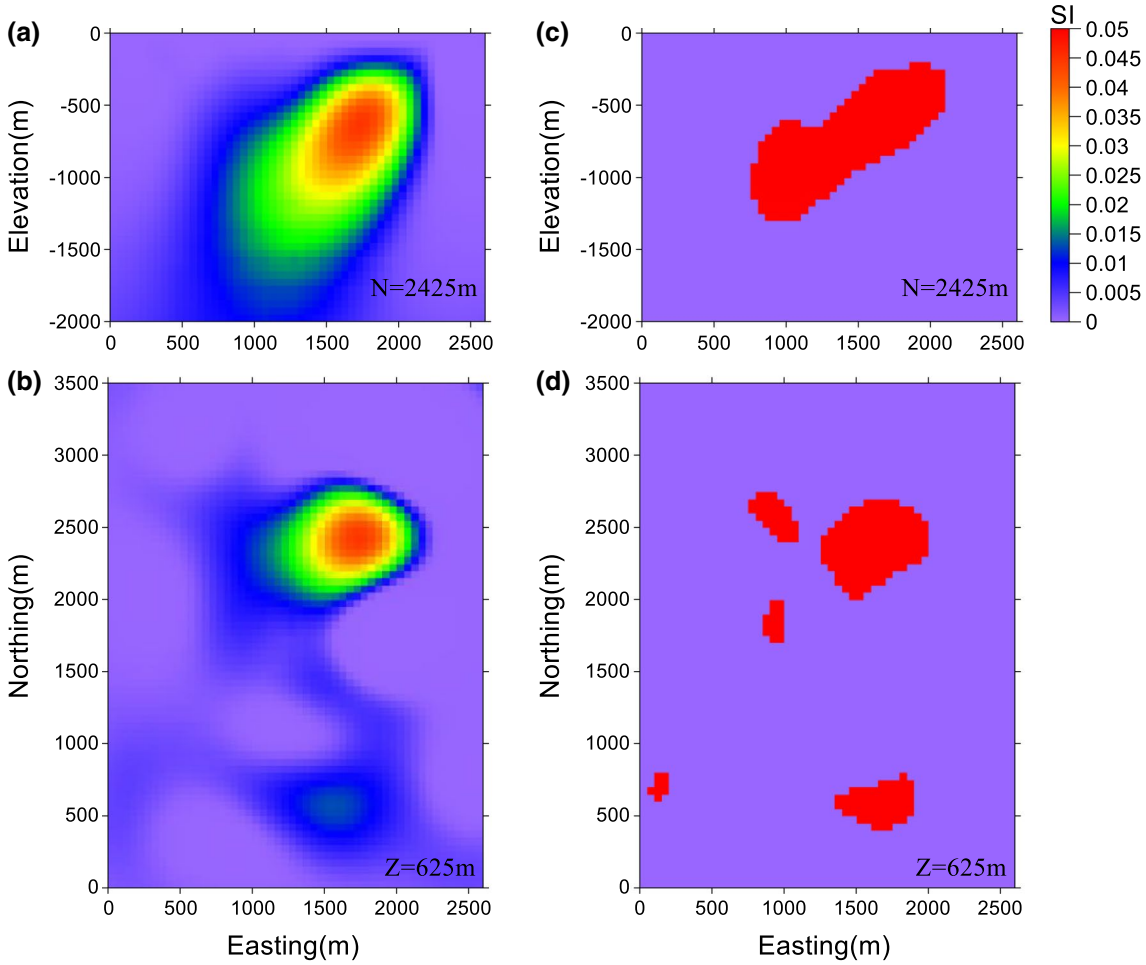

Fig. 8 Cross-sectional views of inversion results of magnetic amplitude data in Fig. 6b. **a–b** The recovered model produced by positivity-constrained L_2-norm inversion. **c–d** The recovered model produced by sparse inversion with the upper bound of 0.05

$$\varphi_\lambda(\boldsymbol{m}) = -\sum_{j=1}^{M}\left[\ln\left(\frac{m_j - m_{\min}}{m_{\max} - m_{\min}}\right) + \ln\left(\frac{m_{\max} - m_j}{m_{\max} - m_{\min}}\right)\right]. \tag{13}$$

Applying one step of Gauss–Newton method for Eq. 12 at the kth iteration, we obtain

$$\begin{aligned}&\left\{(\boldsymbol{J}^{(k)})^T\boldsymbol{W}_d^T\boldsymbol{W}_d\boldsymbol{J}^{(k)} + \mu\boldsymbol{Z}^T\boldsymbol{R}^T\boldsymbol{R}\boldsymbol{Z} + \lambda^{(k-1)}[(\boldsymbol{X}^{(k)})^{-2} + (\boldsymbol{Y}^{(k)})^{-2}]\right\}\Delta\boldsymbol{m}\\ &= (\boldsymbol{J}^{(k)})^T\boldsymbol{W}_d^T\boldsymbol{W}_d[\boldsymbol{d} - \boldsymbol{F}(\boldsymbol{m}^{(k-1)})] - \mu\boldsymbol{Z}^T\boldsymbol{R}^T\boldsymbol{R}\boldsymbol{Z}\boldsymbol{m}^{(k-1)} + \lambda^{(k-1)}[(\boldsymbol{X}^{(k)})^{-1} + (\boldsymbol{Y}^{(k)})^{-1}]\mathbf{1},\end{aligned} \tag{14}$$

where $\boldsymbol{J}^{(k)}$ is the Jacobian matrix (Li et al. 2010) at the kth iteration, $\Delta\boldsymbol{m}$ is the descent direction of objective function, $\boldsymbol{X}^{(k)}$ and $\boldsymbol{Y}^{(k)}$ are diagonal matrixes with $\boldsymbol{m}^{(k-1)} - \boldsymbol{m}_{\min}$ and $\boldsymbol{m}^{(k-1)} - \boldsymbol{m}_{\max}$ on their main diagonals, and $\mathbf{1}$ is the column vector with all entries 1. Once the descent direction has been computed, the solution of Eq. 11 can be iteratively solved with appropriate choice of a step length and careful update of the barrier parameter. The algorithm for solving Eq. 11 is summarized as follows:

1. Initialize $\boldsymbol{m}^{(0)} = \mathbf{0.001}$, $\lambda^{(0)} = \varphi_c(\boldsymbol{m}^{(0)})/\varphi_\lambda(\boldsymbol{m}^{(0)})$, and $k = 1$.
2. Form $\boldsymbol{X}^{(k)}$ and $\boldsymbol{Y}^{(k)}$ from $\boldsymbol{m}^{(k-1)}$.
3. Solve Eq. 14 for $\Delta\boldsymbol{m}$.
4. $\boldsymbol{m}^{(k)} \leftarrow \boldsymbol{m}^{(k-1)} + \gamma\beta^{(k)}\Delta\boldsymbol{m}$, where $\gamma = 0.925$ and

$$\beta^{(k)} = \begin{cases} 1, \text{if } \boldsymbol{m}_{\max} > \boldsymbol{m}^{(k-1)} + \Delta\boldsymbol{m} > \boldsymbol{m}_{\min} \\ \min\left(\min\limits_{\Delta m_i<0} \frac{\boldsymbol{m}_i^{(k-1)} - m_{\min}}{|\Delta \boldsymbol{m}_i|}, \min\limits_{\Delta m_i>0} \frac{m_{\max} - \boldsymbol{m}_i^{(k-1)}}{\Delta \boldsymbol{m}_i} \right), \text{ otherwise.} \end{cases}$$

5. $\lambda^{(k)} \leftarrow [1 - \min(\beta^{(k)}, \gamma)]\lambda^{(k-1)}$.
6. Terminate on convergence or when k attains a specified maximum number of iterations $k_{\max}$. Otherwise, $n \leftarrow n + 1$ and go to Step 2.

References

Abedi M, Fournier D, Devriese SG, Oldenburg DW (2018) Potential field signatures along the Zagros collision zone in Iran. Tectonophysics 722:25–42

Beaton AE, Tukey JW (1974) The fitting of power series, meaning polynomials, illustrated on band-spectroscopic data. Technometrics 16(2):147–185

Beiki M, Clark DA, Austin JR, Foss CA (2012) Estimating source location using normalized magnetic source strength calculated from magnetic gradient tensor data. Geophysics 77(6):J23–J37

Chartrand R, Yin W (2008) Iteratively reweighted algorithms for compressive sensing. In: 2008 IEEE international conference on acoustics, speech and signal processing, pp 3869–3872

Dampney CNG (1969) The equivalent source technique. Geophysics 34(1):39–53

Daubechies I, DeVore R, Fornasier M, Güntürk CS (2010) Iteratively reweighted least squares minimization for sparse recovery. Commun Pure Appl Math 63(1):1–38

Ellis RG, de Wet B, Macleod IN (2012) Inversion of magnetic data for remanent and induced sources. ASEG Ext Abstr 2012(1):1–4

Farquharson CG (2008) Constructing piecewise-constant models in multidimensional minimum-structure inversions. Geophysics 73(1):K1–K9

Farquharson CG, Oldenburg DW (1998) Non-linear inversion using general measures of data misfit and model structure. Geophys J Int 134(1):213–227

Guo L, Meng X, Zhang G (2014) Three-dimensional correlation imaging for total amplitude magnetic anomaly and normalized source strength in the presence of strong remanent magnetization. J Appl Geophys 111:121–128

Holland PW, Welsch RE (1977) Robust regression using iteratively reweighted least-squares. Commun Stat-Theory Methods 6(9):813–827

Hou ZC (1979) Using potential field transformation to build an interpretation system of gravity and magnetic anomalies. Geophys Geochem Explor 3(3):1–10 **(in Chinese with English abstract)**

Krahenbuhl RA, Li Y (2017) Investigation of magnetic inversion methods in highly magnetic environments under strong self-demagnetization effect. Geophysics 82(6):J83–J97

Last BJ, Kubik K (1983) Compact gravity inversion. Geophysics 48(6):713–721

Lelievre PG, Oldenburg DW (2006) Magnetic forward modelling and inversion for high susceptibility. Geophys J Int 166(1):76–90

Lelièvre PG, Oldenburg DW (2009) A 3D total magnetization inversion applicable when significant, complicated remanence is present. Geophysics 74(3):L21–L30

Lelièvre PG, Oldenburg DW, Williams NC (2009) Integrating geological and geophysical data through advanced constrained inversions. Explor Geophys 40(4):334–341

Li SL, Li Y (2014) Inversion of magnetic anomaly on rugged observation surface in the presence of strong remanent magnetization. Geophysics 79(2):J11–J19

Li Y, Oldenburg DW (1996) 3-D inversion of magnetic data. Geophysics 61(2):394–408

Li Y, Oldenburg DW (2003) Fast inversion of large-scale magnetic data using wavelet transforms and a logarithmic barrier method. Geophys J Int 152(2):251–265

Li Y, Sun J (2016) 3D magnetization inversion using fuzzy c-means clustering with application to geology differentiation. Geophysics 81(5):J61–J78

Li Y, Shearer SE, Haney MM, Dannemiller N (2010) Comprehensive approaches to 3D inversion of magnetic data affected by remanent magnetization. Geophysics 75(1):L1–L11

Li ZL, Yao CL, Zheng YM, Meng XH, Zhang YM (2015) 3D data-space inversion of magnetic amplitude data. Chin J Geophys 58(10):3804–3814 **(in Chinese with English abstract)**

Li Z, Yao C, Zheng Y, Wang J, Zhang Y (2018) 3D magnetic sparse inversion using an interior-point method. Geophysics 83(3):J15–J32

Liu S, Hu X, Liu T, Feng J, Gao W, Qiu L (2013) Magnetization vector imaging for borehole magnetic data based on magnitude magnetic anomaly. Geophysics 78(6):D429–D444

Liu S, Hu X, Xi Y, Liu T, Xu S (2015) 2D sequential inversion of total magnitude and total magnetic anomaly data affected by remanent magnetization. Geophysics 80(3):K1–K12

Liu S, Hu X, Zhang H, Geng M, Zuo B (2017) 3D magnetization vector inversion of magnetic data: improving and comparing methods. Pure appl Geophys 174(12):4421–4444

Nabighian MN (1972) The analytic signal of two-dimensional magnetic bodies with polygonal cross-section: its properties and use for automated anomaly interpretation. Geophysics 37(3):507–517

Oldenburg DW, Li Y, Ellis RG (1997) Inversion of geophysical data over a copper gold porphyry deposit: a case history for Mt. Milligan Geophys 62(5):1419–1431

Paine J, Haederle M, Flis M (2001) Using transformed TMI data to invert for remanently magnetised bodies. Explor Geophys 32(3–4):238–242

Pedersen LB (1978) Wavenumber domain expressions for potential fields from arbitrary 2-, 21/2-, and 3-dimensional bodies. Geophysics 43(3):626–630

Pilkington M (1997) 3-D magnetic imaging using conjugate gradients. Geophysics 62(4):1132–1142

Pilkington M (2009) 3D magnetic data-space inversion with sparseness constraints. Geophysics 74(1):L7–L15

Pilkington M, Beiki M (2013) Mitigating remanent magnetization effects in magnetic data using the normalized source strength. Geophysics 78(3):J25–J32

Portniaguine O, Zhdanov MS (1999) Focusing geophysical inversion images. Geophysics 64(3):874–887

Portniaguine O, Zhdanov MS (2002) 3-D magnetic inversion with data compression and image focusing. Geophysics 67(5):1532–1541

Rao BD, Kreutz-Delgado K (1999) An affine scaling methodology for best basis selection. IEEE Trans Signal Process 47(1):187–200

Roest WR, Verhoef J, Pilkington M (1992) Magnetic interpretation using the 3-D analytic signal. Geophysics 57(1):116–125

Rudin LI, Osher S, Fatemi E (1992) Nonlinear total variation based noise removal algorithms. Physica D 60(1–4):259–268

Shearer S, Li Y (2004) 3D inversion of magnetic total gradient data in the presence of remanent magnetization. SEG Tech Progr Expand Abstr 2004:774–777

Stavrev P, Gerovska D (2000) Magnetic field transforms with low sensitivity to the direction of source magnetization and high centricity. Geophys Prospect 48(2):317–340

Sun J, Li Y (2018) Magnetization clustering inversion—Part 1: building an automated numerical optimization algorithm. Geophysics 83(5):J61–J73

Wang MY, Di QY, Xu K, Wang R (2004) Magnetization vector inversion equations and 2D forward and inversed model study. Chin J Geophys 47(3):528–534 **(in Chinese with English abstract)**

Wilson H (1985) Analysis of the magnetic gradient tensor: defence Research Establishment Pacific. Tech Memo 8:5–13

Zhou J, Meng X, Guo L, Zhang S (2015) Three-dimensional cross-gradient joint inversion of gravity and normalized magnetic source strength data in the presence of remanent magnetization. J Appl Geophys 119:51–60

Acta Geophysica (2020) 68:377–388
https://doi.org/10.1007/s11600-020-00403-6

RESEARCH ARTICLE - APPLIED GEOPHYSICS

2D multi-parameter waveform inversion of land reflection seismic data obtained from the particle-motion response from the vertical geophone

Qingyang Li[1,2] · Guochen Wu[1,2]

Received: 24 September 2019 / Accepted: 20 January 2020 / Published online: 25 February 2020

Abstract
Onshore seismic exploration analyzes seismic wave propagation in elastic media, which includes the conversion between P- and S-waves. The development of multi-wave and multi-component seismic exploration methods provides data that enable onshore elastic wave full-waveform inversion. However, most data sets of onshore exploration are single component obtained from the particle-motion response from the vertical geophone. When the aiming area has a low-velocity zone, the ray path of reflected wave that propagates to the detector is nearly perpendicular to the ground surface, so that we call it P-wave data. In this paper, we focus on multi-parameter waveform inversion using P-wave reflection seismic data. Although only P-wave data are received, it still contains the converted P-wave information, and the converted P-wave energy gradually increases as the offset increases. As seismic acquisition technology, observation systems and science develop, the folds and acquisition offset increase significantly, and the seismic data contain important converted P-wave information. In this paper, the first-order elastic velocity–stress equation is decomposed to obtain the scalar-P-wave equation from which the S-wave velocity is included firstly. Then we present the theoretical framework for onshore multi-parameter full-waveform inversion using P-wave data. In order to explore the inversion potential of the P-wave data (extracting the S-wave velocity from the converted P-wave information) and accuracy and stability of the P- and S-wave velocity inverted by our method, we carry out numerical tests via different inversion strategies, by using the P-wave data regarded as containing converted P-wave information, and get successful results.

Keywords Scalar-P-wave equation · Converted P-wave · Onshore seismic full-waveform inversion · P- and S-wave velocity

Introduction

Full-waveform inversion (FWI) is a quantitative data-fitting procedure which minimizes the residuals between the simulated and the observed seismic data to obtain high-resolution subsurface physical parameters such as P-wave velocity, density, impedance, or anisotropic parameters (Virieux and Operto 2009). Lailly (1983) and Tarantola (1984) first proposed the least-squares misfit functional FWI framework and built the gradient of the misfit function by cross-correlating the incident wavefield emitted from the source and the back-propagated residual wavefields. Pratt and Worthington (1990) extended FWI to the frequency domain and pointed out that multi-scale inversion can improve the effectiveness and stability of the inversion. At present, FWI has been successfully applied for both simulated and real seismic data (Shipp and Singh 2002; Sears et al. 2008; Sirgue et al. 2010).

Since the 1990s, the emergence of the ocean bottom cable (OBC) system has caused a dramatic change in marine multi-wave seismic exploration technology. Since 2000, onshore multi-wave multi-component exploration has gradually developed. For multi-component seismic data, elastic wave full-waveform inversion (EFWI) is more suitable for high-precision reconstruction of subsurface elastic parameters than acoustic full-wave inversion (AFWI) (Brossier et al. 2009). In some

✉ Guochen Wu
guochenwu@upc.edu.cn

Qingyang Li
986132055@qq.com

[1] School of Geosciences, China University of Petroleum (East China), Qingdao, China

[2] Laboratory for Marine Mineral Resources, Qingdao National Laboratory for Marine Science and Technology, Qingdao, China

complex areas, AFWI cannot describe elastic wave propagation processes (Barnes and Charara 2009), such as the P/S converted wave and amplitude variation with offset (AVO) effects. EFWI can provide more accurate P- and S-wave velocities for seismic data processing and interpretation, and also provide high-quality parameter information for reservoir description and for oil and gas field development (Tatham and Stoffa 1976).

When multiple parameters are simultaneously processed, the nonlinearity of FWI increases because certain parameters are coupled to each other (Wu and Aki 1985). Many scholars (e.g., Tarantola 1986; Mora 1988; Crase et al. 1990) discussed the elastic wave waveform inversion theory and applied it to simulated and actual data. They developed and improve the forward modeling and inversion theory, iterative optimization method, misfit function, and inversion strategy. Pratt (Pratt et al. 1998, 1999a, b) also proposed the frequency-domain EFWI theory while presenting the AFWI. Crase et al. (1990) used the first-order velocity–stress equation to invert the P-wave impedance, based on various minimization criteria.

Compared with the P- and S-wave velocity parameters, the density variation mainly affects the amplitude information of the seismic wavefield, and has little effect on wave diffusion parameters such as travel time and phase. Therefore, density is the most difficult parameter to be inverted in multi-parameter inversions. Tarantola (1984) proposed a velocity–density inversion strategy based on the acoustic wave equation with variable density. Mora (1987) pointed out that near-offset seismic data are suitable for impedance parameter inversion, while the far-offset data are suitable for velocity parameter inversion, but neither method can adequately invert the density model. Köhn et al. (2012) showed that the use of velocity–density parameterization in multi-parameter EFWI is better than Lame constant-density parameterization. Jeong et al. (2012) proposed a multi-parameter EFWI strategy in the frequency domain, which first inverts the elastic modulus, then simultaneously inverts the velocity and density.

Multi-wave and multi-component seismic exploration technology are still developing, and many problems still need to be solved. At present, most onshore exploration is based on single component, which is collected from obtained from the particle-motion response from the vertical geophone. In this situation, there is a classical assumption that the subsurface is regarded as a fluid (Raknes et al. 2015). When the area has a low-velocity zone, which causes the ray path of reflected wave that propagates to detector is nearly perpendicular by Snell's law working, we call the field data set the P-wave data. Acoustic wave equation is generally used to match the P-wave data, and AFWI is a well-known method in the application of current onshore full-waveform inversion, but it has no possiblity to invert S-wave velocity. However, the seismic data does not contain the S-wave information directly, while it includes a large amount of converted P-wave information, such as P–S–P-wave. It would therefore be possible to establish a scalar-P-wave multi-parameter equation in the elastic wavefield to synthesize record to match the real seismograms.

In this paper, we decompose the elastic first-order velocity–stress equation and obtain the scalar-P-wave equation that includes the S-wave velocity. We apply the conventional acoustic equation, the scalar-P-wave equation and the elastic wave equation to a simple layered model, then analyze the converted wave characteristics of the three equations by comparing the different forward results, and evaluate the S-wave velocity inversion. Then we propose the onshore FWI algorithm based on P-wave data and carry out different inversion strategies using the Marmousi-2 model. Our results confirm the accuracy and stability of the inversion of the P- and S-wave velocities using P-wave data with converted P-wave information.

Method

Why the acoustic approximation can work on land seismic

In exploration geophysics, FWI has come into broad use for applications (Sirgue and Pratt 2004). Generally, scholars make an assumption that subsurface can be considered as a fluid, as we called acoustic approximation (Tarantola 1984). Not considering the limitations in available computer resources, there are two main reasons for this assumption. One is that seismic usually acquire measurements of P-wave, whether current marine data obtained from the pressure response of hydrophone (Vigh et al. 2014) or land data obtained from the particle-motion response from the vertical geophone (details in the next paragraph) correspond to compressional wavefield (Gaiser et al. 2001). The other is that conventional processing focuses on the kinematics of P-waves, and it is well modeled by acoustic wave equation (Raknes et al. 2015).

Different from marine data that obtain pressure response directly, land seismic data usually acquire measurements of the vertical particle velocity (Simmons and Backus 2003). As we all know, the numerical solution of elastic wave equation is more reliable than that of acoustic wave equation to approximate field data (Virieux and Operto 2009). Actually, land seismic data contains converted S-wave, which could have a very strong impact on the acoustic inversion results. Fortunately, the near surface is a low-velocity zone, which causes the ray path of reflected wave that propagates to detector is nearly perpendicular to the ground surface (Snell's law works), as shown in Fig. 1. Thus, land seismic data obtained from the vertical geophone can be considered as P-wave, and it can be assumed that the P- and S-wave are naturally decoupled in land seismic data as shown in Fig. 1. However, this assumption is not applicable in all cases, such as strong anisotropy of

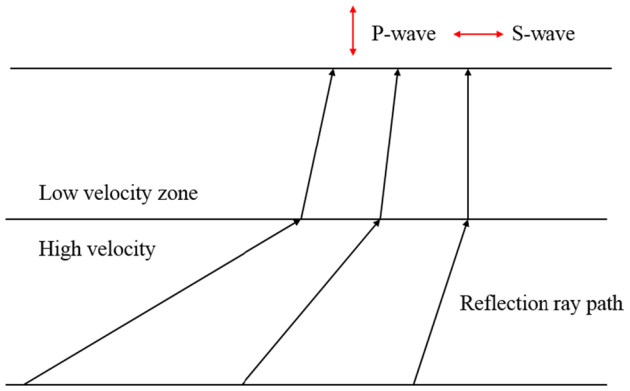

Fig. 1 Ray path of reflection in low-velocity zone

near surface and exposed bedrock environment, which are not considered in this paper.

In acoustic FWI, the subsurface medium is parameterized by density (ρ) and P-wave velocity (v_P), and well inverted (Virieux and Operto 2009). In the field, the land seismic data are obtained only from vertical particle velocity from the vertical geophone, while in the real application, the measurements of seismograms is pressure but not velocity, because the most choice of acoustic equation is second-order system (Ravaut et al. 2004; Operto et al. 2006), in which the vertical particle velocity is implicit. In fact, almost all research use simulated pressure data to match vertical velocity data observed, directly. Then we analyze the relationship between the vertical velocity field and the pressure field and explain that why the seismic data can be modeled by acoustic wave equation in the field.

For the convenience of research, we give the first-order system acoustic wave equation as,

$$\begin{aligned} \frac{\partial v_x}{\partial t} &= \frac{1}{\rho}\frac{\partial P}{\partial x} \\ \frac{\partial v_z}{\partial t} &= \frac{1}{\rho}\frac{\partial P}{\partial z} \\ \frac{\partial P}{\partial t} &= K\left(\frac{\partial v_x}{\partial x}+\frac{\partial v_z}{\partial z}\right)+f \end{aligned}, \tag{1}$$

where P is pressure wavefield, K is bulk modulus, ρ is density, f is the source, $\mathbf{v} = \left(v_x, v_z\right)$ is particle velocity vector, and t is the time.

The pressure and velocity record modeled by acoustic wave equation are shown in Fig. 2a–c, and the travel time and phase information of reflected waveform in vertical velocity record are the same as that in pressure record. For the medium with strong contrasts, the pressure date and velocity data have significant amplitude mismatch at far offsets, which could be solved by data regularization (Hobro et al. 2014). This explains that why the pressure field is used directly to match observed data in conventional land seismic FWI. In this paper, we assume the medium is full elastic, and propose a new multi-parameter waveform inversion method to invert the S-wave velocity (v_S). In our method, the P-wave data are considered to contain rich convert P-wave information to match observed vertical velocity data, which details in the next section.

In addition, the land FWI is also affected by near-surface heterogeneity, anisotropic, attenuation and ground roll, which have a very strong impact on the inversion results and are ignored here.

Scalar-P-wave equation based on elastic decomposition

The application of FWI in industry typically invert two-parameter models, as v_P and ρ. In this work, in additional to aforementioned models, we also try to invert S-wave velocity (v_S). Because of the natural decomposition of P- and S-wave in land seismic data, converted S-wave is not collected directly in vertical geophone, and the S-wave velocity can only be indicated by converted P-wave.

In order to match Methods of decomposition for elastic field are generally divided into three categories. The first is Helmholtz decomposition (Dellinger and Etgen 1990; Sun et al. 2007). The second is vector-based wave equation decomposition (Ma and Zhu 2003; Xiao and Leaney 2010). The third is wavenumber-domain field vector decomposition (Zhang and McMechan 2010). This paper focuses on the elastic

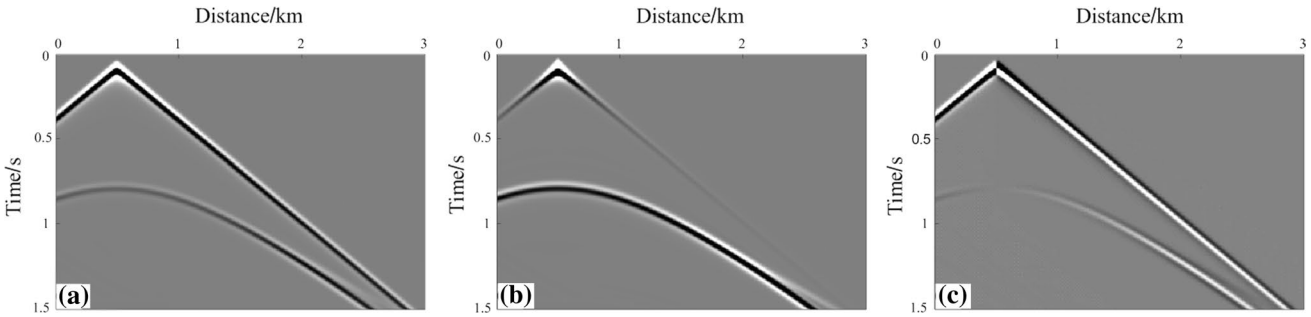

Fig. 2 Pressure (**a**), horizontal (**b**) and vertical (**c**) velocity records modeled by acoustic wave equation

information of P-wavefield based on acoustic approximation and its potential ability to invert v_S. Thus by decomposing constitutive equations into the swell-shrinking (pressure) and shear-rotating forms to decompose the elastic wavefield, we obtain the scalar-P-wave equation (details in "Appendix 1"),

$$\frac{\partial P^2}{\partial t^2} + K\frac{\partial}{\partial x_m}\left[\frac{1}{\rho}\frac{\partial}{\partial x_n}\left(\check{C}_{ijkl}\frac{\partial u_k}{\partial x_l} - P\delta_{ij}\delta_{kl}\delta_{il}\right)\right]\delta_{mn} = f, \quad (2)$$

where $\check{C}_{ijkl}$ is new stiffness tensor, and δ_{ij} is Kronecker's symbol. All indices change from 1 to 3, and rule in Einstein's summation convention over repeated indices.

In isotropic medium, it can be written as:

$$\check{C}_{ijkl} = \underbrace{\lambda\delta_{ij}\delta_{kl} + \mu\left(\delta_{il}\delta_{jl} + \delta_{il}\delta_{jk}\right)}_{C_{ijkl}} - K\delta_{ij}\delta_{kl}. \quad (3)$$

If we set $\mu = 0$, the λ is equal to K,

$$\check{C}_{ijkl} = \lambda\delta_{ij}\delta_{kl} - K\delta_{ij}\delta_{kl} = 0, \quad (4)$$

and scalar-P-wave equation can be rewritten as,

$$\frac{\partial P^2}{\partial t^2} - K\frac{\partial}{\partial x_m}\left(\frac{1}{\rho}\frac{\partial P}{\partial x_n}\right)\delta_{mn} = f. \quad (5)$$

Equation (5) is conventional acoustic wave equation, in which the pure pressure P is different from scalar-P-wave in Eq. (2), which can be regarded as a pseudo-pressure in elastic medium. Like acoustic FWI, we must first study the relationship of the vertical velocity field and the pseudo-pressure field, before the seismic data are modeled by scalar-P-wave equation.

We construct a three-layer elastic model with model size of 2400 × 1500 m, the elastic parameters of first layer are: P-wave velocity of 2500 m/s and S-wave velocity of 1785 m/s; the second layer: P-wave velocity of 3000 m/s and S-wave velocity of 2140 m/s; the third layer: P-wave velocity of 3500 m/s and S-wave velocity of 2500 m/s, while all the density parameter is 1420 kg/m^3. The source, set at (500 m, 10 m), is Ricker wavelet with peak frequency of 20 Hz.

Figure 3a, b shows vertical velocity (v_z) and vertical P-wave (v_{P_z}) velocity elastic wavefield snapshots. Compared with acoustic wavefield (Fig. 3c), elastic v_z field has a lot of converted P- and S-wave, which are decoupled as v_{P_z} and v_{S_z} in land seismic data (see in Sect. 2.1). As shown in Fig. 3b, for the vertical P-wave component, the converted waves generated at the reflection points of two interfaces are visible (Tang and McMechan 2017). Moreover, a converted P–S–P-wave is generated at the second interface, which exists in pseudo-pressure field modeled by scalar-P-wave equation (Fig. 3d) in the same elastic case, but not exist in pure pressure field modeled by acoustic wave equation in acoustic medium (setting $v_S = 0$). Thus v_{P_z} of elastic equation or pseudo-pressure of scalar-P-wave equation can be directly used to match land seismic data in elastic FWI, because of decomposition of P- and S-wave, whose ray path of seismic wave perpendicular to the surface. However, pseudo-pressure modeled by scalar-P-wave equation is a better choice to match observed data. There are two reasons: (1) in order to get v_{P_z}, the computation of elastic modeling by P/S-wave decomposed method(Ren and Liu 2016) requires higher computational cost than scalar-P-wave modeling; (2) conventional processing most focuses on the kinematics of P-waves, and it is well modeled by scalar-P-wave data.

Comparison of v_{P_z} record and pseudo-pressure record as shown in Fig. 4b, d illustrates that converted waves generated of two fields in elastic case are consistent, and this proves the possibility of inversion of S-wave velocity under pseudo-acoustic approximation, which cannot works on acoustic record (Fig. 4c) under pure acoustic approximation.

2D scalar-P-wave equation FWI

Tarantola (1984) defines a local optimization problem of least-squares minimization of the misfit function E between an observed record P_{obs} and simulated data P_{cal},

$$E(m_i) = \frac{1}{2}\sum_{x_r,x_s}\int_t \left(P_{cal} - P_{obs}\right)^t\left(P_{cal} - P_{obs}\right)\mathrm{d}t, \quad (6)$$

where m_i denotes the elastic parameters: v_P,v_S, and ρ, x_r and x_s denote receivers and sources.

The gradient expression of 2D scalar-P-wave equation FWI can be derived by applying the first-order Born approximation (details in "Appendix 2"),

$$\begin{aligned}
\frac{\partial E}{\partial \lambda} &= \int_t -P^*\left(\frac{\partial u}{\partial x} + \frac{\partial w}{\partial z}\right)\mathrm{d}t \\
\frac{\partial E}{\partial \mu} &= \int_t -P^*\left(\frac{\partial u}{\partial x} + \frac{\partial w}{\partial z}\right) + \left(\tau^*_{xx} - \tau^*_{zz}\right)\left(\frac{\partial u}{\partial x} - \frac{\partial w}{\partial z}\right) \\
&\quad + \tau^*_{xz}\left(\frac{\partial u}{\partial z} + \frac{\partial w}{\partial x}\right)\mathrm{d}t \\
\frac{\partial E}{\partial \rho} &= \int_t -\left(u^*\frac{\partial^2 u}{\partial t^2} + w^*\frac{\partial^2 w}{\partial t^2}\right)\mathrm{d}t
\end{aligned} \quad (7)$$

Since the parameterization method using the Lamé constant and density is not a reliable method (Tarantola 1986; Köhn et al. 2012), we chose the velocity–density model parameterization. The gradient of the misfit function with respect to the other parameters can be obtained using the chain rule (Mora 1987):

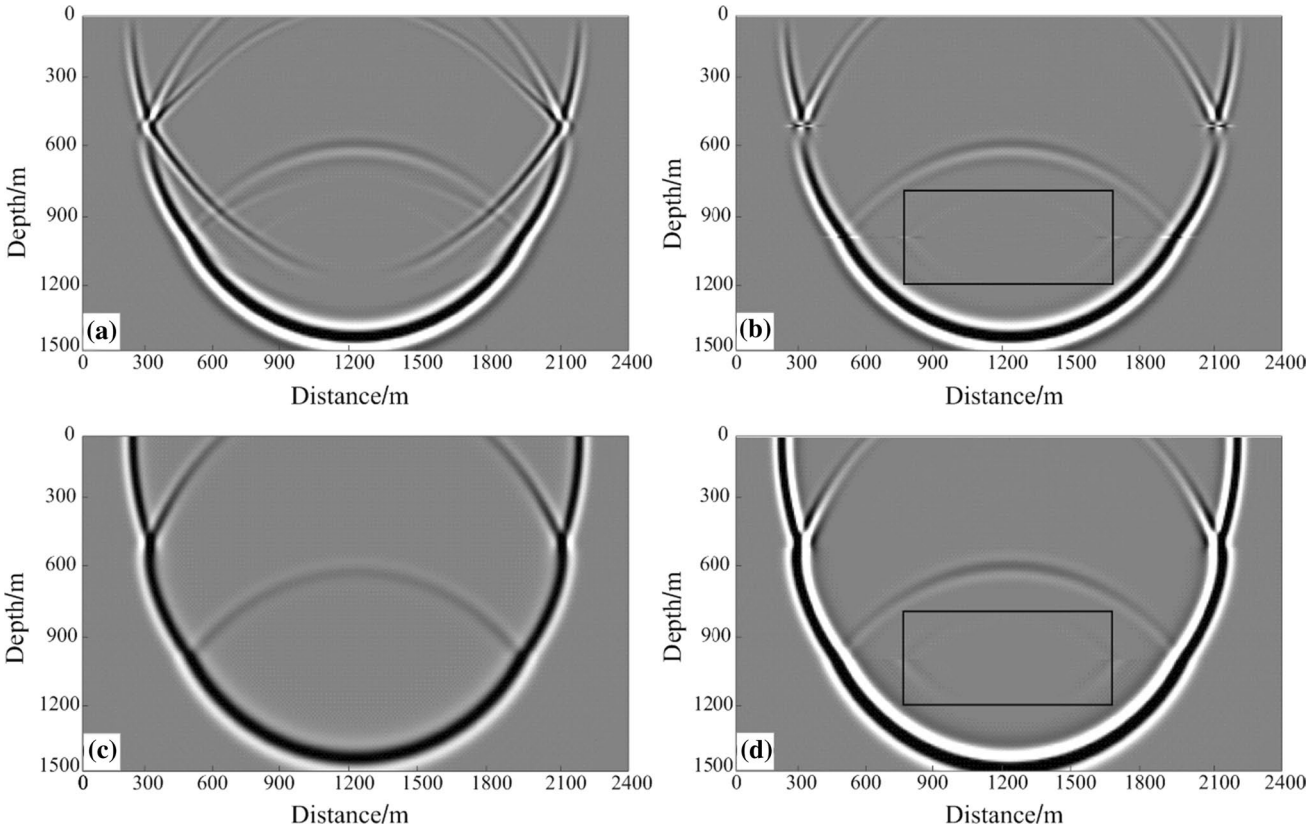

Fig. 3 Layered model forward modeling wavefield snapshots at 0.4 s: **a** v_z of elastic wavefield; **b** v_{P_z} of elastic wavefield; **c** acoustic wavefield; **d** scalar-P-wavefield

$$\begin{aligned}\frac{\partial E}{\partial v_P} &= \frac{\partial E}{\partial \lambda}\frac{\partial \lambda}{\partial v_P} + \frac{\partial E}{\partial \mu}\frac{\partial \mu}{\partial v_P},\\ \frac{\partial E}{\partial v_S} &= \frac{\partial E}{\partial \lambda}\frac{\partial \lambda}{\partial v_S} + \frac{\partial E}{\partial \mu}\frac{\partial \mu}{\partial v_S}\end{aligned} \tag{8}$$

Thus, the velocity–density gradient of the elastic multi-parameter inversion can be expressed as,

$$\begin{aligned}\frac{\partial E}{\partial v_\mathrm{p}} &= \int_t -2\rho v_\mathrm{p} P^*\left(\frac{\partial u}{\partial x}+\frac{\partial w}{\partial z}\right)\mathrm{d}t\\ \frac{\partial E}{\partial v_\mathrm{s}} &= \int_t 2\rho v_\mathrm{s}\begin{bmatrix} P^*\left(\frac{\partial u}{\partial x}+\frac{\partial w}{\partial z}\right)+\tau_{xz}^*\left(\frac{\partial u}{\partial z}+\frac{\partial w}{\partial x}\right)\\ +\tau_{xx}^*\left(\frac{\partial u}{\partial x}-\frac{\partial w}{\partial z}\right)+\tau_{zz}^*\left(\frac{\partial w}{\partial z}-\frac{\partial u}{\partial x}\right)\end{bmatrix}\mathrm{d}t\\ \frac{\partial E}{\partial \rho} &= \int_t -\left(u^*\frac{\partial^2 u}{\partial t^2}+w^*\frac{\partial^2 w}{\partial t^2}\right)\mathrm{d}t.\end{aligned} \tag{9}$$

There are various inversion algorithms used in FWI, such as Gauss–Newton, conjugate-gradient, and Newton method. This paper we apply the conjugate-gradient method (Fletcher and Reeves 1964) to update elastic parameters model with the following steps,

$$\begin{aligned} g_n &= \nabla_{m_i} E\\ \beta &= \frac{g_n^t g_n}{g_{n-1}^t g_{n-1}}\\ k_n &= \begin{cases} -g_0 & \text{if } (n=0)\\ \beta k_{n-1} - g_n & \text{if } (n>0)\end{cases}\\ m_i^{n+1} &= m_i^n - \alpha_n k_n,\end{aligned} \tag{10}$$

where n denotes the current iteration round, t denotes vector transpose operator, α represents the iteration step length, calculated by a one-dimensional line search, and $\nabla_{m_i} E$ represents the gradient of the misfit function with respect to the elastic parameters, k_n is update direction.

Model testing

Marmousi model example

In this section, we test the scalar-P-wave FWI with the well-known 2D Marmousi model. The model shown in Fig. 6 has a grid size of 551 × 251, a sampling interval of 10 m, and a time interval of 0.8 ms. The source excited 8 m under the

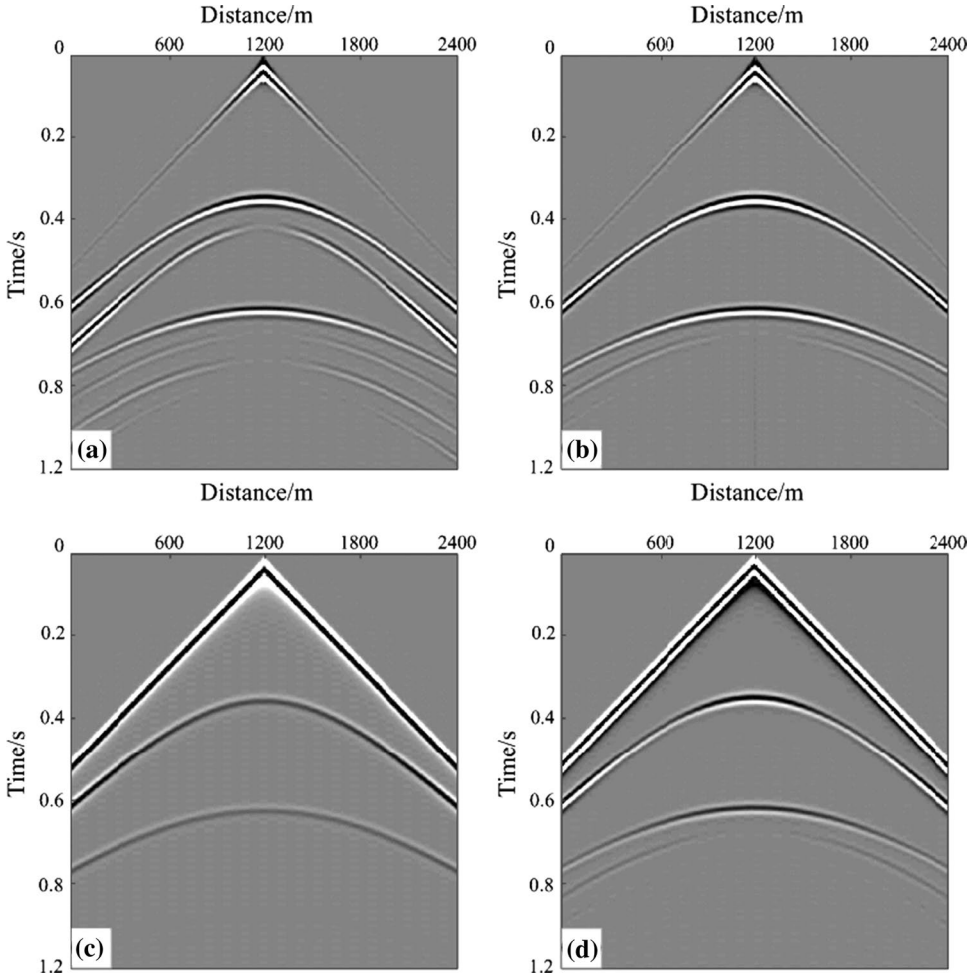

Fig. 4 Layered model forward modeling record: **a** v_z of elastic wave; **b** v_{P_z} of elastic wave; **c** acoustic wave; **d** scalar-P-wave

ground. The source wavelet is a Ricker wavelet with peak frequency of 7 Hz. Fifty-six shots totally are exploded with the 10 m distance between adjacent sources. The geophones were placed on the surface. We generate elastic pseudo-pressure data by Eq. (2), and Fig. 5 shows the real and initial velocity models.

We now carry out two tests: (1) one step: invert P- and S-wave velocities simultaneously by scalar-P-wave FWI; (2) two steps: firstly invert P-wave velocity singly, then invert S-wave velocity. The density is regarded as a constant of 1500 kg/m^3 in all tests.

We apply the one-step inversion method to the elastic multi-parameter waveform inversion: the P- and S-wave velocity are inverted simultaneously. The inversion results are shown in Fig. 6. As we can see, the P-wave velocity inverted model is more reliable, but the S-wave velocity looks worse because of the crosstalk effects between various parameters.

To overcome the drawbacks of the one-step inversion method, we applied the two-step inversion method to the elastic multi-parameter waveform inversion: first, the S-wave velocity (Fig. 5d) is not updated and the P-wave velocity is inverted; then, the S-wave velocity is inverted by using the inverted result from the first step as the initial P-wave velocity model. The results are shown in Fig. 7, and the S-wave velocity inverted model is much better than that inverted simultaneously.

Figures 8 and 9 show the depth profiles of P- and S-wave from the true, initial and inverted (singly and simultaneously) models at x-axis locations of 1, 2, 3, 4, and 5 km. The trace contrast curve (Fig. 8) extracted from the P-wave velocity models shows that the resolution of two inverted models computed singly and simultaneously are similar. The depth profiles of S-wave velocity model derived from the singly inversion results (Fig. 9) are greatly improved compared with the simultaneous inversion method, and the S-wave velocity is well recovered. Although the singly inversion produces good results, the cross talk effects between the various parameters still exist and cause some deviation from the true value in the deep layer, which could be mitigated effectively by resorting to Hessian-based method. In conclusion, the two-step inversion strategy is a better option for multi-parameter waveform inversion.

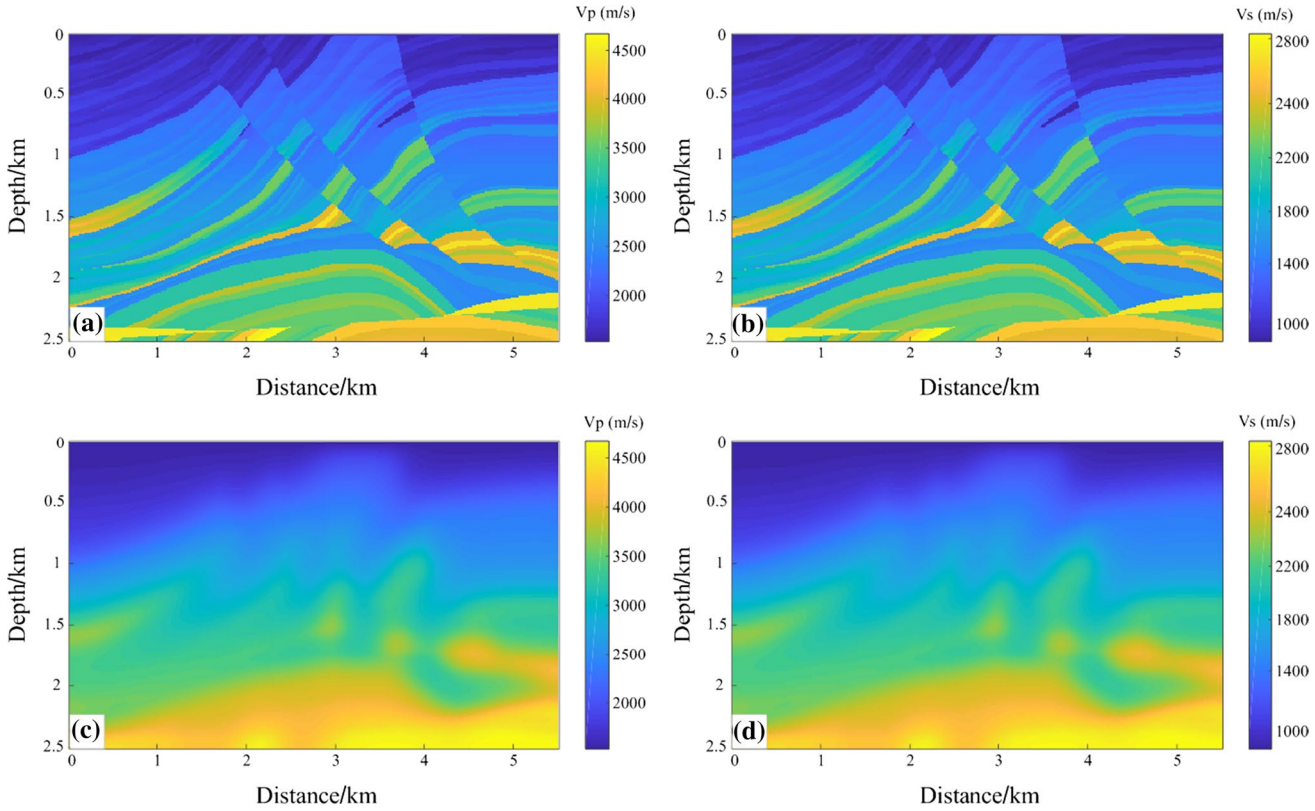

Fig. 5 Marmousi model: **a** real Vp; **b** real Vs; **c** initial Vp; **d** initial Vs

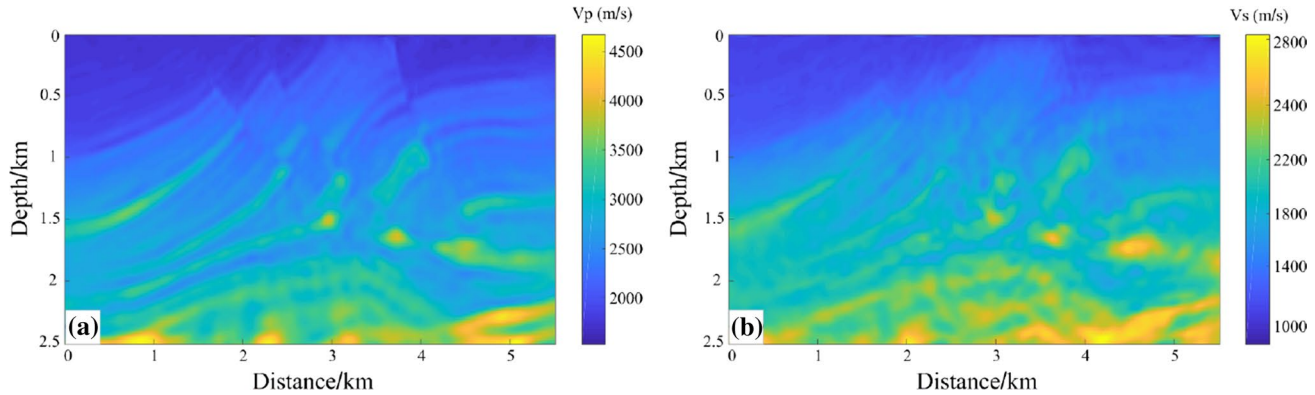

Fig. 6 Inverted simultaneously model: **a** Vp; **b** Vs

Field data example

In this section, we apply a real 2D seismic data set obtained from the particle-motion response from the vertical geophone to verify the scalar-P-wave equation FWI method. This area has a low-velocity zone in near surface, so that the ray path of reflected wave is nearly perpendicular to the ground surface, thus the data set can be regarded as P-wave data, which can be implemented with our scalar-P-wave FWI method.

We use a Fourier transform method to make data interpolation. The sources and receivers are set at the surface. There are 40 shots from $x = 1$ to 5 km and the shot space is 100 m, and the largest offset is 4 km. The receiver spacing is 10 m. The time spacing is 0.8 ms, and maximum time is 2.88 s. The source wavelet is obtained from seismograms analysis.

Figure 10 shows the initial P-wave velocity models computed by migration velocity analysis (MVA), while S-wave velocity model and density are not given. Thus we must find a perfect match empirical relationship between elastic parameters. In

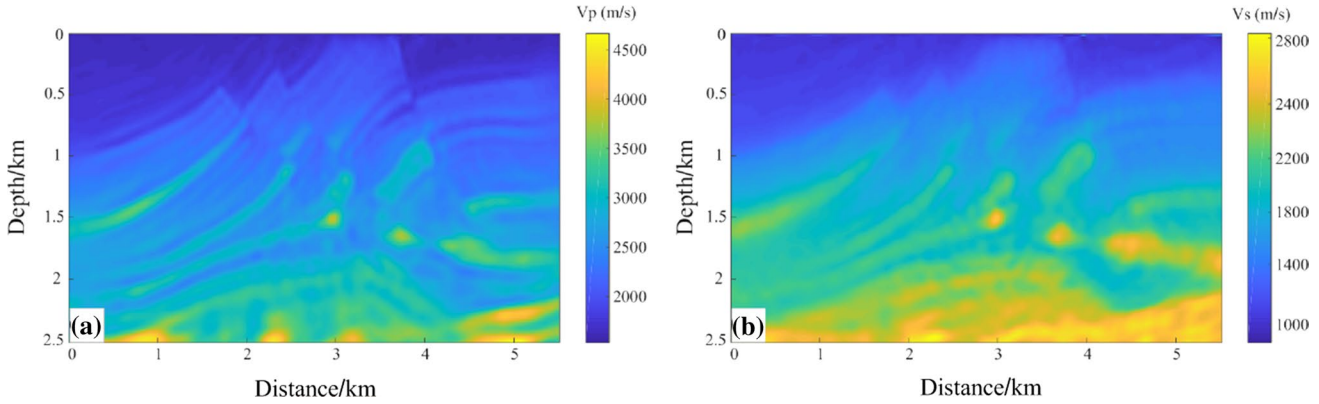

Fig. 7 Inverted singly model: **a** Vp; **b** Vs

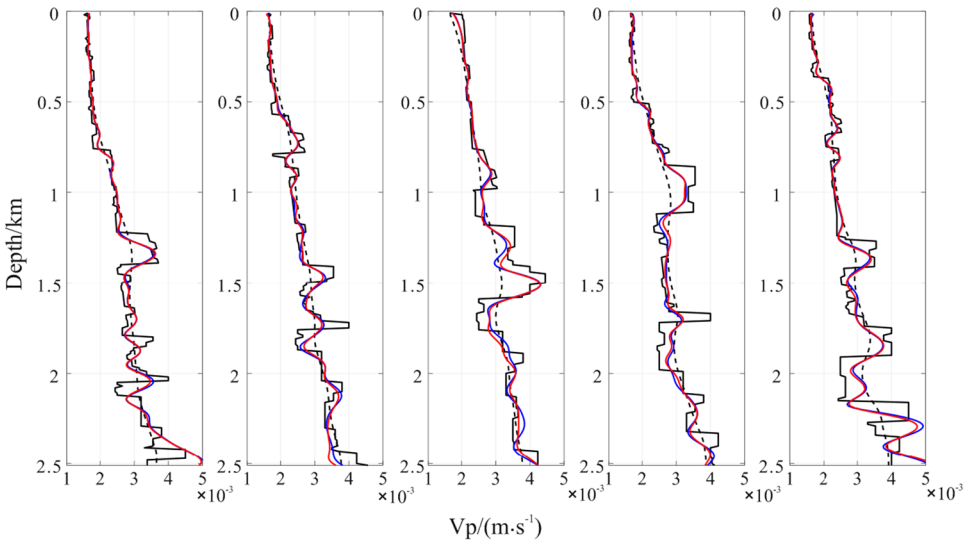

Fig. 8 Depth profiles of *Vp* from the true (black solid line), initial (black dashed line), one-step inverted (blue line) and two-step inverted (red line) model at *x*-axis locations of 1, 2, 3, 4, and 5 km

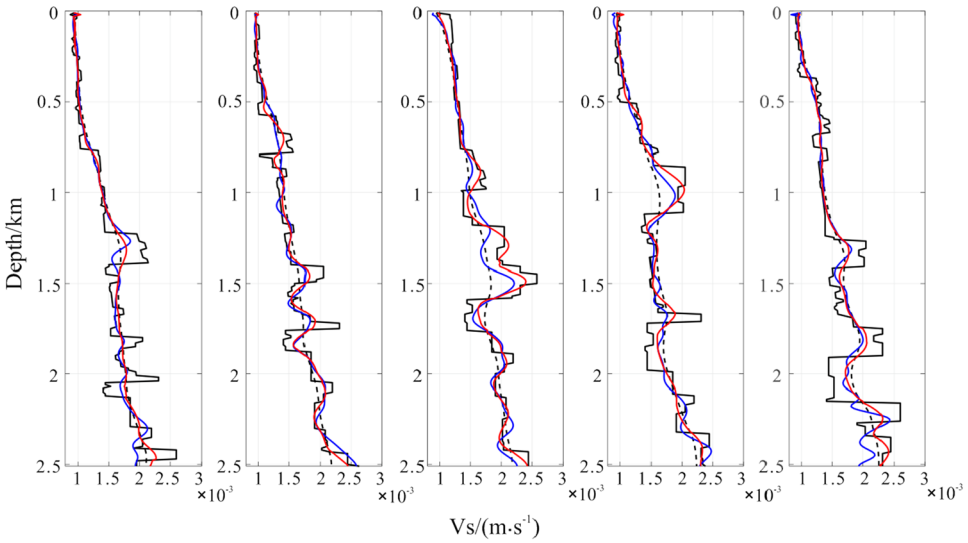

Fig. 9 Depth profiles of Vs from the true (black solid line), initial (black dashed line), inverted (blue line) and two-step inverted (red line) model at *x*-axis locations of 1, 2, 3, 4, and 5 km

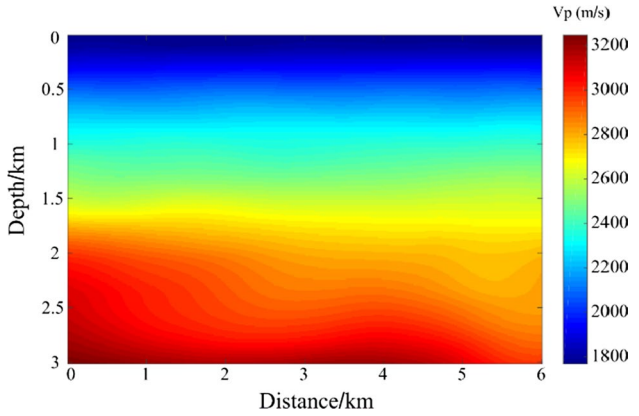

Fig. 10 Initial P-wave velocity model

this test, density model is given by well-known Gardner's relationship: $\rho = 310 \times \left(v_p\right)^{0.25}$ (Gardner et al. 1974), and S-wave velocity model is given by relationship: $v_s = v_p/1.41$. Figure 11 displays the P- and S-wave velocity inversion results simultaneously after 23 iterations. As we can see, the reflections in P-wave velocity model is more continuous. However, there are some discontinuous events and noise in low depth area in S-wave velocity models, and there are two reasons: (1) the trade-off between P- and S-wave; (2) the data set mainly contains P-wave information. We synthesize one shot record by finite difference forward modeling method with inverted P- and S-velocity model, and we compare them with the real seismogram in the same picture, which is illustrated in Fig. 12. Except for surface wave and direction cut in inversion, the main reflections match well.

Conclusions

In this paper, we propose a multi-parameter full-waveform inversion method using the P-wave data with high-quality converted P-wave information. The following conclusions were drawn from model testing.

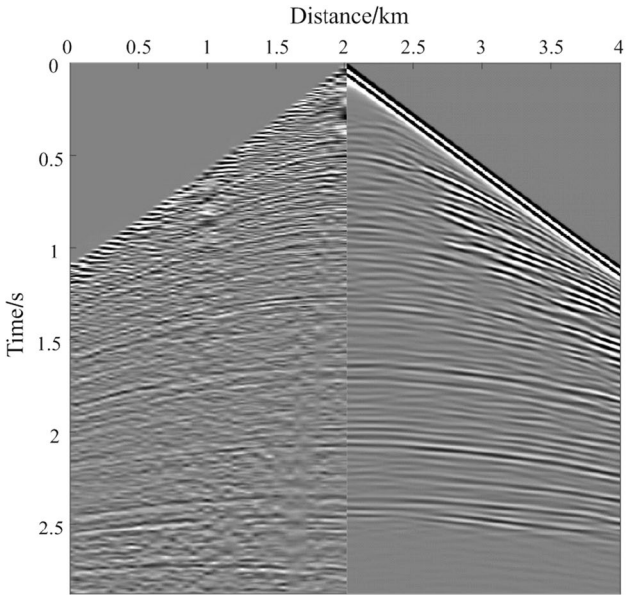

Fig. 12 the synthetic record (right side) modeled by inverted models compared with real seismograms (left side)

1. The scalar-P-wave equation obtained by decoupling the first-order velocity–stress equation contains only P-wave information, unlike the conventional acoustic and elastic wave equations. Compared with the acoustic equation, scalar-P-wave equation can simulate the converted P-waves at the elastic interface, hence it can indicate the variability of the S-wave velocity. This provides information similar to that of the elastic wave equation. The P-wave information received from actual seismic data obtained from the particle-motion response from the vertical geophone is also similar, when the aiming area has a low-velocity zone.
2. The scalar-P-wave equation proposed in this paper has the ability to simulate the converted P-waves, and can invert the P- and S-wave velocity and density parameters.

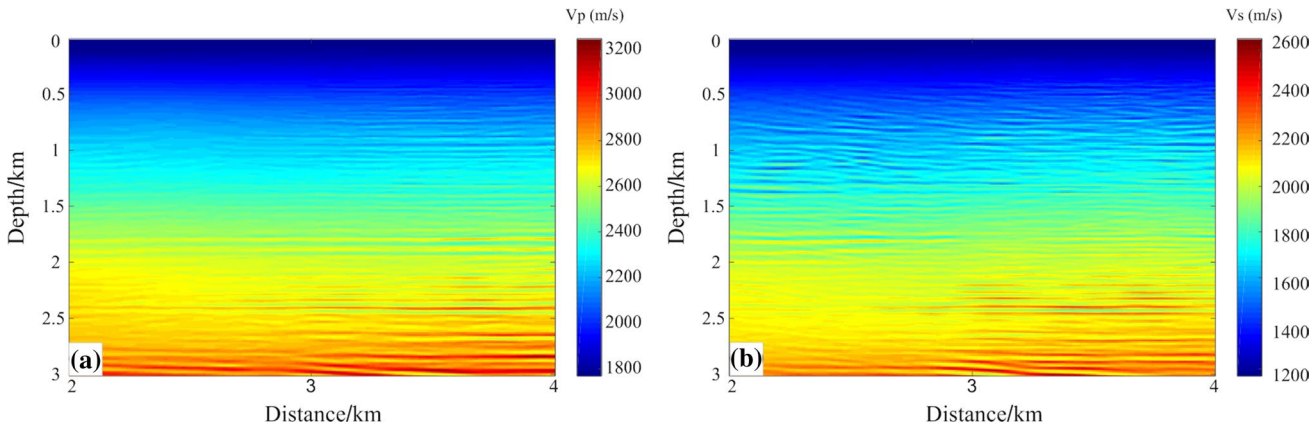

Fig. 11 P- (**a**) and S-wave velocity (**b**) inversion results

Because of the strong crosstalk effects between the density and the other elastic parameters, density can be generally regarded as a constant. We compared the different inversion methods and their effect on the elastic multi-parameter inversion results, and the singly inversion method performed better in the Marmousi-2 model inversion test.

3. The scalar-P-wave multi-parameter inversion method is the only method that evolves from P-wave exploration to multi-wave and multi-component exploration. As P-wave data still dominates onshore seismic surveys, the proposed method has great significance for inverting S-wave velocity parameters based on P-wave.

Acknowledgements The authors would like to acknowledge the support of the National Science and Technology Major Project, China: 2016ZX05024-001-008, and thank the reviewers for their valuable comments which helped to improve this article.

Appendix 1

Combining the relationship between the elastic wave velocity and elastic modulus and density, the three basic equations of elastic dynamics are used to derive the two-dimensional elastic wave equations in homogeneous isotropic media,

$$\begin{aligned}
\rho\frac{\partial^2 u}{\partial t^2} &= \frac{\partial \tau_{xx}}{\partial x} + \frac{\partial \tau_{xz}}{\partial z}\\
\rho\frac{\partial^2 w}{\partial t^2} &= \frac{\partial \tau_{zz}}{\partial z} + \frac{\partial \tau_{xz}}{\partial x}\\
\tau_{xx} &= (\lambda+2\mu)\frac{\partial u}{\partial x} + \lambda\frac{\partial w}{\partial z},\\
\tau_{zz} &= (\lambda+2\mu)\frac{\partial w}{\partial z} + \lambda\frac{\partial u}{\partial x}\\
\tau_{xz} &= \mu\left(\frac{\partial u}{\partial x} + \frac{\partial w}{\partial z}\right)
\end{aligned} \tag{11}$$

where u and v are the displacement components.

The conventional first-order displacement–stress elastic wave equations [Eq. (11)] have been used by many scholars to study EFWI (Tarantola 1986; Mora 1987, 1988; Crase et al. 1990; Pratt and Worthington 1990). In practical applications, multi-wave and multi-component data need to be acquired to provide the displacements in different directions in the equation. As mentioned above, onshore exploration depends on P-wave data. Therefore, our aim is to decompose the elastic wave equation and obtain a multi-parameter equation containing only pure P-wave information. Using the equivalent representation of the constitutive equation, the constitutive equations in the swell-shrinking (pressure) and shear-rotating forms can perform the decomposition of the elastic waves. The constitutive relationship of the pressure form of the media is,

$$P = -3K\theta_{\mathrm{p}}, \tag{12}$$

where K is the bulk modulus and

$$P = -\frac{\tau_{xx}+\tau_{yy}+\tau_{zz}}{3}, \quad \theta_{\mathrm{p}} = \frac{\varepsilon_{xx}+\varepsilon_{yy}+\varepsilon_{zz}}{3}. \tag{13}$$

The constitutive relationship in the shear-rotating form is

$$\boldsymbol{S}_{i,j} = 2\mu\boldsymbol{T}_{i,j}, \tag{14}$$

And the tensors $\boldsymbol{S}_{i,j}$ and $\boldsymbol{T}_{i,j}$ are,

$$\begin{aligned}
\boldsymbol{S}_{i,j} &= \begin{pmatrix} \tau_{xx}+P & \tau_{yx} & \tau_{zx} \\ \tau_{xy} & \tau_{yy}+P & \tau_{zy} \\ \tau_{xz} & \tau_{yz} & \tau_{zz}+P \end{pmatrix},\\
\boldsymbol{T}_{i,j} &= \begin{pmatrix} \varepsilon_{xx}+\theta_{\mathrm{p}} & \varepsilon_{yx} & \varepsilon_{zx} \\ \varepsilon_{xy} & \varepsilon_{yy}+\theta_{\mathrm{p}} & \varepsilon_{zy} \\ \varepsilon_{xz} & \varepsilon_{yz} & \varepsilon_{zz}+\theta_{\mathrm{p}} \end{pmatrix},
\end{aligned} \tag{15}$$

Equations (12) and (15) represent the constitutive equations in the swell-shrinking and shear-rotating forms. Combining Eq. (11), the two-dimensional scalar-P-wave equation consisting of K and μ can then be obtained,

$$\begin{aligned}
\rho\frac{\partial^2 u}{\partial t^2} &= \frac{\partial S_{xx}}{\partial x} + \frac{\partial \tau_{xz}}{\partial z}\\
\rho\frac{\partial^2 w}{\partial t^2} &= \frac{\partial S_{zz}}{\partial z} + \frac{\partial \tau_{xz}}{\partial x}\\
P &= -K\left(\frac{\partial u}{\partial x} + \frac{\partial w}{\partial z}\right) + f\\
\tau_{xx} &= \mu\left(\frac{\partial u}{\partial x} - \frac{\partial w}{\partial z}\right)\\
\tau_{zz} &= \mu\left(\frac{\partial w}{\partial z} - \frac{\partial u}{\partial x}\right)\\
\tau_{xz} &= \mu\left(\frac{\partial u}{\partial x} + \frac{\partial w}{\partial z}\right),
\end{aligned} \tag{16}$$

where f is the source term and the P-wave source is loaded onto the P-wave component in this paper.

Equation (9) decomposes the elastic wave equation into a first-order pressure–displacement–stress equation, thereby separating the pressure term, which corresponds to

the P-wave data received onshore, and this form is equal to Eq. 2.

Appendix 2

The scalar-P-wave Eq. (15) also satisfies the wave equation in the background model. In the Born approximation, the model $\boldsymbol{m}$ can be decomposed as the background model $\boldsymbol{m}_0$ and the perturbation $\delta\boldsymbol{m}$,

$$\boldsymbol{m} = \boldsymbol{m}_0 + \delta\boldsymbol{m}, \tag{17}$$

where δ represent the perturbation, and $\boldsymbol{m}$ is

$$\begin{aligned}
\rho &= \rho_0 + \delta\rho \\
\lambda &= \lambda_0 + \delta\lambda \\
\mu &= \mu_0 + \delta\mu,
\end{aligned} \tag{18}$$

The wavefields can be similarly decomposed as

$$\begin{aligned}
P &= P_0 + \delta P \\
u &= u_0 + \delta u \\
w &= w_0 + \delta w \\
\tau_{xx} &= \tau_{xx} + \delta\tau_{xx} \\
\tau_{zz} &= \tau_{zz0} + \delta\tau_{zz} \\
\tau_{xz} &= \tau_{xz0} + \delta\tau_{xz},
\end{aligned} \tag{19}$$

Subtracting Eq. (21) from the equation satisfied by the background media,

$$\begin{aligned}
\rho\frac{\partial^2\delta u}{\partial t^2} &= \frac{\partial\left(\delta\tau_{xx}+\delta P\right)}{\partial x} - \delta\rho\frac{\partial^2 u_0}{\partial t^2} + \frac{\partial\delta\tau_{xz}}{\partial z} \\
\rho\frac{\partial^2\delta w}{\partial t^2} &= \frac{\partial\left(\delta\tau_{zz}+\delta P\right)}{\partial z} - \delta\rho\frac{\partial^2 w_0}{\partial t^2} + \frac{\partial\delta\tau_{xz}}{\partial x} \\
\delta P &= -(\lambda+\mu)\left(\frac{\partial\delta u}{\partial x}+\frac{\partial\delta w}{\partial z}\right) \\
&\quad -\delta\lambda\left(\frac{\partial u_0}{\partial x}+\frac{\partial w_0}{\partial z}\right) - \delta\mu\left(\frac{\partial u_0}{\partial x}+\frac{\partial w_0}{\partial z}\right) \\
\delta\tau_{xx} &= \delta\mu\left(\frac{\partial u_0}{\partial x}-\frac{\partial w_0}{\partial z}\right) \\
\delta\tau_{zz} &= \delta\mu\left(\frac{\partial w_0}{\partial z}-\frac{\partial u_0}{\partial x}\right) \\
\delta\tau_{xz} &= \delta\mu\left(\frac{\partial u_0}{\partial z}+\frac{\partial w_0}{\partial x}\right)
\end{aligned} \tag{21}$$

The above expression can be written as

$$\frac{\delta\boldsymbol{\Phi}}{\delta m} = L(\tilde{s})\left(\delta\lambda\cdot s^1 + \delta\mu\cdot s^2 + \delta\rho\cdot s^3\right), \tag{22}$$

where $\tilde{s}$ is the virtual source

$$\tilde{s} = \delta\lambda\cdot s^1 + \delta\mu\cdot s^2 + \delta\rho\cdot s^3, \tag{23}$$

and

$$\begin{aligned}
s^1 &= \left(0,0,-\left(\frac{\partial u_0}{\partial x}+\frac{\partial w_0}{\partial z}\right),0,0,0\right)^t \\
s^2 &= \left(0,0,-\left(\frac{\partial u_0}{\partial x}+\frac{\partial w_0}{\partial z}\right),\left(\frac{\partial u_0}{\partial x}-\frac{\partial w_0}{\partial z}\right),\left(\frac{\partial w_0}{\partial z}-\frac{\partial u_0}{\partial x}\right),\left(\frac{\partial u_0}{\partial z}+\frac{\partial w_0}{\partial x}\right)\right)^t \\
s^3 &= \left(-\frac{\partial^2 u_0}{\partial t^2},-\frac{\partial^2 w_0}{\partial t^2},0,0,0,0\right)^t,
\end{aligned} \tag{24}$$

Substituting Eqs. (18) and (19) into Eq. (17), we obtain

$$\begin{aligned}
(\rho_0+\delta\rho)\frac{\partial^2\left(u_0+\delta u\right)}{\partial t^2} &= \frac{\partial\left(\tau_{xx0}+\delta\tau_{xx}+P_0+\delta P\right)}{\partial x} + \frac{\partial\left(\tau_{xz0}+\delta\tau_{xz}\right)}{\partial z} \\
(\rho_0+\delta\rho)\frac{\partial^2\left(w_0+\delta w\right)}{\partial t^2} &= \frac{\partial\left(\tau_{zz0}+\delta\tau_{zz}+P_0+\delta P\right)}{\partial z} + \frac{\partial\left(\tau_{xz0}+\delta\tau_{xz}\right)}{\partial x} \\
P_0+\delta P &= -\left(\lambda_0+\delta\lambda+\mu_0+\delta\mu\right)\left(\frac{\partial\left(u_0+\delta u\right)}{\partial x}+\frac{\partial\left(w_0+\delta w\right)}{\partial z}\right) \\
\tau_{xx0}+\delta\tau_{xx} &= \left(\mu_0+\delta\mu\right)\left(\frac{\partial\left(u_0+\delta u\right)}{\partial x}-\frac{\partial\left(w_0+\delta w\right)}{\partial z}\right) \\
\tau_{zz0}+\delta\tau_{zz} &= \left(\mu_0+\delta\mu\right)\left(\frac{\partial\left(w_0+\delta w\right)}{\partial z}-\frac{\partial\left(u_0+\delta u\right)}{\partial x}\right) \\
\tau_{xz0}+\delta\tau_{xz} &= \left(\mu_0+\delta\mu\right)\left(\frac{\partial\left(u_0+\delta u\right)}{\partial z}+\frac{\partial\left(w_0+\delta w\right)}{\partial x}\right)
\end{aligned} \tag{20}$$

Therefore, the gradient can be calculated as

$$\frac{\partial E}{\partial m} = \frac{\partial\boldsymbol{\Phi}}{\partial m}\left(P_{\text{obs}}-P_{\text{cal}}\right) = L(\tilde{s})\left(P_{\text{obs}}-P_{\text{cal}}\right) = \tilde{s}L^*\left(P_{\text{obs}}-P_{\text{cal}}\right), \tag{25}$$

Thus, the Lame constant-density gradient is expressed as

$$\begin{aligned}
\frac{\partial E}{\partial\lambda} &= -P^*\left(\frac{\partial u}{\partial x}+\frac{\partial w}{\partial z}\right) \\
\frac{\partial E}{\partial\mu} &= -P^*\left(\frac{\partial u}{\partial x}+\frac{\partial w}{\partial z}\right) + \left(\tau_{xx}^*-\tau_{zz}^*\right)\left(\frac{\partial u}{\partial x}-\frac{\partial w}{\partial z}\right) + \tau_{xz}^*\left(\frac{\partial u}{\partial z}+\frac{\partial w}{\partial x}\right). \\
\frac{\partial E}{\partial\rho} &= -\left(u^*\frac{\partial^2 u}{\partial t^2}+w^*\frac{\partial^2 w}{\partial t^2}\right)
\end{aligned} \tag{26}$$

References

Barnes C, Charara M (2009) The domain of applicability of acoustic full-waveform inversion for marine seismic data. Geophysics 74:WCC91–WCC103

Brossier R, Operto S, Virieux J (2009) Seismic imaging of complex onshore structures by 2D elastic frequency-domain full-waveform inversion. Geophysics 74:WCC105–WCC118

Crase E, Pica A, Noble M, Mchdonald J, Tarantola A (1990) Robust elastic nonlinear waveform inversion: application to real data. Geophysics 55:527–538

Dellinger J, Etgen J (1990) Wave-field separation in two-dimensional anisotropic media. Geophysics 1990(55):914–919

Fletcher R, Reeves CM (1964) Function minimization by conjugate gradients. Comput J 7:149–154

Gaiser J, Moldoveanu N, Macbeth C et al (2001) Multicomponent technology: the players, problems, applications, and trends: Summary of the workshop sessions. Lead Edge 20(9):974–977

Gardner G, Gardner L, Gregory A (1974) Formation velocity and density—the diagnostics basics for stratigraphic traps. Geophysics 39:770–780

Hobro JWD, Chapman CH, Robertsson JOA (2014) A method for correcting acoustic finite-difference amplitudes for elastic effects. Geophysics 79:T243–T255

Jeong W, Lee HY, Min DJ (2012) Full waveform inversion strategy for density in the frequency domain. Geophys J Int 188:1221–1242

Köhn D, Nil DD, Kurzmann A, Bohlen T (2012) On the influence of model parametrization in elastic full waveform tomography. Geophys J Int 191:325–345

Lailly P (1983) The seismic inverse problem as a sequence of before stack migrations: conference on inverse scattering, theory and application. Society for Industrial and Applied Mathematics, Philadelphia, pp 206–220

Ma D, Zhu G (2003) Numerical modeling of P wave and S wave separation in elastic wavefield. Oil Geophys Prospect 38:482–486 **(in Chinese)**

Mora P (1987) Nonlinear two-dimensional elastic inversion of multioffset seismic data. Geophysics 52:1211–1228

Mora P (1988) Elastic wave-field inversion of reflection and transmission data. Geophysics 53:750–759

Operto S, Virieux J, Dessa JX et al (2006) Crustal seismic imaging from multifold ocean bottom seismometer data by frequency domain full waveform tomography: application to the eastern Nankai trough. J Geophys Res Solid Earth 111:B9

Pratt RG (1999) Seismic waveform inversion in the frequency domain, part 1: theory and verification in a physical scale model. Geophysics 64:888–901

Pratt RG, Shipp RM (1999) Seismic waveform inversion in the frequency domain, part 2: fault delineation in sediments using crosshole data. Geophysics 64:902–914

Pratt RG, Worthington MH (1990) Inverse theory applied to multisource cross-hole tomography. Part 1: acoustic wave-equation method. Geophys Prospect 38:287–310

Pratt RG, Shin C, Hick GJ (1998) Gauss-Newton and full Newton methods in frequency-space seismic waveform inversion. Geophys J Int 133:341–362

Raknes EB, Arntsen B, Weibull W (2015) Three-dimensional elastic full waveform inversion using seismic data from the Sleipner area. Geophys J Int 22:1877–1894

Ravaut C, Operto S, Improta L et al (2004) Multiscale imaging of complex structures from multifold wide-aperture seismic data by frequency-domain full-waveform tomography: application to a thrust belt. Geophys J Int 159:1032–1056

Ren Z, Liu Y (2016) A hierarchical elastic full-waveform inversion scheme based on wavefield separation and the multistep-length approach. Geophysics 2016(81):R99–R123

Sears TJ, Singh SC, Barton PJ (2008) Elastic full waveform inversion of multi-component OBC seismic data. Geophys Prospect 56:843–862

Shipp RM, Singh SC (2002) Two-dimensional full wavefield inversion of wide-aperture marine seismic streamer data. Geophys J Int 151:325–344

Simmons J, Backus M (2003) An introduction—multicomponent. Lead Edge 22:1227–1262

Sirgue L, Pratt R (2004) Efficient waveform inversion and imaging: a strategy for selecting temporal frequencies. Geophysics 69:231–248

Sirgue L, Barkved OI, Dellinger J, Etgen J, Albertin U, Kommedal JH (2010) Full waveform inversion: the next leap forward in imaging at Valhall. First Break 28:65–70

Sun R, McMechan GA, Lee CS et al (2007) Prestack scalar reverse-time depth migration of 3D elastic seismic data. Geophysics 71:S199–S207

Tang C, McMechan GA (2017) Multidirectional-vector-based elastic reverse time migration and angle-domain common-image gathers with approximate wavefield decomposition of P-and S-waves. Geophysics 83:S57–S79

Tarantola A (1984) Inversion of seismic reflection data in the acoustic approximation. Geophysics 49:1259–1266

Tarantola A (1986) A strategy for nonlinear elastic inversion of seismic reflection data. Geophysics 51:1893–1903

Tatham RH, Stoffa PL (1976) Vp/Vs—a potential hydrocarbon indicator. Geophysics 41:837–849

Vigh D, Jiao K, Watts D, Sun D (2014) Elastic full-waveform inversion application using multicomponent measurements of seismic data collection. Geophysics 79:R63–R77

Virieux J, Operto S (2009) An overview of full-waveform inversion in exploration geophysics. Geophysics 74:WCC1–WCC26

Wu RS, Aki K (1985) Scattering characteristics of elastic waves by an elastic heterogeneity. Geophysics 50:582–595

Xiao X, Leaney WS (2010) Local vertical seismic profiling (VSP) elastic reverse-time migration and migration resolution: salt-flank imaging with transmitted P-to-S waves. Geophysics 75:S35–S49

Zhang Q, McMechan GA (2010) 2D and 3D elastic wavefield vector decomposition in the wavenumber domain for VTI media. Geophysics 75:D13–D26

Acta Geophysica (2020) 68:389–401
https://doi.org/10.1007/s11600-020-00405-4

RESEARCH ARTICLE - APPLIED GEOPHYSICS

Desert seismic noise suppression based on multimodal residual convolutional neural network

Shengnan Wang[1] · **Yue Li**[1] · **Yuxing Zhao**[1]

Received: 24 October 2019 / Accepted: 27 January 2020 / Published online: 5 February 2020

Abstract

Seismic exploration is an important means of oil and gas detection, but affected by complex surface and near-surface conditions, and the seismic records are polluted by noise seriously. Particularly in the desert areas, due to the influence of wind and human activities, the complex desert noise with low-frequency, nonstationary and non-Gaussian characteristics is produced. It is difficult to extract effective signals from strong noise using existing denoising methods. To address this issue, the paper proposes a new denoising method, called multimodal residual convolutional neural network (MRCNN). MRCNN combines convolutional neural network (CNN) with variational modal decomposition (VMD) and adopts residual learning method to suppress desert noise. Since CNN-based denoisers can extract data features based on massive training set, the impact of noise types and intensity on the denoised results can be ignored. In addition, VMD algorithm can sparsely decompose signal, which will facilitate the feature extraction of CNN. Therefore, using VMD algorithm to optimize the input data will conducive to the performance of the network denoising. Moreover, MRCNN adopts reversible downsampling operator to improve running speed, achieving a good trade-off between denoising results and efficiency. Extensive experiments on synthetic and real noisy records are conducted to evaluate MRCNN in comparison with existing denoisers. The extensive experiments demonstrate that the MRCNN can exhibit good effectiveness in seismic denoising tasks.

Keywords Residual learning · Desert seismic record · Noise suppression · Variational mode decomposition

Introduction

Driven by the development of national economy and the improvement in science and technology, the requirement of seismic exploration technology has gradually developed from enhancing effective signals to "three high" (high signal-to-noise ratio, high resolution and high precision) demands. In the "three high" requirements, high signal-to-noise ratio (SNR) is the foundation. However, in the desert area, due to the influence of wind (Shoulong et al. 2014; Li et al. 2015; Wang et al. 2017), surface conditions (Michael et al. 2018) and human noise of near field and far field (Li et al. 2017), seismic noise has complex natures. Firstly, desert noise shares the same frequency band with the effective signal (Li and Li 2016), which makes the time–frequency domain filtering algorithm unable to extract the effective signal while suppressing the noise; secondly, most of the desert noise is non-Gaussian (Zhong et al. 2015), so some current methods of suppressing Gaussian noise cannot be applied to desert noise. Meanwhile, high intensity and irregular interference make the random noise more complex than the common noise. Therefore, it is necessary to develop a high-performance denoising method for desert noise.

Many traditional denoising methods have been proposed and successfully applied to the seismic data denoising (Cobelli 2010; Pilikos and Faul 2017; Liu and Ma 2018). These methods are not limited to the simple or direct applications, and the corresponding improved algorithms (Gan et al. 2016; Liu et al. 2017; Yuan et al. 2018a; Yu and Ma 2017) or the algorithms combined with other methods (Baron et al. 2008; Bagheri et al. 2017) have also been proposed to improve their deficiencies in denoising. These methods and their extension algorithms have performed

✉ Yue Li
liyue@jlu.edu.cn

Shengnan Wang
2667938494@qq.com

Yuxing Zhao
zhaoyx18@mails.jlu.edu.cn

[1] Department of Information, College of Communication Engineering, Jilin University, Changchun 130012, China

well in suppressing noise with specific characteristics. However, since the denoising algorithms often rely on the priori assumptions of signal or noise models (Makitalo and Foi 2012; Yuan and Wang 2013), the denoising methods need to meet certain applicable conditions: For example, the SNR cannot be too low, the noise needs to obey the specific distribution (e.g., Gaussian distribution, white noise) and satisfy some characteristics (e.g., uniformity, linearity), and so on. For desert noise, due to its complex characteristics, it is gradually difficult to process low-quality desert seismic data by existing techniques.

Deep learning (DL) is based on a large amount of samples and obtains more abstract high-layer information by combining low-layer information to acquire the latent features of data, thus realizing intelligent processing and analyzing of data (Hao et al. 2016). At present, many DL-based networks have been successfully applied in the field of seismic exploration: For example, Yuan et al. (2018b) have realized seismic waveform classification and first-time picking and Ross et al. (2018) have detected seismic body-wave phases. For seismic noise attenuation, Li et al. (2019) used a small amount of collected prestack noise as the training set to train the network which can suppress ground roll. However, the prestack noise cannot fully reflect all the characteristics of noise, so the obtained network cannot suppress the noise that is not included in the training set. To solve the problem of inadequate training set, in Yu et al. (2018), both the synthesized data and the field data are used as the training set to train the network. Random noise, linear noise and multiple noise are successfully removed by using the obtained network model. Nevertheless, due to the limited richness of the synthesized training set, the suppression effect of seismic noise still needs to be improved.

Residual network (ResNets) was proposed by He et al. (2016) at the CVPR in 2016. The network utilizes residual learning to deepen the layers of network and has made remarkable achievements in the field of denoising since it was proposed. Zhang et al. (2016) proposed a denoising convolutional neural network called DnCNN and applied it to image denoising tasks. DnCNN combines residual learning and batch normalization to speed up the training process as well as boost the denoising performance, and removes the latent clean image with the operations in the hidden layers to predict the residual image, i.e., the difference between the noisy observation and the latent clean image. Zhao et al. (2019) successfully applied DnCNN algorithm to seismic denoising, which proves that the effective combination of residual learning and batch normalization is suitable for the seismic noise.

This paper proposes a novel desert seismic denoising method, namely multimodal residual convolutional neural network (MRCNN). This method sparsely processes desert seismic data in VMD domain and extracts the desert noise by the feature extraction capability of DnCNN. In addition, in order to improve the execution efficiency and reduce the computational load, similar to the FFDNet method proposed in Zhang et al. (2018), MRCNN adopts subpixel convolution operation proposed by Shi et al. (2016) to process the data in the downsampling subspace. The experimental results of synthetic and field seismic records show that our algorithm can effectively suppress the seismic noise and recover the effective reflections almost completely. By comparing the proposed algorithm with other denoising algorithms (band-pass filter, VMD filter and DnCNN), it is proved that MRCNN has the best denoising performance in suppressing noise and protecting signals. The structure of this paper is as follows. "Theory" section introduces the denoising theory of proposed method, including the decomposition principle of VMD, the denoising principle of DnCNN and the denoising principle of MRCNN. "Experiments and result" section analyzes the denoising performance of MRCNN through synthetic and field records. The last section is the conclusion and discussion of this paper.

Theory

Variational mode decomposition

VMD is an adaptive signal decomposition method proposed by Dragomiretskiy and Zosso (2014). It mainly determines the bandwidth and center frequency of component modes by solving the variational problem of modal components and decomposes the input signals into a series of sparse signals. The variational optimization problem can be described as:

$$\begin{aligned} &\min_{\{\mu_k\},\{\omega_k\}} \left\{ \sum_k \left\| \partial_t \left[\left(\delta(t) + \frac{j}{\pi t} \right) \times \mu_k(t) \right] e^{-j\omega_k t} \right\|_2^2 \right\} \\ &\text{s.t.} \quad \sum_k \mu_k = f \end{aligned} \tag{1}$$

where μ_k and ω_k are shorthand notations for the set of all modes and their center frequencies, respectively. Use both quadratic penalty term and Lagrangian multipliers, λ, in order to render Eq. (1) unconstrained. The above problem can be written as follows:

$$\begin{aligned} L(\{\mu_k\},\{\omega_k\},\lambda) := \alpha \sum_k \left\| \partial_t \left[\left(\delta(t) + \frac{j}{\pi t} \right) \times \mu_k(t) \right] \mathrm{e}^{-j\omega_k t} \right\|_2^2 \\ + \left\| f(t) - \sum_k \mu_k(t) \right\|_2^2 + \left\langle \lambda(t), f(t) - \sum_k \mu_k(t) \right\rangle \end{aligned} \tag{2}$$

where α is used to constrain data fidelity.

After that, minimization of Eq. (2) is solved with alternating direction method of multipliers (ADMM). The ADMM is used to update alternately the parameters according to Eqs. (3) and (4) to solve the above variational problems until the convergence condition Eq. (5) is satisfied:

$$\hat{\mu}_k^{n+1}(\omega) = \frac{\hat{f}(\omega) - \sum_{i\neq k}\hat{\mu}_i(\omega) + \frac{\hat{\lambda}(\omega)}{2}}{1 + 2\alpha(\omega - \omega_k)^2}$$
$$\omega_k^{n+1} = \frac{\int_0^\infty \omega\left|\hat{\mu}_k^{n+1}\right|^2 d\omega}{\int_0^\infty \left|\hat{\mu}_k^{n+1}(\omega)\right|^2 d\omega} \tag{3}$$

where $\hat{\mu}_k$ is the Fourier transform of μ_k.

$$\hat{\lambda}^{n+1}(\omega) \leftarrow \hat{\lambda}^n(\omega) + \tau(\hat{\mathrm{f}}(\omega) - \sum_k \hat{\mu}_k^{n+1}(\omega)) \tag{4}$$

$$\sum_{\mathrm{k}} \frac{\left\|\hat{\mu}_{\mathrm{k}}^{n+1} - \hat{\mu}_{\mathrm{k}}^{n}\right\|}{\left\|\hat{\mu}_{\mathrm{k}}^{n}\right\|_2^2} < \varepsilon \tag{5}$$

where ε is the convergence value.

Denoising principle of DnCNN

Denoising convolutional neural network (DnCNN) (Zhang et al. 2016) adopts residual learning to predict the residual data and gradually separate effective signal from the noisy observation through the hidden layers. Since the type of noise removed by DnCNN is mainly determined by training set, the network can suppress the desert seismic noise as long as we design the training set reasonably. Figure 1 shows the network architecture of the DnCNN, which includes the convolutional layer (Conv), batch normalization layer (BN) and rectified linear unit (RELU). Specifically, the convolutional layer consists of a stack of convolution kernels, which can extract seismic noise through the convolution operation of convolution kernel and seismic data. The batch normalization layer can make the input of each layer have approximately the same distribution, which effectively avoids the problem of vanishing gradient and improves the convergence speed of the network. Rectified linear unit is an activation function commonly used in artificial neural networks, which can also overcome the vanishing gradient problem and accelerate the network training.

The input of DnCNN is a noisy observation

$$y = s + n \tag{6}$$

where s represents the effective signal, n represents the desert noise and y represents the noisy record. DnCNN employs the residual learning formulation to train a residual mapping, and the learning target of the network is

$$n = y - s \approx R(y;\Theta) \tag{7}$$

where θ is the network parameter including weight W and bias b. Then, we can get the clean data

$$s = y - R(y;\theta). \tag{8}$$

To make $R(\bullet)$ and n as close as possible, the averaged mean squared error between the desired residual data and estimated ones from noisy input

$$L(\Theta) = \frac{1}{2N}\sum_{i=1}^{N}\left\|R(y_i;\Theta) - n_i\right\|_F^2 \tag{9}$$

can be adopted as the loss function to learn θ, and $\{y_i, n_i\}_{i=1}^N$ represents N noisy–noise training data pairs.

Denoising principle of MRCNN

Desert seismic data have complex noise structure, which will not conducive to extracting the seismic events directly. The VMD method can decompose the seismic data into a set of band-limited modes with obvious characteristics, which will facilitate the feature extraction. Meanwhile, as the VMD method is shift-invariant, the noisy decomposed modes can be processed in a patch-by-patch manner using the convolution operator. Therefore, the paper proposes to use VMD method to sparsely decompose the input data, which will facilitate feature extraction of the network.

Subpixel convolution is an ingenious method of super-resolution proposed by Shi et al. (2016), which can improve the operational efficiency of deep networks. According to Zhang et al. (2018), MRCNN samples decomposed modes

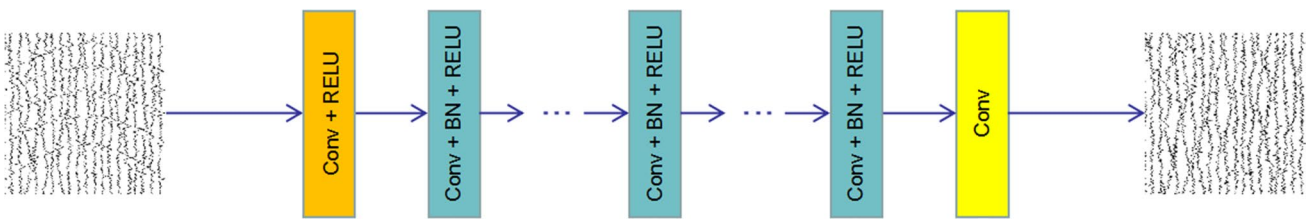

Fig. 1 Architecture of the DnCNN

into subdata as input of DnCNN. At the output end, the periodic shuffling operator (Shi et al. 2016) method is used to reconstruct the final output. By doing so, we effectively reduce the network parameters and increase the receptive field while maintaining the accuracy of the results.

Figure 2 illustrates the architecture of the proposed algorithm. The first layer is the decomposition layer. We decompose the input data into multiple modes by 1D VMD and arrange the same mode into a two-dimensional data. Figure 3 shows the decomposition results of noisy records with different SNRs (−5.6890 dB, −9.2108 dB and −11.7096 dB) at different decomposition times (4–6), where the red boxes are the modes with effective signals and the blue boxes are the modes without effective signals. It can be seen from the two modal distributions that the effective signals are concentrated in mode 1 and mode 2 when decomposed for four times, and the reflection events are retained well. When the decomposition times are 5 and 6, a small amount of effective signals remain in the third mode, which will affect the accuracy of the network to extract effective signals. Therefore, the decomposition times of VMD are set as 4 in this paper.

The second layer is a reversible downsampling operator, which reshapes the modes of size $W \times H$ into tensors of size $\frac{W}{r} \times \frac{H}{r} \times r^2$. Here, r is the downsampling factor and the paper sets r to 2 since it can largely improve the speed without reducing modeling capacity. The third layer to the penultimate layer is 16-channel DnCNN. In the previous theory, we decompose the dataset into four modes, and each mode is reshaped into four ($r^2 = 4$) subdata, so the DnCNN inputs data through 16 channels. For the last layer, we adopt the subpixel convolution to reverse the downsampling process to estimate the noise modes, and all estimated modes are added together to obtain the ultimate estimated noise. The denoised record is the difference between the noisy seismic observation and the predicted noise.

Experiments and result

Experiments on synthetic record

This paper designs a 2D synthetic data to verify the MRCNN for desert noise suppression. Figure 4a exhibits a synthetic noise-free record which contains 17 reflections with 90 receivers, each receiver with 1000 samples; the dominant frequencies of the record include 20 Hz, 25 Hz and 30 Hz; and the signal amplitude is decremented from shallow to deep. In addition, the field seismic data are prone to fail to meet the sampling theorem due to the influence of acquisition factors, resulting in the loss of seismic traces. Therefore, we add some sparse areas to the synthetic seismic data to reflect the phenomenon of missing seismic traces, as shown in the red boxes in Fig. 4a. Figure 4c shows a noisy synthetic record with the SNR of −6.5707 dB, which is gained by adding real desert noise to the noise-free record shown in Fig. 4b. Figure 4d–f shows the *f*–*k* spectrum of Fig. 4a–c, respectively. From the *f*–*k* spectrum, we can conclude that the noise in desert area has the characteristic of low frequency, and the frequency of effective signal and noise overlap seriously.

We set the parameters of MRCNN according to Table 1, and the rules for selecting network parameters are as follows:

1. *Patch size* Patch-based image denoising techniques commonly use a patch of size 40×40. According to Levin and Nadler (2011), high noise level usually requires

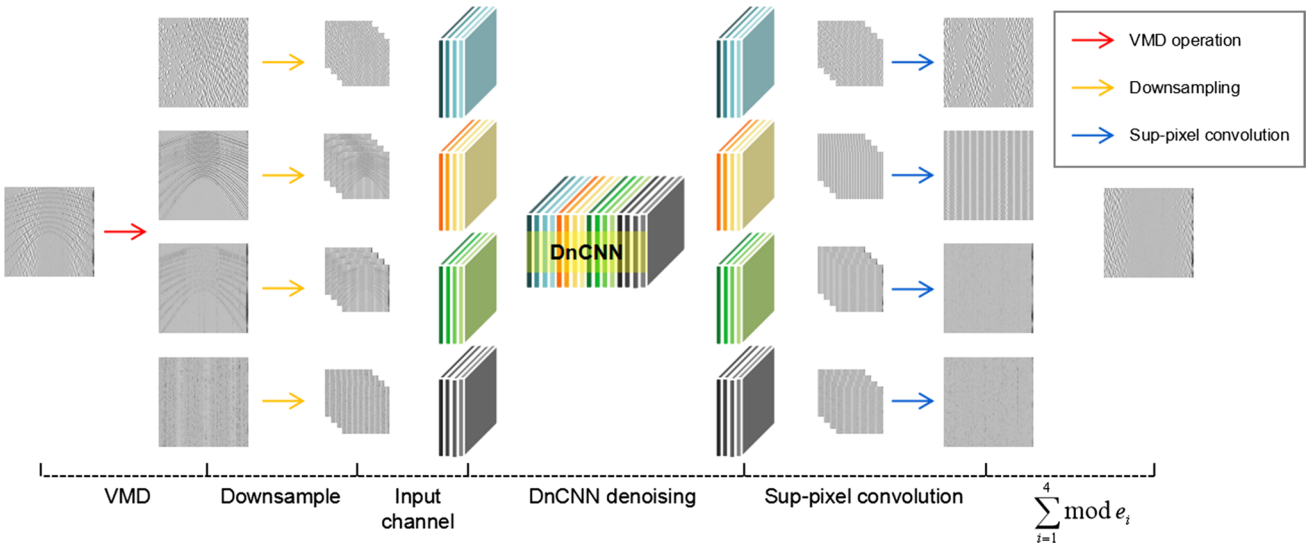

Fig. 2 Architecture of the MRCNN

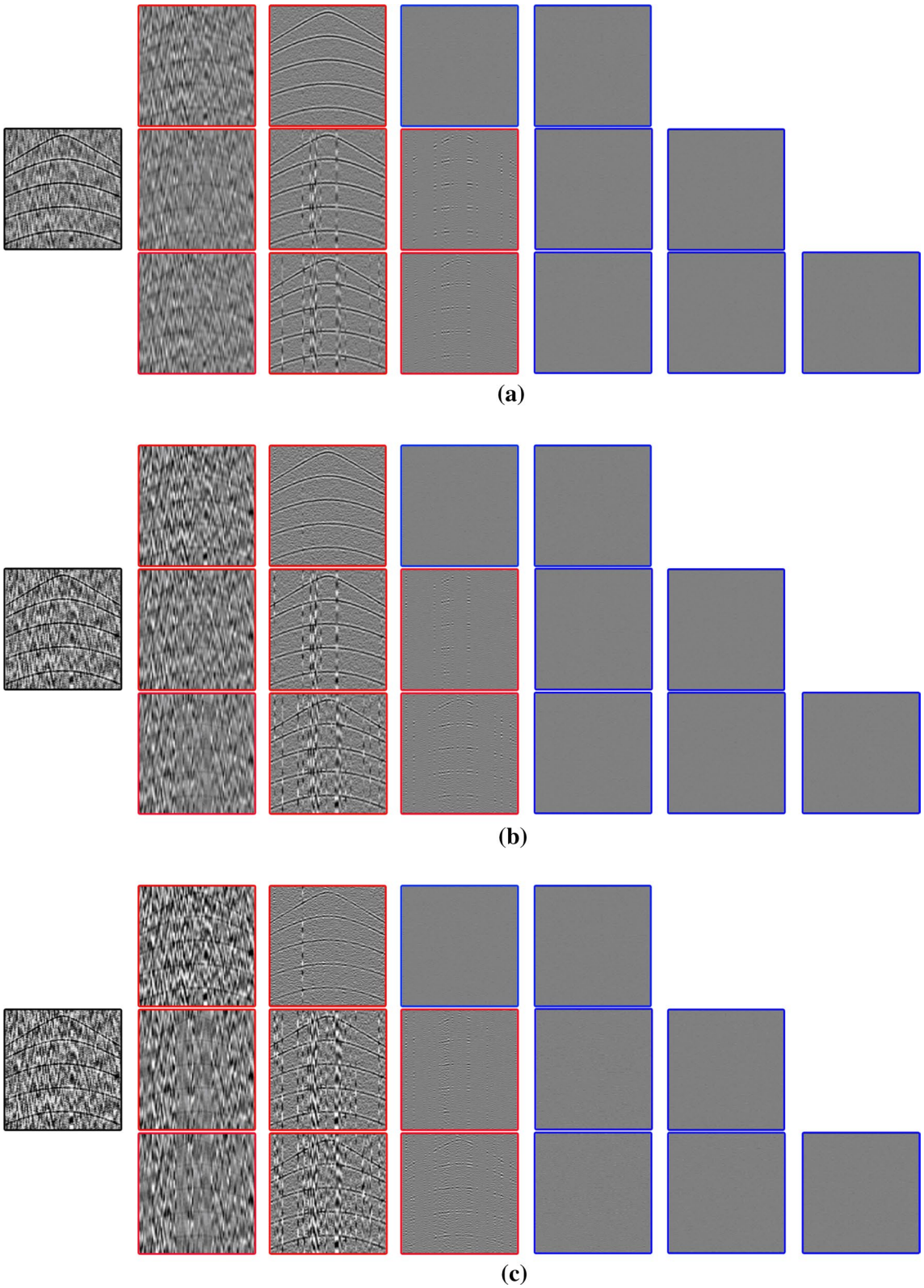

Fig. 3 Decomposition results of seismic records with different SNRs at different decomposition times (four, five and six times). **a** Decomposition results of seismic record with a SNR of −5.6890 dB, **b** decomposition results of seismic record with a SNR of −9.2108 dB, **c** decomposition results of seismic record with a SNR of −11.7096 dB

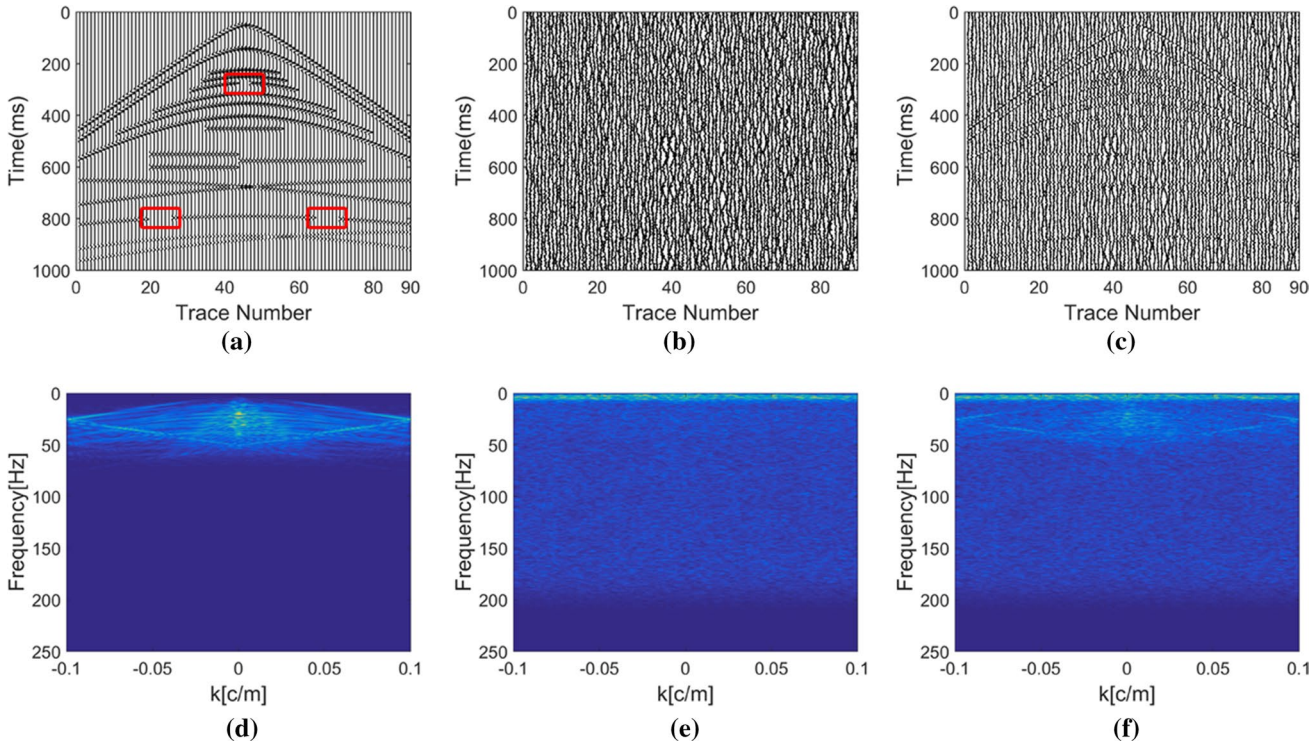

Fig. 4 Synthetic record processing. **a** Noise-free record, **b** desert noise, **c** noisy record, **d** *f*–*k* spectrum of noise-free record, **e** *f*–*k* spectrum of desert noise, **f** *f*–*k* spectrum of noisy record

Table 1 Network training parameters

Training environment	Specification
Patch size	50×50
Batch size	128
Convolution kernels	First layer: 3× 3 × 16×128 Last layer: 3× 3 × 128×16 Other layers: 3× 3 × 128×128
Epoch	50
Network depth	18
Learning rate range	[10^{-3}–10^{-5}]

larger effective patch size to capture more context information for signal recovery. Considering that desert seismic data are usually seriously polluted by random noise and regular noise, a larger patch size should be applied to extract sufficient effective information. However, the increasing patch size will increase the difficulty of network training, so we conduct a large number of simulations and practical experiments and find that the network has the best performance when the patch size is 50×50. Therefore, we finally determine the patch size in this paper is 50×50.

2. *Convolution kernel size* In order to reduce the network parameters and improve the nonlinearity of the network, we use a stack of multiple small convolution kernels instead of a larger one. The convolution kernel size of the first convolutional layer in DnCNN (the third layer of MRCNN) is set to 3×3×16×128 (the reason for choosing 16 channels is explained in Part C of "Theory" section), and the convolution kernel size of the last convolutional layer in DnCNN (the penultimate layer of MRCNN) is set to 3×3×128×16. For the remaining convolutional layers of DnCNN, convolution kernels of size 3×3×128×128 are used.
3. *Network depth*: Theoretically, deeper networks have stronger ability to extract features. However, when the network depth reaches a certain level, the network performance tends to be stable. Excessive increase in the network depth will not only increase the computational cost, but also may lead to network overfitting. In order to find the appropriate network depth, we use the control variable method to train the network. Specifically, we only change the network depth (nine layers to 24 layers) and maintain other hyperparameters unchanged (set the other hyperparameters according to Table 1), and then test the denoising performance of MRCNN at different layers by the variation in SNR. Figure 5 shows that the SNR has no significant improvement after 18 layers,

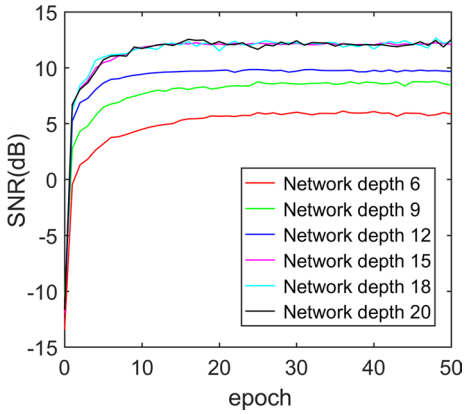

Fig. 5 SNR of a synthetic seismic data after being processed by MRCNN with different network depths (nine layers, 12 layers, 15 layers, 18 layers, 21 layers and 24 layers)

but the network training time will be greatly increased. Therefore, taking into account the ability of network denoising and training efficiency, we finally determine the depth of the MRCNN to be 18.

In this paper, signal set consists of simulated seismic events, including Ricker wavelets of different apparent velocities, different dominant frequencies and different amplitudes. The noise used in the construction of training set is collected in the field or extracted from the field seismic data. The main factors of pollution desert seismic data are random noise and surface wave, so this paper mainly extracts these two kinds of noise to train the network. For random noise, the noise data are collected from the desert area of Tarim Basin in Western China. There are a total of 2300 receivers, each receiver with 30,000 samples, and the sampling rate is 500 Hz. Figure 6a shows part of the random noise. For surface wave, the noise data are extracted from the field seismic data in the western desert region of China. There are a total of 800 receivers, each receiver with 1200 samples, and the sampling rate is 500 Hz. Figure 6b shows part of the surface wave. The noisy training set is obtained by adding the noise training set and the signal set.

Figure 7d shows the denoised record using the proposed algorithm, and the SNR can reach 13.2438 dB. This paper compares the denoising performance of MRCNN with band-pass filter, VMD filter and DnCNN algorithm. Figure 7a shows the result of band-pass filter, and the SNR is 2.5023 dB. Figure 7b shows the result of VMD filter (the mode number of decomposition is 4) with the SNR of 3.9436 dB). The DnCNN algorithm with the same set as the MRCNN is used to process the synthetic record, and the result is shown in Fig. 7c, with the SNR of 7.2031 dB. For the execution time of the algorithm, the introduction of sub-pixel convolution mitigates the time loss caused by VMD. With the same network parameters (including the number of network layers, number of training sets, patch size, epoch, etc.), the training time of DnCNN and MRCNN is 22.45 h and 10.62 h, respectively.

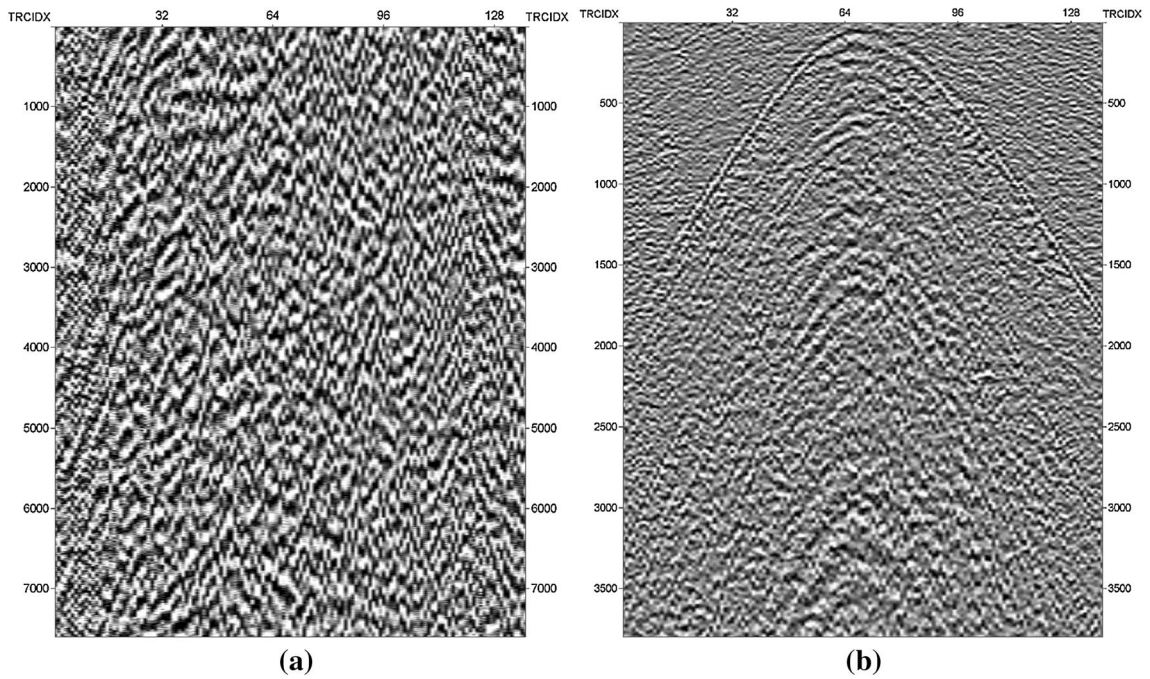

Fig. 6 Partial random noise (**a**) and surface wave (**b**)

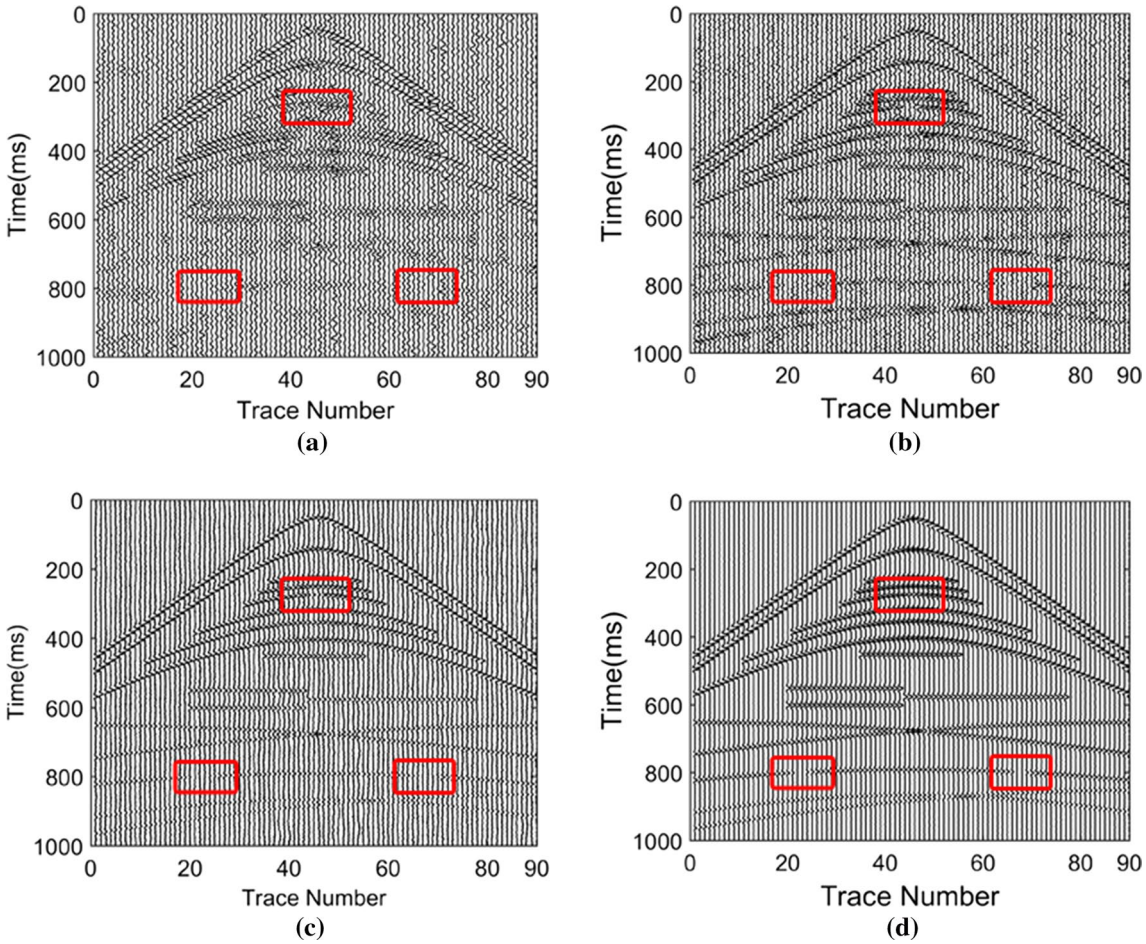

Fig. 7 Comparison of synthetic record. **a** Band-pass denoised record, **b** VMD denoised record, **c** DnCNN denoised record, **d** MRCNN denoised record

From Fig. 7, we have the following observations. The denoising results of band-pass filter and VMD filter are very poor. In these results, the noise cannot be suppressed effectively and there is serious energy loss of reflections. The result of DnCNN is better, reflection events can be recovered clearly, but the denoised record still contains a certain amount of noise. In comparison, the result of MRCNN is the best. It can almost completely suppress the desert noise without the signal energy loss. The red boxes in Fig. 7 show that both MRCNN and DnCNN have the ability to recover the lost seismic events, but the MRCNN can recover the seismic reflections more continuously.

Figure 8a–d shows the single-trace contrast figures of the 46th trace, where the green curves represent the noisy records, the black curves represent the noise-free records and the red curves represent denoised records. The comparison shows that although most of the low-frequency noise has been effectively suppressed after being processed by the band-pass filter, the noise sharing the same frequency band with the signal still exists and the signals have energy loss. Compared with band-pass denoised record, VMD denoising result has less energy loss. However, the suppression of desert noise is still incomplete. MRCNN and DnCNN have similar performances in amplitude preservation of signals, but MRCNN algorithm can suppress noise more thoroughly. The black boxes in the figures represent the missing seismic traces. The comparison shows that the attenuation of signal for MRCNN denoising result is less than 10%, and it is significantly better than the DnCNN.

Figure 9a–d shows residual maps of synthetic record, that is, difference between noisy record and denoised record. The comparison shows that (1) there are some effective signal's residues in the residual map of band-pass filter, which indicates that this method cannot protect the signals effectively; (2) VMD algorithm cannot suppress the desert noise completely; and (3) there is no significant difference between the residual maps of DnCNN and MRCNN, indicating that the two algorithms have similar ability to protect signals and noise.

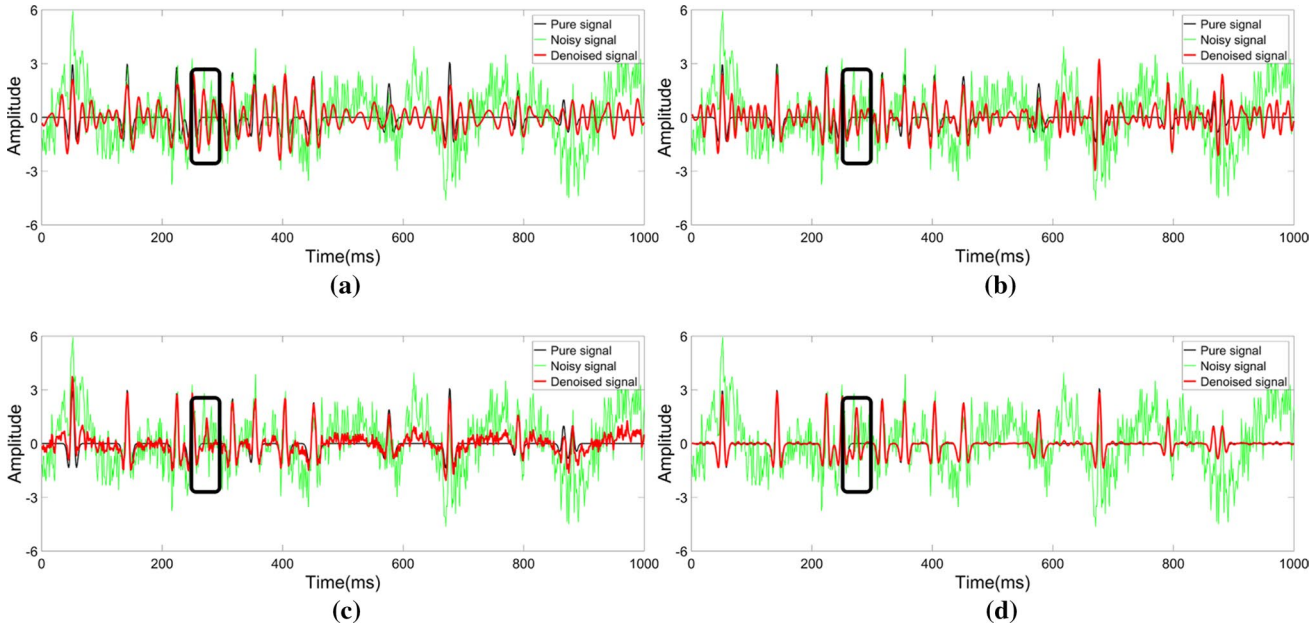

Fig. 8 Single-trace contrast of the 46th trace. **a** 46th trace in band-pass denoising result, **b** 46th trace in VMD denoising result, **c** 46th trace in DnCNN denoising result, **d** 46th trace in MRCNN denoising result

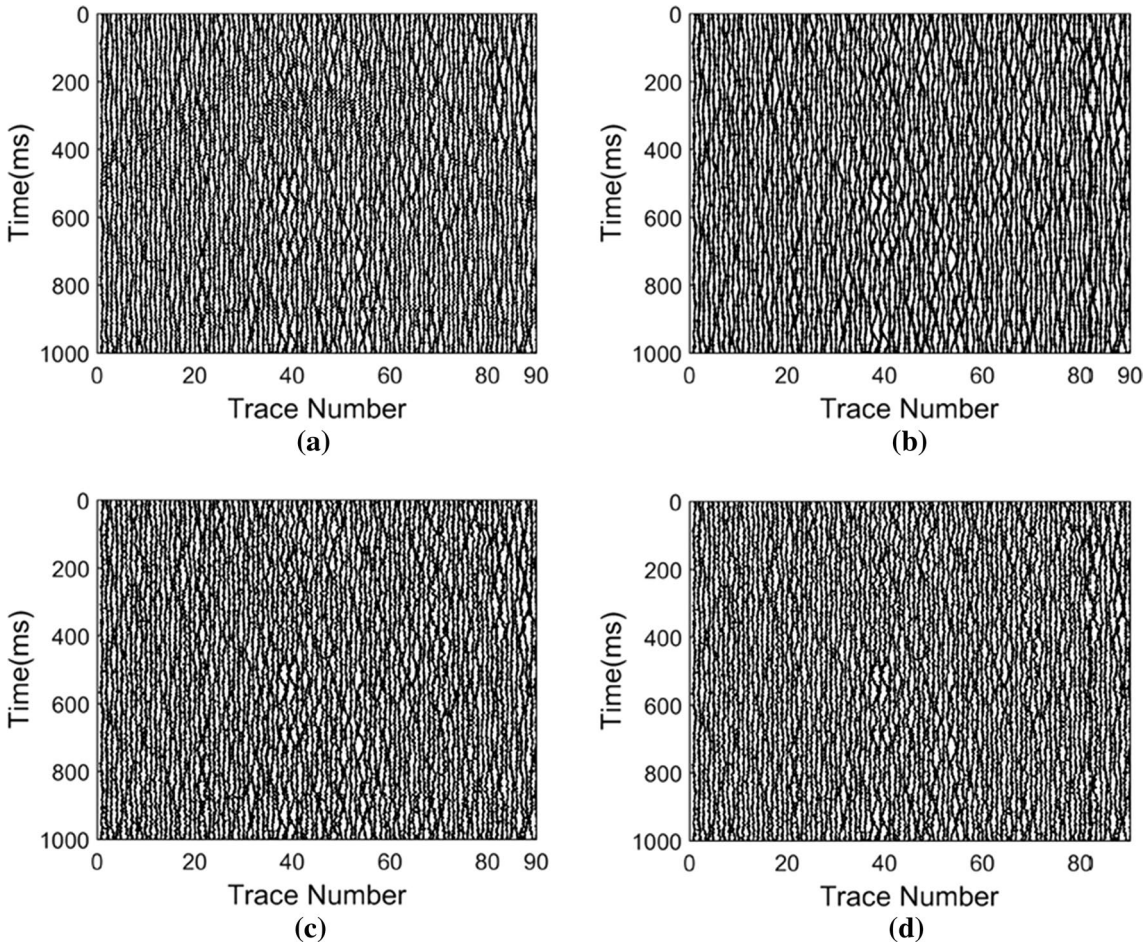

Fig. 9 Residuals comparison of synthetic record. **a** Band-pass denoised residuals, **b** VMD denoised residuals, **c** DnCNN denoised residuals, **d** MRCNN denoised residuals

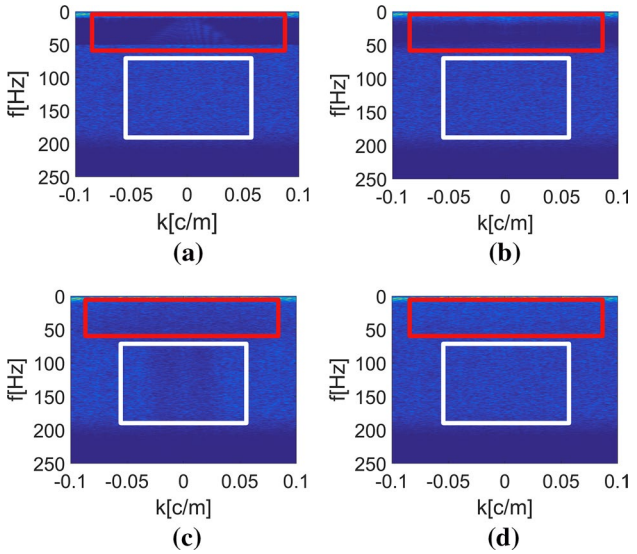

Fig. 10 *f–k* spectrum of residual map. **a** *f–k* spectrum of residual map for band-pass, **b** *f–k* spectrum of residual map for VMD, **c** *f–k* spectrum of residual map for DnCNN, **d** *f–k* spectrum of residual map for MRCNN

Figure 10a–d demonstrates the *f–k* spectrum of the residual maps, and the results obtained from the time-domain analysis can be further verified in the frequency domain. From the red boxes, we can see that the band-pass filter and VMD filter cannot separate the signal from the noise in the overlapping of frequency band, and the residual of the seismic reflections can be clearly seen in the band-pass residual. The white boxes exhibit that DnCNN algorithm cannot completely suppress the desert noise in the middle- and high-frequency band, and some noise remains in the record after denoising. Only the residual of MRCNN is closest to the actual noise, which reflects that the denoising effect of MRCNN is the best.

Furthermore, to verify the denoising ability of MRCNN for noisy data with different levels of noise, we adopted the four algorithms above to process five kinds of noisy records. SNR and mean squared error (MSE) are used to measure the noise suppression ability and the amplitude preservation ability of these four algorithms, respectively, shown in Table 2. In each noise level, the SNR of MRCNN denoised result is higher than the other three algorithms, and the MSE of MRCNN denoised result is lower than the other three algorithms, which proves that the performance of MRCNN is better. In particular, when the SNR of synthetic records is low, the other three algorithms fail in processing ultralow-quality seismic data, whereas MRCNN can still achieve excellent denoising effect.

Experiments on field record

In this paper, we apply the four algorithms to the field common-shot-point record shown in Fig. 11a, which is polluted by both random noise seriously and surface waves. The denoised results of the four algorithms are shown in Fig. 11b–e, respectively. We can see that band-pass filter, VMD filter and DnCNN algorithms have a limited suppression ability to desert noise. Particularly for the surface wave, there are obvious noise residues in the results of the other three algorithms. Moreover, for random noise, VMD and DnCNN cannot suppress it either. In comparison, MRCNN performs the best. MRCNN can remove the desert noise completely and recover seismic reflection events clearly and continuously. Meanwhile, we compare the difference before and after denoising by using selected methods (Fig. 12). From the removed noise, we can see that Fig. 12a, b shows a large number of effective signal remains. In Fig. 12c, the random noise reduction is not complete. Only in Fig. 12d, the effective signal has no energy loss and the noise is suppressed thoroughly.

Conclusion and discussion

This paper proposes a new denoising method—MRCNN, which adopts the VMD method to decrease the complexity of the seismic data and enhance the accuracy of residual network denoising. The contributions of this work are summarized as follows:

(a) Due to the complex characteristics of desert seismic noise, some denoising methods cannot separate the signal from noise effectively. This paper uses discrimina-

Table 2 Suppressing performance of noisy record with different noise levels

Original record		Band-pass filter		VMD filter		DnCNN		MRCNN	
SNR (dB)	MSE	SNR (dB)	MSE	SNR (dB)	MSE	SNR (dB)	MSE	SNR (dB)	MSE
2.3032	0.0518	5.6899	0.0283	7.9207	0.0146	13.2394	0.0038	19.9070	0.0010
− 2.1338	0.1697	5.0720	0.0330	5.1390	0.0328	9.3692	0.0095	16.0520	0.0014
− 6.5707	0.3162	2.5023	0.0492	3.9436	0.0430	7.2031	0.0162	13.2438	0.0019
− 8.653	0.6860	− 0.4777	0.1043	− 5.0391	0.3023	2.2804	0.0504	7.9557	0.0132
− 12.175	1.2790	− 3.0589	0.1862	− 7.7828	0.5306	− 3.3102	0.1966	3.0943	0.0501

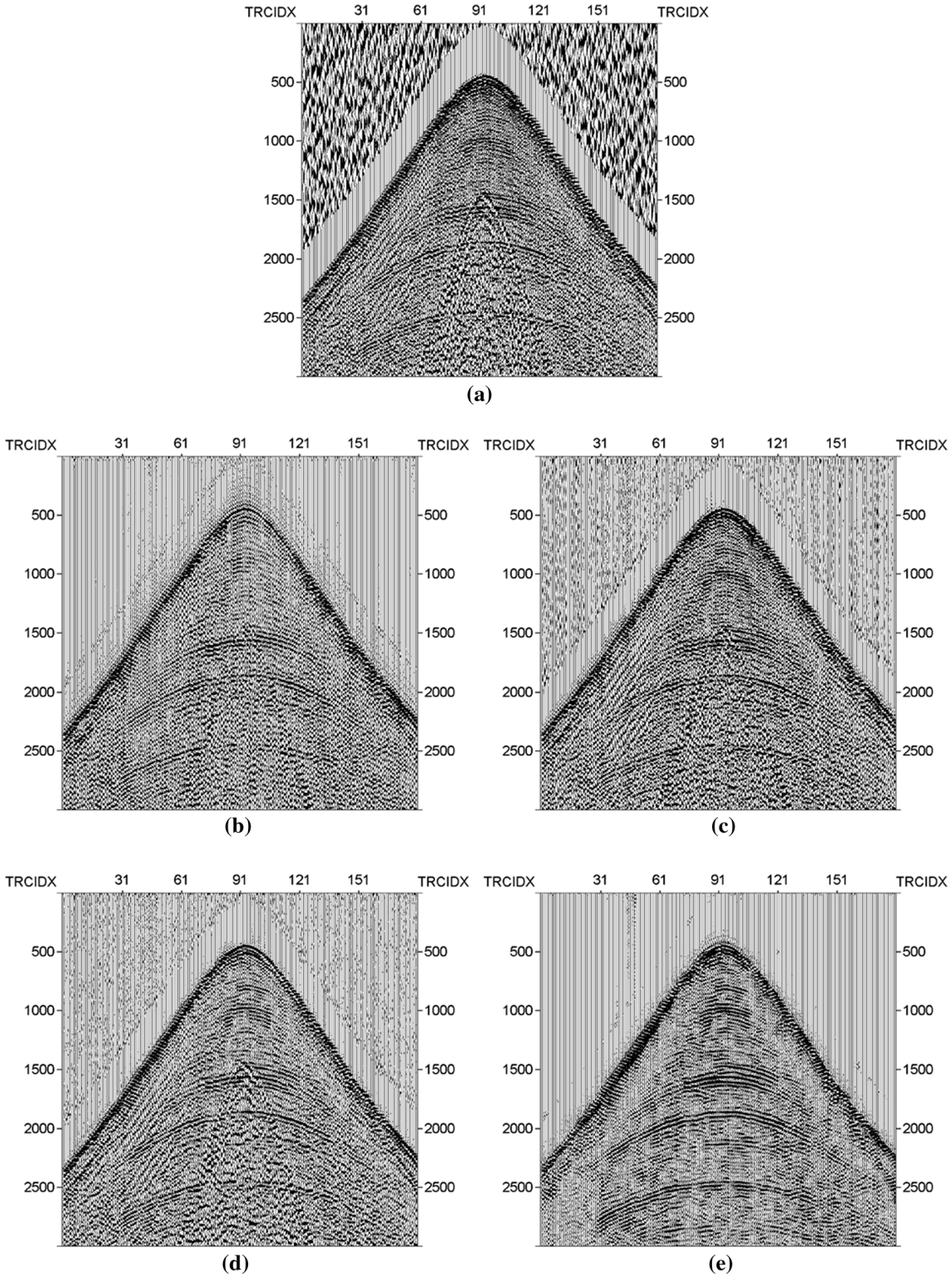

Fig. 11 Comparison of field record. **a** Field seismic data, **b** band-pass denoised result, **c** VMD denoised result, **d** DnCNN denoised result, **e** MRCNN denoised result

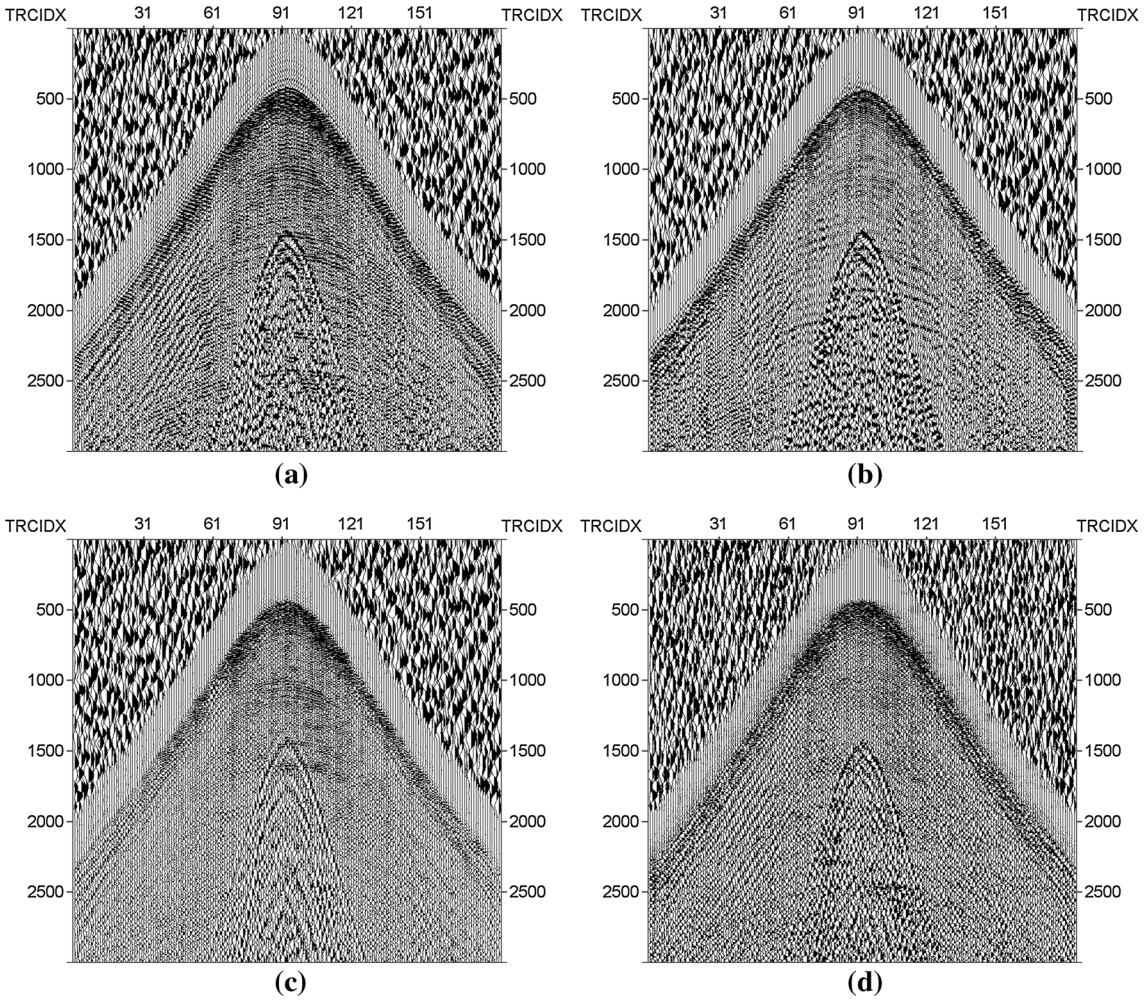

Fig. 12 Residual comparison of real desert seismic record before and after denoising. **a** Band-pass denoised residuals, **b** VMD denoised residuals, **c** DnCNN denoised residuals, **d** MRCNN denoised residuals

tive learning method to separate the signal and noise by feature extraction, which avoids the influence of complex noise characteristics on the denoised result.

(b) This paper integrates the VMD algorithm into CNN-based network. VMD has excellent ability to sparsely decompose data, which can simplify the learning requirements of network and increase the capacity to predict the noise.

(c) Efficiency is also a crucial issue in practical CNN-based denoising. We adopt the subpixel convolution to improve the running speed of the network and predict the desert noise in the subdata space.

The excellent performance of MRCNN has been proven by both synthetic and field experiments. The proposal of MRCNN provides a new solution for the denoising task of desert seismic data.

However, the VMD algorithm applied in MRCNN is still a 1D VMD algorithm, which causes the neglect of the global feature of the dataset. In the future, we will try to combine MRCNN with multidimensional VMD algorithm or with other decomposition algorithms which contain the global feature to improve the MRCNN network.

Acknowledgements This research is supported by the National Natural Science Foundation of China (Under Grants 41730422).

References

Bagheri M, Riahi MA, Hashemi H (2017) Denoising and improving the quality of seismic data using combination of DBM filter and FX deconvolution. Arab J Geosci 10(19):440

Baron D, Sarvotham S, Baraniuk RG (2008) Bayesian compressive sensing via belief propagation. IEEE Trans Signal Process 58(1):269–280

Cobelli C (2010) An online self-tunable method to denoise CGM sensor data. IEEE Trans Biomed Eng 57(3):634–641

Dragomiretskiy K, Zosso D (2014) Variational mode decomposition. IEEE Trans Signal Process 62(3):531–544

Gan SW, Wang SD, Chen YK, Chen JL, Zhong W, Zhang CL (2016) Improved random noise attenuation using f–x empirical mode decomposition and local similarity. Appl Geophys 13(1):127–134

Hao X, Zhang G, Ma S (2016) Deep learning. Int J Semant Comput 10(03):417–439

He, K. M., Zhang, X., Ren, S., & Sun, J. (2016). Deep residual learning for image recognition. IEEE Conference on Computer Vision and Pattern Recognition, 770-778

Levin, A. & Nadler, B. (2011). Natural image denoising: Optimality and inherent bounds, Proceedings of the IEEE Computer Society Conference on Computer Vision and Pattern Recognition, 2833-2840

Li G, Li Y (2016) Random noise of seismic exploration in desert modeling and its applying in noise attenuation. Chin J Geophys 59(2):682–692

Li G, Li Y, Yang B (2015) Effect of wind on seismic exploration random noise on land: modeling and analyzing. J Appl Geophys 119:106–118

Li G, Li Y, Yang B (2017) Seismic exploration random noise on land: modeling and application to noise suppression. IEEE Trans Geosci Remote Sens 55(99):1–14

Li, H., Yang, W. & Yong, X. (2019). Deep learning for ground-roll noise attenuation. 2018 SEG International Exposition and Annual Meeting

Liu L, Ma J (2018) Structured graph dictionary learning and application on the seismic denoising. IEEE Trans Geosci Remote Sens 57(4):1883–1893

Liu W, Cao S, Chen Y (2017) Applications of variational mode decomposition in seismic time-frequency analysis. IEEE J Sel Top Appl Earth Obs Remote Sens 9(8):3821–3831

Makitalo M, Foi A (2012) Optimal inversion of the generalized Anscombe transformation for Poisson–Gaussian noise. IEEE Trans Image Process 22(1):91–103

Michael J, Andrey B, Robert S (2018) Making time-lapse seismic work in a complex desert environment for CO_2 EOR monitoring—design and acquisition. Lead Edge 37(8):598–607

Pilikos G, Faul AC (2017) Bayesian feature learning for seismic compressive sensing and denoising. Geophysics 82(6):O91–O104

Ross ZE, Meier M, Hauksson E, Heaton TH (2018) Generalized seismic phase detection with deep learning. Bull Seismol Soc Am 108(5):2894–2901

Shi, W., Caballero, J., Huszar, F., Totz, J., Aitken, A. P., Bishop, R., Rueckert, D., & Wang, Z. (2016). Real-time single image and video superresolution using an efficient sub-pixel convolutional neural network. IEEE Conference on Computer Vision and Pattern Recognition, 1874-1883

Shoulong X, Wutang B, Pizhe L, Zhaotai Q, Prospecting G (2014) Application examples of q compensation in 3d seismic prospecting data processing in aeolian desert areas. Coal Geol China 26(9):61–64

Wang F, Li Y, Kang XT (2017) Aeolian environmental system modeling of desert area in seismic exploration. Prog Geophys 32(6):2545–2551

Yu S, Ma J (2017) Complex variational mode decomposition for slop-preserving denoising. IEEE Trans Geosci Remote Sens 56(99):586–597

Yu, S., Ma, J., & Wang, W. (2018). Deep learning tutorial for denoising. Electrical Engineering and Systems Science

Yuan S, Wang S (2013) Edge-preserving noise reduction based on Bayesian inversion with directional difference constraints. J Geophys Eng 10(2):1742–2132

Yuan S, Wang S, Luo C, Wang T (2018a) Inversion-based 3-D seismic denoising for exploring spatial edges and spatio-temporal signal redundancy. IEEE Geosci Remote Sens Lett 15(11):1682–1686

Yuan S, Liu J, Wang S, Wang T, Shi P (2018b) Seismic waveform classification and first-break picking using convolution neural networks. IEEE Geosci Remote Sens Lett 15(2):272–276

Zhang K, Zuo W, Chen Y, Meng D, Zhang L (2016) Beyond a Gaussian Denoiser: residual learning of deep CNN for image denoising. IEEE Trans Image Process 26(7):3142–3155

Zhang K, Zuo W, Zhang L (2018) FFDNet: toward a fast and flexible solution for CNN based image denoising. IEEE Trans Image Process 27(9):4608–4622

Zhao Y, Li Y, Dong X, Yang B (2019) Low-frequency noise suppression method based on improved DnCNN in desert seismic data. IEEE Geosci Remote Sens Lett 16(5):811–815

Zhong T, Li Y, Wu N, Pengfei N, Baojun Y (2015) Statistical analysis of background noise in seismic prospecting. Geophys Prospect 63(5):1161–1174

Acta Geophysica (2020) 68:403–412
https://doi.org/10.1007/s11600-020-00408-1

RESEARCH ARTICLE - APPLIED GEOPHYSICS

Denoising of desert seismic signal based on synchrosqueezing transform and Adaboost algorithm

Xiaofu Sun[1] · **Yue Li**[1]

Received: 4 July 2019 / Accepted: 8 February 2020 / Published online: 18 February 2020

Abstract

Seismic data in desert area generally have low signal-to-noise ratio (SNR) due to special surface conditions. Desert noise is characterized as low-frequency, non-Gaussian and non-stationary noise, which makes the noise suppression in desert area more challenging by conventional methods. Conventional methods are effective for the signal with high SNR, but in desert seismic signal, the SNR is low and the signal can easily be obliterated in desert noise. In this paper, we propose an approach that operates in synchrosqueezing transform (SST) domain and use classification techniques obtained from supervised machine learning to identify the coefficients associated with signal and noise. First of all, we transform the real desert seismic data into time–frequency domain by SST. Secondly, we select features by calculating the SST coefficients of signal and noise. And then, we train them in the Adaboost classifier. Finally, when the training is completed, we can obtain the final classifier that can effectively separate the signal from noise. We perform tests on synthetic and field records, and the results show great advantages in suppressing random noise as well as retaining effective signal amplitude.

Keywords Adaboost classifier · Desert low-frequency noise suppression · Seismic low-frequency signal detection · Synchrosqueezing transform

Introduction

Seismic exploration is one of the important methods for prospecting oil and gas resources (Mondol 2010). In the exploration process, the field data in desert area contain a lot of low-frequency noise due to complex geological structures and surface environment, which reduces the SNR (Zhong et al. 2015). Hence, it is important to distinguish the effective signal from noise in desert seismic data. The unsupervised machine learning based on k-means algorithm was proposed to detect the waveform in transform domain, which can effectively detect the main waveform in the data and quickly extract the microseismic signal (Chen 2018). However, this method may lose efficacy under a high noise level. Sparse S transform can be used to obtain the sparse and aggregated time-spectrum with high resolution (Wang et al. 2017), but it is limited by fixed window function and its energy concentration is not as high as SST (Kumar et al. 2017). In addition, the Ricker wavelet kernel using LS-SVM can be adopted in waveform detection of seismic signal to achieve a favorable denoising result (Deng et al. 2007). However, LS-SVM embeds two adjustment parameters. If these parameters are not properly selected, the performance will decrease. Neural network methods have been successfully applied in seismic denoising in recent years (Yuan et al. 2018; Zhao et al. 2019), whereas these methods often require a large number of sample sets for training, resulting in an increase in the complexity during denoising. Besides, there are many methods playing an important role in transform domain analysis such as time-varying median filtering (Liu et al. 2009), vector median filtering (Liu 2013), empirical mode decomposition (Chen and Ma 2014; Bekara and Van der Baan 2009) and others utilizing the coherence of signal (Zhang and Van Der Baan 2018a,b; Zhou et al. 2016; Chen 2017). However, in desert area, most conventional methods are not ideal due to the low-frequency, non-Gaussian, non-stationary and other complex characteristics of desert noise (Li et al 2017; Zhong et al 2015).

✉ Yue Li
liyue@jlu.edu.cn

Xiaofu Sun
sunxf17@mails.jlu.edu.cn

[1] Department of Information, College of Communication Engineering, Jilin University, Changchun 130012, China

In this paper, we propose an approach that operates in time–frequency domain (Qin and Song 2016; Wang et al. 2018; Anvari et al. 2017) and use classification technique adopted from supervised machine learning (Freund and Schapire 1997; Lv et al. 2017) to identify the signal and noise coefficients. Firstly, the noisy desert seismic signal is transformed into time–frequency domain by SST. We use the coefficients in SST domain to extract the features of the signal and the noise. Secondly, these features are trained in the Adaboost classifier. Through the continuous iterations, the final classifier can be obtained and the signal and noise are separated. Finally, we keep the coefficients of the effective signal and transform them back to time domain by the inverse transform of SST. Unlike neural network methods (Yuan et al. 2018; Zhao et al. 2019), Adaboost algorithm in this paper requires a smaller number of samples for training, which reduces the complexity of the algorithm (Freund and Schapire 1997). And it also can enhance its classification accuracy, so as to achieve the optimal classification effect.

Noise reduction method

The proposed method mainly includes two parts: feature extraction and classification. SST (Daubechies and Maes 1996) is selected to realize domain transformation. The features are extracted by the coefficients in SST domain. Adaboost algorithm is used to accurately classify signal and noise features. Once the classification of Adaboost is completed, the SST coefficients of the effective signal can be identified. Therefore, the innovation of this paper is the feature extraction and the classification in transform domain.

Transform domain

SST is a time–frequency method (Daubechies et al. 2011). It is used to solve the problem of speech recognition under noise interference. The main idea is to calculate the speech signal analyzed by wavelet transform and then refocus on the calculated divergent blur values. A detailed theoretical derivation of SST is given by Daubechies et al. (2011). Firstly, the definition of CWT is given:

$$W_s(a,b) = \frac{1}{\sqrt{a}} \int s(t)\varphi^*\left(\frac{t-b}{a}\right)\mathrm{d}t \tag{1}$$

where φ^* is complex conjugate, a is scale factor, b is time shift factor, and $s(t)$ is the signal.

According to Parseval theory in frequency domain (Yuan et al. 2018):

$$W_s(a,b) = \frac{1}{2\pi} \int \frac{1}{\sqrt{a}} \hat{s}(\varepsilon)\mathrm{e}^{-jb\varepsilon}\mathrm{d}\varepsilon \tag{2}$$

where $j = \sqrt{(-1)}$ and ε is the angular frequency.

If we ignore the ambiguity near the time axis, we can calculate the partial derivative of the wavelet transform at (a, b) to obtain the instantaneous frequency; for all $W_s(a,b) \neq 0$, we have:

$$w_s(a,b) = \frac{-j}{2\pi W_s(a,b)} \frac{\partial W_s(a,b)}{\partial b} \tag{3}$$

The signal can be projected from time domain to time–frequency domain using Eq. (3). Convert (a,b) into $(b, w_s(a,b))$. The operation is called synchronous compression.

Taking the scale interval $\Delta a_k = a_{k-1} - a_k$, the value of SST is determined by the frequency range $\left[w_l - \Delta w/2, w_l + w/2\right]$ around the center frequency w_l:

$$T_s\left(w_l, b\right) = \frac{1}{\Delta w} \sum_{\left|w_s(a,b)-w_l\right| \le \Delta w/2} W_s(a_k, b) a^{-3/2} \Delta a_k \tag{4}$$

Among them, the value of a_k is in the interval $\left|w\left(a_k, b\right) - w_l\right| \le \Delta w/2$, w_l is the lth discrete angular frequency, and a_k is the kth discrete scale.

After the synchronous compression, the signal can be reconstructed.

When s is a real signal, there is $\hat{s}(\varepsilon) = \hat{s}^*(-\varepsilon)$, then $s(b) = \frac{1}{\pi}\mathrm{Re}\left[\int_0^\infty \hat{s}(\varepsilon)\mathrm{e}^{ib\varepsilon}\mathrm{d}\varepsilon\right]$, here we make $C_\varphi = \frac{1}{2}\int_0^\infty \hat{\varphi}^* \frac{\mathrm{d}\varepsilon}{\varepsilon}$, then we have:

$$s(b) = \mathrm{Re}\left[C_\varphi^{-1} \sum_l T_s\left(w_l, b\right)(\Delta w)\right] \tag{5}$$

The inverse transformation of SST is:

$$s(t) = s(b) = \mathrm{Re}\left[C_\varphi^{-1} \sum_l T_s(w_l, b)(\Delta w)\right] \tag{6}$$

Examples of clean signal and noisy signal in SST domain are shown in Fig. 1. The SNR of the noisy signal in Fig. 1b is −6.7305 dB. It can be seen that there are significant differences between signal and noise in transform domain. We use SST to map the desert seismic data into time–frequency domain.

Feature extraction and classification

Freund and Schapire (1997) proposed Adaboost algorithm. The key idea is to train the same training set using several weak classifiers and then obtain a final classifier by the weak classifiers. The final classifier can classify the samples more accurately. Figure 2 shows the training workflow

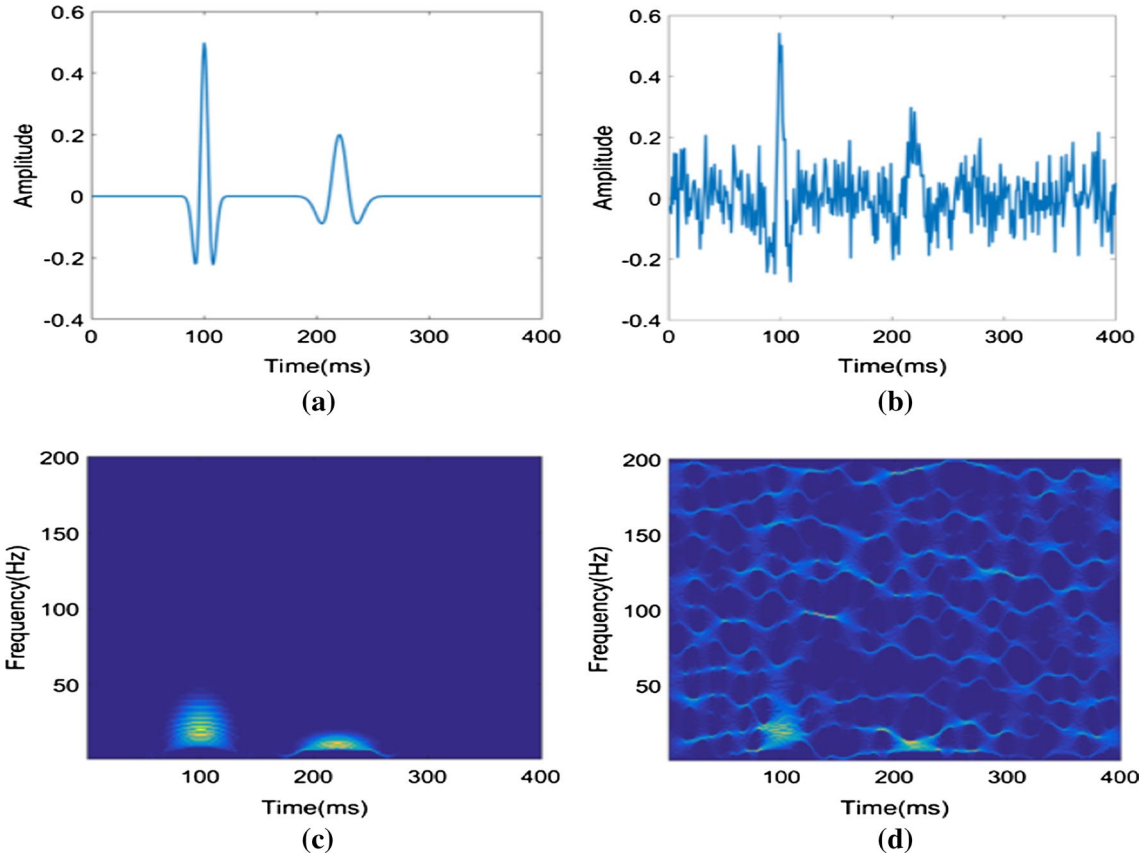

Fig. 1 Time–frequency of the signal in SST domain. **a** Pure signal. **b** Noisy signal. **c** Time–frequency of **a** in SST domain. **d** Time–frequency of **b** in SST domain

of the Adaboost classifier. The obtained weak classifiers are integrated by a voting weight method to generate the final classifier.

For seismic data processing, a set of pure signal and desert noise are transformed into time–frequency domain by SST (Daubechies et al. 2011). Then, we extract features of the noise and the signal in SST domain and train them with the Adaboost classifier. Once the training is completed, we can obtain the final classifier that can effectively identify the signal from noise. After the separation, we can retain the effective signal part. The denoising effect is also achieved during detection.

We use Eqs. (1)–(4) to obtain the coefficients of the pure signal as the positive samples and the coefficients of the noise as the negative samples. All the samples are put into the Adaboost classifier for training. We input the sample set $Q = \{(x_1, y_1), (x_2, y_2), \ldots, (x_i, y_i)\}, y_i \in \{-1,1\}$, where x_i is the sample to be classified, y_i is the label, a positive sample (pure signal point) is set as 1, and a negative sample (noise point) is set as -1. The number of iterations is T, the final strong classifier is $H(x)$, and n is the sum of the samples. Assuming the distribution of the sample to be evenly distributed,$D_t(i) = 1/n$, where $D_t(i)$ is the weights assigned to the sample (x_i, y_i) in the tth iteration. Each sample is of weight $1/n$. The training set is trained according to the D_t sample distribution to obtain the classifier $G_t(x_i)$ (x_i is the ith sample point), whose classification error rate is:

$$e_t = p(G_t(x_i) \neq y_i) \tag{7}$$

where x_i is the sample being classified and y_i is the label. The weighting coefficient α of the $t$thweak classifier is:

$$\alpha_t = \frac{1}{2}\ln\frac{1-e_t}{e_t} \tag{8}$$

where e_t is the classification error rate. The weight of the sample is updated:

$$D_{t+1}(i) = \frac{D_t(i)}{Z_t} \times \begin{cases} e^{-\alpha_t}, G_t(x_i) = y_i \\ e^{\alpha_t}, G_t(x_i) \neq y_i \end{cases} = \frac{D_t(i)\exp(-\alpha_t y_i G_t(x_i))}{Z_t} \tag{9}$$

where Z_t is the normalization factor.

The Adaboost classifier adds new weak classifiers continuously to achieve a sufficiently small error rate. The classifier uses the weight factor of each sample to allocate the probability of entering the next training. The sample correctly

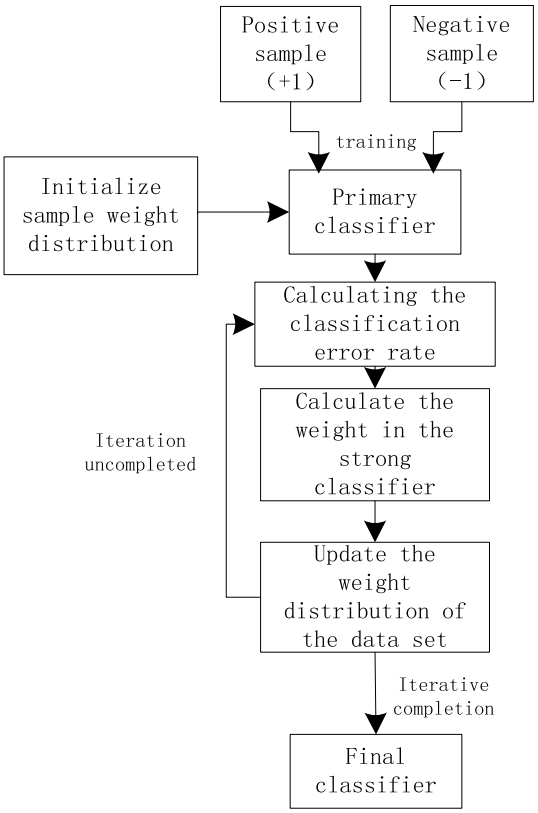

Fig. 2 Training workflow of the Adaboost classifier

classified during the training process should be lowered to reduce the probability of being selected in the next training process. On the contrary, weight of the sample incorrectly classified in the training process will be increased. Following this process, Adaboost can pay more attention to the samples with difficult classification and increase the correct rate in the final classification results (Lv et al. 2017).

The initialized sample weights are constantly changed during the iterations. Once the iteration is terminated, the classification is completed. Then, we can get the final classifier:

$$H(x) = \text{sign}\left(\sum_{t=1}^{T} \alpha_t G_t(x)\right) \tag{10}$$

where $\boldsymbol{x}$ is the sample set and sign is a symbol function.

Once the training is completed, the final classifier in Eq. (10) can be used for the separation of signal and noise.

Desert seismic noise reduction

We use SST coefficients as the input features to train an Adaboost classifier for the signal and noise separation. The main steps are given as follows:

Transform the pure signal and the noise samples into time–frequency domain by SST, and the respective SST coefficients are obtained as features. The coefficient of the signal is set as a positive sample, and the coefficient of the noise is set as a negative sample.

Put the positive and negative samples into the Adaboost classifier for training, and the iterative process is repeated according to the weight. When the iterative process is done, we can obtain the final classifier.

Use the final classifier to identify signal and noise in SST domain, retain the signal coefficients, and discard the noise coefficients.

Convert the effective signal coefficients back to time domain using SST inverse transform.

The workflow is summarized in Fig. 3.

Experiments and results

Implementation

The features of the noisy desert signals in Fig. 1 are extracted in SST domain and sent to the classifier. The classification results are given in Fig. 4. Figure 4a shows the classification result of a pure signal in SST domain. Figure 4b shows the classification result of the SST threshold method in SST domain. The method performs an adaptive threshold on the SST coefficients of the signal in SST domain (Fig. 4b). The signal and the noise are effectively separated in Fig. 4c. In addition, the signal in Fig. 4c is very close to the pure signal shown in Fig. 4a. We keep the signal and eliminate the noise. Then, the inverse SST is used to transform the signal part into time domain. According to the classification results in Fig. 4, it can be concluded that the method proposed is more effective.

Figure 5 shows the results of single-trace processing in Fig. 1b. It implies that the SST threshold method not only causes the incomplete noise removal, but also attenuates the amplitude of signal, which cannot achieve an acceptable denoising result. The proposed method performs better than the SST threshold method in denoising.

Synthetic desert seismic record

We use SNR to verify the effectiveness of a denoising method, which is defined as follows:

$$\text{SNR} = 10\log_{10}\frac{\sum_t |s(f)|^2}{\sum_t |d(f) - s(f)|^2} \tag{11}$$

where $d(f)$ is the denoised signal and $s(f)$ is the original signal.

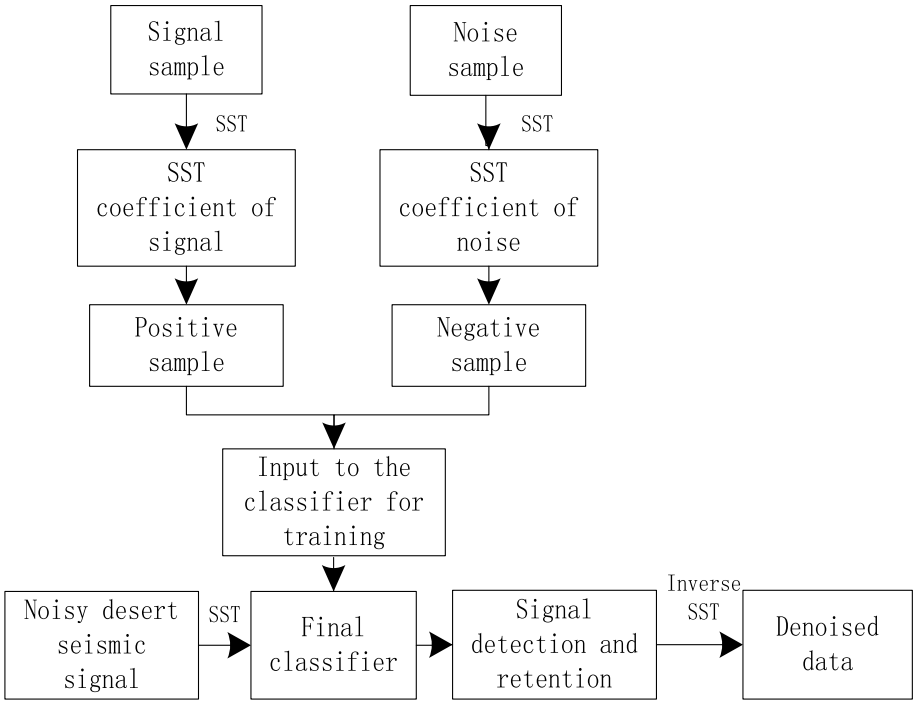

Fig. 3 The workflow of the proposed algorithm

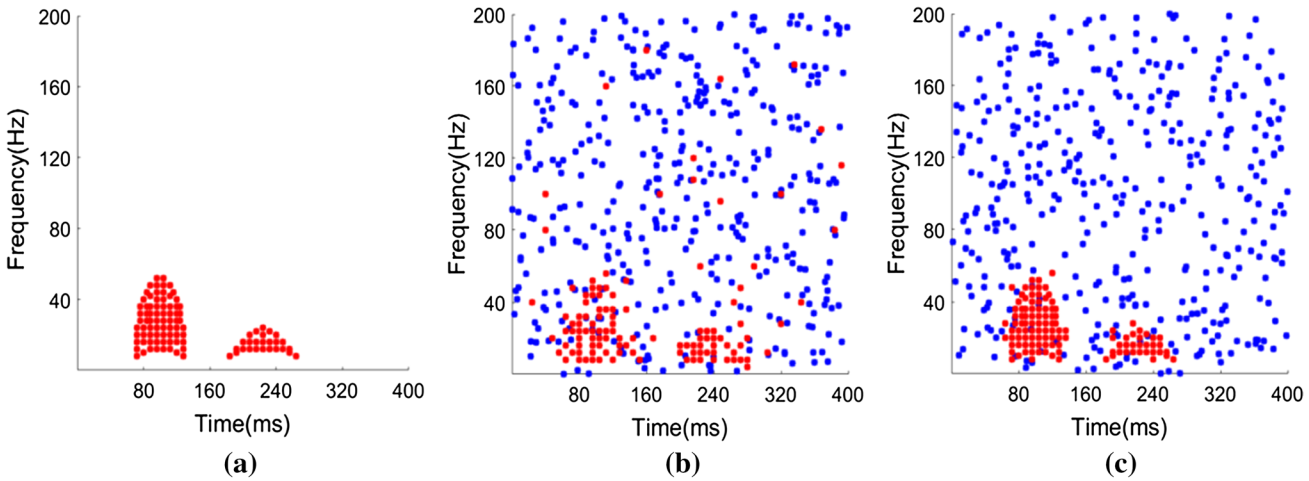

Fig. 4 Coefficient classification results (red and blue dots represent the signal and the noise, respectively). **a** Classification result of pure signal (corresponding to Fig. 1c). **b** Classification result of SST threshold method (corresponding to Fig. 1d). **c** Classification result in this paper (corresponding to Fig. 1d)

Ricker wavelet with dominant frequencies of 15 Hz, 20 Hz, 25 Hz and 30 Hz composes the training set, each of which wavelet has a random amplitude between 0 and 1, and then they are substituted into Eq. (4). After calculating the corresponding SST coefficients, we can get the corresponding SST value of clean signal $T_{s1}(w_l, b) \ldots T_{s40}(w_l, b)$ and the real desert noise $T_{s41}(w_l, b) \ldots T_{s70}(w_l, b)$. Regarding the SST coefficient points, x_1 to x_{40} represent the pure signal, while x_{41} to x_{70} represent the actual desert noise (assuming $n = 70$ and $T = 40$).

Figures 6 and 7 show the denoising results of different simulation records. As we can see from the figures, the method proposed in this paper can suppress noise more effectively, while retaining signal more completely. Furthermore, the proposed method can increase the SNR more. Figure 6 shows a comparison of three methods. The noisy signal in Fig. 6c is composed of Fig. 6a, b. According to the experimental results, the wavelet transform in Fig. 6d remains a lot of random noise, and its signal has great distortion. The SST threshold method in Fig. 6e loses a lot of effective signal

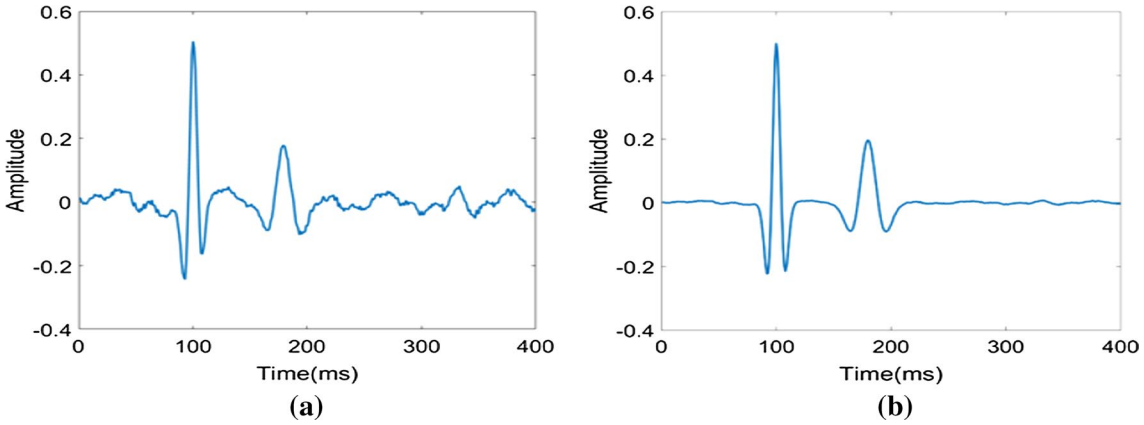

Fig. 5 The results of single-trace processing in Fig. 1b. **a** SST threshold method and **b** the proposed method

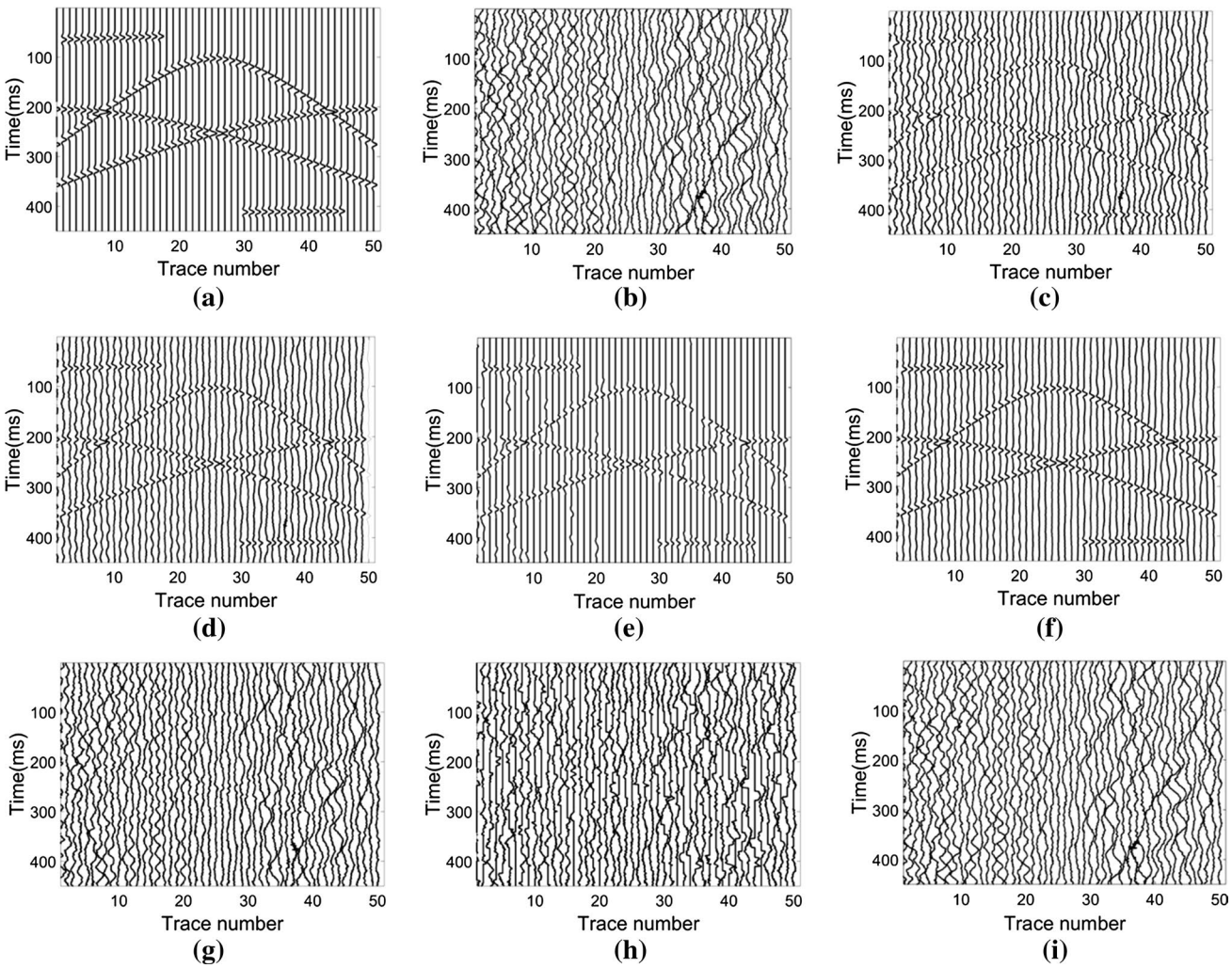

Fig. 6 Synthetic record processing. **a** Pure synthetic signal; **b** desert noise; **c** synthetic records (SNR = − 6.7305 dB); **d** wavelet transform (− 2.1638 dB); **e** SST threshold method (2.2941 dB); **f** proposed method (7.2489 dB); **g** difference between **c** and **d**; **h** difference between **c** and **e**; **i** difference between **c** and **f**

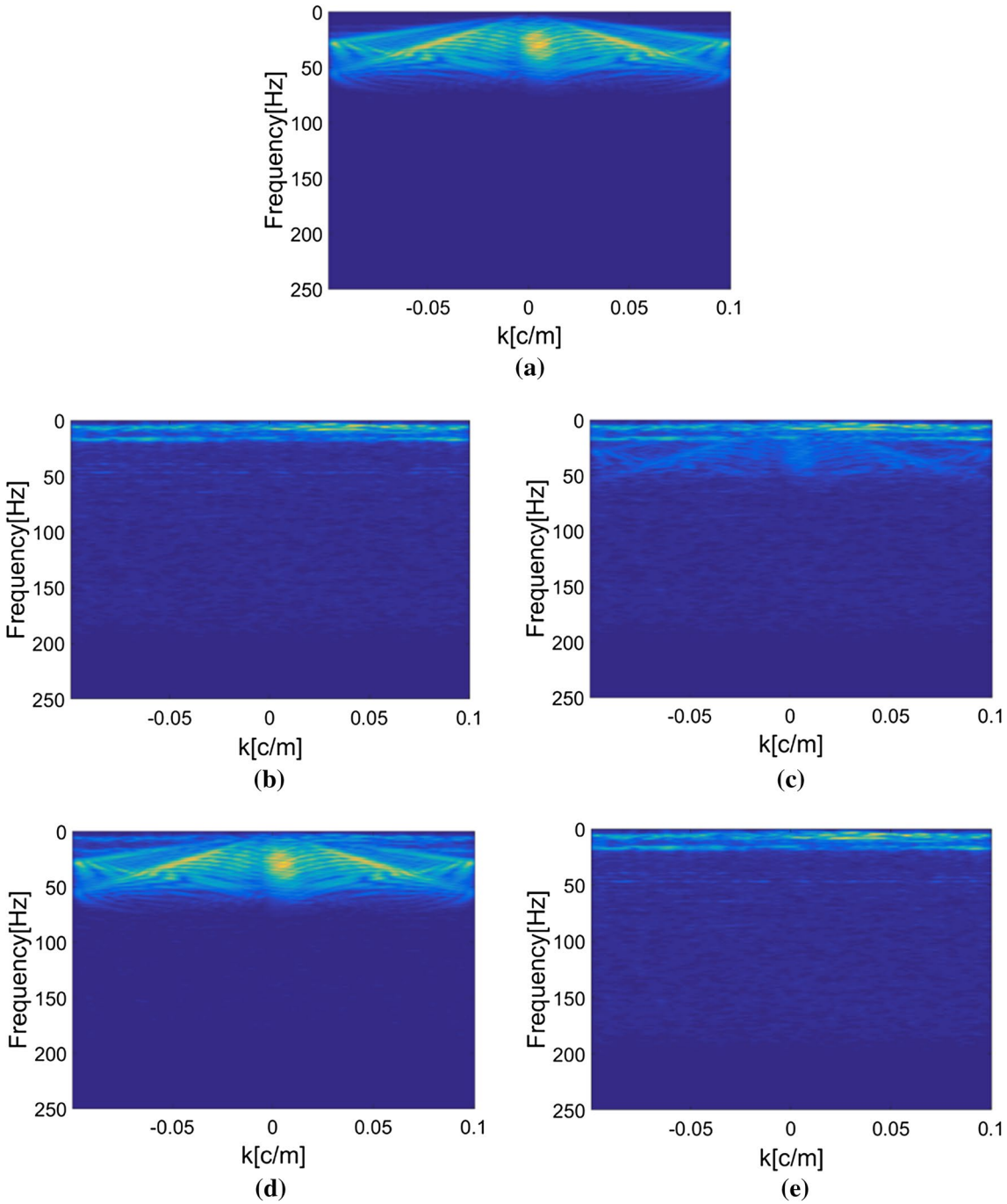

Fig. 7 Synthetic record f–k spectra. **a** Original signal, **b d**esert noise, **c** noisy signal, **d** proposed method, and **e** removed noise in this paper

in denoising process, and there are many inaccuracies in its classification. In contrast, Fig. 6a, f is relatively close, the amplitude of the signal is well preserved, and the noise is suppressed more thoroughly. Figure 6g, h, i shows the results of the removed noise by using wavelet transform, the SST threshold method and the proposed method. We can see that the removed noise (Fig. 6i) is very similar to the desert noise (Fig. 6b), and there is almost no valid signal in this part, which demonstrates superior recovery. However, the wavelet denoising method (Fig. 6g) still has some signal residual after denoising, and the degree of amplitude preservation is not as good as the proposed method. Moreover, the removed noise of the SST threshold method in Fig. 6h also presents some residual signal. Although the denoising effect is better than the wavelet transform, it still has too much signal distortion.

Figure 7 shows f–k spectra in this paper. It can be seen from the comparison among Fig. 7a, c, d that the signal part after denoising is more concentrated and it is close to the pure signal in Fig. 7a. Moreover, there is not much difference between Fig. 7e and b. The effective signal is well preserved in this method. In summary, the proposed algorithm has advantages in desert noise attenuation.

Since the algorithm in this paper has the limitation of the lowest SNR, we add 5 random noises of different levels in the experiments in Fig. 6 and we repeat the same experiment 100 times for each noise level (500 experiments in total). The output SNRs are calculated. The noise level is different in every 100 experiments, and the SNRs have different values, but they are basically in a stable level. As shown in Table 1, the values are represented by SNR. The SNR fluctuates within the range. Obviously, the proposed method has obvious advantages in improving SNR, and it also has a stable effect in denoising.

We also analyze the SNR of the methods mentioned above quantitatively. Figure 8 shows the output SNRs of the three methods (wavelet transform, the SST threshold method, and the proposed method) under different input SNR levels. The line of the proposed algorithm is significantly higher than that of two methods, which demonstrates its superiority. Table 1 gives a more specific comparison among these methods. It shows that the largest SNR values belong to the proposed method.

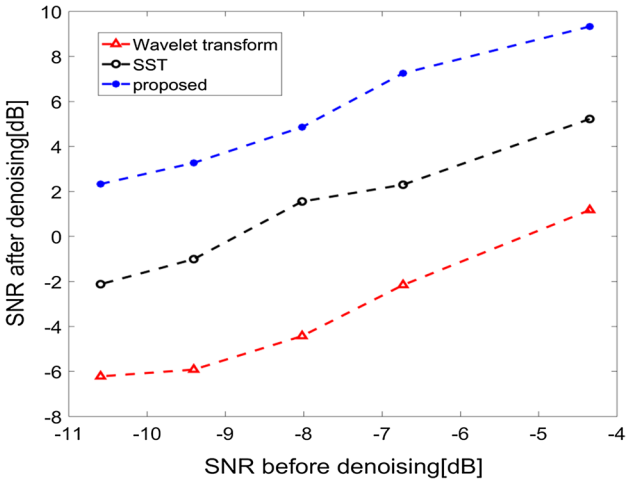

Fig. 8 Comparison of different SNR levels

Field record

We use the field records to test the practical application ability (Fig. 9). The training set is generated by Ricker wavelet with the dominant frequencies from 15 to 30 Hz, each of which is randomly selected with 30 numbers between 0 and 2 as amplitudes, and then they are substituted into Eq. (4). After calculating the corresponding SST coefficients, we can get the corresponding SST value of clean signal $T'_{s1}(w_l, b) \cdots T'_{s480}(w_l, b)$, and the real desert noise $T'_{s481}(w_l, b) \cdots T'_{s1480}(w_l, b)$ from real data set and real surface wave. Regarding the SST coefficient points, x'_1 to x'_{480} represent the pure signal, while x'_{480} to x'_{1480} represent the actual desert noise (assuming $n = 1480$ and $T = 60$). We still compare the algorithm with wavelet transform and SST thresholding algorithm. Figure 9b shows the result of wavelet transform, it can be seen from the circled part of the red frame that the effective signal becomes thicker in Fig. 9b, and the signal on both ends is still aliasing in the noise. Also the high-frequency part loses effective signal. The SST threshold method in Fig. 9c has a better effect, the signal recovery is better than the wavelet transform, and the signal is more continuous on both sides. The proposed method in Fig. 9d has the best denoising effect. The signals are more continuously and clearly recovered. It also completely removes the surface wave. In summary, the effect of the proposed is better than that of the other two methods.

Conclusions

To process complex desert seismic data, we have developed a novel denoising method in time–frequency domain based on supervised machine learning. The method only relies on some small training samples. We adopt the idea of iterative classification in transform domain. We can classify the signal and the noise via the training of Adaboost classifier. The final classifier of the Adaboost classifier can be used to extract the effective signal from desert seismic record. In the training process, we try to use samples with

Table 1 Output SNR with three methods in Fig. 6

Input SNR (dB)	Output SNR (dB)		
	Wavelet transform	SST threshold method	Proposed
−4.3468	1.1689 ± 0.0131	5.2164 ± 0.0063	11.9188 ± 0.0024
−6.7305	−2.1638 ± 0.0206	2.2941 ± 0.0081	7.2489 ± 0.0037
−8.0197	−4.4321 ± 0.0431	1.5488 ± 0.0104	4.8543 ± 0.0052
−9.4013	−5.9232 ± 0.0659	−1.0132 ± 0.0257	3.2647 ± 0.0070
−10.5938	−6.2246 ± 0.0927	−2.1274 ± 0.0449	2.3254 ± 0.0101

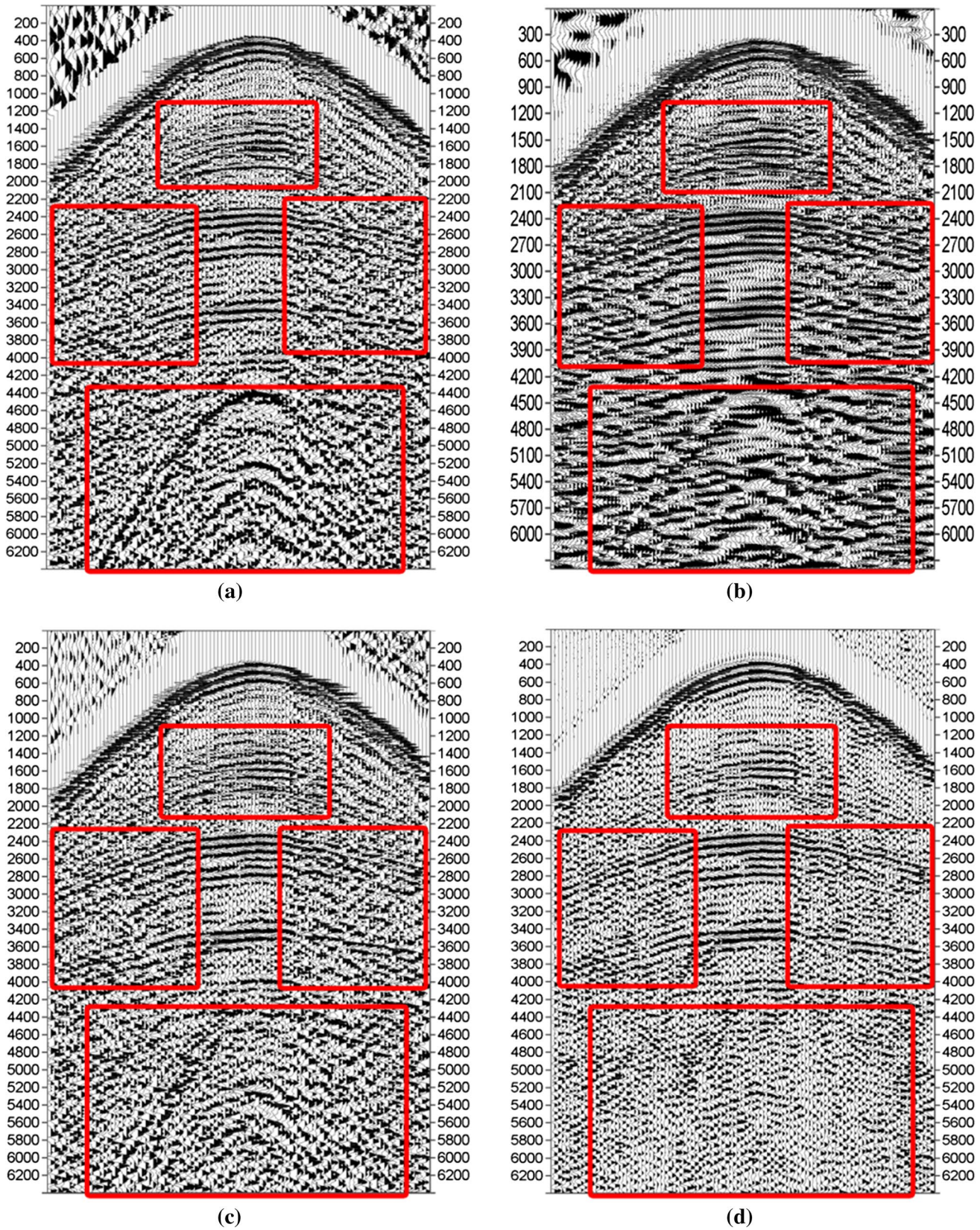

Fig. 9 Real record processing. **a** Original record, **b** wavelet transform, **c** SST threshold method, and **d** proposed method

different dominant frequencies and different intensity noise. The results show the training data set used in this paper is reasonable. Compared with wavelet transform and the SST threshold method, the proposed method achieves a better denoising performance and it is more flexible to be used in practice.

Acknowledgments This work is supported by the National Natural Science Foundation of China (Grant 41730422).

References

Anvari R, Siahsar MAN, Gholtashi S, Roshandel Kahoo A, Mohammadi M (2017) Seismic random noise attenuation using synchrosqueezed wavelet transform and low-rank signal matrix approximation. IEEE Trans Geosci Remote Sens 55(11):6574–6581. https://doi.org/10.1109/TGRS.2017.2730228

Bekara M, van der Baan M (2009) Random and coherent noise attenuation by empirical mode decomposition. Geophysics 74(5):V89–V98. https://doi.org/10.1190/1.3157244

Chen Y (2017) Fast dictionary learning for noise attenuation of multidimensional seismic data. Geophys J Int 209(1):21–31. https://doi.org/10.1093/gji/ggw492

Chen Y (2018) Fast waveform detection for microseismic imaging using unsupervised machine learning. Geophys J Int 215(2):1185–1199. https://doi.org/10.1093/GJI/GGY348

Chen Y, Ma J (2014) Random noise attenuation by f-x empirical-mode decomposition predictive filtering. Geophysics 79(3):81–91. https://doi.org/10.1190/GEO2013-0080.1

Daubechies I, Maes S (1996) A nonlinear squeezing of the continuous wavelet transform based on auditory nerve models. Wavelets Med Biol. https://doi.org/10.1201/9780203734032-20

Daubechies I, Lu J, Wu H (2011) Synchrosqueezed wavelet transforms: an empirical mode decomposition-like tool. Appl Comput Harmon Anal 30(2):243–261. https://doi.org/10.1016/j.acha.2010.08.002

Deng X, Li Y, Yang B (2007) Ricker wavelet LS-SVM and its parameters setting for seismic prospecting signals denoising. In: Paper presented at the second international conference on space information technology 2007, vol 6795. https://doi.org/10.1117/12.773771

Freund Y, Schapire RE (1997) A decision-theoretic generalization of on-line learning and an application to boosting. J Comput Syst Sci 55(1):119–139. https://doi.org/10.1006/jcss.1997.1504

Kumar R, Sumathi P, Kumar A (2017) Synchrosqueezing transform-based frequency shifting detection for earthquake-damaged structures. IEEE Geosci Remote Sens Lett 14(8):1393–1397. https://doi.org/10.1109/LGRS.2017.2714428

Li G, Li Y, Yang B (2017) Seismic exploration random noise on land: modeling and application to noise suppression. IEEE Trans Geosci Remote Sens PP(99):1–14

Liu Y (2013) Noise reduction by vector median filtering. Geophysics 78(3):V79–V86. https://doi.org/10.1190/GEO2012-0232.1

Liu Y, Liu C, Wang D (2009) A 1D time-varying median filter for seismic random, spike-like noise elimination. Geophysics 74(1):V17–V24. https://doi.org/10.1190/1.3043446

Lv T, Yan J, Xu H (2017) An EEG emotion recognition method based on AdaBoost classifier. In: Paper presented at the 2017 Chinese automation congress (CAC), pp 6050–6054. https://doi.org/10.1109/CAC.2017.8243867

Singer SF (1981) Oil exploration. 213(4515):1448

Qin X, Song W (2016) Weak signal extraction method of microseismic data based on synchrosqueezing transform. Geophys Prospect Pet 55(1):60–66

Wang Y, Peng Z, He Y (2017) Time-frequency representation for seismic data using sparse S transform. In: 2nd IEEE international conference on computer and communications (ICCC). IEEE, Chengdu, China. https://doi.org/10.1109/CompComm.2016.7925036

Wang W, Jin Y, Wang B, Li W, Wang X (2018) Chaotic signal de-noising based on adaptive threshold synchrosqueezed wavelet transform. Tien Tzu Hsueh Pao/Acta Electron Sin 46(7):1652–1657. https://doi.org/10.3969/j.issn.0372-2112.2018.07.016

Yuan S, Liu J, Wang S, Wang T, Shi P (2018) Seismic waveform classification and first-break picking using convolution neural networks. IEEE Geosci Remote Sens Lett 15(2):272–276. https://doi.org/10.1109/LGRS.2017.2785834

Zhang C, Van Der Baan M (2018a) A denoising framework for microseismic and reflection seismic data based on block matching. Geophysics 83(5):V283–V292. https://doi.org/10.1190/geo2017-0782.1

Zhang C, van der Baan M (2018b) Multicomponent microseismic data denoising by 3D shearlet transform. Geophysics 83(3):A45–A51. https://doi.org/10.1190/GEO2017-0788.1

Zhao Y, Li Y, Dong X, Yang B (2019) Low-frequency noise suppression method based on improved DnCNN in desert seismic data. IEEE Geosci Remote Sens Lett 16(5):811–815. https://doi.org/10.1109/LGRS.2018.2882058

Zhong T, Li Y, Wu N, Nie P, Yang B (2015) A study on the stationarity and Gaussianity of the background noise in land-seismic prospecting. Geophysics 80(4):V67–V82. https://doi.org/10.1190/geo2014-0153.1

Zhou Q, Gao J, Wang Z, Li K (2016) Adaptive variable time fractional anisotropic diffusion filtering for seismic data noise attenuation. IEEE Trans Geosci Remote Sens 54(4):1905–1917. https://doi.org/10.1109/TGRS.2015.2490158

Acta Geophysica (2020) 68:413–423
https://doi.org/10.1007/s11600-020-00412-5

RESEARCH ARTICLE - APPLIED GEOPHYSICS

Goos–Hänchen induced normal moveout correction for wide-angle reflections

Xiaobo Liu[1] · Fuping Liu[2] · Jingyi Chen[3] · Yifei Bao[3]

Received: 29 October 2019 / Accepted: 22 February 2020 / Published online: 4 March 2020

Abstract
The Goos–Hänchen (GH) lateral shift has been theoretically simulated and observed in lab. GH lateral shift introduces additional traveltime and distance when the incidence angles are larger than the critical angle. For seismic wave, this GH shift is caused by the total reflection of an incident beam of P-wave from low to high impedance medium at near and post-critical angles. Because of its large influences on traveltime and lateral shift displacement, the GH shift should be corrected in normal moveout (NMO) correction for wide-angle reflections in seismic data processing. In this paper, we derive the partial derivatives of reflection coefficients (PP- and PSV-wave) with respect to circular frequency using the Zoeppritz equations. Then, the delay time and NMO correction term with the behavior of GH lateral shift is derived. The characteristics of delay time and GH induced time differences are analyzed. The results show that this GH shift could be either positive or negative and the delay on time has large influences on seismic reflections when the incidence angles are larger than the critical angles. The efficiency of GH induced NMO correction is tested using synthetic seismic data. The GH induced NMO correction should be done for wide-angle reflections during the progress of seismic data processing.

Keywords Delay time · Goos–Hänchen shift · Normal moveout correction · Wide-angle reflections

Introduction

The lateral shift of light was first experimentally observed by Goos and Hänchen (1947). They demonstrated that the beam of reflected light can shift laterally along the reflected interface. This phenomenon is called as Goos–Hänchen (GH) shift (Goos and Hänchen 1949; Ignatovich 2004; Chen et al. 2013; Araújo et al. 2014). This GH lateral shift was further introduced into more physical waves rather than light, such as electromagnetic, acoustic wave and so on (Lotsch 1968; Lakhtakia 2003; Aráujo et al. 2016). In recent years, researchers found that GH shift could be negative and its direction is the same with the direction of energy flow in a negatively refractive medium (Bonnet et al. 2001; Resch et al. 2001; Berman 2002; Chen et al. 2007). However, this GH lateral shift phenomenon was rarely studied in seismic exploration.

Seismic reflection is a method applied in exploring the underground using artificially injected waves (Gardner 1947; Ostrander 1984; Zhang and Wapenaar 2002; Yuan et al. 2020). Sometimes, it is difficult to image oil and gas reservoirs accurately because of the weak transmission energy, which mainly caused by wave scattering, waveform conversion or strong absorption of high frequency content (Brown 1969; Lin et al. 1997; Brittan and Warner 1997). In these areas, the potential ability of wide-angle reflections has been proved (Lerche 1990; Zhang et al. 2004; Sun et al. 2007). However, the lateral shift phenomenon always exist for the wide-angle reflections and the seismic data processing results are significantly affected by the GH effect (Leo and Kraus 2018). Liu et al. (2008) observed that the delay on time is related to the incidence angle, media and frequency. They proved that the GH lateral shift induced delay time is in the same order of magnitude with the wave period. Seismic exploration normally uses low-frequency component which means the wave period is large, so the GH shift cannot be neglected in the seismic data processing.

✉ Xiaobo Liu
liuxiaobo@cugb.edu.cn

[1] School of Geophysics and Information Technology, China University of Geosciences, Beijing 100083, China

[2] Beijing Institute of Graphic Communication, Beijing 102600, China

[3] Seismic Anisotropy Group, Department of Geosciences, The University of Tulsa, Tulsa, OK 74104, USA

Normal moveout (NMO) correction is an important step in seismic data processing, which makes all seismograms to zero-offset seismograms (Rupert and Chun 1975; Yilmaz 1987; Tsvankin 1995; Sedek et al. 2015; Yuan et al. 2019). For the conventional NMO, the delay time caused by GH lateral shift has not been corrected for wide-angle reflections. In seismic exploration, the diffraction phenomenon is a special case of GH shift. Liu et al. (2012) calculated the GH lateral shift displacement of wide-angle reflections. Wang (2015) testified the influence of GH effect on seismic data processing and AVO inversion in attenuating media. Leo and Kraus (2018) derived the closed formulas for the GH phase and determined the lateral displacements for the solid/liquid and liquid/solid scenarios. Based on the previous work, we propose to calculate the delay time caused by the GH lateral shift and derive the GH induced time differences based on NMO correction term for wide-angle reflections.

In this paper, we derive the partial derivatives of Zoeppritz equations with respect to frequency. In addition, the delay on time caused by GH is calculated and the GH induced time differences based on NMO correction is derived for wide-angle reflections. The effects of GH lateral shift on traveltime and NMO correction are analyzed in the numerical examples.

Zoeppritz equations

Zoeppritz equations describe the relationship between the seismic reflection coefficients (PP and PS) and the elastic rock properties (velocities and porosity) (Zoeppritz 1919). The Zoeppritz equations for only P-wave incidence are (Aki and Richards 2002)

$$AR = B \tag{1}$$

where

$$R = \begin{bmatrix} R_{pp} \\ R_{ps} \\ T_{pp} \\ T_{ps} \end{bmatrix}, \quad B = \begin{bmatrix} b_1 \\ b_2 \\ b_3 \\ b_4 \end{bmatrix}, \quad A = \begin{bmatrix} a_{11} & a_{12} & a_{13} & a_{14} \\ a_{21} & a_{22} & a_{23} & a_{24} \\ a_{31} & a_{32} & a_{33} & a_{34} \\ a_{41} & a_{42} & a_{43} & a_{44} \end{bmatrix}, \tag{2}$$

where R_{pp}, R_{ps}, T_{pp} and T_{ps} are the reflection and transmission coefficients of P- and SV-wave, respectively. The elements in matrix A are

$$a_{11} = \sin\alpha, \ a_{12} = \cos\beta, \ a_{13} = -\sin\alpha', \ a_{14} = \cos\beta';$$

$$a_{21} = \cos\alpha, \ a_{22} = -\sin\beta, \ a_{23} = \cos\alpha', \ a_{24} = \sin\beta';$$

$$a_{31} = \cos 2\beta, \ a_{32} = \frac{v_{s1}}{v_{p1}}\sin 2\beta,$$

$$a_{33} = -\frac{\rho_{e2}}{\rho_{e1}}\frac{v_{p2}}{v_{p1}}\cos 2\beta', \ a_{34} = -\frac{\rho_{e2}}{\rho_{e1}}\frac{v_{s2}}{v_{p1}}\sin 2\beta';$$

$$a_{41} = \frac{v_{s1}^2}{v_{p1}^2}\sin 2\alpha, \ a_{42} = \frac{v_{s1}}{v_{p1}}\cos 2\beta,$$

$$a_{43} = \frac{\rho_{e2}}{\rho_{e1}}\frac{v_{s2}^2}{v_{p2}v_{p1}}\sin 2\alpha', \ a_{44} = -\frac{\rho_{e2}}{\rho_{e1}}\frac{v_{s2}}{v_{p1}}\cos 2\beta';$$

$$b_1 = -\sin\alpha, \ b_2 = \cos\alpha, \ b_3 = -\cos 2\beta,$$

$$b_4 = \frac{v_{s1}^2}{v_{p1}^2}\sin 2\alpha = \eta_1^2 \sin 2\alpha.$$

Here, α is the incidence and reflection angle of P-wave; β denotes the reflection angle of SV-wave; α' and β' are the transmission angles of the P- and SV-wave, respectively; v_{pi} and v_{si} denote the P- and SV-wave velocities in layer i, respectively; ρ_i is density in layer i. As shown in Fig. 1, the subscript i ($i = 1, 2$) denotes the upper and lower layers, respectively.

Derivation of partial derivatives of zoeppritz equations with respect to frequency

Letting the circular frequency of seismic wave to be ω, k_{px} and k_{sx} to be the x-component of P- and SV-wave vectors, respectively. The magnitude of P-wave vector is $k_p = \omega/v_p$, and the wave propagation direction is the direction of wave vector. Thus, we have $k_{px} = k_p \sin\alpha = (\omega \sin\alpha)/v_p$. The incidence, reflection and refraction angles of seismic waves at the interface can be expressed using frequency ω. In addition, the reflection coefficients are dependent on ω. So the

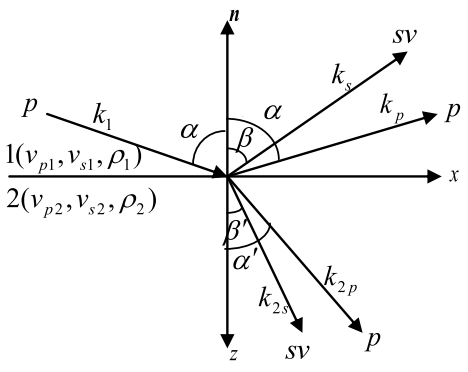

Fig. 1 Reflection and transmission of only P-wave incidence at an interface between two elastic media. n is the normal direction

partial derivatives of Zoeppritz equations with respect to circular frequency ω can be expressed as

$$A\frac{\partial R}{\partial \omega} = -\frac{\partial A}{\partial \omega}R + \frac{\partial B}{\partial \omega}. \tag{3}$$

The reflection coefficient R can be calculated using Zoeppritz Eqs. (1), (2). To get $\frac{\partial R}{\partial \omega}$, the two remaining parameters $\frac{\partial A}{\partial \omega}$ and $\frac{\partial B}{\partial \omega}$ need to be calculated. In the following sections, these two parameters will be calculated, respectively.

The reflection coefficients will become too complex when the incidence angle is larger than the critical angle, $R_{pp} = \eta_p + i\xi_p$ and $R_{ps} = \eta_s + i\xi_s$, where η and ξ denote the real and imaginary parts of reflection coefficients, respectively. The complex angle of reflection coefficient represents the additional phase caused by reflection. The GH lateral shift is the main reason to cause this additional phase (Goos and Hänchen 1947, 1949), the phase angle of P- (δ_p) and SV-wave (δ_s) are

$$\delta_p = \tan^{-1}\frac{\xi_p}{\eta_p}, \tag{4a}$$

$$\delta_s = \tan^{-1}\frac{\xi_s}{\eta_s}. \tag{4b}$$

As shown in Fig. 2, the seismic waves propagate from point C to points E and D. For a given incidence angle α, the phase angle of R_{pp} and R_{ps} can be calculated.

The reflection coefficients of P- and SV-wave can be expressed as $R_{pp} = \frac{E_{pr}}{E_{pi}}$ and $R_{ps} = \frac{E_{sr}}{E_{pi}}$, where $E_{pr}(r,t)$ and $E_{sr}(r,t)$ are the amplitude of reflected P- and SV-wave, respectively. Then, we have

$$E_{pr}(r,t) = E_{pi}e^{-i(k_r\cdot r)+i(\omega t-\delta_p)}, \tag{5a}$$

$$E_{sr}(r,t) = E_{pi}e^{-i(k_r\cdot r)+i(\omega t-\delta_s)}, \tag{5b}$$

here $E_{pi}(r,t)$ denotes the amplitude of incident P-wave. When seismic wave travels from point C to point E and D,

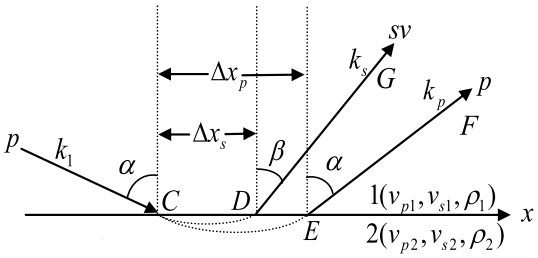

Fig. 2 Sketch of Goos–Hänchen lateral shift of reflected P-and SV-wave

the GH lateral shift induced delay time for P-wave can be expressed as

$$\begin{aligned} t_p &= \frac{\partial \delta_p}{\partial \omega} = \frac{\partial}{\partial \omega}\left(\tan^{-1}\frac{\xi_p}{\eta_p}\right) \\ &= \frac{1}{1+\left(\frac{\xi_p}{\eta_p}\right)^2}\frac{\partial}{\partial \omega}\left(\frac{\xi_p}{\eta_p}\right) \\ &= \frac{\eta_p^2}{\eta_p^2+\xi_p^2}\frac{\eta_p\frac{\partial \xi_p}{\partial \omega} - \xi_p\frac{\partial \eta_p}{\partial \omega}}{\eta_p^2} \\ &= \frac{1}{\eta_p^2+\xi_p^2}\left[\eta_p\xi_{p,\omega} - \xi_p\eta_{p,\omega}\right]. \end{aligned} \tag{6}$$

Similarly, the GH lateral shift induced delay time for SV-wave is

$$t_s = \frac{\partial \delta_s}{\partial \omega} = \frac{1}{\eta_s^2+\xi_s^2}\left[\eta_s\xi_{s,\omega} - \xi_s\eta_{s,\omega}\right], \tag{7}$$

where $\eta_{p,\omega}$ and $\xi_{p,\omega}$ denotes the partial derivatives of the real and imaginary parts of P-wave reflection coefficients with respect to frequency ω, respectively; $\eta_{s,\omega}$ and $\xi_{s,\omega}$ are the partial derivatives of real and imaginary parts of SV-wave reflection coefficients with respect to frequency ω, respectively. These parameters can be obtained through solving Eq. (3).

The partial derivatives of PP and PS reflection coefficients with respect to circular frequency ω are

$$R_{pp,\omega} = \frac{\partial R_{pp}}{\partial \omega} = \eta_{p,\omega} + i\xi_{p,\omega}, \tag{8a}$$

$$R_{ps,\omega} = \frac{\partial R_{ps}}{\partial \omega} = \eta_{s,\omega} + i\xi_{s,\omega}. \tag{8b}$$

To obtain $R_{pp,\omega}$ and $R_{ps,\omega}$, the partial derivatives $\frac{\partial A}{\partial \omega}$ and $\frac{\partial B}{\partial \omega}$ need to be derived. The seismic wave vectors satisfies $\varsigma = k_{1x} = k_{sx} = k_{px} = k_1\sin\alpha = \frac{\omega}{v_{p1}}\sin\alpha$, where $k_1 = \frac{\omega}{v_{p1}}$, $\sin\alpha = \frac{v_{p1}\varsigma}{\omega}$ and $\cos\alpha = \sqrt{1-\left(\frac{v_{p1}\varsigma}{\omega}\right)^2}$. Therefore, we have

$$\frac{\partial \sin\alpha}{\partial \omega} = \frac{\partial}{\partial \omega}\left(\frac{v_{p1}\varsigma}{\omega}\right) = -\frac{v_{p1}\varsigma}{\omega^2} = -\frac{\sin\alpha}{\omega}, \tag{9a}$$

$$\begin{aligned} \frac{\partial \cos\alpha}{\partial \omega} &= \left(v_{p1}^2\varsigma^2/\omega^3\right)\Big/\sqrt{1-\left(\frac{v_{p1}\varsigma}{\omega}\right)^2} \\ &= \frac{\sin^2\alpha}{\omega\cos\alpha} = \frac{1}{\omega}\tan\alpha\sin\alpha. \end{aligned} \tag{9b}$$

According to the Snell's law, $\sin\beta = \frac{v_{s1}}{v_{p1}}\sin\alpha$, $\sin\alpha' = \frac{v_{p2}}{v_{p1}}\sin\alpha$ and $\sin\beta' = \frac{v_{s2}}{v_{p1}}\sin\alpha$. Similarly, $\frac{\partial\sin\beta}{\partial\omega} = -\frac{\sin\beta}{\omega}$, $\frac{\partial\cos\beta}{\partial\omega} = \frac{1}{\omega}\tan\beta\sin\beta$, $\frac{\partial\sin\alpha'}{\partial\omega} = -\frac{\sin\alpha'}{\omega}$, $\frac{\partial\cos\alpha'}{\partial\omega} = \frac{1}{\omega}\tan\alpha'\sin\alpha'$, $\frac{\partial\sin\beta'}{\partial\omega} = -\frac{\sin\beta'}{\omega}$, $\frac{\partial\cos\beta'}{\partial\omega} = \frac{1}{\omega}\tan\beta'\sin\beta'$.

$$\frac{\partial\sin 2\alpha}{\partial\omega} = -\frac{\sin 2\alpha}{\omega}(1-\tan^2\alpha), \tag{10a}$$

$$\frac{\partial\cos 2\alpha}{\partial\omega} = -4\sin\alpha\frac{\partial\sin\alpha}{\partial\omega} = \frac{4}{\omega}\sin^2\alpha. \tag{10b}$$

Similarly, $\sin 2\beta$, $\cos 2\beta$, $\sin 2\alpha'$, $\cos 2\alpha'$, $\sin 2\beta'$ and $\cos 2\beta'$ can be derived, respectively.

Substituting the above derivatives into the Zoeppritz equations, $\frac{\partial A}{\partial\omega}$ and $\frac{\partial B}{\partial\omega}$ are

$$\frac{\partial A}{\partial\omega} = \frac{1}{\omega}\begin{bmatrix} -\sin\alpha & \tan\beta\sin\beta & \sin\alpha' & \tan\beta'\sin\beta' \\ \tan\alpha\sin\alpha & \sin\beta & \tan\alpha'\sin\alpha' & -\sin\beta' \\ 4\sin^2\beta & T_\beta & -\frac{4\rho_2 v_{p2}}{\rho_1 v_{p1}}\sin^2\beta' & T_{\beta'} \\ T_\alpha & 4v_{s1}\sin^2\beta & T_{\alpha'} & -\frac{4\rho_2 v_{s2}}{\rho_1}\sin^2\beta' \end{bmatrix}, \tag{11a}$$

$$\frac{\partial B}{\partial\omega} = \frac{1}{\omega}\begin{bmatrix}\sin\alpha & \tan\alpha\sin\alpha & -4\sin^2\beta & T_\alpha\end{bmatrix}, \tag{11b}$$

where $T_\beta = \frac{v_{s1}}{v_{p1}}\sin 2\beta(1-\tan^2\beta)$, $T_{\beta'} = \frac{\rho_2 v_{s2}}{\rho_1 v_{p1}}\sin 2\beta'(1-\tan^2\beta')$, $T_\alpha = -\frac{v_{s1}^2}{v_{p1}}\sin 2\alpha(1-\tan^2\alpha)$ and $T_{\alpha'} = -\frac{\rho_2 v_{s2}^2}{\rho_1 v_{p2}}\sin 2\alpha'(1-\tan^2\alpha')$. In this way, the partial derivatives of reflection coefficients with respect to frequency ($R_{pp,\omega}$ and $R_{ps,\omega}$) can be calculated for the further calculation of GH lateral shift induced delay time (t_p and t_s).

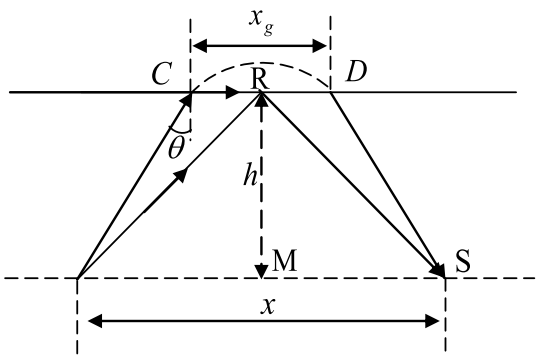

Fig. 3 Sketch of ray path of seismic wave (with Goos–Hänchen lateral shift)

The Goos–Hänchen induced normal moveout correction

In seismic data processing, the normal moveout (NMO) correction is an important procedure. Due to the large influences of Goos–Hänchen (GH) lateral shift for wide-angle reflections, it should be corrected during seismic data processing. As shown in Fig. 3, x_g denotes the GH lateral shift displacement of P- (x_{pp}) or SV-wave (x_{ps}). The source is located at point O, and the receiver is located at point S. The horizontal distance between O and S is x. The traveltime-distance curve for P- and SV-wave without GH shift is $t_{1p} = \frac{1}{V_{p1}}\sqrt{4h^2+x^2}$ and $t_{1s} = \frac{1}{V_{s1}}\sqrt{4h^2+x^2}$, where V_{p1} and V_{s1} are the velocities of P- and SV-wave, respectively (Yilmaz 1987). After considering the GH lateral shift, the seismic wave propagates from O–C–D to point S, the traveltime-distance curve becomes to (GH induced NMO correction)

$$t_{2p} = \frac{2h}{V_{p1}\cos\theta} + t_p, \tag{12a}$$

$$t_{2s} = \frac{2h}{V_{s1}\cos\theta} + t_s, \tag{12b}$$

where t_{2p} and t_{2s} are the traveltime of P- and SV-wave with the consideration of GH lateral shift.

The normal time differences of P- and SV-wave are (Yilmaz 1987)

$$\Delta t_p = \frac{1}{V_{p1}}\sqrt{4h^2+x^2} - \frac{2h}{V_{p1}}, \tag{13a}$$

$$\Delta t_s = \frac{1}{V_{s1}}\sqrt{4h^2+x^2} - \frac{2h}{V_{s1}}, \tag{13b}$$

where $(2h)/V_{p1}$ and $(2h)/V_{s1}$ are the zero-offset traveltime of P- and SV-wave, respectively. After considering the GH lateral shift, the normal time differences can be modified as

$$\Delta t_{\mathrm{pg}} = \frac{2h}{V_{p1}\cos\theta} + t_p - \frac{2h}{V_{p1}}, \tag{14a}$$

$$\Delta t_{sg} = \frac{2h}{V_{s1}\cos\theta} + t_s - \frac{2h}{V_{s1}}, \tag{14b}$$

where t_p and t_s can be calculated using Eqs. (6) and (7), respectively. Combining Eqs. (6), (7), (13) and (14), the GH induced time differences of P- (τ_p) and SV-wave (τ_s) (differences of traveltime with and without GH lateral shift effect) are

$$\tau_p = \Delta t_{\mathrm{pg}} - \Delta t_p = \frac{2h}{V_{p1}\cos\theta} - \frac{1}{V_{p1}}\sqrt{4h^2 + x^2} + \frac{1}{\eta_p^2 + \xi_p^2}\left[\eta_p \xi_{p,\omega} - \xi_p \eta_{p,\omega}\right], \tag{15a}$$

$$\tau_s = \Delta t_{\mathrm{sg}} - \Delta t_s = \frac{2h}{V_{s1}\cos\theta} - \frac{1}{V_{s1}}\sqrt{4h^2 + x^2} + \frac{1}{\eta_s^2 + \xi_s^2}\left[\eta_s \xi_{s,\omega} - \xi_s \eta_{s,\omega}\right]. \tag{15b}$$

Equation (15) can be used to correct the delay time of seismic waves with the consideration of GH effect based on NMO. For all seismic waves received by geophone located at point S, the geometric satisfies

$$x = 2h\tan\theta + x_g. \tag{16}$$

The lateral shift x_g is unique for each incidence angle. The beam of acoustic ray path is unique for a given incidence angle (propagates along O–C–D–S). The energy center of this acoustic wave passes through point S (shown in Fig. 3).

Numerical examples

Characteristics of GH lateral shift

To observe the characteristics and effects of GH lateral shift on seismic wave propagation, the delay time for classic mudstone–sandstone model is calculated. The elastic parameters are Mudstone: $v_{p1} = 1800$ m/s, $v_{s1} = 950$ m/s, $\rho_1 = 2460$ kg/m^3; Sandstone: $v_{p2} = 3850$ m/s, $v_{s2} = 2300$ m/s, $\rho_2 = 2650$ kg/m^3. The frequencies are 25 Hz and 65 Hz. In this numerical example, the contrast of elastic parameters of each medium is relatively large and there are two critical angles, the first and second critical angles are $\alpha_{c1} = 27.9°$ and $\alpha_{c2} = 51.5°$, respectively.

Figure 4 shows the GH lateral shift induced delay time of P- (t_p) and SV-wave (t_s) at the mudstone–sandstone interface when the frequencies are 25 Hz and 65 Hz. In Fig. 4a, there are two break points at the first and second critical angles. For the reflected SV-wave, the delay time is close to zero when the incident angle is close to 90°. Figure 4b, c shows the zoomed in GH shift induced delay time curves of reflected P- and SV-wave between the first and second critical angles. Figure 4d, e shows zoomed in delay time curves with GH shift when the incidence angles are larger than the second critical angle. In the range of these incidence angles, the GH lateral shift induced delay time of P-wave is in the same order of magnitude with the wave period and close to it. When the incidence angles are larger than the second critical angle, the delay time of P-wave becomes smaller and smaller. One can observe that there are some negative points (shown in Fig. 4b, d), which are caused by the negative GH lateral shift. This phenomenon has been observed in optics through theoretical analysis and experiment (Bonnet et al. 2001; Resch et al. 2001; Berman 2002). Figure 4f shows the ratio of delay time ($t_{p\gamma} = t_{p,f_1}/t_{p,f_2}$ and $t_{s\gamma} = t_{s,f_1}/t_{s,f_2}$) when the frequencies are $f_1 = 25$ Hz and $f_2 = 65$ Hz, respectively. For reflected P- or SV-wave, although the delay time varies greatly with different incidence angles, the ratio produced by different frequencies is a constant. It is equal to the ratio of frequencies of P- and SV-wave. In this specific numerical example, $t_{p\gamma} = t_{s\gamma} = 65/25 = 2.6$. The detailed elaboration is shown in the discussion part.

Figure 5 shows the GH shift induced displacement of P- (x_{pp}) and SV-wave (x_{ps}) at the mudstone–sandstone interface when the frequencies are 25 Hz and 65 Hz. Liu et al. (2012) derived the GH shift induced displacement as

$$x_p = -\frac{1}{\eta_p^2 + \xi_p^2}\left[\eta_p \frac{\partial \xi_p}{\partial k_{px}} - \xi_p \frac{\partial \eta_p}{\partial k_{px}}\right], \tag{17a}$$

$$x_s = -\frac{1}{\eta_s^2 + \xi_s^2}\left[\eta_s \frac{\partial \xi_s}{\partial k_{sx}} - \xi_s \frac{\partial \eta_s}{\partial k_{sx}}\right], \tag{17b}$$

where k_{px} and k_{sx} denote the x component of P- and SV-wave vectors, respectively; x_{pp} and x_{ps} are the GH shift induced displacement, respectively. Similar with Fig. 4, there are two break points at two critical angles. One can observe that the influences of GH lateral shift are pretty large and it should be corrected for wide-angle reflections during the NMO correction.

Figure 6 shows the characteristics of GH shift induced time differences for the reflected P- (τ_p) and SV-wave (τ_s) at the mudstone–sandstone interface when the frequencies are 25 Hz and 65 Hz. As shown in Fig. 6a, there are two break points at the first and second critical angles, which mean the effects of GH shift are pretty large around the critical angles. Figure 6b, c are the zoomed in GH shift induced NMO corrections of reflected P- and SV-wave between the first and second critical angles, respectively. The differences between normal time differences with and without GH shift are larger for seismic waves with lower frequencies (for both P- and SV-wave). Figure 6d, e are the GH shift induced NMO corrections of reflected P- and SV-wave when the incidence angles are larger than the second critical angle. Figure 6f shows the ratio of NMO correction with GH lateral shift when the frequencies are 25 Hz and 65 Hz, respectively. One can also observe that frequency influences the corrections of this GH lateral shift. The time differences show similar characteristics with the delay time as shown in Fig. 4. As shown in Fig. 6d, the correction term τ_p of reflected P-wave decreases continuously when the incidence angles are larger than the second critical angle.

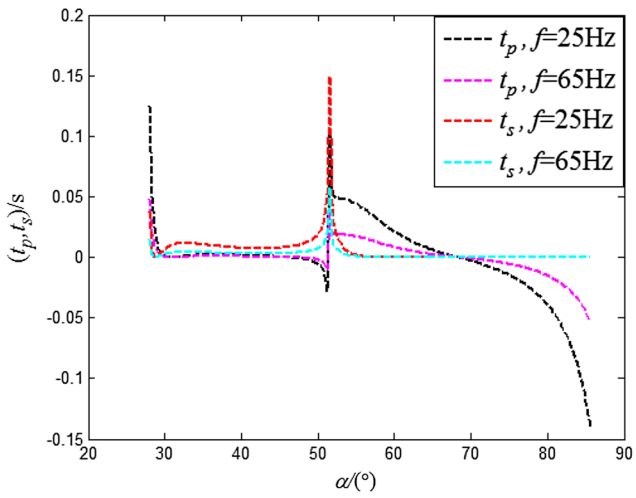
t_p, f=25Hz
t_p, f=65Hz
t_s, f=25Hz
t_s, f=65Hz
(t_p, t_s)/s
α/(°)

(a)

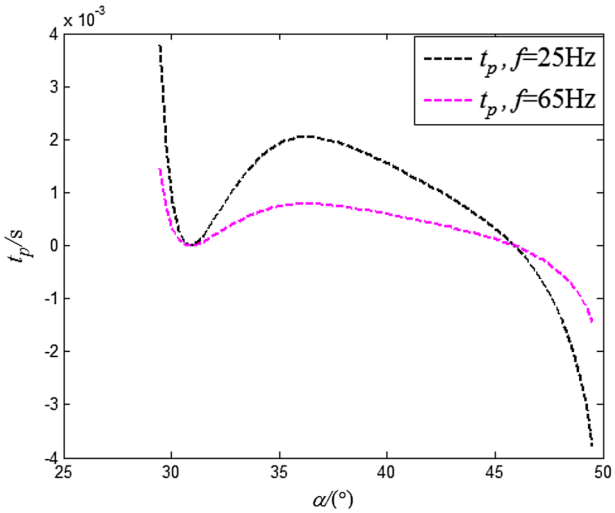
x 10^{-3}
t_p, f=25Hz
t_p, f=65Hz
t_p/s
α/(°)

(b)

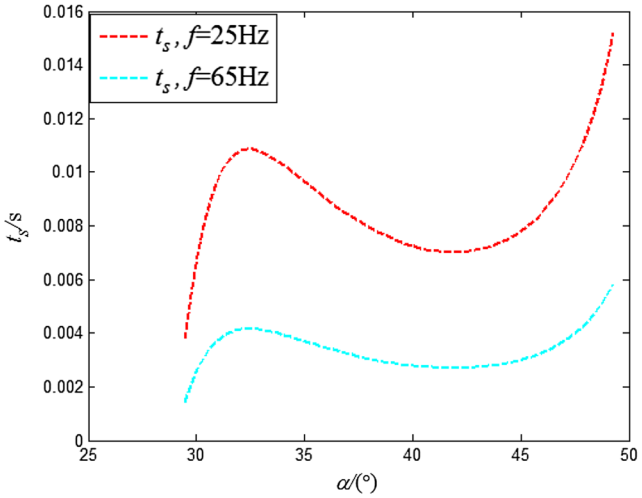
t_s, f=25Hz
t_s, f=65Hz
t_s/s
α/(°)

(c)

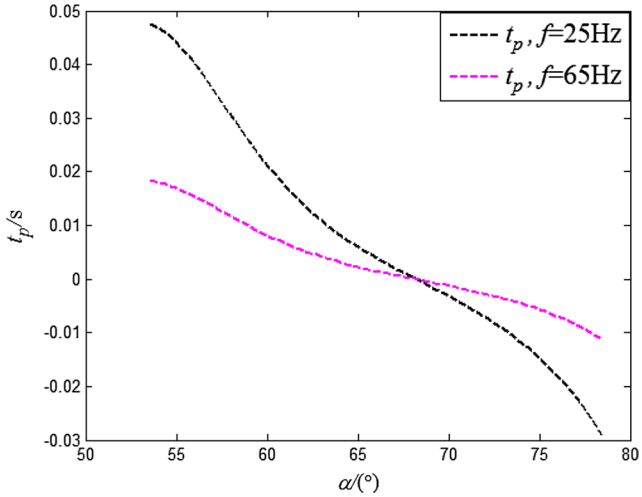
t_p, f=25Hz
t_p, f=65Hz
t_p/s
α/(°)

(d)

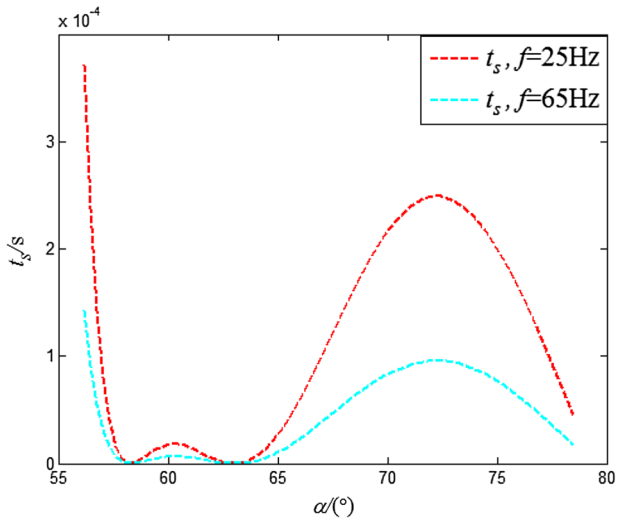
x 10^{-4}
t_s, f=25Hz
t_s, f=65Hz
t_s/s
α/(°)

(e)

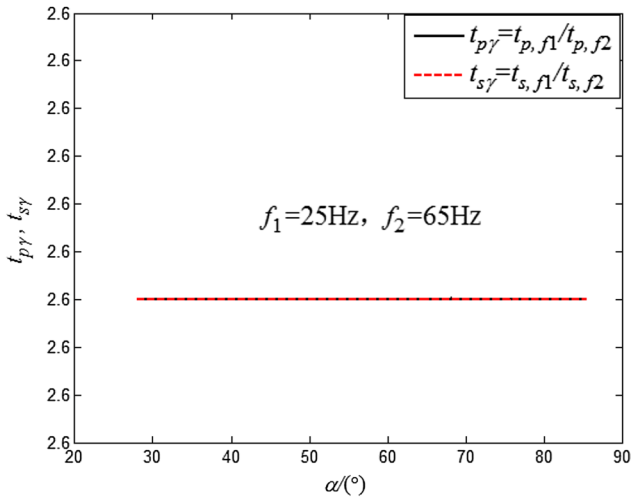
$t_{p\gamma}$=$t_{p,f1}$/$t_{p,f2}$
$t_{s\gamma}$=$t_{s,f1}$/$t_{s,f2}$
f_1=25Hz, f_2=65Hz
$t_{p\gamma}$, $t_{s\gamma}$
α/(°)

(f)

◂**Fig. 4** GH shift induced delay time of P- (t_p) and SV-wave (t_s) at a mudstone–sandstone interface when the frequencies are 25 Hz and 65 Hz, respectively. Black dashed line: delay time of P-wave (t_p) when the frequency is 25 Hz; pink dashed line: delay time of P-wave (t_p) when the frequency is 65 Hz; red dashed line: delay time of SV-wave (t_s) when the frequency is 25 Hz; light blue dashed line: delay time of SV-wave (t_s) when the frequency is 65 Hz

Synthetic seismic data

The efficiency of GH induced NMO correction is further tested for synthetic seismic data. The elastic parameters are Mudstone: $v_{p1}=1800$ m/s, $v_{s1}=950$ m/s, $\rho_1 = 2460$ kg/m^3; Sandstone: $v_{p2}=3850$ m/s, $v_{s2}=2300$ m/s, $\rho_2 = 2650$ kg/m^3. The frequencies are 25 Hz and 65 Hz, respectively.

Figure 7 compares the GH induced NMO correction and conventional NMO correction for P- (Fig. 7a, b) and SV-wave (Fig. 7c, d) when the frequency is 25 Hz. Figure 7a, c shows the seismic gathers with GH induced NMO correction, and Fig. 7b, d shows the seismic gathers with conventional NMO correction. As shown in Fig. 7a, c, the seismic signals of stratigraphy can be corrected to a horizontal interface using GH induced NMO correction no matter the GH lateral shift exist or not. However, the conventional NMO correction method cannot correct seismic signals to a horizontal plane when there is GH lateral shift (shown in Fig. 7b, d).

Figure 8 compares the GH induced NMO correction and conventional NMO correction for P- (Fig. 8a, b) and SV-wave (Fig. 8c, d) when the frequency is 65 Hz. Figure 8a, c shows the seismic gathers with GH induced NMO correction, and Fig. 8b, d shows the seismic gathers with conventional NMO correction. Similar with Fig. 7, GH induced NMO correction can correct the seismic signals to a flat interface. In addition, GH lateral shift with lower frequency have larger impacts on seismic waves. It is necessary to correct the time differences of GH lateral shift for seismic data with large incidence angles.

Discussion

For total reflection, the Goos–Hänchen (GH) shift or displacement is proportional to the wavelength of the laser beam in optics (Alishahi and Mehrany 2010; Araújo et al. 2013, 2016). GH lateral shift delay time and period are in the same order of magnitude (Liu et al. 2008). Therefore, GH lateral displacement or delay time changes with the change of frequency of seismic wave. Based on Zoeppritz equations, the equations of t_p and t_s cannot be expressed explicitly and they are hard to demonstrate theoretically. The explicit expression of group time delay of SH- and SV-wave is (Liu et al. 2009)

$$t_s = -\frac{\partial \delta_s}{\partial \omega} = \frac{2\sin\beta_1}{1+\left(nm\rho_2/\rho_1\right)^2}\frac{n\rho_2}{\omega\rho_1\cos^2\beta_1} \times\left[\frac{n^2\sin\beta_1\cos\beta_1}{\sqrt{\left(n\sin\beta_1\right)^2-1}}+\tan\beta_1\sqrt{n^2\sin^2\beta_1-1}\right], \quad (17)$$

where $n = \frac{V_{s2}}{V_{s1}}$ and $m = \frac{\sqrt{(n\sin\beta)^2-1}}{\cos\beta_1}$. One can observe that t_s and ω are in reverse relationship. When ρ_1, ρ_2, n and β_1 are constant, ω is the only one to affect the value of t_s, then we have

$$t_{s\gamma} = \frac{t_{s,f_1}}{t_{s,f2}} = \frac{\omega_{f2}}{\omega_{f1}} = \frac{2\pi f_2}{2\pi f_1} = \frac{f_2}{f_1} = \frac{T_{f1}}{T_{f2}}, \quad (18)$$

It proves that $t_{s\gamma} = \frac{t_{s,f_1}}{t_{s,f_2}} = \frac{T_{f1}}{T_{f2}}$ for SH-wave. Similarly, the relationship of SV-wave can be demonstrated. The GH shift induced delay time does have a quantitative relationship with the seismic period. For reflected P- or SV-wave, although the delay time varies greatly with different incidence angles, the ratio produced by different frequencies is a constant.

Conclusions

In this paper, we derived the partial derivatives of Zoeppritz equations with respect to frequency. Then, the delay time and Goos–Hänchen (GH) shift induced normal time differences were derived for wide-angle seismic reflections

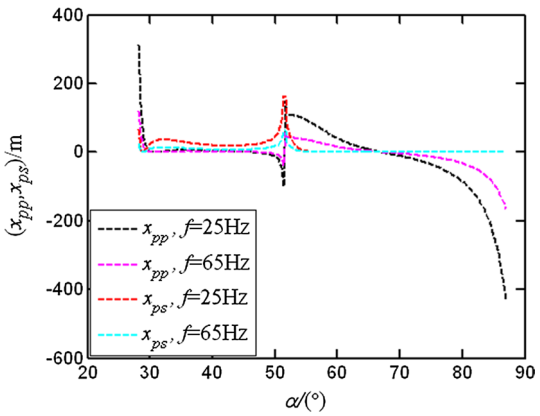

Fig. 5 GH lateral shift induced displacement of P- (x_{pp}) and SV-wave (x_{ps}) at a mudstone–sandstone interface when the frequencies are 25 Hz and 65 Hz, respectively. Black dashed line: GH shift displacement of P-wave (x_{pp}) when the frequency is 25 Hz; Pink dashed line: GH shift displacement of P-wave (x_{pp}) when the frequency is 65 Hz; Red dashed line: GH shift displacement of SV-wave (x_{ps}) when the frequency is 25 Hz; Light blue dashed line: GH shift displacement of SV-wave (x_{ps}) when the frequency is 65 Hz

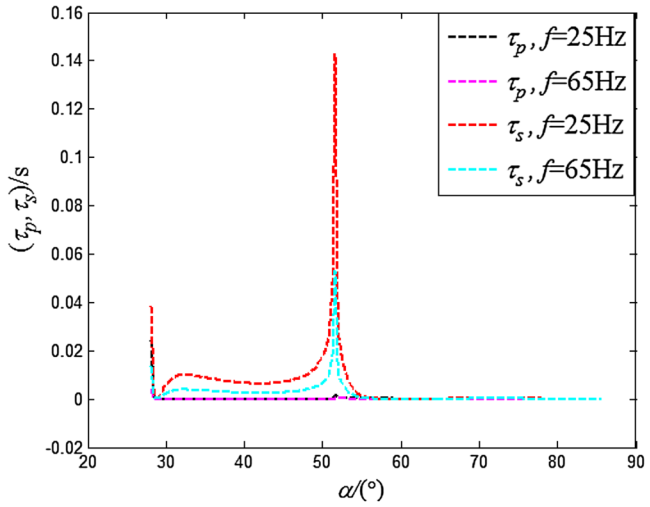
τ_p, f=25Hz
τ_p, f=65Hz
τ_s, f=25Hz
τ_s, f=65Hz
(τ_p, τ_s)/s
α/(°)

(a)

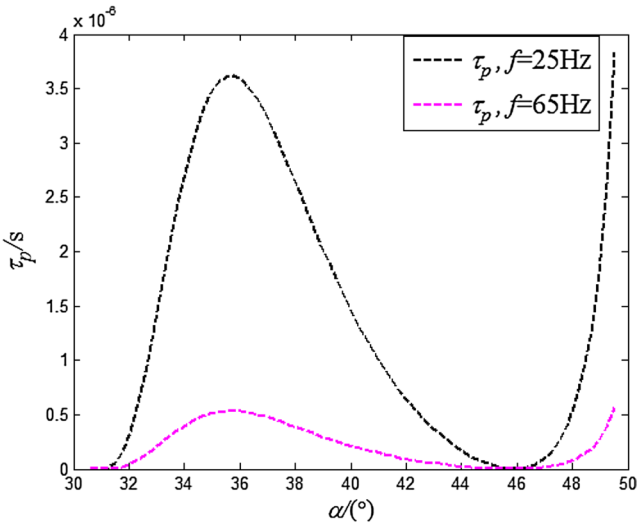
x 10⁻⁶
τ_p, f=25Hz
τ_p, f=65Hz
τ_p/s
α/(°)

(b)

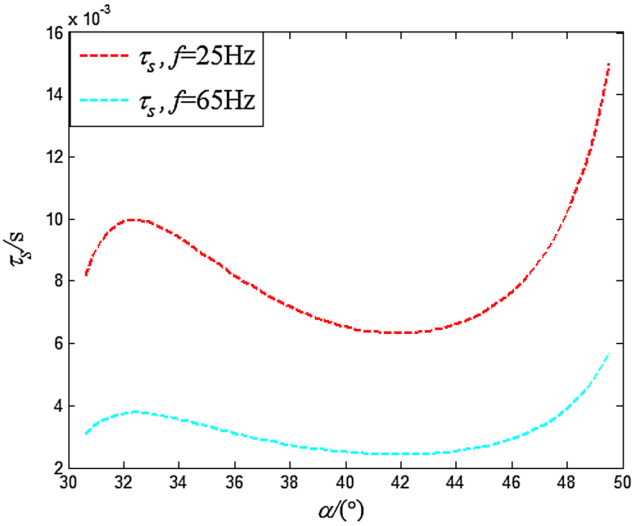
x 10⁻³
τ_s, f=25Hz
τ_s, f=65Hz
τ_s/s
α/(°)

(c)

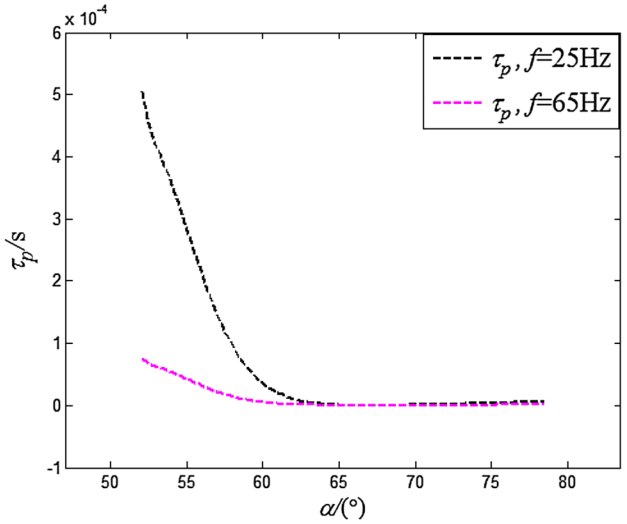
x 10⁻⁴
τ_p, f=25Hz
τ_p, f=65Hz
τ_p/s
α/(°)

(d)

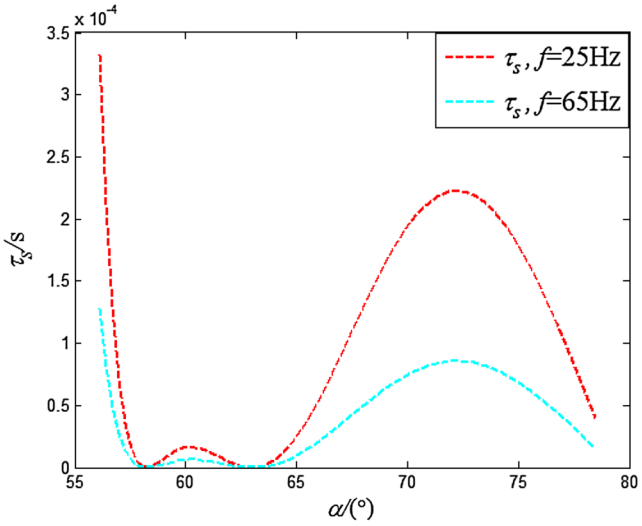
x 10⁻⁴
τ_s, f=25Hz
τ_s, f=65Hz
τ_s/s
α/(°)

(e)

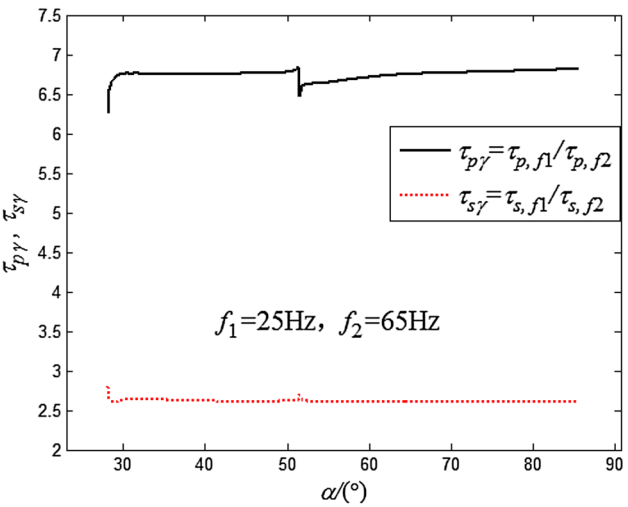
$\tau_{p\gamma}=\tau_{p,f1}/\tau_{p,f2}$
$\tau_{s\gamma}=\tau_{s,f1}/\tau_{s,f2}$
$\tau_{p\gamma}$, $\tau_{s\gamma}$
f_1=25Hz, f_2=65Hz
α/(°)

(f)

◂**Fig. 6** GH induced time differences of P- (τ_p) and SV-wave (τ_s) at a mudstone–sandstone interface when the frequencies are 25 Hz and 65 Hz, respectively. Black dashed line: GH induced NMO correction of P-wave (τ_p) when the frequency is 25 Hz; pink dashed line: GH induced NMO correction of P-wave (τ_p) when the frequency is 65 Hz; red dashed line: GH induced NMO correction of SV-wave (τ_s) when the frequency is 25 Hz; light blue dashed line: GH induced NMO correction of SV-wave (τ_s) when the frequency is 65 Hz

(P- and SV-wave). Numerical examples are carried out to show the characteristics of GH lateral shift induced delay time and time differences. When the incidence angle is larger than the first critical angle, the GH shift induced delay has the same order of magnitude with the wave period. For reflected P- and SV-wave, the ratio produced by different frequencies is a constant. The delay time can become negative for reflected P-wave at some special incidence angles. The results indicate that the delay time influences the results of NMO correction severely for wide-angle reflections. In addition, the efficiency of GH induced NMO correction is further tested for synthetic seismic data. To improve the precision of seismic data processing, the correction of GH induced delay time is needed for wide-angle reflections in the process of NMO correction.

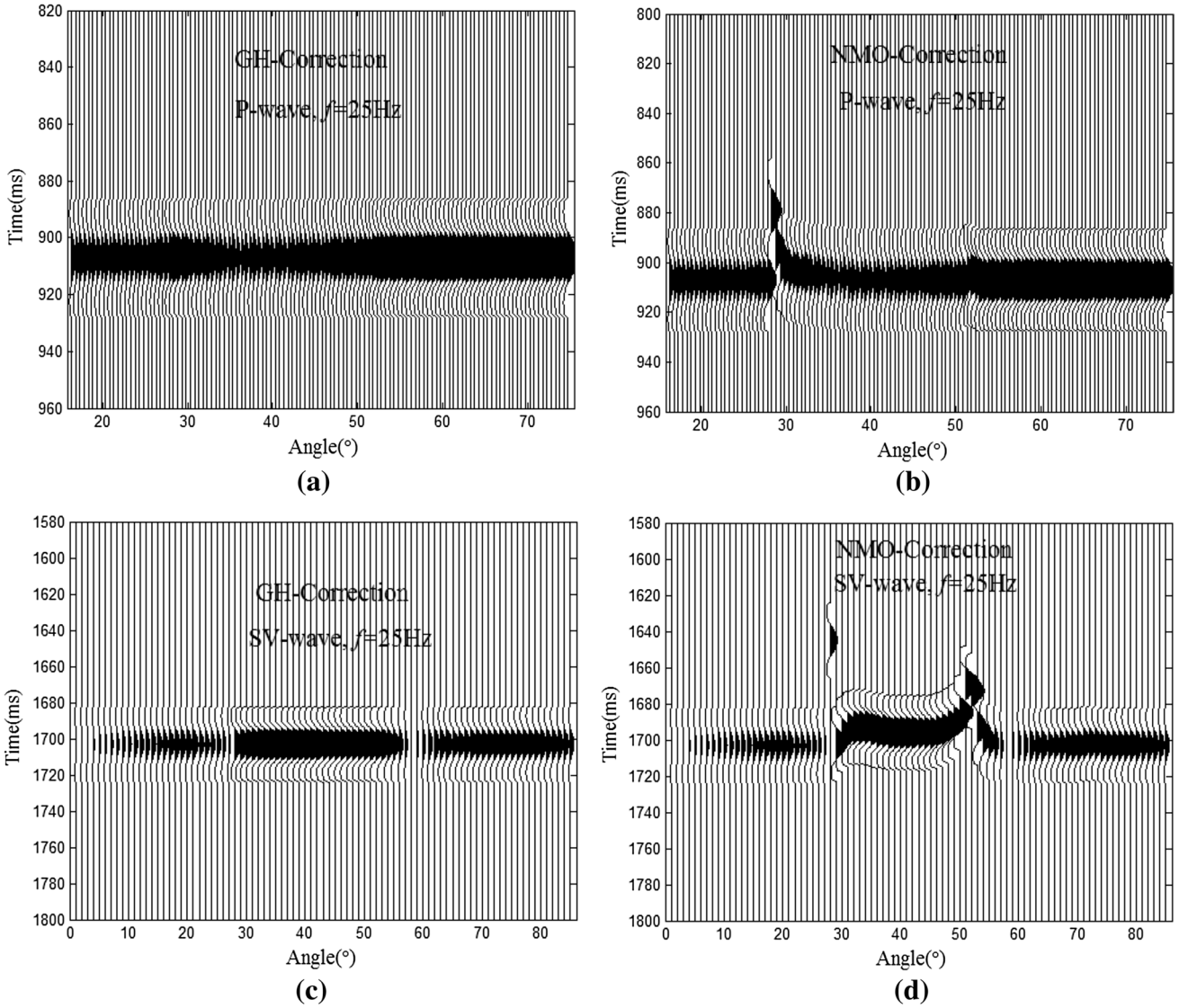

Fig. 7 Comparison of GH induced NMO correction (**a**, **c**) and NMO correction (**b** and **d**) for P- (**a**, **b**) and SV-wave (**c**, **d**) when the frequency is $f = 25$ Hz

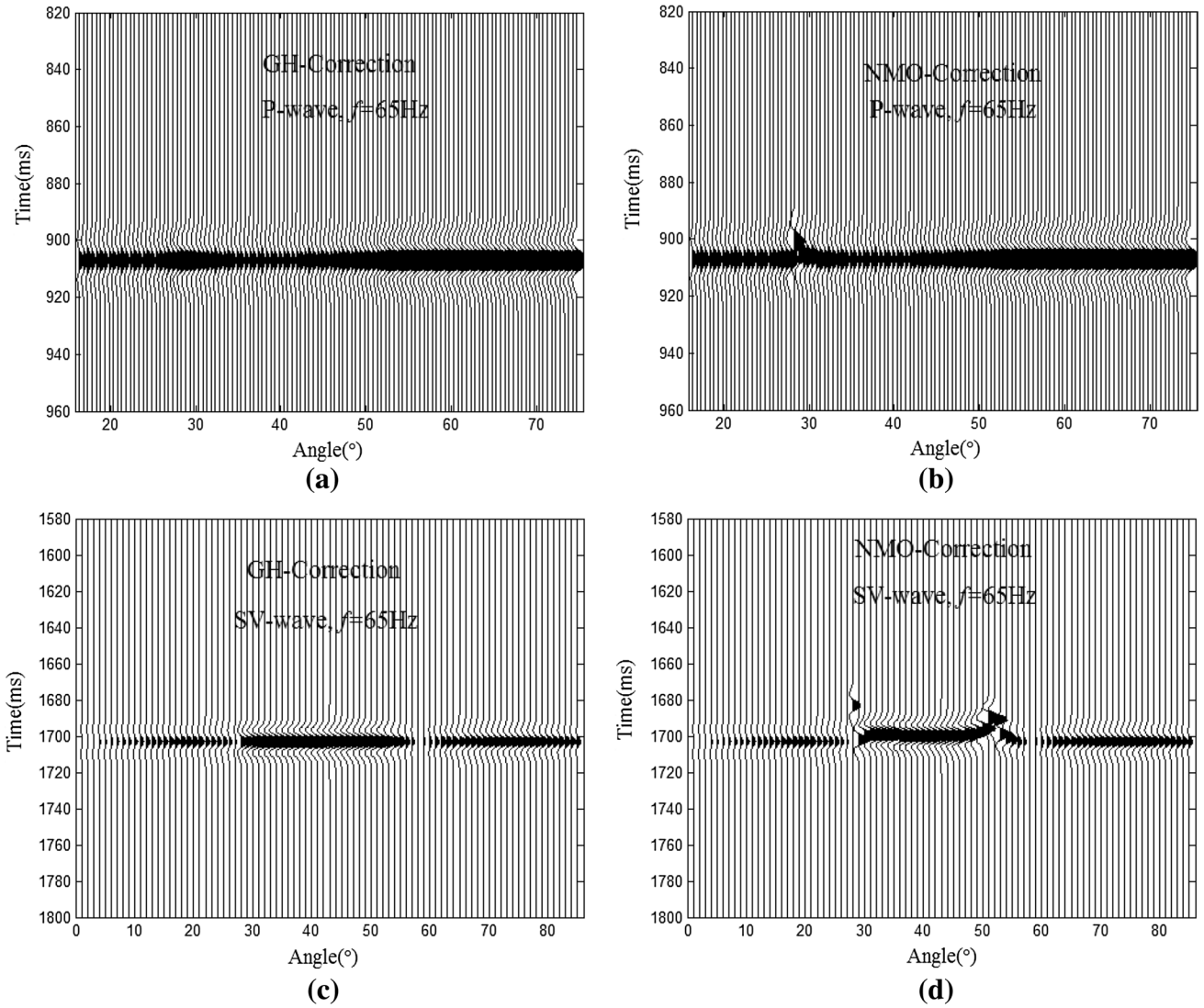

Fig. 8 Comparison of GH induced NMO correction (**a**, **c**) and NMO correction (**b**, **d**) for P- (**a**, **b**) and SV-wave (**c**, **d**) when the frequency is $f = 65$ Hz

Acknowledgements This research was funded by China Postdoctoral Sciences Foundation (2019M660733); the Research and Development Funds of Sinopec (P18070-5); Sinopec Northwest Oilfield Company (34400008-18-ZC0607-0031, 34400008-18-ZC0607-0030); the National Natural Science Foundation of China (41574126) and Beijing Institute of Graphic Communication Project (Ec201803, Ea201806). The suggestions and comments from anonymous reviewers and associate editor Sanyi Yuan are greatly helpful for improving the quality of our paper.

Compliance with ethical standards

Conflict of interest On behalf of all authors, the corresponding author states that there is no conflict of interest.

References

Aki K, Richards PG (2002) Quantitative seismology. University Science Books, Sausalito

Alishahi F, Mehrany K (2010) Analytical expression of giant Goos–Hänchen shift in terms of proper and improper modes in waveguide structures with arbitrary refractive index profile. Opt Lett 35(11):1759–1761

Araújo M, De Leo S, Carvalho S (2013) The frequency crossover for the Goos–Hänchen shift. J Mod Opt 60(20):1772–1780

Araújo M, Carvalho SA, De Leo S (2014) The asymmetric Goos–Hänchen effect. J Opt 16:015702–15707

Araújo M, De Leo S, Maia GG (2016) Closed-form expression for the Goos–Hänchen lateral displacement. Phys Rev A 93(2):23801–23810

Berman PR (2002) Goos–Hänchen shift in negatively refractive media. Phys Rev E Stat Nonlinear Soft Matter Phys 66(6 Pt 2):067603

Bonnet C, Chauvat D, Emile O, Bretenaker F, Le Floch A, Dutriaux L (2001) Measurement of positive and negative Goos–Hänchen effects for metallic gratings near wood anomalies. Opt Lett 26:666–668

Brittan J, Warner M (1997) Wide-angle seismic velocities in heterogeneous crust. Geophys J Int 129(2):269–280

Brown RJS (1969) Normal-moveout and velocity relations for flat and dipping beds and for long offsets. Geophysics 34(2):180–195

Chen L, Cao Z, Ou F, Li H, Shen Q, Qiao H (2007) Observation of large positive and negative lateral shifts of a reflected beam from symmetrical metal-cladding waveguides. Opt Lett 32(11):1432–1434

Chen X, Lu X, Ban Y, Li CF (2013) Electronic analogy of the Goos–Hänchen effect: a review. J Opt 15(3):3001–3012

Gardner LW (1947) Vertical velocities from reflection shooting. Geophysics 12(2):221–228

Goos F, Hänchen H (1947) Ein neurer fundamentaler versuch zur total reflexion. Annalen der Physik 436:333–346

Goos F, Hänchen H (1949) Neumessung des Strahlwersetzungseffektes bei totalreflexion. Annalen der Physik 440:251–252

Ignatovich VK (2004) Neutron from condensed matter, the Goos–Hänchen effect and coherence. Phys Lett A 322(1):36–46

Lakhtakia A (2003) On plane wave remittances and Goos–Hänchen shifts of planar slabs with negative real permittivity and permeability. Electromagnetics 23(1):71–75

Leo SD, Kraus RK (2018) Incidence angles maximizing the Goos–Hänchen shift in seismic data analysis. Pure Appl Geophys 175(6):2023–2044

Lerche I (1990) Reflection of wide-angle acoustic waves from a high velocity interface. Pure Appl Geophys 134(1):109–115

Lin Y, Zhan J, Tseng S (1997) A new method of analyzing the light transmission in leaky and absorbing planar waveguides. IEEE Photon Technol Lett 9(9):1241–1243

Liu F, Gao J, Li R, Wang A, Chen H, Yang C (2008) The influence on normal moveout of total reflected SV-wave by Goos–Hänchen effect at a free surface of stratum. Chin J Geophys 51(3):862–868 **(in Chinese)**

Liu F, Wang A, Li R, Chen H, Yang C (2009) The influence on normal moveout of total reflected SH-wave by Goos-Hänchen effect at an interface of strata. Chin J Geophys 52(8):2129–2134 **(in Chinese)**

Liu F, Meng X, Xiao J, Wang A, Yang C (2012) The Goos–Hänchen shift of wide-angle seismic reflection wave. Sci China Earth Sci 55(5):852–857

Lotsch HKV (1968) Reflection and refraction of a beam of light at a plane interface. J Opt Soc Am 58(4):1358–1361

Ostrander WJ (1984) Plane-wave reflection coefficients for gas sands at nonnormal angles of incidence. Geophysics 49(10):1637–1648

Resch KJ, Lundeen JS, Steinberg AM (2001) Total reflection cannot occur with a negative delay time. IEEE J Quantum Electron 37(6):794–799

Rupert GB, Chun JH (1975) The block move sum normal moveout correction. Geophysics 40(1):17–24

Sedek M, Gross L, Tyson S (2015) Automatic NMO correction and full common depth point NMO velocity field estimation in anisotropic media. Pure Appl Geophys 174(1):305–325

Sun C, Ni C, Li S, Zhang Y (2007) Feature of wide-angle reflection data and correction method. Oil Geophys Prospect 42(1):24–29

Tsvankin I (1995) Normal moveout from dipping reflectors in anisotropic media. Geophysics 60(1):268–284

Wang Z (2015) The influence of the Goos–Haenchen effect on seismic data processing and AVO in attenuating media. J Appl Geophys 122:122–133

Yilmaz O (1987) Seismic data processing. Society of Exploration Geophysics, Tulsa, OK

Yuan S, Liu Y, Zhang Z, Luo C, Wang S (2019) Prestack stochastic frequency-dependent velocity inversion with rock-physics constraints and statistical associated hydrocarbon attributes. IEEE Geosci Remote Sens Lett 16(1):140–144

Yuan S, Wei W, Wang D, Shi P, Wang S (2020) Goal-oriented inversion-based NMO correction using a convex $l_{2,1}$ -norm. IEEE Geosci Remote Sens Lett 17(1):162–166

Zhang J, Wapenaar K (2002) Wavefield extrapolation and prestack depth migration in anelastic inhomogeneous media. Geophys Prospect 50(6):629–643

Zhang W, Guo P, Hu T (2004) Study and practice of wide-angle seismic data processing. Appl Geophys 1(1):31–37

Zoeppritz K (1919) Erdbebenwellen VIII B, uber die reflexion und durchgang seismischer wellen durch unstetigkeitsflachen. Gottinger Nachr 1:66–84

Acta Geophysica (2020) 68:425–434
https://doi.org/10.1007/s11600-020-00413-4

RESEARCH ARTICLE - APPLIED GEOPHYSICS

Seismic signal de-noising using time–frequency peak filtering based on empirical wavelet transform

Naihao Liu[1,2] · Yang Yang[1,2] · Zhen Li[1,2] · Jinghuai Gao[1,2] · Xiudi Jiang[3] · Shulin Pan[4]

Received: 7 November 2019 / Accepted: 22 February 2020 / Published online: 14 March 2020

Abstract

Seismic noise suppression plays an important role in seismic data processing and interpretation. The time–frequency peak filtering (TFPF) is a classical method for seismic noise attenuation defined in the time–frequency domain. Nevertheless, we obtain serious attenuation for the seismic signal amplitude when choosing a wide window of TFPF. It is an unsolved issue for TFPF to select a suitable window width for attenuating seismic noise effectively and preserving valid signal amplitude effectively. To overcome the disadvantage of TFPF, we introduce the empirical wavelet transform (EWT) to improve the filtered results produced by TFPF. We name the proposed seismic de-noising workflow as the TFPF based on EWT (TFPF-EWT). We first introduce EWT to decompose a non-stationary seismic trace into a couple of intrinsic mode functions (IMFs) with different dominant frequencies. Then, we apply TFPF to the chosen IMFs for noise attenuation, which are selected by using a defined reference formula. At last, we add the filtered IMFs and the unprocessed ones to obtain the filtered seismic signal. Synthetic data and 3D field data examples prove the validity and effectiveness of the TFPF-EWT for both attenuating random noise and preserving valid seismic amplitude.

Keywords Seismic signal de-noising · Time–frequency peak filtering (TFPF) · Empirical wavelet transform (EWT) · Preserved valid amplitude

Introduction

Seismic noise attenuation is a fundamental topic in geophysical data processing and interpretation, which facilitates accurate geologic interpretation (Zhou et al. 2016). In recent decades, there are a wealth of effective techniques proposed for seismic noise attenuation (Wang and Gao 2014; Liu et al. 2016c; Zhang et al. 2016; Gemechu et al. 2017), such as the *f*–*x* prediction-based methods (Canales 1984; Harris and White 1997; Naghizadeh 2012), curvelet transform (CLT) and continuous wavelet transform (CWT)-based methods (Donoho and Johnstone 1994; Gao et al. 2006; Shan et al. 2009), EMD and variational mode decomposition (VMD)-based methods (Bekara and van der Baan 2009; Han and van der Baan 2013; Chen and Ma 2014; Chen et al. 2015; Liu et al. 2017; Wu et al. 2019), and Bayesian inversion-based methods (Yuan et al. 2012; Yuan et al. 2018; Yuan and Wang 2013). These de-noising approaches suppress noise contained in seismic data effectively. However, an effective seismic de-noising approach should include noise attenuation and valid signal preservation simultaneously, which is a challenging task for filtering seismic data.

TFPF was proposed by Roessgen and Boashash (1994), which considers the noisy signal as the instantaneous frequency (IF) of a frequency-modulated signal. Afterward, TFPF employs the Wigner–Ville distribution (WVD) (Wigner 1932; Ville 1948) to calculate the time–frequency (TF) spectrum, whose peak frequency is regard as the filtered signal (Arnold et al. 1994). TFPF could achieve an unbiased estimation for the analyzed linear signal with

✉ Zhen Li
lijiasanshao@stu.xjtu.edu.cn

1 School of Information and Communications Engineering, Xi'an Jiaotong University, Xi'an 710049, Shaanxi, China

2 National Engineering Laboratory for Offshore Oil Exploration, Xi'an 710049, Shaanxi, China

3 Geophysics Key Lab, Technology R&D Center, Research Institute of China National Offshore Oil Corporation (CNOOC), and National Engineering Laboratory for Offshore Oil Exploration, Beijing 10028, China

4 School of Earth Science and Technology, Southwest Petroleum University, Chengdu 610500, Sichuan, China

white Gaussian noise (Zahir and Hussain 2000; Yu et al. 2016). However, the TFPF-based approaches work ineffectively for nonlinear signals (Li and Gao 2016). Moreover, the seismic signal is a typical nonlinear and non-stationary signal in real applications (Liu et al. 2016a, 2018b). When de-noising a non-stationary seismic signal using the traditional TFPF, the window length of WVD is a key parameter. For example, we would attenuate noise effectively but achieve a filtered result with an attenuated amplitude when selecting a long window width. On the contrary, we reserve the valid signal amplitude but achieve a result containing too much noise when choosing a short window width. Hence, it is a key step for selecting an appropriate window length of TFPF. To overcome this drawback, Boashash and O'shea (1994) developed a TF digital denoising method employing an invertible wavelet transform (IWT). Lin et al. (2013) built a nonlinearity tool that combines TFPF and a weighted frequency reassignment. Lin et al. (2014) improved TFPF by building an adaptive filtering approach. Liu et al. (2014) combined TFPF and EMD (TFPF-EMD) for attenuating noise in seismic data. Herein, we focus on the TFPF-EMD in this study. EMD is a data-driven algorithm to decompose the analyzed signal into several intrinsic mode functions (IMFs) and a residue (Huang et al. 1998). Note that the IMFs are supposed to be linear. Afterward, TFPF is applied to the selected IMFs. Therefore, the TFPF-EMD-based method works well for attenuating random noise and reserving valid amplitude. Nevertheless, EMD is sensitive to noise (Huang et al. 1998). Additionally, it is with serious mode-mixing issue (Gilles 2013; Li et al. 2018). There are plenty of algorithms proposed for solving the mixing-mode issue, such as the ensemble empirical mode decomposition (EEMD) (Wu and Huang 2009) and EWT (Gilles 2013). EEMD, an extension of EMD, improves the mixing-mode issue but still has no mathematical model (Gilles 2013; Colominas et al. 2014). EWT could decompose a non-stationary signal into a couple of band-limited IMFs adaptively. Moreover, EWT is with theoretical support (Liu et al. 2016b). Hence, we aim to develop an improved workflow for attenuating seismic noise by incorporating TFPF and EWT in this study.

EWT first decomposes a non-stationary seismic signal into a set of band-limited IMFs. Then, we calculate the cross-correlation coefficients to choose which IMFs needed to be filtered. Additionally, we introduce an empirical formula to determine the window width of TFPF. After applying TFPF to the chosen IMFs, we reconstruct the filtered seismic signal by calculating the summation of the denoising IMFs and unprocessed ones. To verify the validity of TFPF-EWT, we apply it to synthetic data and 3D real seismic data.

Method

Time–frequency peak filtering

In this section, we first review TFPF briefly. To explain TFPF in detail, we define a noisy signal $s_n(t)$ as

$$s_n(t) = s(t) + n(t). \tag{1}$$

Here, $s(t)$ and $n(t)$ are the noise-free signal and random noise. Then, TFPF can suppress random noise as a three-step procedure:

Step 1: We first obtain the analytic signal $z_s(t)$ with a unit amplitude by considering $s_n(t)$ as the IF of $z_s(t)$, defined in Eq. (2):

$$z_s(t) = e^{i2\pi\mu\int_0^t s_n(\tau)\mathrm{d}\tau}. \tag{2}$$

Note that μ is a scaling parameter regarded as the FM modulation index (Boashash and Mesbah 2004).

Step 2: As we all know, PWVD provides an effective energy concentration around the IF of the signal (Boashash 2015). Hence, we compute PWVD $W_z(t,f)$ of $z_s(t)$ using a window function $w(\tau)$ as

$$W_z(t,f) = \int_{-\infty}^{\infty} w(\tau) z_s\left(t+\frac{\tau}{2}\right) z_s^*\left(t-\frac{\tau}{2}\right) e^{-i2\pi f\tau}\mathrm{d}\tau, \tag{3}$$

where $(\cdot)^*$ denotes the complex conjugate.

Step 3: Using PWVD, we then estimate the IF $\hat{f}_z(t)$ of the analytic signal $z_s(t)$ as (Boashash and O'shea 1994)

$$\hat{s}_z(t) = \hat{f}_z(t) = \frac{\arg\ \max_f[W_z(t,f)]}{\mu}. \tag{4}$$

Thus, we estimate the filtered signal $\hat{s}(t)$, which equals $\hat{f}_z(t)$.

Note that TFPF achieves an unbiased signal estimation and effective seismic noise reduction (Lin et al. 2016). However, it is difficult to select an appropriate window width of the window function $w(\tau)$ of TFPF (Liu et al. 2014; Li and Gao 2016). For example, a short window width results in reserving the valid amplitude effectively but attenuating random noise inadequately, whereas we would achieve a destructive valid amplitude but a good noise suppression by selecting a long window length. In addition, when the IF of a non-stationary signal changes rapidly (Liu et al. 2018a), it makes the selection of the window length difficult. It may be difficult to obtain an unbiased estimation of a non-stationary signal using Eq. (4). To overcome these drawbacks, Liu et al. (2014) developed a workflow by combining TFPF and EMD. EMD decomposes a non-stationary signal into several IMFs and a residue (Huang et al. 1998). TFPF-EMD works well for attenuating random noise and reserving valid

signal amplitude (Liu et al. 2014). However, EMD suffers from the mode-mixing issue (Gilles 2013; Li et al. 2018). To avoid the mode-mixing issue, we introduce the empirical wavelet transform (EWT) instead of EMD, which is another approach for decomposing a non-stationary signal into several band-limited IMFs (Gilles 2013).

Empirical wavelet transform

EWT decomposes a non-stationary seismic signal into a couple of band-limited IMFs by designing an appropriate wavelet filter bank (Gilles 2013). IMFs with different frequencies are regarded as stationary (Liu et al. 2016b). Using EWT, we calculate the IMF $c_k(t)$ as

$$\begin{aligned} c_0(t) &= W_s^{\epsilon}(0,t) * \phi_1(t), \\ c_k(t) &= W_s^{\epsilon}(n,t) * \psi_k(t), \end{aligned} \tag{5}$$

where $W_s^{\epsilon}(n,t)$ denotes the detailed EWT coefficients, and $\phi_1(t)$ and $\psi_k(t)$ denote the empirical scaling function and empirical wavelets in Fig. 1 (Gilles 2013). Note that there is less mode-mixing of IMFs computed using EWT than those computed using EMD (Gilles 2013). Note that we introduce the automatic detection strategy (Gilles 2013) for defining the number of decomposed IMFs adaptively in this study. After achieving stationary IMFs $c_k(t)$, we can apply TFPF to the stationary IMFs to suppress random noise. We explain the implementation of EWT in Appendix.

TFPF based on EWT

After decomposing a seismic trace into a couple of IMFs with different dominant frequencies using EWT, we then introduce a reference formula to select the IMFs for de-noising processing and then apply TFPF to them to suppress noise. Note that we do not apply TFPF to all decomposed IMFs by EWT. We calculate the correlation coefficients $R_{c_k c_{k+1}}$ of two adjacent IMFs as the reference formula, denoted in Eq. (6):

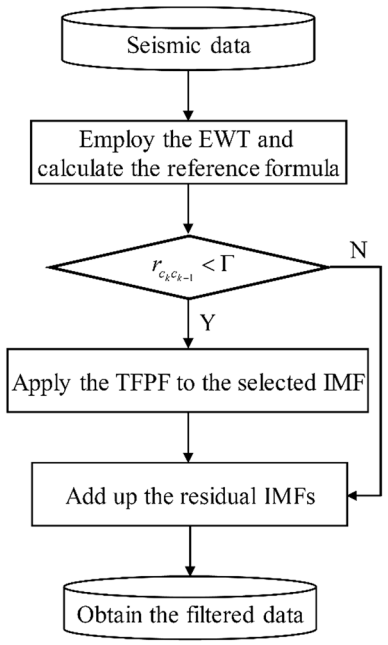

Fig. 2 The workflow of the proposed TFPF based on EWT

$$R_{c_k c_{k+1}} = \frac{\sum_{j=1}^{N_t} \left(c_{k,j} - \bar{c}_k\right)\left(c_{k+1,j} - \bar{c}_{k+1}\right)}{\sqrt{\sum_{j=1}^{N_t} \left(c_{k,j} - \bar{c}_k\right)^2} \sqrt{\sum_{k=1}^{N_t} \left(c_{k+1,j} - \bar{c}_{k+1}\right)^2}}, \tag{6}$$

where N_t is the time sample number, and $R_{c_k c_{k+1}}$ and c_k are the reference formula and the k^{th} IMF, respectively. Obviously, the correlation coefficient of two valid signals is larger than the correlation coefficient of the random noise and valid signal. Therefore, we set a certain threshold value Γ to choose IMFs calculated by EWT to attenuate seismic noise (Liu et al. 2014).

In our workflow, we introduce an empirical formula to determine the window length L_w of TFPF (Lin et al. 2007), denoted in Eq. (7):

$$L_w \le \frac{0.384 f_s}{f_d}. \tag{7}$$

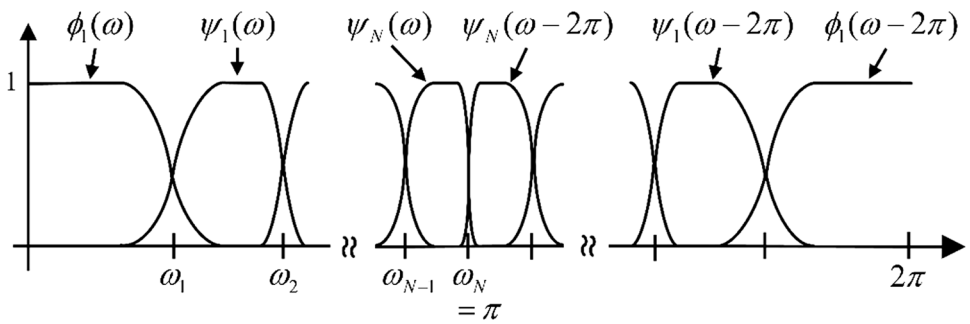

Fig. 1 The empirical scaling function $\phi_1(t)$ and empirical wavelets $\psi_k(t)$

f_d and f_s are the dominant frequency and sampling frequency of the seismic wavelet, respectively. At last, we reconstruct the filtered signal by calculating the summation of the de-noising IMFs and unprocessed ones. The workflow of the proposed de-noising workflow is presented in Fig. 2.

Synthetic data examples

First, we apply the proposed de-noising workflow to synthesized signals to compare its de-noising performance with the conventional TFPF. Note that Lin et al. (2013) have compared the de-noising effectiveness between conventional TFPF- and *f*–*x* filtering-based methods (Harris and White 1997). Hence, we focus on comparing the de-noising effectiveness between a conventional TFPF and the proposed workflow in this section. For a fair comparison, we also used the empirical formula in Eq. (7) to determine the window length of TFPF. Figure 3a presents the noise-free synthetic trace (blue line) and noisy synthetic trace (black line) added with Gaussian white noise. The dominant frequency of the Ricker wavelet equals 30 Hz. The SNR equals 0 dB. We apply TFPF and proposed workflow to the noisy synthetic trace (black line). Figure 3a shows the filtered traces calculated using TFPF (green line) and proposed workflow (red line), which both suppress the noise successfully. The SNR of the filtered traces calculated using TFPF and proposed workflow is 6.31 dB and 9.63 dB, respectively. Note that the proposed workflow suppresses Gaussian white noise more effectively than the conventional TFPF. Moreover, we zoom in the plot in Fig. 3a to show the detail of filtered traces, as presented in Fig. 3b. The de-noised trace calculated using the proposed workflow (red line) preserves the valid amplitude of the Ricker wavelet more effectively than that calculated using TFPF (green line), indicated by the red arrow. Additionally, we add Gaussian white noise to the

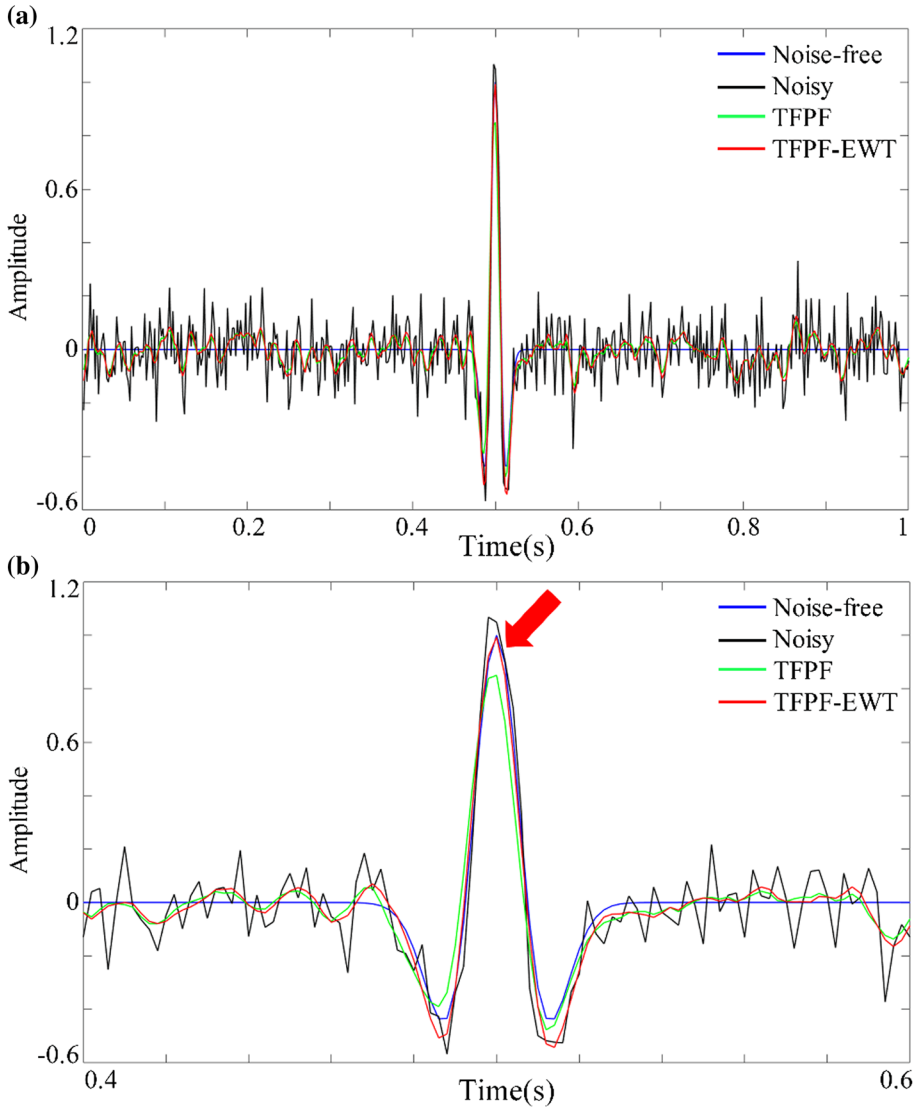

Fig. 3 The synthetic trace de-noising example. **a** The synthetic traces and de-noising traces, **b** the enlarged traces with time duration from 0.4 to 0.6 s. The dominant frequency of the Ricker wavelet is 30 Hz. The SNR equals 0 dB. The blue and black lines denote the noise-free and noisy traces, while the green and red lines represent the de-noising traces calculated using TFPF and proposed workflow

Ricker wavelet with different SNRs. Then, we estimate the SNR of the filtered traces computed using TFPF (blue circle curve) and proposed workflow (red star curve), as shown in Fig. 4. Note that the proposed workflow provides larger SNR values than TFPF for each Ricker wavelet with different SNR values. The SNR curves in Fig. 4 demonstrate the proposed workflow suppresses noise more effectively than the conventional TFPF method.

Then, we generate a synthetic model to test the validity of TFPF-EWT. Figure 5a shows the noise-free synthetic model, while Fig. 5b shows the noisy model. The SNR of Fig. 5b equals 0 dB. Note that we adopt different Ricker wavelets with different dominant frequencies to generate the synthetic model in Fig. 5. Actually, we select Ricker wavelets with dominant frequencies of 30 Hz, 25 Hz, and 15 Hz to generate the first and second seismic events, middle three crossed events, and the last horizontal event. Apparently, the noise reduces the time resolution of synthetic traces. We then apply TFPF and proposed workflow to noisy synthetic data. Figure 6a and b shows the de-noising data calculated using TFPF and TFPF-EWT. Both approaches suppress seismic noise successfully, especially the simple and horizontal events. Afterward, Fig. 6c and d presents the difference profiles calculated using TFPF and proposed workflow. Obviously, the difference profile calculated using TFPF contains some valid reflection events in Fig. 6c, especially the bent seismic event indicated by red arrows. In contrast, the difference profile calculated using TFPF-EWT provides no valid reflection events in Fig. 6d. The plots in Fig. 6 lead us to the conclusion that the proposed workflow not only attenuates noise efficaciously but also reserves the valid amplitude effectually.

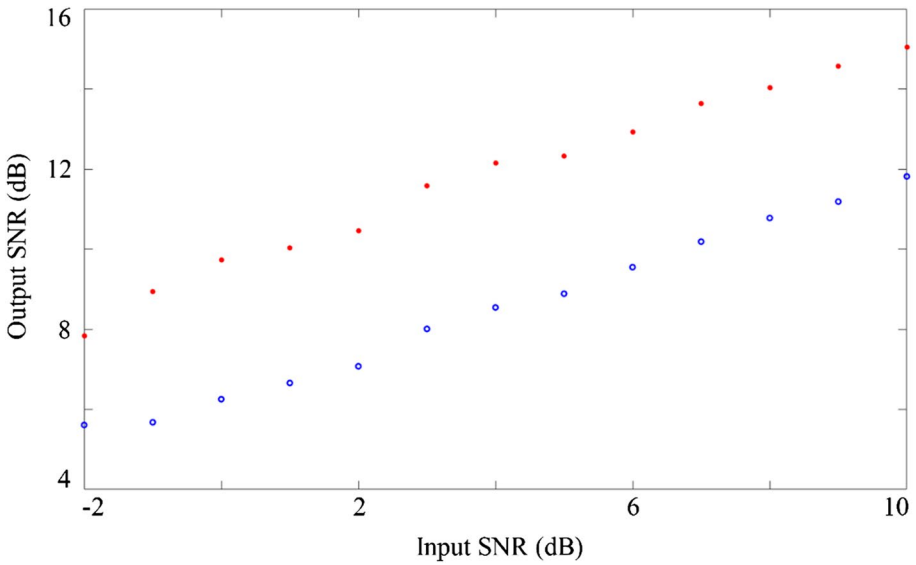

Fig. 4 The output SNR of different filtered traces with different SNRs, computed using TFPF (blue circle curve) and the proposed algorithm (red star curve). The abscissa denotes the input SNR of original synthetic traces added with Gaussian white noise, while the ordinate denotes the output SNR of the filtered traces

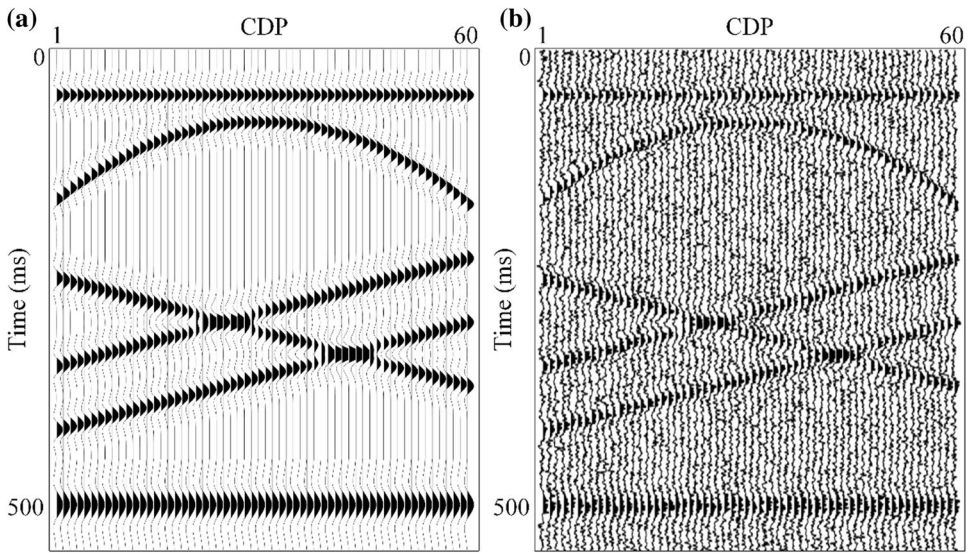

Fig. 5 The synthetic model. **a** Noise-free data and **b** noisy data added with Gaussian white noise. The SNR of **b** is 0 dB. There are six reflection events in the model

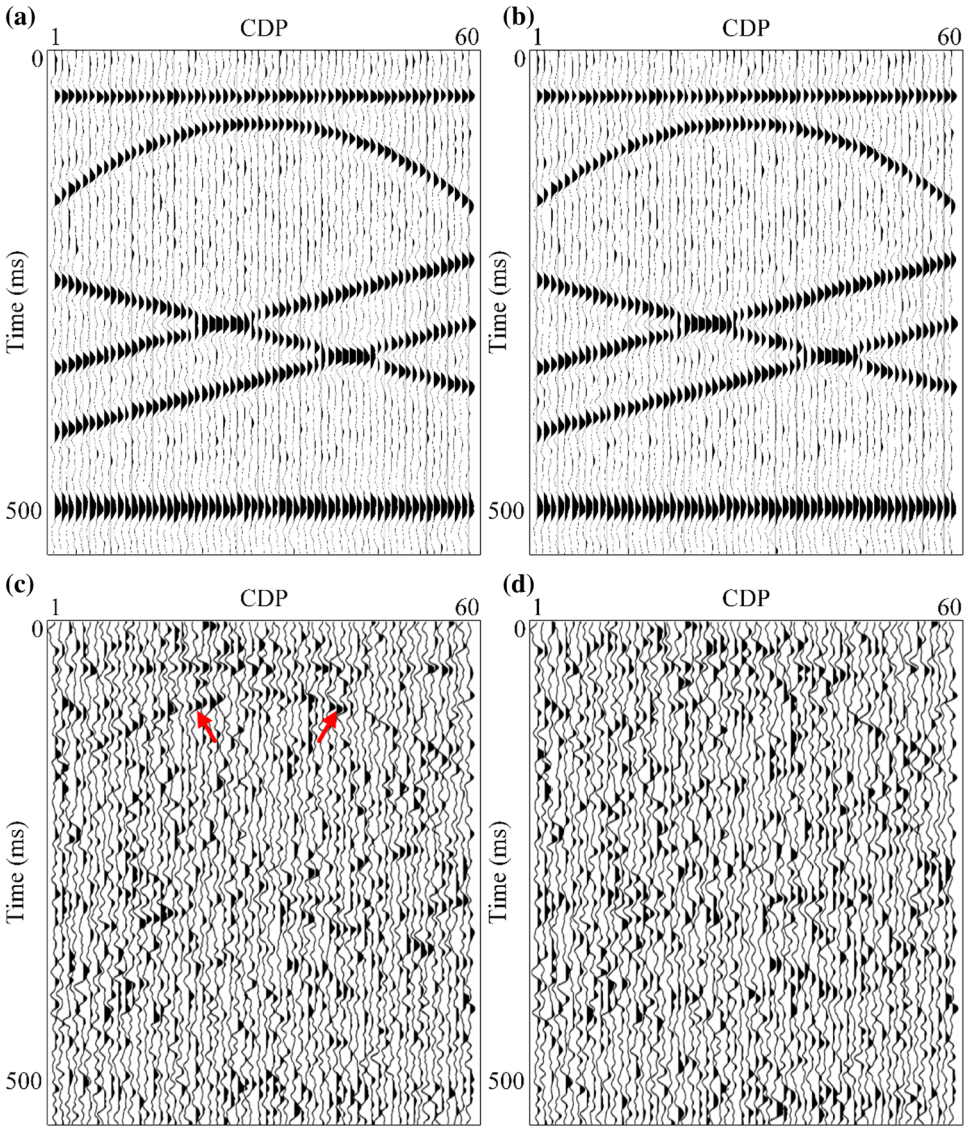

Fig. 6 The de-noising profiles and difference profiles calculated using the noisy data in Fig. 5b. The de-noising profiles calculated using **a** TFPF and **b** proposed workflow, **c** the difference profile between the noisy data and de-noising data calculated using TFPF, and **d** the difference profile between the noisy data and de-noising data calculated using the proposed workflow. Two red arrows indicate valid seismic events contained in the difference profile

Field data applications

To further verify the validity of TFPF-EWT, we apply it to 3D field data and make comparisons with TFPF. Figure 7 shows a horizontal slice of 3D seismic data located in eastern China, i.e., Bohai basin. The data set consists of 1001 Xline and 401 Inline with a time increment of 2 ms, and a 25 m by 12.5 m bin size. In this study area, the seismic reservoir is controlled by shallow-water deltaic systems (Liu et al. 2016a; Liu et al. 2019). The accurate description of geological structures benefits for characterizing the disciplinarian of accumulation of oil and gas. The red line in Fig. 7 indicates the location of Inline 1740. We then apply TFPF and proposed workflow to 3D seismic data to enhance the SNR of this seismic data. Figure 8a and b shows the filtered horizontal slices calculated using TFPF and proposed workflow, respectively. TFPF and proposed workflow both suppress random noise successfully. However, the proposed workflow characterizes fluvial channels more accurately and more continuously than TFPF denoted by red arrows. In addition, green arrows A and B in Fig. 8 indicate two clear channels located at Inline 1740, whose edges are clearer in Fig. 8b than in Fig. 8a. Figure 8c and d presents the difference horizontal slices calculated using TFPF and proposed workflow, respectively. Obviously, the proposed workflow preserves valid seismic amplitude more effectively than TFPF because there is less valid seismic amplitude in Fig. 8d than in Fig. 8c.

At last, we extract a 2D seismic section to testify the de-noising effect of the proposed workflow. Figure 9 shows the 2D seismic section with the Inline number of 1740. The filtered seismic sections and difference seismic sections are shown in Fig. 10. The proposed workflow in

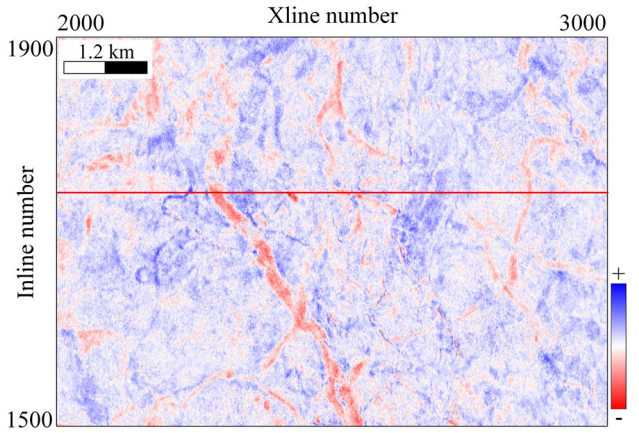

Fig. 7 The horizontal slice of 3D seismic data

Fig. 10b filters random noise more effectively than TFPF in Fig. 10a. This is because the proposed workflow is more appropriate for filtering seismic data than TFPF, which is a typical non-stationary and nonlinear signal. As a result, the proposed workflow characterizes two fluvial channels more precisely than TFPF, indicated by green arrows A and B in Fig. 10a and b. Figure 10c and d shows two difference sections calculated using TFPF and proposed workflow, respectively. Similarly, there is less valid seismic signal in Fig. 10d than in Fig. 10c, especially the fluvial channel indicated by green arrow A. This illustrates that the proposed workflow preserves valid signal amplitude more effectively than TFPF. Therefore, it is easy to conclude that TFPF-EWT provides superior noise attenuation and preserved seismic valid amplitude than TFPF.

Conclusion

In this study, we build a workflow to suppress random noise in seismic data, which is called TFPF based on EWT. EWT decomposes a non-stationary seismic trace

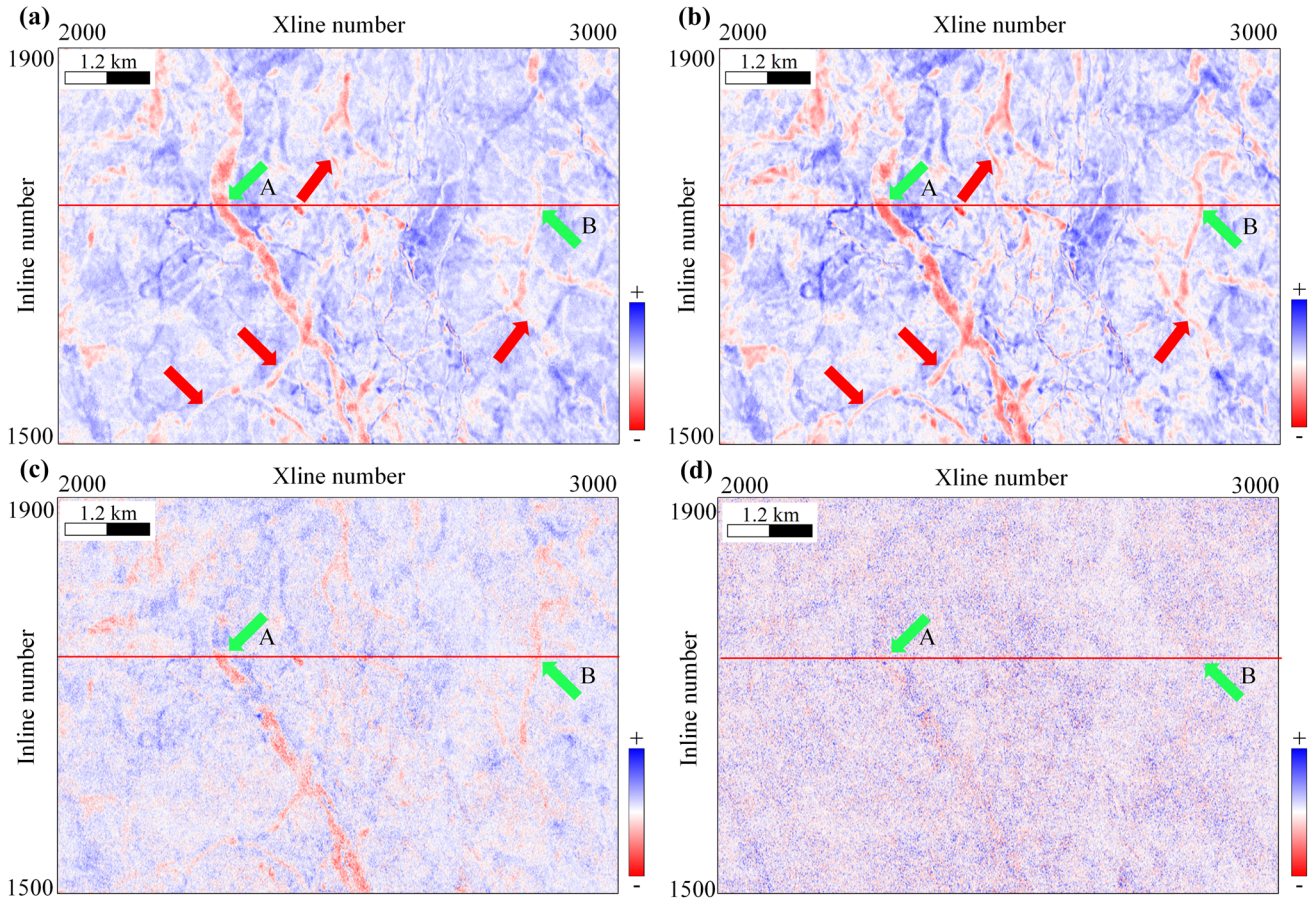

Fig. 8 The de-noising results of the 3D seismic data. The horizontal slices extracted from the filtered data calculated using **a** TFPF and **b** proposed workflow, **c** the difference horizontal slice between the original seismic data and filtered data calculated using TFPF, and **d** the difference horizontal slice between the original seismic data and filtered data calculated using the proposed workflow

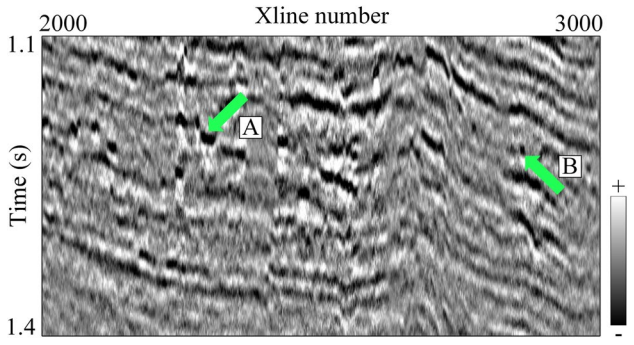

Fig. 9 A 2D seismic section with the Inline number of 1740

to develop TFPF with an adjustable window length for different selected IMFs. For example, we can take dominant frequencies of different IMFs into account when selecting the window length for different IMFs. Synthetic data and filed data applications indicate that the proposed approach provides superior noise attenuation and preserved valid seismic amplitude, which is with minimal impact on the desirable seismic information. The improvements of the proposed workflow have the potential to aid in seismic data processing and interpretation. We can easily conclude that the designed TFPF-EWT would enable the development of effective algorithms to address seismic noise weakening.

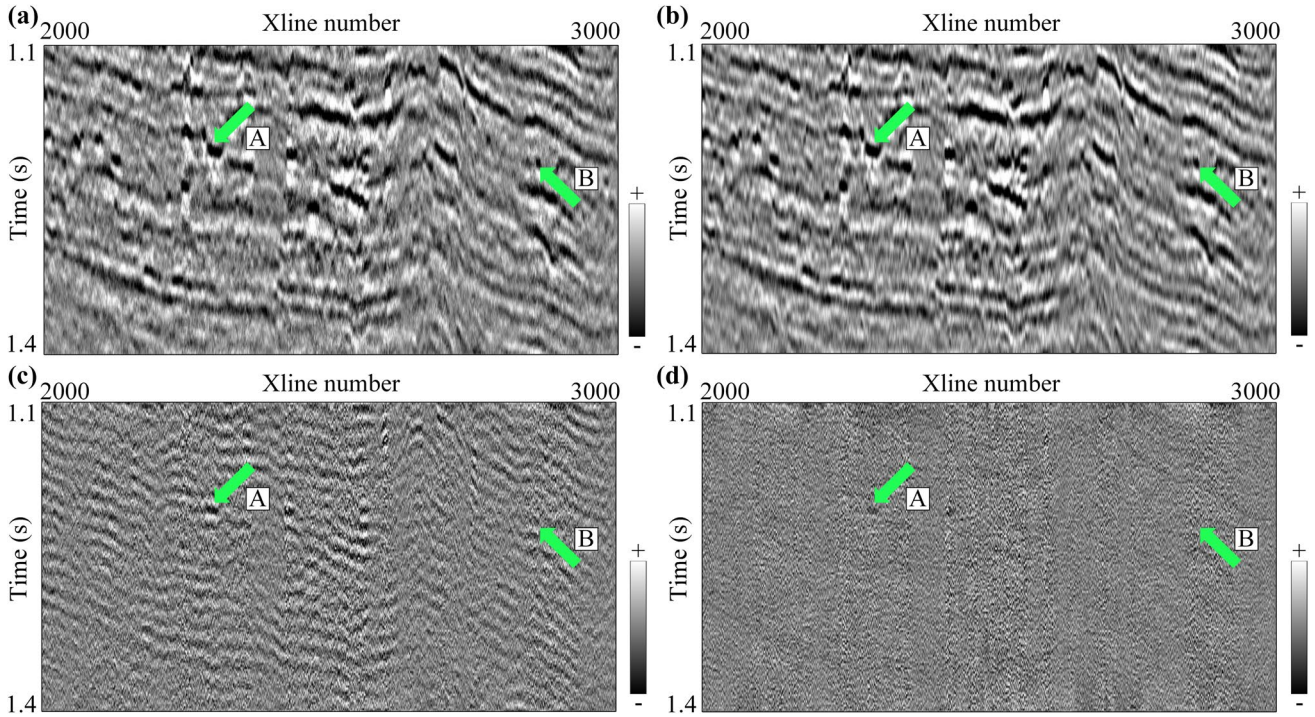

Fig. 10 The de-noising seismic sections and difference profiles of Inline 1740. The de-noising seismic sections calculated using **a** TFPF and **b** proposed workflow, **c** the difference profile between the noisy seismic section and de-noising seismic section calculated using TFPF, and **d** the difference profile between the noisy seismic section and de-noising seismic section calculated using the proposed workflow

into several band-limited IMFs with different dominant frequencies effectively. Each IMF is regarded as stationary. After selecting the IMFs using the proposed reference formula, we apply TFPF to the chosen IMFs to suppress random noise. The summation of the de-noising IMFs is the filtered seismic trace. Note that we choose the same window length defined in Eq. (7) and apply to the selected IMFs in this study. In future work, we would like

Acknowledgments The authors would like to thank National Natural Science Foundation of China (41904102), National Postdoctoral Program for Innovative Talents under grant (BX201900279), China Postdoctoral Science Foundation (2019M653584), National Science and Technology Major Project (2016ZX05024-001-007 and 2017ZX05069), and National Key R&D Program of the Ministry of Science and Technology of China (2018YFC0603501) for their financial support. The authors would also like to thank the Research Institute of CNOOC for providing a license for seismic data used in this study.

Appendix: Empirical wavelet transform

To represent EWT, we first define a non-stationary signal $s_n(t)$ as

$$s_n(t) = \sum_{k=1}^{K} c_k(t) + r(t), \tag{8}$$

where $c_k(t)$ and $r(t)$ are the IMFs and residual, respectively. Based on Eq. (8), we decompose the non-stationary signal $s_n(t)$ into a set of IMFs $c_k(t), k = 1, 2, \ldots, K$ and a residual $r(t)$.

EWT builds adaptive wavelets capable for extracting IMFs using the analyzed signal (Gilles 2013). Each of IMFs has a compact support spectrum. EWT aims to separate different portions of the Fourier spectrum, which corresponds to different IMFs. After segmenting the Fourier support $[0, \pi]$ into N contiguous segments, we denote ω_k to be the limits between each segment, where $\omega_0 = 0$ and $\omega_K = \pi$. Furthermore, each segment is denoted as $\Lambda_k = [\omega_{k-1}, \omega_k]$. Then, EWT is performed in the following steps easily:

(1) We first apply the Fourier transform (FT) to $s(t)$ and obtain the Fourier spectrum. We then assume that there are maxima $\{M_k\}, k = 1, 2, \ldots, K-1$ of the Fourier spectrum.

(2) After obtaining the segments of the Fourier spectrum and the set of the boundaries, the boundaries ω_k of each segmentation are defined as

$$\omega_k = \frac{M_k + M_{k+1}}{2}, \quad k = 1, 2, \ldots, K-1, \tag{9}$$

where $\omega_0 = 0$ and $\omega_K = \pi$.

(3) We define the empirical scaling functions ϕ_k and empirical wavelets ψ_k in Eqs. (10) and (11):

$$\phi_k = \begin{cases} 1, & \omega \le (1-\gamma)\omega_k, \\ \cos\left[\frac{\pi}{2}\alpha(\gamma, \omega_k)\right], & (1-\gamma)\omega_k < |\omega| \le (1+\gamma)\omega_k, \\ 0, & \text{otherwise}, \end{cases} \tag{10}$$

$$\psi_k = \begin{cases} 1, & (1+\gamma)\omega_k \le |\omega| \le (1-\gamma)\omega_{k+1}, \\ \cos\left[\frac{\pi}{2}\alpha(\gamma, \omega_{k+1})\right], & (1-\gamma)\omega_{k+1} < |\omega| \le (1+\gamma)\omega_{k+1}, \\ \sin\left[\frac{\pi}{2}\alpha(\gamma, \omega_k)\right], & (1-\gamma)\omega_k < |\omega| \le (1+\gamma)\omega_k, \\ 0, & \text{otherwise}, \end{cases} \tag{11}$$

where $\alpha(\gamma, \omega_k) = \beta\left(\frac{1}{2\gamma\omega_k}\left[|\omega| - (1-\gamma)\omega_k\right]\right)$. $0 < \gamma < 1$ is a parameter for ensuring no overlap between consecutive transition phases and $\beta(x)$ is a function defined in Eq. (12):

$$\beta(x) = \begin{cases} 0, & x \le 0, \\ 1, & x \ge 1, \end{cases} \quad \text{and} \quad \beta(x) + \beta(1-x) = 1, \quad \forall x \in [0, 1]. \tag{12}$$

(4) We calculate EWT $W_s^{\epsilon}(i, t)$ by the inner product of $s(t)$ with the empirical wavelets ψ_k as

$$W_s^{\epsilon}(n, t) = < s, \psi_k > = \int s(\tau)\overline{\psi}_k(\tau - t)d\tau. \tag{13}$$

In addition, we calculate the approximation coefficients $W_s^{\epsilon}(0, t)$ as

$$W_s^{\epsilon}(0, t) = < s, \phi_1 > = \int s(\tau)\overline{\phi}_1(\tau - t)d\tau, \tag{14}$$

where ϕ_1 and ψ_k are defined in Eqs. (10) and (11).

(5) At last, we calculate IMF $c_k(t)$

$$\begin{aligned} c_0(t) &= W_s^{\epsilon}(0, t) * \phi_1(t), \\ c_k(t) &= W_s^{\epsilon}(n, t) * \psi_k(t). \end{aligned} \tag{15}$$

Moreover, the original signal is reconstructed by

$$s(t) = W_s^{\epsilon}(0, t) * \phi_1(t) + \sum_{k=1}^{K} W_s^{\epsilon}(n, t) * \psi_k(t). \tag{16}$$

Using Eq. (16), EWT decomposes a non-stationary seismic signal into a couple of band-limited IMFs with different dominant frequencies. Then, we could use TFPF-based algorithms to the selected IMFs to suppress seismic noise in this study.

References

Arnold M, Roessgen M, Boashash B (1994) Filtering real signals through frequency modulation and peak detection in the time-frequency plane. IEEE ICASSP 94:345–348

Bekara M, van der Baan M (2009) Random and coherent noise attenuation by empirical mode decomposition. Geophysics 74:V89–V98

Boashash B (2015) Time-frequency signal analysis and processing, 2nd edn. Elsevier, Amsterdam

Boashash B, Mesbah M (2004) Signal enhancement by time-frequency peak filtering. IEEE Trans Signal Process 52:929–937

Boashash B, O'shea PJ (1994) Polynomial Wigner-Ville distributions and their relationship to time-varying higher order spectra. IEEE Trans Signal Process 42:216–220

Canales L (1984) Random noise reduction. In: 54th annal international meeting SEG, pp 525–527

Chen Y, Ma J (2014) Random noise attenuation by *f–x* empirical-mode decomposition predictive filtering. Geophysics 79:V81–V91

Chen Y, Zhang G, Gan S, Zhang C (2015) Enhancing seismic reflections using empirical mode decomposition in the flattened domain. J Appl Geophys 119:99–105

Colominas MA, Schlotthauer G, Torres ME (2014) Improved complete ensemble EMD: a suitable tool for biomedical signal processing. Biomed Signal Process Control 14:19–29

Donoho DL, Johnstone IM (1994) Ideal spatial adaptation by wavelet shrinkage. Biometrika 81:425–455
Fedi M, Lenarduzzi L, Primiceri R, Quarta T (2000) Localized denoising filtering Using the wavelet transform. Pure Appl Geophys 157:1463–1491
Gao J, Mao J, Chen W, Zheng Q (2006) On the denoising method of prestack seismic data in wavelet domain. Chin J Geophys CH 49:1155–1163
Gemechu D, Yuan H, Ma J (2017) Random noise attenuation using an improved anisotropic total variation regularization. J Appl Geophys 144:173–187
Gilles J (2013) Empirical wavelet transform. IEEE Trans Signal Process 61:3999–4010
Han J, van der Baan M (2013) Empirical mode decomposition for seismic time-frequency analysis. Geophysics 78:O9–O19
Harris PE, White RE (1997) Improving the performance of *f–x* prediction filtering at low signal-to-noise ratios. Geophys Prospect 45:269–302
Huang NE, Shen Z, Long SR, Wu MC, Shih HH, Zheng Q, Yen NC, Tung CC, Liu HH (1998) The empirical mode decomposition and the Hilbert spectrum for nonlinear and non-stationary time series analysis. Proc R Soc Lond Ser A 454:903–995
Li Z, Gao J (2016) Random noise attenuation by an amplitude-preserved time-frequency peak-based on empirical wavelet transform predictive filtering. In: 86th annual international meeting SEG, pp 16–21
Li F, Zhang B, Verma S, Marfurt KJ (2018) Seismic signal denoising using thresholded variational mode decomposition. Explor Geophys 49:450–461
Lin H, Li Y, Yang B (2007) Recovery of seismic events by time-frequency peak filtering. IEEE Int Conf Image Process 5:V441–V444
Lin H, Li Y, Yang B, Ma H (2013) Random denoising and signal nonlinearity approach by time-frequency peak filtering using weighted frequency reassignment. Geophysics 78:V229–V237
Lin H, Li Y, Yang B, Ma H, Zhang C (2014) Seismic random noise elimination by adaptive time-frequency peak filtering. IEEE Geosci Remote Sens Lett 11:337–341
Lin H, Li Y, Ma H, Yang B, Dai J (2015) Matching-pursuit-based spatial-trace time-frequency peak filtering for seismic random noise attenuation. IEEE Geosci Remote Sens Lett 12:394–398
Lin H, Li Y, Ma H, Xu L (2016) Simultaneous seismic random noise attenuation and signal preservation by optimal spatiotemporal TFPF. J Appl Geophys 128:123–130
Liu Y, Li Y, Lin H, Ma H (2014) An amplitude-preserved time–frequency peak filtering based on empirical mode decomposition for seismic random noise reduction. IEEE Geosci Remote Sens Lett 11:896–900
Liu N, Gao J, Zhang Z, Jiang X, Lv Q (2016a) High resolution characterization of geological structures using synchrosqueezing transform. Interpretation 5:T75–T85
Liu W, Cao S, Chen Y (2016b) Seismic time–frequency analysis via empirical wavelet transform. IEEE Geosci Remote Sens Lett 13:28–32
Liu Y, Dang B, Li Y, Lin H, Ma H (2016c) Applications of Savitzky–Golay filter for seismic random noise reduction. Acta Geophys 64:101–124
Liu W, Cao S, Wang Z (2017) Application of variational mode decomposition to seismic random noise reduction. J Geophys Eng 14:888–899
Liu N, Gao J, Jiang X, Zhang Z, Wang P (2018a) Seismic instantaneous frequency extraction based on the SST-MAW. J Geophys Eng 15:995–1007
Liu N, Gao J, Zhang B, Li F, Wang Q (2018b) Time-frequency analysis of seismic data using a three parameters S transform. IEEE Geosci Remote Sens Lett 15:142–146
Liu N, Gao J, Zhang B, Wang Q, Jiang X (2019) Self-adaptive generalized s-transform and its application in seismic time-frequency analysis. IEEE Trans Geosci Remote Sens 57:7849–7859
Naghizadeh M (2012) Seismic data interpolation and denoising in the frequency-wavenumber domain. Geophysics 77:V71–V80
Roessgen M, Boashash B (1994) Time–frequency peak filtering applied to FSK signals. In: IEEE-SP international symposium on time-frequency and time-scale analysis, vol 17, pp 516–519
Shan H, Ma J, Yang H (2009) Comparisons of wavelets, contourlets and curvelets in seismic denoising. Journal of Applied Geophysics 69:103–115
Ville J (1948) Théorie et applications de la notion de signal analytique. Cables et transmission 2:61–74
Wang Y (1999) Random noise attenuation using forward-backward linear prediction. J Seism Explor 8:133–142
Wang D, Gao J (2014) A new method for random noise attenuation in seismic data based on anisotropic fractional-gradient operators. J Appl Geophys 110:135–143
Wigner E (1932) On the quantum correction for thermodynamic equilibrium. Phys Rev 40:749–759
Wu Z, Huang NE (2009) Ensemble empirical mode decomposition: a noise-assisted data analysis method. Adv Adapt Data Anal 1:1–41
Wu H, Zhang B, Lin T, Li F, Liu N (2019) White noise attenuation of seismic data by integrating variational mode decomposition and convolutional neural network. Geophysics 84:1–56
Yu P, Li Y, Lin H, Wu N (2016) Removal of random noise in seismic data by time-varying window-length time–frequency peak filtering. Acta Geophys 64:1703–1714
Yuan S, Wang S (2013) Edge-preserving noise reduction based on Bayesian inversion with directional difference constraints. J Geophys Eng 10:025001
Yuan S, Wang S, Li G (2012) Random noise reduction using Bayesian inversion. J Geophys Eng 9:60–68
Yuan S, Wang S, Luo C, Wang T (2018) Inversion-based 3-D seismic de-noising for exploring spatial edges and spatio-temporal signal redundancy. IEEE Geosci Remote Sens Lett 15:1682–1686
Zahir M, Hussain B (2000) Adaptive instantaneous frequency estimation of multicomponent FM signal using quadratic time–frequency distributions. IEEE Trans Signal Process 50:657–660
Zhang B, Lin T, Guo S, Davogustto OE, Marfurt KJ (2016) Noise suppression of time-migrated gathers using prestack structure-oriented filtering. Interpretation 4:SG19–SG29
Zhou Q, Gao J, Wang Z, Li K (2016) Adaptive variable time fractional anisotropic diffusion filtering for seismic data noise attenuation. IEEE Trans Geosci Remote Sens 54:1905–1916

Acta Geophysica (2020) 68:435–444
https://doi.org/10.1007/s11600-020-00414-3

RESEARCH ARTICLE - APPLIED GEOPHYSICS

Simulation of seismic wave propagation in poroelastic media using vectorized Biot's equations: an application to a CO_2 sequestration monitoring case

Emmanuel Anthony[1,3] · **Nimisha Vedanti**[1,2]

Received: 4 November 2019 / Accepted: 26 February 2020 / Published online: 10 March 2020

Abstract
Wave propagation through porous media allows us to understand the response and interaction that occur between the elastic rock matrix and the fluid. This interaction has been described by Biot in his theory of poroelasticity. Seismic wave simulation using Biot's formulations is computationally expensive when compared with the acoustic and elastic cases. This computational burden can be reduced by reformulating the numerical derivative operators to improve the efficiency. To achieve this, we used a staggered-grid finite difference operator to discretize 2D velocity stress equations as given by Biot's theory. A vectorized derivative is applied on the staggered grid by shifting the coordinates. The reformulated equations were applied to compute the seismic response of a reservoir, where CO_2 is being injected and the effect of injected CO_2 in the formation is clearly seen in the synthetic data generated. The algorithm was coded in Python and to test its efficiency, the simulation run-time was compared for both serial and vectorized equations, and the speed-up ratio was calculated. Our results show a decrease in the simulation run-time for the vectorized execution with over a factor of a hundred percent (100%). We further observed that the amplitudes of the events increase with an increase in CO_2 saturation in the formation. This matches well with the real data.

Keywords Poroelasticity · CO_2 injection · Staggered grid · Finite difference · Seismic wave

Introduction

The theory of wave propagation in a porous media enables us to understand the interaction between the solid matrix and the fluid properties. Acoustic and elastic wave equations consider single-phase medium and have been used to solve various geological problems (Sheen et al. 2006). However, properties of the fluid in the pore such as viscosity and density of the fluid have been ignored in the single-phase medium. These fluid properties can be incorporated by using Biot's theory, which predicts the existence of two types of compressional waves and one shear wave (Biot 1956a, b, 1962). The first compressional wave is called the "fast p wave," and the second compressional wave is called the "slow p wave." However, the existence of the second type of compressional wave (slow p) was confirmed through the experiments carried out with artificial rocks (Berryman 1980; Plona 1980). Burridge and Keller (1982), Pride et al. (1992) and Pride and Berryman (1998) have also shown the applicability of the Biot's model to porous media.

When a seismic wave propagates through a porous medium, a pressure gradient is created or we can say a pressure relaxation is achieved. This pressure difference leads to fluid flow as the fluid moves in the pores with respect to the solid. This process is referred to as wave-induced fluid flow, and it is accompanied by the dissipation of energy. The wave-induced fluid flow can be used to monitor the time-lapse seismic response of a reservoir, due to change in the fluid properties such as the injection of CO_2 into a reservoir (Morency et al. 2011).

In a CO_2 sequestration project, large amount of CO_2 is stored in a deep geological formation and to understand the

✉ Emmanuel Anthony
tonyndokalemma@gmail.com

Nimisha Vedanti
nimisha@ngri.res.in

[1] AcSIR-NGRI, Hyderabad 500007, India

[2] CSIR-National Geophysical Research Institute, Hyderabad 500007, India

[3] Department of Physics, Imo State University, Owerri, Nigeria

time-lapse behavior of CO_2 in the formation, Biot's equations can be used. Several authors Dai et al. (1995), Boutin and Bonnet (1986) and Burridge and Vargas (1978) have given analytical solutions to the Biot's equations using simple homogeneous poroelastic media. However, a reservoir under CO_2 injection does not behave like simple media; hence, analytical solutions cannot be used. To model a complex medium, numerical methods like finite difference method (FDM) (Zhu and McMechan 1991; Dai et al. 1995; Wenzlau and Muller 2009; Itz et al. 2016; O'Brien 2010; Zhang et al. 2018), pseudo-spectral methods (Carcione 1996b, a; Ozdenvar and McMechan 1997), finite element method (Roberts and Garboczi 2002) and spectral element (Morency 2008) have been used. In the present work, we used the FDM to solve the Biot's equations for the poroelastic media.

The simulation of seismic waves in a poroelastic medium is computationally intensive. Hence, to overcome this issue, it is required to optimize the algorithm for faster computations. Malkoti et al. (2018) demonstrated a vectorized scheme to increase the speed of the elastic wave simulations over the staggered grid. On a similar line in this paper, we developed an efficient scheme for simulations of seismic waves in a poroelastic media, using vectorized derivative operators. Further, we demonstrated the application of this algorithm on a model derived from the Sleipner for CO_2 sequestration case.

Theory

Biot (1956a, b, 1962) established the theory of poroelasticity with these assumptions:

1. The fluid phase is continuous
2. The porous medium should be statistically isotropic
3. Seismic wavelength is larger than the pore size
4. Deformations on the elastic rock matrix should be small

The Biot's poroelastic equations for an isotropic medium are given by

$$\rho\ddot{\mathbf{u}} + \rho_{\mathrm{f}}\ddot{\mathbf{w}} = (\lambda_{\mathrm{c}} + \mu)\nabla\nabla.\mathbf{u} + \mu\nabla^2\mathbf{u} + \alpha M\nabla\nabla.\mathbf{w} \tag{1}$$

$$\rho_{\mathrm{f}}\ddot{\mathbf{u}} + m\ddot{\mathbf{w}} = \alpha M\nabla\nabla.\mathbf{u} + M\nabla\nabla.\mathbf{w} - b\dot{\mathbf{w}} \tag{2}$$

where u is the solid displacement and w the displacement of the fluid relative to the solid.

The stress and pressure are given by

$$\tau_{ij} = 2\mu e_{ij} + \delta_{ij}(\lambda_{\mathrm{c}} e_{kk} + \alpha M w_{k,k}) \tag{3}$$

$$p = -\alpha M e_{kk} - M w_{k,k} \tag{4}$$

where e_{ij} is the strain tensor, δ_{ij} is the Kronecker delta

The physical parameters used in the equations above are listed in Table 1.

Discretization of the poroelastic equations

The poroelastic equations can be written using velocity–stress formation proposed by (Virieux 1984)

$$\dot{v}_i = (m\rho - \rho_{\mathrm{f}}^2)^{-1}(m\tau_{ij,j} + \rho_{\mathrm{f}} p_{,i} + \rho_{\mathrm{f}} b w_i) \tag{5}$$

$$\dot{w}_i = (m\rho - \rho_{\mathrm{f}}^2)^{-1}(-\rho_{\mathrm{f}}\tau_{ij,j} - \rho p_{,i} - \rho b w_i) \tag{6}$$

Table 1 Table of constants

Name	Symbol	Units	
Density of the solid mineral	ρ_{s}	kg/m^3	
Density of the fluid	ρ_{f}	kg/m^3	
Density	ρ	kg/m^3	$\phi\rho_{\mathrm{s}} + (1-\phi)\rho_{\mathrm{f}}$
Effective fluid density	m	kg/m^3	$T\rho_{\mathrm{f}}/\phi$
porosity	ϕ		
Fluid viscosity	η	Pa s	
Permeability of the medium	κ	m^2	
Tortuosity	T		
Mobility of the fluid	b	Pa s/m^2	η/κ
Lame constant	λ	Pa	
Lame constant of the porous medium	λ_{c}	Pa	$\lambda + \alpha^2 M$
Shear modulus	μ	Pa	
Fluid storage coefficient	M	Pa	$K_{\mathrm{s}}(1 - \phi - K_{\mathrm{d}}/K_{\mathrm{s}} + \phi K_{\mathrm{s}}/K_{\mathrm{f}})^{-1}$
Coefficient of effective stress	α	Pa	$1 - K_{\mathrm{d}}/K_{\mathrm{s}}$
Solid bulk modulus	K_{s}	Pa	
Fluid bulk modulus	K_{f}	Pa	
Drained bulk modulus	K_{d}	Pa	$\lambda + 2/3\mu$

$$\dot{\tau}_{ij} = \mu(v_{i,j} + v_{j,i}) + (\lambda_c v_{k,k} + \alpha M w_{k,k})\delta_i j \tag{7}$$

$$\dot{p} = -\alpha M v_{i,i} - M w_{i,i} \tag{8}$$

The finite difference (FD) method is one of the numerical methods frequently applied in geophysical research for wave propagation modeling (Virieux 1984, 1986; Bohlen 2002). The basic concept of this method is the approximation of the differential operators by finite differences on a discrete mesh in space and time. In this method, an approximate solution of the wave equation is obtained at the mesh grid points. Staggered grids are used to improve the accuracy and efficiency of the numerical modeling. The outstanding feature of this method is the fact that differential operators are naturally centered at the same point in space and time (Sheen et al. 2006). The poroelastic wave equations (Eqs. 5–8) can be discretized after assigning field variables at different positions on the staggered grid, as shown in Fig. 1.

After assigning the fields variable, the poroelastic wave equations can be written as

$$\begin{aligned} D_t^0 v_i|^n = {} & (m\rho - \rho_f^2)^{-1}(mD_j^+ \tau_{ij}|^n \delta_{ij} \\ & + D_j^- \tau_{ij}|^n (1 - \delta_{ij}) + \rho_f D_i^+ p|^n + \rho_f b w_i|^n) \end{aligned} \tag{9}$$

$$\begin{aligned} D_t^0 w_i|^n = {} & (m\rho - \rho_f^2)^{-1}(\rho_f D_j^+ \tau_{ij}|^n \delta_{ij} \\ & + D_j^- \tau_{ij}|^n (1 - \delta_{ij}) - \rho D_i^+ p|^n + \rho b w_i|^n) \end{aligned} \tag{10}$$

$$\begin{aligned} D_t^0 \tau_{ij}|^{n+\frac{1}{2}} = {} & \lambda_c D_k^- v_k|^{(n+\frac{1}{2})} \delta_{ij} + 2\mu D_j^- v_i|^{(n+\frac{1}{2})} \delta_{ij} \\ & + \alpha M(D_k^- w_k|^{(n+\frac{1}{2})} + D_j^- w_i|^{(n+\frac{1}{2})}) \delta_{ij} \\ & + \mu(D_j^+ v_i|^{(n+\frac{1}{2})} + D_i^+ v_j|^{(n+\frac{1}{2})}) \times (1 - \delta_{ij}) \end{aligned} \tag{11}$$

$$\begin{aligned} D_t^0 p|^{(n+\frac{1}{2})} = {} & -\alpha M(D_i^- v_i|^{(n+\frac{1}{2})} + D_j^- v_j|^{(n+\frac{1}{2})}) \\ & - M(D_i^- w_i|^{(n+\frac{1}{2})} + D_j^- w_j|^{(n+\frac{1}{2})}) \end{aligned} \tag{12}$$

where the Kronecker delta function is given by

$$\delta_{ij} = \begin{cases} 1 & \text{if } i=j \\ 0 & \text{if } i \neq j \end{cases}$$

D_t^0 is the time central derivative, D^+ and D^- are the forward and backward spatial derivative operators.

The fourth-order staggered-grid finite difference approximation centered at location i is given by

$$\begin{aligned} D_x f(i) = \frac{1}{\Delta x} \Big\{ & 9/8(f(i+\frac{1}{2}) - f(i-\frac{1}{2})) \\ & - 1/24(f(i+\frac{3}{2}) - f(i-\frac{3}{2})) \Big\} \end{aligned} \tag{13}$$

The derivative operator can be reformulated in the forward and backward derivative operators by shifting the center of Eq. 13. This step is required for vectorization that leads to an increase in computational speed (Fig. 2).

Defining the shift operator as $\Delta^n f(x) = f(x + n\Delta x)$. The reformulated operator(s) can be written as

$$D^+ f(i) = \frac{1}{24}(\Delta^{-1} - 27\Delta^0 + 27\Delta^{+1} - \Delta^{+2}) f(i) \tag{14}$$

$$D^- f(i) = \frac{1}{24}(\Delta^{-2} - 27\Delta^{-1} + 27\Delta^0 - \Delta^{+2}) f(i) \tag{15}$$

Using the reformulated staggered-grid operator, the entire computational domain is considered as a vector, as shown in Fig. 3. The top vector is considered as the entire domain, and the others are considered as a single derivative operator. This formulation enables the entire domain to be updated at once and hence leads to an increase in computational speed.

This reformulated scheme can be extended to 2D, but the shifts are done in just one direction. The direction of the shift is usually the same as the direction of the derivative.

We can relate derivatives on the right-hand side with that on the left-hand side shifted coordinates by attaching different coordinates to each of the field variables f (i.e., velocities, stresses, pressure) as A^f, as shown in Fig. 2. The grid systems are defined by $A^f(I^f, J^f)$, where f can be v_i, w_i, τ_{ij}, p.

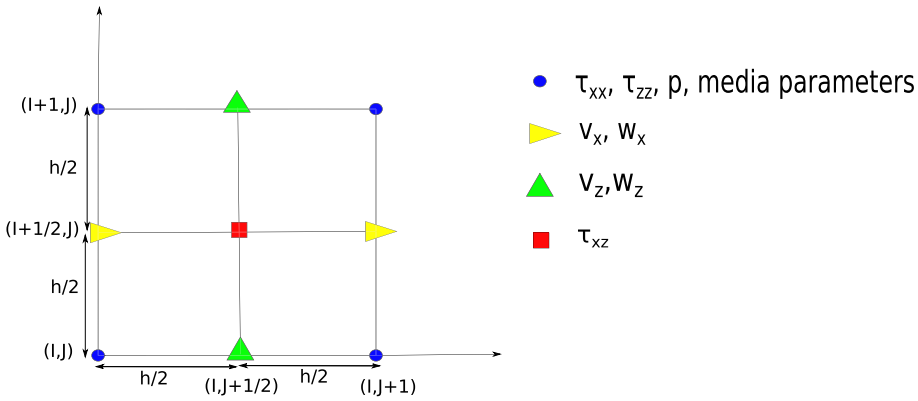

Fig. 1 Staggered-grid finite difference method for poroelastic wave equation

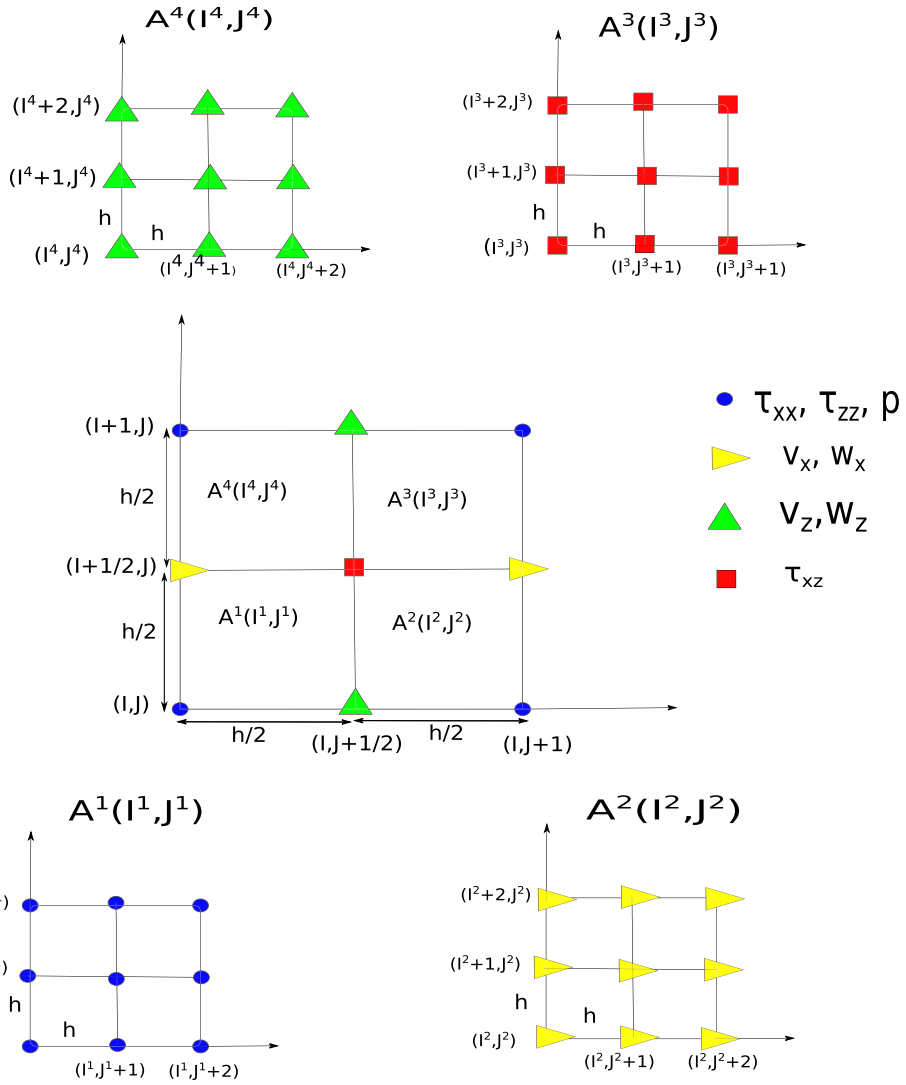

Fig. 2 Main computational grid and four decomposed simpler equispaced subgrid

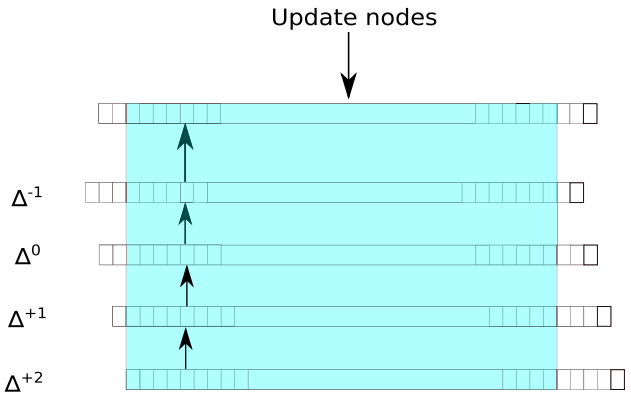

Fig. 3 Vectorized nodes update

Four independent grids A^1, A^2, A^3, A^4 corresponding to field variables are shown in Fig. 2. The poroelastic wave equations can be written using these independent grids as

$$\begin{aligned} D_t^+ v_i(I^{v_i}, J^{v_i}) = (m\rho - \rho_f^2)^{-1}(mD_j^+ \tau_{ij}(I^{\tau_{ij}}, J^{\tau_{ij}})\delta_{ij} \\ + D_j^- \tau_{ij}(I^{\tau_{ij}}, J^{\tau_{ij}})(1-\delta_{ij}) \\ + \rho_f D_i^+ p(I^p, J^p) + \rho_f b w_i(I^{w_i}, J^{w_i})) \end{aligned} \tag{16}$$

$$\begin{aligned} D_t^+ w_i(I^{w_i}, J^{w_i}) = (m\rho - \rho_f^2)^{-1}(\rho_f D_j^+ \tau_{ij}(I^{\tau_{ij}}, J^{\tau_{ij}})\delta_{ij} \\ + D_j^- \tau_{ij}(I^{\tau_{ij}}, J^{\tau_{ij}})(1-\delta_{ij}) \\ - \rho D_i^+ p(I^p, J^p) + \rho b w_i(I^{w_i}, J^{w_i})) \end{aligned} \tag{17}$$

$$\begin{aligned} D_t^+ \tau_{ij}(I^{\tau_{ij}}, J^{\tau_{ij}}) = \lambda_c D_k^- v_k(I^{v_k}, J^{v_k})\delta_{ij} \\ + 2\mu D_j^- v_i(I^{v_i}, J^{v_i})\delta_{ij} + \alpha M(D_k^- w_k(I^{w_k}, J^{w_k}) \\ + D_j^- w_i(I^{w_i}, J^{w_i})\delta_{ij} + \mu(D_j^+ v_i(I^{v_i}, J^{v_i}) \\ + D_i^+ v_j(I^{v_j}, J^{v_j}) \times (1-\delta_{ij}) \end{aligned} \tag{18}$$

Table 2 Poroelastic medium properties (Morency 2008)

Name	Symbol/unit	Value
Solid density	ρ_s (kg/m^3)	2650
Fluid density	ρ_f (kg/m^3)	880
Porosity	ϕ	0.1
Solid bulk modulus	K_s (GPa)	12.2
Fluid bulk modulus	K_f (GPa)	1.985
Frame bulk modulus	K_{dry} (GPa)	9.6
Shear bulk modulus	μ (GPa)	5.1
Fast P-wave	v_f (ms^{-1})	2339
Slow P-wave	v_s (ms^{-1})	960
S-wave	v_s (ms^{-1})	1449

$$\begin{aligned} D_t^+ p(I^p, J^p) = & -\alpha M(D_i^- v_i(I^{v_i}, J^{v_i}) + D_j^- v_j(I^{v_j}, J^{v_j})) \\ & - M(D_i^- w_i(I^{w_i}, J^{w_i}) + D_j^- w_j(I^{w_j}, J^{w_j})) \end{aligned} \tag{19}$$

Absorbing boundary condition

The seismic simulation requires absorbing boundary condition (ABC) to truncate artificial reflections in an unbounded medium. The perfectly matched layer (PML) absorbing boundary condition proposed by (Berenger 1994) is derived by replacing the coordinate variables in the frequency domain with a complex stretched variable defined as

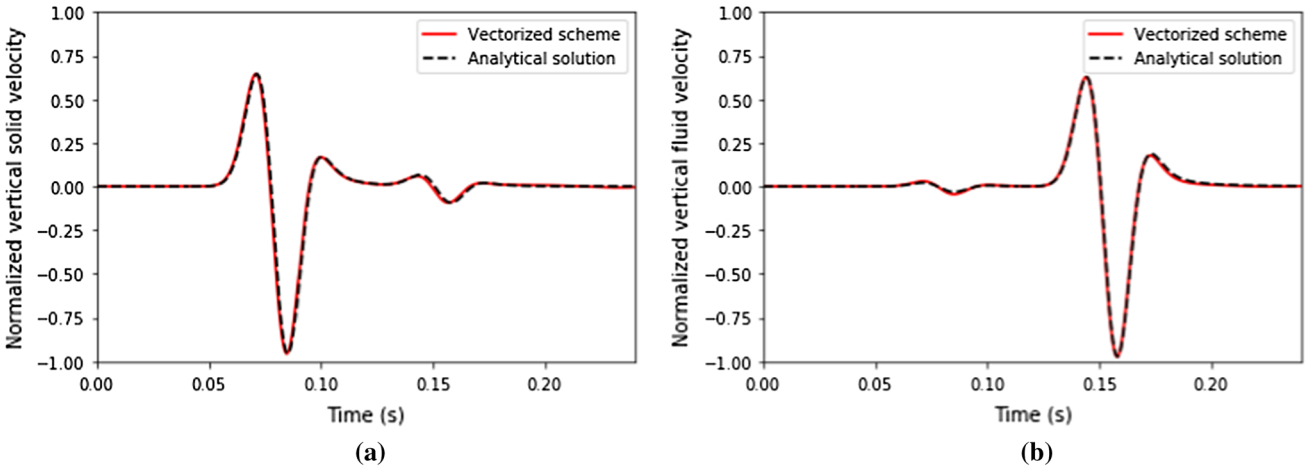

Fig. 4 Plots of analytical and vectorized scheme for the model given in Table 2 at (140 m, 250 m). **a** The normalized vertical solid velocity of the vectorized scheme and analytical solution, and **b** the normalized vertical fluid velocity of the vectorized scheme and analytical solution

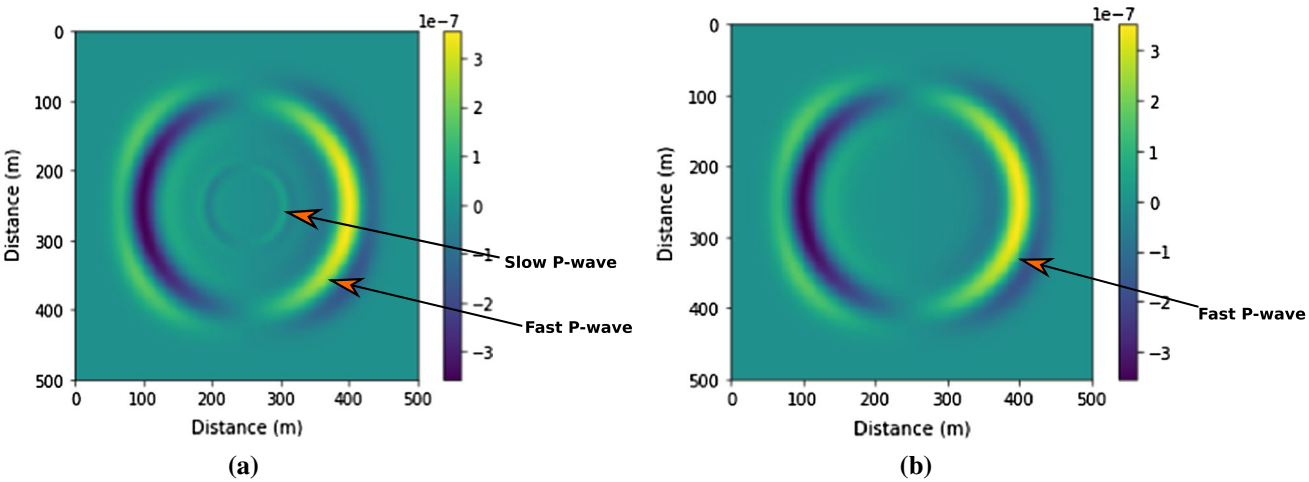

Fig. 5 Snapshots of vertical component of particle velocity, v_x at 0.101 s. **a** Below the Biot's frequency and **b** above the Biot's frequency

$$\tilde{y} = \int_0^{y_i} z_i(y_i)\mathrm{d}y_i$$

where $z_i(y_i) = 1 - \frac{b_i}{i\omega}$, b_i is the damping factor, y_i is the direction and ω is the temporal frequency. The damping factor $b_i = \log(\frac{1}{R})(\frac{3v_p}{2})(\frac{i^2}{L^3})$

R is the coefficient of reflection, and L is the thickness of the PML. In this study, PML is used to truncate the computational domain.

Seismic source

An explosion source generates P-wave without S-wave assuming the explosion is spherical and the surrounding medium is homogenous and isotropic, and can also be called the center of compression (Yijie and Jinghuai 2019). A Ricker wavelet can be used as a time function in the simulation of poroelastic wave propagation and is defined as

$$s(t) = (1 - 2\pi^2 f^2 (t - t_0)^2 e^{-\pi^2 f^2 (t-t_0)^2})$$

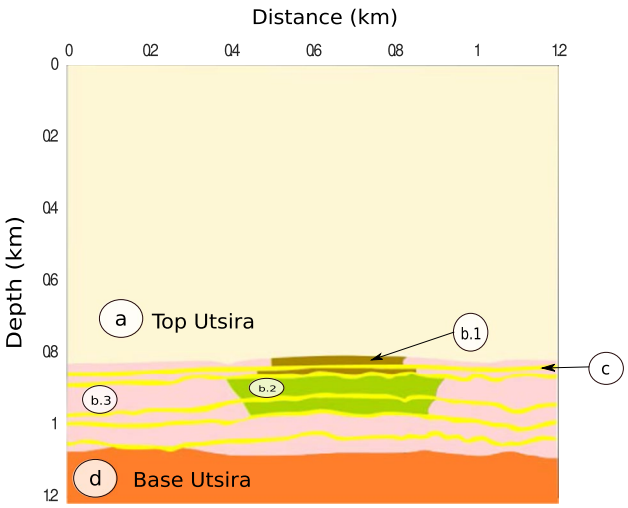

Fig. 6 Geological model of Utsira Formation. a, b, c, d, and correspond to the material properties in Table 3 (Carcione et al. 2006)

where f is the source frequency, t is the time, and t_0 is the time shift. The weights $M_s = (1 - \phi)$ and $M_f = \phi$ can be used to multiply the moment density sources in the solid and fluid phases, respectively, in order to partition it linearly (Yijie and Jinghuai 2019).

Where M_s and M_f are the weighting factor for the solid stresses and fluid pressure, ϕ is the porosity. In this work, an explosion source is used to generate the source vibration.

The above-discussed methodology was used to develop an efficient algorithm for simulation of seismic waves in a poroelastic media.

Validation of algorithm

A numerical scheme is generally validated by comparing it with an analytical solution. Thus, to validate our vectorized scheme, we compared our solution with the analytical solution for seismic wave propagation in a porous medium, as given by Dai et al. (1995). We considered a uniform homogeneous model with dimension 500 m × 500 m, with the model parameters given in Table 2. Ricker wavelet is used as an explosive source with a dominant frequency of 30 Hz and a time delay of $t_0 = 0.004$ s. The source is located in the middle of the grid, that is $(x, z) = (250\text{ m}, 250\text{ m})$. The grid size and time step are 2 m and 0.2 ms, respectively.

Figure 4 shows the normalized vertical solid and fluid velocities of the vectorized scheme and the analytical solution. We observed that the vectorized scheme perfectly approximates the computed analytical solution. Similarly, Fig. 5 shows the snapshot of the vertical component of solid particle velocity, v_x at 0.101 s, when the diffusive parameter $b = 0$ and $b = 4 \times 10^7$, which corresponds to low and high frequencies, respectively. Biot (1956a, b) in establishing this theory predicts a second type of compressional wave usually referred as slow compressional wave. In line with the Biot's theory, this second type of compressional wave is generated by our algorithm, as shown in Fig. 5a. This validates the application of our algorithm.

Table 3 Reservoir properties for Utsira Formation, Sleipner field, Norway

Medium	ρ(kg/m^3)	ρ_f(kg/m^3)	ρ_s(kg/m^3)	K_s (GPa)	K_{dry} (GPa)	K_f (GPa)	μ (GPa)	ϕ	T	η_f (cP)	κ (Darcy)
a	2097	1030	2600	20	1.50	2.25	0.73	0.32	4	1.2	0.1
b.1	1940	715	2600	40	1.33	0.042	0.85	0.35	2.8	0.3	1.6
b.2	2017	935	2600	40	1.33	0.12	0.85	0.35	2.8	0.7	1.6
b.3	2051	1032	2600	40	1.33	2.61	0.85	0.35	2.8	1.2	1.6
c	2207	1030	2600	20	4.70	2.25	0.99	0.25	5	1.2	0.001
d	2286	1030	2600	20	6.49	2.25	1.16	0.2	5	1.2	0.01

b.1: $S_w - 40\%$; b.2:$S_w - 80\%$; b.3: $S_w - 100\%$

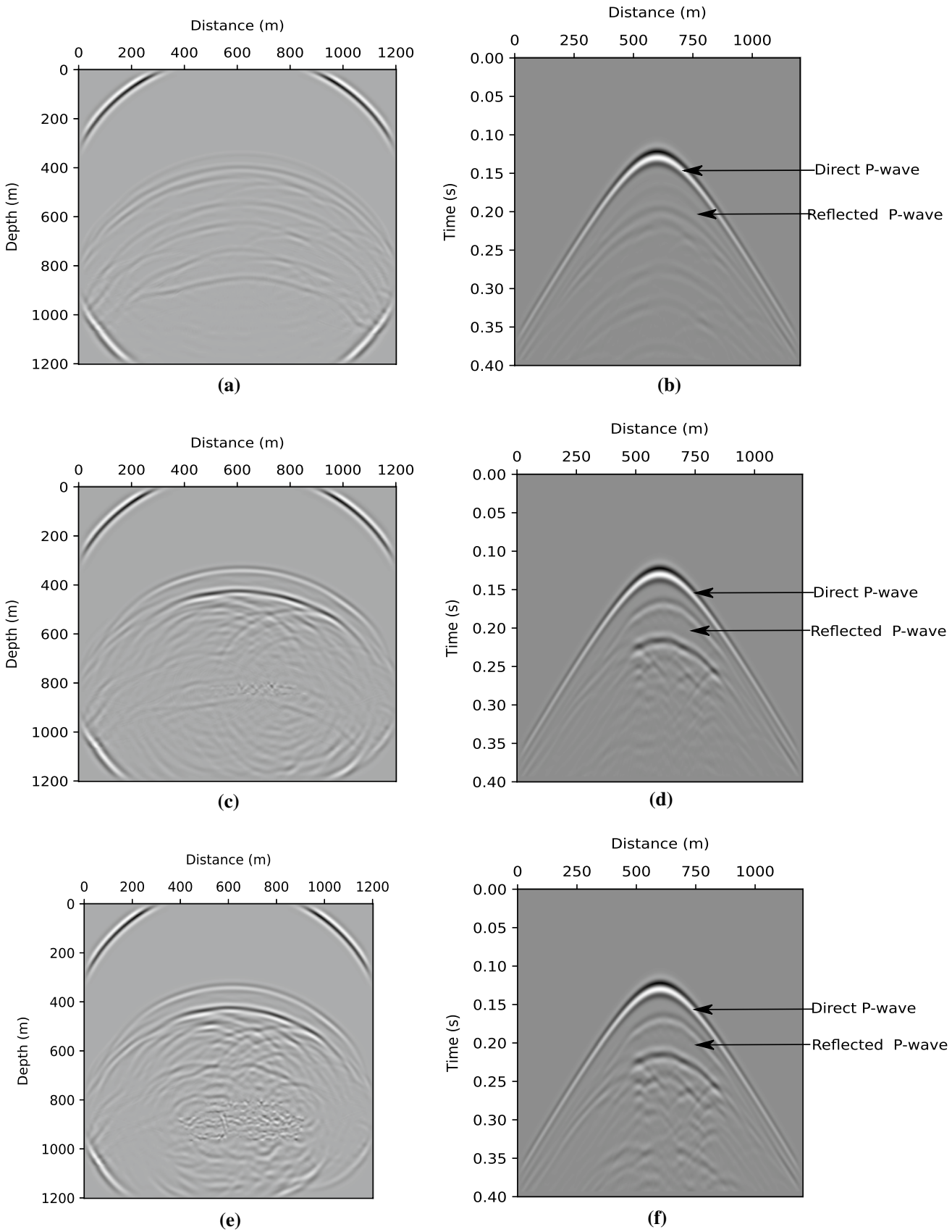

Fig. 7 Snapshots of the solid component of particle velocity and seismic response. **a**, **b** Represent the pre-injection (100% brine saturated) case, **c**, **d** represent first monitored case (80% brine saturated) and **e** and **f** represent the second monitored case (40% brine saturated)

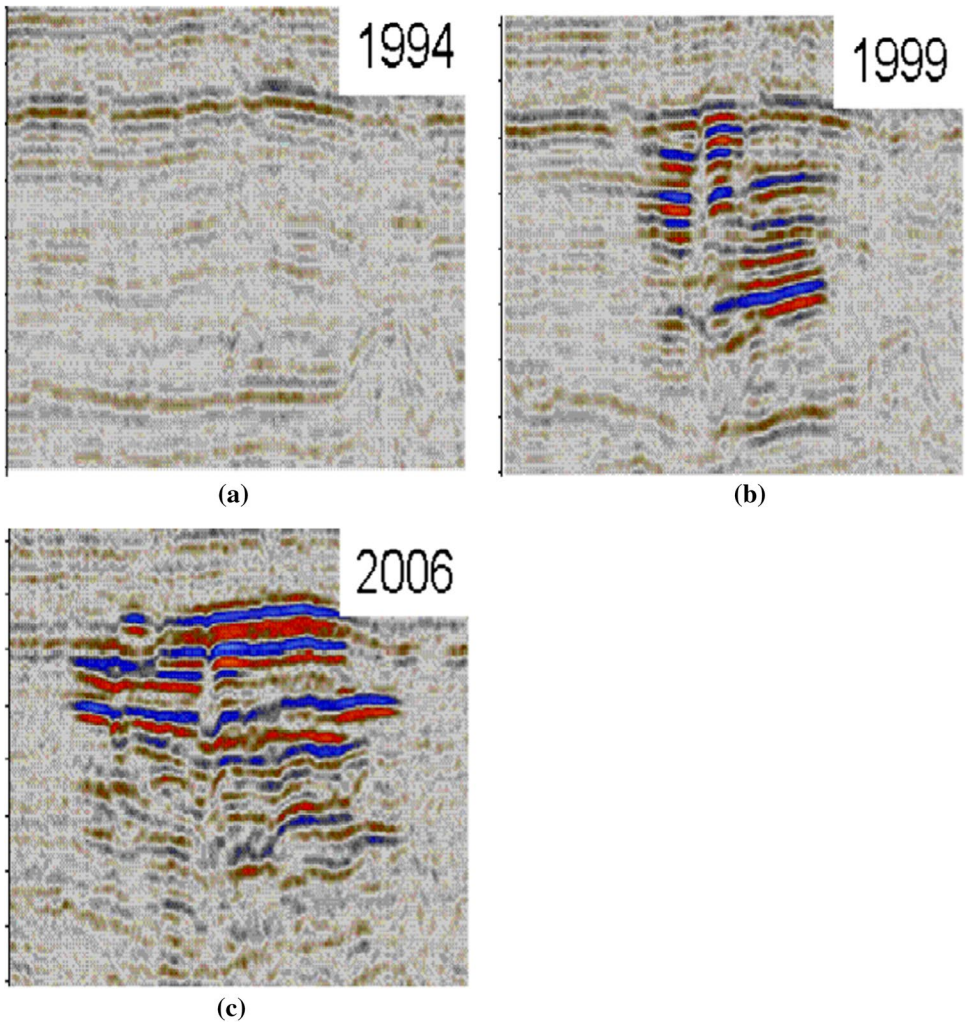

Fig. 8 Observed data from Utsira Sleipner project. **a** Observed data before injection in 1994, **b** observed data after injection in 1999 and **c** observed data after injection in 2006. From Statoil (now Equinor)

Application to a CO_2 injection monitoring case

The developed algorithm discussed above was used to monitor the injection of CO_2 into a saline aquifer called the Utsira Formation in the Sleipner field, North Sea. The Utsira Formation is 800m below the sea and is a highly permeable and porous sandstone. We used a geometrical and physical model of the Utsira Formation given by Carcione et al. (2006) for simulation. The model is shown in Fig. 6. The alphabets a, b, c, and d correspond to the layer properties, as shown in Table 3 (Carcione et al. 2006).

The properties shown in a, b.3, c, and d represent the baseline (pre-injection) case, and the properties a, b.1, c, d, and a, b.2, c, d correspond to the subsequent monitor cases, representing the post-injection scenarios.

Injection of CO_2 in Utsira Formation changes the reservoir properties like the density, viscosity, and the bulk modulus which in turn will change the velocities. Thus new properties are used to model the monitor cases, as shown in Table 3. The CO_2 is injected at a depth greater than 800 m because at such depth CO_2 is in the supercritical state, making it dense but a liquid with measurable wave speed anomalies (Morency et al. 2011).

For the simulations, we considered a model of dimension 1.2 km × 1.2 km with 1.5-m grid spacing on both sides and a time step of 0.2 ms. The source time function is Ricker wavelet with a dominant frequency of 50 Hz. To truncate artificial reflections, 40 PML layers were used.

The snapshots of the solid particle velocity component and the seismic response are shown in Fig. 7a–f for pre- and post-injection scenarios. Figure 7a, b show reflections coming from the top of the Ustira model and the shale that made up the layers. These events become prominent when CO_2 is injected into the formation, as can be seen in Fig. 7c, d when the formation is saturated partially with CO_2. These reflected events are further enhanced as the saturation of CO_2 increases in the formation with time (Fig. 7e, f). This is in agreement with what is observed in the real data, as shown in Fig. 8a–c.

Table 4 Comparison of computation run-time between serial execution (SE) and vectorized execution (VE) on Python programming language

Size	Time step	Run-time (s)		SPR
N_xN_z	N_t	SE	VE	$\frac{\text{SE}}{\text{VE}}$
100^2	100	66.917	0.557	121.667
	200	138.346	1.107	124.974
	500	343.444	2.723	126.127
	1000	657.237	5.319	123.564
	2000	1384.766	10.995	125.945
	4000	2720.452	22.035	123.460
200^2	100	276.458	2.058	134.333
	200	569.219	4.170	136.503
	500	1459.990	10.589	137.878
	1000	2886.344	21.303	135.502
	2000	5598.012	41.699	134.248
	4000	11401.527	83.048	137.288
500^2	100	1861.03	11.903	156.349
	200	3733.67	23.988	155.647
	500	9828.380	62.120	158.216
	1000	18482.831	118.76	155.627
	2000	36024.058	236.079	152.593
	4000	69184.337	465.577	148.599
1000^2	100	7251.710	60.163	120.534
	200	13949.750	121.572	114.743
	500	35800.17	2.723	117.176
	1000	73274.31	613.121	119.510
	2000	143997.500	1231.579	116.921
	4000	288996.253	2476.813	116.681

Test for efficiency

To test the efficiency of the developed algorithm, we compared the total run-time of the simulation (T_{sim}) using a Python platform with the serial execution. The simulations were carried out on HP Z420 workstation with Intel Xeon 3.6 GHz (octa-core) processors. The simulation run-time recorded and the speed-up ratio (SPR), which is the ratio of the serial execution (SE) to the vectorized execution (VE), are listed in Table 4. As observed from Table 4, the vectorized execution (VE) performs better than the serial execution (SE) as the efficiency is increased by a factor of over 100%.

Conclusions

The seismic wave simulation in a porous media using Biot's theory was carried out using vectorized derivative operators to improve the efficiency of computation. The developed algorithm was used to monitor the changes in seismic response of the Sleipner reservoir, North Sea. The effect of CO_2 saturation in the reservoir is picked efficiently by our algorithm, and we could see the brightening of reflections with an increase in CO_2 saturation. These results match well with the real data. The simulation run-time for the vectorized algorithm was compared with the serial execution (SE), and a reduction in run-time for the vectorized execution with over a hundred percent (100%) was reported.

Acknowledgements Emmanuel Anthony wishes to acknowledge CSIR-TWAS for the award of the fellowship. Authors are grateful to the Director NGRI and AcSIR coordinator for their support and permission to publish this work. Equinor is acknowledged for the seismic data.

References

Berenger J (1994) A perfectly matched layer for the absorption of electromagnetic waves. J Comput Phys 114:185–200

Berryman J (1980) Confirmation of biot's theory. Appl Phys Lett 37:168–178

Biot M (1956a) Theory of propagation of elastic waves in a fluid saturated porous solid, part i: low frequency range. J Acoust Soc Am 28(2):168–178

Biot M (1956b) Theory of propagation of elastic waves in a fluid saturated porous solid, part ii: high frequency range. J Acoust Soc Am 28(2):179–191

Biot M (1962) Mechanics of deformation and acoustic propagation in porous media. J Appl Phys 33(4):1482–1498

Bohlen T (2002) Parallel 3-d viscoelastic finite-difference seismic modelling. Comput Geosci 28(8):887–899

Boutin C, Bonnet PY (1986) Green's functions solutions and associated sources in infinite and stratified poroelastic media. J Geophys Res 90:521–550

Burridge R, Keller J (1982) Poroelasticity equations derived from microstructure. J Acoust Soc 70:1140–1146

Burridge R, Vargas CA (1978) The fundamental solution in dynamic poroelasticity. J Geophys Res 58:61–90

Carcione J (1996a) Full frequency-range transient solution for p-wave in a fluid-saturated viscoacoustic porous medium. Geohys Prospect 44:99–129

Carcione J (1996b) Wave propagation in anisotropic, saturated porous media: plane-wave theory and numerical simulation. J Acoust Soc Am 99:2655–2666

Carcione JM, Picotti S, Gei D, Rossi G (2006) Physics and seismic modeling for monitoring CO_2 storage. Pure Appl Geophys 163:175–207

Dai N, Vafidis A, Kanasewich ER (1995) Wave propagation in heterogeneous, porous media: a velocity-stress, finite-difference method. Geophysics 60(2):327–340

Itz R, Iturrarn-Viveros U, Parra JO (2016) Optimal implicit 2-D finite differences to model wave propagation in poroelastic media. Geophys J Int 206(2):1111–1125

Malkoti A, Nimisha V, Tiwari RK (2018) An algorithm for fast elastic wave simulation using a vectorized finite difference operator. Comput Geosci 116:23–31

Morency C, Luo Y, Tromp J (2011) Acoustic, elastic and poroelastic simulations of CO_2 sequestration monitoring based on spectral-element and adjoint methods. Geophys J Int 185:955–966

Morency CTJ (2008) Spectral-element simulations of wave propagation in porous media. Geophys J Int 175:301–345

O'Brien GS (2010) 3D rotated and standard staggered finite-difference solutions to biots poroelastic wave equations: Stability condition and dispersion analysis. Geophysics 75(4):T111–T119

Ozdenvar T, McMechan G (1997) Algorithms for staggered-grid computations for poroelastic, elastic, acoustic, and scalar wave equations. Geophys Prospect 45:403–420

Plona TJ (1980) Observation of a second bulk compressional wave in porous medium at ultrasonic frequencies. Appl Phys Lett 36(4):259–261

Pride S, Berryman J (1998) Connecting theory to experiment in poroelasticity. J Mech Phys Solids 46:719–747

Pride S, Gangi A, Morgan F (1992) Deriving the equations of motion for porous isotropic media. J Acoust Soc 92:3278–3290

Roberts AP, Garboczi EJ (2002) Computation of the linear elastic properties of random porous materials with a wide variety of microstructure. Proc R Soc Lond 458:1033–1054

Sheen D-H, Tuncay K, Baag C-E, Peter JO (2006) Parallel implementation of a velocity-stress staggered-grid finite-difference method for 2-D poroelastic wave propagation. Comput Geosci 32:1182–1191

Virieux J (1984) Sh-wave propagation in heterogeneous media: velocity-stress finite-difference method. Geophysics 49(11):1933–1942

Virieux J (1986) P-sv wave propagation in heterogeneous media: velocity-stress finite-difference method. Geophysics 51(4):889–901

Wenzlau F, Muller TM (2009) Finite-difference modeling of wave propagation and diffusion in poroelastic media. Geophysics 74(4):T55–T66

Yijie Z, Jinghuai G (2019) Tutorial: source simulation for 3D poroelastic wave equations. Geophysics 84(6):W33W45

Zhang Y, Gao J, Peng J (2018) Variable-order finite difference scheme for numerical simulation in 3-D poroelastic media. IEEE Trans Geosci Remote Sens 56(5):2991–3001

Zhu X, McMechan G (1991) Finite difference modeling of the seismic response of fluid saturated, porous, elastic solid using biot theory. Geophysics 56(3):328–339

Acta Geophysica (2020) 68:445–458
https://doi.org/10.1007/s11600-020-00416-1

RESEARCH ARTICLE - APPLIED GEOPHYSICS

A robust data-driven AVO inversion with logarithm absolute error loss function

Siyuan Du[1] · Jiashu Zhang[1] · Guangmin Hu[2]

Received: 25 August 2019 / Accepted: 29 February 2020 / Published online: 14 March 2020

Abstract
Amplitude variation with offset (AVO) inversion is a widely used approach to obtain reliable estimates of elastic parameter. Tikhonov and total variation regularization are commonly used methods to address ill-posed problem of AVO inversion. However, these model-driven methods are only for special geological structure such as smoothness or blockiness. In this letter, a robust data-driven-based regularization method with logarithm absolute error loss function (DDI-Log) for AVO inversion is proposed. In DDI-Log, the information of well-log data and the complex geology are considered in a sparse representation framework. In pre-stack seismic data, outlier noise can negatively influence inversion results. Thus, different from the previous data-driven inversion based on L_2 norm loss function, we extend the logarithm absolute error function as the loss function. In the iteration, a new spectral PRP conjugate gradient method is used to solve the large-scale optimization problem. The synthetic data and field data tests illustrate that the proposed approach is robust against outlier noise and that the resolution and accuracy of the solutions are improved.

Keywords AVO inversion · Dictionary learning · Logarithm absolute error function

Introduction

Pre-stack amplitude variation with offset (AVO) inversion aims to deduce the geological structure and obtain reliable estimates of P-wave velocity, S-wave velocity and density with observed seismic data (Buland and Omre 2003; Zhang et al. 2013; Fan et al. 2015; Liu et al. 2015; Zong et al. 2017). Typically, the AVO inversion problem can be formulated as optimization problem in which the goal is to find a model that minimizes the error between the observed data and the modeled data. Assuming the seismic data were contaminated by Gaussian noise, the optimization problem most often formulated as a least-squares problem. That is, L_2 norm of the error between the observed data and modeled data is minimized. However, the performance of the least square algorithm degrades severely when the seismic data contain outlier noise. On the other hand, the AVO inversion is a typical ill-posed problem, and there usually exist several solutions that honor the observed data. In order to deal with this issue, prior knowledge should be utilized to restrict scope of solutions. Therefore, how to design a robust and high precision algorithm is vital for the AVO inversion tasks.

In order to estimate reliable elastic parameter, regularization is one of the most popular method as prior knowledge. Assuming that the stratum satisfies smoothness prior, L_2 norm-based regularization such as the Tikhonov regularization is often used in seismic inversion (Sen and Roy 2003). However, the Tikhonov regularization method will lead to an over-smoothed solution in the cases of models with sharp interfaces. A common alternative to the Tikhonov regularization is total variation (TV) regularization which is based on L_1 norm. The TV regularization is appropriate for the seismic inversion problems when the stratum has blockiness prior. For example, in full wave inversion (FWI), TV regularization was used to capture sharp interfaces

✉ Jiashu Zhang
jszhang@home.swjtu.edu.cn

Siyuan Du
siyuandu.92@gmail.com

Guangmin Hu
hgm@uestc.edu.cn

[1] Sichuan Province Key Lab of Signal and Information Processing, Southwest Jiaotong University, Chengdu 610031, China

[2] School of Resources and Environments, Center for Information Geoscience, University of Electronic Science and Technology of China, Chengdu 611731, China

(Epanomeritakis et al. 2008 and Anagaw and Sacchi 2011). Yuan et al. (2015) presented a L1-norm regularization of multitrace impedance to stabilize the inversion, reduce the influence of high-wavenumber noise on the inverted result, and explore spatial continuities of structures. Gholami (2015) utilized TV regularization to recover the impedance maps with blocky structures. Yuan et al. (2018) adopted simultaneous sparsity constraints of the first-order differences of signals along the time direction and two spatial directions to propose an inversion-based 3-D seismic denoising method. She et al. (2019b) proposed high-order total variation regularization for different models. In recent years, some more complex mathematical formulas were used to tackle complex geological models [e.g., mixed smooth and blocky features (Sun and Li 2014) and piecewise smooth model (Li et al. 2017)]. However, two main problems are still existing for the mixed regularization methods. First, it does not make full use of the information of well-log data. Second, the aforementioned regularization methods are model-driven approaches which rely on mathematical models from prior information, and they are only suitable for a specific geology. That is, they are inappropriate for complex area where the features are complex.

Recently, dictionary learning has been extensively studied in many fields (Zhou et al. 2016; Siahsar et al. 2017; She et al. 2018; Tao et al. 2019). For instance, sparse dictionary learning was used in noise attenuation of 3D seismic data (Siahsar et al. 2017). She et al. (2018) proposed a data-driven inversion method for the AVO inversion problem. Also, considering that outlier noise can lead to unstable results, L_1 norm was often used as the loss function because the L_1 norm is insensitivity to outlier errors (Guitton and Verschuur 2004; Pyun et al. 2009; Li and Zhang 2017; Fujin and Jiashu 2013). However, these L_1 norm inversion methods may suffer singularity trouble. Although the iterative algorithm called iteratively reweighted least squares (IRLS) has been used to solve L_1 norm minimization problems (Zhang et al. 2000; Ji 2006; Li and Zhang 2017), the IRLS algorithm is time-consuming on updating the re-weighting factors at each iteration in large-scale problem.

In summary, we propose a new method for AVO inversion, using dictionary learning-based sparse representation framework with logarithm absolute error loss function. The dictionary learning-based sparse representation offers a powerful mechanism of combining the information of well-log data and complex geology simultaneously. Unlike using the previous L_2 norm and L_1 norm as the loss function, we propose a robust logarithm absolute error function to cope with the outlier errors , and the singularity problem which is not differentiable at zero point is also avoided. In addition, we use a new spectral Polak–Ribière–Polyak (PRP) conjugate gradient method to solve the large-scale optimization problem (Wan et al. 2011). The synthetic data show that the proposed algorithm is robust and has higher precision compared with the existing state-of-the-art method. Field seismic data tests also demonstrate the validity of our algorithm.

Conventional regularization methods

Forward model

As usual, on the basis of the convolutional model and Aki-Richards approximation equation (Aki and Richards 2002), the forward model of the AVO inversion can be expressed as a large-scale ill-posed linear equation (Hampson et al. 2005)

$$\boldsymbol{d} = \boldsymbol{G}\boldsymbol{m} + \boldsymbol{n}. \tag{1}$$

where $\boldsymbol{d}$ is the observed seismic data, $\boldsymbol{G}$ is a matrix representing the forward linearized operator, $\boldsymbol{m}$ represents a vector of the model parameters to be estimated and $\boldsymbol{n}$ is the noise term. Hampson et al. (2005) build the model parameter $\boldsymbol{m}$ with a nonlinear transformation of the elastic parameter $\boldsymbol{x}$ using the linear relationship between the logarithms of elastic parameters (P-impedance, S-impedance and density). It is worth noting that vector $\boldsymbol{m} \in \mathbb{R}^{3N_{\text{layer}}}$ (N_{layer} is the number of each model parameter) is a simple concatenation of multiple components

$$\boldsymbol{m} = \left[\boldsymbol{m}_{LP}, \boldsymbol{m}_{\Delta LS}, \boldsymbol{m}_{\Delta LD}\right]. \tag{2}$$

and

$$\begin{aligned} \boldsymbol{m}_{LP} &= \left[m_L P^1, \ldots, m_L P^i, \ldots, m_L P^{N_{\text{layer}}}\right] \\ \boldsymbol{m}_{\Delta LS} &= \left[m^1_{\Delta LS}, \ldots, m^i_{\Delta LS}, \ldots, m^{N_{\text{layer}}}_{\Delta LS}\right] \\ \boldsymbol{m}_{\Delta LD} &= \left[m^1_{\Delta LD}, \ldots, m^i_{\Delta LD}, \ldots, m^{N_{\text{layer}}}_{\Delta LD}\right] \end{aligned} \tag{3}$$

Next, we use φ to denote positive conversion of elastic parameter and model parameter

$$\varphi(\boldsymbol{x}_P, \boldsymbol{x}_S, \boldsymbol{x}_\rho)\begin{cases} \boldsymbol{m}_{LP} = ln(\boldsymbol{x}_p \otimes \boldsymbol{x}_d) \\ \boldsymbol{m}_{\Delta LS} = ln(\boldsymbol{x}_s \otimes \boldsymbol{x}_d) - a\boldsymbol{m}_{LP} - b \\ \boldsymbol{m}_{\Delta LD} = ln(\boldsymbol{x}_d) - c\boldsymbol{m}_{LP} - d \end{cases} \tag{4}$$

where $\otimes$ denotes the element-wise multiplication between two vectors. $\boldsymbol{x}_p, \boldsymbol{x}_s, \boldsymbol{x}_d$ represent P-wave velocity vector, S-wave velocity vector and density vector, respectively, and a, b, c, d are the constant linear fitting coefficients which are learned from well-log data set. Similarly, once we get the model parameter, the elastic properties $\boldsymbol{x}_p, \boldsymbol{x}_s, \boldsymbol{x}_d$ can be obtained from a backward conversion φ^{-1}

$$\varphi^{-1}(\boldsymbol{m}_{LP}, \boldsymbol{m}_{\Delta LS}, \boldsymbol{m}_{\Delta LD}) \begin{cases} \boldsymbol{x}_p = e^{\boldsymbol{m}_{LP}}/\boldsymbol{x}_d \\ \boldsymbol{x}_s = e^{\boldsymbol{m}_{\Delta LS}+a\boldsymbol{m}_{LP}+b}/\boldsymbol{x}_d \\ \boldsymbol{x}_d = e^{\boldsymbol{m}_{\Delta LD}+c\boldsymbol{m}_{LP}+d} \end{cases} \tag{5}$$

Conventional regularization methods

To be concrete, one seeks the perfect estimate of the model parameter $\boldsymbol{m}$ from a knowledge of $\boldsymbol{d}$ and $\boldsymbol{G}$. However, the inversion problem is ill-posed, equation (1) is mostly inverted by minimizing the following objection function:

$$\boldsymbol{J} = \|\boldsymbol{d} - \boldsymbol{G}\boldsymbol{m}\|_2^2 + \kappa\boldsymbol{\Phi}(\boldsymbol{m}) \tag{6}$$

where we call the first term the loss function term. $\boldsymbol{\Phi}(\boldsymbol{m})$ is the regularization term and κ represents regularization parameter. The Tikhonov regularization (TK) and TV regularization are the two most popular regularization methods. The Tikhonov regularization approach based on L_2 norm can exhibit smooth solutions:

$$\boldsymbol{J} = \|\boldsymbol{d} - \boldsymbol{G}\boldsymbol{m}\|_2^2 + \kappa\|\boldsymbol{L}\boldsymbol{m}\|_2^2 \tag{7}$$

By minimizing the L_1 norm of the gradient of model $\boldsymbol{m}$, the TV regularization method attempts to obtain solutions with block effect

$$\boldsymbol{J} = \|\boldsymbol{d} - \boldsymbol{G}\boldsymbol{m}\|_2^2 + \kappa\|\boldsymbol{L}\boldsymbol{m}\|_1 \tag{8}$$

where $\boldsymbol{L}$ is the first-order difference operator for the gradient of model $\boldsymbol{m}$. However, there exists two main issues for the two popular regularization methods. On the one hand, it does not make full use of the information of well-log data. On the other hand, these methods are model-driven approaches that are only for specific geological structure.

Theory

She et al. (2018) have shown that data-driven inversion (DDI) method via learned dictionaries and sparse representation can offer more promising performance. Since the unit of our proposed model is dictionary learning-based sparse representation, we will give brief to introduce the data-driven inversion framework.

Data-driven inversion

Within a survey area, since the deposition of the subsurface layers is relatively stable, the physical properties tend to have a certain similarity. Thus, we can make a

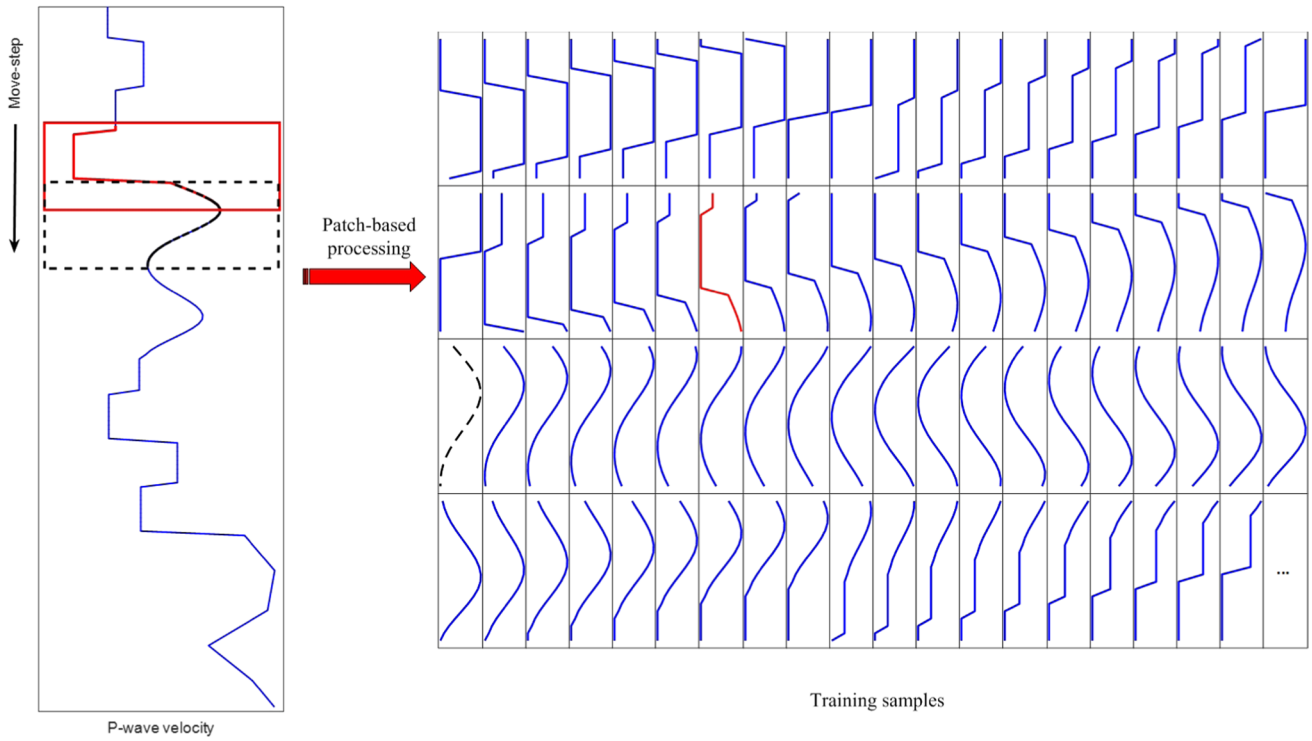

Fig. 1 The patch-based processing approach schematic diagram

reasonable assumption that the sparse dictionary learned from real well-log data can be used as global sparse dictionary. Next, we will describe the dictionary learning method in detail. First, we divide the well-log data into small patches as a training set $\boldsymbol{S} = [\boldsymbol{s}_1, \boldsymbol{s}_2, \ldots, \boldsymbol{s}_n]$. n is the number of small patches with length of M. The training data set is generated using patch-based processing approach that divides the well-logs into patches. Figure 1 shows the patch-based processing approach schematic diagram of the P-wave velocity.

Then, the goal of the dictionary learning is to seek the over-complete dictionary $\boldsymbol{D}$ and sparse approximation $\boldsymbol{A} = [\boldsymbol{a}_1, \boldsymbol{a}_2, \ldots, \boldsymbol{a}_n]$. The process can be expressed as

$$\begin{aligned} &\left\{\hat{\boldsymbol{D}}, \hat{\boldsymbol{A}}\right\} = arg\ min \|\boldsymbol{S} - \boldsymbol{D}\boldsymbol{A}\|_F^2 \\ &subject\ to\ \forall i : \left|\boldsymbol{a}_i\right|_0 \le K (K \ll L) \end{aligned} \tag{9}$$

where $\hat{\boldsymbol{D}}$ and $\hat{\boldsymbol{A}}$ are the learned optimal dictionary and sparse approximation, respectively. $|\cdot|_0$ denotes the L_0 norm that counts nonzero coefficients in a vector and K represents the sparsity level, which is much less than the number of atoms in dictionary $\boldsymbol{D}$. To solve the complex optimization problem, we exploit a flexible and highly efficient K-singular-value decomposition (K-SVD) algorithm (Aharon et al. 2006).

According to the assumption that is mentioned above, once the dictionary is learned, we can represent each unknown elastic parameter block using a few atoms (sparse approximation coefficients) and the dictionary. Thus, the objective function can be described as follows:

$$\begin{aligned} \boldsymbol{J} = &\|\boldsymbol{d} - \boldsymbol{G}\boldsymbol{m}\|_2^2 + \mu_1 \sum_{i=1}^{n} \left\|\boldsymbol{D}_P \alpha_P^i - \boldsymbol{y}_P^i\right\|_2^2 \\ &+ \mu_2 \sum_{i=1}^{n} \left\|\boldsymbol{D}_S \alpha_S^i - \boldsymbol{y}_S^i\right\|_2^2 + \mu_3 \sum_{i=1}^{n} \left\|\boldsymbol{D}_\rho \alpha_\rho^i - \boldsymbol{y}_\rho^i\right\|_2^2 \\ &\text{subject to } \forall i \in \{1, 2, \ldots, n\} : \boldsymbol{R}^i \boldsymbol{m} = \varphi(\boldsymbol{y}_P^i, \boldsymbol{y}_S^i, \boldsymbol{y}_\rho^i) \end{aligned} \tag{10}$$

where n is the number of patches and the subscripts P, S, and ρ denote the P-wave velocity, S-wave velocity, and density, respectively. Taking P-wave velocity as an example, $\boldsymbol{D}_P$ represents the dictionary which is learned through the sparse dictionary learning process above. α_P^i is the sparse coding of $\boldsymbol{y}_P^i$ which is the ith patch of the given P-wave velocity, and the same for S-wave velocity and density. In the sparse representation process, orthonormal matching pursuit (OMP) algorithm is used to get sparse coding α_P^i. Once the sparse coding is done, we can search for dictionary. After several iterations, we can obtain appropriate dictionary and sparse coding. $\boldsymbol{R}^i$ is a matrix that extracts the ith block from the model parameter $\boldsymbol{m}$. In order to eliminate the equality constraints, we use the inverse transformation φ^{-1}. Then, the objective function can be rewritten as

$$\begin{aligned} \boldsymbol{J} = &\|\boldsymbol{d} - \boldsymbol{G}\boldsymbol{m}\|_2^2 \\ &+ \lambda_1 \sum_{i=1}^{n} \left\|\boldsymbol{R}_{LP}^i \boldsymbol{m} - \boldsymbol{m}_{LP}^i\right\|_2^2 \\ &+ \lambda_2 \sum_{i=1}^{n} \left\|\boldsymbol{R}_{\Delta LS}^i \boldsymbol{m} - \boldsymbol{m}_{\Delta LS}^i\right\|_2^2 \\ &+ \lambda_3 \sum_{i=1}^{n} \left\|\boldsymbol{R}_{\Delta LD}^i \boldsymbol{m} - \boldsymbol{m}_{\Delta LD}^i\right\|_2^2 \end{aligned} \tag{11}$$

where $\boldsymbol{m}_{LP}^i$, $\boldsymbol{m}_{\Delta LS}^i$ and $\boldsymbol{m}_{\Delta LD}^i$ are the sparse representation of the ith patch of model parameters. $\boldsymbol{R}_{LP}^i$ is a matrix that extracts the ith block of the logarithm of P-impedance from the model parameter $\boldsymbol{m}$, and similarly for $\boldsymbol{R}_{\Delta LS}^i$ and $\boldsymbol{R}_{\Delta LD}^i$, and λ_1, λ_2 and λ_3 are the regularization parameters.

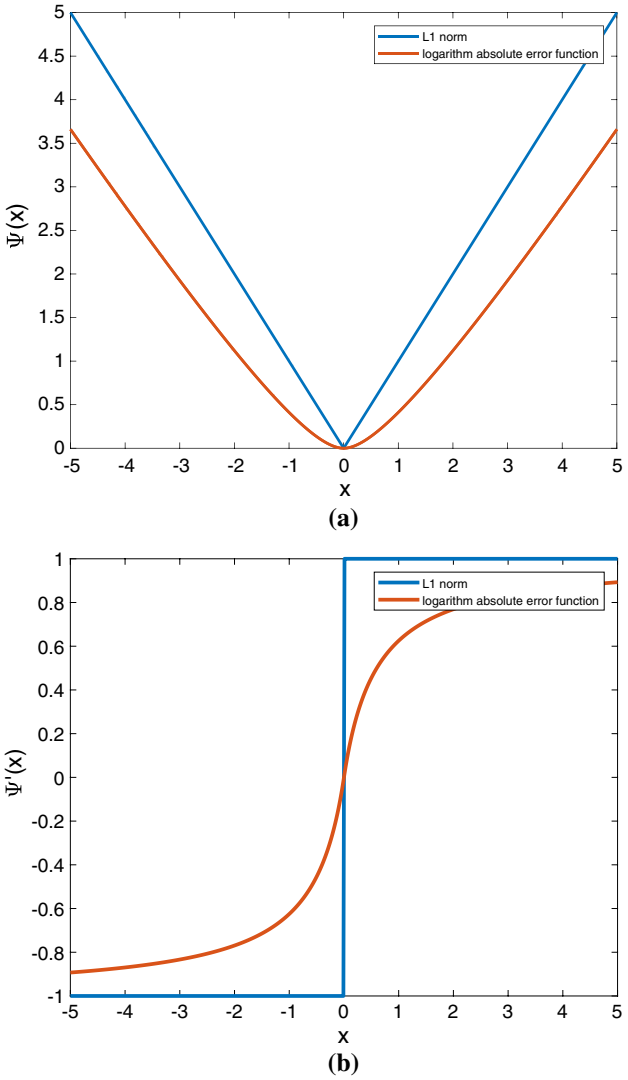

Fig. 2 Comparison curves. **a** L_1 norm and logarithm absolute error function, **b** the derivatives of L_1 norm (blue line) and the derivatives of logarithm absolute error function (orange line)

Proposed method

The noise in real pre-stack seismic data can come from various sources, such as wind motion, poorly planted geophones, or electrical noise, and some of this seismic random noise invariably exhibits spike-like characteristics (Liu et al. 2009). Although the noise produced in seismic data acquisition has been partly eliminated in the denoising process, there are also some noise produced in seismic data processing, such as normal moveout (NMO) correction. The outlier may not get corrected quite enough while its neighbors might be slightly NMO over-correction or under-correction. So, it is important to research robust inversion algorithm.

These L_2 norm loss function methods for AVO inversion usually suffer from drawback that they are highly sensitive to outlier errors. Many studies have shown that L_1 norm-based methods are less affected by outlier errors (Li and Zhang 2017; Guitton and Verschuur 2004). However, L_1 norm method has singularity problem at zero point. Based on the fact above, we propose a new robust data-driven-based regularization method with logarithm absolute error loss function for AVO inversion.

In order to avoid the singularity, we propose the logarithm absolute error loss function:

$$\Psi\Psi(\boldsymbol{e}) = \sum_{i=1}^{N} \left(|e_i|_1 - \alpha ln\left(1 + \frac{1}{\alpha}|e_i|_1\right)\right) \tag{12}$$

where e_i represents the ith component of error vector $\boldsymbol{e}$, N is the length of vector $\boldsymbol{e}$ and $\alpha > 0$ is a design parameter.

Compared to the L_1 norm of error vector(i.e., $\|\boldsymbol{e}\|_1 = \sum_{i=1}^{N} |e_i|_1$), the proposed logarithm absolute error loss function introduces a penalty term in L_1 norm. From Fig. 2a, b, we can see that the logarithm absolute error function solves the problem of non-differentiable at zero point by incorporating the logarithm penalty function into L_1 norm.

Now, we rewrite the forward matrix $\boldsymbol{G}$ and seismic data $\boldsymbol{d}$ in the following form

$$\begin{aligned} \boldsymbol{G} &= \left[\boldsymbol{G}_1, \boldsymbol{G}_2, \ldots, \boldsymbol{G}_N\right]^{\mathrm{T}} \\ \boldsymbol{d} &= \left[d_1, d_2, \ldots, d_N\right]^{\mathrm{T}} \end{aligned} \tag{13}$$

where $\boldsymbol{G}_i$ and d_i represent the ith row of forward matrix $\boldsymbol{G}$ and seismic data $\boldsymbol{d}$, respectively. Thus, we can rewrite the error e_i as

$$e_i = d_i - \boldsymbol{G}_i \boldsymbol{m} \tag{14}$$

To be concrete, the proposed objective function for AVO inversion is formulated as

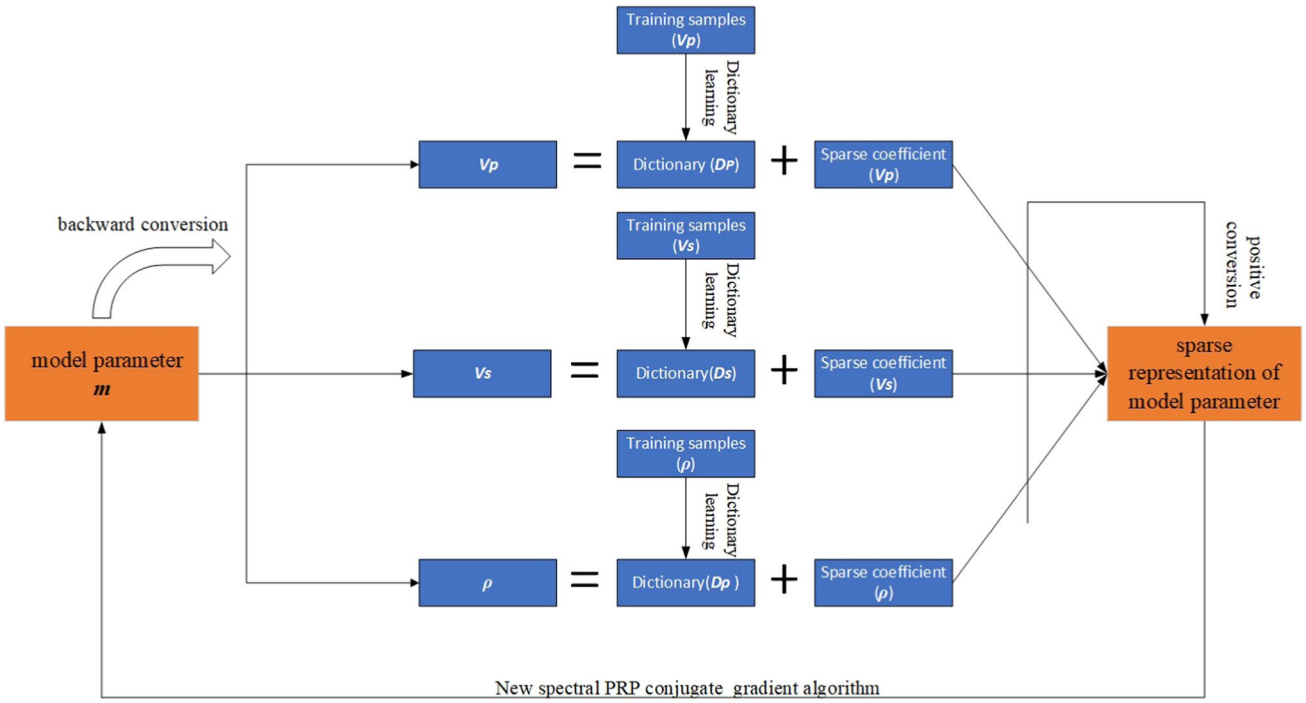

Fig. 3 The flowchart of the whole inversion process

$$
\begin{aligned}
\boldsymbol{J} = & \sum_{i=1}^{N}\left(|e_i|_1 - \alpha ln\left(1+\frac{1}{\alpha}|e_i|_1\right)\right) \\
& + \lambda_1 \sum_{i=1}^{n}\left\|\boldsymbol{R}^i_{LP}\boldsymbol{m} - \boldsymbol{m}^i_{LP}\right\|_2^2 \\
& + \lambda_2 \sum_{i=1}^{n}\left\|\boldsymbol{R}^i_{\Delta LS}\boldsymbol{m} - \boldsymbol{m}^i_{\Delta LS}\right\|_2^2 \\
& + \lambda_3 \sum_{i=1}^{n}\left\|\boldsymbol{R}^i_{\Delta LD}\boldsymbol{m} - \boldsymbol{m}^i_{\Delta LD}\right\|_2^2
\end{aligned} \tag{15}
$$

Minimizing the objective function is difficult because of its high nonlinearity. It is well-known that the conjugate gradient methods are successful methods for solving the large-scale optimization problems due to their simplicity and low storage. Recently, the most widely used conjugate gradient method is the Polak–Ribière–Polyak (PRP) conjugate gradient algorithm. However, the search direction of PRP method is not always a descent direction. Therefore, to make the proposed scheme tractable, we adopt new spectral PRP conjugate gradient algorithm (Wan et al. 2011) to minimize the objective function. More specifically, the iterative process is given by

$$
\boldsymbol{m}_{k+1} = \boldsymbol{m}_k + \mu \boldsymbol{p}_k \tag{16}
$$

where k denotes the kth iteration, μ is iterative step length and $\boldsymbol{p}_k$ is the search direction defined by

$$
\boldsymbol{p}_k = \begin{cases} -\boldsymbol{g}_k, & \text{if } k = 0 \\ -\theta_k \boldsymbol{g}_k + \beta_k^{\mathrm{PRP}} \boldsymbol{p}_{k-1}, & \text{if } k > 0 \end{cases} \tag{17}
$$

In this search direction, the $\beta_k^{\mathrm{PRP}} \in \mathbb{R}$ represents PRP conjugate gradient parameter

$$
\beta_k^{\mathrm{PRP}} = \frac{(\boldsymbol{g}_{k+1} - \boldsymbol{g}_k)^{\mathrm{T}} \boldsymbol{g}_{k+1}}{\boldsymbol{g}_k^{\mathrm{T}} \boldsymbol{g}_k} \tag{18}
$$

and

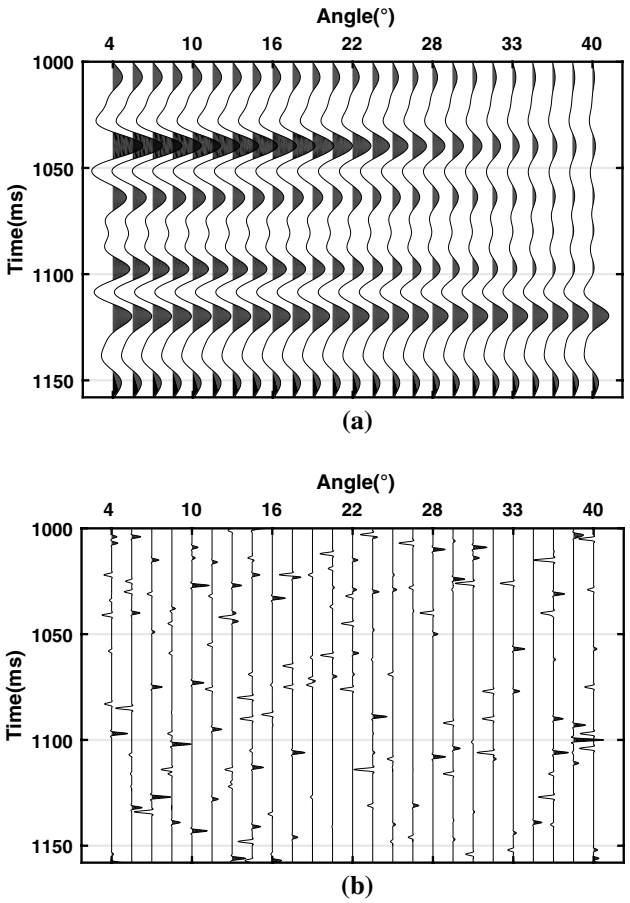

Fig. 5 **a** Synthetic angle gathers; **b** outlier noise with Pr = 0.05

$$
\theta_k = \frac{\boldsymbol{p}_{k-1}^{\mathrm{T}} \boldsymbol{y}_{k-1}}{\left\|\boldsymbol{g}_{k-1}\right\|^2} - \frac{\boldsymbol{p}_{k-1}^{\mathrm{T}} \boldsymbol{g}_k \boldsymbol{g}_k^{\mathrm{T}} \boldsymbol{g}_{k-1}}{\left\|\boldsymbol{g}_k\right\|^2 \left\|\boldsymbol{g}_{k-1}\right\|^2} \tag{19}
$$

and $\boldsymbol{g}_k$ is gradient of the object function

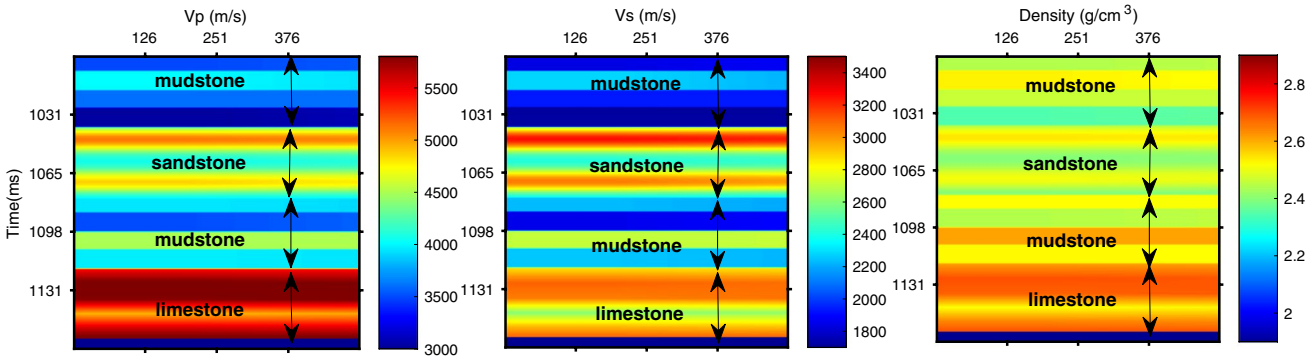

Fig. 4 The multiple lithology model is made up by four segments. Besides, these three subfigures represent P-wave velocity, S-wave velocity and density, respectively

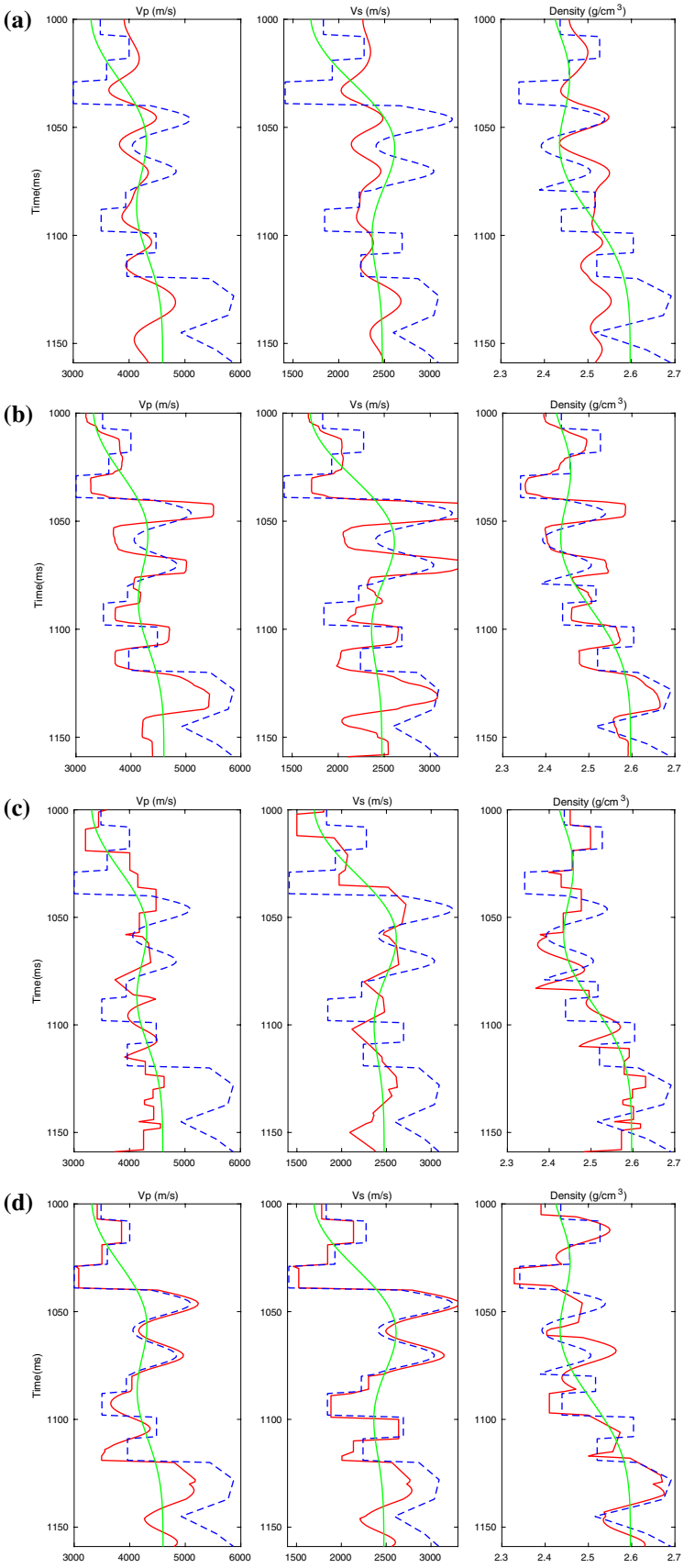

Fig. 6 The retrieved P-wave velocity, S-wave velocity and density using **a** TK, **b** TV, **c** DDI-L2 and **d** DDI-Log methods. (The blue dotted line in each figure shows the true parameter, the green solid line shows the initial model and the red solid line shows the inverted parameter)

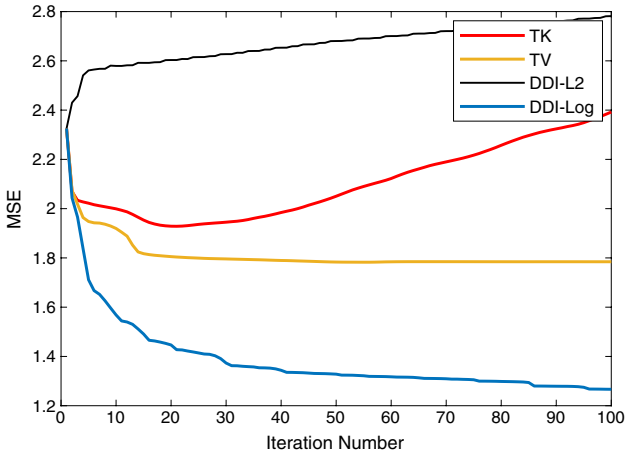

Fig. 7 The convergence curves comparison of the TK, TV, DDI-L2 and DDI-Log methods

$$\begin{aligned}\boldsymbol{g}_k = &\sum_{i=1}^{N}\frac{-\boldsymbol{G}_i e_{k,i}}{\alpha+\left|e_{k,i}\right|}+\lambda_1\sum_{i=1}^{n}(\boldsymbol{R}_{LP}^{i})^{\mathrm{T}}(\boldsymbol{R}_{LP}^{i}\boldsymbol{m}_k-\boldsymbol{m}_{LP(k)}^{i})\\&+\lambda_2\sum_{i=1}^{n}(\boldsymbol{R}_{\Delta LS}^{i})^{\mathrm{T}}(\boldsymbol{R}_{\Delta LS}^{i}\boldsymbol{m}_k-\boldsymbol{m}_{\Delta LS(k)}^{i})\\&+\lambda_3\sum_{i=1}^{n}(\boldsymbol{R}_{\Delta LD}^{i})^{\mathrm{T}}(\boldsymbol{R}_{\Delta LD}^{i}\boldsymbol{m}_k-\boldsymbol{m}_{\Delta LD(k)}^{i})\end{aligned}\tag{20}$$

where $\boldsymbol{m}_{LP(k)}^{i}$, $\boldsymbol{m}_{\Delta LS(k)}^{i}$ and $\boldsymbol{m}_{\Delta LD(k)}^{i}$ are the sparse representation of the ith patch of model parameters at the kth iteration. In particular, the low-frequency model (the initial model) is very important for geophysical inversion problems, which are characterized by ill-posedness (Yuan et al. 2019). Thus, to reduce the instability and recover the low-frequency components of the models, we use a common strategy to guess the initial model $\boldsymbol{m}_0$ from the known well-log data. We will find that every iteration needs an OMP operation if we use formula (20) to update the model parameters directly. In fact, this is time-consuming and unnecessary. Therefore, we update the model parameters using internal and outer loop manners. That is to say, the update method consists of two main loops, an outer loop to update $\boldsymbol{m}_{LP(k)}^{i}$, $\boldsymbol{m}_{\Delta LS(k)}^{i}$ and $\boldsymbol{m}_{\Delta LD(k)}^{i}$ and an inner loop to obtain model parameters using the new spectral PRP conjugate gradient algorithm. Assuming that the whole iteration process includes Q outer loop iterations and K inner loop iterations, the gradient of qth outer loop iteration and kth inner loop iteration can be rewritten as

$$\begin{aligned}\boldsymbol{g}_{(q-1)K+k} = &\sum_{i=1}^{N}\frac{-\boldsymbol{G}_i e_{(q-1)K+k,i}}{\alpha+\left|e_{(q-1)K+k,i}\right|}\\&+\lambda_1\sum_{i=1}^{n}(\boldsymbol{R}_{LP}^{i})^{\mathrm{T}}(\boldsymbol{R}_{LP}^{i}\boldsymbol{m}_{(q-1)K+k}-\boldsymbol{m}_{LP(q)}^{i})\\&+\lambda_2\sum_{i=1}^{n}(\boldsymbol{R}_{\Delta LS}^{i})^{\mathrm{T}}(\boldsymbol{R}_{\Delta LS}^{i}\boldsymbol{m}_{(q-1)K+k}-\boldsymbol{m}_{\Delta LS(q)}^{i})\\&+\lambda_3\sum_{i=1}^{n}(\boldsymbol{R}_{\Delta LD}^{i})^{\mathrm{T}}(\boldsymbol{R}_{\Delta LD}^{i}\boldsymbol{m}_{(q-1)K+k}-\boldsymbol{m}_{\Delta LD(q)}^{i})\end{aligned}\tag{21}$$

In the process of updating model parameters, the choice of step size is also critical. Small step size will result in low steady-state error and slow convergence speed, and large step size may lead to fast convergence speed and unstable convergence results. To ensure convergence, sufficient decrease and discard unacceptably short steps, the step length μ is obtained by the Wolfe-type line search (Sun and Yuan 2006):

$$\boldsymbol{J}(\boldsymbol{m}_k+\mu\boldsymbol{p}_k)\le\boldsymbol{J}(\boldsymbol{m}_k)+\zeta_1\mu\nabla\boldsymbol{J}(\boldsymbol{m}_k)^{\mathrm{T}}\boldsymbol{p}_k\tag{22}$$

$$\left\|\nabla\boldsymbol{J}(\boldsymbol{m}_k+\mu\boldsymbol{p}_k)^{\mathrm{T}}\boldsymbol{p}_k\right\|_1\le\zeta_2\left\|\nabla\boldsymbol{J}(\boldsymbol{m}_k)^{\mathrm{T}}\boldsymbol{p}_k\right\|_1\tag{23}$$

where $0<\zeta_1<\zeta_2<1$, $\|\cdot\|_1$ is L_1 norm, ζ_1 and ζ_2 are chosen as 0.0001 and 0.9, respectively. A flowchart of the whole inversion process can be found in Fig. 3.

Numerical examples

In this section, we will compare the proposed data-driven inversion method with logarithm absolute error loss function (DDI-Log) with data-driven inversion with L_2 norm (DDI-L2), TK and TV methods using synthetic data and field data.

Synthetic data examples

First, we use a multiple lithology model (MLM) (She et al. 2019a) as an example. The MLM of size 160×500 consists of three different kinds of lithologies with different structural features, including mudstone (block), sandstone (smooth) and limestone (linear gradient). As shown in Fig. 4, from top to bottom, the lithologies are mudstone, sandstone, mudstone and limestone. For each trace, the synthetic data are generated by forward model (1) with 30-Hz Ricker wavelet. In order to test the robustness of the proposed method, Bernoulli–Gaussian (BG) noise with signal-to-noise ratio (SNR) of 4dB and Pr = 0.05

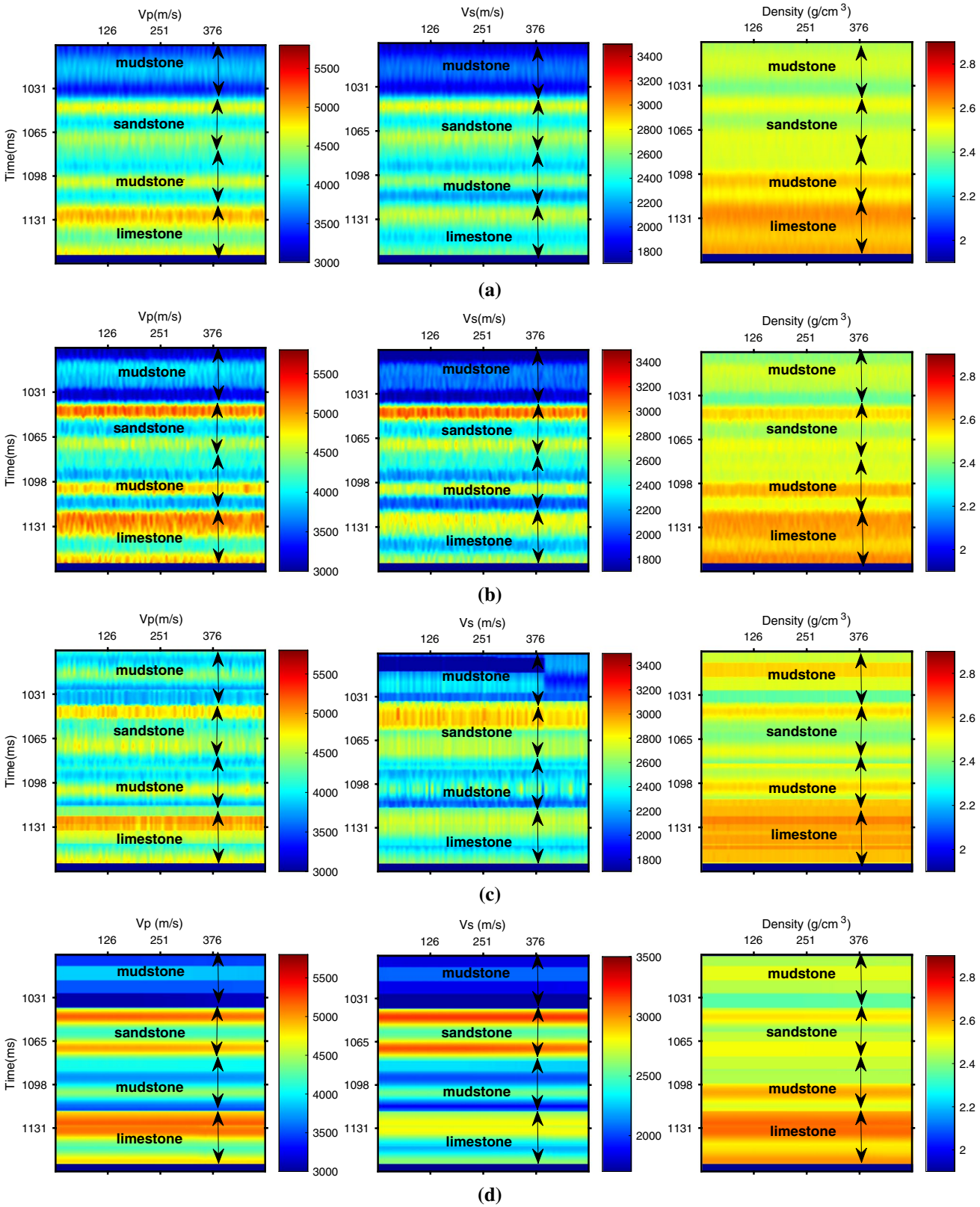

Fig. 8 The retrieved P-wave velocity, S-wave velocity and density profiles of the MLM. Where **a** TK, **b** TV, **c** DDI-L2 and **d** DDI-Log

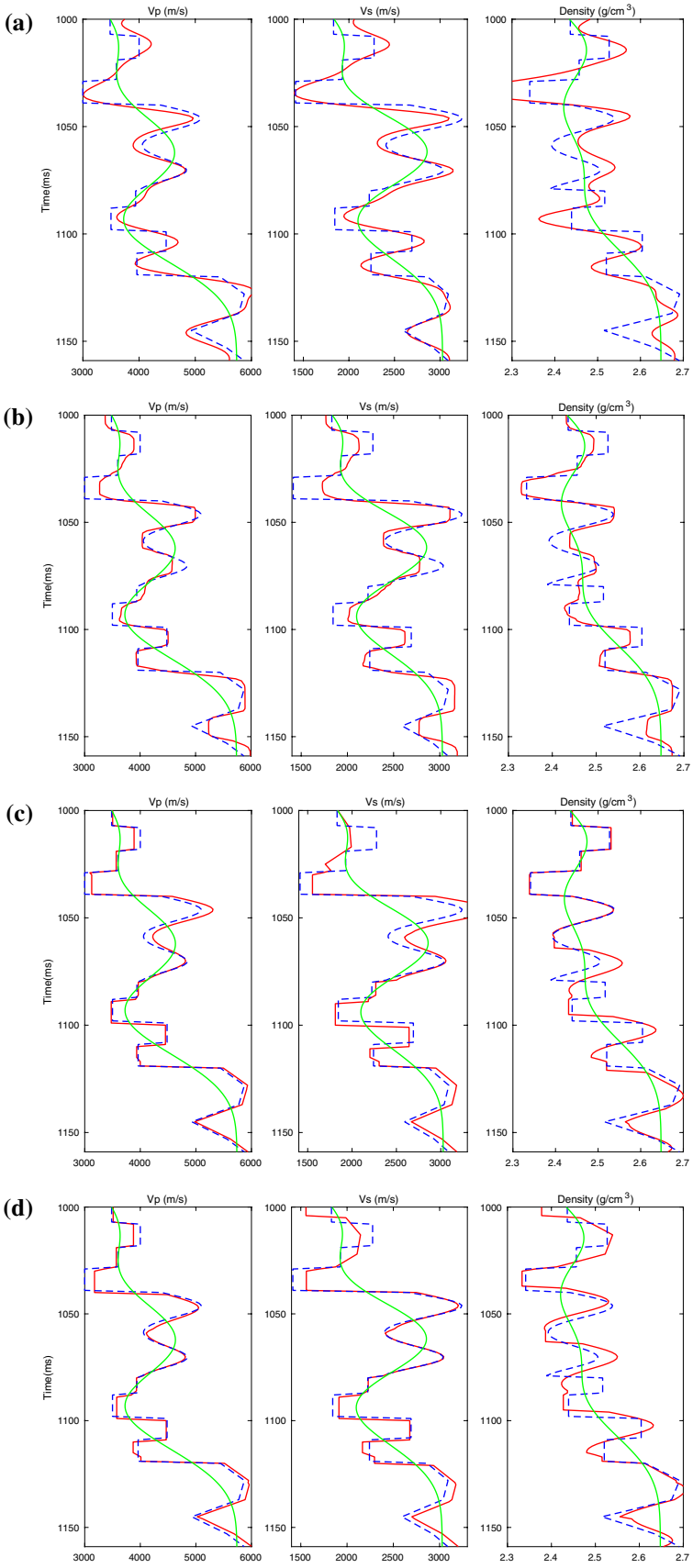

Fig. 9 The retrieved P-wave velocity, S-wave velocity and density using **a** TK, **b** TV, **c** DDI-L2 and **d** DDI-Log methods at the condition of SNR = 5 Gaussian noise (The blue dotted line in each figure shows the true parameter, the green solid line shows the initial model and the red solid line shows the inverted parameter)

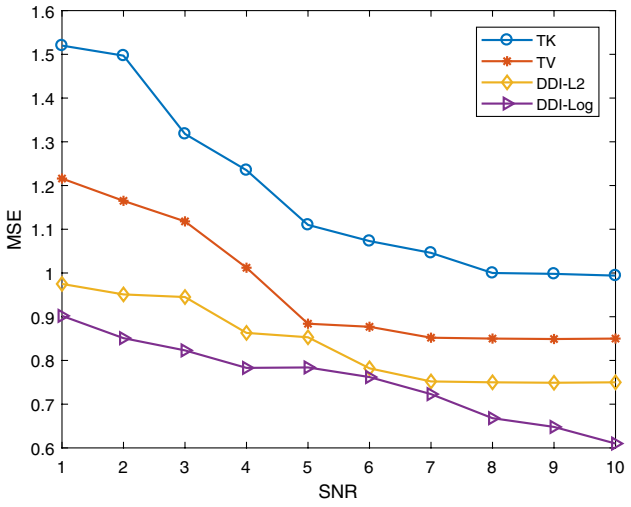

Fig. 10 A plot of average MSE over 10 runs versus SNR for TK (blue circle line), TV (orange star line), DDI-L2 (yellow diamond line) and DDI-Log (purple right triangle line)

is added to the synthetic data. Taking the 128th trace for example, the synthetic data are shown in Fig. 5a. As is shown in Fig. 5b, the BG noise here is used for modeling the outlier noise. This signal is generated as the product of a Bernoulli process and a Gaussian process such that $n(k) = B(k)G(k)$, where $G(k)$ is a white Gaussian random sequence with a mean of zero and variance δ^2, and $B(k)$ is a Bernoulli process with the probability mass function given as $P(B) = 1 - Pr$ for $B = 0$, and $P(B) = Pr$ for $B = 1$, where Pr is a probability that satisfies values of $0 < Pr \leq 1$.

We adopt the same parameter settings as those in She et al. (2018). Considering the MSE and computation cost, we finally choose dictionary size 30×2000 with corresponding sparsity level $K = 1$. Also, we set regularization parameters λ_1, λ_2 and λ_3 to be the same (denoted by λ). In these methods mentioned above, we employ the L-curve criterion to determine the regularization parameter. With regard to parameter α, we use a small value 0.001 to avoid the singularity problem of L_1 norm.

Taking the 128th trace for example, Fig. 6 displays the AVO inversion results for the elastic parameters when the synthetic data are contaminated by outlier noise, and Fig. 6a–d shows the results of TK, TV, DDI-L2 and DDI-Log methods, respectively. Curves in blue dotted lines, respectively, denote original real P-wave velocity, S-wave velocity and density. The green lines and red solid lines are initial models and inversion results, respectively. As can be seen, the TK and DDI-L2 methods give the worst inversion results when the observed data are polluted by outlier noise. The results also indicate that these two methods are highly sensitive to outlier noise. On the other hand, with the inaccuracy of inversion parameters, the sparse representation process cannot accurately affect the geological structure. Thus, the inappropriate sparse representation in turn affects inversion results. So, we will find that the inversion results of DDI-L2 method are worse than TK method. The TV regularization method can mitigate the outlier noise to some extent. But, this TV method is only good for blocky geological structure and is inappropriate for geological areas with different geological features. Compared to TK, TV and DDI-L2 methods, the proposed DDI-Log method can suppress outlier noise and can protect complex geological structure characteristics. The MSE (the mean square error of model parameters) curves shown in Fig. 7 also indicate the proposed method is robust to outlier noise and converges to a satisfying solution. However, the other three methods give relatively poor inversion results and convergence performance. Next, we will show profile inversion results (shown in Fig. 8) of these four methods. Compared with the other three methods, the inversion results of the proposed DDI-Log algorithm are significantly better in the degree of consistency with the real model.

At last, we will test the robustness of the proposed algorithm under the condition of Gaussian noise, because the seismic data also contain the frequent occurrence of Gaussian noise. As can be seen from the inversion results shown in Fig. 9, the DDI-L2 and DDI-Log methods can grasp different structures more accurately. The proposed algorithm has higher accuracy compared with DDI-L2. In addition, Fig. 10 illustrates the statistical performance with respect to different noise conditions. It can be markedly noted that the DDI-Log method is better than the other three methods.

Field data example

In this section, the field pre-stack seismic data of Anyue work area from Western China are used to test the applicability of the proposed algorithm. In this work area, we use 12 well-logs to train dictionary. Next, we apply the learned dictionary to other trace because of the similarity and lateral continuity within a certain range. First, we focus on real well-logs inversion as is shown in Fig. 11. It is worth noting that the proposed algorithms have more similar trends compared with the other three methods. Afterward, we focus on inversion profile. Figure 12 shows the inverted P-wave velocity profile, S-wave velocity profile and density profile using (a) TK, (b) TV, (c) DDI-L2 and (d) DDI-Log methods, respectively. From these inversion results, we will find that the layered structure of TK

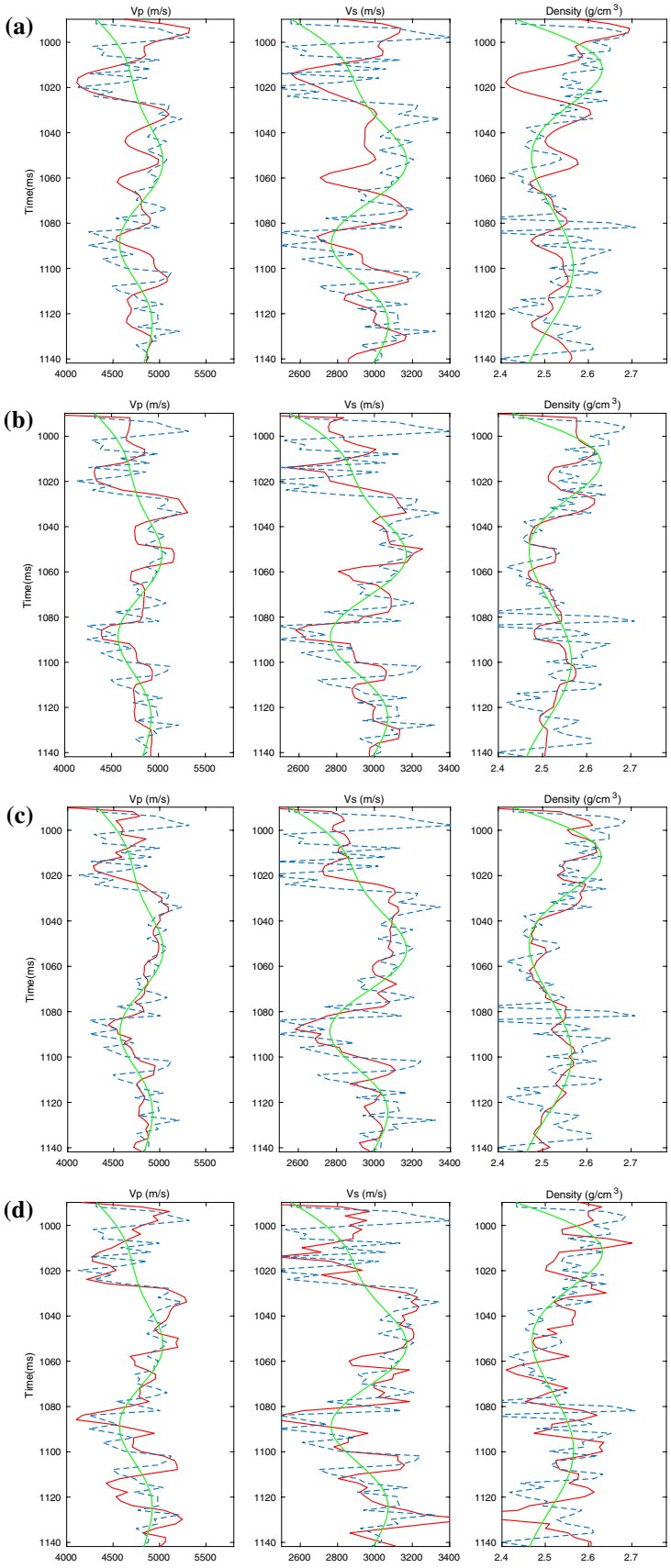

Fig. 11 The retrieved P-wave velocity, S-wave velocity and density using **a** TK, **b** TV, **c** DDI-L2 and **d** DDI-Log methods, respectively (the blue dotted line in each figure shows the true parameter, the green solid line shows the initial model and the red solid line shows the inverted parameter)

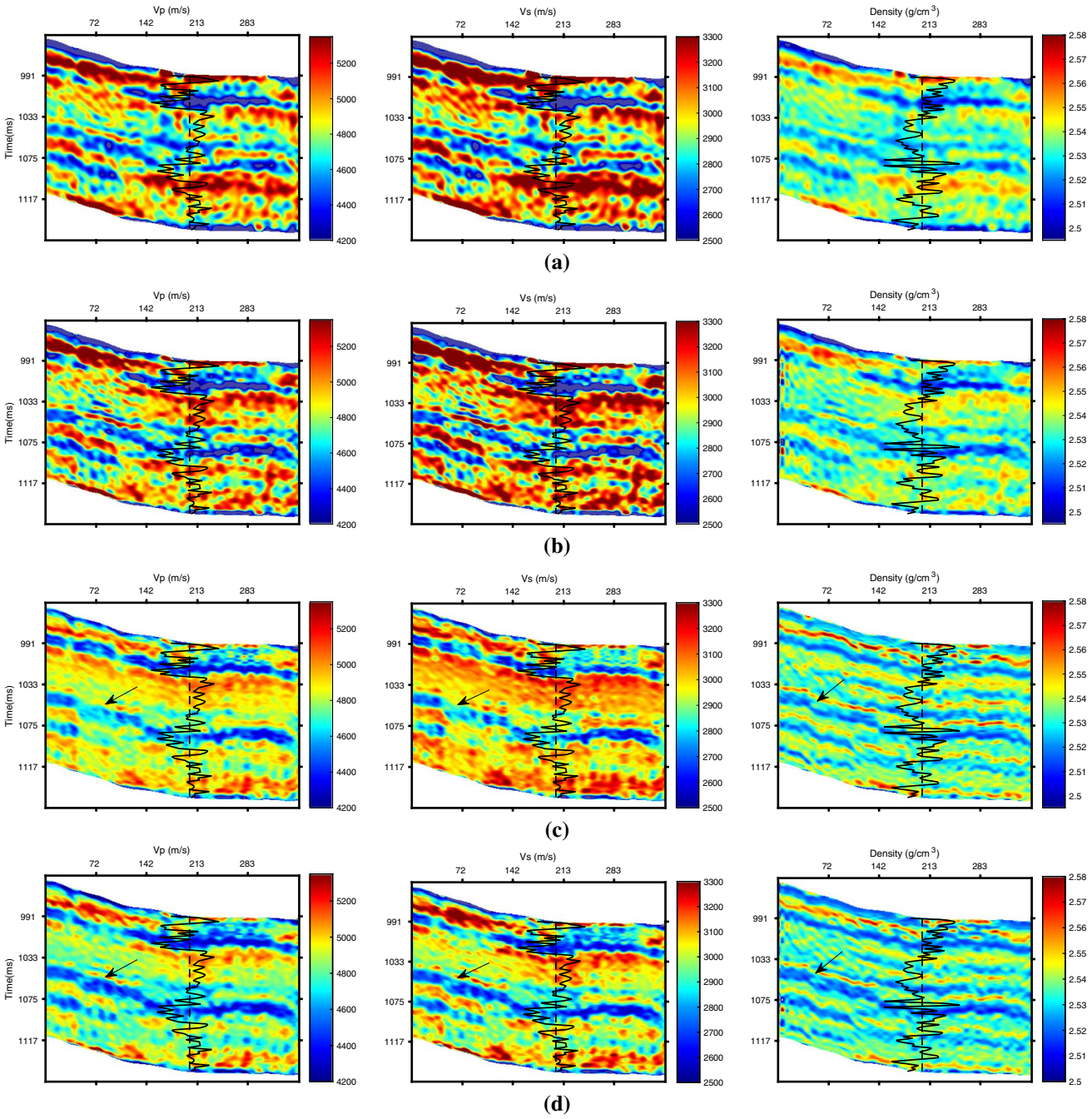

Fig. 12 The inverted P-wave velocity, S-wave velocity, density profile using **a** TK, **b** TV, **c** DDI-L2 and **d** DDI-Log methods, respectively

and TV methods is disorganized. Instead, the DDI-L2 and DDI-Log methods have much better lateral continuity and consistency with the real well-log (black curve). However, compared with DDI-L2, the proposed method has higher resolution and lateral continuity as shown in the black arrows. The inversion results of the proposed algorithm can better distinguish the upper and lower interfaces of geological bodies. These tests demonstrate that the proposed method is effective and reliable.

Conclusion

In this letter, we propose a robust data-driven-based regularization method with logarithm absolute error loss function for AVO inversion. The data-driven-based regularization method has drawn a lot of attention because it can tackle complex geology. However, the inversion result is instable when the pre-stack seismic data are contaminated by outlier noise. Thus, we utilize the logarithm absolute error function as the

loss function. In addition, the new loss function can avoid singularity problem. To minimize this objective function, a simplicity and low-storage spectral PRP conjugate gradient algorithm is used. The synthetic examples verify that the proposed method can address outlier noise problem and can improve inversion accuracy. Field seismic data tests also illustrate that the proposed method has higher inversion resolution.

Acknowledgements This work was supported by the National Nature Science Foundation of China (Grant: 61271341 and U1562218).

References

Aharon M, Elad M, Bruckstein A (2006) K-SVD: an algorithm for designing overcomplete dictionaries for sparse representation. IEEE Trans Signal Process 54(11):4311–4322

Aki K, Richards PG (2002) Quantitative seismology. University Science Books

Anagaw AY, Sacchi MD (2011) Full waveform inversion with total variation regularization. In: Recovery-CSPG CSEG CWLS convention

Buland A, Omre H (2003) Bayesian linearized avo inversion. Geophysics 68(1):185–198

Epanomeritakis I, Akçelik V, Ghattas O, Bielak J (2008) A Newton-CG method for large-scale three-dimensional elastic full-waveform seismic inversion. Inverse Probl 24(3):034015

Fan C, Song Y, Zhang Y, Jiang Z (2015) An amplitude-normalized pseudo well-log construction method and its application on avo inversion in a well-absent marine area. Acta Geophys 63(3):761–775

Fujin Z, Jiashu Z (2013) Linear discriminant analysis based on l1-norm maximization. IEEE Trans Image Process 22(8):3018–3027

Gholami A (2015) Nonlinear multichannel impedance inversion by total-variation regularization. Geophysics 80(5):R217–R224

Guitton A, Verschuur D (2004) Adaptive subtraction of multiples using the l1-norm. Geophys Prospect 52(1):27–38

Hampson DP, Russell BH, Bankhead B (2005) Simultaneous inversion of pre-stack seismic data. In: SEG technical program expanded abstracts 2005, Society of Exploration Geophysicists, pp 1633–1637

Ji J (2006) Hybrid L1/L2 norm IRLS method with application to velocity-stack inversion. In: 68th EAGE Conference and Exhibition incorporating SPE EUROPEC 2006

Li C, Zhang F (2017) Ava inversion based on the L1-norm-based likelihood function and the total variation regularization constraint. Geophysics 82(3):1–54

Li Z, Hu G, She B (2017) A hybrid regularization approach for AVA inversion of the piecewise smooth model

Liu Y, Liu C, Wang D (2009) A 1d time-varying median filter for seismic random, spike-like noise elimination. Geophysics 74(1):V17–V24

Liu Y, Zhang J, Hu G (2015) Iterative reweighted least m-estimate avo inversion. Explor Geophys 46(2):159–167

Pyun S, Son W, Shin C (2009) Frequency-domain waveform inversion using an l 1-norm objective function. Explor Geophys 40(2):227–232

Sen MK, Roy IG (2003) Computation of differential seismograms and iteration adaptive regularization in prestack waveform inversion. Geophysics 68(6):2026–2039

She B, Wang Y, Liang J, Liu Z, Song C, Hu G (2018) A data-driven amplitude variation with offset inversion method via learned dictionaries and sparse representation. Geophysics 83(6):R725–R748

She B, Wang Y, Liang J, Hu G (2019a) Data-driven simultaneous seismic inversion of multiparameters via collaborative sparse representation. Geophys J Int 218(1):313–332

She B, Wang Y, Zhang J, Wang J, Hu G (2019b) Avo inversion with high-order total variation regularization. J Appl Geophys 161:167–181

Siahsar MAN, Gholtashi S, Kahoo AR, Wei C, Chen Y (2017) Data-driven multi-task sparse dictionary learning for noise attenuation of 3d seismic data. Geophysics 82(6):V385–V396

Sun J, Li Y (2014) Adaptive lp inversion for simultaneous recovery of both blocky and smooth features in a geophysical model. Geophys J Int 197(2):882–899

Sun W, Yuan YX (2006) Optimization theory and methods: nonlinear programming, vol 1. Springer, Berlin

Tao L, Jiang X, Li Z, Liu X, Zhou Z (2019) Multiscale incremental dictionary learning with label constraint for sar object recognition. IEEE Geosci Remote Sens Lett 16(1):80–84

Wan Z, Yang Z, Wang Y (2011) New spectral PRP conjugate gradient method for unconstrained optimization. Appl Math Lett 24(1):16–22

Yuan S, Wang S, Luo C, He Y (2015) Simultaneous multitrace impedance inversion with transform-domain sparsity promotion. Geophysics 80(2):R71–R80

Yuan S, Wang S, Luo C, Wang T (2018) Inversion-based 3-d seismic denoising for exploring spatial edges and spatio-temporal signal redundancy. IEEE Geosci Remote Sens Lett 15(11):1682–1686

Yuan S, Wang S, Luo Y, Wei W, Wang G (2019) Impedance inversion by using the low-frequency full-waveform inversion result as an a priori model. Geophysics 84(2):R149–R164

Zhang Z, Chunduru RK, Jervis MA (2000) Determining bed boundaries from inversion of em logging data using general measures of model structure and data misfit. Geophysics 65(1):76–82

Zhang J, Lv S, Liu Y, Hu G (2013) Avo inversion based on generalized extreme value distribution with adaptive parameter estimation. J Appl Geophys 98:11–20

Zhou Y, Gao J, Chen W, Frossard P (2016) Seismic simultaneous source separation via patchwise sparse representation. IEEE Trans Geosci Remote Sens 54(9):5271–5284

Zong Z, Li K, Yin X, Zhu M, Du J, Chen W, Zhang W (2017) Broadband seismic amplitude variation with offset inversion. Geophysics 82(3):M43–M53

Acta Geophysica (2020) 68:459–475
https://doi.org/10.1007/s11600-020-00401-8

REVIEW ARTICLE - HYDROLOGY

On the main components of landscape evolution modelling of river systems

Michael Nones[1]

Received: 31 July 2019 / Accepted: 8 January 2020 / Published online: 23 January 2020

Abstract
Currently, the use of numerical models for reproducing the evolution of river systems and landscapes is part of the day-by-day research activities of fluvial engineers and geomorphologists. However, despite landscape evolution modelling is based on a rather long tradition, and scientists and practitioners are studying how to schematize the processes involved in the evolution of a landscape since decades, there is still the need for improving the knowledge of the physical mechanisms and their numerical coding. Updating past review papers, the present work focuses on the first aspect, discussing six main components of a landscape evolution model, namely continuity of mass, hillslope processes, water flow, erosion and sediment transport, soil properties, vegetation dynamics. The more common schematizations are discussed in a plain language, pointing out the current knowledge and possible open questions to be addressed in the future, towards an improvement of the reliability of such kind of models in describing the evolution of fluvial landscapes and river networks.

Keywords Basin erosion · Landscape evolution model · Numerical modelling · Surface processes · River networks

Introduction

The present paper reviews the state of the art about modelling of landscape evolution, with a particular focus on the main components typically schematized in numerical codes that can be applied for modelling fluvial terrains shaped by the interaction of internal and external processes, such as precipitation, water flow and sediments, as well as vegetation and soil properties. Nowadays, often the term "model" refers to both the underlying theory and the computer programs used to calculate approximate solutions of the governing equations, involving possible misunderstandings. Numerical models represent an indispensable tool for assisting geomorphologists in reproducing the origins and dynamics of surface landscapes, combining a quantitative characterization of terrain with various theories describing the modification of river system topography by the variety of processes that sculpt it (Mark 1975; Tucker and Hancock 2010; Baas 2017).

✉ Michael Nones
mnones@igf.edu.pl

[1] Department of Hydrology and Hydrodynamics, Institute of Geophysics, Polish Academy of Science, Ksiecia Janusza 64, 01-452 Warsaw, Poland

In the last decades, the ability of engineers and geomorphologists to measure the topography of river beds and hillslopes has grown tremendously, moving from topography maps, very imprecisely and requiring a massive work to be revised, towards digital elevation models and digital maps, generally having a higher resolution and covering the majority of the emerged landmasses (Gesch et al. 2006), and more easily updatable. In addition, the recent development of high-resolution mapping tools like laser scanners and cameras, as well as satellites, assured a detailed and reliable description of the changes of the Earth's surface, also in regions where the access could be more complicated. At the same time, theories and models of landscape evolution have grown, accounting for more processes and for a more sophisticated description of them. As recently as the second half of the last century, a landscape evolution model was intended as the sequential evolution of a landscape over the geological time. By the end of the century, this term had been associated with a more scientific meaning: a mathematical theory describing how the actions of a multitude of geomorphic processes interact during the time to shape the basin topography.

Aside from their physical meaning, the complexity of the governing equations of landscape evolution requires a numerical solution method to be solved in a closed form.

The growing complexity introduced in landscape evolution models, accompanied by the advances in computing techniques and acquisition of topographic data, has revolutionized the ability of geomorphologists and fluvial engineers to measure and model landforms and their rate of change, as well as to investigate and numerically reproduce how such forms and dynamics arise from the physics of geomorphic processes (Coulthard 2001; Chen et al. 2014; Willgoose 2018).

In geophysics, primary drivers are generally described by means of a system of partial differential equations, which originate from the classical mechanical theory (e.g. equations describing water and sediment transport, rock mechanics, heat transfer, river hydraulics). The scale dependence of such processes complicates the analysis of feedbacks and interactions between them (Bracken et al. 2015). Therefore, depending on the representation scale, models can be computationally intensive and thus typically limited to a small spatial scale of few metres if strictly adherent to the theory, or addressing large scales problems like the evolution of a whole river basin (10^2–10^5 km^2) with a reduced computational effort, but introducing simplified equations (Khosronejad et al. 2014; Larsen et al. 2016). For addressing problems acting at the landscape scale and therefore involving a great number of coupled state variables, a variety of approaches and methodologies is nowadays available. Currently, in fact, landscape evolution models can combine hillslope, channel, tectonic and vegetation processes by linking physically based equations, which represent simplifications of the real world (e.g. De St. Venant equations for the water flow, geomorphic transport laws, erosion/deposition and sediment transport equations), with semiempirical approaches (e.g. organic accumulation, vegetation growth, the presence of external drivers like fire or wind). In addition, these models are able to couple stochastic (e.g. probabilities of sediment detachment, vegetation encroachment and density, distribution of precipitation) and deterministic (e.g. water flow velocities, bank failure) dynamics (Willgoose 2005; Fagherazzi et al. 2012).

Typically, many of the most used landscape evolution models are run over large domains and are therefore computationally intensive (Salles 2016). Consequently, geoscientists are facing the challenge of reducing the computational effort to a minimal level for performing more effectively. As an example, Stark and Passalacqua (2014) developed a simplified landscape evolution model as a set of coupled dynamic systems, aiming to evaluate the changes of biomass and regolith under mass wasting and run-off erosion. An even more simplified approach was proposed by Franzoia and Nones (2017) and tested by Nones et al. (2019), who described the very long-term evolution of a river watershed by applying, at the watershed scale, a 0-D lumped hydromorphological model. The popular, alternative strategy of cellular automata modelling involves describing the physics governing fluid flow or sediment transport by means of discrete rules that control water, air and sediment transport processes on the basis of information from surrounding model grid cells (Willgoose et al. 1991; Liu and Coulthard 2017). This cellular automata strategies have made it possible to reproduce shallow-water flows for hydrological purposes (Adams et al. 2017; Caviedes-Voullième et al. 2018), but also to simulate the development of braided streams (Murray and Paola 2003), floodplains (Coulthard and Van De Wiel 2006), sand dunes (Zhang et al. 2012), wetland landscape pattern (Williams et al. 2016) and river deltas (Liang et al. 2016), for evaluating their response to global changes and human drivers. Aside from cellular automata, precipiton methods can be applied for simulating the evolution of a river landscape, given their ability in mimicking self-organized emerging properties of geomorphological systems, from high-resolution braided patterns to drainage network organization (Davy et al. 2017). Even if based on dissimilar approaches, these two methods have multiple similarities, like the computational effort needed for simulating large domains or the complexity correlated with solving the hydrodynamics in detail.

The rationale of the research

In the 1950s and 1960s, the discipline of geomorphology turned from a qualitative approach, widely applied at the beginning of the XX century, towards a more quantitative analysis of landscape evolution (Kamp and Owen 2013). Starting from the 1970s, there have been a growing number of excellent review papers covering landscape evolution models and various aspects of geomorphic modelling, offering a very wide vision on the field (see, among many others, Carson and Kirkby 1972; Kirkby 1996; Coulthard 2001; Martin and Church 2004; Khosronejad et al. 2014) and proposing several open questions to be addressed in representing the evolution of the Earth's surface through a mathematical model. As stated by Kamp and Owen (2013), mathematical models were and are still paramount in understanding the landscape processes and the feedback between the involved components, and the recent technological development contributed in increasing their use worldwide.

The aim of the present paper is to discuss six main components usually considered in modelling the evolution of river systems, where the major part of sediments generated on the hillslopes is transported through the drainage network by the water flow. On the one part, river basins are the fundamental geomorphic unit (Chorley 1969), and fluvial landscapes cover most of the Earth's surface. On the other part, being one of the most human-impacted environments, they need particular attention and their future evolution should

be addressed with proper methodologies that also account for climate change. For better focusing on river basins, are here not considered additional erosional systems like eolian landscapes, karstified terrains, ocean floors and glacial landscapes. The application of landscape evolution models to river basins can provide additional insights on the physicochemical processes that interact to shape the surface of a fluvial system, transferring the mass from one area to another. Moreover, the opportunity to have a graphical representation of the basin evolution enhances the ability of scientists and non-experts to interpret possible changes of the surface and to quantify the consequences of various hypotheses about fluvial dynamics.

In addition, landscape evolution models can also be applied for evaluating the development of specific features like passive margins (Tucker and Slingerland 1994; Ruetenik et al. 2016; Braun 2018) or mountain chains (Miller and Slingerland 2006). Numerical models can be focused on the long-term evolution of landscape (Bishop 2007) and river systems (Coulthard and Macklin 2001; Di Silvio and Nones 2014; Varrani et al. 2019) or on evaluating tectonics (Beaumont et al. 2000) and other surface processes. Under an environmental point of view, landform evolution models can be used as a methodology for evaluating and managing degraded landscapes such as abandoned mines (Hancock et al. 2000; Hancock and Willgoose 2018) and contaminated sites (Evans 2000), or for projects involving landscapes affected by disturbance of soil and/or vegetation (Coulthard et al. 2002). Because these models allow to visually evaluate the temporal changes of the basin in terms of elevation, catchment size and shape, they can also be applied to support the study of dynamic phenomena like gully network development and valley alluviation or river avulsion, which is generally not possible with fixed-terrain models based on the classic USLE approach (Karydas et al. 2014). In addition, the flexibility of these models permits to evaluate and potentially combine simulations of processes acting at different spatiotemporal scales, spanning from short-term soil loss along single hillslopes (Montgomery and Dietrich 1992; Hancock et al. 2008) to catchment-scale assessments over geologic time (Hancock et al. 2015; Varrani et al. 2019), eventually coupling geomorphic and tectonic models (Beaumont et al. 2000) or accounting for the mobility of the whole river network (Whipple et al. 2017).

Regarding the mathematical description of erosion and transport rate adopted in landscape models, in the past, Carson and Kirkby (1972) discussed a variety of 1-D models of hillslope evolution under different geomorphic scenarios, while Dietrich et al. (2003) provided an overview of rate laws for both hillslope and channel processes. In their reviews on landscape evolution modelling, Coulthard (2001), Chen et al. (2014) and Willgoose (2018) provided a perspective on their strengths and weaknesses, showing that several solutions for reproducing the evolution of terrestrial landscapes exist. Recently, a thorough review on the fundamental equations implied in landscape evolution models was provided by Chen et al. (2014), who pointed out that the numerical implementation is a non-trivial problem, particularly in simulating water flow and sediment transport in an efficient and highly accurate way.

In the past, many contributions were focused on discussing general and philosophical issues relevant to geomorphic modelling. As an example, Carson and Kirkby (1972) firstly and then Kirkby (1996) pointed out the theoretical foundations of the modelling approach adopted in several fluvial landscape evolution models, showing their role in reducing the gap between the theory and the experimental approach. Focusing not only on landscape evolution models but also on the numerical modelling in general, Oreskes et al. (1994) provided a perspective on the codes' structure and problems associated with their verification and validation. Mimicking this approach, other works (Martin and Church 2004; Larsen et al. 2016) showed the limitation of adopting numerical models for describing the nature complexity proposing open questions to be addressed in the future by means of new methodologies.

Moving from the important review proposed by Tucker and Hancock (2010) and maintaining a similar structure because of its effectiveness in driving the message, the present paper summarized their conclusions on the structure and the constitutive equations of landscape evolution models in a relatively simplified way, using a plain language to provide the readers with a general overview rather than with a complex mathematical description of the phenomena involved, as proposed by Chen et al. (2014). Indeed, the review is mostly devoted to students and young researchers that want to understand the basic mechanisms of landscape evolution models, aiming to design their own approach on the problem.

In addition to what was done in previous reviews, this work discusses the importance of soil processes and vegetation dynamics in shaping fluvial landscapes, and the need of a deeper understanding of the feedback between all these processes for adequately implementing them in a numerical code. The next section is divided into six subsections, and each component is analysed individually. In detail, being the basic component of a landscape evolution model, the conservation of mass is firstly reviewed, and then, the hillslope processes are addressed. Two of the main components in landscape evolution models are the water flow and the sediment behaviour (erosion/deposition and transport) and are discussed in the following two subsections. Aside from these four components, which are included in landscape modelling since the very beginning of this research field, for the future, a major effort should be dedicated to evaluating the effects of soil properties and vegetation dynamics in

changing the Earth's surface. Final conclusions and open questions for researchers and scholars are summarized at the end of the manuscript, aiming to provide the readers with possible paths to follow in developing landscape evolution models more capable to reproduce the variety and feedback of mechanisms interrelating in nature.

Simulating the evolution of a river system via a landscape evolution model

To simulate the creation and evolution of a river system, landscape evolution models can be applied. Based on geometrical, morphometric, hydrological and additional (e.g. wind, vegetation, snow, ice, fire, herbivorous) inputs, a landscape evolution model combines such quantities for simulating the future changes of the Earth's surface. These models are based on a system of equations that schematizes the mass continuity, specific geomorphic transport functions for describing the generation and movement of sediments and solutes on the basin hillslopes, as well as to reproduce the erosion phenomenon, the water flow and the transport of water–sediment mixtures along the river network (Dietrich et al. 2003). Depending on the modellers' needs and the structure of the code, a series of numerical methods can be adopted for discretizing the solution in space and time, aiming to obtain more or less approximated solutions of the governing equations.

For adequately reproduce the evolution of a fluvial landscape, the single components should be effectively characterized, as well as the feedback between them. In the following subsections, six main components are described, summarizing the results already available in the literature and pointing out the opportunity to focus the future research on some of them (i.e. vegetation dynamics, soil properties, sediment transport), given that classical mechanisms (i.e. mass continuity, hillslope properties, water flow) are studied since decades (Mark 1975; Tucker and Hancock 2010).

Exchange of mass

Geomorphic systems are rather basic systems, where the mass is conserved absolutely. However, in the case of landscape evolution, there are examples where the mass is not conserved because of sediment detachment, such as models based on stream power erosion formulas (Warren et al. 2019). Moreover, the mass of water is not always conserved, because it also depends on the flow routing assumptions typical of each model. Therefore, in studying the evolution of fluvial landscapes, there are many possible frameworks for addressing the continuity of the mass, depending on the kind of process reproduced, the circumstances under study and the numerical scheme adopted. Given that each of these possible approaches has its own assumptions and limitations, with their pros and cons, system modelling can be considered, to some degree, as a subjective research field. In fact, the included components, the adopted methodology and technology, as well as the modelling schematization, are arbitrarily assumed by the researcher depending on the case study and the research aims, as well as the modeller experience.

In general, the rate of change in a given control volume V can be derived by comparing the mass rate entering the volume with the one going out (Fig. 1). In other words, the process (rate of change) can be computed as a result of the nature and geometry of the idealized model (mass rate difference in–out).

One of the most common continuity expressions in geomorphic models assumes that the control volume can be schematized by means of a vertical column of rock and/or soil. Starting from this general theory, the modeller can introduce multiple simplifications related to the density or the thickness of the considered material, as well as on its porosity and grain size. Several landscape evolution models consider that all the surface is composed by rock or by a combination of rock and sand. In the first case, assuming that the surface height is a single-valued function of the horizontal position involves the impossibility to describe vertical faces and overhangs. In addition, changes in height due to compaction/expansion of the underlying soil are generally ignored, as well as variations in the thickness of the soil layer. This latter hypothesis means that effects like the dependence of sediment transport rate on the regolith thickness (Carson and Kirkby 1972; Kirkby 1992; Braun et al. 2001; Skinner et al. 2018), the feedbacks between soil water storage capacity, the run-off generation and its effective rate or the weathering and sediment transport processes (Kirkby 1976; Saco et al. 2006; Dochez et al. 2014) are ignored. On the other part, assuming that a contact between the loose, mobile regolith and the underlying rock exists, provides a slightly more complete approach, but still many

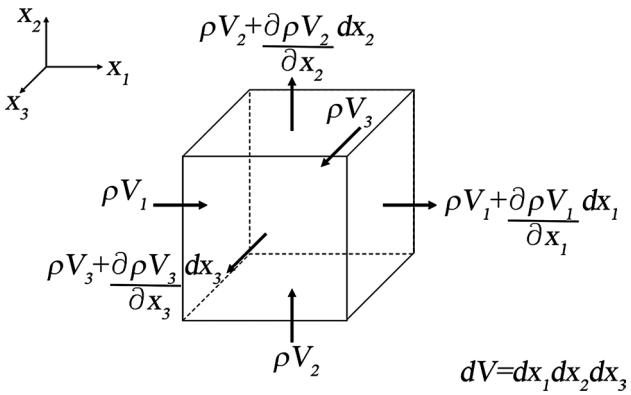

Fig. 1 Schematic representation of the mass continuity in volume V

simplifications are present (Ahnert 1976, 1987; Heimsath et al. 2001; Strudley et al. 2006).

Despite being largely adopted in landscape evolution modelling, the vertical-column continuity approach can sometimes result in being too much simplistic. In fact, there are several landforms that do not fit this framework, such as cliffs, waterfalls and gully headscarps, which have vertical or overhanging faces. Moreover, the 2-D continuity framework commonly implemented in landscape models is often very simple and not able to simulate vertical variations in weathering rates, shallow flows and rock properties. For overcoming these limitations, a fully 3-D approach is therefore necessary, subdividing the column vertically and introducing additional equations to describe the vertical variations of the soil properties (Kirkby 1976; Vanwalleghem et al. 2013). Other approaches included the vertical exchange of mass flux due to the soil strain and the advection of soil layers towards (away from) the eroding (aggrading) land surface, or the consideration of additional drivers like gravitational compaction or changes in mineralogy and geochemistry (Fritsch et al. 2011).

Hillslope erosion processes

Landscape evolution models are based on geomorphic transport functions, which, usually, have a rather general formulation but adopt site-specific parameters, developed for a specific scope (Chen et al. 2014). Moreover, classical approaches to hillslope erosion processes such as the RUSLE (Renard et al. 1997; Nasir and Selvakumar 2018) or the WEPP (Flanagan et al 2012; Nearing et al. 2017) aggregate various geomorphic processes within a given area. (Namely, they can be considered as lumped models.) However, for better addressing the physics of landscape evolution, geomorphic process regimes like sheet flow and gullies should be treated separately (Momm et al. 2018). In the following, a brief overview of the main hillslope erosion processes is reported, showing the need for addressing every single component separately.

Based on long-lasting research, Nearing et al. (2017) defined the critical zone as the region between the top of the forest canopy and the base of the weathering horizon. Processes acting in such zone weaken the rock via mechanisms like mechanical wedging, fracturing, chemical alteration, biological disruption, etc. Although the weathering processes are well studied under a qualitative point of view, their mathematical representation is a rather new field of research, which is mainly focused on predicting rates of change and patterns of rock disintegration induced by specific chemical and physical processes (Cohen et al. 2009; Murphy et al. 2016). Moving from the original intuition proposed by Gilbert (1877), later revised and analytically expressed by Ahnert (1976), one can observe that, assuming a constant rate of regolith production from bare bedrock and a fixed characteristic decay length scale, under quasi-steady conditions (i.e. the regolith thickness varies very slowly with respect to the surface erosion), an inverse relationship between thickness and erosion rate exists. This relationship has been verified against several field data, resulting in being consistent in different environments, ranging from semi-arid and coastal environments to high alpine terrains (Ahnert 1987; McKean et al. 1993). The mathematical formulation of this process can imply several assumptions, but, generally, the obtained decay curve has an exponential trend (Anderson 2002; Saco et al. 2006; Strudley et al. 2006). In the last century, Kirkby (1985) proposed an alternative to the exponential decay models: instead of assuming a sharp contact between bedrock and regolith, he described the transition from rock to regolith as a gradational process having the deficit of soil as a state variable. Such a deficit can be represented by the fraction of unweathered rock remaining at a certain level in the soil profile. He demonstrated that this schematization can be more appropriated in effectively describing a wide interface region between unaltered material and fully weathered soil. Indeed, even if successfully verified in several case studies, the exponential decay rules cannot be considered as a definitive solution for describing the observed regolith thickness patterns, but rather just a relatively simple and appealing method to be used until better approaches will be available. In this sense, further research on the physical mechanics and chemistry of weathering processes is needed for obtaining a better mathematical relationship to correlate rock disintegration rates to factors like subsurface temperature, stresses and mineral alteration (Anderson 1998; Fletcher et al. 2006).

As described in detail in the past (Carson and Kirkby 1972; Tucker and Hancock 2010), to reproduce the long-term phenomenon of soil creep on low-gradient basins, a linear slope-dependent transport function can be adopted (Fernandes and Dietrich 1997), accounting for the convex-upward hillslope profiles. Even if widely and successfully applied in many studies since decades, including fault scarps and fluvial systems, as well as marine and lake-shore terraces (Avouac 1993; Arrowsmith and Rhodes 1994; Pelletier et al. 2006), and calibrated against field data derived from cosmogenic nuclide mass-balance measurements (McKean et al. 1993; Heimsath and Ehlers 2005), the calibration constant is still the main source of uncertainty. In fact, an estimate of its magnitude can be obtained from a variety of approaches and for specific processes (Kirkby 1971; Black and Montgomery 1991; Anderson 2002), but, under a general point of view, it should be treated as an empirical parameter. Although a linear relationship, with a constant parameter, provides reliable results, physical considerations suggest that the regolith thickness can influence the soil creep equation. Therefore, many depth-dependent creep functions have been suggested

in the literature (Ahnert 1976, 1987; Strudley et al. 2006), spanning from very simplified (Rosenbloom and Anderson 1994) to more sophisticated (Braun et al. 2001; Anderson 2002) approaches. However, despite the rising of specific studies, it is evident that more research is needed, especially considering landscapes having steeper gradients, close to the angle of repose for natural soils (Heimsath et al. 2001). A few nonlinear relationships were proposed (Ferdowsi et al. 2018), but, generally, being developed on specific datasets, such formulas result too site-related and therefore not applicable in different contexts. For the future, additional studies should be performed, also involving new technologies like radiometry, laser scanning and micromorphology (Pawlik and Šamonil 2018).

Aside from fluvial processes, transport functions adopted for describing mass movements like shallow, rapid landsliding are more problematic. In fact, there are two general approaches that can be adopted for describing these phenomena: flux-based and event-based models. The first type approximates a series of events in terms of the long-term average rate of mass transfer by means of a transport function (Kirkby 1987). These models are capable to describe the time-averaged sediment transport at a time-scale relevant to landform evolution, but only at the very local spatial scale: the flux in a specific point is represented as a function of the local variables, neglecting the effects of the surroundings and the significance of long-distance transport events on steep slopes (Howard 1994). In the last decades, multiple attempts were made for incorporating the long-distance transport effects into landscape evolution models by accounting for the expected flow paths. However, many uncertainties are still evident, mainly because of the probabilistic behaviour of the sediments and the influence of the soil properties. Indeed, the evident connection between transport statistics, topography and morphological evolution suggests the use of event-based models, but, even if they are more physically rooted being grounded on the current knowledge of landslide triggering and motion (Tucker and Bradley 2010), at the same time, they are computationally not really efficient and therefore not widely applied and tested.

Run-off processes

As well known, the transport of sediment by the flowing water is a fundamental feature of the Earth's processes (Lorang and Hauer 2017). Indeed, geomorphic works in a drainage basin are mostly correlated with surface water, and, therefore, knowing how the water flow is handled in landscape evolution modelling represents a central issue. Despite the possible spatial discretization methods that can be adopted, a common feature between the various models is the need to combine short-time scales (minutes to seasons) associated with hydrologic processes with much longer timescales (years to centuries) that are related to sediment transport and landform evolution.

Typically, in a 2-D model, the flow field is described by means of the De St. Venant (shallow-water) equations, which represent the vertically integrated form of the Navier–Stokes equations for incompressible, free surface flow. They contain a description of the continuity of mass and momentum in the two horizontal dimensions and a friction function to describe the relationship between flow velocity and bed resistance, accounting for four main forces: inertia, gravity, fluid pressure and boundary friction. Being these equations highly complex and generally not analytically solvable, simplified numerical solutions should be applied, accounting for several limitations, as pointed out in the following.

Typically, because channelized flows accelerate only slowly in space (considering a reach-wise averaged velocity), the gradually varied flow approximation is introduced, assuming that the inertial terms in the momentum equation can be neglected. In addition, dropping the time derivative yields the diffusion wave approximation, which is valid in the case of flows mainly driven by pressure and gravity gradients. In the case of small changes of the flow depth in the stream-wise direction with respect to the bed morphology, the gravity represents the main driver of the flow, and the pressure-gradient term can be neglected for obtaining the kinematic-wave equations. In this case, the water gravity-related acceleration is everywhere balanced by the friction. For gravity-driven (kinematic) flows, the local bed shear stress can be represented as a function of the fluid density (water and sediment mixture), the local water/sediment discharge and the bed slope and friction. In a 2-D schematization, this approximation means that the flow lines follow the surface topography.

Based on this approach, many landscape evolution models use a cellular routing algorithm, imposing that the water flows from a cell to the adjacent one, following the steepest descent. As one can easily figure out, cellular routing algorithms are closely correlated with the spatial discretization of the domain. Indeed, in a numerical model, the continuous landscape surface is typically represented by discrete elements, which can be square cells, leading to pretty simple finite-difference solutions. However, in some cases, such square cells are not flexible enough for representing the computation domains in a proper manner. Therefore, to account for more complex domains, triangular elements associated with a finite-element solution (Maniatis et al. 2009) or triangular irregular (unstructured) cells having the nodes connected using a Delaunay triangulation and the surface nodes area described via Voronoi or Thiessen polygons can be adopted, such as made in common landscape models like the CASCADE and CHILD codes (Forte et al. 2016). Despite Caviedes-Voullième et al. (2012) demonstrated the utility of using triangular unstructured meshes for keeping

a low computational cost while ensuring accuracy, only a few models allow for using such a structure (Costabile et al. 2017). The advantages of a cell-routing approach are the simplicity and the speed, but many drawbacks are also present. Firstly, it is hard to handle diverging flows, which is typical of complex river systems. Moreover, the kinematic convergence of the flow depends on the width, which can be supposed equal to the width of the cells, leading to a grid-size dependence of water depth and current velocity (Willgoose et al. 1991). Alternatively, the flow can be assumed as confined to sub-grid cell features, which should have a predetermined (empirical) width (Howard 1994; Tucker and Slingerland 1994). A few landscape models have a less strict approach, relaxing the single-flow-direction assumption by introducing explicit numerical solutions of the steady 2-D kinematic-wave equations (Morgan 1980) or using multiple directions algorithms, which assume that the flow going out from a cell is split among the downslope neighbours, weighted according to the gradient in each direction. Given that this latter type of algorithms provides a better description of shallow overland flow (sheet flow as described by Morgan in 1980) on convex hillslopes and fans (Pelletier 2004), its use is fast spreading. In fact, common and well-known codes like CAESAR (Van De Wiel et al. 2007) or recent examples such as the Landlab (Hobley et al. 2017) use multiple flow-direction algorithms, accounting for all the possible directions of flow propagation. These models provide an effective way to approximate time-varying, 2-D flow fields without the computational effort required by the traditional solution of the shallow-water equations, which could be very high especially for large domains (Garcia-Navarro 2016; Shustikova et al. 2019). Commonly, cell-based or kinematic-wave water routing is associated with a steady flow. As an example, the SIBERIA and the DELIM models compute the water discharge as a power function of the watershed area, assuming the local equilibrium between rainfall and run-off (Willgoose et al. 1991; Howard 1994). However, as Sólyom and Tucker (2004) demonstrated, the local geomorphology can highly affect the hydrological behaviour. Moreover, many studies pointed out the importance of the spatial variability of run-off generation, finding out that the run-off excess (saturation) tends to enhance both the hillslope convexity and the hillslope–channel transitions in equilibrium landscapes (Ijjász-Vásquez et al. 1992).

The kinematic-wave theory represents a reliable approximation for channelized flows, but some problems arise in describing the 2-D evolution of landscapes. Indeed, errors can be hindered behind a series of questionable assumptions that lead to the right solutions (Izumi and Parker 2000). On the one part, the problem of flow convergence along valley axes can represent an obstacle to properly capture the transition from distributed to channelized flow, which can be somehow handled only posing major attention on the spatial resolution of the model (Kirkby 1994; Perron et al. 2008). In fact, to overcome such problems, fine-detailed models using the diffusive wave theory can be developed, but there is still the need of employing more powerful computers for evaluating the long-term evolution of large areas, which can hinder their application to real-time forecasts.

Obviously, there are differences in terms of timescale in simulating the run-off which could be observed during a storm event or the long-term evolution of a river watershed. The majority of landscape evolution models deal with this aspect imposing a geomorphically effective run-off event to describe the basin erosion. Namely, such codes assume a single, steady run-off coefficient is equivalent, in terms of geomorphic effectiveness, to a series of run-off events. There are many examples dealing with this approach, spanning from imposing a relationship between a time-averaged sediment transport discharge and the average water flow peak discharge to more complex approaches (Willgoose et al. 1989). However, all these methods assume that the event is somehow stable, while many researchers pointed out the need to consider the role of the discharge variability in time (Lague et al. 2005; Huang and Niemann 2006; Molnar et al. 2006). Regardless of the detail of each method, they commonly agreed that erosion and transport rates increase with the temporal increment in discharge fluctuations, because they depend more than linearly on the water discharge. While there are several examples for which such effective event assumption is reasonable, recent studies proved that the time variability in hydrologic forcing can have a great impact on the landscape dynamics and, therefore, should be incorporated in the landscape evolution modelling, possibly through a stochastic description of both the rainfall and the run-off events (Tucker and Bras 2000; Whipple and Tucker 2002; Armitage et al. 2018).

In the future, many challenges related to modelling the feedback effects between a changing climate, hydrology and landscape evolution in a coupled way should be faced, aiming to account for different spatiotemporal scales and overcome the simplifications generally applied in practice (Sólyom and Tucker 2004; Huang and Niemann 2006; Anders et al. 2008). Moreover, the randomness in the temporal dynamics of run-off processes requires the development of new high-flow statistics for better describing the evolution of landscapes like river floodplains, which are more impacted by extreme flows.

Sediment transport from the hillslopes to the river system

In shaping a river channel, the water flow erodes the bed with a rate limited by the detachment of particles (supply-limited systems) or by the capacity of the flow to transport sediment particles (capacity-limited systems), with a multitude

of intermediate behaviours (Carson and Kirkby 1972; Hajigholizadeh et al. 2018; Shobe et al. 2018). Thus, each system needs a different schematization, and the complexity varies depending also on the erosion rate: supply-limited systems result in being the simplest in terms of numerical modelling. In fact, in such systems, the sediment particles disappear as soon as they are eroded (Bagnold 1966; Howard 1994). Therefore, in this case, the erosion rate is assumed as a function of the bed shear stress, which, in its turn, depends on the local slope and discharge, giving rise to the so-called stream power erosion law (Bagnold 1966; Howard and Kerby 1983; Warren et al. 2019). A key property of these systems is the wave-like nature: there is a tendency to form erosional fronts that propagate upstream (Tucker and Whipple 2002). In the case of capacity-limited river systems, the erosion rate is a function of the unbalance between sediments entering and going out from the system, assuming a local morphological equilibrium, where the transport rate is everywhere equal to the local carrying capacity. The capacity-based approach is most applicable for describing bedload transport in gravel-bed rivers, given that coarser particles have shorter travel distances, so the assumption of immediate adaptation of the transport rate to changes of water discharge or slope is quite reasonable (Einstein 1950). On the other part, in the case of systems mostly driven by the suspended load like sandy rivers, this approach tends to fail because it essentially ignores the time required for sediment grains to settle in the water column in response to transient hydrology. Indeed, the mechanism requires to define an equation representing the mass continuity for sediments in the water column, as well as detachment and settling functions, which are generally correlated with the local shear stress and grain size (Bracken et al. 2015). There are many formulas that can be adopted to describe the erosion and sediment transport phenomena in a river system, but, despite this, they perform in a very similar manner if looking at the long-term longitudinal river-profile evolution under steady conditions (Whipple and Tucker 2002; Varrani et al. 2019). However, many differences arise in applying the models in transient conditions (Attal et al. 2008; Franzoia and Nones 2017), suggesting the need for using natural experiments to test landscape models (Tucker 2009).

For effectively describing the natural environment and the formation of a river system, a landscape evolution model must correctly reproduce the transition dynamics from the hillslopes to the channel, and the degree to which the surface changes as a function of factors like relief elevation, local climate and river basin lithology (Kirkby 1987; Di Silvio and Nones 2014). The distinction between channels and hillslopes can be explicitly treated, but introducing hardly describable parameters (Willgoose et al. 1991), or representing the channels as sub-grid-scale features where the flow width is prescribed in an empirical way (Howard et al. 1994; Tucker and Slingerland 1994). Depending on the problem under study, models can be built for representing large-scale mechanisms without requiring a very fine detail (Kooi and Beaumont 1994; Lindim et al. 2016) or to reproduce the evolution of small-scale landforms, implying a grid resolution that can be smaller than the channel width (Perron et al. 2008). For having the order of magnitude of the scales involved, one can consider a regime equation in its original form, correlating the river width with a power of the bankfull discharge (Leopold et al. 1964). One can easily notice that channels are typically some orders of magnitude smaller than the whole basin, meaning that they can be effectively handled as sub-grid features in landscape evolution models. The channel geometry is paramount in defining the volume of sediments available: the narrower is the channel, the more confined is the flow. Assuming that other parameters like the bed slope are constant, a narrow channel means an increase in the bed shear stress and the unit stream power, which translates in a bigger rate of sediment detachment and transported by the current (Lague 2014; Armitage et al. 2018).

The complexity of fluvial morphodynamics needs to be simplified for speeding up the computation, especially in the case of large river basins. However, in doing that, some models lose their physical meaning, imposing that the erosion can be directly computed from the total discharge rather than from the specific one (Willgoose et al. 1989; Kooi and Beaumont 1994) or assuming empirical regime equations (Howard 1994; Tucker and Whipple 2002) hardly verifiable. On the one part, the use of empirical scaling laws has the advantage to explicitly calculate the cross-sectional averaged shear stress and stream power and to permit the application of physically based erosion and transport functions that depend on such quantities. On the other part, relying on simple scaling laws for describing the channel geometry has some drawbacks like the application of an equilibrium assumption to describe non-equilibrium dynamics (Nones and Di Silvio 2016) or the impossibility to describe rivers affected by external forcing factors like tectonics or lithological discontinuities (Nones et al. 2019). In the last years, many models have been developed for reproducing bedrock channel evolution (Stark 2006; Wobus et al. 2008; Langston and Tucker 2018) and changes in channel width (Attal et al. 2008; Nones and Di Silvio 2016), as well as debris and granular flows (Howard 1998; Stock and Dietrich 2006), but there is ample room for improving them towards a more reliable estimate of landscape evolution, accounting for physically based laws, as well as spatially and temporally variable functions, for better incorporating the geological and climatological variability.

Soil properties

For terrestrial life, the soil represents one of the most important substances, supporting both the life (Lin 2011) and being a medium for transport and storage of water and gases (Strahler and Strahler 2006). Indeed, hydrological and morphological processes are a function of the soil characteristics (Bryan 2000), but also depend on the ratio between soil and rock coverage (Poesen and Lavee 1994). Therefore, the understanding of the formation, global distribution and functional properties of the soil is paramount in catching the mechanisms driving the landscape dynamics.

Aiming to link the small scale of soil characteristics to the large scale of landscape evolution, in the past years, many statistical methods have been developed for determining and mapping different soil properties depending on other soil characteristics and the basin geomorphology (Behrens and Scholten 2006). However, one of the shortcomings of such an approach is the need of having a very large and detailed dataset of soil attributes, such as the particle size distribution or the amount of organic matter, which is needed for predicting hardly measurable soil properties like the water content. In fact, even if applicable at the small scale, analyses at large (basin-wide) scale require distributed samples, which can be prohibitively expensive and definitely time-consuming (Scull et al. 2003).

While the spatial mapping of soil properties is important, understanding the evolution of these properties and processes at the required scale is also fundamental. For quantifying such processes and predicting the time evolution of the soil characteristics, modellers can apply process-based models (Hoosbeek and Bryant 1992; Minasny et al. 2008; Schoorl and Veldkamp 2016). On the other hand, the most tested but out-of-date process-based models cannot be applied to large domains due to an excessive need of computational resources; therefore, new methods based on state-space matrix methodology were recently introduced (Cohen et al. 2009), also accounting for multiple soil layers (Welivitiya et al. 2016). These models are able to adequately predict the soil properties of an individual pixel, but failed in modelling the spatial interconnectivity between the various parts of the soil catena that result from transport-limited erosion and deposition. To correctly predict the temporal changes of the spatially distributed soil properties, since the end of the last century, many researchers tried to couple the soil profile evolution with the landform evolution. As an example, Minasny and McBratney (2001) modelled the influence of soil and weathering processes on landform evolution using a single layer of soil, while Vanwalleghem et al. (2013) developed the MILESD code, which accounts for four layers (the bottommost bedrock layer and three soil layers above it) for reproducing the evolution of landforms, with a particular focus on Australia. Recently, the soil evolution module adopted in MILESD has been modified adding additional layers (Temme and Vanwalleghem 2016). Indeed, limiting the description of the topsoil to only three layers can hinder the importance of soil characteristics like the particle size distribution, which can be an index of various soil attributes such as the soil moisture content (Schaap et al. 2001; Minasny et al. 2015). As a matter of fact, future landscape evolution models should consider soil characteristics like depth and water holding capacity explicitly, preferably via a physically based approach, because they constrain the grading and amount of material eroded across the river basin.

Vegetation dynamics

Both the soil formation and the establishment of vegetation are paramount in changing the hydrological fluxes by accommodating soil moisture and facilitating the formation of sub-surface flow paths, affecting the form and the magnitude of erosion, sediment transport (Ebel et al. 2007) and deposition (Molina et al. 2009). Therefore, numerical models devoted to predicting the evolution of landscape features are highly dependent on vegetation properties (Casadei et al. 2003; Collins et al. 2004; Istanbulluoglu and Bras 2005; Yetemen et al. 2010). In addition, plants convert solar energy into geomorphic forces with very significant impacts from the regional to the global scales (Phillips 2009). Amundson et al. (2015) summarized the importance of vegetation in landscape evolution in a few points: (1) if water is available, a world without plants would likely have little or no soil on hillslopes; (2) plants may control the soil thickness; (3) soil production rates may be very high with respect to outcrop erosion rates (around one order of magnitude); (4) given that the soil residence times are constrained within a broad window of nutrient sufficiency/optimization, environments characterized by high weathering and low denudation rates can suffer from a deficit of rock-derived elements; (5) local feedbacks between plants, nutrients and soil thickness are possible; (6) at the very long-term (millennia), the vegetation evolution can impact (and be impacted by) geomorphic conditions.

As for the soil, the inclusion of vegetation dynamics in landscape evolution models is related to the spatial scale. Indeed, for adequately simulating how soils and biota interact with climate and bedrock (Corenblit and Steiger 2009), and, consequently, for modulating the geomorphic response at the catchment scale, it is necessary to collect detailed data spatially distributed across the basin. To reduce the computational effort in creating such a dataset, generally spatial analyses of remotely sensed images and digital maps of elevation, geology, soils and vegetation in relation to the local climate and sediment yield are developed (Newton et al. 2009). Aside from creating new databases, the attention of

geomorphologists and soil scientists is now focused on qualitatively and quantitatively understand the effects of vegetation on the landscape physical processes, aiming to provide a more reliable schematization of them to be included in numerical codes. In this sense, the present major challenge is how to explicitly and quantitatively account for the role of biota in the production of soil from bedrock and its transport downslope, investigating the combined evolution and feedback of soil, plants, hydrology and climate.

Conclusions and open questions

Using a plain language, the present review proposes a short summary about landscape evolution modelling and the main components of such codes, showing that, even if characterized by a quite long history, this research field is still very active and several improvements are forecasted for the future for answering to a series of open questions towards a more reliable representation of the Earth's surface (Willgoose 2018). In fact, the understanding of landscape dynamics requires a deeper knowledge of the recursive, multi-scale interactions among abiotic and biotic states and processes (Phillips and Van Dyke 2017).

As for the geomorphic transport functions, in the future, additional research should be performed towards a better evaluation of the dynamics associated with sediment characteristics such as a varying grain size distributions, the role of the basin lithology and the horizontal movement of geomorphic features due to processes like scarp retreat and tectonic displacement.

Most importantly, for obtaining a consistent schematization of the natural landscape, the dynamics of soils must be incorporated in new numerical models, overcoming limitations shown by past codes. In fact, the soil represents one of the most important substances found on the Earth, given that, covering its uppermost layer, it provides the support for all the terrestrial organisms and guarantees the terrestrial life (Lin 2011). In the last decade, many tentative were made for incorporating the soil behaviour into landscape evolution models, as well as in combining soilscape and landscape modelling (Ebel et al. 2007; Welivitiya et al. 2019). Indeed, on the one part, the soil controls the interaction between vegetation and water, as well as the atmosphere in terms of carbon and nutrient cycling. On the other part, in combination with the vegetation, the soil determines the rate of erosion and deposition and therefore cannot be ignored in adequately simulating the long-term dynamics of fluvial landscapes (Wilkes et al. 2019).

Aiming to draw a more complete picture of the evolution of a natural landscape, research should be directed also in including the role of biota, the dynamics of stream-channel adjustment, the erosion and transport of sediments and material by means of woody and debris flows or other mass movements and the formation and evolution of the critical zone (Anderson et al. 2008). In summary, there is an evident need for a better understanding of mechanics and feedback of the physical, chemical and biological controls that can have a role in shaping the landscape forms. Even if the importance of the sediment dynamics is well recognized (Schumm and Lichty 1965; Robinson and Slingerland 1998), a major focus should be posed towards the study of the soil properties, improving the understanding on the influence of grain size, transport and sorting in shaping river systems, given that such aspects received some attention only recently (Gasparini et al. 2004; Di Silvio and Nones 2014; Sklar et al. 2017). Moreover, further research shall be devoted in better interpreting and modelling the links between local climate, relief and grain size delivery to sedimentary basins, aiming to obtain a most reliable estimate of the processes acting at the watershed scale. In fact, fluvial transport capacity and competence are highly sensitive to grain size composition, and, consequently, phenomena like abrasion, weathering and armouring can have a significant impact on the transport mechanisms (Gasparini et al. 2004; Attal and Lave 2006), pinpointing the opportunity to account for them in landscape models at the small scale (Willgoose and Sharmeen 2006; Román-Sánchez et al. 2019) or to justify their absence in the case of basin-wide simplified approaches (Nones et al. 2019; Varrani et al. 2019).

The geometry of river represents another challenge for landscape evolution modelling given that size and shape of a channel controls (and is indirectly controlled by) the distribution of friction and energy dissipation across its wetted perimeter. There are an increasing number of numerical and experimental studies focused on evaluating how the channel geometry follows the changes of base-level controls, tectonic tilting and water and sediment supply (Stark 2006; Finnegan et al. 2007; Wobus et al. 2008; Davy et al. 2017; O'Hara et al. 2019), but these relationships are far to be fully understood. Even if landscape evolution models that couple surface changes with vegetation dynamics have begun to appear in the last decades and now are becoming a major research field (Murray and Paola 2003; Nones and Di Silvio 2016), the scientific community has just started to find a consensus on the quantitative relationships between hydrological, biological and geomorphic processes. In addition, challenges posed by modelling such mechanisms are related also to their spatiotemporal scales, which could be significantly different.

Aside from the theoretical and physical understanding of the mechanisms involved, as well as their mathematical schematization and the associated computing challenges, one of the greatest limitations in widely applying landscape evolution models is the evident lack of data and methods to test them. As stated by Mark (1975), the reliability of a

landscape model can be assessed through four ways, depending on the process under evaluation. First, in the case of rapid landform development measurable in timescales of months or years, such as in the case of gully formation and post-mining landscape (Hancock 2006; Hancock et al. 2017), the model predictions can be tested against direct observations. However, because of uncertainties in understanding delayed effects of processes like vegetation encroachment and weathering, problems can arise in extrapolating information from such newly created landscapes to the long term (Moliere et al. 2002). Second, there are situations where real-time measurements of sediment and solute fluxes can provide a useful basis for evaluating the model performance, even in the case of a slow rate of landform variation (Montgomery and Dietrich 1992). Third, the development of landscapes can be evaluated by means of scaled experiments, where the involved process can be adequately measured in a controlled environment. Since decades, laboratory experiments are very helpful in addressing specific issues focusing on a few geomorphic features (Hasbargen and Paola 2000; Pelletier 2008), but, generally, they perform well only under a qualitative point of view. The recent boom in high-speed computing resources and digital photogrammetry permits to overcome the operative limitations present in the past towards a more quantitative estimation of the landscape evolution at the laboratory scale, which could ultimately support numerical models. Indeed, because of many limitations correlated with laboratory tests and parameters uncertainty (Skinner et al. 2018), physical experiments and numerical model should be combined to adequately reproduce complex landscape changes. Fourth, landscape models can be tested by comparison with natural experiments, which are case studies having sufficiently constraints to allow for a quantitative comparison between field observations and numerical outputs (Montgomery and Dietrich 1992; Tucker 2009). While, since years, there is a great potential in combining natural experiments and modelling runs (Hancock and Willgoose 2001), the need to develop probabilistic frameworks and robust statistical measures for discriminating between dissimilar natural landscapes and scales remains (Schumer et al. 2017).

As visible from the present review, landscape evolution models can be extremely complicated, depending on the processes considered. In fact, the basin surface is not simply shaped by the interaction between water and sediment, but also many other factors can play a major role. As an example, in different parts of the world, the landscape is shaped by wind (Okin and Gillette 2001), snow (Liston and Elder 2006), ice (Ugelvig et al. 2016) or the fire (Scott 2018) since millennia. However, the description of such phenomena is outside the scope of the present work and is therefore not addressed here.

Human-induced alterations of river channels and basins as well as the climate change are actually having a major role in reshaping geomorphic systems, altering the natural relationship between the components and posing additional challenges to river modellers. As suggested by recent studies, topography and climate are generally coupled, and precipitation increases because of orographic effects during the uplift of a high mountain till an elevation of about 1000–2000 m (Bookhagen and Burbank 2006). Therefore, altered climatic conditions can drive to a change in precipitation patterns, with consequences on the watershed topography. However, the landscape sensitivity to the timescale of climatic variations is not yet completely understood and represents a hot research topic for the future (Moussirou and Bonnet 2018). In addition to the large-scale effects of climate change, local changes on the landscape can be also caused by the presence of animals like herbivorous. Nowadays, the correlation between animals and landscape evolution is generally studied only at the local level (Butler et al. 2007), and a general framework is still missing because of the high complexity of considering the presence of human beings and animals.

The present review showed that substantial progress has been made in quantitative modelling the evolution of the Earth's surface in terms of water–sediment–vegetation interactions, but much still remains to be accomplished and there are many open questions that can be addressed in the future. On the one part, there is the need for refining and testing landscape evolution models in a larger variety of cases to cover a multitude of spatial and temporal scales, by means of new and improved computing techniques. On the other part, one of the major challenges lies in developing experimental and field-based datasets for testing and validating numerical models across a wide range of spatiotemporal scales and covering different geomorphic environments (Rixhon et al. 2017).

Funding The work was also supported within statutory activities No. 3841/E-41/S/2019 of the Ministry of Science and Higher Education of Poland.

Compliance with ethical standards

Conflict of interest The author states that there is no conflict of interest.

References

Adams JM, Gasparini NM, Hobley DE, Tucker GE, Hutton E, Nudurupati SS, Istanbulluoglu E (2017) The Landlab v1. 0 OverlandFlow component: a Python tool for computing shallow-water flow across watersheds. Geosci Model Dev. https://doi.org/10.5194/gmd-10-1645-2017

Ahnert F (1976) Brief description of a comprehensive three dimensional model of landform development. Z fur Geomorphol Suppl Band 25:29–49

Ahnert F (1987) Approaches to dynamic equilibrium in theoretical simulations of slope development. Earth Surf Proc Land 12(1):3–15. https://doi.org/10.1002/esp.3290120103

Amundson R, Heimsath A, Owen J, Yoo K, Dietrich WE (2015) Hillslope soils and vegetation. Geomorphology 234:122–132. https://doi.org/10.1016/j.geomorph.2014.12.031

Anders AM, Roe GH, Montgomery DR, Hallet B (2008) Influence of precipitation phase on the form of mountain ranges. Geology 36(6):479–482. https://doi.org/10.1130/G24821A.1

Anderson RS (1998) Near-surface thermal profiles in alpine bedrock: implications for the frost weathering of rock. Arct Alp Res 30(4):362–372

Anderson RS (2002) Modeling the tor-dotted crests, bedrock edges, and parabolic profiles of high alpine surfaces of the Wind River Range Wyoming. Geomorphology 46(1–2):35–58. https://doi.org/10.1016/S0169-555X(02)00053-3

Anderson SP, Bales RC, Duffy CJ (2008) Critical zone observatories: building a network to advance interdisciplinary study of Earth surface processes. Mineral Mag 72(1):7–10. https://doi.org/10.1180/minmag.2008.072.1.7

Armitage JJ, Whittaker AC, Zakari M, Campforts B (2018) Numerical modelling of landscape and sediment flux response to precipitation rate change. Earth Surf Dyn 6(1):77–99. https://doi.org/10.5194/esurf-6-77-2018

Arrowsmith JR, Rhodes DD (1994) Original forms and initial modifications of the Galway Lake Road scarp formed along the Emerson fault during the 28 June 1992 Landers, California, earthquake. Bull Seismol Soc Am 84(3):511–527

Attal M, Lave J (2006) Changes of bedload characteristics along the Marsyandi River (central Nepal): implications for understanding hillslope sediment supply, sediment load evolution along fluvial networks, and denudation in active orogenic belts. In: Willett SD, Hovius N, Brandon MT, Fisher D (eds) Tectonics, climate, and landscape evolution, vol 398. Geological Society of America, Boulder, pp 143–171

Attal M, Tucker GE, Whittaker AC, Cowie PA, Roberts GP (2008) Modeling fluvial incision and transient landscape evolution: Influence of dynamic channel adjustment. J Geophys Res Earth Surf 113(F3):F03013. https://doi.org/10.1029/2007JF000893

Avouac JP (1993) Analysis of scarp profiles: evaluation of errors in morphologic dating. J Geophys Res Solid Earth 98(B4):6745–6754. https://doi.org/10.1029/92JB01962

Baas AC (2017) Models in geomorphology. Int Encycl Geogr People the Earth Environ Technol People Earth Environ Technol. https://doi.org/10.1002/9781118786352.wbieg0882

Bagnold RA (1966) An approach to the sediment transport problem from general physics. United States Geological Survey Professional Paper, 422I. US Government Printing Office, Washington DC, USA

Beaumont C, Kooi H, Willett S (2000) Coupled tectonic-surface process models with applications to rifted margins and collisional orogens. In: Summerfield MA (ed) Geomorphology and global tectonics. Wiley, Hoboken, pp 29–55

Behrens T, Scholten T (2006) Digital soil mapping in Germany-a review. J Plant Nutr Soil Sci 169(3):434–443. https://doi.org/10.1002/jpln.200521962

Bishop P (2007) Long-term landscape evolution: linking tectonics and surface processes. Earth Surf Proc Land 32(3):329–365. https://doi.org/10.1002/esp.1493

Black TA, Montgomery DR (1991) Sediment transport by burrowing mammals, Marin County California. Earth Surf Process Landf 16(2):163–172. https://doi.org/10.1002/esp.3290160207

Bookhagen B, Burbank DW (2006) Topography, relief, and TRMM-derived rainfall variations along the Himalaya. Geophys Res Lett 33(8):L08405. https://doi.org/10.1029/2006GL026037

Bracken LJ, Turnbull L, Wainwright J, Bogaart P (2015) Sediment connectivity: a framework for understanding sediment transfer at multiple scales. Earth Surf Proc Land 40(2):177–188. https://doi.org/10.1002/esp.3635

Braun J (2018) A review of numerical modeling studies of passive margin escarpments leading to a new analytical expression for the rate of escarpment migration velocity. Gondwana Res 53:209–224. https://doi.org/10.1016/j.gr.2017.04.012

Braun J, Heimsath AM, Chappell J (2001) Sediment transport mechanisms on soil-mantled hillslopes. Geology 29(8):683–686. https://doi.org/10.1130/0091-7613(2001)029%3c0683:STMOSM%3e2.0.CO,2

Bryan RB (2000) Soil erodibility and processes of water erosion on hillslope. Geomorphology 32(3–4):385–415. https://doi.org/10.1016/S0169-555X(99)00105-1

Butler LG, Kielland K, Scott RT, Hanley TA (2007) Interactive controls of herbivory and fluvial dynamics on landscape vegetation patterns on the Tanana River floodplain, interior Alaska. J Biogeogr 34(9):1622–1631. https://doi.org/10.1111/j.1365-2699.2007.01713.x

Carson MA, Kirkby MJ (1972) Hillslope form and process. Cambridge University Press, Cambridge

Casadei M, Dietrich WE, Miller NL (2003) Testing a model for predicting the timing and location of shallow landslide initiation in soil-mantled landscapes. Earth Surf Proc Land 28(9):925–950. https://doi.org/10.1002/esp.470

Caviedes-Voullième D, García-Navarro P, Murillo J (2012) Influence of mesh structure on 2D full shallow water equations and SCS Curve Number simulation of rainfall/runoff events. J Hydrol 448:39–59. https://doi.org/10.1016/j.jhydrol.2012.04.006

Caviedes-Voullième D, Fernández-Pato J, Hinz C (2018) Cellular automata and finite volume solvers converge for 2D shallow flow modelling for hydrological modelling. J Hydrol 563:411–417. https://doi.org/10.1016/j.jhydrol.2018.06.021

Chen A, Darbon J, Morel JM (2014) Landscape evolution models: a review of their fundamental equations. Geomorphology 219:68–86. https://doi.org/10.1016/j.geomorph.2014.04.037

Chorley RJ (1969) The drainage basin as the fundamental geomorphic unit. In: Chorley RJ (ed) Water, earth and man. Methuen & Co. Ltd., London, pp 77–98

Cohen S, Willgoose G, Hancock G (2009) The mARM spatially distributed soil evolution model: A computationally efficient modeling framework and analysis of hillslope soil surface organization. J Geophys Res Earth Surf 114(F3):F03001. https://doi.org/10.1029/2008JF001214

Collins DBG, Bras RL, Tucker GE (2004) Modeling the effects of vegetation-erosion coupling on landscape evolution. J Geophys Res Earth Surf 109(F3):F03004. https://doi.org/10.1029/2003JF000028

Corenblit D, Steiger J (2009) Vegetation as a major conductor of geomorphic changes on the Earth surface: toward evolutionary geomorphology. Earth Surf Proc Land 34(6):891–896. https://doi.org/10.1002/esp.1788

Costabile P, Costanzo C, Macchione F (2017) Performances and limitations of the diffusive approximation of the 2-d shallow water equations for flood simulation in urban and rural areas. Appl Numer Math 116:141–156. https://doi.org/10.1016/j.apnum.2016.07.003

Coulthard TJ (2001) Landscape evolution models: a software review. Hydrol Process 15(1):165–173. https://doi.org/10.1002/hyp.426

Coulthard TJ, Macklin MG (2001) How sensitive are river systems to climate and land-use changes? A model-based evaluation. J Quat Sci 16(4):347–351. https://doi.org/10.1002/jqs.604

Coulthard TJ, Van De Wiel MJ (2006) A cellular model of river meandering. Earth Surf Process Landf 31(1):123–132. https://doi.org/10.1002/esp.1315

Coulthard TJ, Macklin MG, Kirkby MJ (2002) A cellular model of Holocene upland river basin and alluvial fan evolution. Earth Surf Proc Land 27(3):269–288. https://doi.org/10.1002/esp.318

Davy P, Croissant T, Lague D (2017) A precipiton method to calculate river hydrodynamics, with applications to flood prediction, landscape evolution models, and braiding instabilities. J Geophys Res Earth Surf 122(8):1491–1512. https://doi.org/10.1002/2016JF004156

Di Silvio G, Nones M (2014) Morphodynamic reaction of a schematic river to sediment input changes: analytical approaches. Geomorphology 215:74–82. https://doi.org/10.1016/j.geomorph.2013.05.021

Dietrich WE, Bellugi DG, Sklar LS, Stock D, Heimsath AM, Roering JJ (2003) Geomorphic transport laws for predicting landscape form and dynamics. In: Wilcock P, Iverson R (eds) Prediction in geomorphology. American Geophysical Union Monograph, Washington, pp 103–132. https://doi.org/10.1029/135GM09

Dochez S, Laouafa F, Franck C, Guedon S, Martineau F, d'Amato J, Saintenoy A (2014) Multi-scale analysis of water alteration on the rockslope stability framework. Acta Geophys 62(5):1025–1048. https://doi.org/10.2478/s11600-014-0232-7

Ebel BA, Loague K, Dietrich WE, Montgomery DR, Torres R, Anderson SP, Giambelluca TW (2007) Near-surface hydrologic response for a steep, unchanneled catchment near Coos Bay, Oregon: 1 Sprinkling experiments. Am J Sci 307(4):678–708. https://doi.org/10.2475/04.2007.02

Einstein HA (1950) The bed-load function for sediment transport in open channel flow. Technical Bulletin, 1026, US Department of Agriculture, USA

Evans KG (2000) Methods for assessing mine site rehabilitation design for erosion impact. Aust J Soil Res 38(2):231–248. https://doi.org/10.1071/SR99036

Fagherazzi S, Kirwan ML, Mudd SM, Guntenspergen GR, Temmerman S, D'Alpaos A, Koppel J, Rybczyk JM, Reyes E, Craft C, Clough J (2012) Numerical models of salt marsh evolution: ecological, geomorphic, and climatic factors. Rev Geophys 50(1):RG1002. https://doi.org/10.1029/2011RG000359

Ferdowsi B, Ortiz CP, Jerolmack DJ (2018) Glassy dynamics of landscape evolution. Proc Natl Acad Sci 115(19):4827–4832. https://doi.org/10.1073/pnas.1715250115

Fernandes NF, Dietrich WE (1997) Hillslope evolution by diffusive processes: the timescale for equilibrium adjustments. Water Resour Res 33(6):1307–1318. https://doi.org/10.1029/97WR00534

Finnegan NJ, Sklar LS, Fuller TK (2007) Interplay of sediment supply, river incision, and channel morphology revealed by the transient evolution of an experimental bedrock channel. J Geophys Res Earth Surf 112(F3):F03S11. https://doi.org/10.1029/2006JF000569

Flanagan DC, Frankenberger JR, Ascough JC II (2012) WEPP: model use, calibration, and validation. Trans ASABE 55(4):1463–1477. https://doi.org/10.13031/2013.42254

Fletcher RC, Buss HL, Brantley SL (2006) A spheroidal weathering model coupling porewater chemistry to soil thicknesses during steady-state denudation. Earth Planet Sci Lett 244(1–2):444–457. https://doi.org/10.1016/j.epsl.2006.01.055

Forte AM, Yanites BJ, Whipple KX (2016) Complexities of landscape evolution during incision through layered stratigraphy with contrasts in rock strength. Earth Surf Proc Land 41(12):1736–1757. https://doi.org/10.1002/esp.3947

Franzoia M, Nones M (2017) Morphological reactions of schematic alluvial rivers: long simulations with a 0-D model. Int J Sediment Res 32(3):295–304. https://doi.org/10.1016/j.ijsrc.2017.04.002

Fritsch E, Balan E, Do Nascimento NR, Allard T, Bardy M, Bueno G, Derenne S, Melfi AJ, Calas G (2011) Deciphering the weathering processes using environmental mineralogy and geochemistry: towards an integrated model of laterite and podzol genesis in the Upper Amazon Basin. CR Geosci 343(2–3):188–198. https://doi.org/10.1016/j.crte.2010.11.002

Garcia-Navarro P (2016) Advances in numerical modelling of hydrodynamics workshop, University of Sheffield, UK, March 24–25, 2015. Appl Math Model 17(40):7423. https://doi.org/10.1016/j.apm.2016.06.045

Gasparini NM, Tucker GE, Bras RL (2004) Network-scale dynamics of grain-size sorting: implications for downstream fining, stream-profile concavity, and drainage basin morphology. Earth Surf Proc Land 29(4):401–421. https://doi.org/10.1002/esp.1031

Gesch B, Muller J, Farr TG (2006) The shuttle radar topography mission-Data validation and applications. Photogramm Eng Remote Sens 72(3):233–235

Gilbert GK (1877) Report on the geology of the Henry Mountains. US Geographical and Geological Survey of the Rocky Mountain Region, Washington, DC

Hajigholizadeh M, Melesse A, Fuentes H (2018) Erosion and sediment transport modelling in shallow waters: a review on approaches, models and applications. Int J Environ Res Public Health 15(3):518. https://doi.org/10.3390/ijerph15030518

Hancock GR (2006) The impact of different gridding methods on catchment geomorphology and soil erosion over long timescales using a landscape evolution model. Earth Surf Proc Land 31(8):1035–1050. https://doi.org/10.1002/esp.1306

Hancock G, Willgoose G (2001) Use of a landscape simulator in the validation of the SIBERIA catchment evolution model: declining equilibrium landforms. Water Resour Res 37(7):1981–1992. https://doi.org/10.1029/2001WR900002

Hancock GR, Willgoose GR (2018) Sustainable mine rehabilitation—25 years of the SIBERIA landform evolution and long-term erosion model. In: From start to finish: a life-of-mine perspective. Australian Institute of Mining and Metallurgy, Carlton

Hancock GR, Evans KG, Willgoose GR, Moliere DR, Saynor MJ, Loch RJ (2000) Medium-term erosion simulation of an abandoned mine site using the SIBERIA landscape evolution model. Aust J Soil Res 38(2):249–264. https://doi.org/10.1071/SR99035

Hancock GR, Loughran RJ, Evans KG, Balog RM (2008) Estimation of soil erosion using field and modelling approaches in an undisturbed Arnhem Land catchment, Northern Territory Australia. Geogr Res 46(3):333–349. https://doi.org/10.1111/j.1745-5871.2008.00527.x

Hancock GR, Lowry JBC, Coulthard TJ (2015) Catchment reconstruction-erosional stability at millennial time scales using landscape evolution models. Geomorphology 231:15–27. https://doi.org/10.1016/j.geomorph.2014.10.034

Hancock GR, Verdon-Kidd D, Lowry JBC (2017) Soil erosion predictions from a landscape evolution model–An assessment of a post-mining landform using spatial climate change analogues. Sci Total Environ 601:109–121. https://doi.org/10.1016/j.scitotenv.2017.04.038

Hasbargen LE, Paola C (2000) Landscape instability in an experimental drainage basin. Geology 28(12):1067–1070. https://doi.org/10.1130/0091-7613(2000)28%3c1067:LIIAED%3e2.0.CO,2

Heimsath AM, Ehlers TA (2005) Quantifying rates and timescales of geomorphic processes. Earth Surf Proc Land 30(8):917–921. https://doi.org/10.1002/esp.1253

Heimsath AM, Dietrich WE, Nishiizumi K, Finkel RC (2001) Stochastic processes of soil production and transport: Erosion rates, topographic variation and cosmogenic nuclides in the Oregon Coast Range. Earth Surf Proc Land 26(5):531–552. https://doi.org/10.1002/esp.209

Hobley DE, Adams JM, Nudurupati SS, Hutton EW, Gasparini NM, Istanbulluoglu E, Tucker GE (2017) Creative computing with Landlab: an open-source toolkit for building, coupling, and exploring two-dimensional numerical models of Earth-surface dynamics. Earth Surf Dyn 5(1):21–46. https://doi.org/10.5194/esurf-5-21-2017

Hoosbeek MR, Bryant RB (1992) Towards the quantitative modeling of pedogenesis—a review. Geoderma 55(3–4):183–210. https://doi.org/10.1016/0016-7061(92)90083-J

Howard AD (1994) A detachment-limited model of drainage basin evolution. Water Resour Res 30(7):2261–2285. https://doi.org/10.1029/94WR00757

Howard AD (1998) Long profile development of bedrock channels, interaction of weathering, mass wasting, bed erosion, and sediment transport. In: Tinkler KJ, Wohl E (eds) Rivers over rock, fluvial processes in bedrock channels. American Geophysical Union, Washington DC, pp 297–319

Howard AD, Kerby G (1983) Channel changes in badlands. Geol Soc Am Bull 94(6):739–752. https://doi.org/10.1130/0016-7606(1983)94%3c739:CCIB%3e2.0.CO,2

Howard AD, Dietrich WE, Seidl MA (1994) Modeling fluvial erosion on regional to continental scales. J Geophys Res Solid Earth 99(B7):13971–13986. https://doi.org/10.1029/94JB00744

Huang X, Niemann JD (2006) An evaluation of the geomorphically effective event for fluvial processes over long periods. J Geophys Res Earth Surf. https://doi.org/10.1029/2006JF000477

Ijjász-Vásquez EJ, Bras RL, Moglen GE (1992) Sensitivity of a basin evolution model to the nature of runoff production and to initial conditions. Water Resour Res 28(10):2733–2741. https://doi.org/10.1029/92WR01561

Istanbulluoglu E, Bras RL (2005) Vegetation-modulated landscape evolution: effects of vegetation on landscape processes, drainage density, and topography. J Geophys Res Earth Surf 110(F2):F02012. https://doi.org/10.1029/2004JF000249

Izumi N, Parker G (2000) Linear stability analysis of channel inception: downstream-driven theory. J Fluid Mech 419:239–262. https://doi.org/10.1017/S0022112000001427

Kamp U, Owen LA (2013) Polygenetic landscapes. In: Treatise on geomorphology, vol 5. Elsevier, pp 370–393

Karydas CG, Panagos P, Gitas IZ (2014) A classification of water erosion models according to their geospatial characteristics. Int J Digital Earth 7(3):229–250. https://doi.org/10.1080/17538947.2012.671380

Khosronejad A, Kozarek JL, Sotiropoulos F (2014) Simulation-based approach for stream restoration structure design: model development and validation. J Hydraul Eng 140:04014042. https://doi.org/10.1061/(ASCE)HY.1943-7900.0000904

Kirkby MJ (1971) Hillslope process-response models based on the continuity equation. Inst Br Geogr Spec Publ 3:15–30

Kirkby MJ (1976) Deterministic continuous slope models. Z für Geomorphol Suppl Band 25:1–19

Kirkby MJ (1985) A model for the evolution of regolith-mantled slopes. In: Models in geomorphology, Allen and Unwin, Boston, pp 213–237

Kirkby MJ (1987) Modelling some influences of soil erosion, landslides and valley gradient on drainage density and hollow development. Catena Suppl 10:1–14

Kirkby MJ (1992) An erosion-limited hillslope evolution model. Catena Suppl 23:157–187

Kirkby MJ (1994) Thresholds and instability in stream head hollows, a model of magnitude and frequency for wash processes. In: Kirkby MJ (ed) Process models and theoretical geomorphology. Wiley, New York, pp 295–314

Kirkby MJ (1996) A role for theoretical models in geomorphology? In: The scientific nature of geomorphology, vol 27. Wiley, Hoboken, pp 257–272

Kooi H, Beaumont C (1994) Escarpment evolution on high-elevation rifted margins: Insights derived from a surface processes model that combines diffusion, advection, and reaction. J Geophys Res Solid Earth 99(B6):12191–12209. https://doi.org/10.1029/94JB00047

Lague D (2014) The stream power river incision model: evidence, theory and beyond. Earth Surf Proc Land 39(1):38–61. https://doi.org/10.1002/esp.3462

Lague D, Hovius N, Davy P (2005) Discharge, discharge variability, and the bedrock channel profile. J Geophys Res Earth Surf 110(F4):F04006. https://doi.org/10.1029/2004JF000259

Langston AL, Tucker GE (2018) Developing and exploring a theory for the lateral erosion of bedrock channels for use in landscape evolution models. Earth Surf Dyn 6:1–27. https://doi.org/10.5194/esurf-6-1-2018

Larsen LG, Eppinga MB, Passalacqua P, Getz WM, Rose KA, Liang M (2016) Appropriate complexity landscape modeling. Earth Sci Rev 160:111–130. https://doi.org/10.1016/j.earscirev.2016.06.016

Leopold LB, Wolman MG, Miller JP (1964) Fluvial processes in geomorphology. Freeman, W.H. and Co., San Francisco

Liang M, Van Dyk C, Passalacqua P (2016) Quantifying the patterns and dynamics of river deltas under conditions of steady forcing and relative sea level rise. J Geophys Res Earth Surf 121(2):465–496. https://doi.org/10.1002/2015JF003653

Lin H (2011) Three principles of soil change and pedogenesis in time and space. Soil Sci Soc Am J 75(6):2049–2070. https://doi.org/10.2136/sssaj2011.0130

Lindim C, Van Gils J, Cousins IT (2016) A large-scale model for simulating the fate & transport of organic contaminants in river basins. Chemosphere 144:803–810. https://doi.org/10.1016/j.chemosphere.2015.09.051

Liston GE, Elder K (2006) A distributed snow-evolution modeling system (SnowModel). J Hydrometeorol 7(6):1259–1276. https://doi.org/10.1175/JHM548.1

Liu B, Coulthard TJ (2017) Modelling the interaction of aeolian and fluvial processes with a combined cellular model of sand dunes and river systems. Comput Geosci 106:1–9. https://doi.org/10.1016/j.cageo.2017.05.003

Lorang MS, Hauer FR (2017) Fluvial geomorphic processes. In: Hauer FR, Lamberti G (eds) Methods in stream ecology, vol 1. Academic Press, Cambridge. https://doi.org/10.1016/B978-0-12-416558-8.00005-6

Maniatis G, Kurfeß D, Hampel A, Heidbach O (2009) Slip acceleration on normal faults due to erosion and sedimentation—results from a new three-dimensional numerical model coupling tectonics and landscape evolution. Earth Planet Sci Lett 284(3–4):570–582. https://doi.org/10.1016/j.epsl.2009.05.024

Mark DM (1975) Geomorphometric parameters: a review and evaluation. Geografiska Annaler: Ser A Phys Geogr 57(3–4):165–177. https://doi.org/10.1080/04353676.1975.11879913

Martin Y, Church M (2004) Numerical modelling of landscape evolution: geomorphological perspectives. Prog Phys Geogr 28(3):317–339. https://doi.org/10.1191/0309133304pp412ra

McKean JA, Dietrich WE, Finkel RC, Southon JR, Caffee MW (1993) Quantification of soil production and downslope creep rates from cosmogenic 10Be accumulations on a hillslope profile. Geology 21(4):343–346. https://doi.org/10.1130/0091-7613(1993)021%3c0343:QOSPAD%3e2.3.CO,2

Miller SR, Slingerland RL (2006) Topographic advection on fault-bend folds: Inheritance of valley positions and the formation of wind gaps. Geology 34(9):769–772. https://doi.org/10.1130/G22658.1

Minasny B, McBratney AB (2001) A rudimentary mechanistic model for soil formation and landscape development: II. A two-dimensional model incorporating chemical weathering. Geoderma 103(1–2):161–179. https://doi.org/10.1016/S0016-7061(01)00075-1

Minasny B, McBratney AB, Salvador-Blanes S (2008) Quantitative models for pedogenesis-a review. Geoderma 144(1–2):140–157. https://doi.org/10.1016/j.geoderma.2007.12.013

Minasny B, Finke P, Stockmann U, Vanwalleghem T, McBratney AB (2015) Resolving the integral connection between pedogenesis and landscape evolution. Earth Sci Rev 150:102–120. https://doi.org/10.1016/j.earscirev.2015.07.004

Moliere DR, Evans KG, Willgoose GR, Saynor MJ (2002) Temporal trends in erosion and hydrology for a post-mining landform at Ranger Mine, Northern Territory. Supervising Scientist Report, 165, Supervising Scientist, Darwin NT, USA

Molina A, Govers G, Cisneros F, Vanacker V (2009) Vegetation and topographic controls on sediment deposition and storage on gully beds in a degraded mountain area. Earth Surf Proc Land 34(6):755–767. https://doi.org/10.1002/esp.1747

Molnar P, Anderson RS, Kier G, Rose J (2006) Relationships among probability distributions of stream discharges in floods, climate, bed load transport, and river incision. J Geophys Res Earth Surf 111(F2):F02001. https://doi.org/10.1029/2005JF000310

Momm HG, Wells RR, Bennett SJ (2018) Disaggregating soil erosion processes within an evolving experimental landscape. Earth Surf Proc Land 43(2):543–552. https://doi.org/10.1002/esp.4268

Montgomery DR, Dietrich WE (1992) Channel initiation and the problem of landscape scale. Science 255(5046):826–830. https://doi.org/10.1126/science.255.5046.826

Morgan RPC (1980) Field studies of sediment transport by overland flow. Earth Surf Process 5(4):307–316. https://doi.org/10.1002/esp.3760050403

Moussirou B, Bonnet S (2018) Modulation of the erosion rate of an uplifting landscape by long-term climate change: an experimental investigation. Geomorphology 303:456–466. https://doi.org/10.1016/j.geomorph.2017.12.010

Murphy BP, Johnson JP, Gasparini NM, Sklar LS (2016) Chemical weathering as a mechanism for the climatic control of bedrock river incision. Nature 532(7598):223. https://doi.org/10.1038/nature17449

Murray AB, Paola C (2003) Modelling the effect of vegetation on channel pattern in bedload rivers. Earth Surf Process Landf 28:131–143. https://doi.org/10.1002/esp.428

Nasir N, Selvakumar R (2018) Influence of land use changes on spatial erosion pattern, a time series analysis using RUSLE and GIS: the cases of Ambuliyar sub-basin India. Acta Geophys 66(5):1121–1130. https://doi.org/10.1007/s11600-018-0186-2

Nearing MA, Lane LJ, Lopes VL (2017) Modeling soil erosion. In: Soil erosion research methods, Routledge, pp 127–158

Newton AC, Hill RA, Echeverría C, Golicher D, Rey Benayas JM, Cayuela L, Hinsley SA (2009) Remote sensing and the future of landscape ecology. Prog Phys Geogr 33(4):528–546. https://doi.org/10.1177/0309133309346882

Nones M, Di Silvio G (2016) Modeling of river width variations based on hydrological, morphological, and biological dynamics. J Hydraul Eng 142(7):04016012. https://doi.org/10.1061/(ASCE)HY.1943-7900.0001135

Nones M, Varrani A, Franzoia M, Di Silvio G (2019) Assessing quasi-equilibrium fining and concavity of present rivers: a modelling approach. CATENA 181:104073. https://doi.org/10.1016/j.catena.2019.104073

O'Hara D, Karlstrom L, Roering JJ (2019) Distributed landscape response to localized uplift and the fragility of steady states. Earth Planet Sci Lett 506:243–254. https://doi.org/10.1016/j.epsl.2018.11.006

Okin GS, Gillette DA (2001) Distribution of vegetation in wind-dominated landscapes: Implications for wind erosion modeling and landscape processes. J Geophys Res Atmos 106(D9):9673–9683. https://doi.org/10.1029/2001JD900052

Oreskes N, Shrader-Frechette K, Belitz K (1994) Verification, validation, and confirmation of numerical models in the earth sciences. Science 263(5147):641–646. https://doi.org/10.1126/science.263.5147.641

Pawlik Ł, Šamonil P (2018) Soil creep: The driving factors, evidence and significance for biogeomorphic and pedogenic domains and systems–a critical literature review. Earth Sci Rev 178:257–278. https://doi.org/10.1016/j.earscirev.2018.01.008

Pelletier J (2008) Quantitative modeling of earth surface processes. Cambridge University Press. https://doi.org/10.1017/CBO9780511813849

Pelletier JD, DeLong SB, Al-Suwaidi AH, Cline M, Lewis Y, Psillas JL, Yanites B (2006) Evolution of the Bonneville shoreline scarp in west-central Utah: Comparison of scarp-analysis methods and implications for the diffusion model of hillslope evolution. Geomorphology 74(1–4):257–270. https://doi.org/10.1016/j.geomorph.2005.08.008

Perron JT, Dietrich WE, Kirchner JW (2008) Controls on the spacing of first-order valleys. J Geophys Res Earth Surf 113(F4):F04016. https://doi.org/10.1029/2007JF000977

Phillips JD (2009) Biological energy in landscape evolution. Am J Sci 309(4):271–289. https://doi.org/10.2475/04.2009.01

Phillips JD, Van Dyke C (2017) State-and-transition models in geomorphology. Catena 153:168–181. https://doi.org/10.1016/j.catena.2017.02.009

Poesen J, Lavee H (1994) Rock fragments in top soils: significance and processes. CATENA 23(1–2):1–28. https://doi.org/10.1016/0341-8162(94)90050-7

Renard KG, Foster GR, Weesies GA, McCool DK, Yoder DC (1997) Predicting soil erosion by water: a guide to conservation planning with the Revised Universal Soil Loss Equation (RUSLE), 703. United States Department of Agriculture, Washington, DC

Rixhon G, Briant RM, Cordier S, Duval M, Jones A, Scholz D (2017) Revealing the pace of river landscape evolution during the Quaternary: recent developments in numerical dating methods. Quatern Sci Rev 166:91–113. https://doi.org/10.1016/j.quascirev.2016.08.016

Robinson RA, Slingerland RL (1998) Origin of fluvial grain-size trends in a foreland basin, the Pocono Formation on the central Appalachian Basin. J Sediment Res 68(3):473–486. https://doi.org/10.2110/jsr.68.473

Román-Sánchez A, Willgoose G, Giráldez JV, Peña A, Vanwalleghem T (2019) The effect of fragmentation on the distribution of hillslope rock size and abundance: Insights from

contrasting field and model data. Geoderma 352:228–240. https://doi.org/10.1016/j.geoderma.2019.06.014
Rosenbloom NA, Anderson RS (1994) Hillslope and channel evolution in a marine terraced landscape, Santa Cruz, California. J Geophys Res Solid Earth 99(B7):14013–14029. https://doi.org/10.1029/94JB00048
Ruetenik GA, Moucha R, Hoke GD (2016) Landscape response to changes in dynamic topography. Terra Nova 28(4):289–296. https://doi.org/10.1111/ter.12220
Saco PM, Willgoose GR, Hancock GR (2006) Spatial organization of soil depths using a landform evolution model. J Geophys Res Earth Surf. https://doi.org/10.1029/2005JF000351
Salles T (2016) Badlands: a parallel basin and landscape dynamics model. SoftwareX 5:195–202. https://doi.org/10.1016/j.softx.2016.08.005
Schaap MG, Leij FJ, Van Genuchten MT (2001) Rosetta: a computer program for estimating soil hydraulic parameters with hierarchical pedotransfer functions. J Hydrol 251(3–4):163–176. https://doi.org/10.1016/S0022-1694(01)00466-8
Schoorl JM, Veldkamp A (2016) Multiscale soil-landscape process modeling. In: Environmental soil-landscape modeling: geographic information technologies and pedometrics, CRC Press, pp 417–435
Schumer R, Taloni A, Furbish DJ (2017) Theory connecting nonlocal sediment transport, earth surface roughness, and the Sadler effect. Geophys Res Lett 44(5):2281–2289. https://doi.org/10.1002/2016GL072134
Schumm SA, Lichty RW (1965) Time, space, and causality in geomorphology. Am J Sci 263(2):110–119. https://doi.org/10.2475/ajs.263.2.110
Scott AC (2018) Burning planet: the story of fire through time. Oxford University Press, Oxford
Scull P, Franklin J, Chadwick OA, McArthur D (2003) Predictive soil mapping: a review. Prog Phys Geogr 27(2):171–197. https://doi.org/10.1191/0309133303pp366ra
Shobe CM, Tucker GE, Barnhart KR (2018) The SPACE 1.0 model: a Landlab component for 2-D calculation of sediment transport, bedrock erosion, and landscape evolution. Geosci Model Dev 10(12):4577–4604. https://doi.org/10.5194/gmd-10-4577-2017
Shustikova I, Domeneghetti A, Neal JC, Bates P, Castellarin A (2019) Comparing 2D capabilities of HEC-RAS and LISFLOOD-FP on complex topography. Hydrol Sci J 64(14):1769–1782. https://doi.org/10.1080/02626667.2019.1671982
Skinner CJ, Coulthard TJ, Schwanghart W, Wiel MJ, Hancock G (2018) Global sensitivity analysis of parameter uncertainty in landscape evolution models. Geosci Model Dev 11(12):4873–4888. https://doi.org/10.5194/gmd-11-4873-2018
Sklar LS, Riebe CS, Marshall JA, Genetti J, Leclere S, Lukens CL, Merces V (2017) The problem of predicting the size distribution of sediment supplied by hillslopes to rivers. Geomorphology 277:31–49. https://doi.org/10.1016/j.geomorph.2016.05.005
Sólyom PB, Tucker GE (2004) Effect of limited storm duration on landscape evolution, drainage basin geometry, and hydrograph shapes. J Geophys Res Earth Surf. https://doi.org/10.1029/2003JF000032
Stark CP (2006) A self-regulating model of bedrock river channel geometry. Geophys Res Lett. https://doi.org/10.1029/2005GL023193
Stark CP, Passalacqua P (2014) A dynamical system model of eco-geomorphic response to landslide disturbance. Water Resour Res 50(10):8216–8226. https://doi.org/10.1002/2013WR014810
Stock JD, Dietrich WE (2006) Erosion of steepland valleys by debris flows. Geol Soc Am Bull 118(9–10):1125–1148. https://doi.org/10.1130/B25902.1
Strahler AH, Strahler AN (2006) Introducing physical geography, 4th edn. Wiley, Hoboken
Strudley MW, Murray AB, Haff PK (2006) Regolith thickness instability and the formation of tors in arid environments. J Geophys Res Earth Surf. https://doi.org/10.1029/2005JF000405
Temme AJ, Vanwalleghem T (2016) LORICA–a new model for linking landscape and soil profile evolution: development and sensitivity analysis. Comput Geosci 90(B):131–143. https://doi.org/10.1016/j.cageo.2015.08.004
Tucker GE (2009) Natural experiments in landscape evolution. Earth Surf Proc Land 34(10):1450–1460. https://doi.org/10.1002/esp.1833
Tucker GE, Bradley DN (2010) Trouble with diffusion: reassessing hillslope erosion laws with a particle-based model. J Geophys Res Earth Surf. https://doi.org/10.1029/2009JF001264
Tucker GE, Bras RL (2000) A stochastic approach to modeling the role of rainfall variability in drainage basin evolution. Water Resour Res 36(7):1953–1964. https://doi.org/10.1029/2000WR900065
Tucker GE, Hancock GR (2010) Modelling landscape evolution. Earth Surf Proc Land 35:28–50. https://doi.org/10.1002/esp.1952
Tucker GE, Slingerland RL (1994) Erosional dynamics, flexural isostasy, and long-lived escarpments: a numerical modeling study. J Geophys Res Solid Earth 99(B6):12229–12243. https://doi.org/10.1029/94JB00320
Tucker GE, Whipple KX (2002) Topographic outcomes predicted by stream erosion models: sensitivity analysis and intermodel comparison. J Geophys Res Solid Earth 107(B9):ETG-1. https://doi.org/10.1029/2001JB000162
Ugelvig SV, Egholm DL, Iverson N (2016) R. Glacial landscape evolution by subglacial quarrying: a multiscale computational approach. J Geophys Res Earth Surf 121(11):2042–2068. https://doi.org/10.1002/2016JF003960
Van De Wiel MJ, Coulthard TJ, Macklin MG, Lewin J (2007) Embedding reach-scale fluvial dynamics within the CAESAR cellular automaton landscape evolution model. Geomorphology 90(3–4):283–301. https://doi.org/10.1016/j.geomorph.2006.10.024
Vanwalleghem T, Stockmann U, Minasny B, McBratney AB (2013) A quantitative model for integrating landscape evolution and soil formation. J Geophys Res Earth Surf 118(2):331–347. https://doi.org/10.1029/2011JF002296
Varrani A, Nones M, Gupana R (2019) Long-term modelling of fluvial systems at the watershed scale: examples from three case studies. J Hydrol 574:1042–1052. https://doi.org/10.1016/j.jhydrol.2019.05.012
Warren SD, Ruzycki TS, Vaughan R, Nissen PE (2019) Validation of the unit stream power erosion and deposition (USPED) model at yakima training centre Washington. Northwest Sci 92(sp5):338–345. https://doi.org/10.3955/046.092.0504
Welivitiya WDP, Willgoose GR, Hancock GR (2016) Exploring the sensitivity on a soil area-slope-grading relationship to changes in process parameters using a pedogenesis model. Earth Surf Dyn 4(3):607–625. https://doi.org/10.5194/esurf-4-607-2016
Welivitiya WDP, Willgoose GR, Hancock GR (2019) A coupled soilscape–landform evolution model: model formulation and initial results. Earth Surf Dyn 7(2):591–607. https://doi.org/10.5194/esurf-7-591-2019
Whipple KX, Tucker GE (2002) Implications of sediment-flux-dependent river incision models for landscape evolution. J Geophys Res Solid Earth 107(B2):ETG 3-1–ETG 3-20. https://doi.org/10.1029/2001JB000162
Whipple KX, Forte AM, DiBiase RA, Gasparini NM, Ouimet WB (2017) Timescales of landscape response to divide migration and drainage capture: implications for the role of divide mobility in landscape evolution. J Geophys Res Earth Surf 122(1):248–273. https://doi.org/10.1002/2016JF003973

Wilkes MA, Gittins JR, Mathers KL, Mason R, Casas-Mulet R, Vanzo D, Mckenzie M, Murray-Bligh J, England J, Gurnell AM, Jones JI (2019) Physical and biological controls on fine sediment transport and storage in rivers. Wiley Interdiscip Rev Water 6(2):e1331. https://doi.org/10.1002/wat2.1331

Willgoose GR (2005) Mathematical modeling of whole landscape evolution. Annu Rev Earth Planet Sci 33:443–459. https://doi.org/10.1146/annurev.earth.33.092203.122610

Willgoose GR (2018) Principles of soilscape and landscape evolution. Cambridge University Press, Cambridge

Willgoose GR, Sharmeen S (2006) A one-dimensional model for simulating armouring and erosion on hillslopes: 1. model development and event-scale dynamics. Earth Surf Process Landf 31(8):970–991. https://doi.org/10.1002/esp.1398

Willgoose GR, Bras RL, Rodriguez-Iturbe I (1989) A physically based channel network and catchment evolution model. TR322. Ralph M. Parsons Laboratory, Massachusetts, USA

Willgoose GR, Bras RL, Rodriguez-Iturbe I (1991) A physically based coupled network growth and hillslope evolution model: 1 Theory. Water Resour Res 27:1671–1684. https://doi.org/10.1029/91WR00935

Williams RD, Brasington J, Hicks DM (2016) Numerical modelling of braided river morphodynamics: review and future challenges. Geography Compass 10(3):102–127. https://doi.org/10.1111/gec3.12260

Wobus CW, Kean JW, Tucker GE, Anderson RS (2008) Modeling the evolution of channel shape: Balancing computational efficiency with hydraulic fidelity. J Geophys Res Earth Surf 113(F2):F02004. https://doi.org/10.1029/2007JF000914

Yetemen O, Istanbulluoglu E, Vivoni ER (2010) The implications of geology, soils, and vegetation on landscape morphology: Inferences from semi-arid basins with complex vegetation patterns in Central New Mexico, USA. Geomorphology 116(3–4):246–263. https://doi.org/10.1016/j.geomorph.2009.11.026

Zhang D, Narteau C, Rozier O, Courrech du Pont S (2012) Morphology and dynamics of star dunes from numerical modelling. Nat Geosci 5:463–467. https://doi.org/10.1038/ngeo1503

Acta Geophysica (2020) 68:477–493
https://doi.org/10.1007/s11600-019-00398-9

RESEARCH ARTICLE - HYDROLOGY

Integration of interval rough AHP and fuzzy logic for assessment of flood prone areas at the regional scale

Mehdi Sepehri[1] · Hossein Malekinezhad[1] · Farshid Jahanbakhshi[1] · Ali Rerza Ildoromi[2] · Javad Chezgi[3] · Omid Ghorbanzadeh[4] · Elham Naghipour[1]

Received: 28 July 2019 / Accepted: 26 December 2019 / Published online: 28 January 2020

Abstract
This study was conducted to prepare a flood susceptibility map in northwest of Hamadan Province, Iran. For this purpose, six criteria related to flood (i.e., distance to discharge channel, slope (%), elevation, soil texture and land use, topographic wet index, and check dams) were chosen. Then, based on the role of these criteria on degree of flood susceptibility, were weighted both in the context of inter-weighting (fuzzy logic) and outer-criteria (Interval Rough Analytic Hierarchy Process). Finally, by combining these primary weights by weight overlay method in GIS, the flood susceptibility mapping was prepared in the study area. The resulted map based on *K*-means clustering and Silhouette function was divided into 9 clusters, whereas the lower clusters show low susceptibility to flood and vice versa. To assess the accuracy of the produced map, 102 flood observation points were overlaid on the clustered flood susceptibility map. The results showed that among these 102 flood points, 66 points are located in the clusters 8 and 9 and 3 points are located on cluster 7. These values show that the produced flood susceptibility mapping has a high accuracy.

Keywords Flood · AHP · Fuzzy logic · IRAHP · *K*-means

Introduction

Floods are known among the most conventional and devastating natural disaster causes to serious financial and life loses throughout the worlds (Kowalzig 2008; Kourgialas and Karatzas 2011). Therefore, the flood has been addressed by many studies on natural disasters. Since the combination of multi-criteria decision analysis (MCDA) and GIS allows the management of a large volume of spatial data (Fernández and Lutz 2010; Sepehri et al. 2019a), it is regarded as a powerful tool for analyzing and controlling natural disasters. Smithson (2012) divided the MCDA method into objective and subjective categories. In the objective category, the natural distribution of the criteria is used to assess their effect on the study objective. Fuzzy logic is one of the well-known broadly used methods in the objective category, used in various studies into natural hazards including flood susceptibility mapping (Perera and Lahat 2015; Hong et al. 2018), forest fire delineation (Iliadis 2005; Bolourchi and Uysal 2013), and groundwater contamination (Dixon 2005; Pathak and Hiratsuka 2011). For example, Sepehri et al. (2019b) used the fuzzy logic to prioritize suburban basins in terms of flood severity in Hamadan City. Yazdi and Neyshabouri (2014) employed fuzzy logic to identify low impact development (LID) strategies for reducing flood consequences. Jun et al. (2013) applied a fuzzy multi-criteria approach to delineate flood susceptibility mapping of South Korea, considering the impacts of climate change. Chen and Chang (2010) applied and developed fuzzy operators to consider the decision-making barriers and limitations in water resource redistribution in two neighboring river basins. Kanani-Sadat et al. (2019) developed a new approach to delineate the flood hazard mapping in ungagged and data-scarce areas based on a fuzzy multi-criteria decision approach.

✉ Ali Rerza Ildoromi
a.ildoromi@yahoo.com

[1] Department of Watershed Management, Faculty of Natural Resources, Yazd University, Yazd, Iran

[2] Department of Watershed Management, Faculty of Natural Resources, Malayer University, Hamadan, Iran

[3] Department of Watershed Management, Faculty of Natural Resources, Birjand University, Birjand, Iran

[4] Department of Geoinformatics Z_GIS, University of Salzburg, Salzburg, Austria

The major characteristic of fuzzy logic is its inter-criteria feature, in that the weight of each criterion is considered separately. Since there are several criteria in multi-criteria studies (natural hazard studies) with unique weight, inter-criteria dependencies are regarded as a limitation. To consider the relative weight of the criteria (outer-criteria), it is a necessity to use the subjective and objective methods together. The analytic hierarchy process (AHP), developed by Saaty in 1989, is one of the most popular methods of the subjective category used in natural hazard studies.

Mahmoud and Gan (2018) delineated flood susceptibility mapping by using 10 criteria in arid regions of the Middle East. These criteria were weighted based on their roles in the flood severity using AHP. Sepehri et al. (2017) used the AHP method for flood hazard mapping in Gonbad chi region. The AHP method was used to determine the relative weights of the flood criteria. Souissi et al. (2019) employed GIS-based MCDM-AHP modeling for flood hazard mapping using eight flood criteria including elevation, land use/land coverage, lithology, and rainfall intensity. Noori et al. (2015) used the AHP method to determine the effect Rock check dams on flood reducing in Northwest Hamadan.

Since in AHP and other subjective methods, the relative weight of the criteria is determined based on the decision maker's preferences, it causes high uncertainty in the final objective of the study. Therefore, in recent years, researchers have tried to reduce this uncertainty by using interval rough numbers (IRN) (Gigović et al. 2017; Pamucar et al. 2017).

This study aimed to make a flood susceptibility map of Ilanlu Watershed in Hamadan by integrating interval rough AHP (IRAHP) and fuzzy logic and using GIS. It is a highly affected region by the flood. Therefore, this study was organized with five sections. In "Description of the study area" section, a brief description of the case and the details of used materials and methods are presented. "Methodology" section analyzes the employed materials and methods. "Analysis and results" section discusses the results. The final section draws a brief conclusion of the study.

Description of the study area

The Ilanlu Watershed, located in Northwest Hamadan Province (31°24′45″ to 31°27′29″ north; 41°55/20″ to 41°57/34″ east), was selected as the case study because it lacked a flood map. This watershed covers an area of about 15 km^2 with a semi-humid climate. Based on field observations and local information, many huge flood disasters occurred in the past decades causing substantial economic loss to agricultural lands in which approximately 70% of the residents are occupationally involved. Due to some features of the case, such as rugged topography and geological structures, floods are likely to occur. Figure 1 shows features of the case and layout of check dams constructed in recent years for flood control.

Methodology

For flood susceptibility mapping, it is first necessary to define related flood criteria. Next, we investigated the fuzzy logic for inter-criteria weighting. Then, the IRAHP method was used for outer-criteria weighting. Finally, the flood hazard map, made based on the combination of the inter- and outer-criteria weights, was classified into flood hazard susceptibility areas using *K*-means clustering and silhouette function. The accuracy of the prepared flood hazard mapping was assessed using the relative operating characteristics (ROC) method. Flowchart of the study stages is shown in Fig. 2, which includes the criteria related to flood studies and manipulation of them in a GIS environment, multi-criteria decision analysis and assessment of the model accuracy.

Preparing the criteria

Based on data availability and literature reviews on flood susceptibility mapping (Fernández and Lutz 2010; Gigović et al. 2017; Mahmoud and Gan 2018), six criteria that are supposed to influence flood process [i.e., distance to discharge channel (**C1**), slope (**C2**), elevation (**C3**), STLU (**C4**), TWI (**C5**), and check dams (**C6**)] were selected (Fig. 3). Among these criteria, the format of soil texture and land use and check dams, that were extracted from 1/250,000 digital maps of database of department of Natural Resources of Hamadan Province, were polygon and point shape files (common formats in ArcGIS software), respectively, which were converted to raster format. Other criteria were directly extracted from The SRTM DEM (30 m) was downloaded from United States Geological Survey (USGS) (2011).

Assigning weights and ranking criteria

In the present study, according to the knowledge-based method, the weights of criteria (inter-criteria and outer-criteria) were measured using the fuzzy logic and IRAHP methods. Using the fuzzy logic method, both dimensions of the criteria that are different were removed and the role and importance of the values of each criterion in the context of the flood degree were defined. The IRAHP that it is known the improved method of AHP allows removing the subjectivity and ambiguity that occurs in group decision making. Thus, this method can be considered as a better method for reducing the uncertainty of the final flood spatial map.

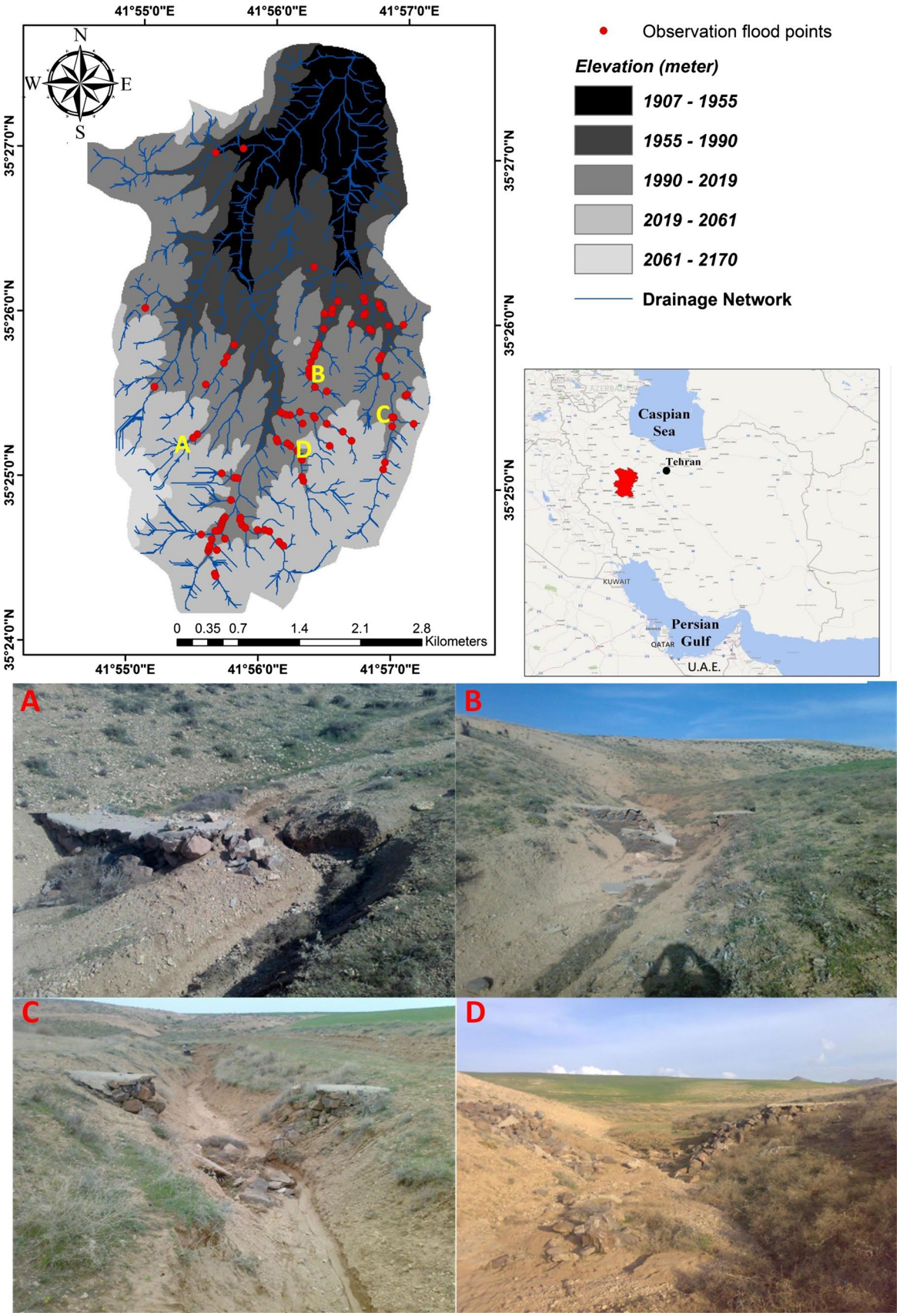

Fig. 1 Location of the study are in Iran and Hamadan Province and photos of flood in the case study

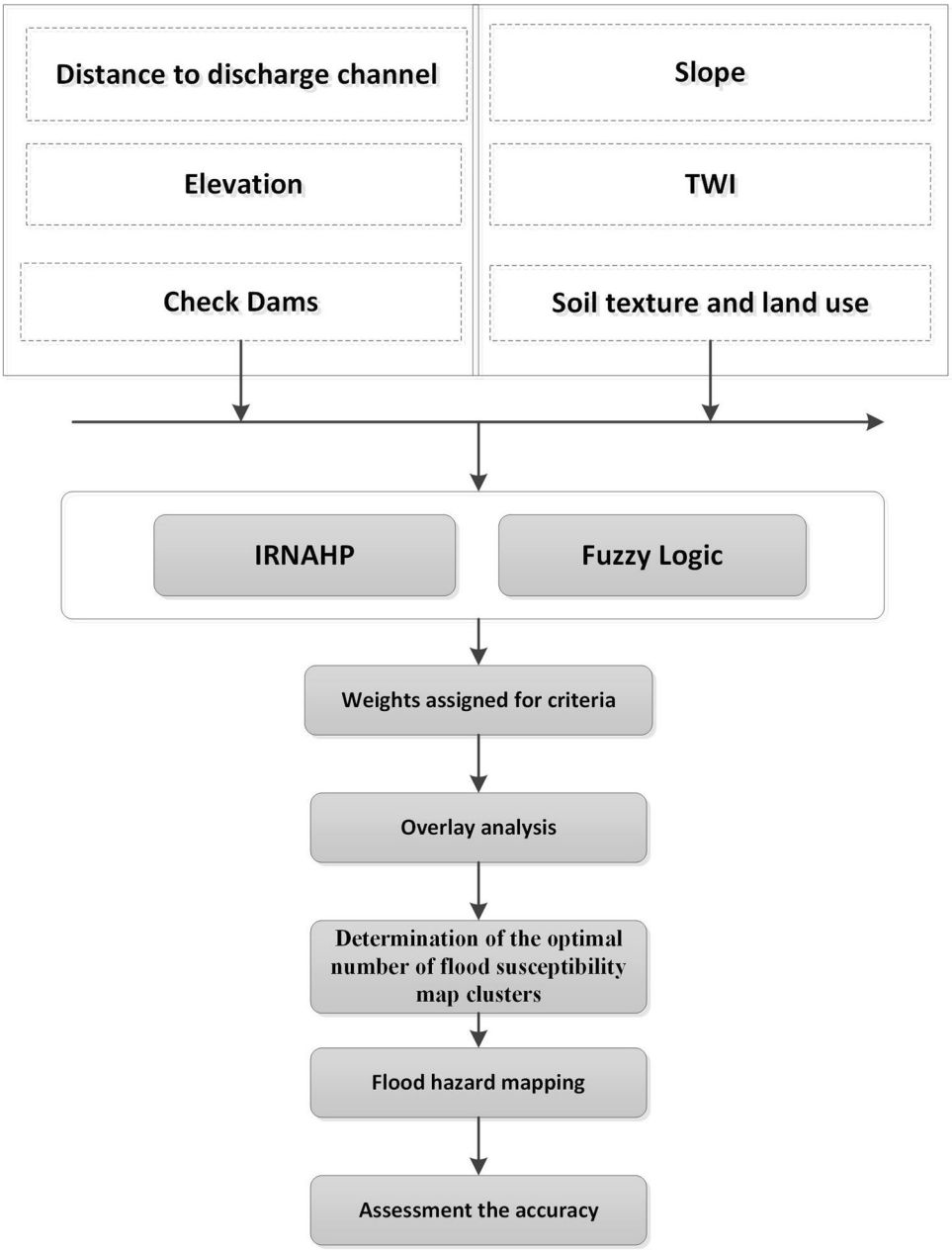

Fig. 2 Flowchart for the preparation of flood hazard map

Fuzzy logic method

Fuzzy theory was introduced by Zadeh (1965). The fuzzy logic contains all theories that employ the basic concepts of fuzzy sets or membership functions. To determine the values of a set, the membership function must be defined. In the membership function, the values of any criteria can vary from 0 to 1. The 0 values mean that the desired value has no membership in that set and, on the contrary, the value of 1 is completely a member of that set. Other values fall between 0 and 1 based on their degree of membership. One of the main challenges in fuzzy studies is that there is no optimum method for determining the kind of membership function and its parameters. These membership functions are generally selected based on the priorities of decision makers in the field of study (Shahabi et al. 2015).

Therefore, the inter-weighing of all the effective criteria in the production of flood maps seems to be more or less similar in various studies. In this study, to weight the criteria that have a direct relationship with the degree of a flood, Eq. (1) was chosen. For other criteria that have an inverse relationship with the degree of a flood, the inverse of Eq. 1 (i.e., Eq. 2) was chosen. Among the applied criteria, the check dam's criteria have two sub-criteria. After assigning the weights to each sub-criteria using Eqs. (1) and (2), these two sub-criteria are combined using gamma fuzzy (Eq. 3),

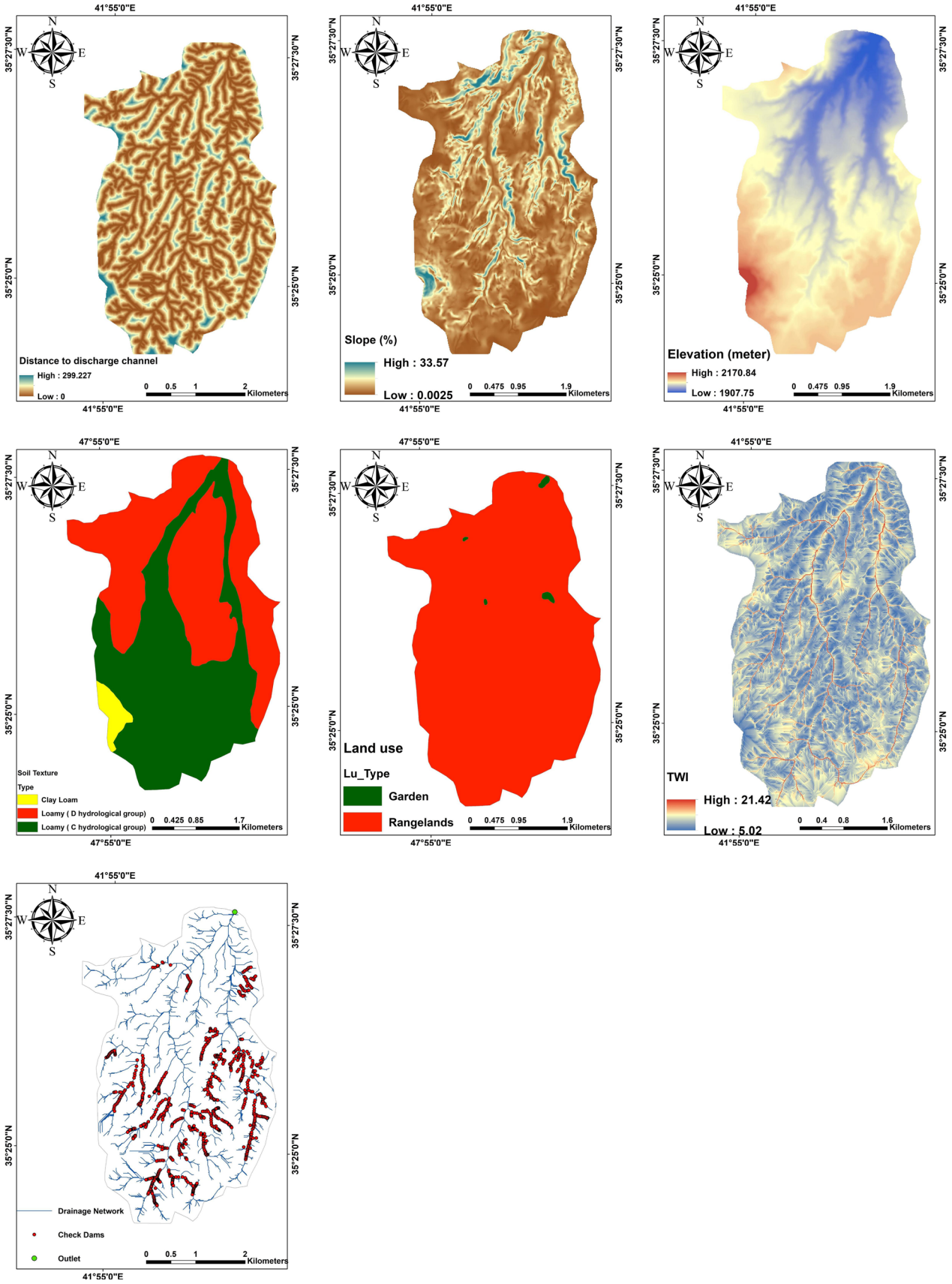

Fig. 3 Images showing the variables incorporated within the model as GIS layers

which is composed of two sum and product functions (Eq. 3) (Ramesh et al. 2016; Sema et al. 2017):

$$f(x;a,b) = \begin{cases} 0, x \le a \\ \frac{x-a}{b-a}, \quad a \le x \le b \\ 1, b \le x \end{cases} \tag{1}$$

$$f^{-1}(x;a,b) = f(x;b,a) = \begin{cases} 1, x \le a \\ 1 - \frac{x-a}{b-a}, \quad a \le x \le b \\ 0, b \le x \end{cases} \tag{2}$$

$$\mu_{gamma} = \mu_{al,sum}^{\gamma} * \mu_{al,prod}^{1-\gamma} = \left[\prod_{i}^{n} \mu_i\right]^{\gamma} * \left[1 - \prod_{i}^{n} (1-\mu_i)\right]^{1-\gamma} \tag{3}$$

Interval rough numbers (IRN)

In this study, it was tried to measure the uncertainty and errors in the data based on a new approach in the theory of IRN-based rough numbers. The process of group decision making can be accompanied by a series of mistakes and subjectivities. In this regard, decision makers face a dilemma during assigning a certain value to criteria. Let us assume that a feature of the decision must be scored with a qualitative scale that ranges from 1 to 9. Also, assume that there are three decision makers in the process of evaluating the criteria. The first decision maker may assume that the desired criteria have a value in the range of 5–6. The decision maker 2 also believes that this criterion should have a value between 6 and 7. Finally, the last decision makers based on his knowledge chose a vale in the range of 6–7. Then, using operations on the rough numbers (further explanations are provided in the next sections), we generate attribute values to explain the mentioned ambiguity. Therefore, the ambiguity of decision maker 1 can be described by IRN ([5, 5.67], [6, 6.67]) (Pamucar et al. 2017). Also, for decision maker 2 and decision maker 3, these values may be ([5. 67, 6], [6.67, 7]), and ([5. 67, 6], [6.67, 7]), respectively (Pamucar et al. 2017).

Considering the novelty of the IRN methodology, there are few studies regarding the application of IRN in multi-criteria decision making. Therefore, the other objective of this study is to encourage other authors for applying IRN in multi-criteria decision-making studies, because the benefits of IRN method can serve as a strong motivation for its widespread use. Suppose there is a universe set that consists of two subsets. The first subset includes K classes that its components indicate preferences of the decision makers $R = (J1, J2, \ldots, JK)$ with $J1 < J2 <, \cdots, < JK$ constraint. The other subset also shows K classes of the decision makers' preferences $R^* = (I1, I2, \ldots, I3)$, where each object class is displayed as $I_i = \{I_{li}, I_{ui}\}$ with the condition of $Ili \le Iui (1 \le i \le m)$ and $Ili, Iui \in R$; I_{li} and I_{ui} represent the limits of lower interval and upper interval of class I, respectively. If the condition of $I_{l1}^* \prec I_{l2}^* \prec, \cdots, \prec I_{lj}^*, I_{u1}^* \prec I_{u2}^* \prec, \cdots, \prec I_{uk}^* (1 \le j, k \le m)$ is established in both limits, then two new sets $R_l^* = (I_{l1}^*, I_{l2}^*, , \ldots, I_{lj}^*)$ (lower class of object) and $R_u^* = (I_{u1}^*, I_{u2}^*, \ldots, I_{uk}^*)$ (upper class of object) are defined. So, for each class of $I_{li}^* \in R (1 \le i \le j)$ and $I_{ui}^* = R (1 \le i \le k)$, lower approximation I_{li}^* and I_{ui}^* will be (Pamučar et al. 2017):

$$\underline{Apr}(I_{li}^*) = \cup \left\{ Y \in u / R_l^*(Y) \le I_{li}^* \right\} \tag{4}$$

$$\underline{Apr}(I_{ui}^*) = \cup \left\{ Y \in u / R_u^*(Y) \le I_{ui}^* \right\} \tag{5}$$

And upper approximation of I_{li}^* and I_{ui}^* is defined as:

$$\overline{Apr}(I_{li}^*) = \cup \left\{ Y \in u / R_l^*(Y) \ge I_{li}^* \right\} \tag{6}$$

$$\overline{Apr}(I_{ui}^*) = \cup \left\{ Y \in u / R_l^*(Y) \ge I_{ui}^* \right\} \tag{7}$$

Upper and lower classes I_{li}^* and I_{ui}^* are described by $\underline{\lim}(I_{li}^*)$ and $\underline{\lim}(I_{ui}^*)$ (lower limits) and $\overline{\lim}(I_{li}^*)$ and $\overline{\lim}(I_{ui}^*)$ (upper limits), respectively:

$$\underline{Lim}(I_{li}^*) = \frac{1}{M_L} \sum R_l^*(Y) | \mathrm{Y} \in \underline{\mathrm{Apr}}(\mathrm{I}_{li}^*) \tag{8}$$

$$\underline{Lim}(I_{ui}^*) = \frac{1}{M_L^*} \sum Ru(Y) | \mathrm{Y} \in \underline{\mathrm{Apr}}(\mathrm{I}_{ui}^*) \tag{9}$$

where M_l and M_l^* denote the number of objects that are located in the lower approximation of the class of objects I_{ui}^* and I_{li}^*, respectively.

$$\overline{Lim}(I_{li}^*) = \frac{1}{M_u} \sum R_l^*(Y) | \mathrm{Y} \in \underline{\mathrm{Apr}}(\mathrm{I}_{li}^*) \tag{10}$$

$$\overline{Lim}(I_{ui}^*) = \frac{1}{M_u^*} \sum Ru(Y) | \mathrm{Y} \in \underline{\mathrm{Apr}}(\mathrm{I}_{ui}^*) \tag{11}$$

where M_u and M_u^* show the number of objects located in the upper approximation of the class of objects I_{ui}^* and I_{li}^*, respectively.

The rough boundary interval for I_{li}^* (RB (I_{li}^*)), which shows the interval between the upper and lower limits, is as follows:

$$RB(I_{li}^*) = \overline{Lim}(I_{li}^*) - \underline{Lim}(I_{li}^*) \tag{12}$$

For I_{ui}^*, the rough boundary interval is defined as:

$$RB(I_{ui}^{*}) = \overline{Lim}(I_{ui}^{*}) - \underline{Lim}(I_{ui}^{*}) \tag{13}$$

Then, the uncertainty class of objects I_{li}^{*} and I_{ui}^{*}, which is described by their lower and upper limits, is shown as follows:

$$RN(I_{li}^{*}) = [\overline{Lim}(I_{li}^{*}), \underline{Lim}(I_{li}^{*})] \tag{14}$$

$$RN(I_{ui}^{*}) = [\overline{Lim}(I_{ui}^{*}), \underline{Lim}(I_{ui}^{*})] \tag{15}$$

As can be seen, each class of objects is defined with its lower and upper limits forms an IRN, which is described as follows:

$$IRN(I_{i}^{*}) = [RN(I_{li}^{*}), RN(I_{ui}^{*})] \tag{16}$$

IR'AHP mathematical model

The AHP developed by Thomas L. Saaty (1980) is one of the most comprehensive systems designed for decision making with multiple criteria. The AHP is widely used in various policy issues, especially in solving problems related to determining the weighting of indices. This method provides the ability to measure the stability of decision makers' preferences in group decision making and allows manipulating quantitative and qualitative criteria (Papaioannou et al. 2015; Ghosh and Kar 2018; Radwan et al. 2019). The final decision to use the AHP method is based on the judgment of the decision maker. Hence, due to the subjectivity and ambiguity that occurs in group decision making, this study used the combination of IRN with the AHP method to exploit that mentality. This combination method can be summarized in five steps as follows (Gigović et al. 2017; Pamucar et al. 2017):

1. Organizing a hierarchical structure of evaluation criteria

At this stage, we chose a group of K experts to select the criteria and define the hierarchy of problem. In this hierarchy, the global purpose is placed at the top of this hierarchy, and at the lower levels, the selected criteria are defined.

2. Filling the paired comparisons matrix

Experts compare the evaluation criteria in pairs to determine the weight of the criteria. This benchmark of comparison is based on Saaty's 9-level linguistic scale (Table 1). Each eth expert exhibits his comparison in the form of a matrix (Eq. 17).

$$Z_k = \begin{bmatrix} 1 & x_{12}^{e};x_{12}^{e'} & \cdots & x_{1n}^{e};x_{1n}^{e'} \\ x_{21}^{e};x_{21}^{e'} & 1 & \ldots & x_{2n}^{e};x_{2n}^{e'} \\ \vdots & \vdots & \ddots & \vdots \\ x_{n1}^{e};x_{n1}^{e'} & x_{n2}^{e};x_{n2}^{e'} & \cdots & 1 \end{bmatrix}_{n\times n} ; \quad 1 \le i,j \le e \le k \tag{17}$$

In the above matrix, the values related to x_{ij}^{k} and $x_{ij}^{k'}$ are based on the Saaty's 9-level linguistic scale and using K expert in order to provide a pairwise comparison of the criteria.

If, an expert K has uncertainty toward a pair of criteria (i, j) and cannot choose between the Saaty's 9-level linguistic scale, then $x_{ij}^{k} \neq x_{ij}^{k'}$ is established. On the other hand, if there is no uncertainty in decision making of expert k, then this expert chooses a number from the Saaty's 9-level linguistic scale (Table 1). In this case, the value of pair comparison of the index (i, j) would be $x_{ij}^{k} = x_{ij}^{k'}$.

3. Establishing the weight coefficients of the experts

For each comparative matrix Z_k, the consistency of the values given by the experts should be determined. In this study, the consistency method by Saaty (1980) was used in order to determine the consistency of decision making by experts. This computational rate consists of two steps.

- Calculating the consistency rate $CI = (\lambda_{\max} - n)/(n-1)$, where n is related to matrix rank and $\lambda_{\max}$ is the maximum eigenvalue of the comparison matrix.

Table 1 The comparison scale between two criteria (Saaty 1980)

Preference factor	Degree of preference	Explanation
1	Equally	Two factors contribute equally to the objective
3	Moderately	Experience and judgment slightly to moderately favor one factor over another
5	Strongly	Experience and judgment strongly or essentially favor one factor over another
7	Very strongly	A factor is strongly favored over another and its dominance is showed in practice
9	Extremely	The evidence of favoring one factor over another is of the highest degree possible of an affirmation
2, 4, 6, 8	Intermediate	Used to represent compromises between the preferences in weights 1, 3, 5, 7 and 9
Reciprocals	Opposites	Used for inverse comparison

- Calculating the consistency rate $CR = CI/RI$, where CI and RI are the consistency index and random index, respectively. The random index depends on the matrix rank and its values are determined by randomly creating 500 matrices.
- Step 4: Generating an averaged interval rough comparison matrix

At this stage, using matrix (17) of all experts, two matrices of the sequence of aggregated experts' X^{*L} and $X^{*\prime u}$ are obtained as follows:

$$X^{*L}\begin{bmatrix} x_{11}^{1L}, x_{11}^{2L}, \ldots, x_{11}^{kL} & x_{12}^{1L}, x_{12}^{2L}, \ldots, x_{12}^{kL} & \cdots & x_{1n}^{1L}, x_{1n}^{2L}, \ldots, x_{1n}^{kL} \\ x_{21}^{1L}, x_{21}^{2L}, \ldots, x_{21}^{kL} & x_{22}^{1L}, x_{22}^{2L}, \ldots, x_{22}^{kL} & \cdots & x_{2n}^{1L}, x_{2n}^{2L}, \ldots, x_{2n}^{kL} \\ \cdots & \cdots & \cdots & \cdots \\ x_{n1}^{1L}, x_{n1}^{2L}, \ldots, x_{n1}^{kL} & x_{n2}^{1L}, x_{n2}^{2L}, \ldots, x_{n2}^{kL} & \cdots & x_{nn}^{1L}, x_{nn}^{2L}, \ldots, x_{nn}^{kL} \end{bmatrix}_{n\times n} \tag{18}$$

$$X^{*\prime u}\begin{bmatrix} x_{11}^{1\prime u}, x_{11}^{2u}, \ldots, x_{11}^{k\prime u} & x_{12}^{1\prime u}, x_{12}^{2\prime u}, \ldots, x_{12}^{k\prime u} & \cdots & x_{1n}^{1\prime u}, x_{1n}^{2\prime u}, \ldots, x_{1n}^{k\prime u} \\ x_{21}^{1\prime u}, x_{21}^{2u}, \ldots, x_{21}^{k\prime u} & x_{22}^{1\prime u}, x_{22}^{2\prime u}, \ldots, x_{22}^{k\prime u} & \cdots & x_{2n}^{1\prime u}, x_{2n}^{2\prime u}, \ldots, x_{2n}^{k\prime u} \\ \cdots & \cdots & \cdots & \cdots \\ x_{n1}^{1\prime u}, x_{n1}^{2\prime u}, \ldots, x_{n1}^{k\prime u} & x_{n2}^{1\prime u}, x_{n2}^{2\prime u}, \ldots, x_{n2}^{k\prime u} & \cdots & x_{nn}^{1\prime u}, x_{nn}^{2\prime u}, \ldots, x_{nn}^{k\prime u} \end{bmatrix}_{n\times n} \tag{19}$$

$x_{ij}^{L} = \left\{x_{ij}^{1L}, x_{ij}^{2L}, \ldots, x_{ij}^{kL}\right\}$ and $x_{ij}^{\prime u} = \left\{x_{ij}^{1\prime u}, x_{ij}^{2\prime u}, \ldots, x_{ij}^{k\prime u}\right\}$. These matrices are sequences that express the importance of the criteria i relative to the criteria j. Then, using Eqs. (4–16), each sequence of x_{ij}^{k} and $x_{ij}^{k'}$ is transferred to $RN(x_{ij}^{KL}) = [\underline{Lim}(x_{ij}^{KL}), \overline{Lim}(x_{ij}^{KL})]$ and $RN(x_{ij}^{K'u}) = [\underline{Lim}(x_{ij}^{K'u}), \overline{Lim}(x_{ij}^{K'u})]$, respectively, where $\underline{Lim}(x_{ij}^{KL})$ and $\underline{Lim}(x_{ij}^{K'u})$ are called lower limits while $\overline{Lim}(x_{ij}^{KL})$ and $\overline{Lim}(x_{ij}^{K'u})$ are upper limits of $RN(x_{ij}^{KL})$ and $RN(x_{ij}^{K'u})$, respectively. Such a rough sequence is defined in matrices 18 and 19. Therefore, rough matrices are obtained $X^{1L}, X^{2L}, \ldots, X^{mL}$ for the first rough sequence $RN(x_{ij}^{KL})$ and $X^{1'u}, X^{2'u}, \ldots, X^{m'u}$ for the second rough sequence $RN(x_{ij}^{K'u})$, where the subindex m expresses the number of experts.

The rough sequence in the first $(X^{1L}, X^{2L}, \ldots, X^{mL})$ and second $(X^{1'u}, X^{2'u}, \ldots, X^{m'u})$ groups of rough matrices at (i, j) is defined as $RN(x_{ij}^{L}) = \left\{\left[\underline{Lim}(x_{ij}^{1L}), \overline{Lim}(x_{ij}^{1L})\right], \left[\underline{Lim}(x_{ij}^{2L}), \overline{Lim}(x_{ij}^{2L})\right], \ldots, \left[\underline{Lim}(x_{ij}^{mL}), \overline{Lim}(x_{ij}^{mL})\right]\right\}$ and $RN(x_{ij}^{\prime u}) = \left\{\left[\underline{Lim}(x_{ij}^{1'u}), \overline{Lim}(x_{ij}^{1'u})\right], \left[\underline{Lim}(x_{ij}^{2'u}), \overline{Lim}(x_{ij}^{2'u})\right], \ldots, RN(x_{ij}^{\prime u}) = \left\{\left[\underline{Lim}(x_{ij}^{1'u}), \overline{Lim}(x_{ij}^{1'u})\right], \left[\underline{Lim}(x_{ij}^{2'u}), \overline{Lim}(x_{ij}^{2'u})\right], \ldots, \left[\underline{Lim}(x_{ij}^{2'u}), \overline{Lim}(x_{ij}^{2'u})\right], \ldots, \left[\underline{Lim}(x_{ij}^{m'u}), \overline{Lim}(x_{ij}^{m'u})\right]\right\}$

The average of rough sequences is also calculated using the following equations:

$$RN(Z_{ij}^{L}) = RN(x_{ij}^{1L}, x_{ij}^{2L}, \ldots x_{ij}^{eL}) = \left\{\begin{matrix} Z_{ij}^{L} = \frac{1}{m}\sum_{e=1}^{m} x_{ij}^{eL} \\ Z_{ij}^{u} = \frac{1}{m}\sum_{e=1}^{m} x_{ij}^{eu} \end{matrix}\right\} \tag{20}$$

$$RN(Z_{ij}^{\prime u}) = RN(x_{ij}^{1'u}, x_{ij}^{2'u}, \ldots x_{ij}^{e'u}) = \left\{\begin{matrix} Z_{ij}^{L} = \frac{1}{m}\sum_{e=1}^{m} x_{ij}^{e'L} \\ Z_{ij}^{u} = \frac{1}{m}\sum_{e=1}^{m} x_{ij}^{e'u} \end{matrix}\right\} \tag{21}$$

where e represented the number of experts ($e = 1: m$) while $RN(Z_{ij}^{L})$ and $RN(Z_{ij}^{\prime u})$ show the lower and upper limit of IRN, $IRN(zij) = \left[RN(Z_{ij}^{L}), RN(Z_{ij}^{\prime u})\right]$.

Therefore, the matrix z that expresses the average interval rough comparison matrix in pairs of evaluation criteria is calculated as follows:

$$z = \begin{bmatrix} 1 & IRN(z_{12}) & \cdots & IRN(z_{1n}) \\ IRN(z_{21}) & 1 & \cdots & IRN(z_{2n}) \\ \vdots & \vdots & \ddots & \vdots \\ IRN(z_{n1}) & IRN(z_{n2}) & \cdots & 1 \end{bmatrix}_{n\times n} \tag{22}$$

5. Calculating the priority vector

The priority vector represents the interval rough weight coefficient $IRN(w_i)$, which is determined for each n of the evaluation criteria. $IRN(w_i)$ is determined using Eqs. (23–26). Using Eq. (23), the elements of the z matrix are collected through the columns.

$$IRN(a_{ij}^{'}) = \sum_{j=1}^{n} IRN(z_{ij}) = \left(\left[\sum_{j=1}^{n} z_{ij}^{L}, \sum_{j=1}^{n} z_{ij}^{u}\right], \left[\sum_{j=1}^{n} z_{ij}^{'L}, \sum_{j=1}^{n} z_{ij}^{'u}\right]\right) \tag{23}$$

Dividing the elements of matrix (22) to the elements of matrix (23) gives matrix (24), which is called the normalized matrix of weight coefficients w, matrices (25) (26).

$$IRN(w_{ij}) = \left(\left[w_{ij}^{L}, w_{ij}^{u}\right], \left[w_{ij}^{'L}, w_{ij}^{'u}\right]\right) = \frac{IRN(z_{ij})}{\sum_{j=1}^{n} IRN(z_{ij})} = \frac{\left(\left[z_{ij}^{L}, z_{ij}^{u}\right], \left[z_{ij}^{'L}, z_{ij}^{'u}\right]\right)}{\left(\left[\sum_{j=1}^{n} z_{ij}^{L}, \sum_{j=1}^{n} z_{ij}^{u}\right], \left[\sum_{j=1}^{n} z_{ij}^{'L}, \sum_{j=1}^{n} z_{ij}^{'u}\right]\right)} \tag{24}$$

$$w = \begin{bmatrix} 1 & \left(\left[w_{12}^{L}\right], \left[w_{12}^{u}\right], \left[w_{12}^{'L}\right], \left[w_{12}^{'u}\right]\right) & \cdots & \left(\left[w_{1n}^{L}\right], \left[w_{1n}^{u}\right], \left[w_{1n}^{'L}\right], \left[w_{1n}^{'u}\right]\right) \\ \left(\left[w_{21}^{L}\right], \left[w_{21}^{u}\right], \left[w_{21}^{'L}\right], \left[w_{21}^{'u}\right]\right) & 1 & \cdots & \left(\left[w_{2n}^{L}\right], \left[w_{2n}^{u}\right], \left[w_{2n}^{'L}\right], \left[w_{2n}^{'u}\right]\right) \\ \vdots & \vdots & \ddots & \vdots \\ \left(\left[w_{n1}^{L}\right], \left[w_{n1}^{u}\right], \left[w_{n1}^{'L}\right], \left[w_{n1}^{'u}\right]\right) & \left(\left[w_{n2}^{L}\right], \left[w_{n2}^{u}\right], \left[w_{n2}^{'L}\right], \left[w_{n2}^{'u}\right]\right) & \cdots & 1 \end{bmatrix}_{n\times n} \tag{25}$$

Eventually, for each evaluation criterion, $IRN(w_i)$ (rough interval weights coefficients) is calculated as:

$$IRN(w_i) = \left(\left[\sum_{j=1}^{n} w_{ij}^{L}, \sum_{j=1}^{n} w_{ij}^{u} \right], \left[\sum_{j=1}^{n} w_{ij}^{'L}, \sum_{j=1}^{n} w_{ij}^{'u} \right] \right) / n \quad (26)$$

Weighted overlay method (WOM)

In this study, after assigning weights to criteria earthier by inter-criteria (i.e., fuzzy logic) or by outer-criteria (IRAHP), for a combination of these criteria and preparing flood susceptibility map, the WOM was used. One of the most important characteristics of this widely used method is its replacement property (Raj and Shaji 2017; Thapa et al. 2017). Using this property, a criterion providing lower scores can be replaced by another criterion that has a high score. The mathematical representation of the WOM method for combining the criteria is as follows:

$$FH = \sum w_i x_i \quad (27)$$

where w_i is the weight of inter-criteria of i index and x_i is also the weight of outer-criteria of i index.

Determination of the optimal number of flood susceptibility map clusters

In this study, the K-Means clustering method was used to classify the flood susceptibility map. This clustering method has been recently used because of its easy quantification and high performance. One of the most important questions that should be considered when using K-means clustering is the optimal number of clusters (Weatherill and Burton 2009; Xu et al. 2018). One of the ways that can be used for determining the number of clusters is the use of the Silhouette function (Eq. 28), which presents a coherent degree of the similarity of each object (data) to its own cluster compared to the other clusters (Gaitani et al. 2010; Xu et al. 2018).

$$\mathrm{Si} = \frac{\min(b_i) - a_i}{\max[a_i, \min(b_i)]}, i = 1, 2, \ldots, n \quad (28)$$

where a_i is equivalent to the distance from ith points from other points in the cluster and b_i is the mean distance from points in the cluster. The optimal number of clusters is determined when the Si value has the highest mean and lowest number of negative numbers.

K-means cluster analysis

K-means clustering algorithm is a clustering technique that attempts to determine a non-overlapping cluster with the goal of maximizing cluster variance and minimizing in-cluster variance (Fernandez et al. 2016; Xu et al. 2018; Malekinezhad et al. 2011). The main steps of the clustering K-means algorithm are summarized as follows (Xu et al. 2018):

1. The random start of cluster centers $c_1, c_2, \ldots, c_k$
2. Estimating Euclidean distance d_{ij} between point jth q_j and cluster center c_i (Eq. 29), where n is the number of points

$$d_{ji} = \| q_j - c_i \|, 1 \le j \le n \text{ and } 1 \le i \le k \quad (29)$$

3. The movement of each point qj to the nearest cluster center
4. Updating cluster centers that the data are disconnected or allocated from those center
5. Determination of the objective function j (Eq. 30). If J converges, then cluster centers do not change from the previous iteration and the algorithm obtains the final cluster centers. Steps 2–5 are repeated until the target function j converges.

$$J = \sum_{i=1}^{k} \sum_{j=1}^{n} \left\| q_j - c_i \right\|^2, \quad 1 \le j \le n \& 1 \le i \le k \quad (30)$$

Analysis and results

Floods can be considered as one of the most serious threats in areas and countries where natural hazards can occur. The flood in the Ilanlu Watershed is affected by these criteria. Weighting methods for criteria are:

Inter-criteria weighting

Distance to discharge channel plays a crucial role in flood degree. Based on local reports, the areas near to discharge channel have the most susceptibility to flooding degree. Therefore, in this criteria, also Eq. (1) was used for inter-criteria weighting (Sepehri et al. 2019a; Mahmoud and Gan 2018).

The slope map is used for determining the water velocity and flooding potential (Fernández and Lutz 2010). In this case study, the values of slope criteria vary from 33% (maximum value) to 10% (minimum value). The areas with high slope located in the northern and middle parts of the case study. So, the areas with a low slope have more importance on flood degree. Equation (1) was used for assigning the inter-criteria weighting of this criterion.

The maximum and minimum values of the elevation criteria in the case study are 1907 and 2170 m, respectively. In this criteria like slope map, the lower values of these criteria have more importance on flood degree. Therefore, again

Eq. (1) was used for determining of inter-criteria weighting (Mahmoud and Gan 2018).

The TWI is a criterion that describes the role of topography on the saturation rate. This criterion that is a function of flow direction and flow accumulative has a major role in flood susceptibility. According to this criterion, areas with high values of TWI are more susceptible to flooding. In this criterion, which its values vary from − 10 to 25, Eq. (2) was used for assigning the scores (Fernández and Lutz 2010; Mahmoud and Gan 2018; Ildoromi et al. 2019).

Check dams play an important role in flood control. In a local scale, these dams trap the deposits in the upstream area of the dam and reduce the flow rate in the downstream area. It should be noted that evaluating the effectiveness of check dams in local scale is the function of the distance from the check dam; thus, the areas closer to check dams are affected more than those far away from the dam. Besides, the total behavior of every check dam in the watershed scale leads to changing in hydrological continuity.

In the present study, the following steps were taken for evaluating the role of check dams in flood hazard reduction:

1. Preparing the map of check dams' performance on a local scale and preparing its fuzzy map

The height of the check dams is one of the most important characteristics that control their performance on a local scale (Hartman et al. 2016). Therefore, in the present research, considering the primary data of check dams as point shape file format, the inverse distance weighted (IDW) interpolation method was used to prepare a raster map of check dams' performance in local scale. In this method, the location and height of the check dam were used as inputs. The IDW is an interpolation method in which the value of each pixel is as same as adjacent pixels; and with this much similarity with the further pixels, it reaches the lowest value. It is of note that local-scaled check dams depend on the distance and by increasing the distance the performance is reduced. In the second step, considering the important role of check dams in the reduction of flood hazard, Eq. (2) was used to convert the prepared map to a fuzzy map.

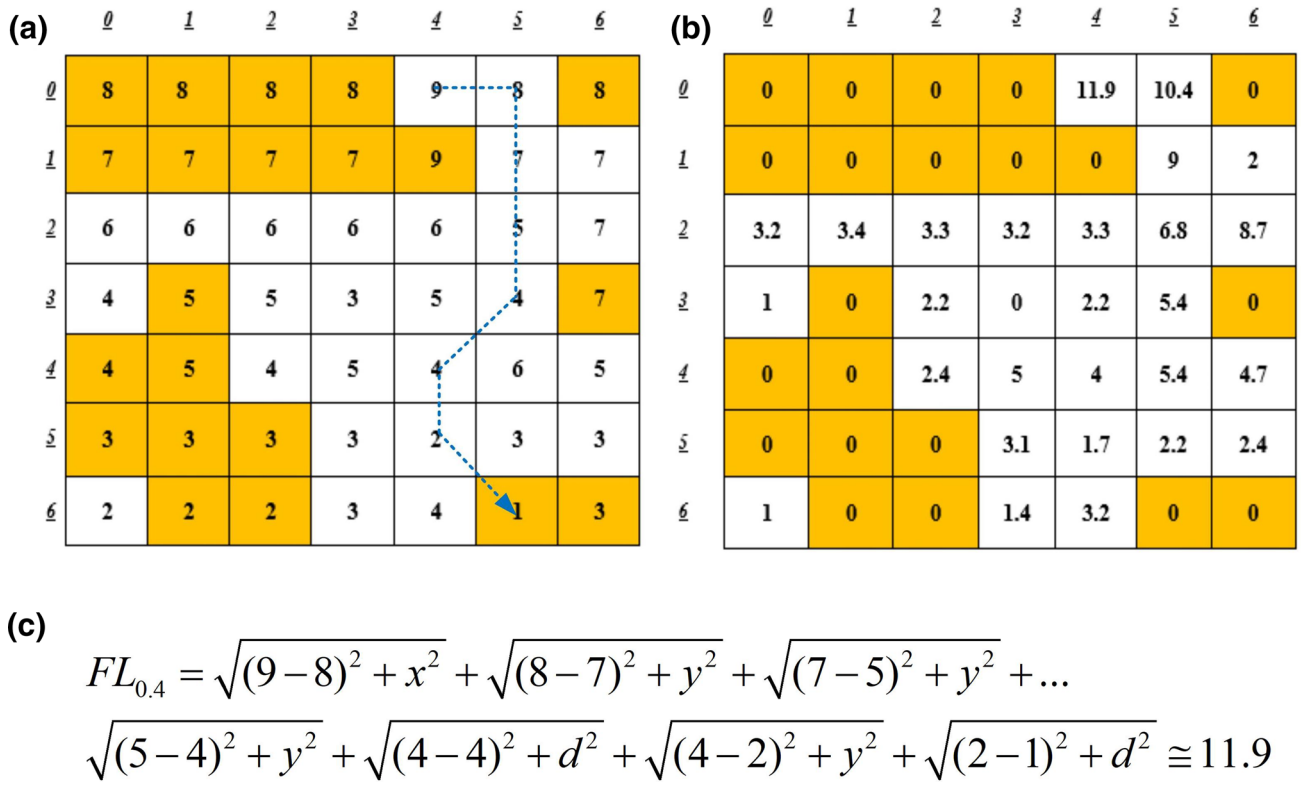

Fig. 4 The graphical illustration of flow length index calculation; **a** the attitude map and the corrective operations of an assumed hillslope. The color pixels indicate the area with corrective operations and white pixels are those without any operations; **b** the map of calculating the flow length of each pixel. The value of flow length index (for example 2.5) is calculated as an average of all flow length in the map; **c** the way of calculating the flow length index along the dash line path. In Fig. 2a, the path length of the flow between two consecutive pixels in a given path is determined as the slope length determined by the difference in height between the two pixels and the horizontal distance between them. The pixel size here is considered as 1 × 1, so the horizontal distance between two adjacent pixels is along with the two main directions as $x = 1$ and $y = 1$ and along the diameter as $FL_{0.4}$ relates to the calculation of flow length pixel with 0 row and 4 columns coordinates (Mayor et al. 2008)

2. Preparing the check dams' performance maps in watershed scale and providing its fuzzy map

There are several methods to prepare the hydrological continuity map and to evaluate the behavior of the watershed-scaled check dams (Mayor et al. 2008). In the present study, the flow length index was used for calculating the hydrological continuity. One of the most important advantages of flow length index, which is defined as the algebraic sum of the distance from the center of each pixel to the adjacent pixel along the slope, is its high efficiency in describing topographic characteristics, vegetation, and corrective operations (such as check dams). These factors are weighted in the range of 0–1 (1: no vegetation or corrective operations (source runoff), other values relate to the weighted value of corrective operations or vegetation in runoff reduction (sink runoff)) (Mayor et al. 2008) (Fig. 4). Hence, in the present study, the flow length index with a weight factor of local-scaled check dams sub-criteria was used for calculating the hydrological continuity, where the sub-criteria of hydrological continuity are 0–1220 m. Considering that higher sub-criteria of hydrological continuity lead to the greater amounts of runoff generated and thus more flooding, so Eq. (1) was used for fuzzy scoring of the index.

3. Combining two performance sub-criteria of local and watershed-scaled check dam

Two sub-criteria of the check dams were combined using gamma function. The most important point in using the gamma function is the gamma coefficient, which varies between 0 and 1 (Ramesh et al. 2016; Sema et al. 2017). When the value is close to 0, the gamma function is converted to product function and if the value is close to 1 it will be converted to sum function. The product function reduces the property; in other words, the final value of fuzzy function produced moves from the combination of fuzzy indices toward a certain fuzzy function with the minimum value across the sun function. In addition, in the sum function, the final value of the combined fuzzy function moves toward a certain fuzzy function with the maximum value. Since the check dams are structures built in the drainage networks, they receive the maximum score of the index. As a result, when the gamma coefficient is assumed to be 0, it results in observing the 0 fuzzy number in the whole area except draining networks. However, the gamma coefficient equivalent to 1 leads to having a fuzzy number higher than 1 for non-draining network areas. In most of the studies, to balance sum and product functions, the gamma coefficient has been considered to be between 0.5 and 0.6. In the present study, since the importance of check dams role in local scale in the reduction of flood hazard and because the check dams in watershed scale is a function of local scale, the numerical gamma coefficient is considered to be 0.7.

STLU are two main criteria affecting on the infiltration and surface runoff (Thapa et al. 2017; Ildoromi et al. 2019). Both criteria have low diversity in the case study. So, in the present study, we have just two kinds of soil texture (i.e., loam and clay loam) and thus they do not play a major role in the distribution of the flood characteristics. To overcome this problem, the loam soil texture of the case study, based on the hydrological condition that is determined by some features such as soil depth or surface vegetation cover, was divided into two groups: (1) loam soil texture with the

Table 2 Initial combination of soil texture and land use by permutation law

	Soil type	Loamy (Group C)	Loamy (Group D)	Clay Loam
	Primary Score	1	2	3
Reclassify slope base on natural break method	0_6%	1	1	2	3
	6-14%	2	2	4	6
	14_22%	3	3	6	9
	22-34%	4	4	8	12
	34-67%	5	5	10	15

Land Cover	Garden	rangelands
Primary Score	3	6

Soil Type * Land Cover (STLU) =

3	6	9
6	12	18
9	18	27
12	24	36
15	30	45

6	12	18
12	24	36
18	36	54
24	48	72
30	60	90

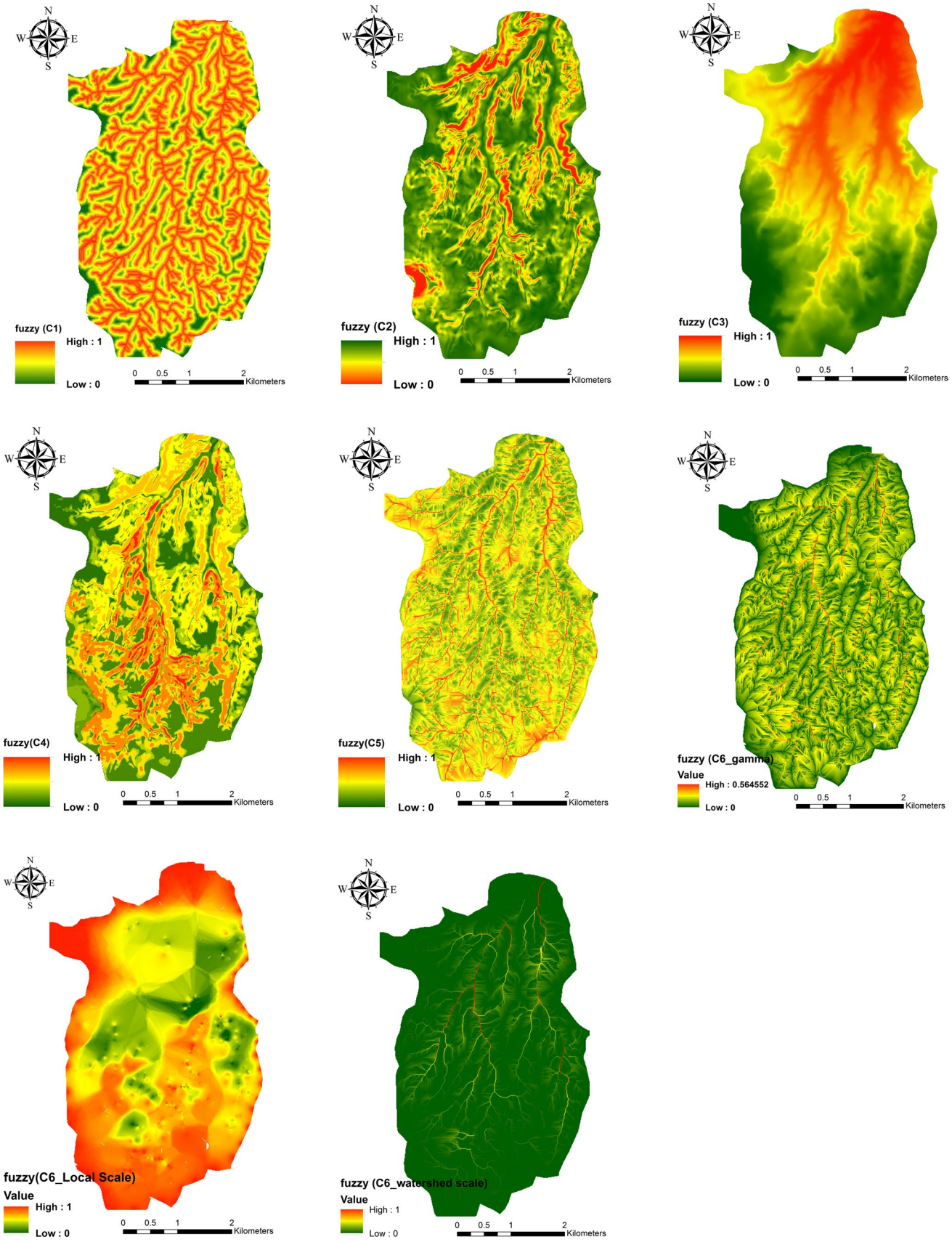

Fig. 5 Schematic maps of inter-weighted criteria for the case study

Table 3 Matrices of experts' pairwise comparison of evaluation criteria

	C_1	C_2	C_3	C_4	C_5	C_6
Expert 1						
C_1	*(1; 1)*	(4; 4)	(4; 5)	(5; 6)	(4; 5)	(1; 2)
C_2	(0.25; 0.25)	*(1; 1)*	(1; 2)	(2; 3)	(2; 2)	(0.5; 0.5)
C_3	(0.2; 0.25)	(0.5; 1)	*(1; 1)*	(2; 3)	(2; 2)	(0.33; 0.33)
C_4	(0.16; 0.2)	(0.33; 0.5)	(0.33; 0.2)	*(1; 1)*	(1; 1)	0.25; 0.33)
C_5	(0.2:0.25)	(0.5; 0.5)	(0.5; 0.5)	(1; 1)	*(1; 1)*	(0.25; 0.33)
C_6	(0.5; 0.1)	(2; 2)	(3; 3)	(3; 4)	(3;3)	*(1; 1)*
Expert 6						
C_1	*(1; 1)*	(4; 5)	(4; 5)	(5; 6)	(4; 5)	(1; 2)
C_2	(0.2; 0.25)	*(1; 1)*	(1; 2)	(3; 4)	(1; 2)	(0.33; 0.5)
C_3	(0.2; 0.5)	(0.5; 1)	*(1; 1)*	(2; 3)	(2; 2)	(0.25; 0.33)
C_4	(0.16; 0.2)	(0.25; 0.33)	(0.33; 0.5)	*(1; 1)*	(1; 2)	(0.2; 0.25)
C_5	(0.2; 0.25)	(0.5; 1)	(0.5; 0.5)	(0.5; 1)	*(1; 1)*	(0.25; 0.25)
C_6	(0.5; 1)	(2; 3)	(3; 4)	(4; 5)	(4; 4)	*(1; 1)*

Table 4 Consistency ratio for comparing the matrices

Expert	CR^e	$CR^{e'}$	CR^e
E1	0.098	0.1	0.099
E2	0.09	0.099	0.094
E3	0.015	0.097	0.05
E4	0.01	0.012	0.01
E5	0.098	0.09	0.094
E6	0.095	0.099	0.097

hydrological status of C and (2) loam soil texture with the hydrologic status of D. Next, these two categories based on the natural gradient of the slope map (5 slope variation were considered in this study) were transferred to 10 different classes. For land use, there exists only rangeland and garden coverage. In the case study, a scale ranging from 1 to 10 was used for assigning a primary score to these land use types based on their role on flood degree. The score 1 means that the lowest impact on flood degree and number 10 means the most impact on flood degree. Eventually, by merging of the soil texture and land use by low of permutation (Table 2), a map was generated in which the higher the values, the stronger their effect is on flood degree, and vice versa (Fig. 5). Finally, Eq. (1) was used for inter-weighting this criterion.

Outer-criteria weighting

After inter-criteria weighting, decision makers must consider the relative importance of criteria. Hence, the next section examines the weight of the criteria relative to each other. In this study, six experts were chosen to evaluate the relative importance of criteria (Table 3).

Table 3 presents matrices of experts' pairwise comparison of evaluation criteria. According to that, there is uncertainty in experts' opinions.

For instance, at the location of **C1–C4**, Expert 1 is uncertain between choosing the two values of 5 and 6. When there was no uncertainty, Expert 1 used a specific value for the relative importance of the criteria.

After filling the comparison matrices in pairs for each matrix, the consistency ratio was calculated. As in matrix (17), there are two values for each position (i, j) and thus two consistency ratios were calculated. One of these consistency ratios is for lower comparison value (CR^e) and the other is

Table 5 Interval rough average matrix

	C1	C2	…	C5	C6
C1	([1, 1], [1, 1])	([2.8, 3.6], [3.2, 4.1])	**…**	([4, 4.3], [4.7, 5])	([1.5, 2.5], [2.2, 3.1])
C2	([0.3, 0.3], [0.3, 0.4])	([1, 1], [1, 1])	…	([1.4, 1.9], [2.1, 2.6])	([0.4, 0.5], [0.5, 0.8])
C3	([0.2, 0.3], [0.3, 0.3])	([0.5, 0.8], [0.8, 1])	…	([1.4, 1.9], [1.7, 2.3])	([0.3, 0.4], [0.3, 0.6])
C4	([0.2, 0.2], [0.2, 0.2])	([0.3, 0.3], [0.4, 0.5])	…	([0.4, 0.8], [0.6, 1.3])	([0.2, 03], [0.3, 0.4])
C5	([0.2, 0.2], [0.2, 0.2])	([0.4, 0.5], [0.6, 0.8])	…	([1.1], [1, 1])	([0.3, 0.4], [0.4, 0.7])
C6	([0.3, 0.5], [0.5, 0.8])	([1.4, 2.2], [2.1, 2.6])	…	([1.9, 3.4], [2.6, 4.1])	([1, 1], [1, 1])

Table 6 Normalized matrix of weight coefficients

	C1	C2	…	C5	C6
C1	([0.06, 0.05], [0.05, 0.04])	([0.15, 0.17], [0.15, 0.17])	…	([0.23, 0.21], [0.22, 0.20])	([0.08, 0.12], [0.11, 0.13])
C2	([0.04, 0.04], [0.03, 0.04])	([0.16, 0.13], [0.12, 0.1])	…	([0.23, 0.25], [0.25, 0.25])	([0.06, 0.06], [0.06, 0.08])
C3	([0.04, 0.04], [0.04, 0.04])	([0.10, 0.11], [0.13, 0.12])	…	([0.29, 0.28], [0.28, 0.27])	([0.06, 0.06], [0.05, 0.07])
C4	([0.06, 0.05], [0.06, 0.05])	([0.12, 0.10], [0.13, 0.11])	…	([0.17, 0.25], [0.20, 0.31])	([0.09, 0.09], [0.09, 0.10])
C5	([0.06, 0.04], [0.06, 0.04])	([0.12, 0.10], [0.13, 0.13])	…	([0.29, 0.20], [0.24, 0.16])	([0.08, 0.09], [0.09, 0.12])
C6	([0.04, 0.03], [0.04, 0.05])	([0.15, 0.16], [0.17, 0.15])	…	([0.20, 0.24], [0.21, 0.24])	([0.11, 0.07], [0.08, 0.06])

Table 7 The interval rough weight coefficients for evaluation criteria

	IRN(Wi)	Rank
C1	([0.42, 0.51], [0.5, 0.59])	1
C2	([0.13, 0.16], [0.17, 0.21])	3
C3	([0.1, 0.14], [0.12, 0.17])	4
C4	([0.05, 0.07], [0.06, 0.09])	6
C5	([0.07, 0.1], [0.09, 0.13])	5
C6	([0.21, 0.31], [0.28, 0.38])	2

for upper comparison value ($CR^{e'}$). Then, the final consistency ratio for each position (i, j) is the average of lower and upper consistency ratio (CR_e) (Table 4):

The elements of matrix Z_k are transferred to IRN (ze *ij*) based on Table 2 and Eqs. (1–16). It has to be noted that 6 IRN (ze *ij*) were calculated in this study. Then, using Eqs. (23) and (24), the average interval rough comparison matrix in pair evaluation of the criteria was calculated (Table 5).

Matrix w (Table 6), which shows the normalized matrix of weight coefficients, is calculated based on Eqs. (26–27) and Table 5.

Finally, the interval rough weight coefficients (Table 7) for evaluation criteria are obtained using Eq. (29):

Flood susceptibility mapping

Using MCDA and GIS technique, flood susceptibility mapping was provided by aggregating criteria in the WOM method.

$$FH = x_D w_D + x_S w_S + x_E w_E + x_{STLU} w_{STLU} + x_{CheckDams} w_{CheckDams} \quad (34)$$

Discussion

The key features of the employed methodology are its simplicity and applicability with a focus on the criteria related to control water routing when the peak is higher than the drainage network capacity. MCDA is generally used for ranking, accepting, rejecting, and determining the number of optimal options (Fernández and Lutz 2010). In the present study, IRAHP and fuzzy logic used as two MCDA methods for criteria weighting.

After weighing the criteria and preparing the flood susceptibility map in the study area, the optimum number of clusters was determined for classifying the prepared map using the silhouette function. The optimal number of clusters and the related silhouette value are shown in Fig. 4. The analysis of clusters was started with 3 clusters and ended with 10 clusters. According to Fig. 4, the mean silhouette value is maximum for 9 clusters and their negative numbers are minimum. Therefore, nine clusters were used for flood risk zoning map, where Clusters 9 and 1 represent the highest and lowest flood probability, respectively (Fig. 6).

One of the most important differences between this study and other studies (Haghizadeh et al. 2017; Siahkamari et al. 2018; Darabi et al. 2019; Radwan et al. 2019a) is the difference in flood susceptible zones. For example, the probable overestimation or underestimation of the flood susceptibility by some studies, depending on their criteria weighting method, can result in false precision of flood hazard zoning map. There are two main causes of these overestimation and underestimation are:

1. Multi-criteria decision methods: The application of the subjective methods alone for flood hazard mapping is associated with some limitations in weighting indices; therefore, it is necessary to classify the criteria into subclasses and then give initial weights to these subclasses. In this way the variety of spatial distribution of criteria will reduce, resulting in rigid maps (Sepehri et al. 2019a). In this study, the integration of fuzzy logic and IRAHP method, as objective and subjective methods, was used to overcome this problem.
2. Classification of final flood hazard mapping: A major factor that affects the accuracy of the developed flood hazard map, regardless of the classification method, is the number of classes in final flood hazard mapping. If the number of classes is less or more than optimal numbers, the area in flood hazard classes will be over-

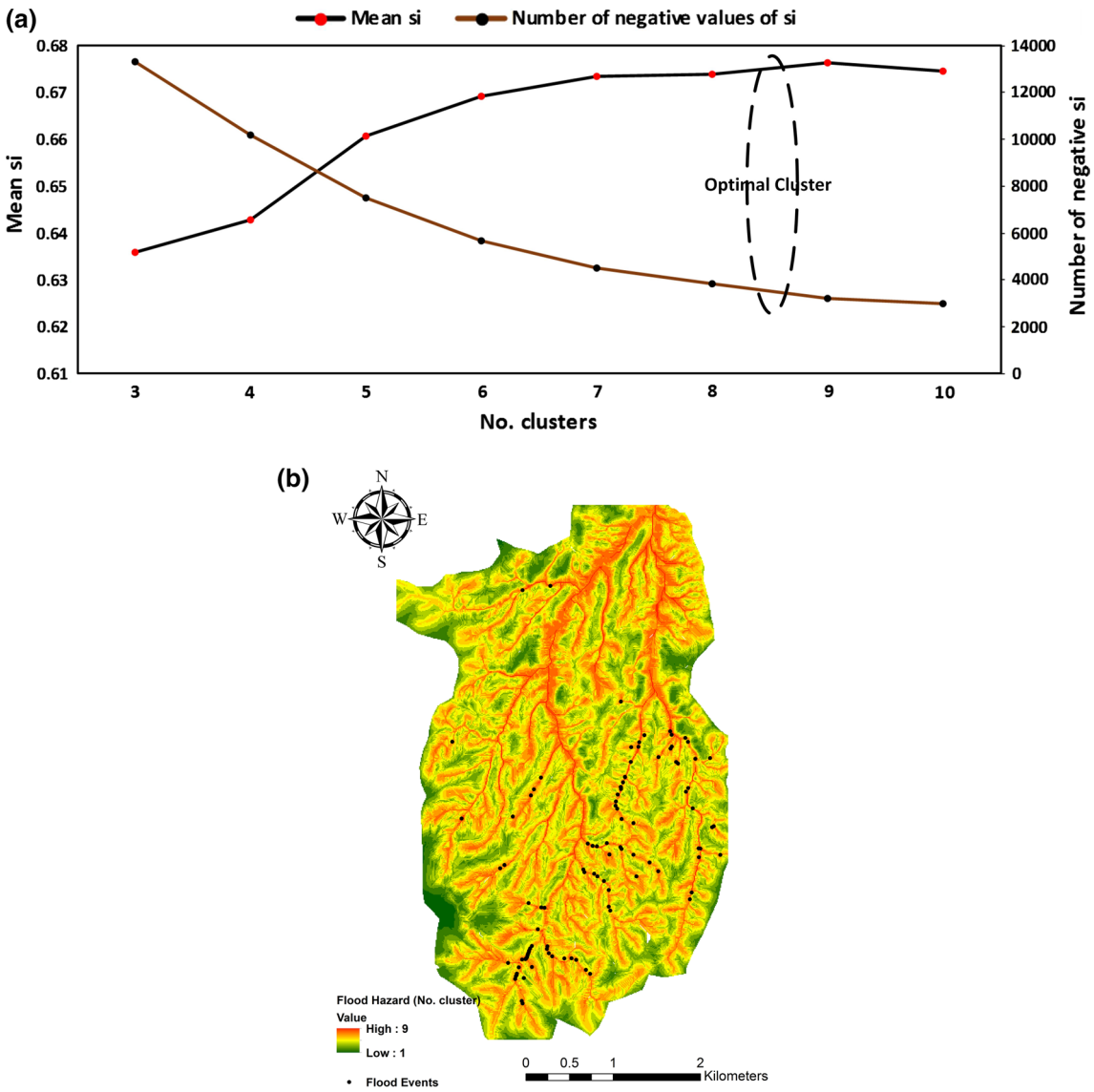

Fig. 6 **a** The features of the silhouette function (number of Silhouette negative values Si and mean Silhouette values Si) and **b** flood susceptibility mapping of the case study

estimated or underestimated (Xu et al. 2018). Moreover, to avoid this problem, the silhouette function was a statistical method for determining an optimal number of classes.

Finally, to verify the accuracy of the map, the flood observation points were overlaid with the given map. Among 102 points (Fig. 4), 66 points were in Clusters 8 and 9, 30 points in Cluster 7, and 6 points in other clusters. Since the majority of points were in Clusters 7, 8, and 9, the flood hazard map achieved acceptable accuracy.

Conclusion

Although prevention of flood occurrence, as the most common and catastrophic natural disaster, is impossible, the use of a suitable method in flood susceptibility mapping can predict vulnerable areas while preventing potential damage. In the present study, the six most effective flooding criteria selected, including distance to drainage network, slope, elevation, soil texture and land use, TWI, and check dams. These criteria were weighted based on their effects on flooding using subjective (IRAHP) and an objective (fuzzy logic) methods. Finally, the weighted criteria were overlaid to produce a flood zoning map of the study area. The conclusion could be drawn that (1) the distance

to drainage network is the most prominent criterion; (2) more than 90% of observed flood points are mainly concentrated in the high flood susceptibility areas; therefore, (3) the integration of IRAHP-Fuzzy logic-GIS has high capability in investigation of flood susceptibility zones.

Finally, it must be noted that the flood hazard studies consider the physical and climatic features of the study case. Therefore, future studies are recommended to provide good management of land use planning, so as to reduce future damages. To this end, it is better to combine the social and economic features of the case to make the flood hazard maps.

References

Bolourchi P, Uysal S (2013) 2013 fifth international conference on computational intelligence, communication systems and networks. IEEE, pp 83–87

Chen H-W, Chang N-B (2010) Using fuzzy operators to address the complexity in decision making of water resources redistribution in two neighboring river basins. Adv Water Resour 33:652–666

Darabi H, Choubin B, Rahmati O, Haghighi AT, Pradhan B, Kløve B (2019) Urban flood risk mapping using the GARP and QUEST models: a comparative study of machine learning techniques. J Hydrol 569:142–154

Fernández D, Lutz M (2010) Urban flood hazard zoning in Tucumán Province, Argentina, using GIS and multicriteria decision analysis. Eng Geol 111(1–4):90–98

Fernandez P, Mourato S, Moreira M, Pereira L (2016) A new approach for computing a flood vulnerability index using cluster analysis. Phys Chem Earth Parts A/B/C 94:47–55

Gaitani N, Lehmann C, Santamouris M, Mihalakakou G, Patargias P (2010) Using principal component and cluster analysis in the heating evaluation of the school building sector. Appl Energy 87(6):2079–2086

Ghosh A, Kar SK (2018) Application of analytical hierarchy process (AHP) for flood risk assessment: a case study in Malda district of West Bengal, India. Nat Hazards 94(1):349–368

Gigović L, Pamučar D, Bajić Z, Drobnjak S (2017) Application of GIS-interval rough AHP methodology for flood hazard mapping in urban areas. Water 9(6):360

Haghizadeh A, Siahkamari S, Haghiabi AH, Rahmati O (2017) Forecasting flood-prone areas using Shannon's entropy model. J Earth Syst Sci 126:39

Hartman BD, Bookhagen B, Chadwick OA (2016) The effects of check dams and other erosion control structures on the restoration of Andean bofedal ecosystems. Restor Ecol 24(6):761–772

Hong H, Tsangaratos P, Ilia I, Liu J, Zhu A-X, Chen W (2018) Application of fuzzy weight of evidence and data mining techniques in construction of flood susceptibility map of Poyang County, China. Sci Total Environ 625:575–588

Ildoromi AR, Sepehri M, Malekinezhad H, Kiani-Harchegani M, Ghahramani A, Hosseini SZ, Artimani MM (2019) Application of multi-criteria decision making and GIS for check dam Layout in the Ilanlu Basin, Northwest of Hamadan Province, Iran. Phys Chem Earth Parts A/B/C 114:102803

Iliadis LS (2005) A decision support system applying an integrated fuzzy model for long-term forest fire risk estimation. Environ Model Softw 20:613–621

Jun K-S, Chung E-S, Kim Y-G, Kim Y (2013) A fuzzy multi-criteria approach to flood risk vulnerability in South Korea by considering climate change impacts. Expert Syst Appl 40:1003–1013

Kanani-Sadat Y, Arabsheibani R, Karimipour F, Nasseri M (2019) A new approach to flood susceptibility assessment in data-scarce and ungauged regions based on GIS-based hybrid multi criteria decision-making method. J Hydrol 572:17–31

Kourgialas NN, Karatzas GP (2011) Flood management and a GIS modelling method to assess flood-hazard areas—a case study. Hydrol Sci J 56(2):212–225

Kowalzig J (2008) Climate, poverty, and justice: what the Poznan UN climate conference needs to deliver for a fair and effective global deal. Oxfam Policy Pract Clim Change Resil 4(3):117–148

Mahmoud SH, Gan TY (2018) Multi-criteria approach to develop flood susceptibility maps in arid regions of Middle East. J Clean Prod 196:216–229

Malekinezhad H, Nachtnebel H, Klik A (2011) Comparing the index-flood and multiple-regression methods using L-moments. Phys Chem Earth Parts A/B/C 36:54–60

Mayor ÁG, Bautista S, Small EE, Dixon M, Bellot J (2008) Measurement of the connectivity of runoff source areas as determined by vegetation pattern and topography: a tool for assessing potential water and soil losses in drylands. Water Resour Res 44:1–13. https://doi.org/10.1029/2007wr006367

Noori H, Iildoromi AR, Sepehri M, Sepehri N, Artimani MM (2015) Assesment of mechanicaloperationson hydrodynamic features of flood. Iran J Ecohydrol 2(3):245–252. https://doi.org/10.22059/ije.2015.57294

Pamučar D, Mihajlović M, Obradović R, Atanasković P (2017) Novel approach to group multi-criteria decision making based on interval rough numbers: hybrid DEMATEL-ANP-MAIRCA model. Expert Syst Appl 88:58–80

Papaioannou G, Vasiliades L, Loukas A (2015) Multi-criteria analysis framework for potential flood prone areas mapping. Water Resour Manag 29(2):399–418

Pathak DR, Hiratsuka A (2011) An integrated GIS based fuzzy pattern recognition model to compute groundwater vulnerability index for decision making. J Hydro-Environ Res 5:63–77

Perera EDP, Lahat L (2015) Fuzzy logic based flood forecasting model for the Kelantan River basin, Malaysia. J Hydro-Environ Res 9(4):542–553

Radwan F, Alazba A, Mossad A (2019) Flood risk assessment and mapping using AHP in arid and semiarid regions. Acta Geophys 67(1):215–229

Raj D, Shaji E (2017) Fluoride contamination in groundwater resources of Alleppey, southern India. Geosci Front 8(1):117–124

Ramesh V, Phaomei T, Baskar M, Anbazhagan S (2016) Application of fuzzy gamma operator in landslide susceptibility mapping along Yercaud Ghat Road section, Tamil Nadu, India. In: Geostatistical and geospatial approaches for the characterization of natural resources in the environment. Springer, pp 545–553

Saaty TL (1980) The Analytic Hierarchy process: planning, priority setting, l~esource Allocation. M cGraw Hill, New York

Sema HV, Guru B, Veerappan R (2017) Fuzzy gamma operator model for preparing landslide susceptibility zonation mapping in parts of Kohima Town, Nagaland, India. Model Earth Syst Environ 3(2):499–514

Sepehri M, Ildoromi AR, Malekinezhad H, Hosseini SZ, Talebi A, Goodarzi S (2017) Flood hazard mapping for the gonbad chi region, Iran. J Environ Eng Sci 12(1):16–24

Sepehri M, Malekinezhad H, Hosseini SZ, Ildoromi AR (2019a) Assessment of flood hazard mapping in urban areas using entropy weighting method: a case study in Hamadan city, Iran. Acta Geophys 67(5):1435–1449

Sepehri M, Malekinezhad H, Hosseini SZ, Ildoromi AR (2019b) Suburban flood hazard mapping in Hamadan city, Iran. Paper presented at the proceedings of the institution of civil engineers-municipal engineer

Shahabi H, Hashim M, Ahmad BB (2015) Remote sensing and GIS-based landslide susceptibility mapping using frequency ratio, logistic regression, and fuzzy logic methods at the central Zab basin, Iran. Environ Earth Sci 73:8647–8668

Siahkamari S, Haghizadeh A, Zeinivand H, Tahmasebipour N, Rahmati O (2018) Spatial prediction of flood-susceptible areas using frequency ratio and maximum entropy models. Geocarto Int 33:927–941

Smithson M (2012) Ignorance and uncertainty: emerging paradigms. Springer, Berlin

Souissi D, Zouhri L, Hammami S, Msaddek MH, Zghibi A, Dlala M (2019) GIS-based MCDM-AHP modeling for flood susceptibility mapping of arid areas, southeastern Tunisia. Geocarto Int. https://doi.org/10.1080/10106049.2019.1566405

Thapa R, Gupta S, Reddy D (2017) Application of geospatial modelling technique in delineation of fluoride contamination zones within Dwarka Basin, Birbhum, India. Geosci Front 8(5):1105–1114

Weatherill G, Burton PW (2009) Delineation of shallow seismic source zones using *K*-means cluster analysis, with application to the Aegean region. Geophys J Int 176(2):565–588

Xu H, Ma C, Lian J, Xu K, Chaima E (2018) Urban flooding risk assessment based on an integrated *k*-means cluster algorithm and improved entropy weight method in the region of Haikou, China. J Hydrol 563:975–986

Yazdi J, Neyshabouri SS (2014) Identifying low impact development strategies for flood mitigation using a fuzzy-probabilistic approach. Environ Model Softw 60:31–44

Zadeh LA (1965) Fuzzy sets. Inf Control 8(3):338–353

Acta Geophysica (2020) 68:495–504
https://doi.org/10.1007/s11600-020-00400-9

RESEARCH ARTICLE - HYDROLOGY

Changing trends of river flows in the Upper Vistula Basin (East-Central Europe)

Marek Górnik[1]

Received: 6 June 2019 / Accepted: 8 January 2020 / Published online: 5 February 2020

Abstract

The mean annual, winter half-year and summer half-year flows at 86 water level gauges in the Upper Vistula Basin in the years 1951–2015 were examined. The Ward's hierarchical cluster analysis was used for grouping sub-catchments in reference to the standardized aforementioned flows. Trends analysis was performed for each cluster of catchments in all combinations of periods not shorter than 20 years. Spatial distribution of clusters of catchments has been analysed according to geographical locations. There are observed different trends in distinguished groups of catchments, wherein the substantial differences concern long-term trends. Changes in trend direction in the years 1951–2015 were revealed, which indicate flow fluctuations. Presumably, physiographical heterogeneity of the Upper Vistula Basin is reflected in no unequivocal trends occurring in clusters of catchments. Some similarities were stated in short-term trends occurring in particular groups of catchments.

Keywords River runoff · Cluster analysis · Multitemporal trends · Mann–Kendall statistics · Poland

Introduction

Increase in air temperature and changes in precipitation have been noted in many areas but their effect on river flow has been difficult to pinpoint. Research on change detection in river flow has not revealed convincing and ubiquitous changes in Europe and worldwide, and there are no clear indications of significant trends of river flow at regional or large scales and there is as yet no evidence that the river flow in recent years is influenced directly by climate change (Kundzewicz ed. 2012; Madsen et al. 2014). Apart from climatic factors, there are other important components which may independently influence river flow variability, namely changes in land cover (reforestation or deforestation, urbanization), capacity of river channels, water intake for municipal, agricultural and industrial purposes, etc. (Slater et al. 2015). River runoff integrates the influence of this complex phenomenon over a watershed; hence, the analysis of long time series of river discharge datasets does not result in unequivocal satisfactory and expected results. From the other site, the search for trends (or lack thereof) in river flow data series has become of scientific interest and practical importance in the last decades as it is essential for adaptation to climate change, in particular water management strategies (Adaptation… 2018).

There are a few studies on long-term river flow trends in Europe in last 200 years. Some trends are increasing but not statistically significant (Pekarova et al. 2003; Lindstrom and Bergstrom 2004). The average annual river flow in the second half of the twentieth and at the beginning of the twenty-first centuries dropped in southern and south-eastern Europe and rose in the rest part of Europe (Stahl et al. 2012; Hannaford et al. 2013).

The analysis of long series of annual river flow showed no trends in Poland (Jokiel and Kożuchowski 1989; Miler 1999; Soja 2002; Stachý 2010), while in the second half of the twentieth century positive trends prevailed (Wrzesiński 2009). The re-analysis of the river flow trends for data on the second half of the twentieth and the beginning of the twenty-first centuries showed a decrease in river flows, with the exception of the Carpathian Mountains rivers where an increase in river flow was observed (Piniewski et al. 2018). Furthermore, numerous researchers point out to a decline in river flow in Europe in the summer half-year and an increase in the winter half-year (Wrzesiński 2009; Stahl et al. 2010; Hannaford et al. 2013; Birsan et al. 2014; Piniewski et al. 2018).

✉ Marek Górnik
marek4891@poczta.fm

[1] Institute of Geography and Spatial Management, Jagiellonian University, Gronostajowa Str. 7, 30-387 Cracow, Poland

There is a region influencing considerably water resources for more than half of the territory of Poland, i.e., the Upper Vistula Basin. There is no detailed study reflecting contemporary trends in river flow with the exception of Piniewski et al.'s (2018) work related to the whole country area. The aim of the paper is an analysis of trends of average annual river flow in the Upper Vistula Basin in the years 1951–2015 and investigation into the spatial differentiation of trends. A multitemporal trend approach was applied to trend analysis, and trends were fitted to every possible combination of start and end years in the time record. This research may partly fill the gap in current research on changes in the river flow and additionally eliminate the impact of the length of data series on the value of calculated trend and is a response to the need for comprehensive studies of river flow trends (Hannaford et al. 2013; Piniawski et al. 2018). It is worth pointing out, however, that multitemporal trend approach does not replace the analysis of individual trends, but yet may be a complementary part of the study.

Study area

The area of the Upper Vistula Basin (at Zawichost gauge) drains a total of 50,731.8 km^2 and covers a large part of the Southern Poland (Fig. 1). This area is about 25% of the total Vistula drainage basin and is shared by Poland (91%), Ukraine (5%) and Slovakia (4%). There are located three geographical regions: the Carpathian Mountains and their foreland, the Subcarpathian Basins and the Lesser Poland Uplands. The highest point within the watershed reaches the altitude of 2438 m a.s.l. in the Tatra Mountains, whereas the lower one is 134 m a.s.l. There are the highest annual precipitations in the Carpathian Mountains reaching 1700 mm. This region includes headwater of most of the tributaries of the Upper Vistula River. Due to significant water resources, the Carpathian Mountains secure water for a number of regions far beyond their boundaries being an important water tower for the rest of the country (Pociask-Karteczka 2016). The share of the outflow from the Upper Vistula Basin in relation to the outflow from the whole Vistula basin amounts to 41%, although it occupies only 25% of the entire Vistula River Basin (Chełmicki 1991). Hence, much of the flood risk in Poland is related to the Upper Vistula River Basin, and its right-bank tributaries significantly contribute to the total flood damage.

Data and methods

The study applied a multitemporal approach, whereby trends are fitted to every possible combination of start and end years in a record (McCabe and Wolock 2002; Hannaford et al. 2013). The datasets of 86 water gauge stations located on 50 rivers in the Upper Vistula Basin with long (1951–2015) hydrometric records were used in the analysis. The average daily river flow provided by the monitoring network system carried out by the Institute of Meteorology and Water Management–National Research Institute (IMGW-BIP) was used in the study. The prevailing length of individual measurement series is 55 years except four records: Czarna—Raków, Prądnik—Ojców, Rudawa—Balice with 45-year series and the Nida—Czarna with a 50-year series.

In the first stage of the study, average annual flow values for each year (SQ_Y), winter half-year (SQ_W) and summer half-year (SQ_S) for each catchment were calculated according to the classical formula for the arithmetic mean based on daily flow values, creating a data series for each catchment.

In the next step, based on the data series received for each catchment, multiannual average flow values for year (SSQ_Y), winter half-year (SSQ_w) and summer half-year (SSQ_S) were calculated (also using the arithmetic mean formula).

Data series created from average annual flow values for each year (SQ_Y), winter half-year (SQ_W) and summer half-year (SQ_S) for each catchment were standardized by their multiannual mean value (respectively, by SSQ_Y, SSQ_w, SSQ_S), so that on all subsequent time series plots, annual values are shown as a proportion of the long-term mean in that indicator. To calculate normalized average flow values (STD SQ), the following formula was used:

$$\text{STD SQ}_n = \frac{\text{SQ}_n}{\text{SSQ}} \tag{1}$$

where n is the certain year of multiannual period.

For the purpose of further calculations, the values obtained in the previous step were combined into annual data series (S_STD SQ_Y), winter half-year data series (S_STD SQ_W) and summer half-year data series (S_STD SQ_S).

Then, the catchments were clustered into a few regions broadly homogenous in terms of standardized annual (S_STD SQ_Y), standardized winter half-year (S_STD SQ_W) and standardized summer half-year (S_STD SQ_S) river flow series in the studied multiannual period. Cluster analysis in each of three groupings was carried out using the agglomerative hierarchical Ward method employing the Pearson's distance matrix ($1-r$). Ward's method was used because it is one of the most popular and commonly used grouping methods in hydrology and meteorology (Hannaford et al. 2013; Wrzesiński and Sobkowiak 2018). It is worth noting that this method is often used due to simple mathematical properties and convenient graphical interpretation. The optimum number of clusters was determined on the basis of the geometry of the dendrogram and the plot of the binding distance. The number of identified groups was selected according to the highest homogeneity in a group in terms of interannual variability of average river flows.

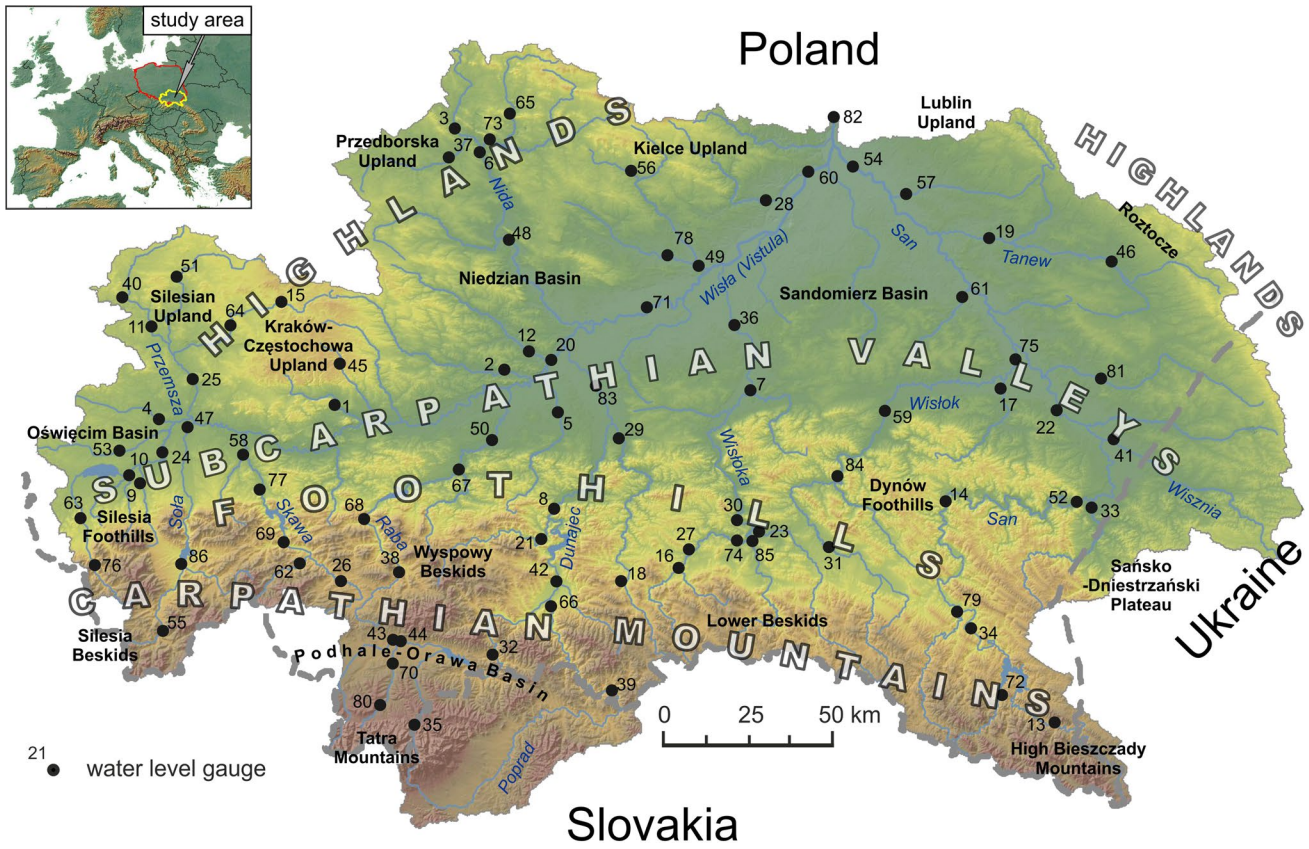

Fig. 1 Research area with locations of water level gauges in the Upper Vistula Basin. 1—the Rudawa at Balice, 2—the Szreniawa at Biskupice, 3—the Wierna Rzeka at Bocheniec, 4—the Gostynia at Bojszowy, 5—the Uszwica at Borzęcin, 6—the Nida at Brzegi, 7—the Wielopolka at Brzeźnica, 8—the Dunajec at Czchów, 9—the Biała at Czechowice–Bestwina, 10—the Iłownica at Czechowice-Dziedzice, 11—the Brynica at Czeladź, 12—the Nidzica at Dobiesławice, 13—the San at Dwernik, 14—the San at Dynów, 15—the Biała Przemsza at Golczowice, 16—the Sękówka at Gorlice, 17—the Mleczka at Gorliczyna, 18—the Biała at Grybów, 19—the Tanew at Harasiuki, 20—the Wisła at Jagodniki, 21—the Łososina at Jakubowice, 22—the San at Jarosław, 23—the Jasiołka at Jasło, 24—the Wisła at Jawiszowice, 25—the Przemsza at Jeleń, 26—the Skawa at Jordanów, 27—the Ropa at Klęczany, 28—the Koprzywianka at Koprzywnica, 29—the Biała at Koszyce Wielkie, 30—the Wisłoka at Krajowiec, 31—the Wisłok at Krosno, 32—the Dunajec at Krościenko, 33—the Wiar at Krówniki, 34—the San at Lesko, 35—the Białka at Łysa Polana, 36—the Wisłoka at Mielec, 37—the Nida at Mniszek, 38—the Raba at Mszana Dolna, 39—the Poprad at Muszyna, 40—the Brynica at Namiarki, 41—the Wisznia at Nienowice, 42—the Dunajec at Nowy Sącz, 43—the Czarny Dunajec at Nowy Targ, 44—the Dunajec at Nowy Targ-Kowaniec, 45—the Prądnik at Ojców, 46—the Tanew at Osuchy, 47—the Soła at Oświęcim, 48—the Nida at Pińczów, 49—the Czarna at Połaniec, 50—the Raba at Proszówki, 51—the Przemsza at Przeczyce, 52—the San at Przemyśl, 53—the Pszczynka at Pszczyna, 54—the San at Radomyśl, 55—the Soła at Rajcza, 56—the Czarna at Raków, 57—the Bukowa at Ruda Jastkowska, 58—the Wieprzówka at Rudze, 59—the Wisłok at Rzeszów, 60—the Wisła at Sandomierz, 61—the Trzebośnica at Sarzyna, 62—the Skawica Dolna at Skawica, 63—the Wisła at Skoczów, 64—the Biała Przemsza at Sławków, 65—the Bobrza at Słowik, 66—the Poprad at Stary Sącz, 67—the Stradomka at Stradomka, 68—the Raba at Stróża, 69—the Skawa at Sucha Beskidzka, 70—the Biały Dunajec at Szaflary, 71—the Wisła at Szczucin, 72—the Solinka at Terka, 73—the Czarna Nida at Tokarnia, 74—the Ropa at Topoliny, 75—the Wisłok at Tryńcza, 76—the Wisła at Ustroń-Obłaziec, 77—the Skawa at Wadowice, 78—the Wschodnia at Wilkowa, 79—the Osława at Zagórz, 80—the Cicha Woda at Zakopane–Harenda, 81—the Lubaczówka at Zapałów, 82—the Wisła at Zawichost, 83—the Dunajec at Żabno, 84—the Wisłok at Żarnowa, 85—the Wisłoka at Żółków and 86—the Soła at Żywiec

In the next step, the average values from standardized flows were calculated for separated groups of catchments separately for each year, each winter half-year and each summer half-year. As a result of this process, average values of standardized group flows were obtained for each year (GrSTD SQY), each winter half-year (GrSTD SQW) and each summer half-year (GrSTD SQS). These calculations were carried out in each of the separated groups using the formula:

$$\mathrm{GrSTD\ SQ}_n = \frac{\sum \mathrm{STD\ SQ}_n}{m} \tag{2}$$

where n is the certain year of multiannual period and m is number of catchments in the group for given n.

The final effect of the procedure, outlined above, was receiving for each group a series of annual data (S_GrSTD SQ_Y), of the winter half-year data (S_GrSTD SQ_W) and of the summer half-year data (S_GrSTD SQ_S).

To check the quality of the data series match, there was determined a relationship between group-averages series (S_GrSTD SQ_Y, S_GrSTD SQ_W, S_GrSTD SQ_S) and standardized average river flow series in particular catchments belonging to a given group (S_STD SQ_Y, S_STD SQ_W, S_STD SQ_S). The coefficient of determination calculated as the square of the Pearson correlation coefficient was used for this purpose. (Only positive correlation coefficients were considered.)

Trend analysis was performed to group-average river flows series (S_GrSTD SQ_Y, S_GrSTD SQ_W, S_GrSTD SQ_S). The nonparametric Mann–Kendall statistic was used to test for trends. It identifies monotonic increases or decreases in a time series by comparing between successive values. The Mann–Kendall test has been advocated for hydrological applications (Kundzewicz and Robson 2004). In order to remove the autocorrelation data from the series, the trend-free prewhitening (TFPW) method was used (Yue et al. 2002). According to McCabe and Wolock (2002), Mann–Kendall's statistics and its statistical significance were calculated for every possible combination of start and end years in the record 1951–2015. The minimum length of the calculation period was 20 years (Hannaford et al. 2013).

Results

Annual river flow

The result of cluster analysis is shown in Fig. 2. Most of the seven distinguished clusters of catchments are geographically coherent within the Upper Vistula Basin. The homogeneity of clusters ($Y_I - Y_{VII}$) varies substantially. The standardized annual average flow series in particular basins (S_STD SQ_Y) has been explained by the standardized group-average annual flow series (S_GrSTD SQ_Y) from 53% (Biała Przemsza–Sławków) to 98% (Brynica–Namiarki). A low homogeneity reveals the highest parts of the Upper Vistula Basin: The average annual river flow in the northern Tatra Mountains (Y_{III}) and the High Bieszczady Mountains catchments (Y_{II}) are poorly explained by the group-average river flow series (S_GrSTD SQ_Y)—from 57 to 74%, respectively—in comparison with other catchments within their groups.

There are clearly substantial differences between the directionality and magnitude of trends over time within particular clusters in the Upper Vistula Basin (Fig. 3). The Y_V upland cluster (Brynica River) is characterized by the predominant positive trends, while trends in the neighbouring group Y_{VII} are mostly negative. Negative trends are found also in the group Y_{VI} comprising the Oświęcim Basin, the Silesian Foothills and the Silesian Beskids Mountains. Within the Carpathian Mountains catchments (groups Y_{II} and Y_{III}), there is a contrast in trend directionality and positive trends prevail. Fluctuations between positive and negative trends over a range of periods remain in two groups Y_I and Y_{IV} representing mostly lowland catchments.

Trends in all groups are positive up to the second half of the 1980s. The decrease in river flow in the following years has weakened these trends, especially in mountain and foothill groups (Y_{II}, Y_{III}) and upland group (Y_V). Within the rest of groups (Y_I, Y_{IV}, Y_{VI}, Y_{VII}), there is a very strong contrast in trend directionality at the end of the 1980s, when trends reversed to negative ending in the end of the 1990s.

Trends after 2000 are mostly positive in the Carpathian catchments (Y_{II}, Y_{III}, Y_{IV}) and Brynica River catchment (Y_V) in contrast to Y_{VI} and Y_{VII} groups, where negative trends prevail. Trends in the group Y_I (eastern part of the Sandomierz Basin and a part of Roztocze) follow a very different pattern. After 2010, trends become weaker.

Trends starting between 1961 and 1981 are all negative up to the 1990s in all groups, and they remain negative in Y_{IV}, Y_{VI} and Y_{VII}. Groups Y_{II}, Y_{III}, Y_V show the change in trend directionality from negative to positive. In the Y_I group, no unambiguous flow trends were found.

For most of the groups, annual river flow trends after 1981 are predominantly positive to all end years. Negative trends over a range of periods after 1991 are common.

Winter half-year river flow

The eight groups of catchments on the basis of homogeneous hydrological behaviour on an S_STD SQ_W using cluster analysis were formed. The clusters are relatively geographically coherent areas within the Upper Vistula Basin (Fig. 4). The standardized group averages of winter half-year flow series (S_GrSTD SQ_W) explain from 33% (Biała–Czechowice-Dziedzice) to 97% (Brynica–Namiarki) of standardized average winter half-year flow series in the catchments (S_STD SQ_W).

In the case of drainage catchments, the northern slopes of the Tatra Mountains and the Bieszczady Mountains (from 51 to 62%) and catchments located within the Oświęcim Basin and the Silesian Foothills (from 33 to 64%) in comparison with winter half-year flow in other catchments inside their group were poorly explained by their mean group (S_GrSTD SQ_W). A considerably low homogeneity reveals W_{VI} and W_{VIII} with catchments within, respectively, the Oświęcim Basin and the Silesian Foothills (from 33 to 64%).

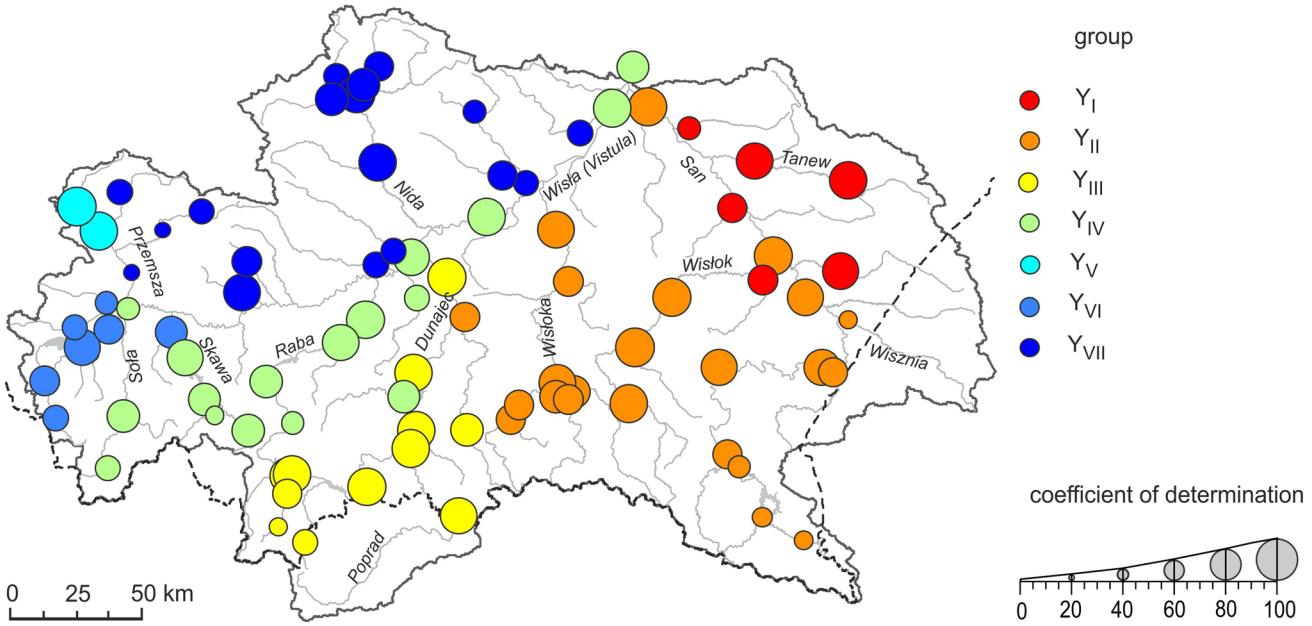

Fig. 2 Location of the catchments grouped into seven homogeneous clusters according to average annual river flow series (S_STD SQ_Y) in the Upper Vistula Basin

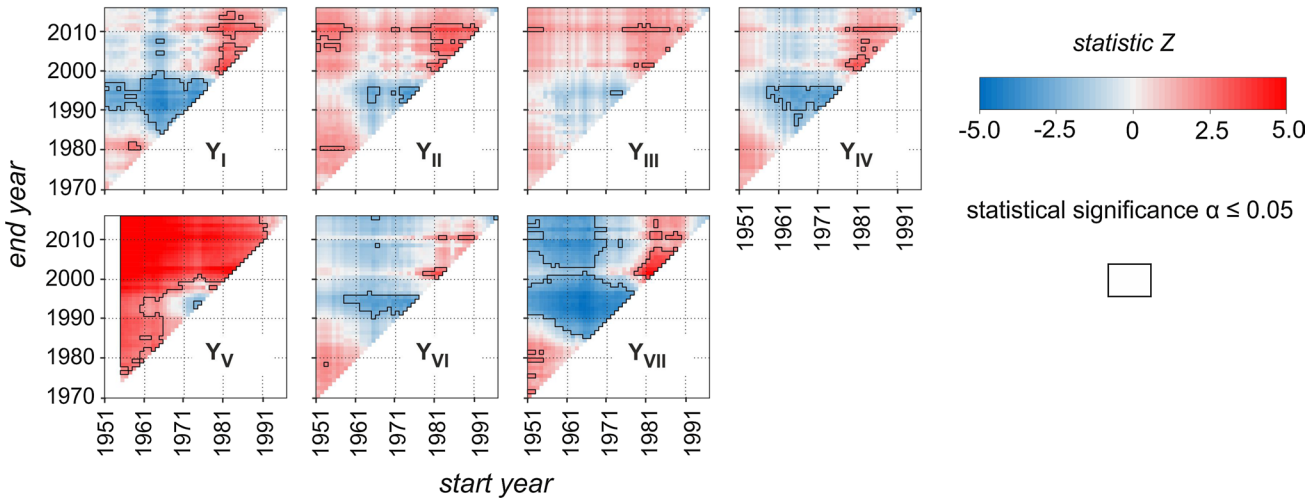

Fig. 3 Multitemporal trend analysis for annual average river flow series (S_GrSTD SQ_Y). *X*-axis shows start year of trend, and *y*-axis shows end. The corresponding pixel is coloured according to the resulting Z statistic (see legend), with red representing positive trends and blue representing negative trends

Overall, the average winter half-year river flows follow various patterns in the period 1951–2015 (Fig. 5). Positive trends prevail in the Brynica River (W_I) and in the Carpathian catchments (W_{II}, W_{IV}, W_V). River flow in the catchments in upland area (W_{VII}, W_{VIII}) and the Vistula River flow (W_{VI}) reveal decreasing trends. In the eastern parts of the Sandomierz Basin and Roztocze (W_{III}), any dominating trend has been observed.

Positive trends prevail strongly up to the second half of the 1980s in all groups except W_V where this prevailing is less apparent. Trends remain positive in the following years in W_I and W_{IV} and become relatively weaker in W_{II} and W_V, while there is a strong contrast in trend directionality over the time series in the groups W_{III}, W_{VI}, W_{VII}, W_{VIII} (positive/negative). Trends starting in the end of the 1990s are positive within the W_I, W_{II}, W_{IV} and W_V groups. However, in

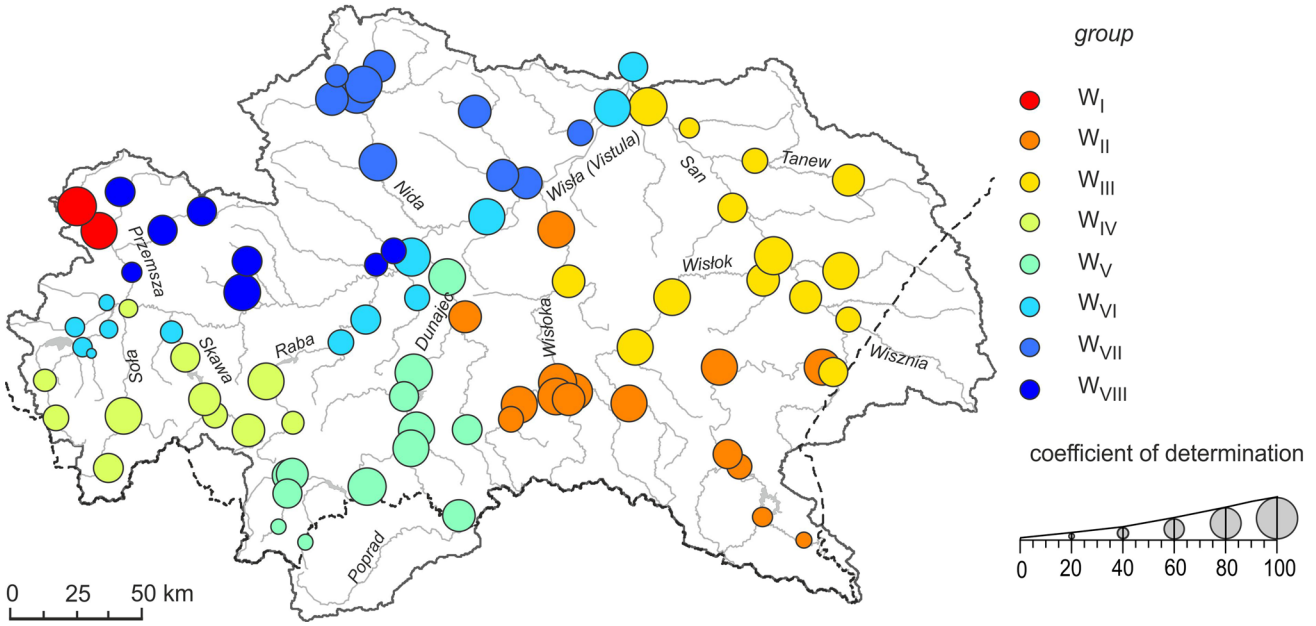

Fig. 4 Location of the catchments grouped into eight homogeneous clusters according to average winter half-year river flow series (S_STD SQ_W) in the Upper Vistula Basin

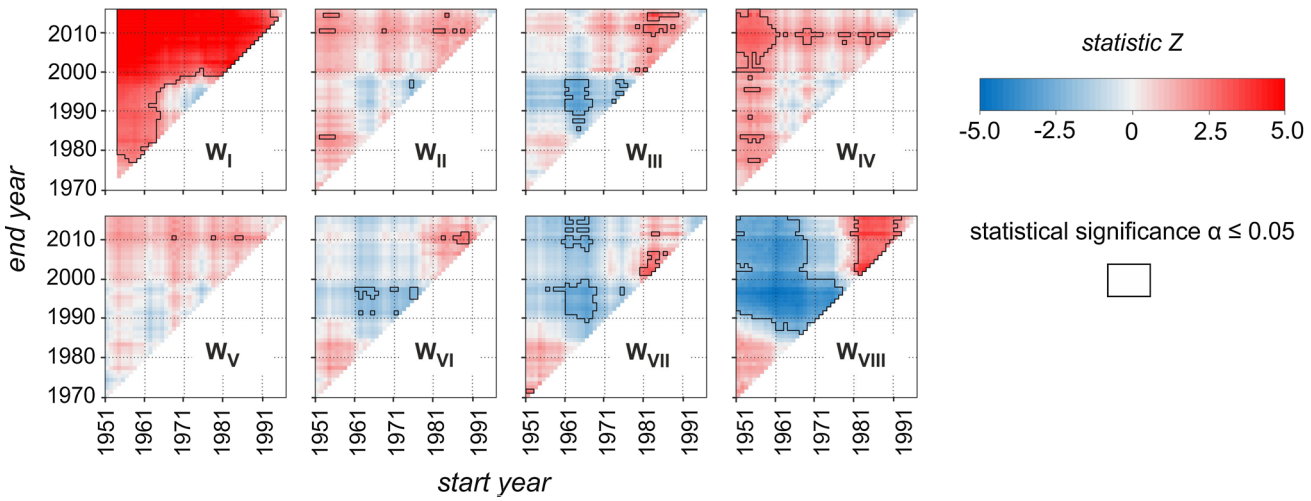

Fig. 5 Multitemporal trend analysis for average winter half-year river flow series (S_GrSTD SQ_W). *X*-axis shows start year of trend, and *y*-axis shows end. The corresponding pixel is coloured according to the resulting *Z* statistic (see legend), with red representing positive trends and blue representing negative trends

the group W_{III}, trend reverses (positive/negative). Negative trends are found in the groups W_{VI}, W_{VII}, W_{VIII} until 2015.

All trends starting in 1965–1981 and ending in 1985–2015 onwards are negative in W_{VI}, W_{VII}, W_{VIII}. In the group W_{III}, trends remain negative to the end of the 1990s and then change toward a positive one. There are fluctuations between positive and negative trends in the groups W_I, W_{II}, W_{IV}, W_V until 2000; afterwards, positive trends increase. Trends starting between 1981 and 1991 are positive in all groups, while those starting after 1991 are mostly negative.

Summer half-year river flow

The catchments are clustered into eight groups, which are broadly homogenous in terms of variability of the summer half-year river flow (Fig. 6). Their geographical coherency

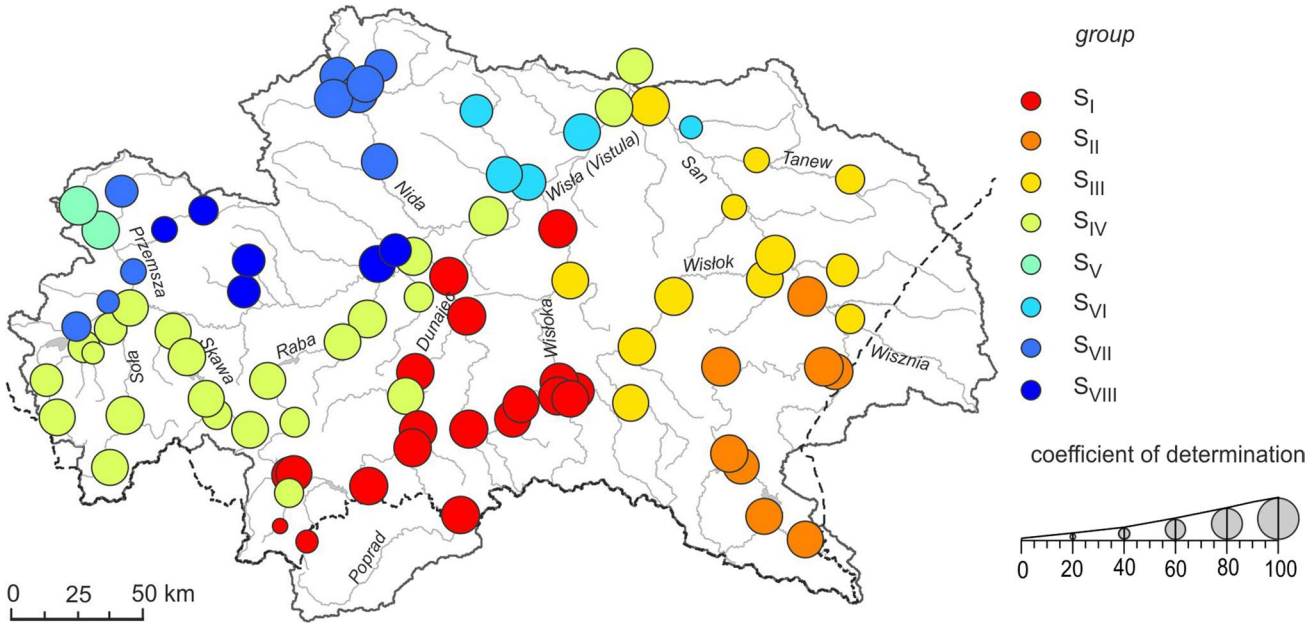

Fig. 6 Location of the catchments grouped into eight homogeneous clusters according to average summer half-year river flow series (S_STD SQ_S) in the Upper Vistula Basin

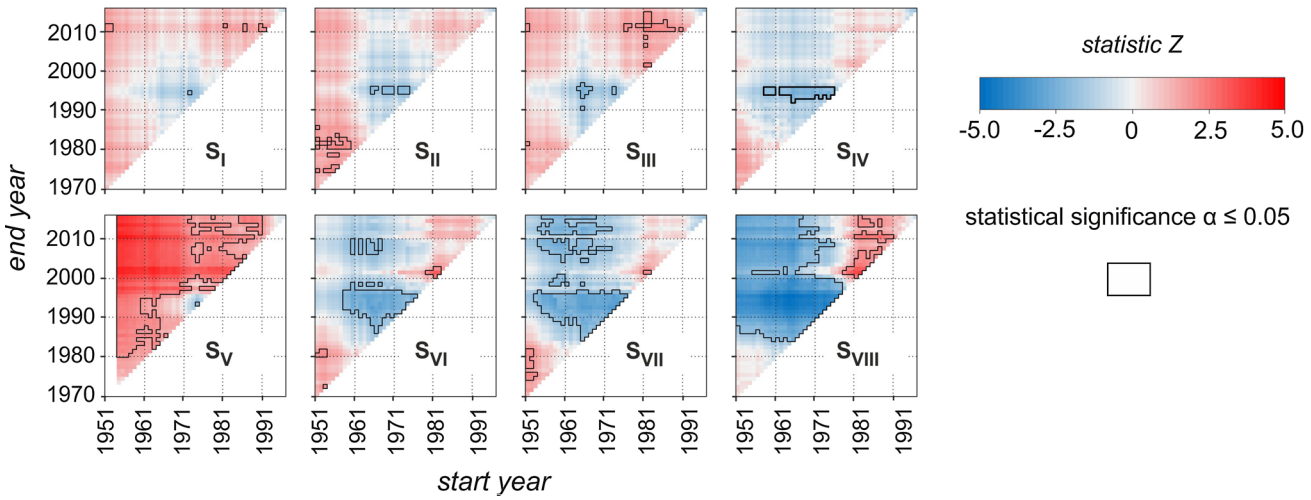

Fig. 7 Multitemporal trend analysis for summer half-year average river flow series (S_GrSTD SQ_S). *X*-axis shows start year of trend, and *y*-axis shows end. The corresponding pixel is coloured according to the resulting Z statistic (see legend), with red representing positive trends and blue representing negative trends

is weaker than in the case of previous grouping. The homogeneity of the group $S_I - S_{VIII}$ differs substantially. The standardized group-average summer flow series (S_GrSTD SQ_S) explains from 55% (Cicha Woda River—Zakopane–Harenda) to 99% (Brynica–Namiarki) standardized summer average flows series in catchments (S_STD SQ_S). A low homogeneity reveals the group S_I where the average summer river flow on the northern slopes of the Tatra Mountains has been poorly weakly explained—from 55% to 68%—by the standardized group—average summer half-year flow series (S_GrSTD SQ_S).

A very strong contrast in trend directionality over the average summer half-year river flow series has been found (Fig. 7). Trends in the catchments at the left-bank part of the Upper Vistula River (S_{VI}, S_{VII}, S_{VIII}) are predominantly negative except the Brynica (S_V). At the right-bank part of the Upper Vistula River basin (S_I, S_{II} and S_{III}), positive trends

prevail with the exception of the S_{IV} group, which shows negative trends.

Trends in particular groups follow very different patterns. Trends of the summer half-year average river flow starting between 1951 and 1961 are positive for the groups S_I, S_{II}, S_{III}, S_V and likewise for the groups S_{IV}, S_{VI} and S_{VII} but only until the middle of the 1980s followed then by negative trends onwards. In the S_{VIII} until the mid-1980s, there have been no trends, while from the second half of the 1980s, negative trends have been observed.

Trends starting in between 1961 and 1981 were largely negative—up to 2015 in groups S_{II}, S_{IV}, S_{VI}, S_{VII} and S_{VIII}. For the S_I and S_{III}, change in trends has been observed from negative to positive. The summer half-year average river flow in the group S_V is firmly dominated by positive trends. Negative trends occur merely in periods starting between 1971 and 1975 and ending in 1995 in this group.

Discussion

The results of multitemporal trend analysis for the annual, winter half-year and summer half-year averages river flow in the Upper Vistula Basin reveal substantial differences in trends in 1951–2015. It is consistent with previous studies carried out for rivers in Poland (Bartnik and Jokiel 1997; Fal and Bogdanowicz 2002; Wrzesiński 2009; Piniewski et al. 2018). Similar findings were observed by Hannaford et al. 2013 for other European rivers. Current research allows to identify in short river flow records an alternating occurrence of periods with positive and negative trends except two groups of catchments W_{IV} and W_V. A shift from positive to negative trends in the first half of the 1960s and the end of the 1980s is typical for a multiannual temporal pattern of trends over a range of catchments (for the Brynica catchment: 1970s and 1980s, respectively). Apparent short-term trends indicate river flow fluctuations as a response of changing precipitation and air temperature associated with atmospheric circulation over Europe driven by large-scale patterns of climatic variability such as the NAO (Pociask-Karteczka et al. 2002–2003; Styszyńska and Tamulewicz 2005; Pociask-Karteczka 2006; Wrzesiński 2011; Wrzesiński and Paluszkiewicz 2011).

Long-term 40–50-year trends—primarily negative—are found in river flow catchments in the highland regions. The strong trends in summer half-year average flow prevail in the western part of highland region, while those in the eastern part are slightly weaker. There is a substantial difference in the Brynica River flow, which is dominated by strong positive trends in cases of both annual and half-year average flows. This catchment is strongly anthropogenically influenced primarily by Silesian coal mine activity. It was reported by Punzet (1973), Dynowska (1984) and Czaja (1988) that pumped groundwater discharge to the river hinders a natural variability of river regime flow. Unsurprisingly, the group-average flow explains very poor average flows in such catchment as it is similar for the catchments on the northern slopes of the Tatras.

Clustering of catchments on the basis of variability of annual and winter half-year average river flows allowed to distinguish two regions in the Carpathian part of the Upper Vistula River basin: the western region and eastern region. This is unsurprising given the increase into the east a climatic continentality (Kożuchowski and Marciniak 1992) associated with predominance of snow over rain precipitation (Dynowska 1971; Ziemońska 1973). The western region spans to the upper part of the Biała Tarnowska River and the Dunajec River catchment, as Dobija (1981) and Chełmicki et al. (1999) indicated in their research on river runoff patterns and river runoff variability. In the case of the summer half-year average river flow, the border spans further to the east to the Wisłoka River (Ziemońska 1973) and to the Nida River in the northern part of uplands.

Conclusions

The conducted studies provide temporal patterns of trends and the evidence of regional hydrological response to the climate and anthropogenic activity in the Upper Vistula Basin.

Clustering of catchments on the basis of variability of annual, winter half-year and summer half-year average river flows allowed to distinguish three groups of catchments, i.e., $Y_I - Y_{VII}$, $W_I - W_{VIII}$ and $S_I - S_{VIII}$, geographically coherent in various degrees.

There are differences between groups of catchments in the directionality of trends over time for any one group of catchment.

Despite the presence of alternation in short-term trends—especially evident in the case of average annual trends—a wide variation in long-term trends was observed in all groups. Their spatial distribution is closely related to the geographical regions. This may indicate a very strong impact of local environmental features on river runoff. This was pointed out in his works by Dobija and Dynowska (1975), Parajka et al. (2009), Wrzesiński (2017) and Wrzesiński and Sobkowiak (2018). Bezak et al. (2015) also referred to significance of the environment in identifying trends. Research conducted by Gutry-Korycka (1996, 1997) indicated lower resistance of lowland rivers to climatic changes compared to upland and mountain rivers. This analysis enables to conclude that two neighbouring groups of river catchments with different environmental conditions may react differently to climate changes and, therefore, have a different trend value.

The considerably higher coefficient of determination between the groups distinguished with average summer

half-year flow likely indicates reasonably higher significance of climatic factors such as precipitation and air temperature than another geographical factors such as landforms and catchment storage on hydrology in the summer season. Further trends in river flow in the future will be dominated by increasing precipitation and air temperature as climate scenario projects for Poland. Therein, a significant increase in river flow will be noted in the winter season (Piniawski et al. 2016, 2017). Despite that, Romanowicz et al. (2016) signalized lack of tendencies in future river flow trends in two catchments in the Upper Vistula Basin and discrepancies in river flow projection for different climate scenarios.

The results of this study indicate considerable variability of trends in time according to the length of analysed time series. Extending or shortening of the time dataset causes strengthening or weakening of trend, or even change in the directionality of trend. Hence, an attempt to extrapolate river flow into past or future of such a selective viewpoint could easily be misleading, as mentioned by Svensson et al. (2006), Chen and Grasby (2009) and Hannaford et al. (2013). Also the underlying assumption of stationarity of river flow should be critically reviewed (Milly et al 2008, 2015; Piniawski et al 2018).

Compliance with ethical standards

Conflict of interest The corresponding author states that there is no conflict of interest.

References

Adaptation to climate change (2018) European Commission. https://ec.europa.eu/clima/policies/

Bartnik A, Jokiel P (1997) Zmiany odpływu na obszarze Polski w latach 1971–1990 w świetle analiz jednorodności szeregów przepływów rzek. Wiad IMGW 4:67–85

Bezak N, Horvat A, Šraj M (2015) Analysis of flood events in Slovenian streams. J Hydrol Hydromech 63:134–144

Birsan MV, Zaharia L, Chendes V, Branescu E (2014) Seasonal trends in Romanian streamflow. Hydrol Process 28:4496–4505

Chełmicki W (1991) Położenie, podział i cechy dorzecza. In: Dynowska I, Maciejowski M (eds) Dorzecze górnej Wisły. Część I, PWN Warszawa, pp 15–29

Chełmicki W, Skąpski R, Soja R (1999) Reżim hydrologiczny rzek karpackich w Polsce, Folia Geogr., Geogr.-Phys., Kom. Nauk Geogr. PAN, Kraków 29/30:67–8

Chen Z, Grasby SE (2009) Impact of decadal and century-scale oscillations on hydroclimate trend analyses. J Hydrol 365:122–133

Czaja S (1988) Zmiany stosunków wodnych w zlewni Brynicy w wyniku gospodarczej działalności człowieka. Geogr Stud Disser 11:60–93

Dobija A (1981) Sezonowa zmienność odpływu w zlewni górnej Wisły (po Zawichost). Zeszyty Naukowe UJ, Prace Geograficzne 53:51–112

Dobija A, Dynowska I (1975) Znaczenie parametrów fizjograficznych zlewni dla ustalenia wielkości odpływu rzecznego. Folia Geogr Ser Geogr Phys 9:77–127

Dynowska I (1971) Typy reżimów rzecznych w Polsce. Zeszyty Naukowe UJ, Prace Geograficzne 28:1–133

Dynowska I (1984) Zmiana reżimu odpływu w wyniku oddziaływania zbiorników retencyjnych. Czasop Geogr 55(3):301–315

Fal B, Bogdanowicz E (2002) Zasoby wód powierzchniowych Polski. Wiad IMiGW 25(2):3–38

Gutry-Korycka M (1996) Długookresowe tendencje elementów obiegu wody w zlewni w istniejących i w przewidywanych warunkach zmian globalnych klimatu. In: Gutry-Korycka M (ed) Studia nad wpływem globalnych zmian klimatu na obieg wody. Wydział Geografii i Studiów Regionalnych UW, Warszawa, p 159

Gutry-Korycka M (1997) Próba oceny odpływu rzek polskich w XXI wieku. Annales UMCS, Sectio B, Lublin 52(8):123–132

Hannaford J, Buysl G, Stahl GK, Tallaksen LM (2013) The influence of decadal-scalevariability on trends in long European streamflow records. Hydrol Earth Syst Sci 17:2717–2733

Jokiel P, Kożuchowski K (1989) Zmiany wybranych charakterystyk hydroklimatycznych Polski w bieżącym stuleciu. Dokumentacja Geograficzna IGPZ PAN 6:7–87

Kożuchowski K, Marciniak M (1992) Kontynentalizm termiczny klimatu na obszarze Polski w okresie 1881–1980. Wiad IMGW 15(4):89–93

Kundzewicz ZW (ed) (2012) Changes in flood risk in Europe, Special IAHS Publication, 10, Wallingford, Oxfordshire, UK

Kundzewicz ZW, Robson AJ (2004) Change detection in hydrological records—a review of the methodology. Hydrol Sci J 49:7–19

Lindstrom G, Bergstrom S (2004) Runoff trends in Sweden 1807–2002. Hydrol Sci 49(1):69–83

Madsen H, Lawrence D, Lang M, Martinkova M, Kjeldsen TR (2014) Review of trend analysis and climate change projections of extreme precipitation and floods in Europe. J Hydrol 519:3634–3650

McCabe GJ, Wolock DM (2002) A step increase in streamflow in the conterminous United States. Geophys Res Lett 29:2189

Miler A (1999) Okresowość i trendy czasowe zmian przepływów Warty w Poznaniu w okresie udokumentowanych obserwacji 1822–1997. In: Chełmicki W, Pociask-Karteczka J (eds) Interdyscyplinarność w badaniach dorzecza. IGUJ, Kraków, pp 99–107

Milly PCD, Betancourt J, Falkenmark M, Hirsch RM, Kundzewicz ZW, Lettenmaier DP, Stouffer RJ (2008) Stationarity is dead: whither water management? Science 319:573–574

Milly PCD, Betancourt J, Falkenmark M, Hirsch RM, Kundzewicz ZW, Lettenmaier DP, Stouffer RJ, Dettinger MD, Krysanova V (2015) On critiques of ''Stationarity is dead: whither water management?'. Water Resour Res 51(9):7785–7789

Parajka J, Kohnova S, Merz R, Szolgay J, Hlavcova K, Blöschl G (2009) Comparative analysis of the seasonality of hydrological characteristics in Slovakia and Austria. Hydrol Sci J 54(3):456–473

Pekarova P, Miklanek P, Pekair J (2003) Spatial and temporal runoff oscillation analysis of the main rivers of the world during the 19th-20th centuries. J. Hydrology 274:62–79

Piniewski M, Szczęśniak M, Mezghani A, Kundzewicz ZW (2016) Hydroclimatic projections for the Upper Vistula Basin. In: Kundzewicz ZW, Stoffel M, Niedźwiedź T, Wyżga B (eds) Flood risk in the Upper Vistula Basin. GeoPlanet: Earth and planetary sciences. Springer, Berlin, pp 331–339

Piniewski M, Szcześniak M, Kundzewicz ZW, Mezghani A, Hov Ø (2017) Changes in low and high flows in the Vistula and the Odra basins: model projections in the European-scale context. Hydrol Process 31(12):2210–2225

Piniewski M, Marcinkowski P, Kundzewicz ZW (2018) Trend detection in river flow indices in Poland. Acta Geophys 66(3):347–360

Pociask-Karteczka J (2006) River hydrology and the North Atlantic oscillation: a general review. AMBIO J Hum Environ 35(6):312–314

Pociask-Karteczka J (2016) Vistula basin—A geographical overview. In: Kundzewicz ZW, Stoffel M, Niedźwiedź, Wyżga B (eds) Flood risk in the Upper Vistula Basin. GeoPlanet: earth and planetary sciences. Springer, Berlin, pp. 3–21

Pociask-Karteczka J, Limanówka D, Nieckarz Z (2002–2003) Wpływ oscylacji północnoatlantyckiej na przepływy rzek karpackich (1951-2000). Folia Geogr Ser Geogr Phys 33–34:89–104

Punzet J (1973) Wpływ zbiorników retencyjnych na prawdopodobieństwo występowania wielkich wód w dorzeczu Górnej Wisły. Gosp Wodna 2:46–49

Romanowicz RJ, Kundzewicz ZW, Meresa HK, Stoffel M, Krysanova V, Doroszkiewicz J (2016) Projections of changes in flood hazard in two headwater catchments of the Vistula in the context of European-scale studies. In: Kundzewicz ZW, Stoffel M, Niedźwiedź T, Wyżga B (eds) Flood risk in the Upper Vistula Basin. GeoPlanet: earth and planetary sciences. Springer, Berlin, pp 341–359

Slater LJ, Singer MB, Kirchner JW (2015) Hydrologic versus geomorphic drivers of trends in flood hazard. Geophys Res Lett 42:370–376

Soja R (2002) Hydrologiczne aspekty antropopresji w polskich Karpatach. Prace Geograficzne 186:7–130

Stachý J (2010) Zmienność odpływu rocznego Odry i Wisły w latach 1901–2008. Monografie Komitetu Inżynierii Środowiska PAN 69:43–53

Stahl K, Hisdal H, Hannaford J, Tallaksen L, Van Lanen HAJ, Sauquet E, Demuth S, Fendekova M, Jordar J (2010) Streamow trends in Europe: evidence from a dataset of near-natural catchments. Hydrol Earth Syst Sci 14:2367–2382

Stahl K, Tallaksen LM, Hannaford J, Van Lanen HAJ (2012) Filling the white space on maps of European runoff trends: estimates from a multi-model ensemble. Hydrol Earth Syst Sci 16:2035–2047

Styszyńska A, Tamulewicz J (2005) Warta river discharges in Poznań and atmospheric circulation in the North Atlantic region. Quaest Geogr 23:63–81

Svensson C, Hannaford J, Kundzewicz ZW, Marsh T (2006) Trends in river floods: why is there no clear signal in observations? In: Frontiers in flood research: proceedings of kovacs colloquium, Paris, June 2006, vol 305. IAHS Publication, Wallingford, UK, pp 1–18

Wrzesiński D (2009) Tendencje zmian przepływu rzek Polski w drugiej połowie XX wieku. Badania fizjograficzne nad Polską Zachodnią, seria A–Geografia Fizyczne 60:147–162

Wrzesiński D (2011) Regional differences in the influence of the North Atlantic Oscillation on seasonal river runoff in Poland. Quaest Geogr 30(3):127–136

Wrzesiński D (2017) Reżim rzek Polski. In: Jokiel P, Marszelewski W, Pociask-Karteczk J (eds) Hydrologia Polski. Wyd. Naukowe PWN, Warszawa, pp 215–222

Wrzesiński D, Paluszkiewicz R (2011) Spatial differences in the impact of the North Atlantic Oscillation on the flow of rivers in Europe. Hydrol Res 42(1):30–39

Wrzesiński D, Sobkowiak L (2018) Detection of changes in flow regime of rivers in Poland. J Hydrol Hydromech 66(1):55–64

Yue S, Pilon P, Phinney B, Cavadias G (2002) The influence of autocorrelation on the ability to detect trend in hydrological series. Hydrol Process 16:1807–1829

Ziemońska Z (1973) Stosunki wodne w Polskich Karpatach Zachodnich. Prace Geograficzne PAN 103:124–127

Acta Geophysica (2020) 68:505–517
https://doi.org/10.1007/s11600-020-00404-5

RESEARCH ARTICLE - HYDROLOGY

Multi-objective optimization of soil erosion parameters using response surface method (RSM) in the Emamzadeh watershed

Mojtaba Shirazi[1] · Ataallah Khademalrasoul[1] · Seyed Mohammad Safieddin Ardebili[2]

Received: 15 October 2019 / Accepted: 25 January 2020 / Published online: 3 February 2020

Abstract

Soil erosion is one of the most leading environmental and public health problems in the world which dislodges considerable volumes of soil annually. In order to control soil erosion, several soil factors should be taken into account. Regarding the importance of soil properties on erosion occurrence, it is necessary to focus on soil properties. The aim of this study is to evaluate the effect of physical parameters that consist of sand %, silt %, clay %, SP % and stone % along with hydraulic properties including theta *s*, theta *r*, alpha *n* and Ks (cm/day) on the amount of soil erosion in Emamzadeh watershed. The above-mentioned factors were optimized using response surface methodology. The soil texture in the study area is mostly silty clay loam, and the main soil orders are Entisols and Inceptisols. Moreover, the main land use in the study area is forest–rangeland. The results proved that both physical and hydraulic valuables illustrated a significant effect on all of the independent parameters. The optimized values of different physical parameters were 60.241 for sand, 14 for silt, 41.025 for clay, 58.729% for SP and 3.83% for stone. A theta *r* of 0.09, theta *s* of 0.457 alpha of 0.014, *n* of 1.3 and Ks of 46.01 were found to be optimal values. The results of this study indicated that at optimal studied parameters, the values of the soil erosion before and after application of management scenarios were found to be 11.537 and − 2.253, respectively. Results show that both physical and hydraulic parameters have significant effects at the 1% level on the soil erosion before and after application of management scenarios. The obtained results could assist policy-makers with decisions aimed at minimizing soil erosion in this watershed. In summary, using the simulation–optimization techniques helps to evaluate the effect of management scenarios, then select and apply the best one to minimize the soil erosion outcomes.

Keywords D-optimal design · Management scenarios · Optimization · Physical and hydraulic parameters · Response surface methodology (RSM)

Introduction

Soil as one of the most important sources of production has been demolished with population growth and industrialization of the world (Meliho et al. 2019). Land degradation through human activities such as deforestation, overgrazing, tillage operations, inappropriate agricultural practices and land-use changes has negative impacts on soil quality indices and soil healthy (Schole et al. 2018; IPBES 2018). Soil erosion by water, as the most prevailing factor of soil degradation, has several outcomes, including mitigation of agricultural productivity, water quality–quantity and environmental impacts (Park et al. 2011; Xu et al. 2013; Xiong et al. 2019). Therefore, effective planning and implementation of soil erosion monitoring program are needed for understanding and estimating of soil erosion severity (Mondal et al. 2017; Nasiri et al. 2017). Moreover, in order to decrease the risk of soil erosion should be considered convenient strategies in the management plan (Sherriff et al. 2018). However, despite widespread researches on soil erosion and conservation (Mhazo et al. 2016), still, there is not a precise technique for soil erosion assessment in the watersheds; this means that, given the importance of the occurrence of erosion processes and the complexity of their mechanisms, it is essential to use new software and techniques with the ability to monitoring complex processes (Diodato et al. 2012; Corella et al. 2019). A convenient tool

✉ Ataallah Khademalrasoul
a.khademalrasoul@scu.ac.ir; Ataalahsoil@gmail.com

[1] Soil Science Department, Faculty of Agriculture, Shahid Chamran University of Ahvaz, Ahvaz, Iran

[2] Biosystems Engineering Department, Faculty of Agriculture, Shahid Chamran University of Ahvaz, Ahvaz, Iran

to estimate soil erosion–deposition and to understand the relations between different effective parameters on soil erosion is the application of soil erosion models. Soil erosion models are beneficial tools for analyzing soil erosion processes in the watersheds (Laflen and Flanagan 2013). Qian et al. (2014) analyzed the relation between water and soil erosion using linear and quadratic regression models and concluded that the runoff rate had a significant linear relationship with the rate of sediment loss. The outputs of soil erosion models are efficient tools which ultimately can be used to provide different scenarios for selecting and implementing a best management practice (Argent et al. 2016). Well-developed and properly calibrated models provide reasonable estimations of soil erosion risks (Giannecchini 2006). Generally, using simulation–optimization techniques are effective tools for planners, managers and executive units which is convenient in achieving management goals. In this regard, should provide backgrounds and contexts for best application of these techniques in order to eventually adopt appropriate management scenarios (Batista et al. 2019).

Regarding the complexity of soil erosion mechanisms and due to deficiency of appropriate management strategies, it is necessary to apply new techniques for simulation and optimization of soil erosion processes (Kirkby et al. 2008; Arnold et al. 2015; Shojaei et al. 2019). Response surface methodology (RSM) is an appropriate technique for monitoring the complicated processes in the watersheds (Chandramohan et al. 2015). The main advantage of RSM is the reduction of experiments to evaluate multiple parameters and their interactions (). Another advantage of this technique is the simplification of complex processes, scrutinizing continuous variables, elimination of problems related to the one-factor and determination of response's sensitivity to each factor. The RSM is an efficient experimental strategy to run optimal conditions for multivariable systems (Long et al. 2019). Indeed, the RSM by providing response levels along with appropriate statistics and ultimately by optimizing them allows selection of the best set of input parameters based on the research objectives (Sharma et al. 2019). The RSM is a collection of useful statistical and mathematical techniques for developing, improving and optimizing processes. It also has essential applications in the design, development and formulation of new products, as well as in the improvement of the existing product designs (Tan et al. 2017). The primary purpose of the RSM is to optimize the response (output variable), which is influenced by several independent variables (input variable) (Kumar et al. 2016). Therefore, according to importance of soil against erosive forces, it is necessary to use RSM technique for optimization and ultimately selection of the best management practices. The specific objective of our study was to optimize soil erosion using response surface methodology based on soil physical and hydraulic parameters which are effective on soil erosion.

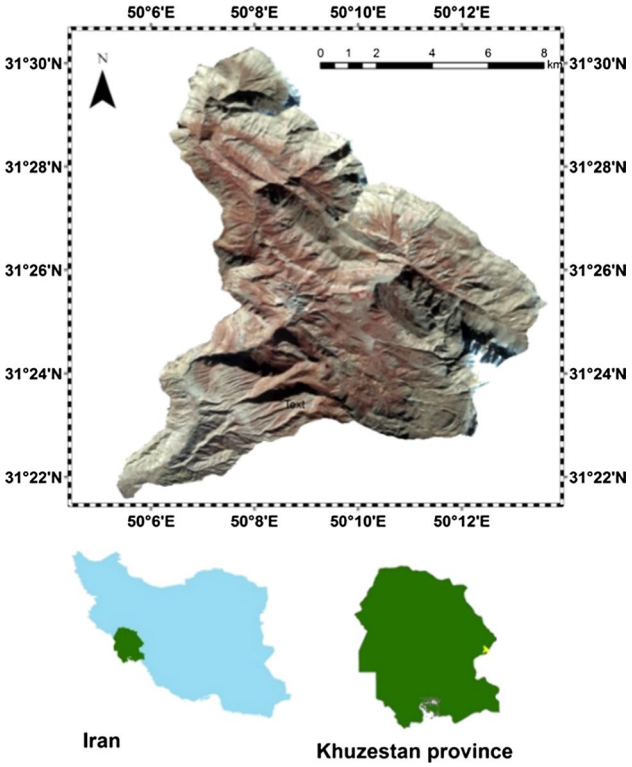

Fig. 1 Location of study area on true color composite of Landsat7 ETM^+ image acquired in March 2018

Methods and material

Location of the study area

The study area is placed in the northeast of Khuzestan Province, Iran country, with the geographical coordination of 31° 18′ to 31° 33′ N and 50° 5′ to 50° 13′ E (Fig. 1). The area of this watershed is approximately 104 km^2 including six hydrological parcels. In this area, the total annual precipitation is around 712 mm, and the average temperature is 23 °C. Furthermore, the soil texture in the study area is mostly silty clay loam (SiCL), and the main soil orders are Entisols and Inceptisols. The main land use in the study area is forest–rangeland.

Soil sampling, measurements and analysis

A composite sample (0–20 cm) was obtained by mixing soil from five separate sampling points in the watershed. Soil samples were air-dried at 20 °C in the laboratory. Afterward, soil texture was measured using hydrometric method. Regarding the heterogeneity of soil texture in different parts of study area, soil samples were collected and analyzed.

In order to measure stone (%) were collected all the stone, gravel and pebble in the 1×1 square meter area on the ground, then weighted. Using these 1×1 m^2 plots in different places, we calculated the average amount of stone on the ground in different parcels of watershed. Cation exchange capacity (CEC) and exchangeable bases were measured by the ammonium acetate method (pH = 7) (Thomas 1982). The soil organic matter (SOM) was measured using Walkley and Block method. Actually, soil organic matter is a key factor to prevent the soil against erosive factors. The saturation percentage (SP) is an index of soil texture; this parameter was measured based on the difference of the soil weight in the dry condition and the saturated condition. For all the soil samples, this parameter was measured three times to find an acceptable average. Albedo coefficient was calculated using the climate data, solar radiations and surface characteristics. This parameter depends on solar radiations and surface characteristics. For the white and flat surfaces, the Albedo coefficient has the highest amount. Compute theta *r*, theta *s*, alpha, *n* and K_S through RETC software.

Soil erosion simulation using the WEPP model

The Water Erosion Prediction Project (WEPP) model is based on surface water flow hydrology and erosion processes which provide the possibility of estimating the spatial and temporal patterns of soil erosion and sedimentation in the watersheds (Boll et al. 2015; Brooks et al. 2016). In the WEPP model, a watershed is defined as one or number of hillslopes, which have been drained into one or more channels (Flanagan and Nearing 1995; Flanagan et al. 2013). In this study, the climate simulation was performed using CLIGEN module (Kinnell et al. 2018; Anache et al. 2018) with data obtained from Izeh synoptic station. Moreover, soil, topography and management layers were defined for each hillslope (Schaap and Leij 2000; Tiwari et al. 2000). Ultimately, the studied watershed was simulated by hillslopes and the hydrographical network to run the model. In this study, in 17 hydrological units, the sediment load was converted to soil erosion values in ton/ha using the relationship between sediment load, sediment delivery ratio (SDR) and soil erosion described in PSIAC (1968) and modifications applied on PSIAC (MPSIAC) by Johnson and Gebhardt (1982). Sediment delivery ratio for each hydrological unit calculated based on the unit area (in mi^2) as above mentioned references (Table 1). Hydrological unit sediment production was obtained from the ministry of agriculture's hydrometric/sediment gauging stations (2009).

Response surface methodology

The second part of this study is the evaluation and optimization of physical and hydraulically parameters effective on soil erosion, which was performed using the RSM method. Design-Expert version 10 was utilized to generate a regression model and to perform the statistical analysis. The RSM shows the general form of the statistical model for predicting the response or dependent variable (Y) based on independent variables ($x_1, x_2, \ldots, x_k$) based on Eq. (1). The dependent variable is response, and independent variable acts as input factors (Muthusamy et al. 2019; Montgomery and Anderson-Cook 2009).

Table 1 The measured erosion, WEPP predicted and measured SDR for hydrological units

N	Overall SDR	Mean of predicted erosion (ton/ha)	Mean of predicted erosion (ton/ha)	Mean hydrological units SDR	Mean hydrological units area
17	30.68	23.04	29.27	61.98	6.15

$$y = f\left(x_1, x_2, \ldots, x_k\right) + \varepsilon \tag{1}$$

f is the response function, which will be finally optimized by the software, while ε shows the variables (error) that are effective in y but are not included in f (Najafi et al. 2015). The general form of the quadratic polynomial model is expressed by Eq. 2:

$$Y = \alpha_0 + \sum_{j=1}^{k} \alpha_j x_j + \sum_{j=1}^{k} \alpha_{jj} x_j^2 + \sum_{j<1} \sum_{l=2}^{k} \alpha_{jl} x_j x_1 + \varepsilon \tag{2}$$

where Y is the response. α_0, α_j, α_{jj} and α_{jl} are regression coefficients for intercept, linear, quadratic and interaction coefficients, respectively ($k = 8$ levels for each factor). x_j and x_l are independent variables and ε unpredicted error (De Oliveira Faber and Ferreira-Leitão 2016).

Response surface methodology is a collection of mathematical and statistical techniques based on the fit of a polynomial equation to the experimental data, which predict the process and optimize the levels of independent variables to attain the best level of dependent variables (Keshtegar et al. 2016; Bezerra et al. 2008). The RSM includes three parts: designing, analysis and optimization (Pattanaik and Rayasam 2018). In the first section, were determined the independent and dependent variables in two levels (− 1 and + 1) for software, and in the next sections, data analysis and optimization were performed (Gao et al. 2016). In the analysis section, there is a possibility to choose PTF (pedotransfer function) for data analysis and a section dedicated to the analysis of variance called ANOVA[1] (Rao and Venkaiah 2015). Then, in the next section, the software shows

[1] Analysis of variance.

the relationship between independent and dependent variables in a way 2D and 3D graphs, contour graphs, one-factor graphs and interaction graphs (Podder and Majumder 2015). First, each parameter must be defined in the upper limit and lower limit for the software. Then, according to the nature of each parameter, the goal of optimization has been defined. Sometimes, the goal of optimization somehow was adjusted that optimization process doing out of this range. But generally, there are five goals in the optimization process, which include: maximize, minimize, target, in rang and equal to (Kumar et al. 2018). In the optimization section, there is a section called importance, which the value of each optimization parameters from 1 to 5 plus is determined according to the optimization goal. Another part of the optimization is related to the solutions step that desirability function shows the probability of reaching optimization paths to the whole goal of research (Dinarvand et al. 2017). Desirability is a goal function that ranges from zero to one at the goal. The numerical optimization finds a point that maximizes the desirability function. The characteristics of a goal may be shifted by regulating the weight or significance. For several responses and factors, all goals combine into one desirability function. Myers and Montgomery (Chabbi et al. 2017) explained a multiple response method called desirability. The method using an objective function, D(X), is called the desirability function. The desirable range for each response (di) is from zero to one. The concurrent objective function is a geometric mean of all converted responses (Eq. 3):

$$D = \left(d_1 \times d_2 \times \cdots \times d_n\right)^{\frac{1}{n}} = \left(\sum_{i=1}^{n} d_i\right)^{\frac{1}{n}} \tag{3}$$

n is the number of responses. If any of the responses was outside of their desirability range, the overall function becomes zero. For synchronic optimization, each response must have a low and high value specified to each goal. On the worksheet, the "goal" field for responses must be one of five choices: "none," "maximum," "minimum," "target," or "in range." Factors will always be included in the optimization, at their design range by default, or as a maximum, minimum of target goal. For simultaneous optimization, all goals have been combined into a desirability function, which is expressed by Eq. (4).

$$D = \left(\left(d_1\right)^{P_1}\left(d_2\right)^{P_2} \ldots \left(d_n\right)^{P_n}\right)^{\frac{1}{\sum P_i}} = \left(\prod_{i=1}^{n} d_i^{Pi}\right)^{\frac{1}{\sum P_i}}. \tag{4}$$

The goals of minimum and maximum for defining desirability (di) were obtained using Eqs. (5) and (6), respectively.

$$d = \begin{cases} 0 & \text{if: } y_i \le y_i^{\min} \\ \left(\frac{y_i - y_i^{\min}}{y_i^{\max} - y_i^{\min}}\right)^{w_i} & \text{if: } y_i^{\min} \le y_i \le y_i^{\max} \\ 1 & \text{if: } y_i \ge y_i^{\max} \end{cases} \tag{5}$$

$$d = \begin{cases} 1 & \text{if: } y_i \le y_i^{\min} \\ \left(\frac{y_i^{\min} - y_i}{y_i^{\max} - y_i^{\min}}\right)^{w_i} & \text{if: } y_i^{\min} \le y_i \le y_i^{\max} \\ 0 & \text{if: } y_i \ge y_i^{\max}. \end{cases} \tag{6}$$

RSM for soil erosion modeling and optimization

The simulation and optimization processes using RSM consist of six consecutive steps (Fig. 2): (1) screening of independent factors and defining dependent factors, (2) selecting the strategy for experimental design, (3) running the experiments and measuring the results, (4) fitting and diagnosing mathematical model, (5) confirming the model using ANOVA and graphs and (6) determination of optimal conditions (Karimifard and Moghaddam 2018). In this study, ten parameters (independent variables) were defined at minimum (−1) and maximum (+1) levels for software (Table 2). Two responses in the output template (R_1 = amount of soil erosion and R_2 = soil erosion amount after management) were determined. The type of applied management scenario was a revision of crop cover and exclosure in the watershed. In the first step, a design for processing was selected. Then, the amounts of each input parameter (independent variables) were defined at minimum (−1) and maximum (+1) levels. In the next step, the processing was begun after selecting the PTF and process order or regression models (mean, linear, 2FI, quadratic and cubic). In the last section of this stage, the software was shown the relationships between parameters as individually and interacting effect on the dependent variable (soil erosion) in the form of 2D and 3D graphs. In the optimization section, the optimization process was accomplished for both of the responses in two ways numerical and graphical that different stages of optimization and response parameters using RSM are shown (Fig. 2).

Results and discussion

Statistical analysis of RSM parameters and model selection

Our results illustrated a significant relationship between all evaluated parameters and soil erosion, before and after application of management scenarios. Regarding the possibility of RSM technique to select the best model among all assessed models using statistical parameters, the quadratic

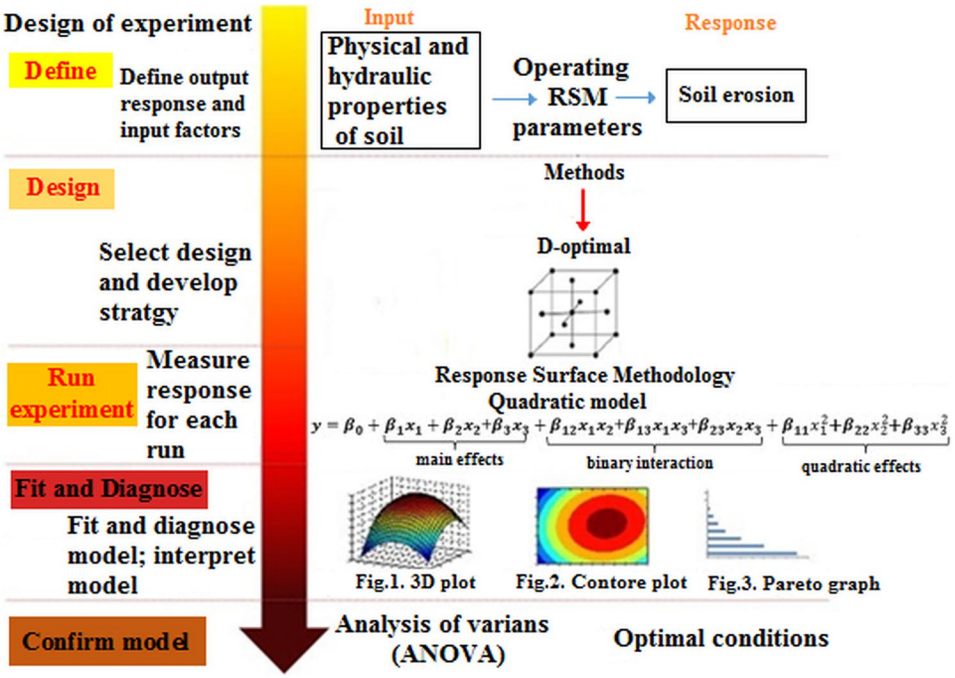

Fig. 2 Steps of experimental design in the response surface methodology

Table 2 The D-optimal design of the independent variables

Parameters	Coded values	
	Min (−1)	Max (+1)
Physical		
Sand	−1.000 = 6.0000	1.000 = 64.0000
Silt	−1.000 = 14.0000	1.000 = 76.0000
Clay	−1.000 = 6.0000	1.000 = 46.0000
SP	−1.000 = 31.6000	1.000 = 68.1000
Stone	−1.000 = 0.0900	1.000 = 5.2000
Hydraulic		
Theta *r*	−1.000 = 0.0339	1.000 = 0.0974
Theta *s*	−1.000 = 0.3856	1.000 = 0.4874
Alpha	−1.000 = 0.0052	1.000 = 0.0291
n	−1.000 = 1.2767	1.000 = 1.6799
K_S	−1.000 = 6.8400	1.000 = 46.0100

model was suggested as the best model (Table 3) (select the highest-order polynomial where the additional terms are significant and the model is not aliased). Based on the statistical analysis, the quadratic model was selected as the best model; therefore in the ANOVA section, all analyses were performed with this selected model. The value of "Prob[2] > *F*" was smaller than 0.05, which defined as the α value of the test with a confidence interval of 95% (Table 4). This means that the quadratic model is significant and independent variables (physical and hydraulic properties of soil) influenced soil erosion. Also, the *F*-value of 99.30 implies that the model is significant. The values of "Prob > *F*" less than 0.05 indicate that our model is significant, whereas the values more than 0.10 stated that the model is not significant. Moreover, the *R*-square of the model with *df* equal to 65 ($df = n - 1$) was greater than 0.99, and the difference between *R*-square and adjusted *R*-square was smaller than 0.01, which illustrated the high accuracy of the obtained model. The "Adeq[3] Precision" measures the signal to noise ratio, and a ratio greater than 4 is desirable (Stat-Ease., 1998). Our results showed that this ratio was 23.73 which confirmed an adequate signal; therefore, this model can be used to navigate the design space. Ultimately based on all above mentioned statistical parameters, the optimization of effective parameters on soil erosion was performed using the quadratic model that suggested with the RSM. Therefore, using the RSM technique (Bezerra et al. 2008), the best model with the highest accuracy for simulation–optimization process was selected.

Interactive effects of sand and clay on soil erosion using RSM

The range of clay content was from 6 to 46%, and for sand content was 4 to 64%; therefore, results illustrated that minimum amount of soil erosion occurred in the maximum levels of both clay and sand contents which soil erosion was equal to 15.4 ton/ha (Fig. 3a). Also, the maximum amount

[2] Probability.

[3] Adequate.

Table 3 Statistical parameters of different regression models based on dependents variables (including R_1 and R_2)

Source	SDEV		*R*-square		Adjusted *R*-square		
Response	R_1	R_2	R_1	R_2	R_1	R_2	
Linear	4.740	2.030	0.2789	0.0911	0.1587	−0.0604	
2FI	3.990	2.100	0.8720	0.7560	0.4027	−0.1389	
Quadratic	0.540	0.260	0.9992	0.9988	0.9892	0.9826	Suggested
Cubic	0	0	1	1	1	1	Aliased

Additionally, mean ± standard deviation (SDEV) is shown ($n = 66$)

Table 4 The ANOVA analysis for response surface quadratic model

ANOVA for response surface quadratic model											
Source	Sum of squares		*df*		Mean square		*F*-value		*p* value prob > *f*		
Response	R_1	R_2	R_1	R_2	R_1	R_2	R_1	R_2	R_1	R_2	
Model	1865.41	270.71	65	65	28.70	4.16	99.30	61.94	< 0.0001	< 0.0001	Significant

of soil erosion (equal to 24 ton/ha) was at the minimum level of clay content and the sand content between 40 and 50% (Fig. 3c). According to the high amount of sand and increasing clay content (Fig. 3a), it was expected that soil erosion was reduced from 22.8 to 15.4 ton/ha. The main reason for this result is the meaningful effect of clay and associated organic matter content on soil aggregation compared to silt and sand particles (Kumar et al. 2016; Mangalassery et al. 2019). Therefore, in the soil conservation plan, one of the most important parts is the soil properties.

Moreover, according to Russell's theory, clay particles owing to small size with high cation exchange capacity and high specific surface area, therefore, enhance soil aggregation and diminish the soil erosion potential (Shaikh et al. 2017; Spagnoli and Shimobe 2019). However, based on the existing management situations in the studied watershed and the interaction effects of sand and clay content, the soil erosion was around 15 ton/ha. To evaluate the effectiveness of management scenarios using WEPP model, the effect of the applied management strategies including revision of crop cover (RC) and exclosure (EX) was assessed as response 2 (R_2) using RSM. Results showed that after the application of management scenarios as R_2, the soil erosion was significantly decreased to around 1–2 ton/ha (Fig. 3b). This meaningful declining of soil erosion clearly confirmed the positive effects of convenient management strategies on soil preserving against erosive forces. Feng et al. (2006) showed that the establishment of a vegetation riparian buffer regarding the crop cover revision is an effective scenario to reduce the on-site and off-site effects of soil erosion. Indeed, the riparian buffer is a permanent vegetation cover which is located between erosion site and water bodies with numerous capabilities to mitigate soil erosion potential. Also, as Fig. 3b illustrates regarding the effectiveness of the applied management scenarios, the amount of deposited soil was −0.06 ton/ha, which means the dramatical effects of the applied management scenarios on soil erosion controlling in the watershed. Results confirmed that the application of convenient management scenarios is able to conserve soil against erosive agents, therefore to mitigate on-site and off-site effects of soil erosion. The evaluated management strategies in our study were non-structural management scenarios which covered the purposes of sustainable management.

Interactive effects of sand and Ks on soil erosion using RSM

Our results depicted that by increasing the sand content and saturated hydraulic conductivity (Ks), the soil erosion was at the minimum level, which was equal to 21.7 ton/ha (Fig. 4a). As Fig. 4a shows by decreasing of sand content and Ks, the soil erosion potential was enhanced to 26 ton/ha while when the Ks was between 10 and 25 cm/day, the soil erosion was at the lowest amount (22 ton/ha) (Fig. 4c). As our results illustrated the hydraulic conductivity and sand content both are effective on soil erosion occurrence and this is an interactive effect. Soil erosion as a dynamic phenomenon is a function of different factors; therefore, despite the increasing of hydraulic conductivity, this parameter is not sufficient to enhance the resistance of soil aggregates against erosive factors (Jarzyna et al. 2019; Barman et al. 2019). Considering the complexity of the soil erosion process, the RSM technique provides an advanced infrastructural analysis to evaluate the interaction effects of different parameters on soil erosion. Utilizing the interactive effects of several parameters on soil erosion is a suitable tool to select and apply the best management practice in the critical area.

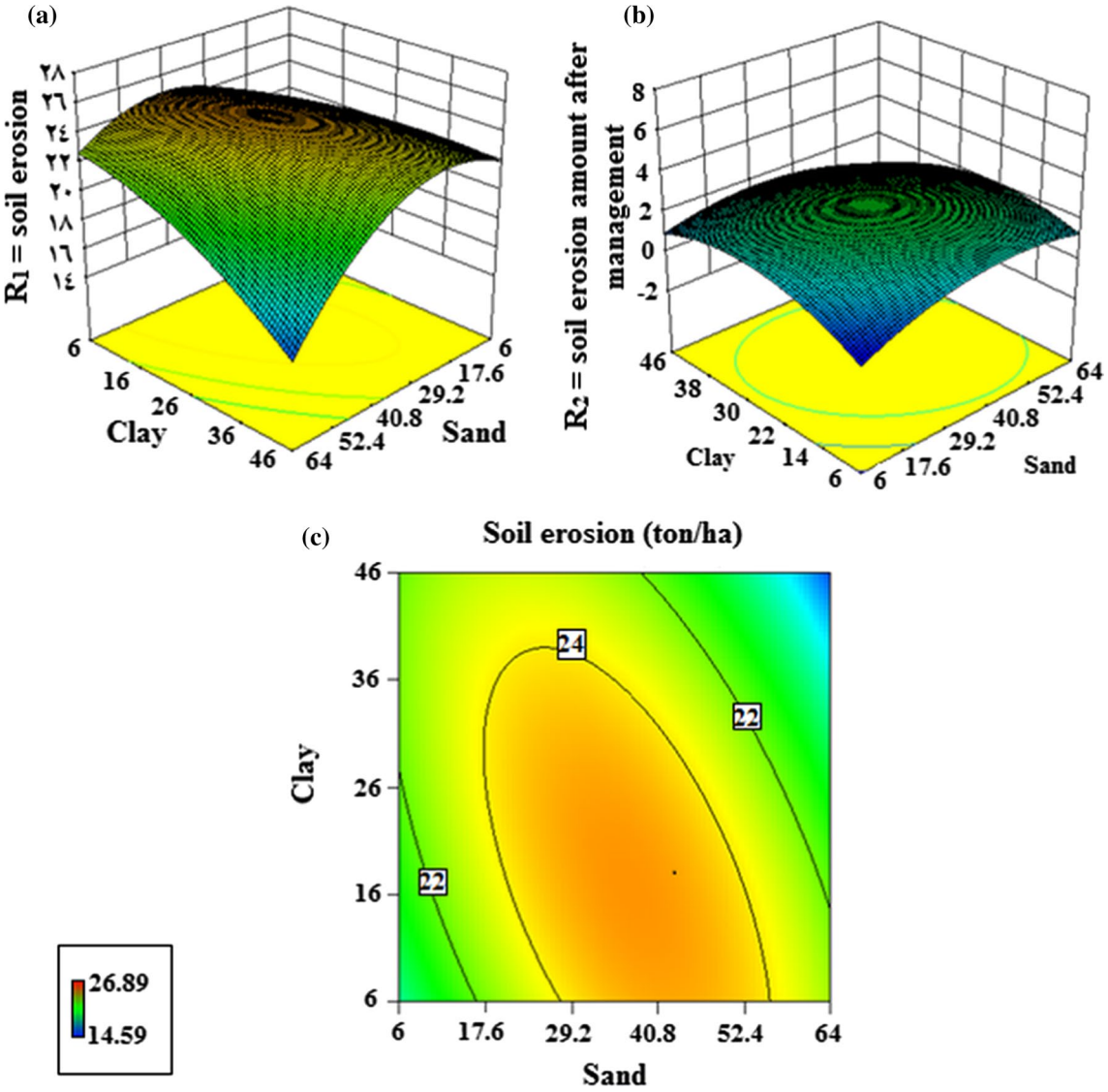

Fig. 3 The 3D diagram of clay and sand effects on the soil erosion. **a** Before application of management scenarios and **b** after application of management scenarios. The contour plot of clay and sand content (**c**)

Also, investigation of interactive factors presents a real situation of soil erosion occurrence in the watershed.

Results of management scenarios applications on soil erosion outcomes illustrated the significant effects of management strategies on soil erosion controlling and diminishing to 1.7–3 ton/ha (Fig. 4b). Actually, this mitigation of soil erosion (at the maximum level, 3 ton/ha) is significantly effective on different parts of conservational plan and reduces the costs of soil preserving. This result confirms the meaningful effects of land use and the type of management operations on soil erosion occurrence.

Interactive effects of clay and theta *r* on soil erosion using RSM

The relation between clay and residual moisture (theta *r*), which is associated with clay content increasing and the theta *r* decreasing, is shown (Fig. 5a). As Fig. 5a shows, by reducing theta *r* and clay content, the soil erosion was at the maximum level (equal to 25.7 ton/ha), whereas by increasing clay content the soil erosion was decreased and illustrated the minimum level (equal to 21.7 ton/ha). The clay particles have an essential role in soil aggregation processes and meaningfully are effective on aggregate stability; therefore, with changing the soil clay content, the magnitude of soil erosion was varied (Arthur et al. 2019). The theta *r* as

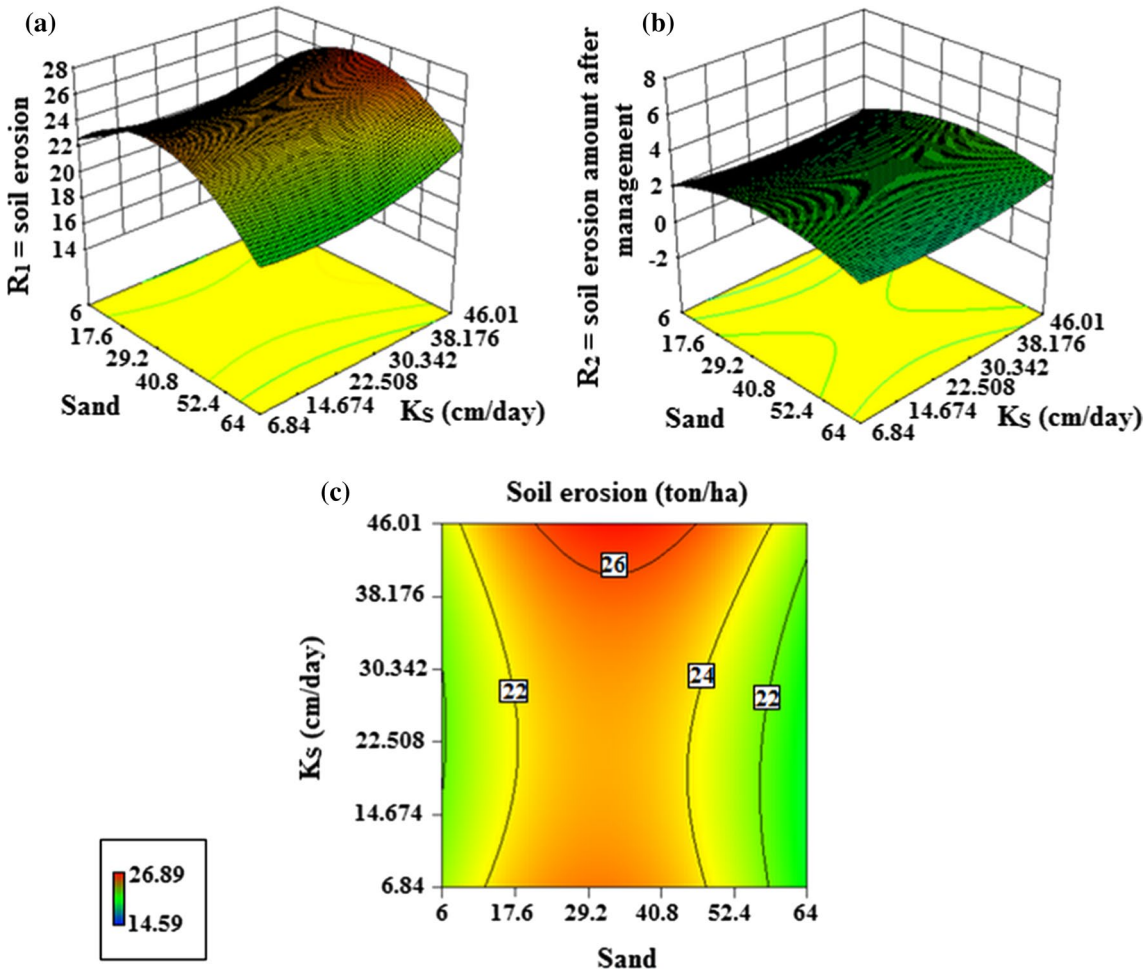

Fig. 4 The 3D diagram of sand content and saturated hydraulic conductivity (Ks) on the soil erosion. **a** Before application of management scenarios and **b** after application of management scenarios. The contour plot of sand content and saturated hydraulic conductivity (**c**)

hydraulic parameter depends on soil porosity, and the heavy textured soils have higher theta *r* values. Our results show that the theta *r* is equal to 0.03393 for silty soils (Fig. 5a) and regarding the structural properties of silt particles, the existence of silt particles in the soil enhanced the soil erosion potential. Also, the interaction between sand particles and theta *r* is same as the interaction between clay particles and theta *r*, because both of them can control the soil erosion occurrence (Wee and Yap 2019). Besides, sand particles reduced the soil erosion by increasing permeability and saturated hydraulic conductivity (Ks) in the critical soils, therefore reduce the runoff potential. Based on the modeling results, the critical area was recognized; then for those areas, the specific management scenarios were defined.

Regarding the effectiveness of those management strategies (R_2 in the RSM), the soil erosion was decreased to 1.6–3.5 ton/ha (Fig. 5b). This significant decreasing in soil erosion confirmed the positive feedbacks of appropriate management scenarios to reduced soil erosion and the off-site effects of erosion. Dybkjær et al. (2012) showed the significant effects of plant cover properties that consist of density, length and width on soil erosion controlling; therefore, the plant operations in the form of management strategies are effective on soil erosional behaviors. Application of RSM technique with responses (mainly R_2) clearly showed the positive impacts of clay particles and management scenarios on soil erosion controlling in the watershed (Fig. 5b). Soil aggregation mainly depends on clay content, and beside the soil clay content, land use (the applied management scenarios) significantly determine the soil status against erosive forces.

Interactive effect of clay and theta *s* on soil erosion using RSM

The interaction effects of soil clay content and saturation moisture (theta *s*) are shown (Fig. 6a). As Fig. 6a illustrates, the minimum level of soil erosion was at the maximum level of clay content and the minimum amount

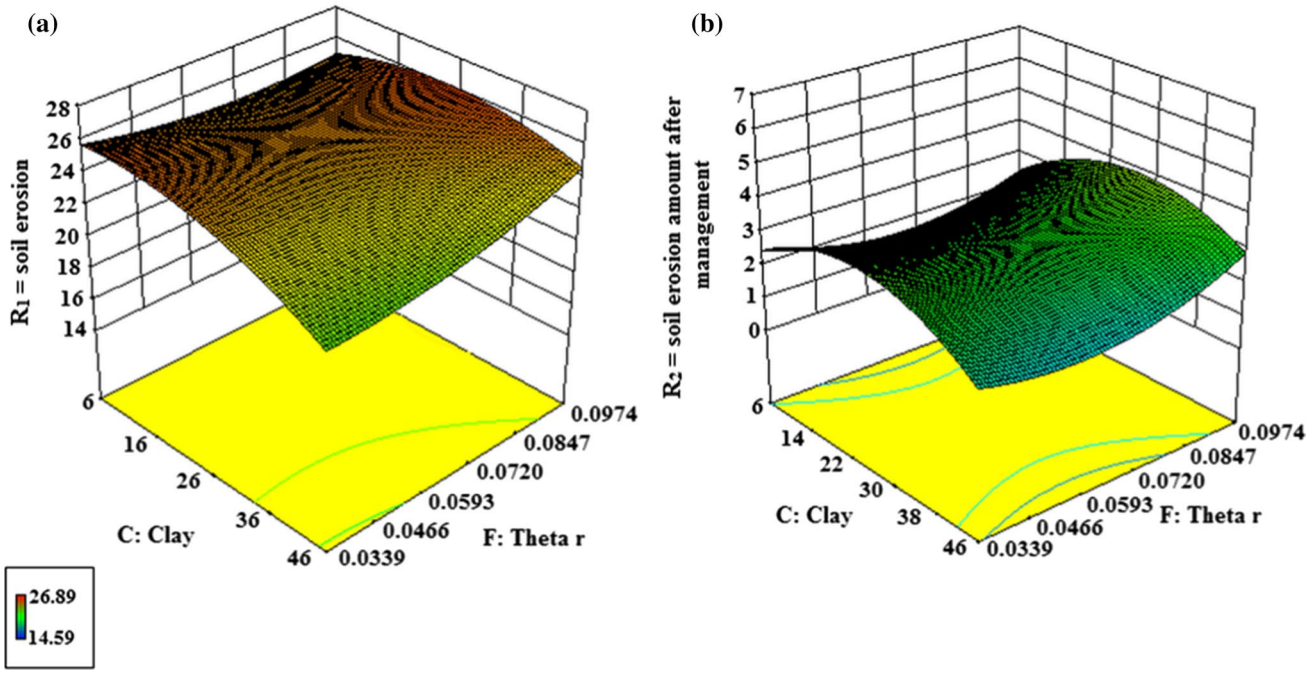

Fig. 5 The 3D diagram of clay content and moisture residual (theta *r*) on the soil erosion. **a** Before application of management scenarios and **b** after application of management scenarios

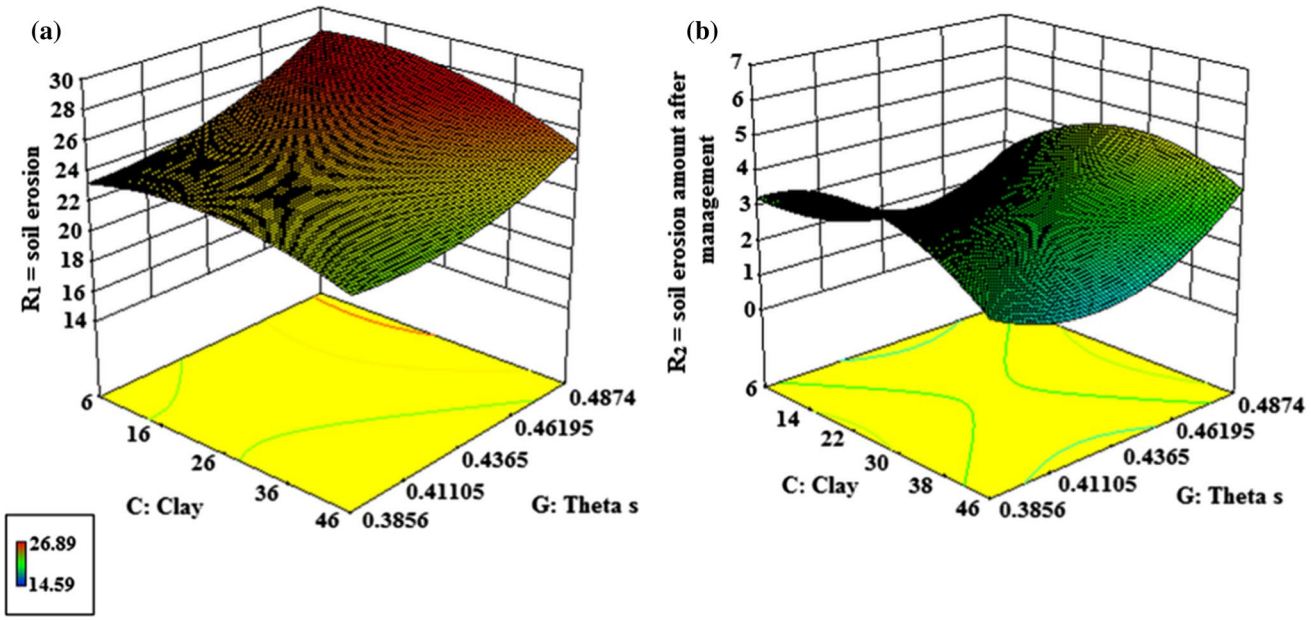

Fig. 6 The 3D diagram of clay and saturation moisture (theta *s*) on the soil erosion. **a** Before application of management scenarios and **b** after application of management scenarios

of theta *s*. As mentioned in other sections of the paper, clay particles are capable of creating and increasing the binding in the soil matrix; therefore by increasing the clay content individually, the soil erosion was decreased (Chen et al. 2014). Our results showed that the theta *s* was equal to 0.38, which means the soil texture could be sandy clay and clay, because theta *s* is an index of soil texture therefore could represent the soil hydrological

Table 5 The ANOVA result of quadratic model for responses (R_1 and R_2)

Response	R_1	R_2	Response	R_1	R_2
SDEV	0.54	0.26	*R*-square	0.9992	0.9988
Mean	20.76	1.48	C.V. %	2.59	17.52

Table 6 The range of input parameters and responses for optimization using RSM

Parameters	Unit	Goal	Lower limit	Upper limit	Importance
A[a]: Sand	%	Is in range	6.0000	64.0000	***[b]
B: Silt	%	Minimize	14.0000	76.0000	*****[b]
C: Clay	%	Is in range	6.0000	46.0000	***
D: SP	%	Is in range	31.6000	68.1000	***
E: Stone	%	Is in range	0.0900	5.2000	***
F: Theta *r*	–	Is in range	0.0339	0.0974	***
G: Theta *s*	–	Is in range	0.3856	0.4874	***
H: Alpha	–	Is in range	0.0052	0.0291	***
J: *n*	–	Is in range	1.2767	1.6799	***
K: Ks	cm/day	Maximize	6.8400	46.0100	****
R_1	ton/ha	Minimize	14.5900	26.8900	*****[b]
R_2	ton/ha	Minimize	0.0900	6.0100	*****

[a]The codes of independent variables

[b]The importance values

group. These results confirmed the relation and interaction effects of clay content and the hydraulic properties. Application of RSM technique in the form of R_2 (Fig. 6b), to evaluate the interaction effects of clay content theta *s* and the management strategies, illustrated the positive effects of management scenarios to reduced soil erosion. Generally, the application of convenient and adaptive management programs in the watershed plays an effective role to diminish soil erosion and deposition. This is a milestone of RSM that based on response 2 (R_2) clearly presents the effectiveness of convenient management operations and is applicable for selecting the best management practice in the watershed. Generally, interactive effects of soil texture components, hydraulic characteristics and land use are effective on soil erosion occurrence (Table 5).

Table 7 The optimal values of input parameters and responses

Parameters	Unit	Goal	Optimum values
A: Sand	%	Is in range	60.241
B: Silt	%	Minimize	14.000
C: Clay	%	Is in range	41.025
D: SP	%	Is in range	58.729
E: Stone	%	Is in range	3.830
F: Theta *r*	–	Is in range	0.090
J: Theta *s*	–	Is in range	0.457
H: Alpha	–	Is in range	0.014
J: n	–	Is in range	1.300
K: Ks	cm/day	Maximize	46.010
R_1	ton/ha	Minimize	11.537
R_2	ton/ha	Minimize	−2.253
Desirability	–	–	1

Optimization of effective factors on erosion using RSM

The design factors, model responses and optimized values are shown (Tables 6, 7). In the optimization phase, the purpose is finding the optimal value of the independent and dependent parameters shown in Table 7. In the present study, the desirability function was used for the optimization (Ardebili et al. 2019). All parameters were weighted equally 1:1 with an importance of 3 for each of them other than silt and K_S parameters that were set in 4. Also, the importance of dependent variables was 5. The bar graph is used to display desirability of the results and is shown as being a variable from to 1 denoting the vicinity of the output. The optimal solution for the problem is achieved with the following design parameters, and the entire results of the model are close to maximum anticipation set for the model (Fig. 7). Finally, the optimal blend was selected based on the result of the desirability function that so equals 1. This technique shows that by defining the K_S parameter in the maximum of goal, silt and dependent variables in the minimum of goal, the R_1 value is 11.54 ton/ha and R_2 is equal −2.25 ton/ha. Thus, the bar graph shows how each design factor is optimally set to get requirements, and total desirability equal 1 is excellent attainment (Fig. 8) (Pour et al. 2018). Therefore, using the RSM technique for selected parameters and the real situation in the studied watershed, the statistical parameters were obtained to apply the best one in the watershed.

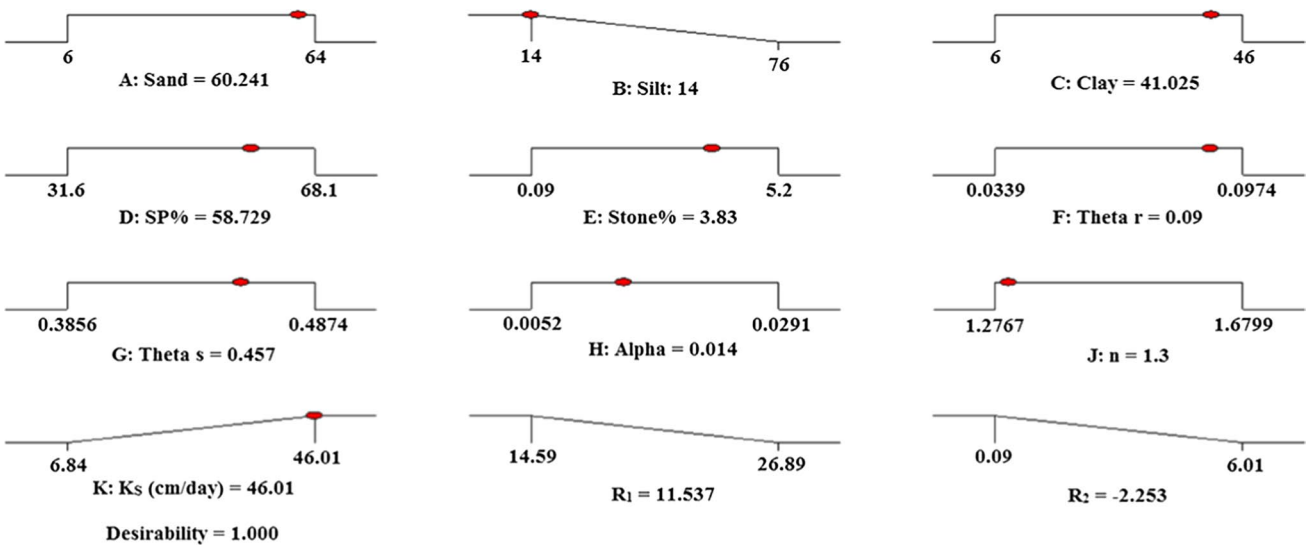

Fig. 7 The ramp graph of optimization using RSM technique

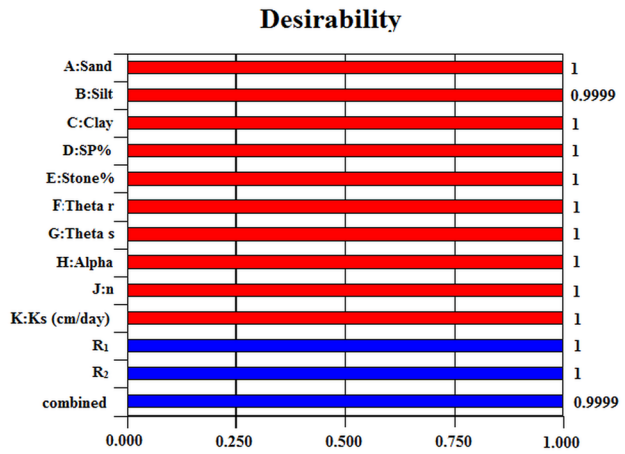

Fig. 8 The bar graph of desirability

Conclusion

RSM as a powerful methodology has high potential and optimizes modeling that can gain in more significant and comprehensive outcomes. Today, using of response surface methodology in optimization processes and analytical methods is expanding because of its benefits as one-variable-a-time and providing large amounts of information from a small number of experiments. Presentation of several optimization scenarios could be ideal for future studies to fully to establish the process of optimization in different and diverse scopes which could result in a better understanding of the process and applicability of the optimization. The purpose of this study was to optimize the physical and hydraulic properties of soil, providing the best management practices according to optimization results. The results showed that changes in physical and hydraulic parameters of soil have a significant effect on soil erosion. Also, the effect of the physical/hydraulic parameters on response variables was discussed using ANOVA results of suggested models. According to ANOVA results, it was found that all of the suggested models were significant at 1% level and the *p* value of model is equal to 0.0001. The optimized values of different physical parameters were 60.241 for sand, 14 for silt, 41.025 for clay, 58.729% for SP and 3.83% for stone. A theta *r* of 0.09, theta *s* of 0.457, alpha of 0.014, *n* of 1.3 and Ks of 46.01 were found to be optimal values. The results of this study indicated that at optimal studied parameters the values of the soil erosion before and after management scenarios were found to be 11.537 and − 2.253, respectively. Results show that both physical and hydraulic parameters have significant effects at the 1% level on the soil erosion. The obtained results could assist policy-makers with decisions aimed at minimizing soil erosion in this watershed.

References

Anache JA, Flanagan DC, Srivastava A, Wendland EC (2018) Land use and climate change impacts on runoff and soil erosion at the hillslope scale in the Brazilian Cerrado. Sci Total Environ 622:140–151

Ardebili SMS, Solmaz H, Mostafaei M (2019) Optimization of fuel oil–Gasoline blend ratio to enhance the performance and reduce emissions. Appl Therm Eng 148:1334–1345

Argent RM, Sojda RS, Giupponi C, McIntosh B, Voinov AA, Maier HR (2016) Best practices for conceptual modelling in environmental planning and management. Environ Model Softw 80:113–121

Arnold JG, Youssef MA, Yen H, White MJ, Sheshukov AY, Sadeghi AM, Haney EB (2015) Hydrological processes and model representation: impact of soft data on calibration. Trans ASABE 58(6):1637–1660

Arthur E, Tuller M, Norgaard T, Moldrup P, de Jonge LW (2019) Improved estimation of clay content from water content for soils rich in smectite and kaolinite. Geoderma 350:40–45

Barman B, Kumar B, Sarma AK (2019) Impact of sand mining on alluvial channel flow characteristics. Ecol Eng 135:36–44

Batista PV, Davies J, Silva ML, Quinton JN (2019) On the evaluation of soil erosion models: Are we doing enough? Earth Sci Rev 102898

Bezerra MA, Santelli RE, Oliveira EP, Villar LS, Escaleira LA (2008) Response surface methodology (RSM) as a tool for optimization in analytical chemistry. Talanta 76(5):965–977

Boll J, Brooks ES, Crabtree B, Dun S, Steenhuis TS (2015) Variable source area hydrology modelling with the water erosion prediction project model. JAWRA J Am Water Resources Assoc 51(2):330–342

Brooks ES, Dobre M, Elliot WJ, Wu JQ, Boll J (2016) Watershed-scale evaluation of the Water Erosion Prediction Project (WEPP) model in the Lake Tahoe basin. J Hydrol 533:389–402

Chabbi A, Yallese MA, Meddour I, Nouioua M, Mabrouki T, Girardin F (2017) Predictive modelling and multi-response optimization of technological parameters in turning of Polyoxymethylene polymer (POM C) using RSM and desirability function. Measurement 95:99–115

Chandramohan T, Venkatesh B, Balchand AN (2015) Evaluation of three soil erosion models for small watersheds. Aquatic Procedia 4:1227–1234

Chen C, Ren T, Hu K, Li B, Wang Y (2014) Estimation of soil clay content using hygroscopic water content at an arbitrary humidity. Soil Sci Soc Am J 78(1):119–124

Corella JP, Benito G, Wilhelm B, Montoya E, Rull V, Vegas T, Valero-Garcés BL (2019) A millennium-long perspective of flood-related seasonal sediment yield in Mediterranean watersheds. Glob Planet Change 177:127–140

De Oliveira Faber M, Ferreira-Leitão VS (2016) Optimization of biohydrogen yield produced by bacterial consortia using residual glycerin from biodiesel production. Biores Technol 219:365–370

Dinarvand M, Rezaee M, Foroughi M (2017) Optimizing culture conditions for the production of intra and extracellular inulinase and invertase from Aspergillus Niger ATCC 20611 by response surface methodology (RSM). Braz J Microbiol 48(3):427–441

Diodato N, Gericke A, Bellocchi G (2012) Modelling the inter-annual variability of sediment yields: a case study for the upper Lech River. Catena 97:12–19

Dybkjær JB, Baattrup-Pedersen A, Kronvang B, Thodsen H (2012) Diversity and distribution of riparian plant communities in relation to stream size and eutrophication. J Environ Qual 41(2):348–354

Feng H, Kurkalova LA, Kling CL, Gassman PW (2006) Environmental conservation in agriculture: land retirement vs. changing practices on working land. J Environ Econ Manag 52(2):600–614

Flanagan DC, Nearing MA (1995) USDA-Water Erosion Prediction Project: Hillslope profile and watershed model documentation, vol 10, pp 1603–1612. NSERL report

Flanagan DC, Frankenberger JR, Cochrane TA, Renschler CS, Elliot WJ (2013) Geospatial application of the water erosion prediction project (WEPP) model. Trans ASABE 56(2):591–601

Gao Y, Xu J, Luo X, Zhu J, Nie L (2016) Experiment research on mix design and early mechanical performance of alkali-activated slag using response surface methodology (RSM). Ceram Int 42(10):11666–11673

Giannecchini R (2006) Relationship between rainfall and shallow landslides in the southern Apuan Alps (Italy). Nat Hazards Earth Syst Sci 6(3):357–364

IPBES (2018) In: Scholes R, Montanarella L, Brainich A, Barger N, ten Brink B, Cantele M, Erasmus B, Fisher J, Gardner T, Holland TG, Kohler F, Kotiaho JS, Von Maltitz G, Nangendo G, Pandit R, Parrotta J, Potts MD, Prince S, Sankaran M, Willemen L (eds) Summary for policymakers of the assessment report on land degradation and restoration of the Intergovernmental Science Policy Platform on Biodiversity and Ecosystem Services. IPBES Secretariat, Bonn

Jarzyna JA, Puskarczyk E, Motyka J (2019) Estimating porosity and hydraulic conductivity for hydrogeology on the basis of reservoir and elastic petrophysical parameters. J Appl Geophys 167:11–18

Johnson CW, Gebhardt KA (1982) Predicting sediment yields from sagebrush rangelands [Pacific Southwest Inter-Agency Committee prediction procedure, southwest Idaho]. Agric Rev Manuals

Karimifard S, Moghaddam MRA (2018) Application of response surface methodology in physicochemical removal of dyes from wastewater: a critical review. Sci Total Environ 640:772–797

Keshtegar B, Allawi MF, Afan HA, El-Shafie A (2016) Optimized river stream-flow forecasting model utilizing high-order response surface method. Water Resour Manag 30(11):3899–3914

Kinnell PIA, Wang J, Zheng F (2018) Comparison of the abilities of WEPP and the USLE-M to predict event soil loss on steep loessal slopes in China. Catena 171:99–106

Kirkby MJ, Irvine BJ, Jones RJ, Govers G, PESERA team (2008) The PESERA coarse scale erosion model for Europe. I.–Model rationale and implementation. Eur J Soil Sci 59(6):1293–1306

Kumar AK, Kalaiselvi B, Sujata K, Nair KM, Singh SK (2016) Characterization of red and lateritic soils formed under varied climates and their management. Clay Res 35(1):43–53

Kumar M, Singh G, Arya SK, Bhatti JS, Sharma P (2018) Artificial Neuro-Fuzzy Inference System (ANFIS) based validation of laccase production using RSM model. Biocatal Agric Biotechnol 14:235–240

Laflen JM, Flanagan DC (2013) The development of US soil erosion prediction and modeling. Int Soil Water Conserv Res 1(2):1–11

Long X, Cai L, Li W (2019) RSM-based assessment of pavement concrete mechanical properties under joint action of corrosion, fatigue, and fiber content. Constr Build Mater 197:406–420

Mangalassery S, Kalaivanan D, Philip PS (2019) Effect of inorganic fertilizers and organic amendments on soil aggregation and biochemical characteristics in a weathered tropical soil. Soil Tillage Res 187:144–151

Meliho M, Nouira A, Benmansour M, Boulmane M, Khattabi A, Mhammdi N, Benkdad A (2019) Assessment of soil erosion rates in a Mediterranean cultivated and uncultivated soils using fallout 137Cs. J Environ Radioact 208:106021

Mhazo N, Chivenge P, Chaplot V (2016) Tillage impact on soil erosion by water: discrepancies due to climate and soil characteristics. Agric Ecosyst Environ 230:231–241

Mondal A, Khare D, Kundu S, Mukherjee S, Mukhopadhyay A, Mondal S (2017) Uncertainty of soil erosion modeling using open source high resolution and aggregated DEMs. Geosci Front 8(3):425–436

Montgomery DC, Anderson-Cook CM (2009) Response surface methodology: process and product optimization using designed experiments. Wiley, New York

Muthusamy S, Manickam LP, Murugesan V, Muthukumaran C, Pugazhendhi A (2019) Pectin extraction from Helianthus annuus (sunflower) heads using RSM and ANN modelling by a genetic algorithm approach. Int J Biol Macromol 124:750–758

Najafi G, Ghobadian B, Yusaf T, Ardebili SMS, Mamat R (2015) Optimization of performance and exhaust emission parameters of a SI (spark ignition) engine with gasoline-ethanol blended fuels using response surface methodology. Energy 90:1815–1829

Nasiri A, Shirokova V, Zareie S, Shojaei S (2017) Assessment of the statue and intensity of water erosion in the river basin Delichai

(Iranian territory) using GIS model. In: International multidisciplinary scientific Geoconference: SGEM: surveying geology and mining ecology management, vol 17, pp 89–96
Park S, Oh C, Jeon S, Jung H, Choi C (2011) Soil erosion risk in Korean watersheds, assessed using the revised universal soil loss equation. J Hydrol 399(3–4):263–273
Pattanaik A, Rayasam V (2018) Analysis of reverse cationic iron ore fines flotation using RSM-D-optimal design–An approach towards sustainability. Adv Powder Technol 29(12):3404–3414
Podder MS, Majumder CB (2015) Modeling of optimum conditions for bioaccumulation of As (III) and As (V) by response surface methodology (RSM). J Environ Chem Eng 3(3):1986–2001
Pour AH, Ardebili SMS, Sheikhdavoodi MJ (2018) Multi-objective optimization of diesel engine performance and emissions fueled with diesel-biodiesel-fusel oil blends using response surface method. Environ Sci Pollut Res 25(35):35429–35439
Qian F, Cheng D, Liu J (2014) Analysis of the water and soil erosion and infiltration characteristic in Ziquejie Terrace. IERI Procedia 9:13–19
Rao MS, Venkaiah N (2015) Parametric optimization in machining of Nimonic-263 alloy using RSM and particle swarm optimization. Procedia Mater Sci 10:70–79
Schaap MG, Leij FJ (2000) Improved prediction of unsaturated hydraulic conductivity with the Mualem-van Genuchten model. Soil Sci Soc Am J 64(3):843–851
Schole RJ, Kanter DR, Musumba M, Wood SL, Palm C, Antle J, Balvanera P, Thornton P (2018) Evaluating agricultural trade-offs in the age of sustainable development. Agric Syst 163:73–88
Shaikh SM, Nasser MS, Hussein I, Benamor A, Onaizi SA, Qiblawey H (2017) Influence of polyelectrolytes and other polymer complexes on the flocculation and rheological behaviors of clay minerals: a comprehensive review. Sep Purif Technol 187:137–161
Sharma AK, Kaith BS, Tanwar V, Bhatia JK, Sharma N, Bajaj S, Panchal S (2019) RSM-CCD optimized sodium alginate/gelatin based ZnS-nanocomposite hydrogel for the effective removal of biebrich scarlet and crystal violet dyes. Int J Biol Macromol 129:214–226
Sherriff SC, Rowan JS, Fenton O, Jordan P (2018) Sediment fingerprinting as a tool to identify temporal and spatial variability of sediment sources and transport pathways in agricultural catchments. Agric Ecosyst Environ 267:188–200
Shojaei S, Ardakani MAH, Sodaiezadeh H (2019) Optimization of parameters affecting organic mulch test to control erosion. J Environ Manag 249:109414
Spagnoli G, Shimobe S (2019) A statistical reappraisal of the relationship between liquid limit and specific surface area, cation exchange capacity and activity of clays. J Rock Mech Geotech Eng 11:874–881
Tan YH, Abdullah MO, Nolasco-Hipolito C, Zauzi NSA (2017) Application of RSM and Taguchi methods for optimizing the transesterification of waste cooking oil catalyzed by a solid ostrich and chicken-eggshell derived CaO. Renew Energy 114:437–447
Thomas GW (1982) Exchangeable cations. In: Page AL (ed) Methods of soil analysis, Part 2, Chemical and microbiological properties, 2nd edn. Agronomy, No. 9, Part 2. American Society of Agronomy, Soil Science Society of America, Madison, WL, pp 159–165
Tiwari AK, Risse LM, Nearing MA (2000) Evaluation of WEPP and its comparison with USLE and RUSLE. Trans ASAE 43(5):1129
Wee SK, Yap YJ (2019) CFD study of sand erosion in pipeline. J Petrol Sci Eng 176:269–278
Xiong M, Sun R, Chen L (2019) A global comparison of soil erosion associated with land use and climate type. Geoderma 343:31–39
Xu L, Xu X, Meng X (2013) Risk assessment of soil erosion in different rainfall scenarios by RUSLE model coupled with Information Diffusion Model: a case study of Bohai Rim, China. Catena 100:74–82

Acta Geophysica (2020) 68:519–535
https://doi.org/10.1007/s11600-020-00407-2

RESEARCH ARTICLE - HYDROLOGY

Multifractal description of streamflow and suspended sediment concentration data from Indian river basins

S. Adarsh[1] · Drisya S. Dharan[1] · A. R. Nandhu[1] · B. Anand Vishnu[1] · Vysakh K. Mohan[1] · M. Wątorek[2,3]

Received: 25 August 2019 / Accepted: 31 January 2020 / Published online: 11 February 2020

Abstract

This study investigated the multifractality of streamflow data of 192 stations located in 13 river basins in India using the multifractal detrended fluctuation analysis (MF-DFA). The streamflow datasets of different river basins displayed multifractality and long-term persistence with a mean exponent of 0.585. The streamflow records of Krishna basin displayed least persistence and that of Godavari basin displayed strongest multifractality and complexity. Subsequently, the streamflow-sediment links of five major river basins were evaluated using the novel multifractal cross-correlation analysis (MFCCA) method of cross-correlation studies. The results showed that the joint persistence of streamflow and total suspended sediments (TSS) is approximately the mean of the persistence of individual series. The streamflow displayed higher persistence than TSS in 60% of the stations while in majority of stations of Godavari basin the trend was opposite. The annual cross-correlation is higher than seasonal cross-correlation in majority of stations but at these time scales strength of their association differs with river basin.

Keywords Streamflow · Multifractal · Sediment · Persistence · Correlation

Introduction

The estimation of local fluctuations and long-term dependency of hydrologic time series is a long standing problem in hydrology. Hurst exponent (Hurst 1951) is perhaps one of the most debated properties of hydro-meteorological datasets, which is mainly used to elucidate the persistence of the time series. Mandelbrot (1982) paved the way of existence of fractal geometry of geophysical fields. Over the years, a large number of methods evolved for estimation of dependency structure and fractal behaviour of hydrologic time series. It includes the rescaled range analysis, double trace moments (Tessier et al. 1996), Fourier spectral analysis (Hurst et al. 1965; Pandey et al. 1998), extended self similarity principles (Dahlstedt and Jensen 2005), wavelet transform modula maxima (WTMM) (Muzy et al. 1991), arbitrary order Hilbert spectral analysis (AOHSA) (Huang et al. 2011; Adarsh et al. 2018a). Peng et al. (1994) proposed an efficient method namely detrended fluctuation analysis (DFA) to perform the fractal analysis based on a detrending procedure. Kantelhardt et al. (2002) proposed the multifractal extension of DFA procedure now popularly known as multifractal DFA (MF-DFA). Multifractal is the appropriate framework for scaling fields of time series and thus can provide the natural framework for analysing and modelling various geophysical processes. For hydrological time series, multifractal description can be regarded as a 'fingerprint' and it serves as an efficient nontrivial test bed for the performance of state-of-the-art precipitation-runoff models (Kantelhardt et al. 2006). Therefore, DFA or MF-DFA was successfully applied for characterization of different hydro-meteorological time series (Yuan et al. 2010; Yu et al. 2014; Baranowski et al. 2015; Krzyszczak et al. 2019; Adarsh et al. 2019).

Kantelhardt et al. (2003) applied the MF-DFA procedure for runoff and precipitation from different parts of globe and compared the results with WTMM method. Koscielny-Bunde et al. (2003) applied DFA, MF-DFA and wavelet

✉ S. Adarsh
adarsh_lce@yahoo.co.in; adarsh1982@tkmce.ac.in

[1] TKM College of Engineering, Kollam, Kerala, India

[2] Complex Systems Theory Department, Institute of Nuclear Physics, Polish Academy of Sciences, ul. Radzikowskiego 152, 31-342 Kraków, Poland

[3] Faculty of Computer Science and Telecommunications, Cracow University of Technology, ul. Warszawska 24, 31–155 Kraków, Poland

analysis to discharge records from 41 hydrological stations around the globe for investigating their temporal correlations and multifractal properties. The study found that the daily runoff records were long-term correlated above some crossover time in the order of weeks, and they were characterized by a correlation function that follow a power-law behaviour with exponents varying between 0.1 to 0.9. Kantelhardt et al. (2006) studied the multifractal behaviour of 99 long-term daily precipitation records and 42 long-term daily runoff records from different parts of the world. They found that the precipitation records generally show short-term persistence while runoff records showed long-term persistence with a mean exponent of 0.73. Zhang et al. (2008) applied the MF-DFA procedure to analyse the multifractal characteristics of streamflow from four gauging stations in Yangtze river in China. The study detected the non-stationarity of different time series and analysed the differences in multifractality among the records from stations at upper and lower Yangtze basin. Zhang et al. (2009) applied MF-DFA method to study the scaling behaviours of the long daily streamflow series of four hydrological stations in the mainstream of East river in China. The results indicated that streamflow series of the East river basin were characterized by anti-persistence and showed similar scaling behaviour at different shorter time scales. Further their study applied the technique to investigate the effect of water storage structures on streamflow records and found that the streamflow magnitude was mainly influenced by the precipitation magnitude while the fluctuations of the streamflow records were affected by the human interventions like construction of control structures. Labat et al. (2011) applied DFA to investigate the multifractality of streamflow series of two karstic watersheds in the southern France, suggesting that the correlation properties exist in small scales and anti-correlated properties exist in large scales. Hirpa et al. (2010) analysed and compared the long-range correlations of river flow fluctuations from 14 stations in the Flint river basin in the state of Georgia in the southeastern USA. The study investigated the effect of basin area on the multifractal characteristics of streamflow time series at different locations and it was found that in general, higher the basin area lower will be the degree of multifractality. Rego et al. (2013) applied the MF-DFA to analyse the multifractality of water level records of 12 principal Brazilian rivers, and the results indicated that the presence of multifractality and long-range correlations for all the stations after eliminating the climatic periodicity. Li et al. (2015) applied the MF-DFA method to the streamflow time series of four stations of Yellow river in China. They detected the crossover point at annual scale in all the time series. After removing the trend by the seasonal trend decomposition, they found that all decomposed series were characterized by the long-term persistence. Also the study noted that the multifractality of streamflow series was because of the correlation properties as well as the probability density function. Tan and Gan (2017) used MF-DFA for determination of multifractal behaviour of 145 streamflow and 100 daily precipitation series of Canada. They reported that all precipitation time series showed long-term persistence (LTP) at both small and large time scales, while streamflow time series generally showed LTP at large time scales. Recently, Adarsh et al. (2018a, b) performed the multifractal analysis of streamflow records of four stations of Brahmani river basin and one station of Kallada river basin in India.

Even though many studies performed multifractal characterization of streamflow employing the MF-DFA procedure worldwide, according to the author's knowledge, no comprehensive study has been reported considering streamflow data from Indian rivers and such an analysis on sediment concentration data is really scarce in the literature. The specific objectives of this paper include: (1) multifractal characterization of streamflow data of different rivers in India; (2) investigate the streamflow–suspended sediment link of five major basins in India using multifractal cross-correlation analysis (MFCCA). The next section presents the theoretical details on MF-DFA and MFCCA. The details of data used in the study are presented in the section thereafter. Subsequently, results of MF-DFA analysis of streamflow and MFCCA on streamflow-total suspended sediment (TSS) links of five major basins are presented along with relevant discussions. Then the major conclusions drawn from the study are presented.

Materials and methods

This section presents the theoretical details on the multifractal detrended fluctuation analysis (MF-DFA) and multifractal detrended cross-correlation analysis (MFCCA) used in this study.

Multifractal detrended fluctuation analysis (MF-DFA)

The multifractal detrended fluctuation analysis (MF-DFA) is a popular tool used for the scaling characterization of non-stationary time series. The different steps involved in MF-DFA computational procedure can be described as follows:

Consider a time series X (x_1, x_2... x_N), where N is the length of the time series. The accumulated deviation of the series (known as 'profile') is calculated as:

$$X(i) = \sum_{k=1}^{i} \left[x_k - \bar{x}\right] \tag{1}$$

where $i = 1, 2, \ldots, N$, $k = 1, 2 \ldots, N$, $\bar{x}$ is the mean of the series x_k.

Divide the profile $X(i)$ into $N_s = \text{int}(N/s)$ non-overlapping segments of length, here s is the segment sample size (so called scale) chosen for the analysis and int (N/s) is the integer part of (N/s). As N need not be a multiple of s always, there is a chance of omission of small portion of the time series at the end, and to include such segments, the same procedure is repeated starting from the opposite end and a total of $2N_s$ segments are considered in the analysis.

Calculate the local trend for each of the $2N_s$ segments by a least squares fit of the series as:

$$F^2(s,\nu) = \frac{1}{s}\sum_{i=1}^{s}\left\{X[(\upsilon-1)s+i] - x_\nu(i)\right\}^2 \text{ for } \upsilon = 1,2,\ldots,N_s \tag{2}$$

And

$$F^2(s,\nu) = \frac{1}{s}\sum_{i=1}^{s}\left\{X\left[N-(\upsilon-N_s)s+i\right] - x_\nu(i)\right\}^2$$
$$\text{for } \upsilon = N_s+1,\ldots,2N_s \tag{3}$$

Here $x_\upsilon(i)$ is the fitting polynomial in segment υ. Linear, quadratic, cubic etc., different types of fitting can be made and accordingly DFA procedure is named as DFA1, DFA2,…..DFAm etc.

Compute the qth order fluctuation function by averaging:

$$F_q(s) = \left\{\frac{1}{2N}\sum_{\nu=1}^{2N_s}\left[F^2(s,\nu)\right]^{q/2}\right\}^{1/q} \tag{4}$$

Here the index variable q can take any real value except zero and the zeroth order fluctuation function is computed by following a logarithmic averaging procedure:

$$F_0(s) = \exp\left\{\frac{1}{4N}\sum_{\nu=1}^{2N_s}\ln\left[F^2(s,\nu)\right]\right\} \tag{5}$$

Analyse the scaling behaviour of the fluctuation functions developing the log–log plots of $F_q(s)$ versus s for each values of q. If the time series is long-range power-law correlated, $F_q(s)$ increases as:

$F_q(s) \sim s^{h\,(q)}$ and $h\,(q)$, the slope of the plot is referred as the generalized Hurst exponent (GHE).For stationary time series, $0 < h\,(q=2) < 1$, is identical to the classical Hurst exponent (Hurst 1951). For an uncorrelated series the value of Hurst exponent is 0.5. If the Hurst exponent falls between 0.5 and 1, it indicates the long-term persistence (long memory process) and if it falls between 0 and 0.5, it indicates a short-term persistence (short memory process). Long-term persistence implies a positive autocorrelation in the time series (i.e. the effect of an observation on future observations remain significant for a long period of time). For example an extreme event would have higher probability being followed by another extreme of same character (i.e. a flood followed by another flood). The selection of scale (s) or segment sample size, the type of polynomial chosen etc., are some of the key issues while applying the MF-DFA method. Generally sufficient segments are chosen between the bounds (minimum and maximum) scale range. Minimum scale can be chosen in such way that it is sufficiently larger than the polynomial order chosen to prevent error in computation of local fluctuations and maximum scale below 1/10 of the sample size. Also the polynomial order can be chosen 1–3 probably sufficient to avoid overfitting problems within small segment sizes (Ihlen 2012; Oświęcimka et al. 2013).

From the GHE, several other types of scaling exponents can also be derived, which is helpful for the multifractal characterization of the time series. The q-order mass exponent $((\tau(q))$ and singularity exponent (α) are derived as follows:

$$\tau(q) = qh(q) - 1 \tag{6}$$

$$\alpha = \frac{\mathrm{d}\tau(q)}{\mathrm{d}q} \tag{7}$$

And

$$f(\alpha) = q\alpha - \tau(q) \tag{8}$$

where $f(\alpha)$ provides the singularity spectrum. The dependency of $h(q)$ on q infer multifractality of the time series and the spread of GHE plot $\Delta h(q)$ refer the strength of multifractality (Grech 2016). If the variation of GHE plot is steeper the time series is more multifractal (higher degree of multifractality) and if it is flatter the series is less multifractal (lower degree of multifractality). The base width of the singularity spectrum (spread of singularity exponent, $\Delta\alpha$) also reflects the strength of the multifractality of the time series. The shape and extent of the singularity spectrum curve contain significant information about the distribution characteristics and the singularity content of the time series. A wider singularity spectrum indicates a higher degree of multifractality and a narrow width indicates lesser degree of multifractality. For a multifractal time series the shape of singularity spectrum will be an inverted parabola whose right- and left-hand wings correspond to negative and positive q, respectively. Asymmetry Index (A_α) is a useful parameter for multifractal analysis derived from the properties of the spectrum. It is obtained by the following relation (Drozdz and Oswiecimka 2015):

$$A_\alpha = \frac{\left(\Delta\alpha_L - \Delta\alpha_R\right)}{\left(\Delta\alpha_L + \Delta\alpha_R\right)} \tag{9}$$

where $\Delta\alpha_L = \alpha_0 - \alpha_{\min}$ and $\Delta\alpha_R = \alpha_{\max} - \alpha_0$ are, respectively, the width of left- and right-hand branches of the

multifractal spectrum curve; their values describe the distribution patterns of high and low fluctuations and α_0 is the singularity exponent for $q=0$. The value of A_α ranges from − 1 to 1. It quantifies the deviations of the multifractal spectrum curve. $A_\alpha>0$ suggests a left-hand deviation of the multifractal spectrum, likely to have resulted from some degree of local high fluctuations; $A_\alpha<0$ suggests a right-hand deviation with local low fluctuations, and $A_\alpha=0$ represents a symmetrical multifractal spectrum. The difference $\Delta f(\alpha)$ between maximum and minimum values of singularity provides an estimate of the spread in changes in fractal patterns. Since $\Delta f(\alpha)$ denotes the frequency ratio of the largest to the smallest fluctuations $\Delta f(\alpha)>0$ means that the largest fluctuations are more frequent than smallest fluctuations.

Multifractal cross-correlation analysis (MFCCA)

In order to determine the inter-relationships between different hydro-meteorological variables, different statistical approaches have been developed and simplest of which is the estimation of Pearson correlation coefficient. However, this coefficient is not robust and can be misleading if outliers are present, as in real-world data characterized by a high degree of nonlinearity and non-stationarity. The Pearson correlation may display the spurious correlations in the presence of trend in non-stationary time series. Podobnik and Stanley (2008) proposed a new method, detrended cross-correlation analysis (DCCA), to investigate power-law cross-correlations between two candidate non-stationarity time series in a multifractal framework. Podobnik et al. (2009a) found that the trends can severely affect the long-range correlations in the time series, leading to crossovers and other spurious deviations from power laws. To circumvent these issues, they proposed a novel statistical significance test for the quantitative analysis of power-law cross-correlations considering the both local and global detrending approaches. Podobnik et al. (2011) presented an analytical examination of the above test considering the Chinese, USA and German financial indices and proposed an improved variant of the statistical test to quantify the existence of cross-correlations between two power-law correlated time series. Some recent studies made detailed comparison on the person correlation and DCCA approach (Piao and Fu 2016). DCCA was extended to multifractal case and named as multifractal detrended cross-correlation analysis (MFDCCA) (Zhou 2008) and multifractal detrending moving average cross-correlation analysis (MFXDMA) (Jiang and Zhou 2011). Later on, Oświęcimka et al. (2014) propounded a more generalized version of cross-correlation analysis namely multifractal cross-correlation analysis (MFCCA) which can also incorporate the sign of fluctuation function to their generalized moments. DCCA and its variants have successfully been applied to financial, biomedical and meteorological time series (Podobnik et al. 2009a, b; Hajian and Movahed 2010; Shi 2014; Vassoler and Zebende 2012; Jiang et al. 2011; Wu et al. 2018; Dey and Mujumdar 2018; Wątorek et al. 2019).

The different steps involved in MFCCA computational procedure can be described as follows:

For two time series x_i and y_i ($i=1, 2, \ldots, N$); determine the profiles as two new series:

$$X(j)=\sum_{i=1}^{j}\left[x_i-\langle x\rangle\right] \tag{10}$$

and

$$Y(j)=\sum_{i=1}^{j}\left[y_i-\langle y\rangle\right] \tag{11}$$

where $i=1, 2, \ldots, N$; $\langle x\rangle$ and $\langle y\rangle$ are the mean of the two series.

Each series x_i and y_i are divided into N_s non-overlapping segments both in progressive and retrograde directions, to avoid any omission of time series data at the beginning or end of the series. For each $2N_s$ segments, local trend of both series x_j and y_j are computed by fitting polynomial of appropriate order (m). The subtraction of the fitted polynomial from the original segment gives the covariance:

$$f_{XY}^2(\upsilon,s)=\left\{\frac{1}{s}\sum_{k=i}^{s}\left[\left(X((\upsilon-1)+k)-p_{X,\upsilon}^{m}(k)\right)\times\left(Y((\upsilon-1)+k)-p_{Y,\upsilon}^{m}(k)\right)\right]\right\} \tag{12}$$

Calculate detrended covariance by summing over all overlapping all segments of length n:

$$F_{XY}^{q}(s)=\frac{1}{2N_s}\sum_{\upsilon=0}^{2N_s-1}\operatorname{sign}\left[f_{XY}^2(\upsilon,s)\right]\left|f_{XY}^2(\upsilon,s)\right|^{q/2} \tag{13}$$

$F_{XY}^{q}(s)$ behaves as a power-law function of s (the scaling behaviour), where s is the segmental sample size:

$$F_{XY}^{q}(s)\sim s^{\lambda(q)} \tag{14}$$

The cross-correlation exponent $\lambda(q)$ similar to the generalized Hurst exponent $h(q)$ in MF-DFA and it can be obtained by observing the slope of log–log plot of $F(s)$ versus s by ordinary least squares.

Determination of cross-correlation coefficient (ρ_{XY})

DCCA cross-correlation coefficient is defined as the ratio between the detrended covariance function F_{XY} and the

detrended variance functions F_X and F_Y (Zebende 2011; Kwapień et al. 2015)

$$\rho_{XY} = \frac{F_{XY}^{q}}{\sqrt{F_X^q F_Y^q}} \tag{15}$$

Theoretically the value of ρ_{XY} ranges between $-1 \le \rho_{XY} \le 1$. If the value range between ± 0.666 to ± 1 cross-correlation it can be considered as strong positive (or negative); ± 0.333 to ± 0.666 it is medium and ± 0 to ± 0.333 it is weak (Brito et al. 2018). The MFCCA analysis facilitate the estimation of scale dependent correlation between two candidate time series, which can provide better insight into the physical association between the variables. It is to be noted that in this study MFCCA is retrieved for the moment order $q = 2$.

Study area and data

In this study long-term daily streamflow data of 192 stations falling in 13 river basins in India are collected from Water Resources Information System (WRIS) India (www.india-wris.nrsc.gov.in) operated by the Central Water Commission (CWC) India, which one of the most reliable database pertaining to India. The map showing different major river basins is presented in Fig. 1. The data ranging from 1969 to 2016 are considered for the study. For brevity, the maximum and minimum data lengths of the basin along with the maximum and minimum drainage area of stations of different basins are provided in Table 1. As the total suspended sediment information is really scarce, the streamflow-sediment link is investigated in five major basins by considering the longest common period for which both the streamflow and sediment data are available.

Results and discussions

In this study, first daily streamflow data of different stations are analysed using the MF-DFA method by selecting moment order in the range − 4 to + 4 and minimum scale as 10, maximum as $N/2$, where N is the data length. Six different prominent multifractal properties such as Hurst exponent (H), spread of generalized Hurst exponent plot $\Delta h(q)$, spread of singularity parameter $\Delta\alpha$ (called as spectral width), Asymmetry index (A_α), $\Delta f(\alpha)$, singularity parameter for zero moment order (α_0) etc. are evaluated. The spatial distribution of the different multifractal parameters is shown in Fig. 2. Further, the non-parametric Kernel density estimator (KDE) is used to develop the probability density function (PDF) and cumulative distribution fuction (CDF) of all the six multifractal parameters, and the results are presented in Fig. 3.

From the results it is noted that most of the streamflow series displayed long-term persistence (71.3%) with a mean value of 0.585, which is less than the universal value of 0.73 reported by Kantelhardt et al. (2006). Similarly the high multifractal width and spread ($\Delta h(q)$) are noted in the database, which shows that there is a large variation in distribution of high and low fluctuations, indicating irregular and non-homogeneous distribution. This is quite obvious because of the high intermittent character of river flows in the basins considered in the study. It is to be noted that the database considered the stations located in the southern/peninsular part of India, where in most of the rivers the streamflow is intermittent in nature and comprising of continuous zero or very low discharge values. In the northern India, abundant alluvial and perennial rivers are present, but most of them are trans-boundary in character for which the data sharing is not flexible. From Fig. 2, it is also noted that river basins Periyar, Cauvery, Pennar, Vaippar, which are near to the southern coastal regions have high degree of multifractality. The Asymmetry index value is positive for most of stations (181 stations out of 192), which indicates left-hand deviations of the spectra with local high fluctuations.

From Fig. 3, it is noted that as expected the distribution of spectral width and spread (which convey the similar message on degree of multifractality) irrespective of their numerical values. The PDF of Hurst exponent shows a density concentration around 0.5–0.7, where Hurst exponent lies in this range for most of the stations (49%). A near symmetrical distribution is noted for the value of $\Delta f(\alpha)$ and the dominant density of α_0 is in the range of 0.8–1.2. Now, for a comparison of multifractal properties of streamflow of different basins, five major basins, namely Godavari, Krishna, Mahanadi, West flowing rivers (WFR) from Tadri to Kanyakumari (WFR T-K) and Cauvery are considered (for which datasets of minimum 10 stations are available). The PDFs and CDFs of different multifractal parameters are presented in Fig. 4.

From the PDFs and CDFs of streamflow data of river basins it is clear that the data of Krishna has least persistence (followed by Mahanadi) as compared with that of other basins. The highest degree of multifractality is noted for the streamflows of Godavari basin which is having over 400 major and minor dams and other regulation structures which control the streamflows. From Fig. 4, it is also noted that streamflows of Godavari basin has higher $\alpha_0$as compared with other basins, which infer the complexity of the series. From the plot of α0 it is noted that the streamflow of Krishna and WFR T-K has almost similar complexity which possess finer structure. In the WFR T-K basin, no major flow regulation structures are present and the drainage areas of different stations are similar in magnitude (varies between 238 and 5755 km^2 from Table 1). To get an insight into the effect of drainage area and data length on the multifractality

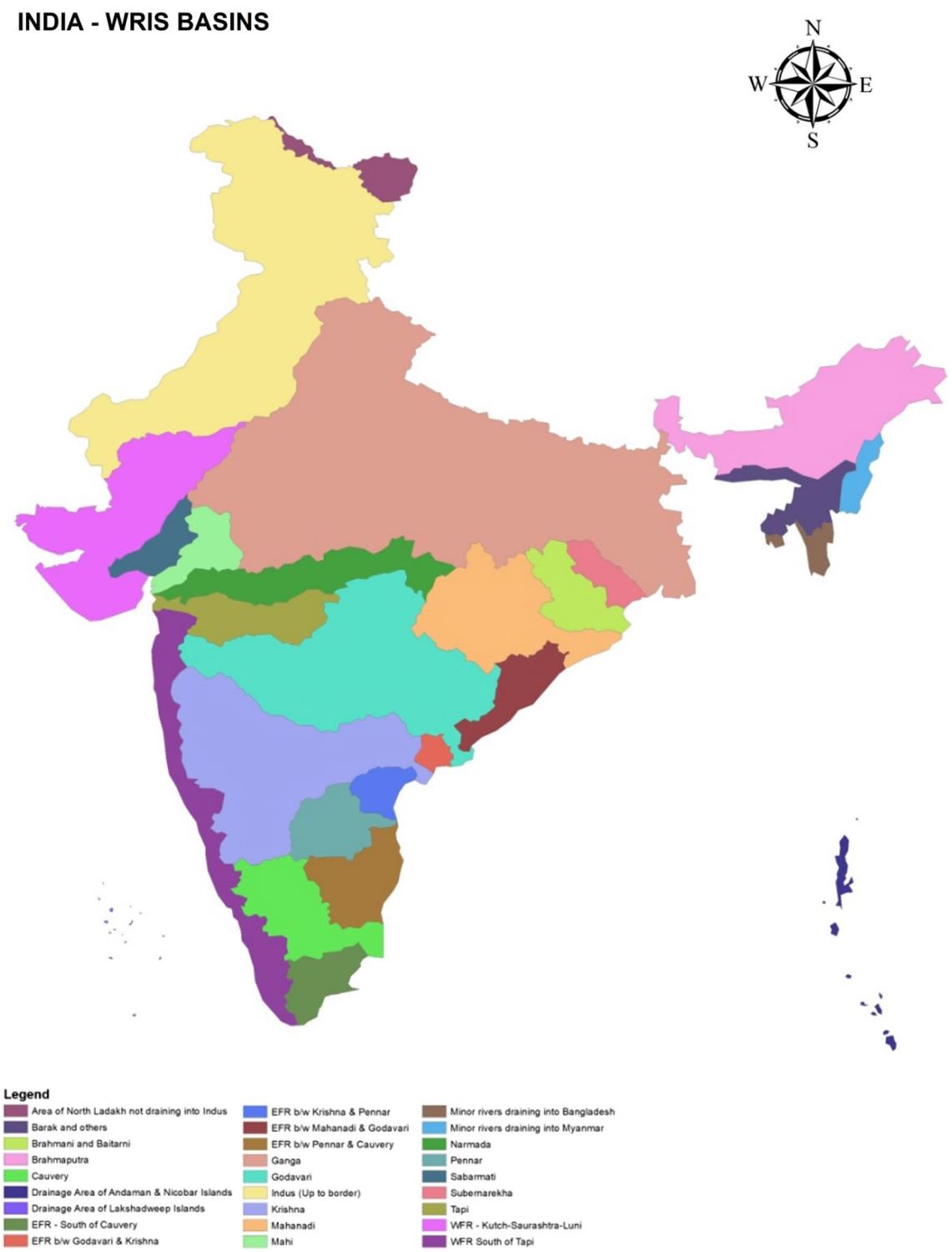

Fig. 1 Map showing river basins in India

and persistence, the plots of drainage area versus H, drainage area versus spectral width, data length versus H and data length versus spectral width are prepared and presented in Fig. 5.

It is evident from Fig. 5 and it is noted that most of the Hurst exponent values are centred around 0.55–0.65 and there is no major change in the value of the Hurst Exponent with drainage area. This evidently concludes that

Table 1 Details of streamflow data used for the study

S. no.	Basin	Number of stations	Drainage area (km^2)		Data length	
			Minimum	Maximum	Minimum	Maximum
1	Krishna	31	1850	251,360	1095	18,615
2	Brahmani-Baitarani	9	830	33,955	4015	15,330
3	Sabarmati	6	1421	19,636	5840	9490
4	Mahi	7	1510	32,510	3285	13,805
5	Mahanadi	19	1100	124,450	4015	15,695
6	Subarnarekha	5	1330	12,649	6205	14,235
7	Tapi	5	8487	58,400	3285	5110
8	Cauvery	31	258	66,243	2555	16,425
9	WFR Tadri-Kanyakumari	28	238	5755	1460	16,425
10	EFR Pennar-Kanyakumari	13	850	16,230	4015	16,060
11	Godavari	23	2500	307,800	1019	13,111
12	Pennar	7	2486	37,981	1245	10,606
13	WFR-Kutch-Saurashtra-Luni	8	345	6960	6865	15,111

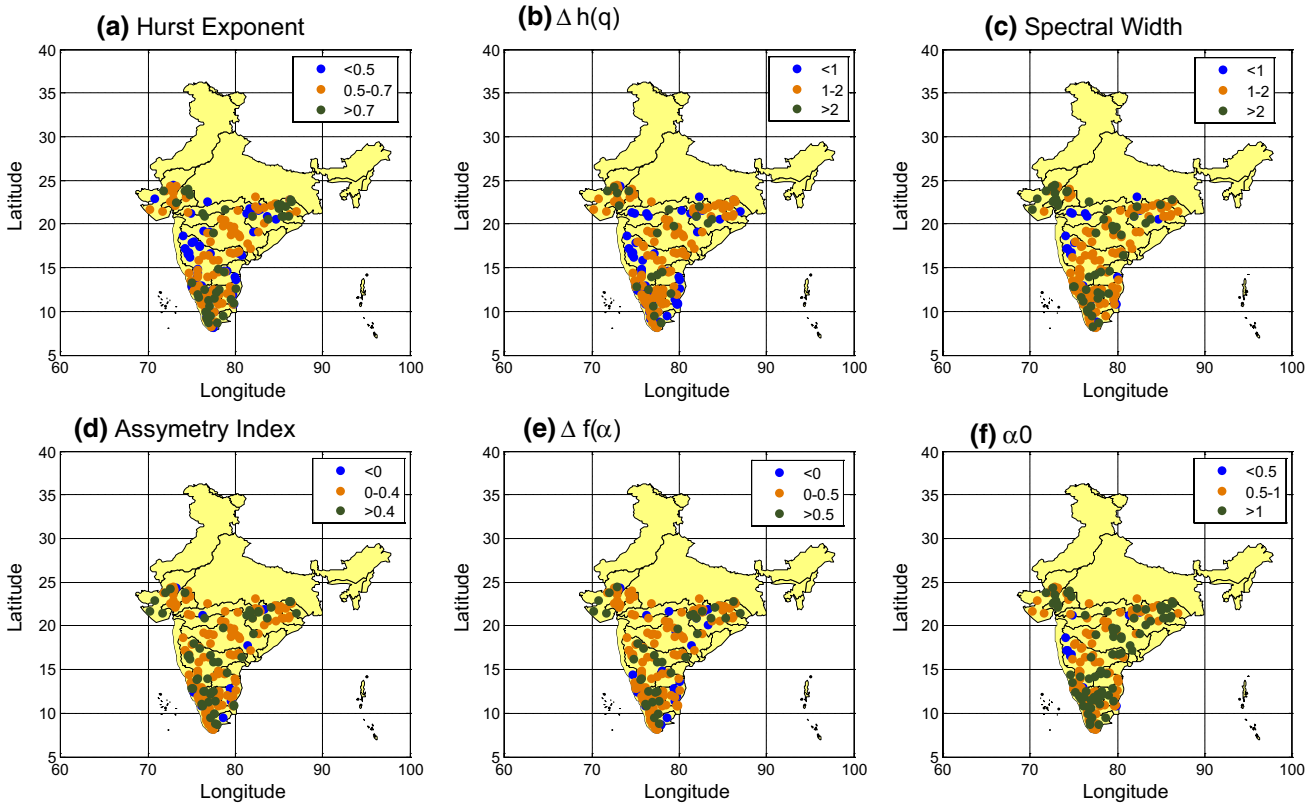

Fig. 2 Spatial distribution of multifractal parameters of streamflow all over India **a** Hurst exponent; **b** $\Delta h(q)$; **c** spectral width; **d** asymmetry index; **e** $\Delta f(\alpha)$; **f** α_0

change in drainage area has no effect on the persistence of the different series. No direct conclusions can be made from the other two plots except that area and data length independently seem to have no significant effect on the multifractality and persistence.

MFCCA between streamflow and suspended sediment

Multifractal cross-correlation analysis (MFCCA) between streamflow and total suspended sediment (TSS) was

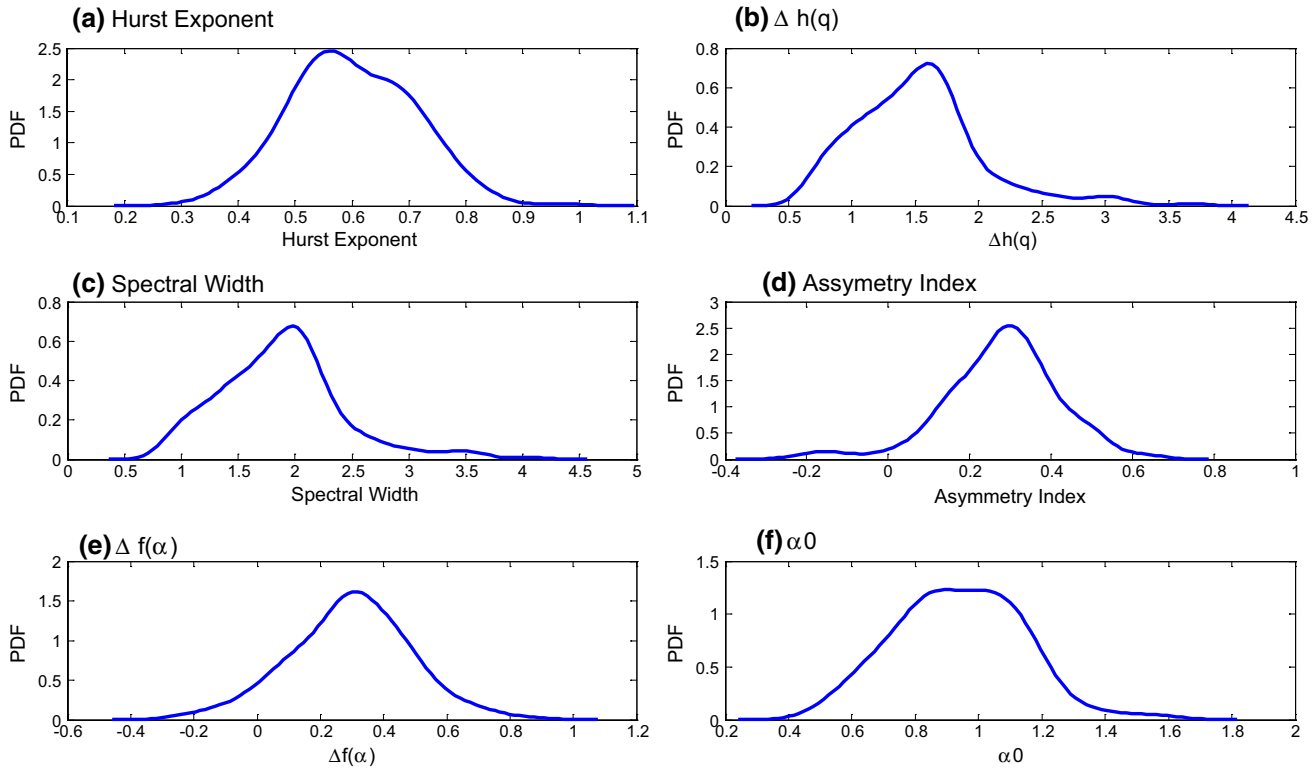

Fig. 3 PDF of different multifractal parameters of streamflow data

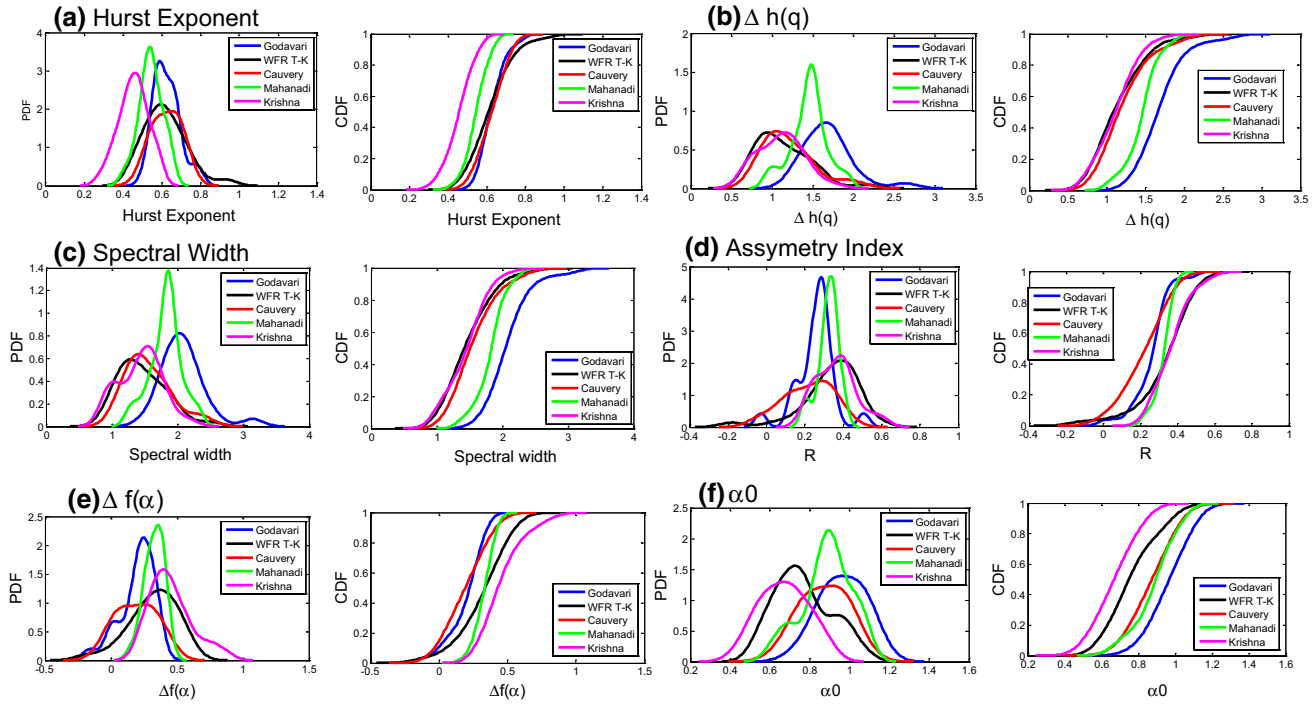

Fig. 4 PDFs and CDFs of different multifractal parameters for basin wise analysis of streamflow datasets

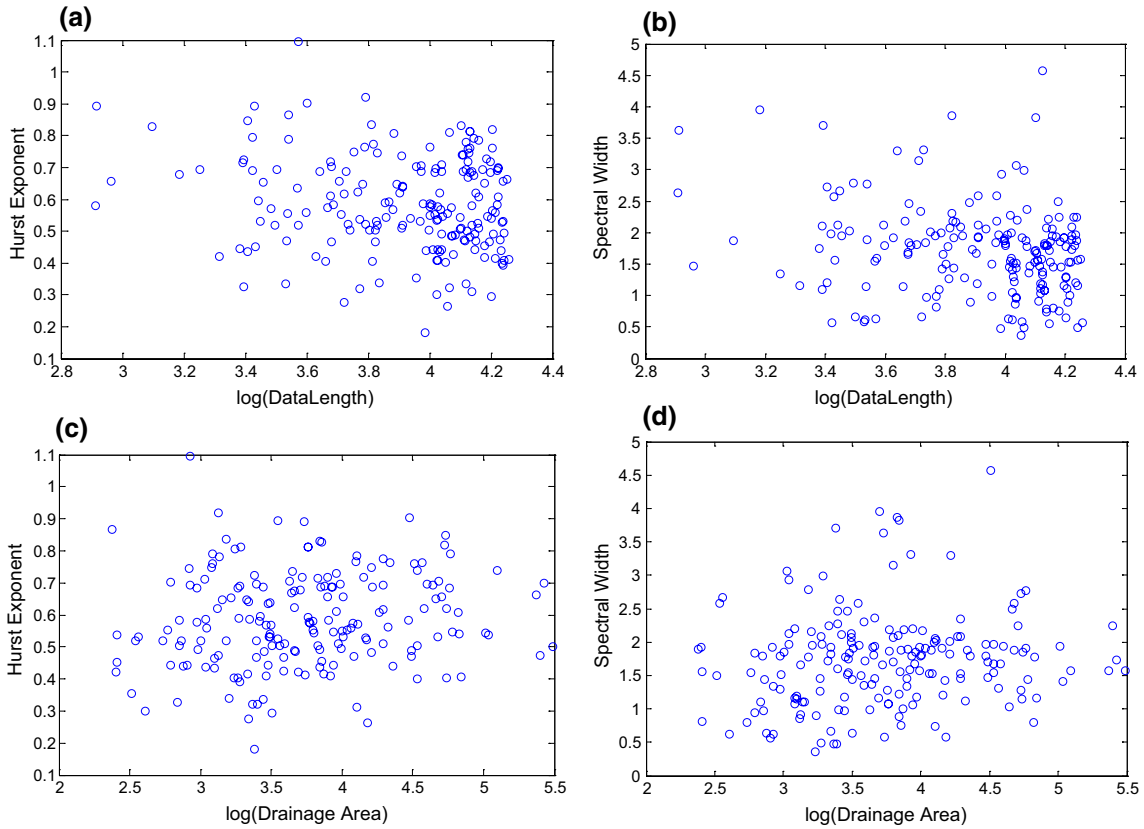

Fig. 5 Influence of drainage area and data length on persistence and multifractality **a** Hurst exponent versus log (data length); **b** spectral width versus log (data length); **c** Hurst exponent versus log (drainage area); **d** spectral width versus log (drainage area)

performed for 5 major basins in India—Cauvery, Krishna, Godavari, Mahanadi and WFR T-K. Choosing the appropriate moment order and scaling ranges are crucial in performing the MFCCA analysis and in this study, we considered the moment order −4 to +4 to avoid any possible bias (Drożdż et al. 2019). It is worth mentioning that due to the highly intermittent rainfall characteristics, many long and continuous zero value stretches may be present in many of the streamflow and suspended sediment series. Addressing this, the minimum scale is selected as more than the length of longest stretch of zero values to avoid any possible inconsistencies in the results (Drożdż et al. 2019). From the MFCCA, the individual persistence, joint persistence and cross-correlation coefficient at annual and the overall correlation are determined for each case. In Cauvery basin, 11 stations for which long and continuous streamflow and TSS data are available are considered for MFCCA analysis. The annual cross-correlation coefficient along with Hurst exponents obtained is given in Table 2. Figure 6 shows typical plots of multifractal analysis along with the variability of cross-correlation with time scale of Kudige station.

Among the different plots, the fluctuation function plots (log ($F(q$, scale)) versus log (scale)) for $q=2$ are presented as the representative sample (Krzyszczak et al. 2019). From the plots of fluctuation function, it is inferred that a definite crossover is noticed between 350 and 400 days (log10(350) − log10(400), i.e. 2.55–2.61) which is corresponding to annual scale. It is to be noted that the multifractal measures are calculated by identifying proper scaling range from the fluctuation function plots. In most of the time series considered in the study, proper scaling in the fluctuation function is noted up to annual scale. Therefore in such series, maximum scale of ~ 365 days was considered in estimation of the different multifractal measures. The annual scale variations are obvious in the streamflow and sediment concentration time series, which could be attributed to the precipitation contributions from the catchment. One cannot ignore the crossover points at intra-seasonal scale ranges in the streamflow and sediment series in certain stations, which could be due to the anthropogenic flow regulation activities performed at the station. Accordingly, this is purely a data dependent property and one cannot generalize the behavioural pattern of the fluctuation function. The scaling exponent plot, mass exponent plot and multifractal spectra of the streamflow and suspended sediment time series derived from the plots of fluctuation function are also presented

Table 2 Hurst exponents of streamflow and TSS data of Cauvery basin along with the cross-correlation

Station	Hx (streamflow)	Hy (TSS)	Scaling Exponent (Hxy)	ρ_{XY} (annual)	ρ_{XY} (overall)
Biligundulu	0.797	0.669	0.733	0.404	0.274
Kodumudi	0.904	0.742	0.823	0.627	0.414
Kollegal	0.736	0.672	0.704	0.428	0.172
Kudige	0.745	0.655	0.700	0.431	0.249
Musiri	0.656	0.641	0.649	0.664	0.504
Muthankera	0.561	0.779	0.670	0.716	0.494
Savandpur	0.752	0.658	0.705	0.450	0.386
T Narasipur	0.781	0.633	0.707	0.208	0.090
TK Halli	0.688	0.673	0.681	0.566	0.415
Tehngudi	0.823	0.883	0.853	0.725	0.360
Thengumarahada	0.839	0.829	0.834	0.241	0.275

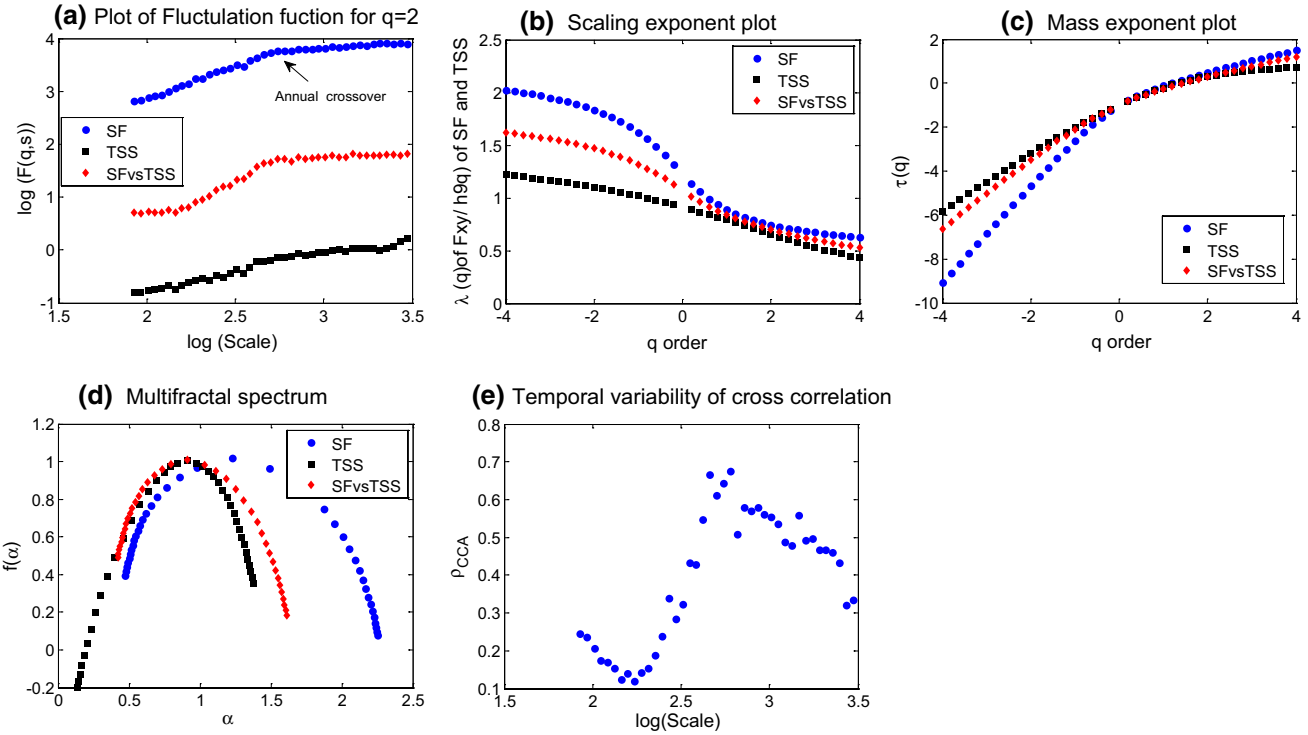

Fig. 6 Plots of multifractal analysis of data of Kudige station along with the variability of cross-correlation **a** log–log plot of fluctuation function versus scale for $q=2$; **b** scaling exponent plot; **c** mass exponent plot; **d** multifractal spectrum; **e** temporal variability of cross-correlation coefficient

in Fig. 6. It can be noted that the scaling exponent plot of cross-correlations is located near the middle of the scaling exponent plots of individual time series (so called GHE plots), which confirms the universal property of the relation between the scaling exponents (Hajian and Movahed 2010). Results obtained by the MFCCA analysis for streamflow and sediment data for Cauvery basin (Table 2) it is noted that the persistence of streamflow is more than that of TSS except for two stations. At all stations of Cauvery basin, the joint persistence is found to be nearly the average of individual persistence of streamflow and TSS. The joint persistence is found to be strong with a mean value of 0.733. The annual correlation is found to be more than 0.5 in five stations, but the overall correlation is found to be weak and it is less than 0.5 in all stations. The mean annual correlation is found to be 0.492 while the mean overall correlation is only 0.33. On examining the correlations it was found that, 7 out of 11 stations weak seasonal correlation (at 90 day scale) was also

detected in this basin. Except for the data of Savandpur and Thengumarahada stations, the annual correlation is found to be more than that of seasonal correlation.

The annual and overall correlation along with Hurst exponents of datasets of different stations of Godavari basin is given in Table 3.

From Table 3, it is noted that unlike for Cauvery basin, for majority of the stations in Godavari basin (i.e. 14 out of 26), the persistence of TSS is more than that of streamflow. The persistence is strong and long term for both streamflow and TSS series with a mean of 0.803 and 0.789, respectively. There exists a strong annual correlation between streamflow and TSS in this basin (mean value of 0.702). The annual correlation is greater than 0.5 in 23 cases, out of which in 17 cases the correlation is more than 0.7. The overall correlation was found to be more than 0.5 in 18 cases out of which the association is strong (> 0.4) in four cases. For the datasets of Bishnur, Bhatpalii and Satrapur stations, both the annual and overall correlation are found to be very weak. It was also noted the seasonal correlation (at 3 month time scale) was also detectable at 16 out of 26 stations and annual correlation was found to be greater than seasonal correlation for data of all stations except Satrapur. At all stations of this basin, the joint persistence is found to be the average of persistence of streamflow and TSS. Figure 7 shows typical plots of multifractal analysis along with the variability of cross-correlation with time scale of Polavaram station in the Godavari basin.

The annual and overall correlation between streamflow and TSS along with Hurst exponents of datasets of Krishna basin is given in Table 4.

From Table 4, it is clear that for 14 out of 23 stations, the persistence of streamflow is more than that of TSS. In this case, the joint persistence (with a mean of 0.614) is found to be the average of the individual persistence of streamflow and TSS. Strong annual correlation (> 0.7) is noted in 7 cases while it is more than 0.5 in 18 cases. In 9 cases seasonal correlation was also noted and the annual correlation is greater than that of seasonal correlation in these stations. The overall correlation was found to be weak (with a mean of 0.375) and in 5 cases the correlation is found to be more than 0.5. Figure 8 shows typical plots of multifractal analysis of streamflow and sediment data along with the variability of Cholachguda station in Krishna basin. The overall and

Table 3 Hurst exponents of streamflow and TSS data of Godavari basin along with the cross-correlation

Station	Hx (streamflow)	Hy (TSS)	Scaling exponent (Hxy)	ρ_{XY} (annual)	ρ_{XY} (overall)
Ashti	0.844	0.920	0.882	0.823	0.602
Babli	0.982	0.959	0.970	0.657	0.442
Bamini(Balharsha)	0.727	0.778	0.752	0.691	0.566
Basar	1.00	0.965	0.994	0.588	0.521
Bhatpalli	0.587	0.644	0.615	0.357	0.267
Bishnur	0.739	0.457	0.598	0.231	0.188
Dhalegaon	0.653	0.669	0.661	0.631	0.460
G.R.Bridge	0.767	0.737	0.752	0.714	0.561
Hivra	0.633	0.570	0.601	0.619	0.498
Jagdalpur	0.838	0.882	0.860	0.713	0.530
Konta	0.786	0.845	0.815	0.811	0.548
Kumhari	0.910	0.893	0.901	0.871	0.599
Mancherial	0.860	0.796	0.828	0.518	0.391
Nandgaon	0.724	0.751	0.737	0.768	0.614
Nowrangpur	0.850	0.877	0.864	0.754	0.662
P.G. (Penganga) Bridge	0.489	0.316	0.402	0.710	0.489
Pathagudem	0.822	0.894	0.858	0.886	0.722
Pauni	0.718	0.782	0.750	0.807	0.575
Perur	0.889	0.898	0.893	0.950	0.915
Polavaram	0.908	0.830	0.869	0.932	0.855
Purna	0.782	0.747	0.764	0.722	0.594
Rajegaon	0.998	1.00	1.000	0.908	0.549
Saigaon	0.597	0.562	0.580	0.769	0.584
Satrapur	0.957	0.877	0.917	0.117	0.277
Tekra	0.848	0.867	0.858	0.884	0.685
Yelli	0.942	0.965	0.953	0.809	0.755

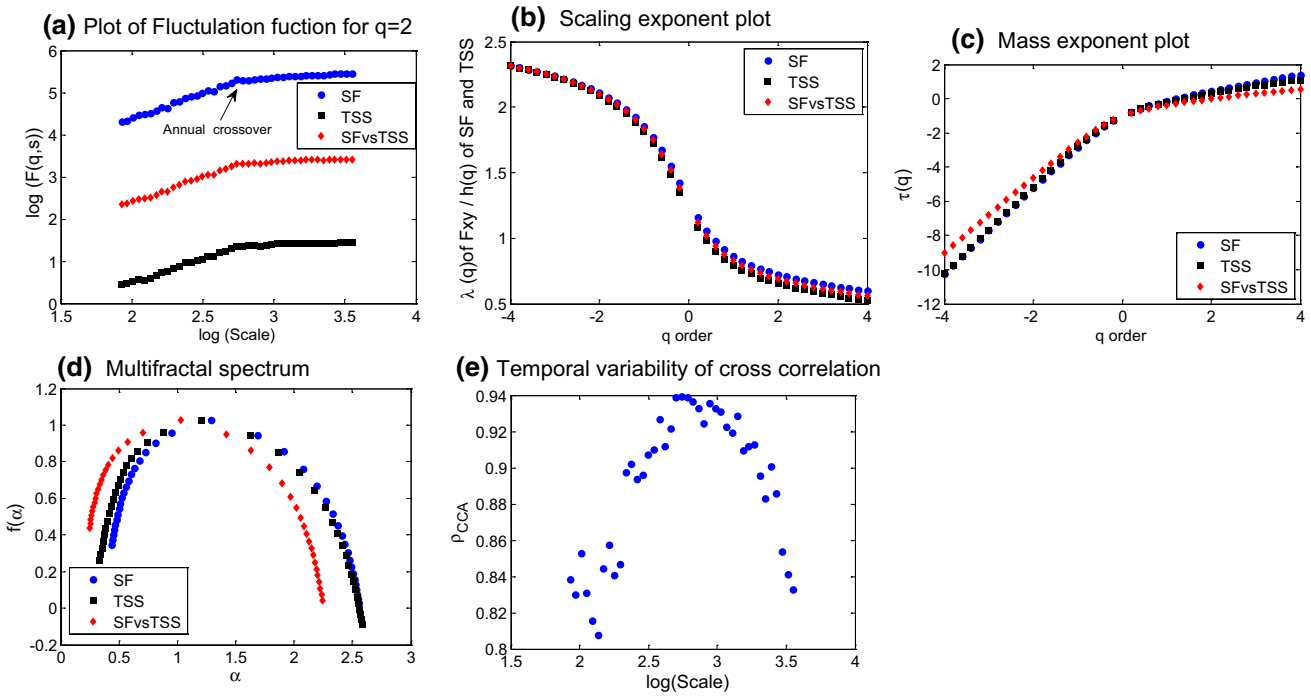

Fig. 7 Plots of multifractal analysis of data of Polavaram station along with the variability of cross-correlation **a** log–log plot of fluctuation function versus scale for $q=2$; **b** scaling exponent plot; **c** mass exponent plot; **d** multifractal spectrum; **e** temporal variability of cross-correlation coefficient

Table 4 Hurst exponents of streamflow and TSS data of Krishna basin along with the cross-correlation

Station	Hx (streamflow)	Hy (TSS)	Scaling exponent (Hxy)	ρ_{XY} (annual)	ρ_{XY} (overall)
Bagalkot	0.540	0.541	0.540	0.441	0.205
Bawapuram	0.577	0.505	0.541	0.644	0.434
Byaladahalli	0.912	0.870	0.891	0.813	0.607
Cholachguda	0.597	0.682	0.639	0.808	0.660
Haralahalli	0.751	0.683	0.717	0.383	0.296
Honnali	0.967	1.027	0.997	0.589	0.194
Huvanahedgi	0.721	0.650	0.685	0.241	0.174
K Agraharam	0.713	0.621	0.667	0.677	0.430
Karaad	0.480	0.449	0.465	0.659	0.346
Keesara	0.591	0.548	0.569	0.570	0.302
Kurundwad	0.420	0.487	0.453	0.938	0.795
Malkhed	0.655	0.639	0.647	0.721	0.210
Mantralayam	0.559	0.557	0.558	0.575	0.353
Marol	0.525	0.578	0.552	0.396	0.143
Pondugala	0.645	0.857	0.751	0.337	0.112
Yadgir	0.490	0.392	0.441	0.686	0.524
Warunji	0.655	0.654	0.654	0.731	0.493
Wadanapalli	0.675	0.750	0.713	0.572	0.336
Wadakbal	0.582	0.558	0.570	0.617	0.484
Vijayawada	0.656	0.590	0.623	0.702	0.330
Takli	0.468	0.365	0.416	0.504	0.232
Shimogs	0.557	0.628	0.592	0.917	0.686
Sarati	0.421	0.446	0.434	0.523	0.320

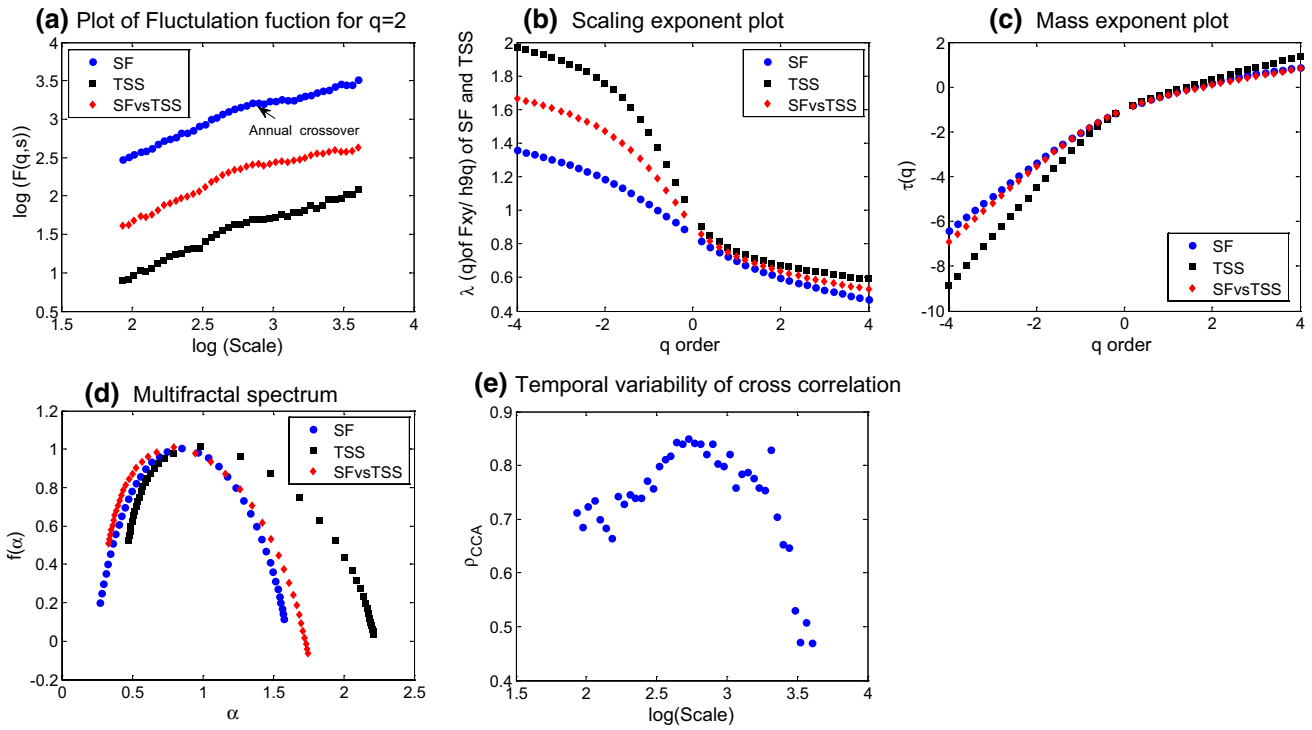

Fig. 8 Plots of multifractal analysis of data of Cholachguda station along with the variability of cross-correlation **a** log–log plot of fluctuation function versus scale for $q=2$; **b** scaling exponent plot; **c** mass exponent plot; **d** multifractal spectrum; **e** temporal variability of cross-correlation coefficient

annual cross-correlation coefficient along with Hurst exponents of datasets of Mahanadi basin is given in Table 5.

From Table 5, it is noticed that in 81% of stations (i.e. 13 out of 16) the persistence of streamflow is more than that of TSS. The seasonal correlation was detected only at Basantpur and Tikarapara stations. The cross-correlation coefficient is more than 0.7 at all stations except Kesinga indicating very strong positive correlation between the parameters in the basin and reasonably good overall correlation (> 0.4) is noted at 14 stations. The mean value of

Table 5 Hurst exponents of streamflow and TSS data of Mahanadi basin along with the cross-correlation

Station	Hx (streamflow)	Hy (TSS)	Scaling exponent (Hxy)	ρ_{XY} (annual)	ρ_{XY} (overall)
Andhiyarkore	0.527	0.341	0.434	0.721	0.490
Bamnidhi	0.517	0.506	0.512	0.759	0.489
Baronda	0.498	0.416	0.457	0.757	0.423
Basantpur	0.691	0.701	0.696	0.816	0.552
Ghatora	1.000	0.991	1.00	0.782	0.629
Jondhra	0.537	0.505	0.521	0.801	0.513
Kantamal	0.538	0.415	0.477	0.726	0.489
Kesinga	0.99	1.000	1.00	0.316	0.364
Kurubhata	0.573	0.571	0.572	0.892	0.740
Manendragarh	0.665	0.777	0.721	0.779	0.528
Rajim	0.499	0.396	0.448	0.700	0.379
Rampur	0.483	0.378	0.430	0.835	0.484
Salebhata	0.462	0.386	0.424	0.763	0.453
Simga	0.487	0.400	0.444	0.720	0.403
Sundaragarh	0.465	0.387	0.426	0.833	0.574
Tikarapara	0.762	0.721	0.741	0.765	0.420

annual correlation is found to be 0.748 while it is 0.495 for overall data. The correlation plot and multifractal plots of Basantpur station are presented in Fig. 9.

The results of MFCCA of streamflow and TSS of WFR Tadri-Kanyakumari (WFR T-K) are given in Table 6. From Table 6, it is clear that the persistence of streamflow is more that of sediment for nine stations. The joint persistenceis nearly the mean of the individual persistence of streamflow and TSS stations of different stations. There exists reasonably good correlation at annual scale with a mean correlation of 0.75 and the overall correlation was also more than 0.5 in 14 cases. The seasonal association was detectable at nine stations and the annual scale correlation is greater than the seasonal correlation for all the stations except for the data of Kumbidi station. The annual cross-correlation is greater than 0.5 in 18 cases out of which in 14 cases the correlation is found to be > 0.7. Figure 10 shows the multifractal plots of Ramamangalam station.

In general, in most of the stations (57 out of 95 stations) the persistence of streamflow is greater than that of TSS. In Godavari basin, majority of the stations the persistence of TSS is more than that of streamflow. The human interventions and flow regulations might have influenced the persistence and multifractality of streamflow in this basin to a great extent. The investigation using MFCCA provides the time (scale) dependent information of the association between streamflow and TSS against the unique and traditional linear correlation between them, i.e. even though the overall correlation between the two are less, at specific time scale the association could be of considerable magnitude. In 45 stations, seasonal (intra-annual) association between streamflow and TSS are also noticed, among which highest number of stations (18 stations) are located in Godavari basin. This also infers the role of flow regulations in streamflow-TSS links of this basin. Even though streamflow-TSS association varies with temporal scales and there is no systematic pattern in this variation for the datasets of different basins. But it is noted that the strength of their association could vary significantly with time scale and their association could significantly depend on the basin and climatic (precipitation) characteristics.

Conclusions

This study first investigated the multifractality of streamflow of 192 stations falling in 13 river basins in India using the multifractal detrended fluctuation analysis (MF-DFA). Subsequently, the multifractal cross-correlation analysis (MFCCA) is employed for investigating the

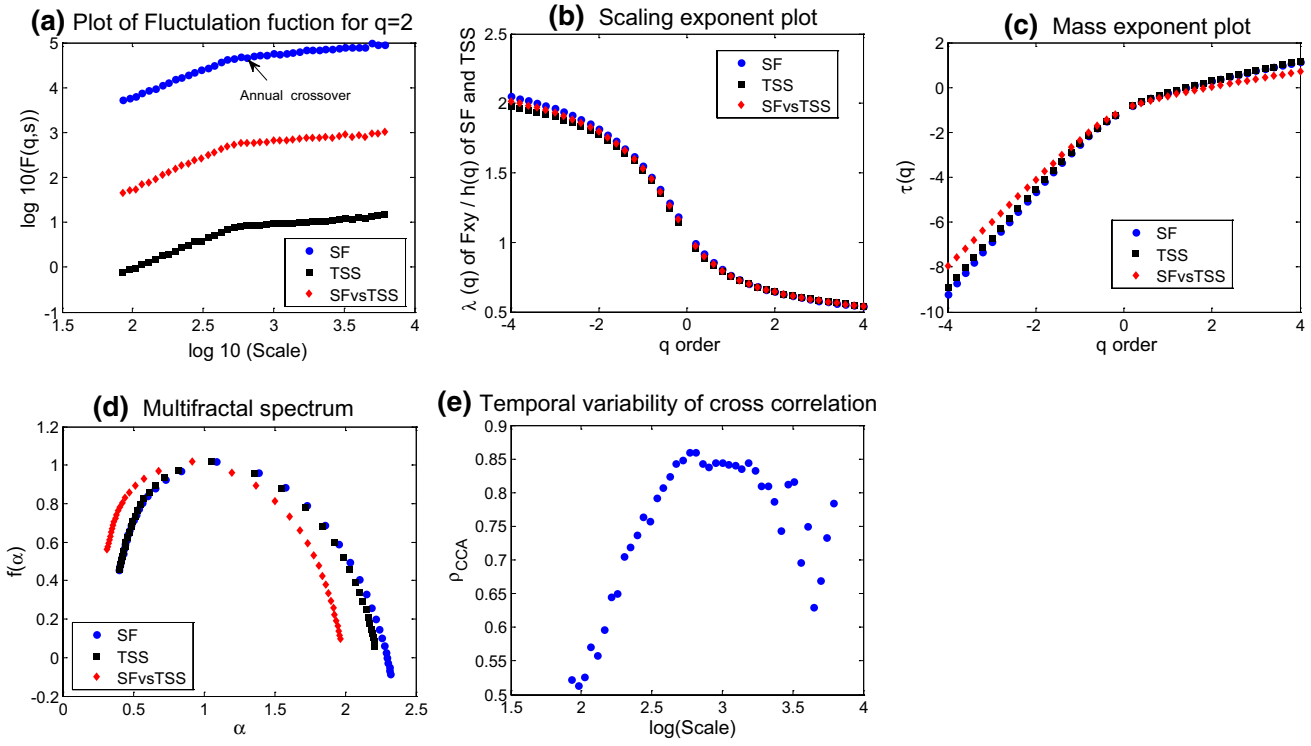

Fig. 9 Plots of multifractal analysis of data of Basantpur station along with the variability of cross-correlation **a** log–log plot of fluctuation function versus scale for $q=2$; **b** scaling exponent plot; **c** mass exponent plot; **d** multifractal spectrum; **e** temporal variability of cross-correlation coefficient

Table 6 Hurst exponents of streamflow and TSS data of WFR Tadri to Kanyakumari basin along with the cross-correlation

Station	Hx (streamflow)	Hy (TSS)	Scaling exponent (Hxy)	ρ_{XY} (annual)	ρ_{XY} (overall)
Ambarampalayam	0.963	0.648	0.806	0.431	0.368
Arangaly	0.500	0.665	0.582	0.855	0.611
Ayilam	0.605	0.558	0.582	0.749	0.581
Bantwal	0.391	0.517	0.454	0.866	0.710
Erinjipuzha	0.722	0.686	0.704	0.897	0.669
Kalampur	0.585	0.636	0.611	0.786	0.564
Kallooppara	0.522	0.593	0.557	0.783	0.420
Karathodu	0.717	0.776	0.747	0.834	0.701
Kidangoor	0.594	0.803	0.699	0.657	0.348
Kumbidi	0.733	0.772	0.752	0.714	0.637
Kuniyil	0.584	0.626	0.605	0.711	0.589
Kuttyadi	1.000	0.997	1.00	0.595	0.415
Malakkara	0.560	0.645	0.603	0.678	0.533
Neeleswaram	1.00	0.916	0.956	0.858	0.615
Pattazhy	0.695	0.685	0.690	0.641	0.555
Perumannu	0.881	0.764	0.822	0.904	0.695
Pulamanthole	0.844	0.772	0.808	0.810	0.621
Ramamangalam	0.681	0.663	0.672	0.782	0.501
Thumpamon	0.595	0.674	0.634	0.730	0.483

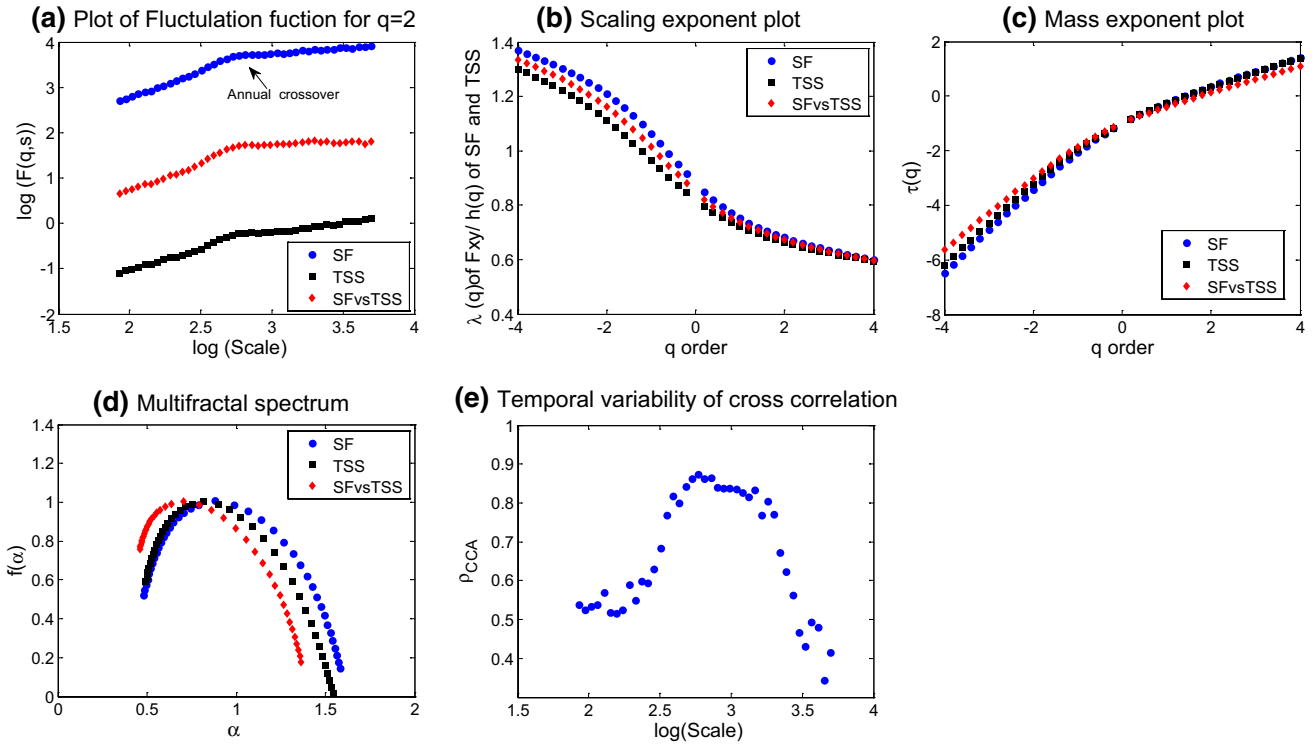

Fig. 10 Plots of multifractal cross-correlation analysis of data of Ramamangalam station along with the variability of cross-correlation **a** log–log plot of fluctuation function versus scale for $q=2$; **b** scaling exponent plot; **c** mass exponent plot; **d** multifractal spectrum; **e** temporal variability of cross-correlation coefficient

streamflow-sediment link in a multifractal perspective. From the results it is noted that the streamflow datasets of different river basins displayed multifractality and long-term persistence with a mean exponent of 0.583. The streamflow records of Krishna basin displayed least persistence and that of Godavari displayed strongest multifractality and complexity. The streamflow-sediment links of five major river basins evaluated using MFCCA showed that the joint persistence is nearly the mean of the persistence of individual series. The streamflow displayed higher persistence than total suspended sediment in majority of the stations except that in Godavari basin. The annual cross-correlation between streamflow and sediment is higher than seasonal and overall cross-correlation but the strength of their association differs with river basin.

Funding The authors received NO funding for performing this research work.

Compliance with ethical standards

Conflict of interest On behalf of all authors, the corresponding author states that there is no conflict of interest.

References

Adarsh S, Drisya SD, Anuja PK, Aggie S (2018a) Unravelling the scaling characteristics of daily streamflows of Brahmani River Basin, India using Arbitrary order Hilbert spectral and detrended fluctuation analyses. SN Appl Sci 1(2018):58. https://doi.org/10.1007/s42452-018-0056-1

Adarsh S, Drisya SD, Anuja PK (2018b) Analyzing the hydrologic variability of Kallada River, India using continuous wavelet transform and fractal theory. Water Conserv Sci Eng. https://doi.org/10.1007/s41101-018-0060-8

Adarsh S, Kumar DN, Deepthi B, Gayathri G, Aswathy SS, Bhagyasree S (2019) Multifractal characterization of meteorological drought in India using detrended fluctuation analysis. J Climatol Int. https://doi.org/10.1002/joc.6070

Baranowski P, Krzyszczak J, Slawinski C, Hoffmann H, Kozyra J, Nieróbca A, Siwek K, Gluza A (2015) Multifractal analysis of meteorological time series to assess climate impacts. Clim Res 65:39–52

Brito AA, Santos FR, de Castro APN, da Cunha Lima AT, Zebende GF, da Cunha Lima IC (2018) Cross-correlation in a turbulent flow: analysis of the velocity field using the σ DCCA coefficient. Europhys Lett 123:20011

Dahlstedt K, Jensen H (2005) Fluctuation spectrum and size scaling of river flow and level. Phys A 348:596–610

Dey P, Mujumdar PP (2018) Multiscale evolution of persistence of rainfall and streamflow. Adv Water Resour 121:285–303

Drożdż S, Oświęcimka P (2015) Detecting and interpreting distortions in hierarchical organization of complex time series. Phys Rev E 91:030902(R)

Drożdż S, Minati L, Oświęcimka P, Stanuszek M, Wątorek M (2019) Signatures of the crypto-currency market decoupling from the Forex. Future Internet 11:154. https://doi.org/10.3390/fi11070154

Grech D (2016) Alternative measure of multifractal content and its application in finance. Chaos, Solitons Fractals 88:183–195

Hajian S, Movahed MS (2010) Multifractal detrended cross-correlation analysis of sunspot numbers and river flow fluctuations. Phys A 389:4942–4957

Hirpa FA, Gebremichael M, Over TM (2010) River flow fluctuation analysis: effect of watershed area. Water Resour Res. https://doi.org/10.1029/2009WR009000

Huang YX, Schmitt FG, Hermand JP, Gagne Y, Lu ZM, Liu YM (2011) Arbitrary-order Hilbert spectral analysis for time series possessing scaling statistics: a comparison study with detrended fluctuation analysis and wavelet leaders. Phys Rev E 84:016208. https://doi.org/10.1103/PhysRevE.84.016208

Hurst HE (1951) Long-term storage capacity of reservoirs. Trans ASCE 116:770–808

Hurst HE, Black RP, Simaika YM (1965) Long-term storage: an experimental study. Constable, London

Ihlen EAF (2012) Introduction to multifractal detrended fluctuation analysis in MATLAB. Front Physiol 3:141. https://doi.org/10.3389/fphys.2012.00141

Jiang ZQ, Zhou WX (2011) Multifractal detrending moving-average cross-correlation analysis. Phys Rev E 84:016106

Jiang ZQ, Wen-Jie X, Zhou WX, Sornette D (2011) Multifractal analysis of financial markets. Quant Finance. http://arxiv.org/abs/1805.04750

Kantelhardt JW, Zschiegner SA, Koscielny-Bunde E, Halvin H, Bunde A, Stanley HE (2002) Multifractal detrended fluctuation analysis of non-stationary time series. Phys A 316:87–114

Kantelhardt JW, Rybski D, Zschiegner SA, Braun P, Koscielny-Bunde E, Livina V, Havlin S, Bunde A (2003) Multifractality of river runoff and precipitation: comparison of fluctuation analysis and wavelet methods. Phys A 330:240–245

Kantelhardt JW, Bunde EK, Rybski D, Barun P, Bunde A, Havlin S (2006) Long-term persistence and multifractality of precipitation and river runoff records. J Geophys Res Atmos 28:1–13

Koscielny-Bunde E, Kantelhardt JW, Braun P, Bunde A, Havlin S (2003) Long-term persistence and multifractality of river runoff records: detrended fluctuation studies. J Hydrol 322:120–137

Krzyszczak J et al (2019) Multifractal characterization and comparison of meteorological time series from two climatic zones. Theoret Appl Climatol 137:1811–1824

Kwapień J, Oświęcimka P, Drożdż S (2015) Detrended fluctuation analysis made flexible to detect range of cross-correlated fluctuations. Phys Rev E 92:052815

Labat D, Masbou J, Beaulieu E, Mangin A (2011) Scaling behavior of the fluctuations in stream flow at the outlet of karstic watersheds, France. J Hydrol 410:162–168

Li E, Mu X, Zhao G, Gao P (2015) Multifractal detrended fluctuation analysis of streamflow in Yellow River Basin, China. Water 7:1670–1686

Mandelbrot B (1982) The fractal geometry of nature. WH Freeman Publishers, New York

Muzy JF, Bacry E, Arneodo A (1991) Wavelets and multifractal formalism for singular signals: application to turbulence data. Phys Rev Lett 67(1991):3515–3518

Oświęcimka P, Drożdż S, Kwapień J, Górski A (2013) Effect of detrending on multifractal characteristics. Acta Phys Pol, A 123:597–603

Oświęcimka P, Drożdż S, Forczek M, Jadach S, Kwapień J (2014) Detrended cross-correlation analysis consistently extended to multifractality. Phys Rev E 89:023305

Pandey G, Lovejoy S, Schertzer D (1998) Multifractal analysis of daily river flows including extremes for basins five to two million square kilometers, one day to 75 years. J Hydrol 208:62–81

Peng CK, Buldyrev SV, Simons M, Stanley HE, Goldberger AL (1994) Mosaic organization of DNA nucleotides. Phys Rev E 49:1685–1689

Piao L, Fu Z (2016) Quantifying distinct associations on different temporal scales: comparison of DCCA and Pearson methods. Sci Rep 6:36759

Podobnik B, Stanley HE (2008) Detrended cross-correlation analysis: a new method for analyzing two non-stationary time series. Phys Rev Lett 100(8):084102

Podobnik B, Grosse I, Horvatic D, Ilic S, Ivanov PCh, Stanley HE (2009a) Quantifying cross-correlations using local and global detrending approaches. Eur Phys J B 71:243–250

Podobnik B, Horvatic D, Petersen AM, Stanley HE (2009b) Cross-correlations between volume change and price change. Proc Natl Acad Sci USA 106:22079–22084

Podobnik B, Jiang Z-Q, Zhou W-X, Stanley HE (2011) Statistical tests for power-law cross-correlated processes. Phys Rev E 84:066118

Rego CRC, Frota HO, Gusmão MS (2013) Multifractality of Brazilian rivers. J Hydrol 495:208–215

Shi K (2014) Detrended cross-correlation analysis of temperature, rainfall, PM_{10} and ambient dioxins in Hong Kong. Atmos Environ 97(2014):130–135

Tan X, Gan TW (2017) Multifractality of Canadian precipitation and streamflow. Int J Climatol 37(S1):1221–1236

Tessier Y, Lovejoy S, Hubert P, Schertzer D, Pecknold S (1996) Multifractal analysis and modeling of rainfall and river flows and scaling, causal transfer functions. J Geophys Res Atmos 101:26427–26440

Vassoler RT, Zebende GF (2012) DCCA cross-correlation coefficient apply in time series of air temperature and air relative humidity. Phys A 391:2438–2443

Wątorek M, Drożdż S, Oświęcimka P, Stanuszek M (2019) Multifractal cross-correlations between the world oil and other financial markets in 2012–2017. Energy Econ 81:874–885

Wu Y, He Y, Wu M, Lu C, Gao S, Xu Y (2018) Multifractality and cross correlation analysis of streamflow and sediment fluctuation at the apex of the Pearl River Delta. Sci Rep 8:16553. https://doi.org/10.1038/s41598-018-35032-z

Yu ZG, Leung Y, Chen YD, Zhang Q, Anh V, Zhou Y (2014) Multifractal analyses of daily rainfall time series in Pearl River basin of China. Phys A 405:193–202

Yuan N, Fu Z, Mao J (2010) Different scaling behaviors in daily temperature records over China. Phys A 389(19):4087–4095

Zebende GF (2011) DCCA cross-correlation coefficient: quantifying level of cross-correlation. Phys A 390:614–618

Zhang Q, Xu CY, Chen DYQ, Gemmer M, Yu ZG (2008) Multifractal detrended fluctuation analysis of streamflow series of the Yangtze river basin, China. Hydrol Process 22:4997–5003

Zhang Q, Chong YX, Yu ZG, Liu CL, Chen DYQ (2009) Multifractal analysis of streamflow records of the East River basin (Pearl River), China. Phys A 388:927–934

Zhou WX (2008) Multifractal detrended cross-correlation analysis for two non-stationary signals. Phys Rev E 77:066211

Acta Geophysica (2020) 68:537–551
https://doi.org/10.1007/s11600-020-00417-0

RESEARCH ARTICLE - HYDROLOGY

Multi-variable calibration of hydrological model in the upper Omo-Gibe basin, Ethiopia

Mudesir Nesru[1,2] · Amba Shetty[1] · M. K. Nagaraj[1]

Received: 31 October 2019 / Accepted: 29 February 2020 / Published online: 9 March 2020

Abstract

The calibration of any hydrological model in any river basin is generally performed using a single hydrological variable. Spatially distributed hydrological modeling provides an opportunity to enhance the use of multi-variable calibration models. The objective of this study is to test the efficiency of satellite-based actual evapotranspiration in the HBV hydrological model to render the catchment water balance using multi-variable calibration in the upper Omo-Gibe basin in Ethiopia. Five years (2000–2004) meteorological data, streamflow, and actual evapotranspiration (ETa) based on remote sensing were used for calibration and validation purposes. The performance of the HBV model and the efficiency of SEBS–ETa were evaluated using certain calibration criteria (objective function). The model is first calibrated using only streamflow data to test HBV model performance and then calibrated using a multi-variable (streamflow and ETa) dataset to evaluate the efficiency of SEBS–ETa. Both model setups were validated in a multi-variable evaluation using streamflow and ETa data. In the first case, the model performed well enough for streamflow and poor for ETa, while in the latter case, the performance efficiency of SEBS–ETa and streamflow data shows satisfactory to good. This implies that the performance of hydrological models is enhanced by employing multi-variable calibration.

Keywords Evapotranspiration · Ethiopia · Hydrological model · Multi-variable · Streamflow

Introduction

Knowing the reliable information on the components of the water balance equation is crucial for water management in a river basin system. Hydrological modeling is an important tool for knowledge grasping on the hydrological responses of the catchment area (Kim et al. 2018) and is a challenging task (Romanowicz et al. 2013). In a conceptual rainfall–run-off model, it is challenging to measure different parameters directly. It requires the optimization of some hydrological variables through calibration in order to achieve good correlation and closely to match between simulated and observed variables. Calibration with historical data is the most common method for the identification of an optimized model parameter set (Wagener et al. 2003; De Vos et al. 2010).

In hydrological modeling, an integrated response parameter streamflow is commonly used for model calibration. However, the use of streamflow compels the assessment of model performance, since the deviation between simulated and observed matching parts comes from different possible reasons. Some of the causes are errors as a result of lack of complete representations of hydrological data, for instance, evapotranspiration and precipitation, the incorrectness of parameter values, deficiencies in model structure, and error due to observations of calibration variables. Furthermore, sources of error related to the use of boundary fluxes and model initialization to permit water to pass through the boundaries of the model are other causes (Carrera and Neuman 1986; Boulet et al. 2002). To overcome these errors for the solution of a practical problem, all of the hydrological models should be calibrated (Gupta et al. 1998). The process of hydrological model calibration can take place either manually or automatically. The former one is done manually using a trial-and-error parameter correction process for

✉ Mudesir Nesru
marude03@yahoo.com

[1] Department of Applied Mechanics and Hydraulics, National Institute of Technology Karnataka, Surathkal, Mangalore 575 025, India

[2] Department of Hydraulic and Water Resource Engineering, Wolaita Sodo University, P.O. Box 138, Wolaita Sodo, Ethiopia

reducing the error of objectives, while in the latter case, according to a specific search scheme for optimization of objective functions, parameters that measure the simulation model goodness of fit are automatically adjusted. Refsgaard (1997) and Wagener et al. (2001) stated that the automated calibration employed without enough hydrological know-how could result in incorrect parameter values, which could lead to an unrealistic model response system that is uncontrolled by measurements. In addition, however, the models are calibrated well in terms of an independent verification dataset parameter values that cannot yield good performance (Shafii et al. 2014).

In rainfall–runoff models, problems with the amendment of parameters can be attributed to different factors. As stated in Gupta et al. (1998), during the calibration period combination of all the remaining parameters into a single objective function does not demonstrate the insufficiency of the model. For instance, in a single objective function, there is difficulty in differentiating between recession and high-flow model behavior. In this regard, understanding the limitation of single objective function encourages to adopt multi-criteria calibration approaches (Franks and Beven 1997; Gupta et al. 1998; Yapo et al. 1998; Legates and McCabe 1999; Madsen 2000; Beven and Freer 2001; Shafii et al. 2014; Poméon et al. 2018). Multi-objective calibration methods are designed to identify certain parameters that better reproduce multiple outputs from the system. Multi-criteria calibration utilizes multi-index to define the features of the error vector resulting from the corresponding set of the multi-objective equivalence optimal parameter values and an objective function interchange curve. In addition, the process of a characteristic multi-criteria calibration model can be able to consist of multiple probability functions utilized for several sets of measurements, such as sediment, discharge, evapotranspiration, snow. However, to simulate a single output flux, the model assessment could be assumed to be of inherently many criteria (Gupta et al. 1998).

Multi-objective calibration of the model varies from a one-objective calibration of the model. To reproduce a record of single independent observation based on the abilities of the model traditional single form of objective calibration attempts to define the model parameter sets (Mccabe et al. 2005). By utilizing both groundwater level and runoff observation based on a modeling system called MIKE SHE, Madsen (2003) suggested a general multi-objective structure of an integrated and distributed hydrological model for automatic calibration. In which case, to optimize the catchment runoff performance index in a multi-objective optimization framework, individual groundwater well's performance indices were grouped into a single certain calibration criterion. Meixner et al. (2002) employed a multi-criteria algorithm to calibrate the hydrochemical model. For assessing the performance of this model, a total of 21 chemicals and hydrological criteria were obtainable. Also, various researchers use a second set of the variable for model output. Such variables are soil moisture or groundwater hydraulic heads for assessment of determining rainfall–runoff model data (Gupta et al. 2008; Khu et al. 2008); graphs of groundwater piezometer (Fenicia et al. 2005; Khu et al. 2008); soil wetness index or simple soil moisture storage indicator (Downer and Ogden 2003); and satellite-based soil moisture estimates (Campo et al. 2006). In addition to streamflow data for 320 Austrian catchments, Parajka et al. (2007a, b) utilized daily snow cover data for the calibration of a conceptual hydrological model. The concept of most hydrological models combination is to combine state variables with streamflow. It has been pointed out that the combination has an indirect impact on closure of water balance term in the rainfall–runoff model. Since the performance evaluation of these procedures is constrained, there is the uncertainty of how best the model reproduces the performance of the water balance of the study area.

Commonly in hydrological modeling, evapotranspiration is assessed through meteorological data, which helps to evaluate reference evapotranspiration (ET_0) and direct measurement data. Since those data may have comparatively insufficient spatial coverage for larger areas of the catchment, it is necessary to substitute data sources, which enhances the spatial coverage of the large area. In general hydrological model requires large numbers of spatiotemporally distributed datasets to characterize the major catchment hydrological processes and its climate. This introduces remote sensing data as a possible source for this model (Chen et al. 2005; Montzka et al. 2008). Remote sensing is utilized to find hydrological parameters; such parameters are rainfall (Wang et al. 2001; Haile et al. 2013; Rientjes et al. 2013a), soil moisture (Hollenbeck et al. 1996; Kim and Barros 2002), and potential evapotranspiration (Stisen et al. 2008). It also distinguishes areal phenomena, such as clouds (Ouillon et al. 1997), inundated areas (Islam and Sado 2002), and snow cover (Tait et al. 2000).

Based on observed values of ground temperature, latent heat, sensible heat, and soil moisture data, the Biosphere–Atmosphere Transfer Scheme was calibrated by Gupta et al. (1999). In their study, they identified that to simulate accurate multi-variant, single output variable calibration is not sufficient. Crow et al. (2003) reported that, relative to individual variable calibration, multi-variable calibration reduces 20% calibration error in actual evapotranspiration (ETa). Also, to calibrate the semi-distributed variable infiltration capacity (VIC) hydrological model, they used streamflow and space-borne radiometric surface temperature data. In the Krishna basin of southern India, Immerzeel and Droogers (2008) incorporated evapotranspiration based on remote sensing into Soil

and Water Assessment Tool (SWAT) model calibration. In their analysis, they compare the monthly sub-basins output of remote sensing-derived ETa and ETa simulated by the physically based hydrological model. In the upper Bhima catchment of southern India, Immerzeel et al. (2008) combined remote sensing data and output of the SWAT model to assess productivity and the use of water. They found that in the watershed, evapotranspiration is the significant water loss term. In the Luangwa River Basin in Zambia using remote sensing ETa in a conceptual semi-distributed hydrological model, Winsemius et al. (2008) measured the values of a land surface-related parameter. To improve the simulation of discharge based on the energy balance approach in a controlled water system, Hartanto et al. (2017) integrate remote sensing-based ETa data with a spatially distributed hydrological model in a low-lying reclamation area of the Rijnland area in the Netherlands. They compared integrated modeled and remote sensing-based ETa to simulated data without integration between modeled and RS ETa. Herman et al. (2018) examined the overall performance improvement of the SWAT model by utilizing integrated satellite-based ETa with the spatially distributed dataset of the hydrological model. They calibrated the model using spatially distributed ETa in Creek Watershed, in Michigan, and a particular record of point streamflow for the Honeyoey Creek-Pine, USA. To calibrate the model, they employed a multi-variable and genetic algorithm. They found that there is a great improvement in the performance of the hydrological model since the integration of satellite-based and spatially distributed hydrological data combines with the right calibration method.

Since actual evapotranspiration is part of water balance terms in hydrological studies, it has not been paying more attention while performing a multi-variable calibration for water balance studies. For this study, the performance evaluation of hydrological studies was accomplished through a multi-variable calibration technique, which utilizes two water balance terms. These water balance terms are satellite-based ETa and streamflow. Within a multi-variable calibration formulation, the hydrological process is likely to be satisfactory for an initial assessment of more than a single uncertainty-based calibration technique. Moreover, this study estimates and tests the utilization of a second calibration variable called satellite-based actual evapotranspiration and gives possibility as the water balance with its model performance. This study aims to test the efficiency of satellite-based actual evapotranspiration in the semi-distributed HBV hydrological model to render the catchment water balance by utilizing daily remote-sensed actual evapotranspiration data and daily streamflow. The HBV light hydrological model (Seibert 1996) was applied to the upper Omo-Gibe basin, Ethiopia.

Materials and methods

Study area background

The upper Omo-Gibe basin (UOGB) covers an area of around 33,276 sq. km including some parts of Southern Nations, Nationalities, and People Regional State (SNNPRS) and some parts of the Oromia region and located between 6° 51′ 55.81″ and 9° 22′ 26.05″ N latitude and 35° 31′ 49.63″–38° 23′ 43.85″ E longitude. The location map of the UOGB is shown in Fig. 1. Based on data collected from the National Meteorological Agency of Ethiopia, the annual rainfall in the UOGB ranges from approximately 2050 mm per year in the Bonga and Wushwush stations to less than 400 mm per year in the Indibir region over the 34 years of recorded data for the twenty-three rain gauge stations. Approximately 58% of the average annual rainfall values occur in the rainy season, and its peak values found in the month of July. In addition, the mean annual temperature in the basin varies from around 16 °C in the highlands of the north near the Gedo rain gauge station to 21 °C near the Areka station, whereas the mean monthly temperature is also higher during the short rainy season (March through May) and lowers during the rainy season (June to mid-September).

The basin topography, all in all, is characterized by environmental variation. The main gorges of the basin are mostly unpopulated and sustain the silvopastoral and silvicultural cover. The southern part of the basin has a higher population of natural vegetation with more sparsely populated, whereas the eastern part of the basin was intensively cultivated and most densely populated areas (Nesru et al. 2020). At the same time, the major soil types found in the basin are Alisols, Leptosols, Luvisols, Nitosols, and Vertisols (data from the Ministry of Water, Irrigation and Energy of Ethiopia).

The UOGB is divided into four sub-catchments based on streamflow measuring station to set up the HBV light hydrological model (Fig. 2). The largest and smallest sub-catchment is Abelti and Wabe, respectively. At the outlets of each of the four sub-catchments, the mean daily streamflow varies from 2.89 to 4.53 m^3/s for the year 2000–2004. Abelti, Wabe, and Gojeb sub-catchments receive streamflow from the upstream of the basin, while Gibe sub-catchment receives from those three sub-catchments.

Methods

Surface energy balance system (SEBS) and actual evapotranspiration

SEBS

To estimate bi-weekly ETa from January 1, 2000, to October 31, 2004, SEBS developed by Su (2002) was used. SEBS

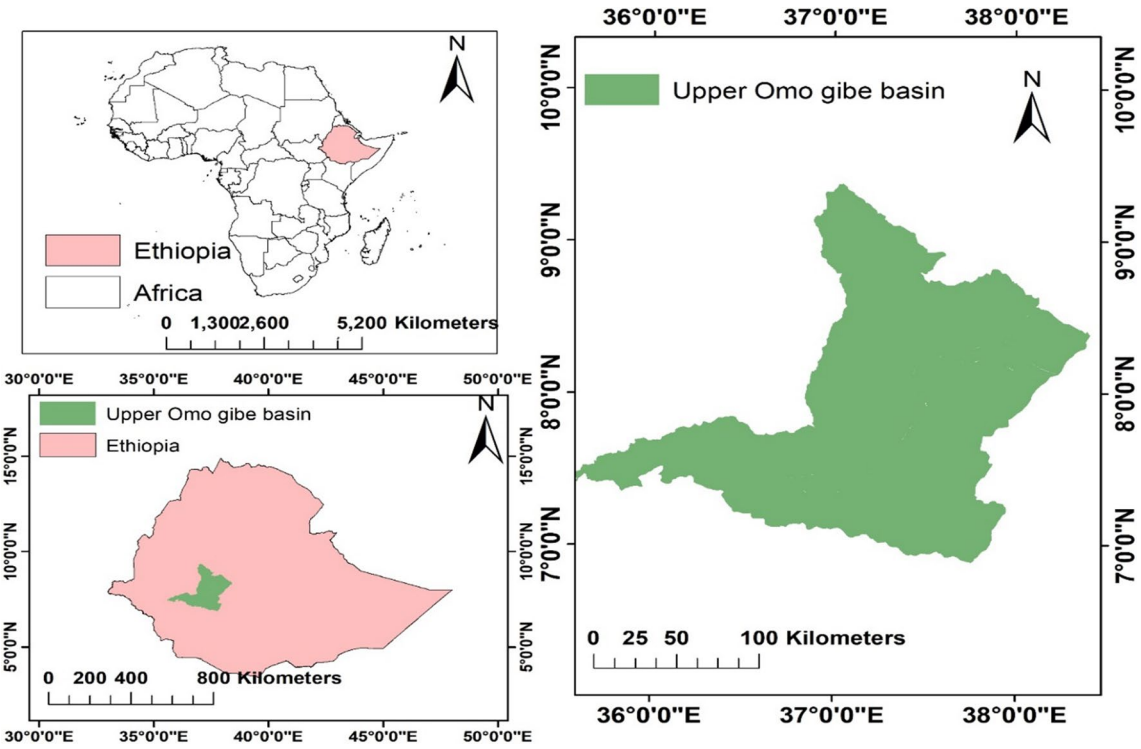

Fig. 1 Location of upper Omo-Gibe basin

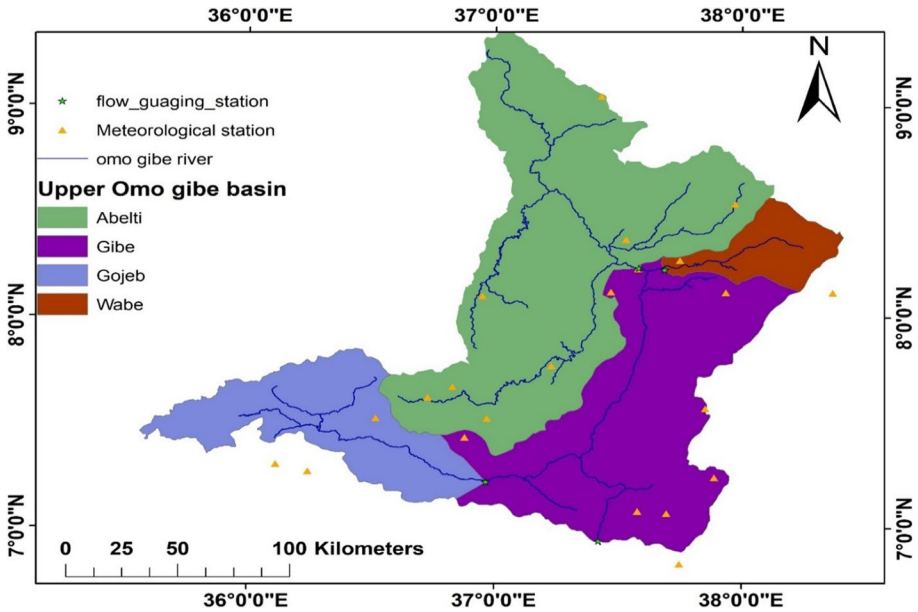

Fig. 2 Sub-catchment and selected meteorological and stream gauging station for UOGB

converts satellite radiance into land surface characteristics such as vegetation index, surface albedo, leaf area index, and surface temperature. The collected daily meteorological data and land surface characteristics were used to solve the energy balance equation, which is read as:

$$\lambda E = R_n - G_0 - H \quad (1)$$

where λE, R_n, G_0, and H are the latent heat flux, net radiation flux at the surface, soil heat flux, and the sensible heat flux to the air, respectively. (All terms are in W/m^2.) The R_n was determined by subtracting all outgoing radiant fluxes from all incoming radiant fluxes and is written as:

$$R_n = R_s^{\downarrow} - \alpha R_s^{\downarrow} + \varepsilon_a.\sigma.T_a^4 - \varepsilon_0.\sigma.T_s^4 \quad (2)$$

where $R_s^{\downarrow}$ is the incoming short wave radiation (W/m^2), σ is the Stefan–Boltzmann constant (W/m^2 K^4), α is the surface albedo (–), ε_a is the air emissivity (–), T_a is the air temperature (K), ε_0 is the surface emissivity (–), and T_s is the surface temperature (K). The soil heat flux is empirically calculated as G_0/R_n fraction or is written as:

$$G_0 = R_n\left[\Gamma_c + \left(1 - f_c\right)\left(\Gamma_s - \Gamma_c\right)\right] \tag{3}$$

where Γ_c is the ratio of soil heat flux to net radiation, which is assumed that 0.315 for bare soil (Kustas and Daughtry 1990) and 0.05 for full vegetation canopy (Monteith 1973), and f_c is the fractional vegetation cover, which can be determined from RS data. Using the f_c value interpolation is then performed between the case of full vegetation and bare soil. The value of H is calculated using air to surface temperature, estimated surface roughness, and observed wind speed. The equation of sensible heat flux reads as:

$$H = \rho_{air}.C_p\frac{dT}{r_{ah}} \tag{4}$$

where C_p is the specific heat of the air (J g^{-1} K^{-1}); dT is the near-surface and air-temperature difference (K) (d$T = T_a - T_s$); ρ_{air} is the air density (kg m^{-3}), and r_{ah} is the aerodynamic resistance to heat transfer (s m^{-1}) over the vertical distance. To estimate ETa, SEBS utilizes evaporative fraction. By knowing sensible, latent, and soil heat flux, it is possible to calculate evaporative fraction Λ (dimensionless). Since there is a related uncertainty in the evaporative fraction and derived latent heat of flux, the sensible heat flux is unconstrained by the available energy. Thus, the meteorological conditions at surface temperature and reference height were used to determine the sensible heat flux. However, this uncertainty is limited in the energy budget consideration at the limiting case in the SEBS algorithm. The sensible heat flux at the dry limit (from available energy) and the wet limit (resulting from a combination equation) constrains the range of actually sensible heat flux (Su 2002). The relative evaporation Λr (dimensionless) is derived by utilizing the sensible heat flux and the calculated sensible heat flux at the dry and wet limits (Su 2002). The relative evaporation Λr and the evaporative fraction Λ, respectively, are written as (Eqs. 5, 6):

$$\Lambda_r = 1 - \frac{H - \lambda E_{wet}}{R_n - G_o} \tag{5}$$

$$\Lambda = \frac{\lambda E}{R_n - G_o} = \frac{\Lambda_r.\lambda E_{wet}}{R_n - G_o} \tag{6}$$

SEBS has various applications in the river basins in different parts of the world. For instance, it is used to estimate ETa over the Heith River Basin in China (Qin et al. 2008), the Yellow River Delta wetland (Jia et al. 2009), in the Karkheh River Basin in Iran (Muthuwatta et al. 2010), the Nagqu River Basin of the Northern Tibetan Plateau (Zhong et al. 2019), the Haihe River Basin in China (Zhao et al. 2019). Also, Wang and Li (2011) used SEBS to estimate the sensible heat flux in the Arou area. Furthermore, Wu et al. (2015) used SEBS to estimate irrigation water efficiency in the Heihe River in northwestern China. In addition, SEBS was used in the upper Omo-Gibe basin in Ethiopia (Nesru et al. 2020) to estimate ETa for assessing the availability of water for crop production.

Time series trends of actual evapotranspiration

For the present study to estimate daily ETa from the period of January 2000 to October 2004, 145 cloud-free calibrated radiance MODIS Level 1B (MOD021KM) with their corresponding geo-location files (MOD03), with a daily temporal and spatial resolution of 1 km^2 collected by the Terra (EOS AM) satellite in the MODIS sensor launched in December 1999, were used (Table 1) (source:

Table 1 Acquisition dates of TERRA-MODIS images in the upper Omo-Gibe basin for the study period. *Source*: http://ladsweb.modaps.eosdis.nasa.gov/

Month	2000	2001	2002	2003	2004
Jan		06, 18, 23	17, 23, 28	01, 04	04
Feb	28	03, 14, 28	02, 11, 27	05, 18, 21	05
Mar	04, 13,22	07, 09, 16	29, 31	06, 16, 25	08
Apr	05, 14, 30	08, 17, 26	07, 13, 23	01, 14, 23	09, 25
May	09, 14, 25	03, 15, 19, 24	15, 25, 31	02, 09, 18	04, 27
Jun	01, 13, 26	02, 04	03, 05, 23	01, 10, 26	12, 28
Jul	01, 24, 30	11, 13	02, 12, 23	17, 28	14
Aug	02, 27	12, 19, 25	13, 22, 29	04, 18	31
Sep	03, 09, 16	10, 24, 27	5, 14, 30	05, 12, 19, 30	16
Oct	02, 11, 29	03, 10, 19, 26	16	07, 16, 23	02, 18
Nov	03, 19, 26	02, 11, 18, 27	01, 05, 14, 26	01	
Dec	05, 22, 31	04, 18, 27	05, 12, 26	03	

https://ladsweb.modaps.eosdis.nasa.gov/search/). Due to cloud coverage over time, the collected imageries were irregularly distributed. Moreover, for the HBV hydrological light model to estimate reference evapotranspiration (ET_0), the Penman–Monteith equation was used. Likewise, to estimate ETa in the spatial and temporal variability, the SEBS model developed by Su (2002) has been applied. The meteorological data used to estimate ETa in this RS model were recorded at 3:00 local time, which is near the time of satellite overpass (i.e., between 2:10 and 2:55 local time). Using the SEBS model, evaporation cannot be estimated for an entire twelve-month period because of cloud-free imageries that cannot be found during the rainy seasons. Accordingly, to calculate ETa for all day without satellite imagery, meteorological data and the Penman–Monteith equation were employed (Bastiaanssen and Bandara 2001; Immerzeel and Droogers 2008). For this purpose, meteorological data for 23 stations on wind speed, precipitation, relative humidity, and temperature were used. Then, using surface energy balance algorithms and MODIS images, the latent heat flux (λE) is calculated. For days when satellite imageries were obtainable, the values of surface resistance (r_s) were inversely determined by replacing λE in the Penman–Monteith equation. For days without satellite imagery r_s value was determined through the preceding imagery of r_s value with recorded daily weather data to all day within the consecutive imageries. The Penman–Monteith equation is given by:

$$\lambda E = \frac{\Delta\left(R_n - G_0\right) + \rho_a C_p \frac{\left(e_s - e_a\right)}{r_a}}{\Delta + \gamma\left(1 + \frac{r_s}{r_a}\right)} \tag{7}$$

where $(e_s - e_a)$ (kPa) is the vapor pressure deficit of the air, Δ (kPa/K) is the slope of the saturated vapor pressure curve, ρ_a (kg/m^3) is the moist air density, r_a, and r_s (s/m) are aerodynamic and surface resistances, respectively, and Υ (kPa/K) is the psychometric constant, and the remaining parameters are described in Eq. 1. To estimate Rn at a daily time, step G_0 is assumed to be zero, and sunshine hours can be used. The difference between ETa and ET_0 is controlled by r_s, which means the reference evapotranspiration lies above actual evapotranspiration, and r_s surpasses a particular minimum value (Bastiaanssen and Bandara 2001). Also, r_s can be explained concerning solar radiation, vapor pressure deficit, soil moisture, and air temperature (Jarvis 1976). For estimating all values in Eq. 1 except the aerodynamic and surface resistances, local daily measurements of wind speed, sunshine hours, minimum and maximum temperature, and relative humidity were obtained from the National Meteorological Agency of Ethiopia. Hence, for all days without satellite imagery, calculating daily values of r_a and r_s permits for ETa estimation.

From the evaporating surface to the air, the transfer of water vapor and heat can be determined by r_a and is written as:

$$r_a = \frac{\ln\left[\frac{\left(Z_m - d\right)}{Z_{om}} - \Psi_m\right] \ln\left[\frac{\left(Z_h - d\right)}{Z_{oh}} - \Psi_h\right]}{k^2 u_2} \tag{8}$$

where Z_m, d, and Z_h (m), respectively, are the height measurements of the wind speed, the zero displacements, and humidity. Z_{oh} and Z_{om} (m), respectively, are the roughness length governing heat and vapor transfer and the momentum transfer, uz is the wind speed at height z (m/s), k is the von Karman's constant (–), and Ψ_h and Ψ_m (–), respectively, are the stability correction functions for heat transport and momentum. The roughness for momentum can be calculated through an experimental relation suggested by Su et al. (2001) and is written as:

$$Z_{om} = 0.005 + 0.5\left(\frac{\mathrm{NDVI}}{\mathrm{NDVI}_{max}}\right)^{2.5} \tag{9}$$

To determine the value of Z_{oh}, the dimensionless quantity kB^{-1} has been developed through the relationship between roughness length for momentum and heat and vapor transfer. Brutsaert (1982) assigns a value of 2.3 for kB^{-1}. The equation reads

$$Z_{oh} = \frac{Z_{om}}{\exp\left(kB^{-1}\right)} \tag{10}$$

In this study, the estimated SEBS–ETa from Nesru et al. (2020) was used to taste the efficiency of remote sensing ETa in the HBV hydrological model. A detailed explanation and procedure for the estimated SEBS–ETa for the production of crops were described there.

Hydrological model

For the simulation of the streamflow using rainfall, potential evapotranspiration, and temperature as input, a modified version of the conceptual semi-distributed hydrological model was selected for this study, which is an HBV light model (Seibert 1996). This model uses sub-basins as the most fundamental units of hydrology. The distribution of lakes, forests, glaciers, open areas, and area elevation is also considered in the HBV model. The sub-basins are considered in the spatial variation of different properties, such as the physical properties or meteorological properties of the basin. The HBV model consists of six different routines; such routines are precipitation accounting routine representing snowmelt, rainfall, and snow accumulation; soil moisture routing where surface and overland flow and actual evapotranspiration are calculated as a function of actual storage of water; a quick

runoff routine representing river discharge, subsurface flow which is represented by the base flow routine; a transformation routine for flow attenuation and delay and a routing routine (Bergström 1992).

The aim of selecting this simplified version of the HBV model is due to comparatively low demand with low complexity for input data and produces better simulation results (Bergström and Forsman 1973). Meanwhile, there have been relatively large sub-catchments in the study area; the transformation function that smoothens the streamflow is not utilized. Even if there were well-known methods for estimation of potential evapotranspiration (Lindström et al. 1997; Merz and Blöschl 2004), the standard Penman–Monteith equation is employed for evaluation of potential evapotranspiration (Allen et al. 1998). The HBV light model was applied in the upper Omo-Gibe basin for each of the given four sub-catchments. Commonly, many years of data on flow, temperature, and precipitation for model calibration are needed for the application of hydrological modeling, but these data are not sufficiently available for all catchments worldwide (Etter et al. 2018). Nowadays, some studies have shown that calibration and validation analysis is carried out over a few years of data (Madsen 2000; Wagener et al. 2003; Rientjes et al. 2013b; Ha et al. 2018; Mohaideen and Varija 2018). For this study, depending on a separate sample test for the periods from January 1, 2000, to December 31, 2002, the model has been calibrated and verified for the periods from January 1, 2003, to December 31, 2004. Figure 3 shows the schematization of the HBV model structure.

General calibration criteria (objective function) Y has been used to test the overall model performance for simulating the behavior of observed streamflow (Akhtar et al. 2009), which combines the relative volume error (RVE) and the Nash–Sutcliffe efficiency coefficient (NSE) (Nash and Sutcliffe 1970). Compared to the measured data variance NSE calculates the relative magnitude of residual difference. NSE refers to the degree to which the plot of the simulated against observed data matches the one-to-one line. One parameter set may show good correlation according to the criterion of NSE but may imply a weak relationship for RVE and vice versa (Seibert 1999). A combination of values of these particular calibration criteria is difficult because various objective functions are not directly comparable. The equations of objective functions are written as:

$$Y = \frac{\mathrm{NSE}}{1 + |\mathrm{RVE}|} \tag{11}$$

$$\mathrm{NSE} = 1 - \frac{\sum_{i=1}^{n} \left(Q_{si} - Q_{oi}\right)^2}{\sum_{i=1}^{n} \left(Q_{0i} - \overline{Q_0}\right)^2} \tag{12}$$

$$\mathrm{RVE} = \frac{\sum_{i=1}^{N} \left(Q_{si} - Q_{oi}\right)}{\sum_{i=1}^{N} Q_{oi}} \tag{13}$$

In Eqs. (11)–(13) Q_s and Q_o are simulated and observed discharge, respectively, i is the time step, N is the total number of time steps, and $\overline{Q_0}$ is the mean of Q_o over the calibration or verification period. The efficiency value of RVE should be close to zero, and the value of Y and NSE should be close to 1 for satisfactory model performance. In addition that as stated by Bergström (1992), NSE values tend to one indicating a perfect fit for the simulation and observation value, while values approach zero, indicating that simulations are as poor or good as the constant value prediction, and also, the values less than zero indicate a very poor fit for the simulation and observation value. The value of Y ranges from 0 (meaning the model performs poorly) to 1 (meaning the model performs well), with typical values up to 0.6 considered poor to satisfactory and higher values indicating less error variance (Rientjes et al. 2013b).

In this study succeeding (Harlin and Kung 1992; Seibert 1999; Wagener et al. 2003; Choi and Beven 2007; Booij and Krol 2010), Monte Carlo simulation (MCS) procedure is employed for parameter optimization to four sub-catchments of the UOGB. In MCS, to evaluate the model performance, a multitude of parameter sets is generated and performed randomly. In the MCS approach, along with various simulations of the model, preeminent objective function values are selected by utilizing randomly generated parameters within the predefined space of the model parameter. Essential characteristics of MCS frameworks are the choice of the objective function(s), the determination of the number of simulations to be performed, the determination of prior parameter spaces, the choice of parameters for calibration, and choosing the likelihood distribution for the calibration parameters.

For calibration of the time series of actual daily evapotranspiration and daily streamflow, parameters have been estimated. Meanwhile, both ETa and Q are major water balance terms to the hydrological model matching each other directly affects one another. Winsemius et al. (2008) stated that estimated HBV-ETa through employing the lumped HBV model is representatives for the sub-catchment scale. To come to the corresponding estimates for comparison SEBS–ETa with HBV-ETa over the sub-catchments, all pixel estimate values are averaged. In order to support irrigation from river discharge channels, estimated ETa are used instead for water abstraction. Hence, for the calibration of the streamflow model, time series of streamflow at the catchment outlets has been used.

Two model calibration cases were defined for this study. The first case is the most common scenario where optimization and calibration of the model parameter are on

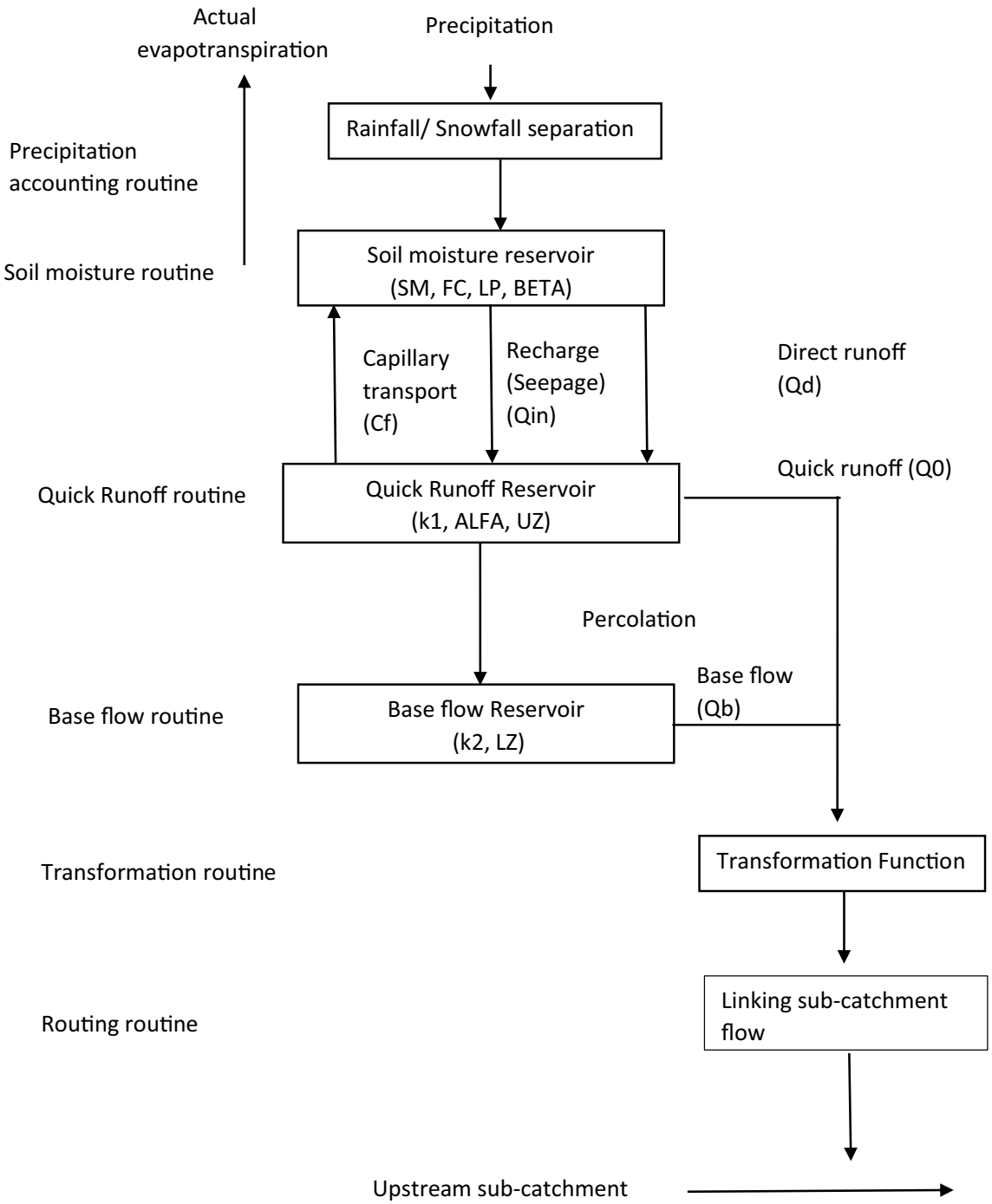

Fig. 3 The HBV hydrological model structure schematization (based on Lindström et al. 1997)

streamflow. Performance measures are merely applied to evaluate how well matches SEBS–ETa with HBV-ETa. In the last case, to optimize the parameter values in model calibration, both actual evapotranspiration and streamflow are used simultaneously. Preference-based objective functions are used for evaluating model performance, which simultaneously reduces the deviation between particular variables.

For HBV hydrological models the selection of sensitivity parameters was based on studies and simple manual sensitivity of Seibert (1997, 1999), Booij (2005), Götzinger and Bárdossy (2005), Wale et al. (2009), Booij and Krol (2010), and Deckers et al. (2010) for the degree-day procedure, for threshold temperature, and for melting factor. The parameters of the model and their prior ranges utilized in the MCS

procedure are shown in Table 2. For all sets of parameters, a uniform distribution has been assumed, and as defined by the values of parameter ranges, the values of parameters are arbitrarily drawn from the space of the variable.

Results and discussion

Time series patterns of actual evapotranspiration

For the given four major sub-catchments, the daily basis time series of SEBS–ETa values were constructed, as shown in Fig. 4.

From Fig. 4, the lowest values of ETa were observed during the wet season, which shows the planting and growing period of crop plants, while the highest values were observed during the dry season, which is due to the reduction of the upper part of the saturated zone.

For the best performing parameter set, the model output of average parameter values for the four major sub-catchments for the given two cases is given in Table 3.

Model calibration and validation on streamflow (case 1)

The simulation was initiated with the default parameter values. The streamflow hydrographs showed comparatively weak matching between the simulated and observed output values. The pairing denotes that when the HBV model is applied in regions other than it was calibrated, it requires

Table 2 Model parameters and their prior ranges used in the MCS procedure

Parameter	Description	Prior range	Unit
TT	Threshold temperature	− 1.5 to 2.5	°C
FC	Maximum soil moisture storage	100–600	mm
ALFA	Nonlinearity coefficient	0.1–0.4	–
BETA	A parameter that determines the relative contribution to runoff from rain or snow	1.0–1.2	–
Lp	Soil moisture value above which ETa reaches ETp	0.1–1.0	–
PERC	Maximal flow from upper to lower box	0.1–1.1	mm/d
*K*1	Recession coefficient (upper box)	0.01–0.1	1/d
*K*2	Recession coefficient (lower box)	0.001–0.15	1/d

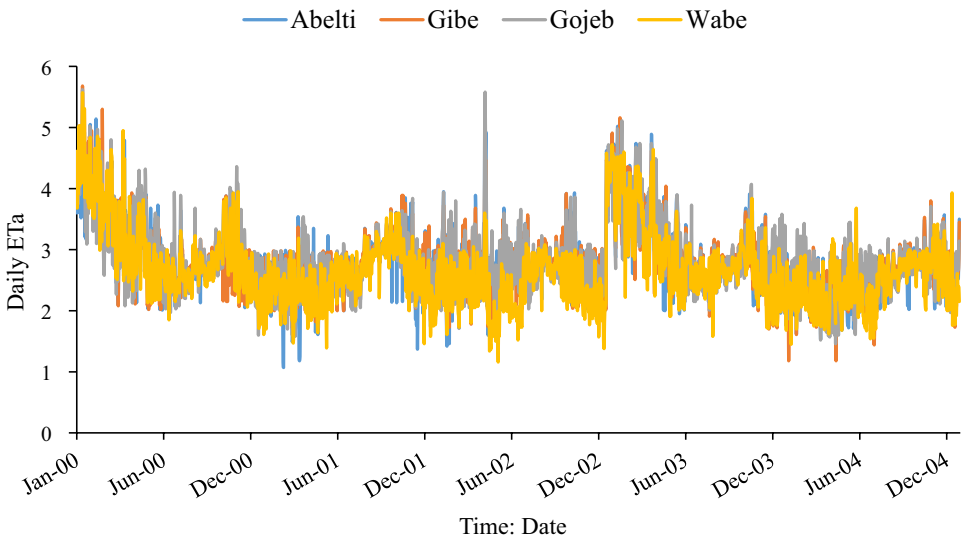

Fig. 4 Time series patterns of SEBS–ETa for the given four major sub-basins

Table 3 Average parameter values for the four major sub-catchments for the given two cases

Parameter	TT	FC	Lp	BETA	PERC	ALFA	*K*1	*K*2
mm	°C	mm	–	–	mm/d	–	1/d	1/d
Case 1	0	400	1	1	1	0	0.1	0.05
Case 2	0	600	1	1	1	0	0.01	0.15

a new calibration. Model calibration aims to improve the accuracy of the model predictions, which was performed in the sensitive HBV flow parameters that are already identified (Table 2) and are subject to minor changes to ensure a good correlation between the observed and the simulated flow. First, the most sensitive parameters are modified, employing a manual calibration process based on the information available in the literature. In this process, the values of the parameters have been iteratively changed within the appropriate ranges to increase the value of NSE (Eq. 12). Autocalibration processes that significantly improved model efficiency were then carried out using sensitive parameters that were defined during sensitivity analysis.

During the calibration step, the first year, i.e., from January 1, 2000, to December 31, 2000, was considered as a model warm-up period to establish proper initial conditions and to stabilize the model. Calibration was then performed for the next step. Commonly, the trial-and-error methods were used to calibrate the HBV light hydrological model (Bergström 1992). Therefore, when determining the calibration result, the subjectivity problem must be addressed. Typically during the calibration process to get good results from the model, the user will start from sensitive parameter values that gave good results in a similar catchment and try to maintain them within specific ranges. For example, in southern Sweden, Bergström (1990) found regional differences for the calibrated values of maximum soil moisture storage (FC). The results indicated that such regional differences occurred may be partially due to what the modeler expects. It begins with one value, and since very different FC values can produce good matches, it is possible to keep this value by adjusting certain parameters. With poorly defined parameters, depending on the start values and method of optimization, automated calibration methods will often point out to different sets of parameters, and the user decides to determine what parameter set to use (Kite and Kouwen 1992). The value of model performance indices obtained for daily streamflow predictions during the calibration and verification periods is summarized in Table 4.

Measured and simulated flows for daily time steps had a favorable comparison during all the four sub-basins (Table 4, Fig. 5). This is evident from the values of NSE varied from 0.79 to 0.97, RVE ranging from 0.06 to 0.48, and *Y* varied from 0.56 to 0.92. Overall, we can say the model performance is very good, consistently across calibration and validation in daily predictions. Figure 5 compares the daily simulated flows with observed daily flows for four sub-basins. It is indicated that simulated flows are consistently more than the observed flows. The simulated streamflow values are plotted against the observed streamflow values, and their distribution is approximately 1:1. During the calibration period for both higher and lower values of observed streamflow, the

Table 4 HBV model performance evaluation for daily streamflow prediction for the four major sub-basins

Model performance index	Calibration (01/01/2000–31/12/2002)				Validation (01/01/2003–31/12/2004)			
	Sub-basin							
	Abelti	Gibe	Gojeb	Wabe	Abelti	Gibe	Gojeb	Wabe
NSE	0.97	0.79	0.85	0.83	0.86	0.87	0.88	0.76
RVE	0.06	0.40	0.31	0.48	0.43	0.41	0.41	0.56
Y	0.92	0.57	0.63	0.56	0.60	0.62	0.62	0.49

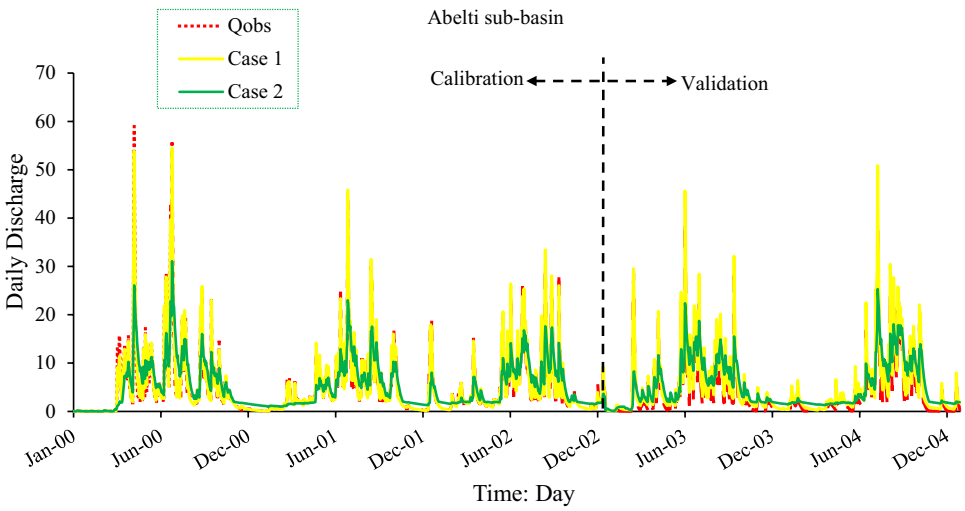

Fig. 5 Time series of observed and simulated daily streamflow for calibration and validation period for Jan 1, 2000–Dec 31, 2004, for Abelti sub-catchment

simulated streamflow is distributed uniformly along the 1:1 line. The mathematical comparison between the observed streamflow and the best simulation result showed a good agreement.

After the model is calibrated, validation of the model at the Omo-Gibe River Basin was performed for an independent dataset, which is different from the calibration periods without further modification of the calibrated parameters. The model has been found to have a good predictive capability with NSE, RVE, and a *Y* value ranging from 0.76 to 0.88, 0.41 to 0.56, and 0.49 to 0.62, respectively, for a daily basis. It has been shown that the parameters of the model in the catchment area represent the processes taking place to the best of their ability. The model validation outcomes for daily streamflow showed a good match between the simulated and the measured values. Through statistical model efficiency during the calibration process, the model performed well. Figure 5 shows the time series of simulated and observed daily streamflow calibration and verification for the Abelti sub-catchment. Therefore, HBV hydrological model can be used in basins having similar characteristics.

Similarly, the efficiency values for ETa were performed for the major four sub-catchments of the upper Omo-Gibe basin. Estimated and simulated ETa values for daily time steps had unfavorable comparisons during all of the four sub-basins (Table 5). Figure 6 shows the time series of observed and simulated daily ETa calibration and verification for the Abelti sub-catchment. The result indicates that the values of NSE varied from 0.18 to 0.28, RVE ranging from 0.05 to 0.08, and *Y* varied from 0.16 to 0.27. Likewise, in the verification periods, the model has been found to have a poor predictive capability with NSE, RVE, and a *Y* value ranging from 0.31 to 0.48, 0.04 to 0.09, and 0.28 to 0.51, respectively, for the daily basis. This suggested that the simulated HBV-ETa does not fit SEBS–ETa well.

Comparatively, some variations between SEBS–ETa and HBV-ETa were observed during the dry seasons, while during the rainy season, most of the estimated ETa values have the same result of the simulated ETa ones. During the dry season, this variation indicates that the HBV-ETa shows lower fluxes. Also, the results showed that as the HBV rainfall–runoff model helps to solve the water balance, the only consideration is on suitably balancing the streamflow. Furthermore, with relatively weak model performance values, the simulated ETa has not represented the estimated ETa well. Therefore, the overall model performance was not fulfilled the minimum values recommended in the literature during both the wet and dry seasons.

Evaluating the performance of SEBS–ETa using multi-variable (case 2)

In this case, multi-variable model calibration and verification were performed for both streamflow and ETa as similar

Table 5 HBV model performance evaluation for daily ETa prediction for the four major sub-basins

Model performance index	Calibration (01/01/2000–31/12/2002)				Validation (01/01/2003–31/12/2004)			
	Sub-basin							
	Abelti	Gibe	Gojeb	Wabe	Abelti	Gibe	Gojeb	Wabe
NSE	0.18	0.22	0.28	0.28	0.48	0.48	0.52	0.31
RVE	0.07	0.08	0.05	0.08	0.05	0.06	0.04	0.09
Y	0.17	0.20	0.27	0.26	0.46	0.46	0.51	0.28

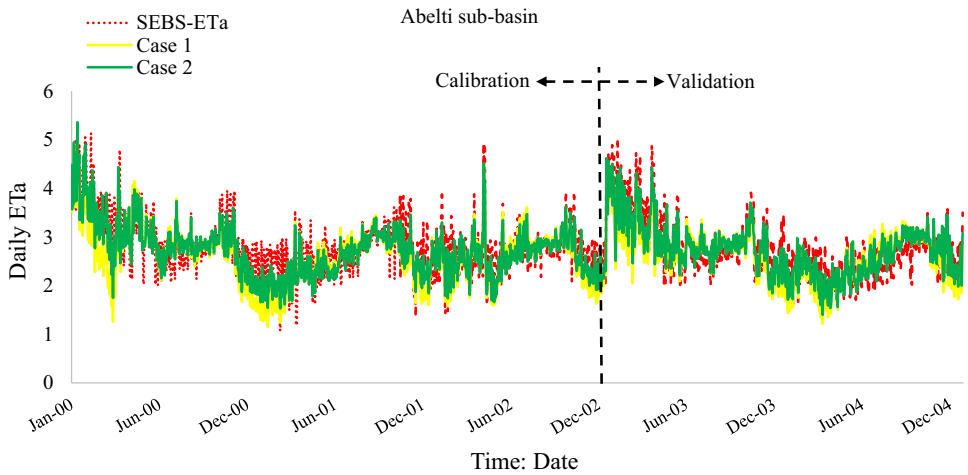

Fig. 6 Time series of observed and simulated daily ETa for calibration and validation period for Jan 1, 2000–Dec 31, 2004, for Abelti sub-catchment

to case 1 to test the effectiveness of SEBS–ETa and with that in mind to test the performance of HBV hydrological model. For both variables, the objective functions were optimized simultaneously and are presented in Table 6.

It was found that the model has a well analytical capability for streamflow with NSE, value ranging from 0.66 to 0.69 and 0.62 to 0.66, respectively, for calibration and verification. Additionally, calibration and verification values range from 0.04 to 0.45 and 0.40 to 0.54, respectively, for the objective function RVR. Also, for the objective function, *Y* values range from 0.50 to 0.67 and 0.42 to 0.47, respectively, for calibration and verification. Similarly, from the model, efficiency values for ETa for the major sub-catchments show that NSE varied from 0.56 to 0.60 and 0.64 to 0.73, RVE ranging from 0.02 to 0.04 and 0.01 to 0.04, and *Y* varied from 0.54 to 0.65 and 0.62 to 0.70, for the calibration and verification period, respectively.

The comparison was executed similarly with case 1 for both streamflow and ETa. From the result, it is shown that as compared to observed data for both streamflow and ETa, the recession and falling limbs were somewhat higher and lower, respectively, in the simulated data. This shows both streamflow and ETa were well represented in a reasonable match for recession and falling limbs. Also, the result shows a good fit for ETa during the wet and dry seasons. Furthermore, as compared to case 1, the results were much better, not only streamflow but also for ETa. This shows the effectiveness of multi-variable model calibration for SEBS–ETa. Overall the result demonstrated that the parameters of the model in the catchment area represent the processes taking place to the best of their ability.

Additionally, in this case, the hydrological catchment behaviors represented as required, and single-variable calibration constraints in case 1 were very weak. Moreover, the model verification outcomes, both for streamflow and for ETa, showed a good match between the simulated and measured values. The model performed well, though the statistical model efficiency measures are good during the calibration process. Furthermore, as shown from all maps, the simulations were below the observed value; this showed an underestimation of the simulated flow over the observed ones. The possibility of underestimating the streamflow may be due to the fact that, in such a complex terrain, rainfall is captured through 23 gauges, and the rainfall varies across the catchment from a minimum of 1019 mm to a maximum of greater than 1439 mm. Finally, the result suggested that the use of more than one water balance term in a hydrological model calibration was beneficial.

Parameter estimation and uncertainty of model parameters

In the HBV rainfall–runoff, model streamflow simulations are directly affected by PERC, *K*1, *K*2, and ALFA. Also, ETa simulation is directly affected by LP, while the other parameters like BETA and FC indirectly affect streamflow and ETa simulation. Generally, the spatial variability of the parameters is an indicator of the uncertainty of measurement data. For some parameters of the model, if the number of iteration increases as the spatial parameter increases, which means increased from the first iteration to second iteration, etc. (Parajka et al. 2007b). In the UOGB, the error caused by time series of measured precipitation and streamflow and estimated ETa affects the uncertainty of parameters of the model. In addition, as compared to rain gauge stations, the availability of streamflow gauging stations was small (i.e., four streamflow gauging stations). This shows that as well as streamflow gauging station, the rain gauge station is not spatially distributed well in the basin. The study area topography, elevation, and influences of cloud affect the accuracy and location of streamflow and rain gauge stations.

Table 6 Efficiency evaluation for daily streamflow and ETa prediction for the four major sub-basins

Variables	Sub-catchment	Performance index					
		Calibration period (01/01/2000–31/12/2002)			Validation period (01/01/2003–31/12/2004)		
		NSE	RVE	Y	NSE	RVE	Y
Streamflow (*Q*)	Abelti	0.69	0.04	0.67	0.68	0.40	0.46
	Gibe	0.68	0.37	0.49	0.66	0.38	0.47
	Gojeb	0.66	0.28	0.52	0.62	0.38	0.45
	Wabe	0.68	0.45	0.47	0.65	0.54	0.42
Actual evapotranspiration	Abelti	0.56	0.03	0.54	0.70	0.01	0.69
	Gibe	0.60	0.04	0.58	0.72	0.03	0.70
	Gojeb	0.66	0.02	0.65	0.73	0.01	0.72
	Wabe	0.66	0.04	0.64	0.64	0.40	0.62

Conclusions

In this study, the conceptual semi-distributed HBV light rainfall–runoff hydrological model was selected and used for calibration and verification based on multi-variable evaluation using streamflow and ETa to test the efficiency of SEBS–ETa in UOGB, Ethiopia. Based on MCS, the model was calibrated and validated in two different cases using more than a single variable (i.e., streamflow and ETa). The performance and applicability of HBV light were successfully evaluated through sensitivity analysis, model calibration, and verification, and reproducing simulated streamflow and ETa. Also, the efficiency of SEBS–ETa using the HBV hydrological model was assessed. The study showed that surface and subsurface water model parameters are sensitive and have physical meaning, especially the FC, LP, BETA, PERC, ALPHA, $K1$, and $K2$ were the most sensitive parameters with regard to streamflow and ETa prediction in the UOGB.

In the first scenario, the calibration and validation process is carried out for HBV hydrological model to verify whether or not the model is applicable in the study area. For calibration and validation of the model, the consideration was only in the streamflow, and the objective function NSE, RVR, and Y for daily ETa show low-performance values (less than satisfactory) for SEBS–ETa. Though the model performance of the HBV for simulating streamflow in the UOGB was very good, this shows the model has relatively high confidence and gives a very good result for the case of streamflow only. Moreover, the simulated streamflow peak was well represented in all of the days.

In the second scenario, the aim is to test the efficiency of SEBS–ETa in the study area and with that in mind to test the performance of the HBV hydrological model. For calibration and validation purposes, the consideration was given to both in streamflow and in satellite-based ETa in multi-variable model calibration. The result shows satisfactory to good performance for SEBS–ETa as well as streamflow. At the same time, the model was well simulated for both streamflow and ETa on the rising and falling limbs of the streamflow and ETa hydrograph during calibration and verification periods. However, the streamflow and ETa peak were represented well and slightly underestimated the peaks for some days. Additionally, the objective function's result shows satisfactory to good performance values contrary to a single-variable calibration for both streamflow and ETa.

For model calibration and verification, the efficiency of the use of satellite-based ETa was confirmed. However, to reproduce the best outcomes from the model for water balance in the catchment during model calibration and verification uses of a combination of streamflow with estimated ETa should be necessary. Therefore, to provide reasonable solutions to reproduce and close the water balance in the catchment, it is required to use the preferred multi-variable calibration method. Moreover, the HBV hydrological model can be used in other basins having similar characteristics.

References

Akhtar M, Ahmad N, Booij MJ (2009) Use of regional climate model simulations as input for hydrological models for the Hindukush–Karakorum–Himalaya region. Hydrol Earth Syst Sci 13:1075–1089

Allen RG, Pereira LS, Raes D, Smith M (1998) Crop evapo-transpiration guidelines for computing crop water requirements. FAO irrigation and drainage paper no. 56. Food and Agriculture Organization of the United Nations, Rome, Italy. https://doi.org/10.1016/j.eja.2010.12.001

Bastiaanssen WGM, Bandara KMPS (2001) Evaporative depletion assessments for irrigated watersheds in Sri Lanka. Irrig Sci 21(1):1–15. https://doi.org/10.1007/s002710100046

Bergström S (1990) Parameter values for the HBV model in Sweden, in Swedish. SMHI Hydrolog Nr28

Bergström S (1992) The HBV model—its structure and application. SMHI RH 4, Norrkoping

Bergström S, Forsman A (1973) Development of a conceptual deterministic rainfall–runoff-model, vol 4. Munksgaard, Copenhagen

Beven K, Freer J (2001) Equifinality, data assimilation, and uncertainty estimation in mechanistic modelling of complex environmental systems using the GLUE methodology. J Hydrol 249(2):11–29. https://doi.org/10.1080/00343404.2011.553520

Booij MJ (2005) Impact of climate change on river flooding assessed with different spatial model resolutions. J Hydrol 303(1–4):176–198. https://doi.org/10.1016/j.jhydrol.2004.07.013

Booij MJ, Krol MS (2010) Balance between calibration objectives in a conceptual hydrological model. Hydrol Sci J 55(6):1017–1032. https://doi.org/10.1080/02626667.2010.505892

Boulet G, Kerr Y, Chehbouni A, Kalma JD (2002) Deriving catchment-scale water and energy balance parameters using data assimilation based on extended Kalman filtering. Hydrol Sci J 47(3):449–467. https://doi.org/10.1080/02626660209492946

Brutsaert W (1982) Evaporation to the atmosphere theory, history, and application. D. Reidel Publishing Co., Boston

Campo L, Caparrini F, Castelli F (2006) Use of multi-platform, multi-temporal remote-sensing data for calibration of a distributed hydrological model: an application in the Arno basin, Italy. Hydrol Process 20(13):2693–2712. https://doi.org/10.1002/hyp.6061

Carrera J, Neuman SP (1986) Estimation of aquifer parameters under transient and steady state conditions. Water Resour Res 22(2):199–210

Chen JM, Chen X, Ju W, Geng X (2005) Distributed hydrological model for mapping evapotranspiration using remote sensing inputs. J Hydrol 305(1–4):15–39. https://doi.org/10.1016/j.jhydrol.2004.08.029

Choi HT, Beven K (2007) Multi-period and multi-criteria model conditioning to reduce prediction uncertainty in an application of TOPMODEL within the GLUE framework. J Hydrol 332(3–4):316–336. https://doi.org/10.1016/j.jhydrol.2006.07.012

Crow WT, Wood EF, Pan M (2003) Multiobjective calibration of land surface model evapotranspiration predictions using streamflow observations and spaceborne surface radiometric

temperature retrievals. J Geophys Res 108(23):1–12. https://doi.org/10.1029/2002JD003292
De Vos NJ, Rientjes THM, Gupta HV (2010) Diagnostic evaluation of conceptual rainfall–runoff models using temporal clustering. Hydrol Proces 24(20):2840–2850. https://doi.org/10.1002/hyp.7698
Deckers DLEH, Booij MJ, Rientjes TM, Krol MS (2010) Catchment variability and parameter estimation in multi-objective regionalisation of a rainfall–runoff model. Water Resour Manag 24(14):3961–3985. https://doi.org/10.1007/s11269-010-9642-8
Downer CW, Ogden FL (2003) Prediction of runoff and soil moistures at the watershed scale: effects of model complexity and parameter assignment. Water Resour Res 39(3):1–13. https://doi.org/10.1029/2002WR001439
Etter S, Strobl B, Seibert J, Ilja Van Meerveld HJ (2018) Value of uncertain streamflow observations for hydrological modelling. Hydrol Earth Syst Sci 22(10):5243–5257. https://doi.org/10.5194/hess-22-5243-2018
Fenicia F, Zhang GP, Rientjes T, Hoffman L, Pfiste L, Savenije HHG (2005) Numerical simulations of runoff generation with surface water–groundwater interactions in the Alzette river alluvial plain (Luxembourg). Phys Chem Earth 30(4–5):277–284. https://doi.org/10.1016/j.pce.2004.11.001
Franks SW, Beven KJ (1997) Bayesian estimation of uncertainty in land surface-atmosphere flux predictions. J Geophys Res 102(D20):23991–23999
Götzinger J, Bárdossy A (2005) Advances in geosciences integration and calibration of a conceptual rainfall–runoff model in the framework of a decision support system for river basin management. Adv Geosci 5:31–35
Gupta HV, Sorooshian S, Yapo PO (1998) Toward improved calibration of hydrologic models: multiple and noncommensurable measures of information. Water Resour Res 34(4):751–763
Gupta HV, Bastida LA, Sorooshian S, Shuttleworth WJ, Yang ZL (1999) Parameter estimation of a land surface scheme using multicriteria methods. J Geophys Res 104(16):19491–19503
Gupta HV, Wagener T, Liu Y (2008) Reconciling theory with observations: elements of a diagnostic approach to model evaluation. Hydrol Proces 22(18):3802–3813. https://doi.org/10.1002/hyp
Ha LT, Bastiaanssen WGM, van Griensven A, van Dijk AIJM, Senay GB (2018) Calibration of spatially distributed hydrological processes and model parameters in SWAT using remote sensing data and an auto-calibration procedure: a case study in a Vietnamese river basin. Water 10(212):1–21. https://doi.org/10.3390/w10020212
Haile AT, Habib E, Rientjes T (2013) Evaluation of the climate prediction center (CPC) morphing technique (CMORPH) rainfall product on hourly time scales over the source of the Blue Nile River. Hydrol Proces 27(12):1829–1839. https://doi.org/10.1002/hyp.9330
Harlin J, Kung C (1992) Parameter uncertainty and simulation of design floods in Sweden. J Hydrol 137(1–4):209–230
Hartanto IM, van der Kwast J, Alexandridis TK, Almeida W, Song Y, van Andel SJ, Solomatine DP (2017) Data assimilation of satellite-based actual evapotranspiration in a distributed hydrological model of a controlled water system. Int J Appl Earth Obs Geoinf 57:123–135. https://doi.org/10.1016/j.jag.2016.12.015
Herman MR, Nejadhashemi AP, Abouali M, Hernandez-Suarez JS, Daneshvar F, Zhang Z, Sharifi A (2018) Evaluating the role of evapotranspiration remote sensing data in improving hydrological modeling predictability. J Hydrol 556:39–49. https://doi.org/10.1016/j.jhydrol.2017.11.009
Hollenbeck KJ, Schmugge TJ, Hornberger GM, Wang JR (1996) Identifying soil hydraulic heterogeneity by detection of relative change in passive microwave remote sensing observations. Water Resour Res 32(1):139–148. https://doi.org/10.1029/95WR02916
Immerzeel WW, Droogers P (2008) Calibration of a distributed hydrological model based on satellite evapotranspiration. J Hydrol 349(3–4):411–424. https://doi.org/10.1016/j.jhydrol.2007.11.017
Immerzeel WW, Gaur A, Zwart SJ (2008) Integrating remote sensing and a process-based hydrological model to evaluate water use and productivity in a south Indian catchment. Agric Water Manag 95:11–24. https://doi.org/10.1016/j.agwat.2007.08.006
Islam MM, Sado K (2002) Development priority map for flood countermeasures by remote sensing data with geographic information system. J Hydrol Eng 7(5):346–355. https://doi.org/10.1061/(ASCE)1084-0699(2002)7:5(346)
Jarvis PG (1976) The interpretation of the variations in leaf water potential and stomatal conductance found in canopies in the field. Philos Trans R Soc Lond B Biol Sci 273(927):593–610. https://doi.org/10.1098/rstb.1976.0035
Jia L, Xi G, Liu S, Huang C, Yan Y, Liu G (2009) Regional estimation of daily to annual regional evapotranspiration with MODIS data in the Yellow River Delta wetland. Hydrol Earth Syst Sci 13(10):1775–1787
Khu S, Madsen H, di Pierro F (2008) Incorporating multiple observations for distributed hydrologic model calibration: an approach using a multi-objective evolutionary algorithm and clustering. Adv Water Resour 31(10):1387–1398. https://doi.org/10.1016/j.advwatres.2008.07.011
Kim G, Barros AP (2002) Space-time characterization of soil moisture from passive microwave remotely sensed imagery and ancillary data. Remote Sens Environ 81(2–3):393–403. https://doi.org/10.1016/S0034-4257(02)00014-7
Kim KB, Kwon HH, Han D (2018) Exploration of warm-up period in conceptual hydrological modelling. J Hydrol 556:194–210. https://doi.org/10.1016/j.jhydrol.2017.11.015
Kite GW, Kouwen N (1992) Watershed modeling using land classifications. Water Resour Res 28(12):3193–3200. https://doi.org/10.1029/92WR01819
Kustas WP, Daughtry CST (1990) Estimation of the soil heat flux/net radiation ratio from spectral data. Agric For Meteorol 49(3):205–223
Legates DR, McCabe GJ Jr (1999) Evaluating the use of "goodness-of-fit" measures in hydrologic and hydroclimatic model validation. Water Resour Res 35(1):233–241
Lindström G, Johansson B, Persson M, Gardelin M, Bergström S (1997) Development and test of the distributed HBV-96 hydrological model. J Hydrol 201(1–4):272–288. https://doi.org/10.1016/S0022-1694(97)00041-3
Madsen H (2000) Automatic calibration of a conceptual rainfall–runoff model using multiple objectives. J Hydrol 235(3–4):276–288
Madsen H (2003) Parameter estimation in distributed hydrological catchment modelling using automatic calibration with multiple objectives. Adv Water Resour 26(2):205–216
Mccabe MF, Franks SW, Kalma JD (2005) Calibration of a land surface model using multiple data sets. J Hydrol 302(1–4):209–222. https://doi.org/10.1016/j.jhydrol.2004.07.002
Meixner T, Bastidas LA, Gupta HV, Bales RC (2002) Multicriteria parameter estimation for models of stream chemical composition. Water Resour Res 38(3):1–9
Merz R, Blöschl G (2004) Regionalisation of catchment model parameters. J Hydrol 287:95–123. https://doi.org/10.1016/j.jhydrol.2003.09.028
Mohaideen MMD, Varija K (2018) Improved vegetation parameterization for hydrological model and assessment of land cover change impacts on flow regime of the upper Bhima basin, India. Acta Geophys 66:697–715. https://doi.org/10.1007/s11600-018-0161-y
Monteith JL (1973) Principles of Environmental Physics. Edward Arnold Press, London
Montzka C, Canty M, Kunkel R, Menz G, Vereecken H, Wendland F (2008) Modelling the water balance of a mesoscale catchment

basin using remotely sensed land cover data. J Hydrol 353(3–4):322–334. https://doi.org/10.1016/j.jhydrol.2008.02.018
Muthuwatta LP, MudD A, Bos MG, Rientjes THM (2010) Assessment of water availability and consumption in the Karkheh river basin, Iran-using remote sensing and geo-statistics. Water Resour Manag 24(3):459–484. https://doi.org/10.1007/s11269-009-9455-9
Nash J, Sutcliffe J (1970) River flow forecasting through conceptual models part I—a discussion of principles. J Hydrol 10:282–290
Nesru M, Nagaraj MK, Shetty A (2020) Assessment of consumption and availability of water in the upper Omo-Gibe basin, Ethiopia. Arab J Geosci 13(13):1–11
Ouillon S, Forget P, Froidfond JM, Naudin JJ (1997) Estimating suspended matter concentrations from SPOT data and from field measurements in the Rhone river plume. MTS J 31(2):15–20
Parajka J, Merz R, Bloschl G (2007a) Uncertainty and multiple objective calibration in regional water balance modelling: case study in 320 Austrian catchments. Hydrol Process 21(4):435–446. https://doi.org/10.1002/hyp.6253
Parajka J, Bloschl G, Merz R (2007b) Regional calibration of catchment models: potential for ungauged catchments. Water Resour Res 43(6):1–16. https://doi.org/10.1029/2006WR005271
Poméon T, Diekkrüger B, Kumar R (2018) Computationally efficient multivariate calibration and validation of a grid-based hydrologic model in sparsely gauged West African river basins. Water 10(10):1–26. https://doi.org/10.3390/w10101418
Qin C, Jia Y, Su Z, Zhou Z, Qiu Y, Suhui S (2008) Integrating remote sensing information into a distributed hydrological model for improving water budget predictions in large-scale basins through data assimilation. Sensors 8(7):4441–4465. https://doi.org/10.3390/s8074441
Refsgaard JC (1997) Parameterisation, calibration and validation of distributed hydrological models. J Hydrol 198(1–4):69–97. https://doi.org/10.1016/S0022-1694(96)03329-X
Rientjes THM, Muthuwatta LP, Bos MG, Booij MJ, Bhatti HA (2013a) Multi-variable calibration of a semi-distributed hydrological model using streamflow data and satellite-based evapotranspiration. J Hydrol 505:276–290. https://doi.org/10.1016/j.jhydrol.2013.10.006
Rientjes T, Tamiru A, Almaw A (2013b) Diurnal rainfall variability over the Upper Blue Nile Basin: a remote sensing based approach. Int J Appl Earth Obs Geoinf 21:311–325. https://doi.org/10.1016/j.jag.2012.07.009
Romanowicz RJ, Osuch M, Grabowiecka M (2013) On the choice of calibration periods and objective functions: a practical guide to model parameter identification. Acta Geophys 61(6):1477–1503. https://doi.org/10.2478/s11600-013-0157-6
Seibert J (1996) HBV light version 2 user's manual. Stockholm University, Department of Physical Geography and Quaternary Geology, Stockholm, p 32
Seibert J (1997) Estimation of parameter uncertainty in the HBV model. Nord Hydrol 28(4/5):247–262
Seibert J (1999) Regionalisation of parameters for a conceptual rainfall–runoff model. Agric For Meteorol 98:279–293
Shafii M, Tolson B, Matott LS (2014) Uncertainty-based multi-criteria calibration of rainfall–runoff models: a comparative study. Stoch Environ Res Risk Assess 28(6):1493–1510. https://doi.org/10.1007/s00477-014-0855-x
Stisen S, Jensen KH, Sandholt I, Grimes DIF (2008) A remote sensing driven distributed hydrological model of the Senegal River basin. J Hydrol 354(1–4):131–148. https://doi.org/10.1016/j.jhydrol.2008.03.006
Su Z (2002) The surface energy balance system (SEBS) for estimation of turbulent heat fluxes. Hydrol Earth Syst Sci 6(1):85–99. https://doi.org/10.5194/hess-6-85-2002
Su Z, Schmugge T, Kustas WP, Massman WJ (2001) An evaluation of two models for estimation of the roughness height for heat transfer between the land surface and the atmosphere. J Appl Meteorol 40(11):1933–1951. https://doi.org/10.1175/1520-0450(2001)040%3c1933:AEOTMF%3e2.0.CO;2
Tait AB, Hall DK, Foster JL, Armstrong RL (2000) Utilizing multiple datasets for snow-cover mapping. Remote Sens Environ 72(1):111–126. https://doi.org/10.1016/S0034-4257(99)00099-1
Wagener T, Boyle DP, Lees MJ, Wheater HS, Gupta HV, Sorooshian S (2001) A framework for development and application of hydrological models. Hydrol Earth Syst Sci 5(1):13–26. https://doi.org/10.5194/hess-5-13-2001
Wagener T, Mcintyre N, Lees MJ, Wheater HS, Gupta HV (2003) Towards reduced uncertainty in conceptual rainfall–runoff modelling: dynamic identifiability analysis. Hydrol Proces 17(2):455–476. https://doi.org/10.1002/hyp.1135
Wale A, Rientjes THM, Gieske ASM, Getachew HA (2009) Ungauged catchment contributions to Lake Tana' s water balance. Hydrol Process 23(26):3682–3693. https://doi.org/10.1002/hyp
Wang Y, Li X (2011) Sensible heat flux estimation using surface energy balance system (SEBS), modis products, and NCEP reanalysis data. In: International geoscience and remote sensing symposium (IGARSS), no 1, pp 4269–4272. https://doi.org/10.1109/igarss.2011.6050174
Wang J, Price KP, Rich PM (2001) Spatial patterns of NDVI in response to precipitation and temperature in the central Great Plains. Int J Remote Sens 22(18):3827–3844. https://doi.org/10.1080/01431160010007033
Winsemius HC, Savenije HHG, Bastiaanssen WGM (2008) Constraining model parameters on remotely sensed evaporation: justification for distribution in ungauged basins? Hydrol Earth Syst Sci 12:1403–1413
Wu X, Zhou J, Wang H, Li Y, Zhong B (2015) Evaluation of irrigation water use efficiency using remote sensing in the middle reach of the Heihe river, in the semi-arid Northwestern China. Hydrol Process 29(9):2243–2257. https://doi.org/10.1002/hyp.10365
Yapo PO, Gupta HV, Sorooshian S (1998) Multi-objective global optimization for hydrologic models. J Hydrol 204(1–4):83–97
Zhao J, Chen X, Zhang J, Zhao H, Song Y (2019) Higher temporal evapotranspiration estimation with improved SEBS model from geostationary meteorological satellite data. Sci Rep 9(1):1–15. https://doi.org/10.1038/s41598-019-50724-w
Zhong L, Xu K, Ma Y, Ziyu H, Wang X, Ge N (2019) Evapotranspiration estimation using surface energy balance system model: a case study in the Nagqu River Basin. Atmosphere 10(268):1–13. https://doi.org/10.3390/atmos10050268

Acta Geophysica (2020) 68:553–563
https://doi.org/10.1007/s11600-020-00419-y

RESEARCH ARTICLE - HYDROLOGY

Simulating Caspian Sea surface water level by artificial neural network and support vector machine models

M. R. Khaledian[1,2] · M. Isazadeh[3] · S. M. Biazar[3] · Q. B. Pham[4]

Received: 3 December 2019 / Accepted: 7 March 2020 / Published online: 17 March 2020

Abstract

Reduction in sea water level can make services in nearshore structures difficult, and sea water level rise increases the risk to residential areas or the surrounding fields. For strategic planning, it is vital to take into account the present and future fluctuations of Caspian Sea water level. In this study, support vector machine and artificial neural network are used to estimate water level of the Caspian Sea. A 34-year period dataset is used as input data for water level on the scale based at Anzali, Iran. Performances of these two models are compared according to some statistical indices. Results of this study indicate that support vector machine with an error of 4.782 mm and $r = 0.96$ simulated the time series better, as compared with artificial neural network with an error of 5.014 mm and $r = 0.957$; furthermore, the uncertainty of this model is lower than that of the artificial neural network, i.e., 0.04 verses 0.22.

Keywords Anzali · Kernel function · Uncertainty

Introduction

Caspian Sea, as the biggest lake in the world, plays its role as a sensor which reflects all hydro-climatic changes in its basin with its sea level fluctuation (Aladin and Plotnikov 2004). Sea level indicates the groundwater levels in the low land coastal areas (Meyer 1989) as well as hydraulic regime of coastal rivers (Thain et al. 2004). Therefore, accurate prediction of sea level in coastal engineering and hydrological studies is needed. Besides, when agricultural lands are located along rivers and in deltas or coastal areas, sea level may temporarily restrict water from draining away. Recently, researchers have used past data to predict sea level changes instead of inputs related to environmental factors (Imani et al. 2014a). Artificial intelligence methods that are used most recently to predict sea level have the ability to fill information gaps and also estimate future values without the need for long-term and extensive observed information (Lee et al. 2007; Makarynska et al. 2009). In fact, the above-mentioned are advantages of intelligent methods in analyzing and predicting sea level.

Many studies have been conducted to estimate sea level with different methods. Ramezani Mouzirji et al. (2011) estimated Caspian Sea water level with fuzzy prediction system. They used a combination of statistical techniques and fuzzy systems for predicting changes in Caspian Sea level fluctuation. They could forecast Caspian Sea level for a 10-year oncoming period. Their results showed that Caspian Sea water level would rise in the future; in fact, in the next few years, Caspian Sea water level would drop initially and then would come up again. In the 10-year forecast period, the minimum level would be – 26.45 m in year 2015, and the maximum levels would be – 26.32 m in years 2017–2011. Rajaei and Shahabi (2014) used wavelet-ANN (artificial neural network) hybrid model to predict short-term changes in Oman sea level in Chabahar port. They evaluated the performance of the combination of ANN and wavelet model to predict short-term sea level fluctuations. Results of this method were compared with those of ANNs and regression models. The results showed the superiority of wavelet-ANN combination outputs compared to the other two

✉ M. R. Khaledian
mkh572000@yahoo.com

[1] Water Engineering Department, University of Guilan, Rasht, Iran

[2] Department of Water Engineering and Environment, Caspian Sea Basin Research Center, 4199613776 Rasht, Iran

[3] Department of Water Engineering, University of Tabriz, Tabriz, Iran

[4] Department of Hydraulic and Ocean Engineering, National Cheng-Kung University, Tainan 701, Taiwan

methods. Makarynska and Makarynska (2008) forecasted sea level in Cocos Islands (Keeling) in India. They used ANN to predict water level in case of danger from one hour to five days using hourly observed data from a tide gauge. They used a 3-layer feed-forward ANN. Results showed that the ANNs had an appropriate performance. Sertel et al. (2008) estimated daily mean sea level height by applying ANNs. They employed five different methods, namely least square of sea level, nonlinear regression, and three different algorithms of ANNs including feed-forward propagation, radial basis function, and generalized regression. They used observed data from a tide gauge in Newlin from January 1991 to December 2005. Results showed that feed-forward propagation model was better than other models. Ghorbani et al. (2010) predicted sea level by genetic programming and compared results with those of ANNs. In that study, genetic programming model was used to predict future changes in sea level for four time steps, namely 12-h, 24-h, 5-day, and 10-day intervals. A comparison of the two models showed that both of them had favorable performances. Karimi et al. (2013) predicted sea level in Darwin Harbour, Australia, by employing neuro-fuzzy and ANNs models. Hourly sea level changes as well as multiple-linear regression were used to select the optimal input combination. They compared results of both ANNs and neuro-fuzzy model with the optimized ARMA model. Results showed that ANNs and neuro-fuzzy model had similar performance, and their results were better than those of ARMA model. Imani et al. (2014b) forecasted Caspian Sea level by employing satellite altimetry data (June 1992–December 2013) based on evolutionary support vector regression algorithms and gene expression programming. They evaluated performances of these two methods. Results indicated that the performance of evolutionary support vector regression algorithm was excellent. Kisi et al. (2015) evaluated daily water level changes in Urmia Lake by using a hybrid of SVM with firefly algorithm. Results of the selected algorithm were compared with those of both genetic programming and ANNs. Results showed that the performance of the selected algorithm was better than those of other two models in predicting Urmia Lake water level.

The use of mean values is one of the innovations of this article because the use of mean and month number reduces the periodic effects of inlet flows to the lake and consequently the periodicity of the lake surface level. Awchi (2014) and Ghorbani et al. (2016) also used the same method.

With respect to the literature, this study attempts to estimate water level of Caspian Sea by SVM and ANN. For more accurate assessment of performances of both models, SVM with three kernel functions and ANNs with 1–20 neurons in the hidden layer are evaluated. One of the most important factors in modeling is the type and the number of model input, whereas in this study, the gamma test is used to select the type and number of model input. In addition, according to other studies, effects of month's index and average monthly index of water level on model performances are evaluated. In the next step, the uncertainty of both models for the determined combinations is evaluated. Finally, the best model and input combination to estimate Caspian Sea level are determined.

Materials and methods

In this study, data used to estimate sea water level are registered in Anzali station. Statistical parameters of time series are listed in Table 1. The dataset is divided into two parts: training and test parts. Indeed, 80% of sea water level data is used for training and 20% is used for test.

Data were standardized before entering the model according to Isazadeh et al. (2017); Deo et al. (2018); Ashrazfzadeh et al. (2019): Naganna et al. (2019): Aghelpour et al. (2019).

Artificial neural network (ANNs)

ANNs are data processing techniques that are essentially a collection of basic processing components of input, output, and generally one or more concealed layers. Although there are different types of neural network architectures, about 90% of them are the feed-forward type (Coulibaly et al. 2000; Li et al. 2019; Aghelpour et al. 2019). The perceptron, the very basic form of an artificial neural network, is a binary classifier and can be described using the following equation:

$$f(z) = \begin{cases} 1 \text{ if } z = w \times X + b > 0 \\ 0 \text{ otherwise} \end{cases} \quad (1)$$

Table 1 Statistical characteristics of the input and output data

Data	Statistical indices					
	Minimum	Average	Maximum	Standard deviation	Skewness	Kurtosis
Total	− 138.00	− 32.58	52.00	47.17	− 0.78	− 0.60
Calibration	− 138.00	− 36.75	52.00	51.22	− 0.55	− 1.10
Validation	− 47.20	− 15.84	22.20	16.58	0.06	− 0.57

where *f(z)* is the heaviside step function (a hard-limit activation function), *w,* the weight vector, and *b*, the bias, are the parameters of the perceptron, and *X* is the input vector. MLP networks learn to simulate the behavior of a complex and nonlinear system through learning algorithms and observed data. Learning algorithms, such as back-propagation (Rumelhart et al. 1988), delta-bar-delta (Jacobs 1988), quickprop (Fombellida and Destiné 1992), conjugate gradient (Charalambous 1992), and Levenberg–Marquardt (Hagan and Menhaj 1994; Deo et al. 2018), are commonly used to find an optimal set of parameters of MLP models. In this study, the MLP model was used with the Levenberg–Marquardt learning algorithm. One to 20 neurons were used in the hidden layer to assess the effect of network structure on its performance in simulating the saline water evaporation. A sigmoid tangent function was utilized to map information from the input layer onto the hidden layer and from hidden layers onto the output layer (Lagos-Avid and Bonilla 2017; Naganna et al. 2019). Seventy percent of data were used for the training period and 20% for the testing period.

Support vector machine

SVM is a popular technique for pattern recognition, classification, regression, and function approximation (Vapnik et al. 1997; Dibike et al. 2001). Vapnik et al. (1997) introduced SVMs for dividing a set of vectors into two classes. SVMs are based on a hyperplane in the form of $w.X + b = 0$ that optimally separates a set of *n*-dimensional vectors ($X_i \in R^n$) into two categories. This optimal hyperplane has the farthest distance from support vectors and the nearest data points from each class. Finding *w* is equivalent to solving a quadratic programming problem. To solve this problem, a trade-off parameter ($c > 0$) needs to be determined. To categorize vectors that are not linearly separable, a kernel function such as degree-d polynomial, radial basis, or hyperbolic tangent and Linear is used to map the observed multidimensional vectors to a space with higher dimensions (Ashrafzadeh et al. 2019; Choubin et al. 2019).

The first application of this method to water problems was proposed by Dibike et al. (2001) to simulate runoff. The support vector machine is an efficient learning system based on bounded optimization theory that utilizes the principle of structural error minimization and results in an optimal solution (Dibike et al. 2001). Figure 1 shows the structure of the support vector machine. In the SVM regression model, a function related to the dependent variable *y*, which is itself a function of several independent variables *x*, is estimated. Like other regression problems, it is assumed to determine the relationship between independent and dependent variables with an algebraic function such as *f*(*x*) plus some perturbation (permissible error 1).

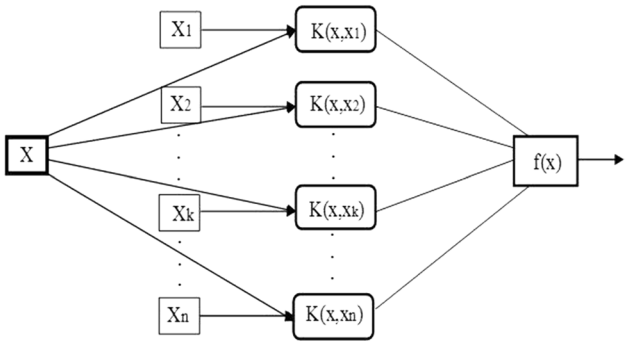

Fig. 1 Structure of support vector machine (*x*: input vector, *x*1 − *xn*: support vector, *K*(*x*, × 1) − *K*(*x*, *xn*): kernel function, *f*(*x*): output)

$$f(x) = W^{\mathrm{T}}.\emptyset(x) + b \tag{2}$$

$$y = f(x) + \text{noise} \tag{3}$$

If *W* is the vector of the coefficients *a* and *b* of the features of the regression function as well as the control function, then the objective is to find a functional form for *f*(*x*). This is accomplished by calibrating the SVM model by a set of samples (calibration set). This procedure involves sequential optimization of the error function. Depending on the definition of this error function, two types of SVM models are defined: type I regression SVM (also known as ε-SVM regression); type II regression SVM (also known as regression ν-SVM). It is worth noting that in this study the ε-SVM regression model for forecasting of the Caspian Sea water level has been used (Dibike et al. 2001).

Therefore, *W* and *b* need to be optimized by the error function of relation (4) in the ε-SVM model, taking into account the conditions contained in (5).

$$\frac{1}{2}W^{\mathrm{T}}.w + C\sum_{i=1}^{N}\varepsilon_i + C\sum_{i=1}^{N}\varepsilon_i^* \tag{4}$$

$$\begin{aligned} &\frac{1}{2}W^{\mathrm{T}}.w + C\sum_{i=1}^{N}\varepsilon_i + C\sum_{i=1}^{N}\varepsilon_i^* \\ &W^{T}.\emptyset\left(x_i\right) + b - y_i \le \varepsilon_i + \varepsilon_i^* \\ &\varepsilon_i, \varepsilon_i^* \ge 0, k \quad i = 1, 2, \ldots, N \end{aligned} \tag{5}$$

In the above equations, *C* is a positive integer, which is the factor determining the penalty when model calibration error occurs. Φ is kernel function, *N* is the number of samples, and $\varepsilon_i, \varepsilon_i^*$ are deficiency variables which specify the upper and lower training errors associated with the allowed error value (Dibike et al. 2001).

In solving problems, it is predicted that the data will fall within the boundary range. Now if the data are out of range,

then there will be an equivalent error. It should also be noted that the SVM model solves the problems of underestimation and over-fitting by simultaneously minimizing the two terms of $\frac{1}{2}W^{\mathrm{T}}.w$ and the instructional error, i.e., $C\sum_{i=1}^{N}\varepsilon_i + C\sum_{i=1}^{N}\varepsilon_i^*$ in relation 4. Therefore, by introducing two Lagrangian coefficients of a_i and a_i^* the optimization problem by numerical maximizing of the quadratic function (relation 6) with conditions in relation 7 will be solved.

$$\sum_{i=1}^{N} y_i\left(a_i - a_i^*\right) - \varepsilon_i \sum_{i=1}^{N}\left(a_i + a_i^*\right) - 0.5\sum_{i,j=1}^{N}\left(a_i - a_i^*\right)\left(\left(a_j - a_j^*\right).\emptyset(x)^{\mathrm{T}} \ldots \emptyset\left(x_j\right)\right) \tag{6}$$

$$\begin{aligned}&\sum_{i=1}^{N}\left(a_i + a_i^*\right) = 0\\ &0 \le a_i \le C\\ &0 \le a_i^* \le C\\ &I = 1, 2, \ldots, N\end{aligned} \tag{7}$$

The objective function of relation 6 is a convex function, and therefore, the solution of relation 6 will be unique and optimal. After defining the Lagrangian coefficients in relation 8, characteristics of w and b in the SVM regression model were calculated using the conditions of Crash–Cohen–Tucker theory, where $W = \sum_{i=1}^{N}\left(a_i + a_i^*\right).\emptyset\left(x_i\right)$. Consequently, we will get a regression SVM model:

$$\sum_{i=1}^{N}\left(a_i + a_i^*\right).\emptyset(x)^{\mathrm{T}}.\emptyset\left(x_j\right) + b. \tag{8}$$

It should be noted that Lagrange's terms can be zero or nonzero. Therefore, only datasets whose $\overline{a_i}$ coefficients are nonzero were included in the final regression equation, and these datasets are the supporting vectors of those data that help to structure the regression function. Among the vectors mentioned are those whose $\left|\overline{a_i}\right|$ values are less than C, called marginal support vectors. When $\left|\overline{a_i}\right|$ support vectors are equal to C, they are known as error support vectors or boundary support vectors. Marginal support vectors are found on the non-sensing border margin, while error support vectors are out of range. Finally, the regression SVM function can be rewritten as follows:

$$f(x) = \sum_{i=1}^{N}\overline{a_i}.\emptyset\left(x_i\right)^{\mathrm{T}}.\emptyset(x) + b. \tag{9}$$

In relation 9, $\overline{a_i}$ is the mean of Lagrangian coefficient. Computing of the $\emptyset(x)$ in its characteristic space can be very complex. To solve this problem, the usual process in the regression SVM model is to select a kernel function. The support vector machine is usually used with three radial basis kernel function, d degree and linear polynomials, where the relation used in each of them is as follows (Guo et al. 2008; Kavzoglu and Colkesen 2009):

$$k\left(X_i, X_j\right) = \exp\left(-x - x_i^2/\sigma^2\right) \tag{10}$$

$$k\left(X_i, X_j\right) = \left(t + \left(x, x_i\right)\right)^d \tag{11}$$

$$k\left(X_i, X_j\right) = x.x_i. \tag{12}$$

Since the most commonly used kernel functions are linear, radial basis, and polynomial kernels (Liu 2011; Vapnik et al. 1997), these three kernel functions have been used in this study. It should be noted that the computational vector machine computation process is based on coding in MATLAB software and the parameters of the kernel functions are optimized through trial and error method. Given that each kernel has its own parameters, therefore, parameters of each kernel were optimized separately. The reason for separately optimizing kernel parameters is that each kernel has its own separate parameters, and the performance of each kernel is different from other kernels as they are known. Therefore, according to the kernel function formulas, the parameters C, d, t, and ε for the polynomial kernel, the parameters C, σ and ε for the radial basis function kernel, and for the linear kernel the parameters C and ε were optimized.

Gamma test (GT)

GT is a nonlinear method which assumes that the observation set is described by the following relationship (Durrant 2001):

$$\{(x_i - y_i)\}, \quad 1 \le i \le M\} \tag{13}$$

where x_{i} is the input observation vector (here, surface water temperature, air temperature, …), and y_{i} is the output of the GT (here, evaporation rate from a distinct concentration), and M is the total number of observations (here, total days for which evaporation was measured). The relationship between the inputs and output can be expressed as:

$$y = f(x) + r \tag{14}$$

where $f(x)$ is the smooth variable and r is the error term. It is assumed that the mean of the distribution fitted to r is zero and its variance is limited. The gamma statistic denoted by (Γ) expresses the variance of those observations; the model

is incapable of its determination. For a distinct input vector xi, the set N [i, k], for $(1 \le k \le p)$, is called the set of closest neighbors.

The gamma test is based on this set (i.e., N [i, k]). The term $X_{[I,k]}$ is the closest neighbor for ith x (i.e., x_i), such that $(1 \le k \le p)$, and$(1 \le i \le m)$. Also p is the maximum number of neighbors that are usually assumed to be between 10 and 50. In order to estimate (Γ), the values of $(\delta_M(k))$ should be calculated according to the input data (Evans and Jones 2002).

$$\delta_M(k) = \frac{1}{M}\sum_{i=1}^{M}\left|x_{N[i,k]} - x_i\right|^2, \quad 1 \le k \le p \tag{15}$$

where $|\ldots|$ denotes the Euclidean distance between vector $x_{N[i,k]}$ and its neighbors. Also, the value of $\gamma_M(k)$ can be estimated using the output data from the following relationship:

$$\gamma_M(k) = \frac{1}{2M}\sum_{i=1}^{M}\left|y_{N[i,k]} - y_i\right|^2, \quad 1 \le k \le p \tag{16}$$

where $y_{N[i,k]}$ is the value of output corresponding to the kth neighborhood of x_i vector. In this manner, the p values for $\delta_M(k)$ and the p values for $\gamma_M(k)$ can be calculated. Then, a relationship between $\{\delta_M(k), \gamma_M(k)\}$ would exist as:

$$\gamma = A\delta + \Gamma \tag{17}$$

The value of Γ statistic is indeed the intercept of the above-mentioned regression model. Also, A is the slope of the line which shows the complexity of model derived from data (Isazadeh et al. 2017; Ashrafzadeh et al. 2019). Another variable usually used in gamma test is dimensionless variable V_{ratio} whose value is between zero and one, determined according to Eq. 14 (Evans and Jone 2002).

$$V_{\text{ratio}} = \frac{\Gamma}{\sigma^2(y)} \tag{18}$$

where $\sigma^2(y)$ is the variance of observed data. The closer is the value of parameter V_{ratio} to zero, the better is the selected combination for modeling. It has been proven that when the value is less than one, the amount of model determination coefficient is obtained.

Uncertainty

To quantify the uncertainty, p-factor and d-factor coefficients were proposed, respectively, to quantify the power of calibration and uncertainty analyses (Abbaspour et al. 2007; Taormina et al. 2015). Equation 15 is used to determine the average width of the band (d-factor) index.

$$d - \text{factor} = \frac{\overline{dx}}{\sigma x} \tag{19}$$

where σx is the standard deviation of observed data and d $\bar{x}$ is the average width of confidence interval that can be attained by using Eq. 16.

$$\overline{dx} = \frac{1}{n}\sum_{t=1}^{K}(X_U - X_L) \tag{20}$$

Percentage of data in the band of 95% (p-factor) confidence interval is computed as follows:

$$\text{Bracketed by 95 PPU} = \frac{1}{k}\text{count}(j|X_L^l \le X_r eg^l \le X_U^l) \times 100 \tag{21}$$

where k is the number of observation data and l is the item number from one to k. X_L^l and X_U^l determine the confidence interval bands of 2.5% and 97.5%, respectively, X_{reg}^l is the observed value on day l, and j is the counter parameter of the number of observed values placed on 95 PPU band. If all values are within the confidence band of uncertainty, then they are bracketed by 95 PPU (p-factor) = 100 (Ghorbani et al. 2016).

Evaluation criteria

Various methods can be used to evaluate and compare the performances of models, one of which is the use of evaluation criteria. Among the evaluation criteria widely used in water engineering science, correlation coefficients (CC), root mean square error (RMSE), and the Nash Sutcliffe (NS) as in Eqs. 18, 19 and 20, respectively, are presented herein. The most accurate model with respect to these criteria is a model for which the values of these three criteria are close to one, zero, and one, respectively.

$$\text{CC} = \sqrt{\frac{(\sum_{i=1}^{N}(x_i - \bar{x})(y_i - \bar{y}))^2}{\sum_{i=1}^{N}(x_i - \bar{x})^2 \sum_{i=1}^{N}(y_i - \bar{y})^2}} \tag{22}$$

$$\text{RMSE} = \sqrt{\frac{1}{N}\sum_{i=1}^{N}(x_i - y_i)^2} \tag{23}$$

$$\text{NS} = 1 - \frac{\sum_{i=1}^{N}(x_i - y_i)^2}{\sum_{i=1}^{N}(x_i - \bar{x})^2} \tag{24}$$

In the above relations, x_i, $\bar{x}$, y_i, $\bar{y}$, and N are the observed values of the flow, mean of observed values, computed flow,

mean of computed flow, and number of data, respectively (Misra et al. 2009).

Results and discussion

In this study, Caspian Sea water level parameters with different lags, month number, and monthly mean Caspian Sea level were used as input variables. Inlet combinations have also been evaluated in four sections. In the first step with the gamma test, the best combination was selected using Caspian Sea Water Level Lags. In the second section, the number of the month was added to the selection of the previous section. In the third section, the Caspian Sea monthly mean water level was selected for the first part of the study, and in the last part, two parameters of the month number and the Caspian Sea monthly mean were added to the selected combination of the first part obtained by gamma test. The sections are compared with each other.

After validation of input data by using the gamma test, the optimal input composition is used to estimate the sea level. Then, by using ANNs and SVM, the calibration and validation processes of the sea level estimation are performed. In the following, different stages of water level estimation are described.

Gamma test

Regarding the periodicity of the surface level of Caspian Sea, 1–15 delays with respect to the sea level are considered as the input of gamma test. Therefore, firstly, the gamma test is performed for the whole data (row 1), and then the test is performed based on the replacement of each of the variables from the total of the fifteen input variables (rows 2 through 16), which are shown in Table 2.

According to the gamma test results in Table 2, the gamma statistics of the sea level with delays of 8 and 11 months (rows 6 and 9) are less than the gamma value of the whole data (row 1). Therefore, the gamma test identifies the sea level elevation with delays of 8 and 11 months as negative inputs parameters. Thus, other input parameters can be employed to estimate the level of sea surface. The use of the data measurement number according to Awchi (2014) and Ghorbani et al. (2016) and application of the monthly measurement number and monthly average of the data on the basis of Isazadeh (2015) can increase the accuracy of model estimation. Therefore, in this study, the combinations in Table 3, which are obtained by using gamma test and other studies, are used to estimate Caspian Sea water level.

In Table 3, $h_{(t-i)}$ is the sea level with the delay of i month, NM is the month number of measurement (1 to 12), and AV is the monthly average of the sea level.

Artificial neural network

In this section, calibration and verification of Caspian Sea level estimation are performed by using the proposed input combinations in Table 3. The number of optimal neurons together with the values of accuracy estimation statistics and uncertainty of models are shown in Table 4.

According to results in Table 4, the estimation of sea level is carried out by using ANN model with very high precision, and results of the model with different combinations

Table 2 Gamma test for all input and output data by replacing each input

Row number	Absent variable	Gamma	Gradient	Error	v
1	–	0.000156	0.059235	0.000658	0.000623
2	$h_{(t-15)}$	0.000252	0.06295	0.000497	0.0010007
3	$h_{(t-14)}$	0.000583	0.057837	0.000449	0.002335
4	$h_{(t-13)}$	0.000314	0.060466	0.000461	0.001255
5	$h_{(t-12)}$	0.000203	0.062732	0.00547	0.000812
6	$h_{(t-11)}$	−0.00021	0.06658	0.000539	−0.00082
7	$h_{(t-10)}$	0.000247	0.062055	0.000557	0.000987
8	$h_{(t-9)}$	0.000505	0.059638	0.000453	0.002019
9	$h_{(t-8)}$	0.000168	0.063507	0.000515	0.000673
10	$h_{(t-7)}$	0.000376	0.031239	0.000495	0.001503
11	$h_{(t-6)}$	0.000509	0.059246	0.000478	0.002036
12	$h_{(t-5)}$	0.000529	0.059421	0.000668	0.002115
13	$h_{(t-4)}$	0.000329	0.061879	0.000668	0.001318
14	$h_{(t-3)}$	0.000466	0.060728	0.000476	0.001864
15	$h_{(t-2)}$	0.000223	0.066546	0.000493	0.00089
16	$h_{(t-1)}$	0.000482	0.077483	0.000643	0.001927

are close to each other. In general, according to all evaluation statistics, the ANN model by using combination No. 4 in Table 3 is able to estimate the level of the Caspian Sea with less error and high precision. Results also show that the use of the month number of measurement (NM) and the average monthly sea level (AV) have a positive effect on the accuracy of the estimates. Of course, the simultaneous use of the month number of measurement and the monthly average of the sea level, along with the first input combination, leads to the best result. The value of the Nash–Sutcliff coefficient, which exceeds 90% during the validation period, also reveals a highly accurate estimation of the ANN model. The uncertainty of superior models also shows that combination No. 3 with a *d*-factor of 0.22 has the least uncertainty.

Support vector machine

Results of sea level estimation with designated input compounds (Table 3) are shown in Table 5 by using SVM with the optimal kernel function.

Due to the negligible error of the SVM in Caspian Sea level estimates for each of the four combinations, the performance of this model is very well. According to results in Table 5, the support model machine by combination No. 4 from Table 3 estimates the sea level with better accuracy, compared to combinations Nos. 1–3. Also, results show that error and accuracy rates of this model are, respectively, lower and higher than those of 2 to 4 combinations as compared with the first combination. Therefore, adding the parameters of the month number and the average monthly sea level reduces the error of this model in the estimation of sea level. Given the higher value of the Nash–Sutcliffe index compared to a limit of 75% in each estimate, the performance of the SVM is proved to be excellent. The low value of the d-factor index for each estimate suggests low uncertainty of the SVM in estimating the surface level of Caspian Sea. The lowest uncertainty index also belongs to the second combination with *d*-factor of 0.005. RMSE values used for the verification stage of SVM for each of the three kernel functions are shown in Fig. 2.

According to Fig. 2, results of all three kernel functions with the first, third, and fourth combinations are close to each other. Only in combination No. 2, the estimation errors of each function are relatively large, necessitating the evaluation of each kernel function by soft computing technique. Regarding Fig. 2, in general, the polynomial kernel function

Table 3 Input combinations in each estimator model

Combination number	Input variables
1	$h_{(t-1)}$, $h_{(t-2)}$, $h_{(t-3)}$, $h_{(t-4)}$, $h_{(t-5)}$, $h_{(t-6)}$, $h_{(t-7)}$, $h_{(t-9)}$, $h_{(t-10)}$, $h_{(t-12)}$, $h_{(t-13)}$, $h_{(t-14)}$, $h_{(t-15)}$
2	$h_{(t-1)}$, $h_{(t-2)}$, $h_{(t-3)}$, $h_{(t-4)}$, $h_{(t-5)}$, $h_{(t-6)}$, $h_{(t-7)}$, $h_{(t-9)}$, $h_{(t-10)}$, $h_{(t-12)}$, $h_{(t-13)}$, $h_{(t-14)}$, $h_{(t-15)}$, NM
3	$h_{(t-1)}$, $h_{(t-2)}$, $h_{(t-3)}$, $h_{(t-4)}$, $h_{(t-5)}$, $h_{(t-6)}$, $h_{(t-7)}$, $h_{(t-9)}$, $h_{(t-10)}$, $h_{(t-12)}$, $h_{(t-13)}$, $h_{(t-14)}$, $h_{(t-15)}$, AV
4	$h_{(t-1)}$, $h_{(t-2)}$, $h_{(t-3)}$, $h_{(t-4)}$, $h_{(t-5)}$, $h_{(t-6)}$, $h_{(t-7)}$, $h_{(t-9)}$, $h_{(t-10)}$, $h_{(t-122)}$, $h_{(t-13)}$, $h_{(t-14)}$, $h_{(t-15)}$, NM, AV

Table 4 The results of Caspian Sea level estimation with artificial neural network model and four selected input combinations

Combination number	Optimized neuron number	Calibration			CC	RMSE (mm)	Validation		
		CC	RMSE (mm)	NS			NS	*d*-factor	*p*-factor (%)
1	12	0.997	4.243	0.993	0.949	5.430	0.893	0.480	50
2	13	0.997	4.173	0.993	0.955	5.030	0.908	0.570	63
3	2	0.996	4.490	0.992	0.950	5.287	0.898	0.220	32
4	16	0.997	4.256	0.993	0.957	5.014	0.909	0.560	58

Table 5 The results of Caspian Sea level estimation with support vector machine with four selected input combinations

Combination number	Optimized kernel function	Calibration			Validation				
		CC	RMSE (mm)	NS	CC	RMSE (mm)	NS	*d*-factor	*p*-factor (%)
1	Linear	0.995	4.917	0.991	0.947	5.428	0.893	0.0012	1.32
2	Polynomial	0.996	4.304	0.993	0.955	5.089	0.906	0.005	1.32
3	Radial basis	0.996	4.428	0.993	0.954	5.115	0.905	0.006	8
4	Radial basis	0.997	4.153	0.993	0.960	4.781	0.917	0.04	4

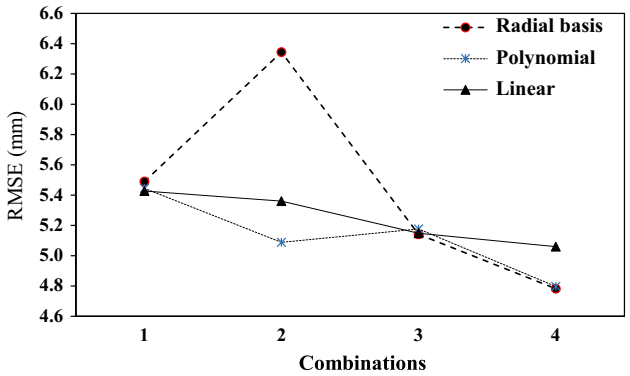

Fig. 2 RMSE value of calibration period of the support vector machine by the radial, polynomial, and linear kernel functions

has less error than two other kernel functions, as also confirmed in the study by Isazadeh et al. (2016).

Performance evaluation of the month number of measurement and mean monthly sea level as input parameters

In this research, the estimation of the sea level with each model according to the combination determined by gamma test is considered as the base estimate (combination No. 1). In the next step, parameters of the month number of measurement and mean monthly sea level, which are added as the month number index and average monthly sea level index to the first combination, are evaluated, as shown in Fig. 3.

According to Fig. 3a, better accuracy of Caspian Sea level estimation by each of the models is obtained with the fourth, second, third, and first combinations. Therefore, it can be concluded that the use of month number and average monthly measurements indices has a positive effect on each model for estimating sea level. This result was also confirmed by Ghorbani et al. (2016) and Isazadeh (2015). Besides, results show that the month number index is more effective than average monthly measurement one, which improves results of sea level estimation. Finally, performances of both models show that the simultaneous use of both the month number indices and the average monthly measurement index is better than their separate use. This is very evident in the performance of the SVM, such that the best performance of the total estimates for the use of these two indices is made by the SVM. Furthermore, Fig. 3b shows that the uncertainty of the SVM is much lower than that of the ANN model for each of the four input combinations. The lower uncertainty of the SVM is one of the features that surpass this model, compared to the ANN model. Figure 4 shows the sea level estimated by SVM and ANN for the superior combination of each model (the fourth combination) and their uncertainty during the validation period.

As shown in Fig. 4, the uncertainty band in the estimation of the SVM is very narrow, indicating a low or high degree of uncertainty in this model. In fact, the difference between the *d*-factor of the ANN (0.56) and that of SVM (0.04) for the superior composition (the fourth composition) is quite clear in Fig. 4. Results are in agreement with those of Ghorbani et al. (2016) and Isazadeh et al. 2017).

In addition to the models used in Imani et al. (2014a, b), this study attempts to use different functions of the SVM model and to use the gamma test to select the appropriate input for the models. Also, the uncertainties of these models have been calculated in this research. It should be noted that the use of the mean value is another innovation of this article. Imani et al. (2014a, b) also used satellite data, whereas the ground station data used in the present study have less errors.

The use of the gamma test avoids over-fitting (Durrant 2001; Evans and Jones 2002; Isazadeh et al. 2017; Ashrafzadeh et al. 2019). Also, the use of the month number and the mean value makes the optimization model more than normal

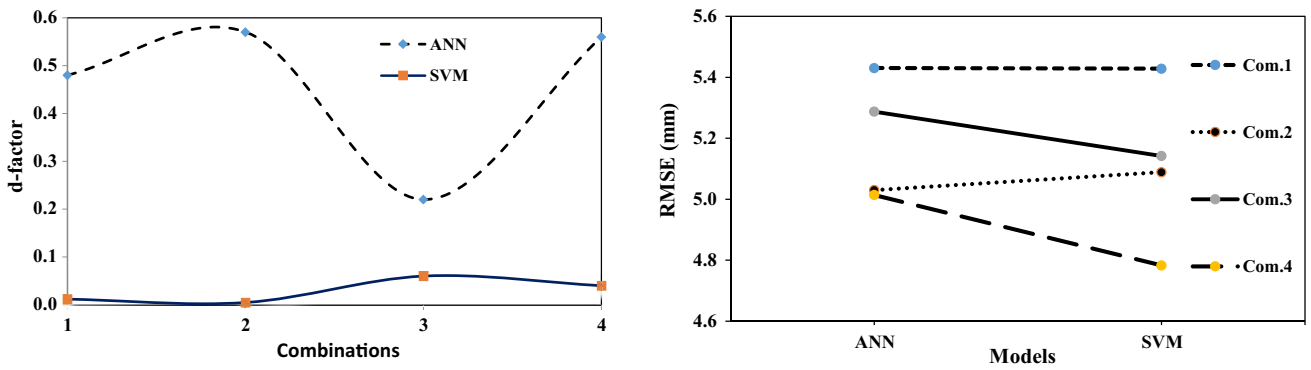

Fig. 3 Performance comparison of the models and combinations (Com.1–5: combination 1–4) used in the process of estimating the Caspian Sea level

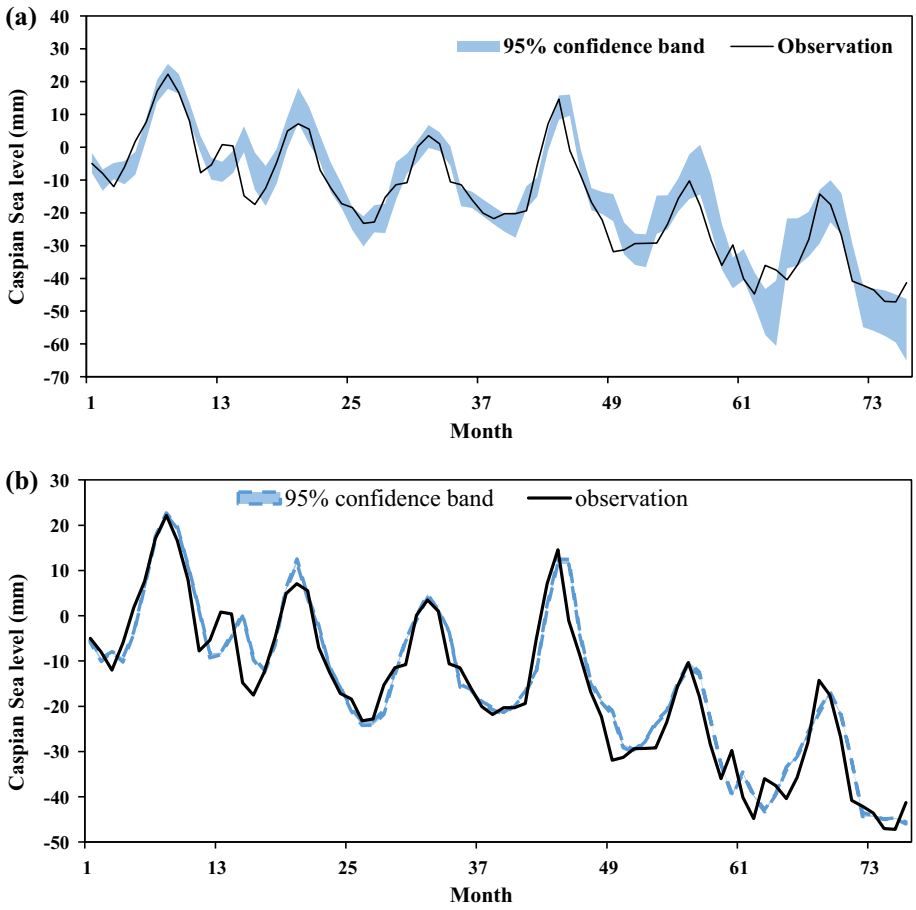

Fig. 4 Observations data of Caspian Sea level along with uncertainty band of ANN (**a**) and SVM (**b**) models due to fourth input

to look around the average data for the desired value and to avoid over-fitting and low-fitting (Awchi 2014; Ghorbani et al. 2016).

Conclusions

The estimation of the Caspian Sea water level is performed by using SVM and ANN models. Four selected inputs are determined based on the gamma test and performed studies to determine sea level. Results indicate that the ANN and SVM models are very good at sea level estimation. Results of the estimations show that the ANN has the best estimation for the sea level with the fourth combination having an error of 5.014 mm and a correlation coefficient of 0.957 in the verification stage. The uncertainty of the ANN with the third combination is 0.22, which is less than the uncertainty of other combinations. The SVM, with the fourth combination having an error and correlation coefficient of 4.782 mm and 0.96, has the best result for the sea level estimation. The uncertainty of this model is low, equal to 0.04 for the fourth combination. Besides, results of SVM with different kernel functions indicate better performance of the polynomial kernel function. The performance of models has improved by adding the auxiliary parameters of the month number of measurement and average monthly sea level indices. Therefore, it is possible to use these parameters in other monthly estimates as efficient inputs. Furthermore, results show that both models have better performance if both the month number of measurement and mean monthly sea level are used simultaneously. The comparison between SVM and ANN models shows that the SVM has better results than any ANN models for each of the four proposed combinations. Moreover, the uncertainty of this model is lower than that of the ANN model for all four input combinations. With reference to the above points, the SVM with minimal error and very low uncertainty can be considered as the superior model in estimating the level of Caspian Sea at Anzali station.

Computer code availability

ANN and SVM codes developed in MATLAB are not available for readers.

References

Abbaspour KC, Yang J, Maximov I, Siber R, Bogner K, Mieleitner J, Zobrist J, Srinivasan R (2007) Modeling hydrology and water quality in the pre-alpine/alpine Thur watershed using SWAT. J Hydrol 333:413–430

Aghelpour P, Mohammadi B, Biazar SM (2019) Long-term monthly average temperature forecasting in some climate types of Iran, using the models SARIMA, SVR, and SVR-FA. Theor Appl Climatol 138(3–4):1471–1480

Aladin NB, Plotnikov IS (2004) The Caspian sea, lake basin management initiative. Casp Bull 4:112–126

ASCE (2000) Task committee on application of artificial neural networks in hydrology artificial neural networks in hydrology. i: preliminary concepts. J Hydrol Eng 2:115–123

Ashrafzadeh A, Ghorbani MA, Biazar SM, Yaseen ZM (2019) Evaporation process modelling over northern Iran: application of an integrative data-intelligence model with the krill herd optimization algorithm. Hydrol Sci J 64(15):1843–1856

Awchi TA (2014) River discharges forecasting in northern Iraq using different ANN techniques. Water Resour Manag 28(3):801–814

Charalambous C (1992) Conjugate gradient algorithm for efficient training of artificial neural networks. IEE Proc G (Circuits, Devices Syst) 139(3):301–310

Cheng CT, Chau KW (2004) Flood control management system for reservoirs. Environ Model Softw 19(12):1141–1150

Cheng CT, Wu XY, Chau KW (2005) Multiple criteria rainfall-runoff model calibration using a parallel genetic algorithm in a cluster of computer. Hydrol Sci J 50(6):1069–1087

Choubin B, Moradi E, Golshan M, Adamowski J, Sajedi-Hosseini F, Mosavi A (2019) An Ensemble prediction of flood susceptibility using multivariate discriminant analysis, classification and regression trees, and support vector machines. Sci Total Environ 651:2087–2096

Coulibaly P, Anctil F, Bobée B (2000) Daily reservoir inflow forecasting using artificial neural networks with stopped training approach. J Hydrol 230:244–257

Dawson CW, Abrahart RJ, Shamseldin AY, Wibly RL (2006) Flood estimation at ungauged sites using artificial neural networks. J Hydrol 319:391–409

Deo RC, Ghorbani MA, Samadianfard S, Maraseni T, Bilgili M, Biazar M (2018) Multi-layer perceptron hybrid model integrated with the firefly optimizer algorithm for windspeed prediction of target site using a limited set of neighboring reference station data. Renew Energy 116:309–323

Dibike Y, Velickov S, Solomatine D, Abbott M (2001) Model induction with of support vector machines. introduction and applications. J Comput Civil Eng 15:208–216

Durrant PJ (2001) Win_gamma TMA non-linear data analysis and modeling tool with applications to flood prediction. Ph.D. Thesis, Department of Computer Science, Cardiff University Wales, UK

Eskandari A, Nouri R, Meraji H, Kiaghadi A (2012) Developing a proper model for online estimation of the 5-day biochemical oxygen demand based on artificial neural network and support vector machine. J Environ Stud 38(1):71–82 **(in Persian)**

Evans D, Jone A (2002) A proof of the gamma test. Proc R Soc Ser A 458:2759–2799

Fombellida M, Destiné J (1992) The extended quickprop. Artif Neural Netw. https://doi.org/10.1016/B978-0-444-89488-5.50032-4

Fotovatikhah F, Herrera M, Shamshirband S, Chau KW, Ardabili SF, Piran MJ (2018) Survey of computational intelligence as basis to big flood management: challenges, research directions and future work. Eng Appl Comput Fluid Mech 12(1):411–437

Ghorbani MA, Khatibi R, Aytek A, Makarynskyy O, Shiri J (2010) Sea water level forecasting using genetic programming and comparing the performance with artificial neural networks. Comput Geosci 36(2010):620–627

Ghorbani MA, Ahmad Zadeh H, Isazadeh M, Terzi O (2016) A comparative study of artificial neural network (MLP, RBF) and support vector machine models for river flow prediction. J Environ Earth Sci 75:1–14

Guo B, Gunn SR, Damper RI, Nelson JD (2008) Customizing kernel functions for SVM-based hyperspectral image classification. IEEE Trans Image Process 17(4):622–629

Hagan MT, Menhaj MB (1994) Training feedforward networks with the Marquardt algorithm. IEEE Trans Neural Netw 5(6):989–993

Hajikhodaverdikhan P, Nazari M, Mohsenizadeh M, Shamshirband S, Chau KW (2018) Earthquake prediction with meteorological data by particle filter-based support vector regression. Eng Appl Comput Fluid Mech 12(1):679–688

Imani M, You RJ, Kuo CY (2014a) Caspian Sea level prediction using satellite altimetry by artificial neural networks. Int J Env Sci Tech 11:1035–1042

Imani M, You RJ, Kuo CY (2014b) Forecasting Caspian Sea level changes using satellite altimetry data (June 1992–December 2013) based on evolutionary support vector regression algorithms and gene expression programming. Glob Planet Change 121:53–63

Isazadeh M (2015) Estimation of ZarrinehRoud River discharge using hybrid artificial intelligence models. MSc. thesis. Faculty of agricultural sciences. University of Tabriz. p 171. (in Persian)

Isazadeh M, Ahmadzadeh H, Ghorbani MA (2016) Assessment of kernel functions performance in river flow estimation using support vector machine. J Water Soil Conserv 23(3):69–89 **(in Persian)**

Isazadeh M, Biazar SM, Ashrafzadeh A (2017) Support vector machines and feed-forward neural networks for spatial modeling of groundwater qualitative parameters. Environ Earth Sci 76(17):6–10

Jacobs RA (1988) Increased rates of convergence through learning rate adaptation. Neural Netw 1(4):295–307

Karimi S, Kisi O, Shiri J, Makarynsky Y (2013) Neuro-fuzzy and neural network techniques for forecasting sea level in Darwin Harbor Australia. Comput Geosci 52(2013):50–59

Kavzoglu T, Colkesen I (2009) A kernel functions analysis for support vector machines for land cover classification. Int J Appl Earth Obs Geoinf 11:352–359

Kisi O, Shiri J, Karimi S, Shamshirband S, Motamedi S, Petkovi´c D, Hashim R (2015) A survey of water level fluctuation prediction in Urmia Lake using Support Vector Machine with firefly algorithm. Appl Math Comput 270:731–743

Lagos-Avid MP, Bonilla CA (2017) Predicting the particle size distribution of eroded sediment using artificial neural networks. Sci Total Environ 581:833–839

Lee TL, Makarynskyy O, Shao CC (2007) A combined harmonic analysis-artificial neural network methodology for tidal predictions. J Coast Res 23:764–770

Li S, Kazemi H, Rockaway TD (2019) Performance assessment of stormwater GI practices using artificial neural networks. Sci Total Environ 651:2811–2819

Lin JY, Cheng CT, Chau KW (2006) Using support vector machines for long-term discharge prediction. Hydrol Sci J 51(4):599–612

Liu GQ (2011) Comparison of regression and ARIMA models with neural network models to forecast the daily streamflow of white clay creek. PhD Thesis, University of Delaware, Newark, USA

Makarynska D, Makarynska O (2008) Predicting sea-level variations at Cocos (Keeling)islands with artificial neural networks. Comput Geosci 34:1910–1917

Makarynska O, Makarynska D, Kuhn M, Featherstone WE (2009) Predicting sea level variations runoff modeling. Water Resour Manag 23:2877–2894

Meyer FW (1989) Hydrogeology, ground-water movement, and subsurface storage in the Florida aquifer system in Southern Florida, United States Geological Survey Professional Paper 1403-G. US Government Printing Office, Washington, p 1989

Misra D, Oommen T, Agarwal A, Mishra SK (2009) Application and analysis of Support Vector machine based simulation for runoff and sediment yield. J Biosyst Eng 103:527–535

Moazenzadeh R, Mohammadi B, Shamshirband S, Chau KW (2018) Coupling a firefly algorithm with support vector regression to predict evaporation in northern Iran. Eng Appl Comput Fluid Mech 12(1):584–597

Naganna SR, Deka PC, Ghorbani MA, Biazar SM, Al-Ansari N, Yaseen ZM (2019) Dew point temperature estimation: application of artificial intelligence model integrated with nature-inspired optimization algorithms. Water 11(4):742

Rajaei T, Shahabi A (2014) Application of ANN and wavelet conjunction model in forecasting short-term sea level variations (case study: chabahar port). Marine Technol 1(2):42–53 **(in Persian)**

Ramezani Mouzirji F, Yaghoobi M, Ghanghermeh A (2011) Caspian Sea level prediction based on fuzzy regressor system. J Water Wastewater 22(3):90–98 **(in Persian)**

Rumelhart DE, Hinton GE, Williams RJ (1988) Learning representations by back-propagating errors. Cogn Model 5(3):1

Sertel E, Cigizoglu HK, Sanli DU (2008) Estimating daily mean sea level heights using artificial neural network. J Coast Res 243:727–734

Taormina R, Chau KW, Sivakumar B (2015) Neural network river forecasting through baseflow separation and binary-coded swarm optimization. J Hydrol 529(3):1788–1797

Thain RH, Priestley AD, Davidson MA (2004) The formation of a tidal intrusion front at the mouth of a macro tidal, partially mixed estuary: a field study of the Dart Estuary UK. Estuar Coast Shelf Sci 61:161–172

Vapnik VN (1999) An overview of statistical learning theory. IEEE Trans Neural Netw 10:988–1000

Vapnik V, Golowich SE, Smola AJ (1997) Support vector method for function approximation, regression estimation and signal processing. In: Mozer M, Jordan M, Petsche T (eds) Advances in neural information processing systems. MIT Press, Cambridge, MA, pp 281–287

Wu CL, Chau KW (2011) Rainfall-runoff modeling using artificial neural network coupled with singular spectrum analysis. J Hydrol 399(3–4):394–409

Wu CL, Chau KW, Li YS (2008) River stage prediction based on a distributed support vector regression. J Hydrol 358(1–2):96–111

Acta Geophysica (2020) 68:565–576
https://doi.org/10.1007/s11600-020-00409-0

RESEARCH ARTICLE – HYDROLOGY

Impact of missing precipitation values on hydrological model output: a case study from the Eddleston Water catchment, Scotland

S. Ruman[1] · P. Krpec[1] · P. Rusnok[2] · A. R. Black[3] · M. Trizna[4] · T. Ball[5]

Received: 23 September 2019 / Accepted: 17 February 2020 / Published online: 27 February 2020

Abstract

A hydrological model was applied to select the best infilling method of missing precipitation (1) and to assess the impact of the length of deleted and filled precipitation data (2). The model was calibrated and validated using the hourly observed discharges from two gauges located in the outlet of the catchment (62.34 km^2) and in the inner sub-catchment (2.05 km^2). Precipitation from four gauges was spatially interpolated over the overall catchment, while the sub-catchment used the precipitation from one gauge. Four scenarios of different lengths of deletion within three high-intensity events were established in the data of this gauge. Three infilling methods were applied and compared: substitution, linear regression and inverse distance weighting (IDW). Substitution showed the best results, followed by linear regression and IDW in both scales. Differences between methods were significant only in 8.3% and 19.4% of all cases (sub-catchment and catchment, respectively). The impact of length was assessed using the substitution only and by comparing differences in discharges and performance statistics caused by four scenarios. Higher differences in discharges were found on the catchment scale compared to the inner sub-catchment and were insignificant for all events and scenarios. The hypothesis that a longer length of deleted and filled data would lead to a greater error in discharges was wrong for 11.1% and 16.7% of all cases (sub-catchment and catchment, respectively). In several cases (33.4% sub-catchment, 27.1% catchment), the model produced better results using the time series with filled gaps compared to the configuration with observed data.

Keywords Missing values · High-intensity rainfall · Infilling methods · Hydrological model · Scotland

Introduction

Accurate precipitation data are essential for the understanding of hydrological processes, water resources planning, proposing flood protection or the mitigation of contamination (Beven 2012). Furthermore, precipitation data are the most important input for the hydrological models (Moulin et al. 2008). However, there remain high uncertainties when precipitation values in the time series are missing, often due to instrument or related failure (Wagner et al. 2012). Infilling methods provide a solution to fill in missing data; however, the right method has to be selected for each gauge due to its unique geographical location (Hwang et al. 2012). Estimations of missing time series are generally based on the measured data from gauges surrounding the targeted gauge (Cole and Moore 2008). The basic source of precipitation data remains the tipping-bucket gauge for the measurement of point rainfall depth (Cole and Moore 2008) often combined with the radar outputs (Jurczyk 2008; Pauthier et al. 2016; Boudevillain et al. 2016).

✉ S. Ruman
stanislav.ruman@osu.cz

1 Department of Physical Geography and Geoecology, Faculty of Sciences, University of Ostrava, Chittussiho 10, 710 00 Ostrava, Czech Republic

2 Institute for Research and Applications of Fuzzy Modeling, University of Ostrava, 30. Dubna 22, 701 03 Ostrava 1, Czech Republic

3 Geography, School of Social Sciences, University of Dundee, Nethergate, Dundee DD1 4HN, Scotland, UK

4 Department of Physical Geography and Geoecology, Faculty of Sciences, Comenius University in Bratislava, Mlynská dolina, Ilkovičova 6, 842 15 Bratislava 4, Slovakia

5 Department of Archaeology, Anthropology and Geography, Faculty of Humanities and Social Sciences, University of Winchester, Sparkford Road, Winchester SO22 4NR, UK

Many studies propose different infilling methods for filling missing values of precipitation and consequently examine these methods using hydrological models (Heistermann and Kneis 2011; Lo Presti et al. 2010; Vicente-Serrano et al. 2010). Concerning the simple methods, substitution (Lo Presti et al. 2010; Vicente-Serrano et al. 2010), IDW (Dirks et al. 1998; Jurczyk 2008) and linear regression (Weisberg 2005) have all been employed for infilling missing values of precipitation. Vicente-Serrano et al. (2010) evaluated these methods during the homogenization of daily time series in north-east Spain and found the substitution as the best method, followed by the IDW and linear regression. Lo Presti et al. (2010) proposed filling gaps in daily precipitation time series in Italy by nonparametric regression in comparison with parametric regression and simple substitution. However, they found out the substitution method can be acceptable when the similarity value tends to be significantly high. Eischeid et al. (2000) used six different interpolation methods for completing daily time series in dependency of estimation biases for every gauge and every month in the western USA. They used, for the most part, multiple regression with the least absolute deviation criterion which outperformed IDW from remaining methods. Bárdossy and Pegram (2014) compared several methods for daily time steps in South Africa and proposed a new cupola-based method. Among the compared methods were the IDW, linear regression and substitution, while the IDW performed the best followed by linear regression and substitution. An artificial neural network (ANN) method with the regression tree was used in the study from the Appalachian Mountain, USA (Kim and Pachepsky 2010), where accuracy of the SWAT model was significantly improved using these infilling methods. Furthermore, the ANN approach was recently used along with the conventional cubic spline algorithm and multivariate linear regression method in the catchment of Southern England (Song et al. 2017) in high temporal resolution of rainfall rate estimation. As noted above, hydrological models were applied in this process, firstly to investigate the impact of missing precipitation data on the simulated outputs (dominantly discharges) and secondly to select the best infilling method (Singh 1997; Arnaud et al. 2002; Bárdossy and Das 2008; Moulin et al. 2008; Reusser et al. 2009; Hwang et al. 2012). Studies from France (Moulin et al. 2008) and Mexico (Arnaud et al. 2002) showed that by using the hydrological model, less detailed hourly rainfall input led to biased flow outputs. These biases can be compensated by model calibration applying the *effective parameters* approach (Beven 2006), but it results in higher output uncertainty. Although most of the studies analyse the effect of filling daily data series (Heistermann and Kneis 2011; Hwang et al. 2012; Kim and Pachepsky 2010), in higher temporal sub-daily resolution, there is a decrease in spatial correlation between gauges (Blenkinsop et al. 2016; Villarini et al. 2008; Lewis et al. 2018). Ficchi et al (2016) investigate the extent to which the performance of hydrological modelling is improved by short time-step data (6 min vs. daily rainfall) in the mesoscale French catchment. They reported significant improvement in performance with shorter time steps.

Generally, rainfall estimation errors increase with decreasing catchment size due to topographic variability, so cases of small catchments are the most problematic. This was shown in the study by Krajewski et al. (2003), where the time interval varied from 1 h to 5 min in the selected rain gauges of various environments. Furthermore, the small urban catchments also require smaller temporal resolution, which was the case of the Twenterand catchment in the Netherlands (Cecinati et al. 2017). We followed these studies and applied hydrological model MIKE SHE/MIKE11 running on an hourly time step to select the best infilling method for the three high-intensity rainfall events. The model was developed in the part of small-scale Eddleston Water catchment and its inner sub-catchment.

Analyses of the extent to which data infilling of precipitation input influences the outputs of hydrological models are rare. The study of Teegavarapu and Nayak (2017) examined the impact of filled precipitation datasets for different lengths of gaps. The result for the period from 1901 to 2006 at 53 rain gauges in south Florida indicated the data infilling does not introduce statistically significant bias in total annual precipitation values but may lead to underestimation of both magnitude and frequency of heavy and very heavy precipitation events. Furthermore, they reported the increase in bias with the increase in the amounts of missing data. We follow this study and assess the impact of gaps of various lengths during three high-intensity rainfall events on the hydrological model outputs.

Thus, the aims of this case study were as follows: firstly, to select the best (optimal) infilling method of high-intensity rainfall events using the hydrological model (1) and, secondly, to assess the impact of different lengths of infilled gaps in high-intensity rainfall events on the outputs of hydrological model (2). Both aims were solved on the sub-catchment and catchment scale to investigate the impact of the catchment area.

Study area

The Eddleston Water, near Peebles, Scottish Borders, UK, has a topography ranging from 150 to 700 m and the average rainfall of 980 mm year^{-1} (Fig. 1). The high-intensity rainfall events are primarily caused by frontal precipitation. The Kidston Mill stream gauge is located at the main river of the Eddleston Water (river kilometre 2.53), which is a right (16.39 km long) tributary of River Tweed. The average discharge is 1.27 m^3 s^{-1}, river slope is equal to 0.0069 m/m,

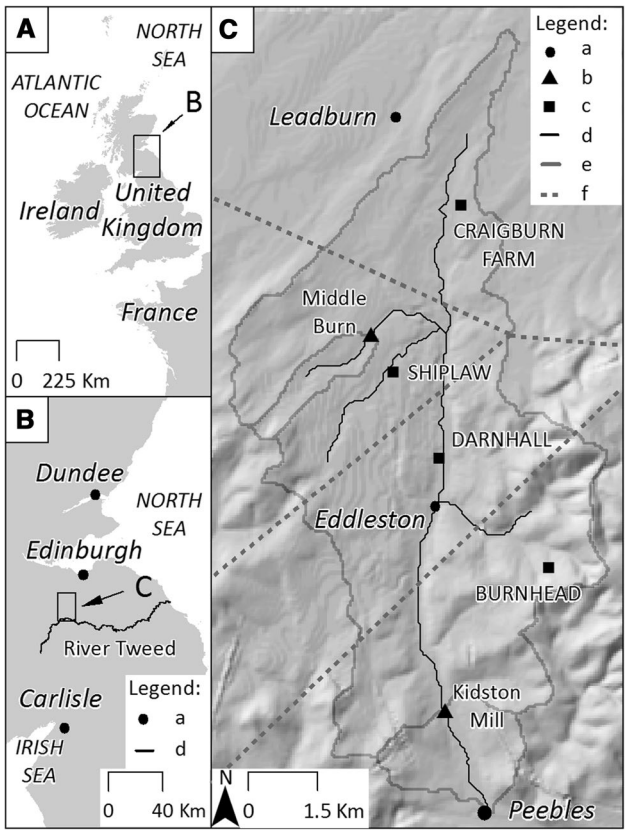

Fig. 1 Geographical position of the study area. A—localization within Western Europe, B—position within south-west Scotland, C—geographical situation of close surroundings of the Eddleston Water catchment. Legend: a—municipalities, b—stream gauges, c—rain gauges, d—waterways, e—sub-catchment borders, f—Thiessen polygons. Data sources: Eurostat, Ordnance Survey; Geographic Coordinate System: GCS OSGB 1936

and the sub-catchment area is 62.34 km^2 with the slope equal to 13.97%. The Middle Burn stream gauge (river kilometre 2.2) is located at the stream of the identical name with the length of 4.1 km, slope equal to 0.0215 m/m and average discharge equal to 0.06 $m^3\ s^{-1}$. The stream is a right tributary of the Eddleston Water, located in the north-west part of the catchment (Fig. 1). The sub-catchment area is 2.05 km^2, and the sub-catchment slope is 7.59%. Geologically, it is mantled by complex post-glacial ice-margin deposits, surface strata (O'Dochartaigh et al. 2012) that overlay generally low-permeability Silurian greywackes (Pearce et al. 2014). The main river stem runs, from approximately its catchment midpoint, down a wide alluvium-infilled valley. Soils within the catchment are dominantly sandy loams (53%) followed by loamy sands (20%), peats (17%) and loam (10%; JHI 2014). Catchment land use is mostly grass (67%) followed by coniferous forest (10%, predominantly in the Middle Burn sub-catchment). Marsh, shrubs and mixed forest each account for 5% of the total catchment area. Urban development, stripes of arable land, water and broadleaf forest cover the remaining area. Since 2011, the catchment has been equipped with rain and stream gauges (Fig. 1). Research undertaken under the auspices of the Eddleston Water Project (Tweed Forum 2016) has investigated the effects of catchment management and restoration measures that have been implemented for both ecological improvements and as a means to alleviate local flood risk (Archer et al. 2013; Tweed Forum 2016). These measures were implemented at the end of August 2013 (Tweed Forum 2016) and thus did not influence the results of this study.

Methods

Hydrological model set-up, calibration and validation

A coupled rainfall–runoff/hydraulic model of the Eddleston Water catchment was developed using MIKE SHE/MIKE 11 (DHI 2014). This established modelling system has been employed in a wide range of situations from small catchments or parts of catchments (e.g. Sahoo et al. 2006; Thompson et al. 2014; Thompson 2012) to large river basins (e.g. Andersen et al. 2001; Singh et al. 2011; Thompson et al. 2013, 2014). A 200 m × 200 m computational grid was employed, resulting in the catchment being discretized into 8000 cells. A digital terrain model (DTM) at 10 m grid resolution was created from contours with root mean square error/RMSE/± 2.5 m. The model structure used the gravity flow method for the unsaturated zone formulation (MIKE SHE 2011). This comprised two layers for soils (JHI 2014) and bedrock (Hughes 1996) or superficial geology. A similar two-layer (upper zone: soils and lower zone: bedrock) approach was used in the finite difference saturated zone set-up with superficial geology represented as lenses. Hydraulic parameters for the unsaturated (saturated hydraulic conductivity, van Genuchten parameters) and saturated (horizontal and vertical hydraulic conductivity, specific storage and specific yield) zones were initially taken from the literature (Morris and Johnson 1967; O'Dochartaigh et al. 2012; MacDonald et al. 2012; Thompson 2012; Foster and Allen 2015) and were subject to manual calibration (Table 1).

The model used the finite difference approach for overland flow computation and the Kristensen–Jensen method for evapotranspiration. In the latter, a daily time series of reference evapotranspiration was computed (Allen et al. 1998) from the Darnhall meteorological station (as the climate data were available only in this station) and uniformly distributed over the catchment (see Fig. 1). Hourly precipitation from the four rain gauges for period 20/3/2011–23/6/2012 ('the study period') within the catchment was distributed using Thiessen polygons (Fig. 1). Although other methods

Table 1 Principal calibrated parameter values used in the model

Parameter	Average	Min	Max
Grid resolution (m)	200	–	–
Overland flow			
Manning *M*	3.0	1.0	20.0
Root depth (m)	–	0.0	1.5
Leaf area index	–	1.0	7.0
Crop coefficient	–	1.0	1.1
Detention storage (mm)	5.0	–	–
Unsaturated zone			
Saturated moisture content	0.4	0.4	0.5
Residual moisture content	0.0	0.0	0.1
Alpha	0.1	1.0E−02	0.4
N	1.6	1.5	1.8
SHC (m s^{-1})	1.8E−05	1.0E−13	7.0E−05
Saturated zone			
HHC (m s^{-1})	4.8E−06	1.9E−13	1.3E−05
VHC (m s^{-1})	9.7E−07	1.9E−13	3.7E−06
Specific yield	0.1	0.0	0.2
Specific storage	3.1E−02	1.0E−05	0.1

SHC saturated hydraulic conductivity, *HHC* horizontal hydraulic conductivity, *VHC* vertical hydraulic conductivity

of spatial interpolation of the precipitation were tried (e.g. Kriging), only the Thiessen polygon method allowed the overall area of the Middle Burn sub-catchment to gain precipitation from a single rain gauge. The MIKE 11 1D hydraulic model used the dynamic wave approximation of the St. Venant equations. Four branches were delineated using the Arc Hydro extension of ArcGIS (Maidment 2002) and DTM (Fig. 1). A total of 200 cross-sections were specified throughout the channel model and were based on the topographic survey (June 2013). Stream discharges were measured and rated at the Middle Burn and Kidston Mill gauge stations. The hydrological model of Middle Burn sub-catchment used data from a rain gauge situated directly in an adjoining sub-catchment area (the Shiplaw Burn), 0.9 km away. The second (Kidston Mill) integrates all four rain gauges as sources of rainfall. The maximum allowed time step for all components of the MIKE SHE model was set to one hour, while a fixed time step of 5 s was applied in the MIKE 11 hydraulic model. Due to the relatively short length of the simulation period and the limited availability of hydrological data to drive the model, period of 1.3 years (20/3/2011–23/6/2012) of rainfall and reference evapotranspiration inputs were repeated for a warm-up period immediately prior to the simulation period in order to establish initial conditions.

The calibration strategy was aimed to build the hydrological model able to reflect the hydrological response of the catchment not only during high-intensity events but also for the study period. The calibration procedure was as follows: the overall data for rainfall and discharge were subdivided into calibration (20/3/2011–19/3/2012) and validation (20/3/2012–23/6/2012) periods. The model was run and manually calibrated. The Nash–Sutcliffe efficiency index (NSE) was set as an objective function and was computed using the following equation:

$$\mathrm{NSE} = 1 - \frac{\sum_{t=1}^{T}\left(Q_m^t - Q_o^t\right)^2}{\sum_{t=1}^{T}\left(Q_o^t - Q_{\bar{o}}^t\right)^2} \quad (1)$$

where Q_m is simulated discharge, Q_o is observed discharge and $Q_{\bar{o}}$ is average observed discharge. Following Ritter and Muñoz-Carpena (2013), a threshold for satisfactory model performance, the value of NSE equal to 0.65 was deemed acceptable. This threshold was evaluated also for the selected events. During the calibration and validation, the *modified* Nash–Sutcliffe efficiency index (MNSE) and absolute total difference error were also assessed:

$$\mathrm{MNSE} = 1 - \frac{\sum_{t=1}^{T}\left(Q_m^t - Q_o^t\right)}{\sum_{t=1}^{T}\left(Q_o^t - Q_{\bar{o}}^t\right)} \quad (2)$$

$$\mathrm{ATD}\ \% = \left(\mathrm{abs}\left(\sum_{t=1}^{T} Q_o^t - \sum_{t=1}^{T} Q_m^t\right) \Big/ \sum_{t=1}^{T} Q_m^t \times 100\right) \quad (3)$$

The ATD % provides information about the volume changes and is crucial for flood volume balance. The MNSE uses the power of one, having a higher sensitivity to systematic errors (Krause et al. 2005). Furthermore, during every model run, water balance error (WBE) was calculated by the model as an additional measure of model performance.

Selection of the best gap-filling method and impact of the length of deleted and filled precipitation data

The Shiplaw rain gauge station was selected as a source of precipitation data for further steps. Three events of different lengths were chosen from the study period, using the criteria of maximal hourly rainfall, aiming for a spread of both duration and intensity. Based on this, three events with the maximal hourly rainfall over the study period were selected. The shortest was event 1 (63 h), followed by the lower-intensity multi-peak event 2 (366 h) and event 3 (72 h; Table 2). The event 1 produced the highest peak discharge equal to 20-year recurrence interval at Eddleston Village.

Four scenarios of data deletion within these events were established, to make the proportion deleted equally to 10%, 30%, 50% and 70% from the event total length. Deleted data were afterwards filled using the three methods of filling missing values of precipitation. In the simple substitution

Table 2 Observed characteristics of three events used in the study

Event	No. of hours	Kidston Mill				Middle Burn			
		Rainfall (mm h^{-1})		Discharge (m^3 s^{-1})		Rainfall (mm h^{-1})		Discharge (m^3 s^{-1})	
		Max	Cum	Max	Cum	Max	Cum	Max	Cum
1 (10/08/2011–11/08/2011)	63	6.6	56.7	16.6	500.3	6.6	60.2	1.1	28.8
2 (19/11/2011/–04/12/2011)	366	6.4	85.8	8.7	832.2	6.4	103	0.6	42.1
3 (02/01/2012/–05/01/2012/)	72	7.4	30.9	13.4	316	7	41.6	0.8	15.4

Max maximal hourly variable (rainfall/discharge), *Cum* cumulative value of a variable over the event

method, gaps were filled directly, using data obtained from the most similar station. Station similarity was assessed by correlation between stations expressed using Pearson's coefficient values (Lo Presti et al. 2010). For the linear regression, a substitute station was found using the same method as above. This station was then used as an explanatory variable for fitting a linear function by the least-squares method, and the equation obtained was then used for missing data prediction (Weisberg 2005). In the case of IDW, missing values were obtained as a weighted mean from all surrounding gauges, where the weight is proportional to the distance. The power value of three has been found most suitable for hourly data (Dirks et al. 1998), so this was adopted.

Four scenarios of synthetically deleted and filled precipitation time series of three events were varied in the hydrological model. While the start of the simulation for each of the events was the same as for the study period, the end of the simulation was set to the end of the particular event. The same model performance statistics (NSE, MNSE, and ATD%) were applied as for the model calibration and validation periods to select the best method of filling missing values of precipitation and to assess the impact of the event total length. However, three types of performance statistics were computed. The first type (T1) was calculated using Eqs. (1)–(3), applying the observed discharges and discharges produced by the hydrological model, which used four scenarios of synthetically deleted and filled precipitation data. Instead of using the observed discharges in Eqs. (1)–(3), the simulated discharges produced by the hydrological model using gap-free precipitation time series were applied for the second type (T2). The last type (T3) was calculated using Eqs. (1)–(3), but applying the observed and synthetically deleted and filled precipitation data instead of discharges. While the first two types (T1 and T2) allowed us to distinguish between the errors caused by inaccurate model and errors caused by each method of filling missing values of precipitation, the latter type was used to assess the transfer of the precipitation error to the model results. Performance statistics of all types were computed for the overall event length, not just for the deleted part. To select the best method of filling missing values of precipitation, all scenarios and events were evaluated together and median and interquartile ranges of performance statistics (Lo Presti et al. 2010) were compared. The impact of length was assessed for the best method of filling missing values of precipitation only. Mann–Whitney test was applied to the discharges to judge whether the differences caused by four scenarios of synthetically deleted and filled precipitation were significant.

Results

Hydrological model calibration and validation

While overall fits between the modelled and observed data were qualitatively good, simulated peaks were characteristically advanced compared with the observed flows (Fig. 2). These shifts in the timing of peak flows were higher in the Kidston Mill record; thus, better performance statistics were reported for the Middle Burn.

The NSE was equal to 0.84 (calibration) and 0.85 (validation) for the Middle Burn sub-catchment. Lower values were found for the Kidston Mill, when the NSE of all methods was equal to 0.74 and 0.73 for calibration and validation, respectively. Higher ATD% was found in Kidston Mill compared to Middle Burn, with the highest value for calibration equal to 22.8%. The best NSE values were reported for the event 3, followed by event 2 and event 1 in the Middle Burn, while the change in the second and third places occurred for the Kidston Mill. Detailed information for all performance statistics for the calibration and validation period and also for the three events is shown in Table 3. The average value for WBE was computed from all of the simulations. This was equal to 1.74% for the Middle Burn and 0.27% for the Kidston Mill catchment, indicating a lower computational error for the larger catchment.

Selection of the best filling method and evaluation of the impact of the length of deleted and filled precipitation data

The selection of the best method was based on the median and interquartile range of the NSE, MNSE and ATD% (Fig. 3). Substitution was found to be the best method, followed by linear regression and IDW for Middle Burn using the median as the criterion. All three types of performance

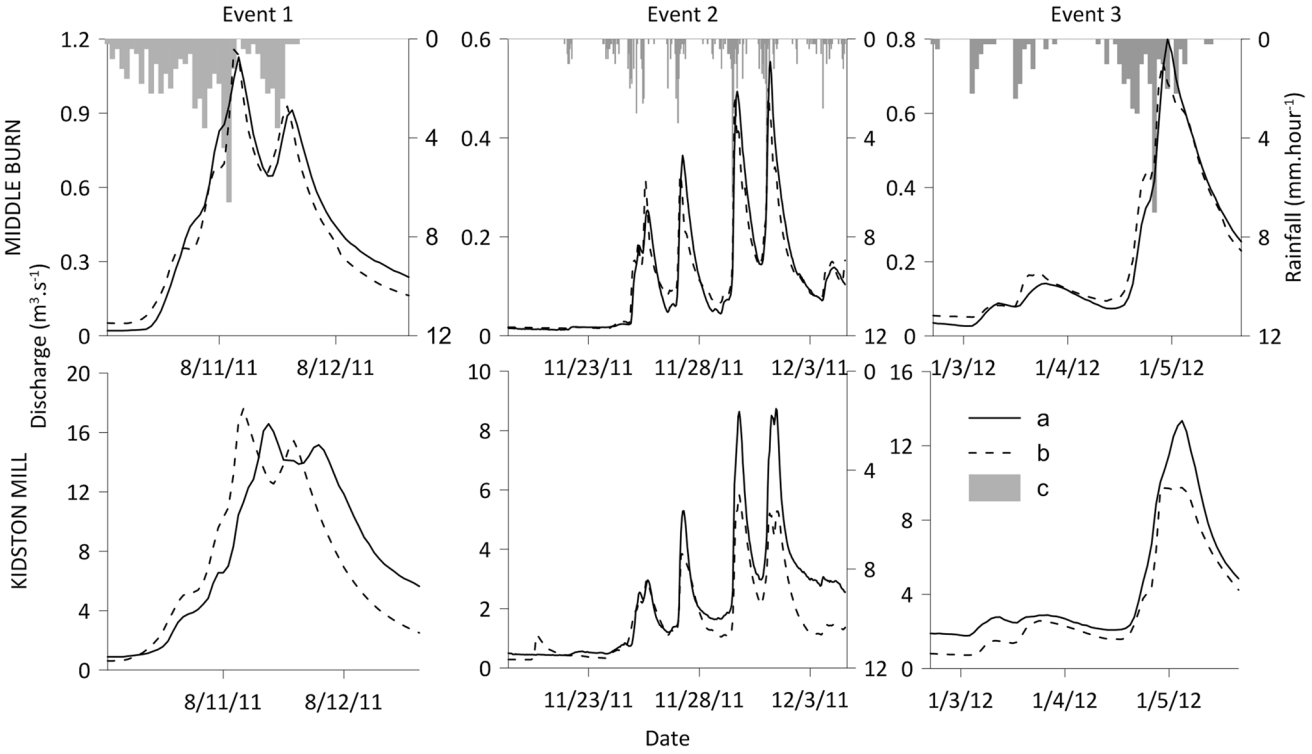

Fig. 2 Observed and simulated discharges in Middle Burn and Kidston Mill for three high-intensity events simulated by the hydrological model. Legend: a—observed, b—simulated, c—rainfall

Table 3 Hydrological model performance

Performance statistics	Period/event	Catchment	
		Middle Burn	Kidston Mill
NSE	Calibration	0.84	0.74
	Validation	0.85	0.73
	Event 1	0.94	0.65
	Event 2	0.93	0.74
	Event 3	0.97	0.86
MNSE	Calibration	0.65	0.49
	Validation	0.66	0.50
	Event 1	0.73	0.43
	Event 2	0.79	0.57
	Event 3	0.84	0.63
ATD%	Calibration	6.57	22.83
	Validation	6.72	12.18
	Event 1	7.09	9.27
	Event 2	0.82	24.49
	Event 3	5.93	23.54

statistics (T1, T2 and T3) agreed in this result. However, different results were found comparing the performance statistics T1 and T2 in the case of Kidston Mill. Applying the T1, the linear regression was favoured, while the T2 marked the substitution as the best method on the catchment scale.

Contradictory results among the best method selection were found applying the IQR criterion. For the Middle Burn, assessing the NSE, substitution produced the lowest IQR for all three types of performance statistics. Using IQR of MNSE and ATD%, the substitution was the best for the T2 and T3; however, IDW performed best for the T1 statistic. Similar contradictory outputs occurred on the catchment level: using the NSE and MNSE, the IDW performed the best applying the T1, while substitution was the best applying the T2. For the ATD%, the linear method produced the lowest IQR using the T1, but the substitution was the best applying the T2.

High Pearson's correlation coefficients (minimal value 0.95, maximal 0.99 from all events) were found when the three methods of filling missing values of precipitation were compared. The Mann–Whitney test showed the differences between methods were significant ($p < 0.005$) only in 8.3% of all of scenarios and events for the Middle Burn. These significant differences occurred during the longest event 2 between the IDW and linear regression for the scenarios 50% and 70% and between the IDW and substitution for the scenario 70%. Higher numbers of significant differences between the methods (19.4% of all cases) were found at Kidston Mill and occurred during the event 2, between the

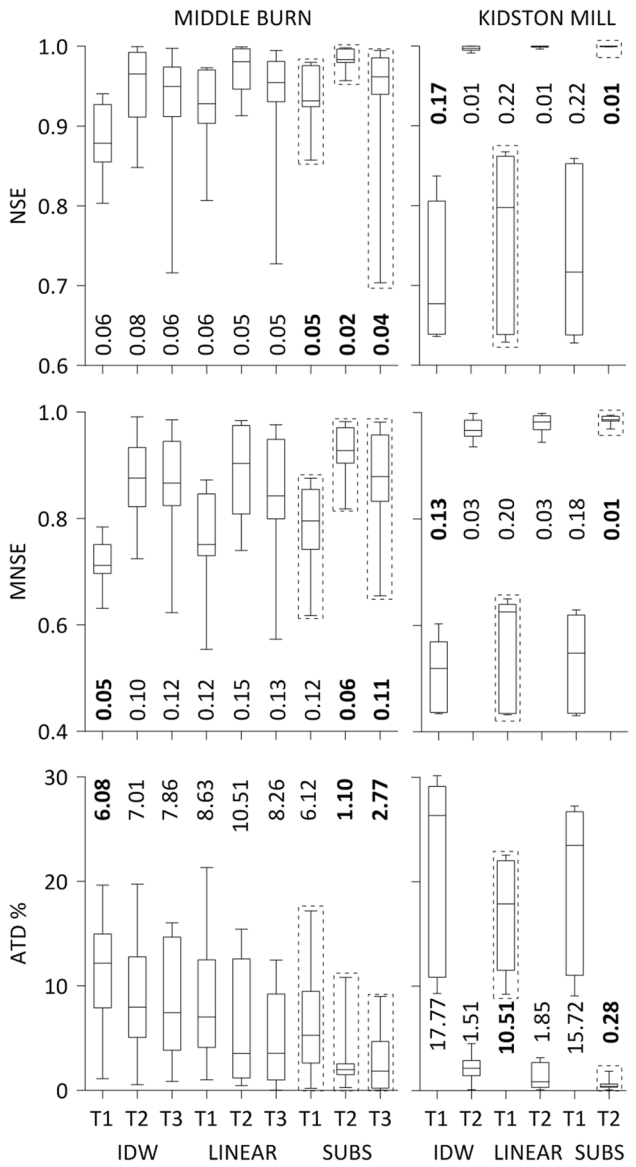

Fig. 3 Comparison of performance statistics of three methods infilling missing values of precipitation. Single box plot was created using the performance statistic of all events and all scenarios ($n = 12$ for every single box plot; Whiskers = Max and Min). The best method based on the median is marked by the dotted rectangle. Numbers denote the values of IQR. Bolded values denote the lowest IQR among three methods

substitution and linear regression, IDW and linear regression for the scenarios 30, 50 and 70% and between the IDW and linear regression for the scenario 10%.

The transfer of precipitation error to the simulated discharges is visible in Fig. 3, by comparing three types of performance statistics (T1, T2 and T3). The performance statistics computed from precipitation data (T2) were generally better than statistics computed using observed and simulated discharges (T2), but worse than statistics computed using simulated discharges. Thus, the hydrological model lowered the error in the precipitation (T1 and T3).

The impact of the length of deleted and filled precipitation data was assessed using the substitution method only as this provided the best results. Differences between the simulation with observed precipitation data and four scenarios of deleted and filled precipitation data are visualized in Fig. 4. Higher differences in discharges were found on the catchment scale compared to the inner sub-catchment. Differences in performance statistics were higher on the sub-catchment scale and are shown in Fig. 5. These were caused by various scenarios of synthetically deleted and filled precipitation data for three high-intensity events and three infilling methods.

By assessing all events and performance statistics on the sub-catchment scale, in 33.4% of cases, the model produced better results when synthetically deleted and filled gaps were used in the hydrological model compared to the configuration with the observed precipitation data. Amount of cases was lower (27.1%) on the catchment scale. Most of these situations occurred for the event 3, followed by the event 2.

Furthermore, the higher length of deleted and filled data produced better results compared to the shorter length. This happened for 27.1% of all cases for the Middle Burn, while lower values (6.3%) were calculated for the Kidston Mill. This happened mainly during the event 3 on both scales. The most sensitive performance statistic for this detection was the ATD%.

Significant differences were reported for the event 2 and event 3 by the Mann–Whitney test for the Kidston Mill catchment, while all differences were marked as insignificant for the Middle Burn. This test used the simulated discharges produced by the model set-up with the four scenarios of deleted and filled precipitation data and the observed discharges.

Differences in performance statistics of the second type (T2) are shown in Fig. 6. Similarly, in results in Fig. 5, higher differences were reported for the Middle Burn than for the overall catchment and differences for the event 1 were the highest.

We further found out in several cases (11.1% of all cases for the Middle Burn) greater length of deleted and filled data led to better results compared to the shorter length. Higher values (16.7%) were calculated for the Kidston Mill. This happened dominantly during the event 3 on both scales. The most sensitive performance statistic for this detection was again the ATD%.

Differences were insignificant comparing discharges produced by four scenarios to the discharges simulated by the model with observed precipitation data for all events and scenarios.

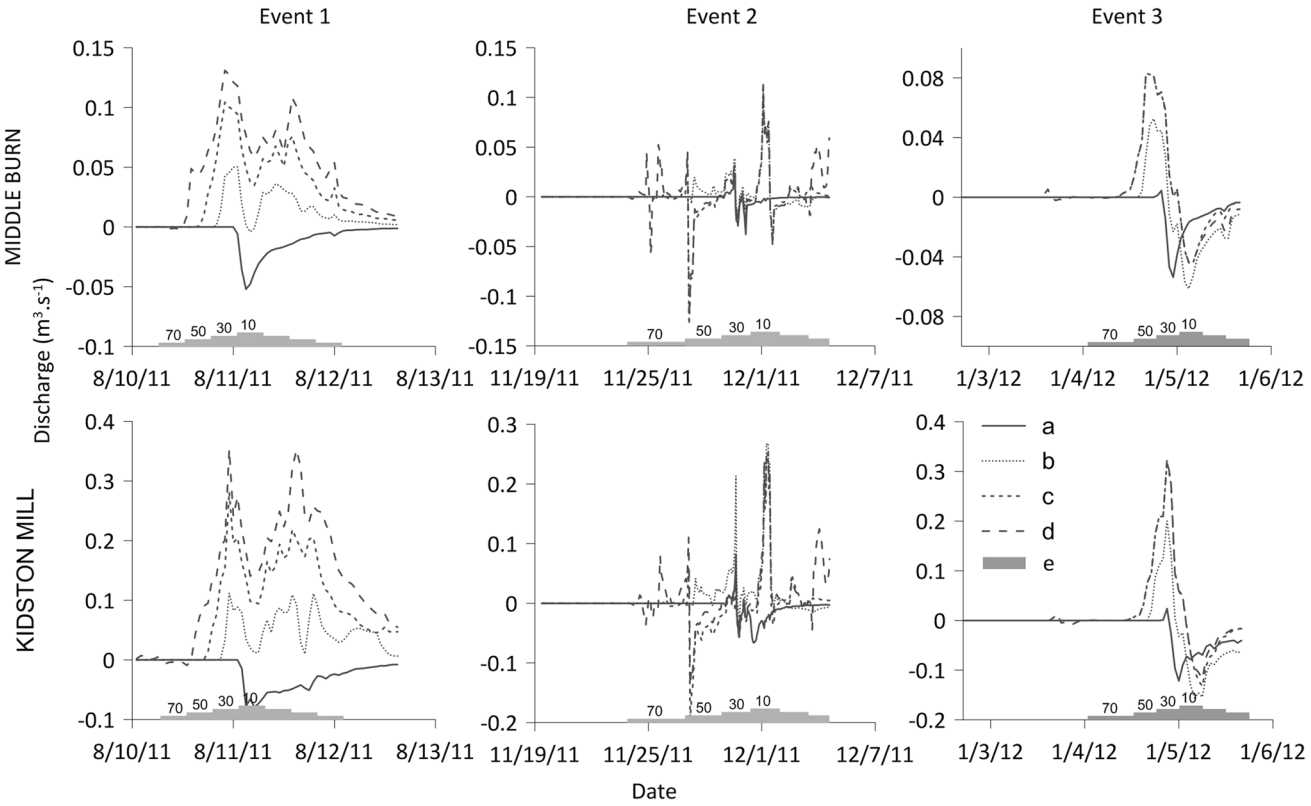

Fig. 4 Differences in discharges for four scenarios. Differences were computed between the simulation with observed precipitation data and four scenarios of deleted and filled precipitation data using the substitution. Legend: a—10% of deleted and filled data, b—30%, c—50%, d—70%, e—length of a particular scenario

Discussion

In this study, we applied the precipitation data to a fully distributed, physically based hydrological model. This type of modelling is based on the main premise; a high level of spatial resolution should lead to both improved representation of catchment behaviour and better simulation of the effects of changes in catchment processes and characteristics. As noted by Beven (2012), every single model requires its own model structure and own effective parameters (Vázquez and Hample 2014). Various models could produce different outputs as shown in the study of Huisman et al. (2009), where the effect of land cover change was examined; thus, results of this study (selection of the optimal infilling method) should be confirmed by different hydrological models.

Following the NSE criteria of model evaluation defined by Ritter and Muñoz-Carpena (2013), the model applied in this study was 'good' on the sub-catchment scale and 'acceptable' on the catchment scale for both the calibration and validation periods. All three events used in this study were marked as very good in the Middle Burn, while event 3 was good, and event 1 and event 2 were acceptable in the Kidston Mill. The computational error (WBE) for the Kidston Mill catchment were comparable to other studies (Foster and Allen 2015; Rahim et al. 2012). Higher errors in the WBE for Middle Burn could be caused by coarse-grid resolution (200 m), which might have been unable to account for sub-catchment hydrological processes. The length of the validation period was restricted to 3 months due to the hydrological data availability. Although a longer period (several years) would be essential to model variability of flood regime, we believe the results of this case study were not influenced by the length of the validation period as documented by fulfilling the criteria of model evaluation defined by Ritter and Muñoz-Carpena (2013). Various lengths of the IQR in the results could be caused by the model sensitivity of the input data reported by Beven (2006) and Vázquez and Hample (2014).

Three widely used methods for filling synthetically created gaps in the precipitation time series were assessed. Of the three methods used, the simple substitution produced the best results, followed by linear regression and IDW. This result is in agreement with the work of Lo Presti et al. (2010), where authors reported acceptable results by using the substitution when similarity among gauges was high. This can be a consequence of high correlation coefficient of the surrounding gauges. The correlation coefficient may be used as a weight in the IDW method rather than the

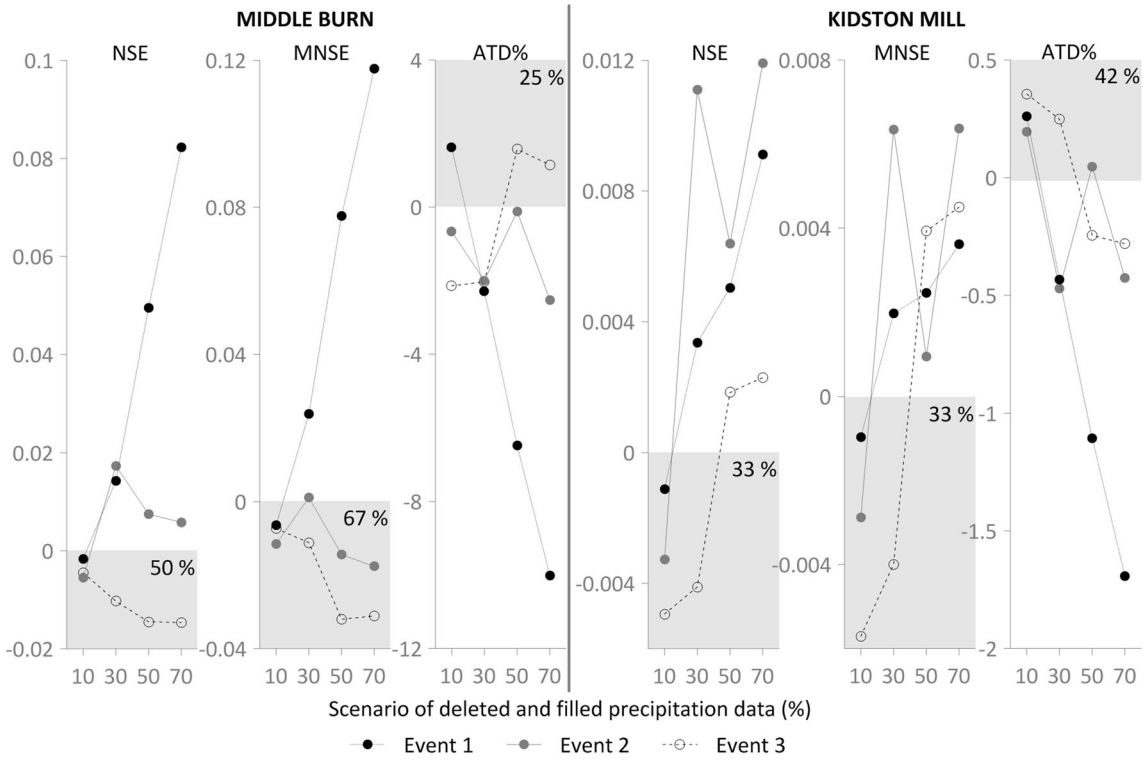

Fig. 5 Differences in performance statistics of type 1. Grey areas and percentage mark the simulations when the model produced better results using the time series with filled gaps compared to the set-up with gaps-free data

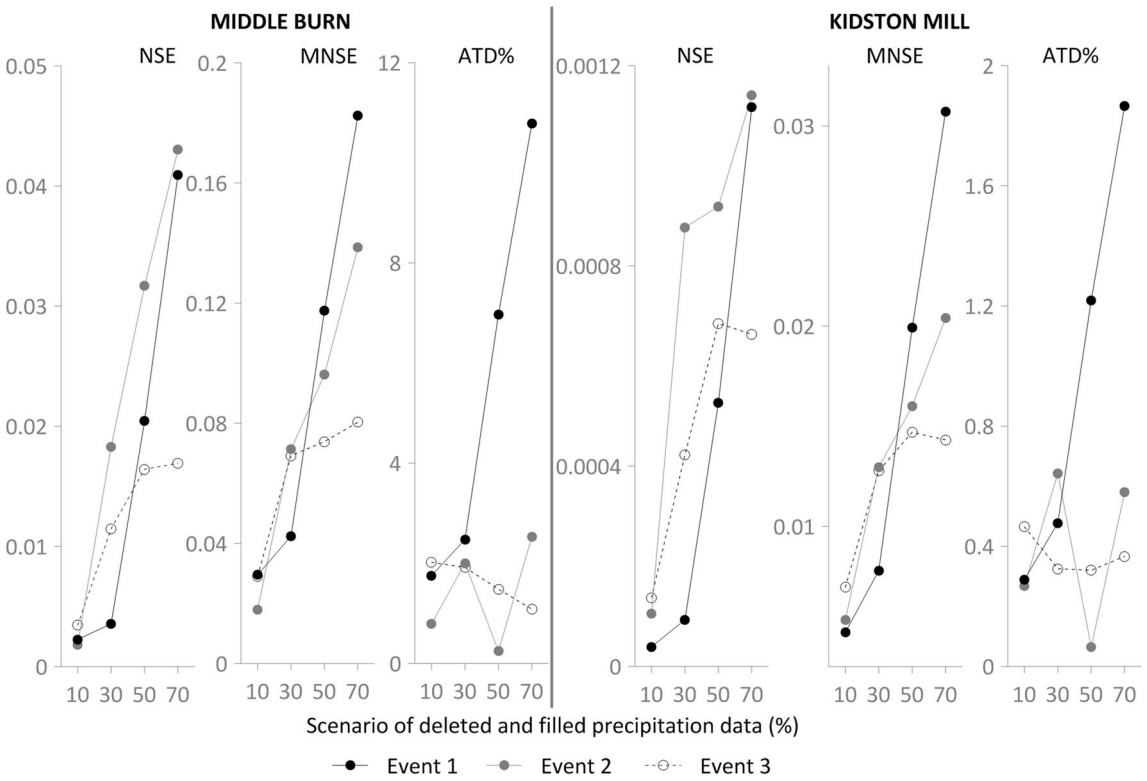

Fig. 6 Differences in performance statistics of type 2

distance (Vicente-Serrano et al. 2010) to improve results of this method.

Three performance statistics (NSE, MNSE and ATD%) were applied for both aims of this study. Contradictory conclusions were drawn in the selection of the best method and in assessing the impact of the length of deleted and filled precipitation data in the several cases using these statistics. This happened because each of the statistics was sensitive to different model (catchment) behaviour (e.g. high errors, water balance). This emphasizes the necessity of application of several performance statistics to obtain a holistic view of the outputs of the hydrological model (Moriasi et al. 2007; Ritter and Muñoz-Carpena 2013).

We computed three different types of performance statistics (T1, T2 and T3). While two of them were used for the hydrological model (T1 and T2), the latter was applied to the precipitation only. Transfer of precipitation errors to the results of the hydrological model was shown comparing all types of statistics. This is in agreement with other studies (Sun et al. 2000; Kuczera and Williams 1992; Kim and Pachepsky 2010). The model configured to use the synthetically deleted and filled precipitation data produced better performance than the model configured to use observed precipitation data, in several cases. In other words, the low-quality data lead to better model performance than high-quality input. This was revealed applying the T1, and it is a consequence of the effective parameters (Beven 2006) which were able to balance the inadequate representation of input data (Vázquez and Hample 2014; Alvarenga et al. 2016). Contradictory output in the selection of the best infilling method was found, comparing the T1 and T2 on the catchment scale. One remark needs to be done concerning the T1, T2 and T3. While T1 is independent of calibration results, T2 is based on the quality of the calibration (the better the calibration, the better the performance statistic). We propose to apply the T2 to select the best infilling method, as this type is using the simulated discharges produced by the model configured to use observed precipitation instead of the observed discharge.

Typically, distributed models employ the highest resolution of spatial data. However, the resolution of spatial data varies through the model (e.g. hydraulic properties of sediment and rocks, soils, land use data, digital terrain model, etc.) and is based purely on the data availability. The level of this availability allows the modeller to select more or less sophisticated model structure (Beven 2012). Furthermore, the application of the finest scale data does not necessarily provide the best agreement with observation. This was shown in the studies of Vázquez and Hample (2014) and Alvarenga et al. (2016), where datasets of lower quality (evapotranspiration in the first case and land cover in latter) produced superior model outputs over the higher quality data. In this study, the longer period of deleted and filled precipitation data used in the model leads to better model performance compared to shorter period in several cases, again because of effective parameters. Although it is highly possible, the more detailed calibration would eliminate this conflict; results of this study confirmed the problems associated with calibration of physically based, distributed hydrological models (Freeze and Harlan 1969; Beven 1993; Walker et al. 2003; Fatichi et al. 2016).

The length of deleted and filled precipitation data was assessed using four scenarios for three events of different lengths and rainfall intensities. In a majority of cases, we reported increase in bias with the increase in length of gaps, which is in agreement with the study of Teegavarapu and Nayak (2017). When comparing three infilling methods, significant differences were reported only for the longest event 2. Assessing the impact of the length, significant differences were reported for the longest event 2, followed by event 3. Thus, the length of the event had a crucial bearing to the modelled discharges. We further suppose the low magnitude of the events leads to the conclusion of this study: the impact of the length of deleted and filled precipitation data on the outputs of hydrological model is insignificant in a majority of cases. More events of higher recurrence interval should be applied to correctly investigate the impact of the length of deleted and filled precipitation data. This remark is based also on the study of Teegavarapu and Nayak (2017), where authors mark the events of heavy and very heavy rainfall as the most problematic.

The aims of the study were solved on two scales: overall catchment and inner sub-catchment. On the catchment scale, the differences between the simulated discharges produced by a model with a 'gaps-free' configuration and with four scenarios of deleted and filled precipitation data were higher than on the sub-catchment scale because of a larger area (Thiessen polygon), from where the information about the precipitation was spatially interpolated. Differences in performance statistics of both types (T1 and T2) were higher on the sub-catchment scale compared to the overall catchment. This is because the inner sub-catchment had the only one source of precipitation—the Shiplaw rain gauge station, from which data were synthetically deleted and filled. The overall catchment also used data from this station, but another three rain gauges with observed data were applied and spatially interpolated. Thus, the influence of missing precipitation data on the result of the hydrological model is greatest at the sub-catchment level and decreases with increasing catchment area due to synergic effects of other gauging stations. This finding is in agreement with the conclusion of Krajewski et al. (2003). However, more catchments should be examined in order to evaluate the impact of the length of deleted and filled precipitation data.

We applied a manual calibration strategy and approach of optimal parameter set to calibrate the model to hourly

observed discharges in two gauging stations. Indeed, manual calibration remains a subjective approach, and a series of drawbacks in this approach were reported (Boyle et al. 2001; Vázquez and Hample 2014); the advantages of this approach are also known (Vaze et al. 2012). In the study of Vázquez and Hample (2014), authors found contrasting results for the manual and automatic calibration procedures.

Conclusion

We compared three infilling methods of precipitation for filling missing precipitation data. Our results showed the substitution provided the best results followed by linear regression and IDW, probably as a consequence of high correlation coefficient among rain gauges. Thus, in the case of gauges with the high correlation coefficient, the substitution can be used.

In our case study, the length of the event had a crucial bearing on the outputs of the hydrological model. However, only in a minority of cases, significant differences were reported between four scenarios of deleted and filled data, probably as a consequence of low magnitude of the events. Further analyses with events of higher magnitude should be carried out, and longer events should be evaluated to fully support this hypothesis.

Our results further indicate the data of lower quality (deleted and filled time series of precipitation) led to better model performance in several cases than the higher-quality data (original precipitation time series). This happened firstly when the hydrological model was fed by the original data and model performance was compared with the four scenarios and, secondly, when four scenarios of deleted and filled time series were compared between each other. Both cases were connected with the uncertainty associated with hydrological models, and modellers should be aware of this uncertainty and should carefully explain the results when the aim of the study is to compare the data of different qualities (not only the precipitation but also static catchment characteristics such as land use, soil texture and geological characteristics).

Lastly, the impact of the deleted and filled data on the model performance was higher on the sub-catchment scale. This is because the source of the precipitation data for this sub-catchment was from the gauge when the time series was deleted and filled. On the catchment scale, the impact was reduced by the synergic effect of four gauges. This emphasizes the necessity of close investigation of precipitation quality for the catchment where the source of data comes from the only single rain gauge.

Acknowledgements This work was supported by the research Project SGS01/UVAFM/2016 financed by the University of Ostrava and by Scottish Government Funding via Eddleston Water Project. We would like to thank Mr. Matěj Horáček for providing support to this work and to the Tweed Forum for the permission to use outputs of the gauged network set-up under the project.

Compliance with ethical standards

Conflict of interest On behalf of all authors, the corresponding author states that there is no conflict of interest.

References

Allen RG, Pereira LS, Raes D, Smith M (1998) Crop evapotranspiration—guidelines for computing crop water requirements. FAO Irrigation and drainage paper 56. Food and Agriculture Organization, Rome

Alvarenga LA, de Mello CR, Colombo A, Cuartas LA, Bowling LC (2016) Assessment of land cover change on the hydrology of a Brazilian headwater watershed using the Distributed Hydrology–Soil–Vegetation Model. Catena 143(2016):7–17

Andersen J, Refsgaard JC, Jensen KH (2001) Distributed hydrological modelling of the Senegal river basin—model construction and validation. J Hydrol 247(3–4):200–214

Archer NL, Bonell M, Coles N, MacDonald AM, Auton R (2013) Soil characteristics and landcover relationships on soil hydraulic conductivity at a hillslope scale: a view towards local flood management. J Hydrol 497:208–222

Arnaud P, Bouvier C, Cisneros L, Dominguez R (2002) Influence of rainfall spatial variability on flood prediction. J Hydrol 260(1–4):216–230

Bárdossy A, Das T (2008) Influence of rainfall observation network on model calibration and application. Hydrol Earth Syst Sci Discuss 3(6):3691–3726

Bárdossy A, Pegram G (2014) Infilling missing precipitation records—a comparison of a new copula-based method with other techniques. J Hydrol 519:1162–1170

Beven K (1993) Prophecy, reality and uncertainty in distributed hydrological modelling. Adv Water Resour 16:41–51

Beven K (2006) A manifesto for the equifinality thesis. J Hydrol 320(1):18–36

Beven K (2012) Rainfall–runoff modelling: the primer, 2nd edn. Wiley, Chichester, p 455

Blenkinsop S, Lewis E, Chan SC, Fowler HJ (2016) Quality-control of an hourly rainfall dataset and climatology of extremes for the UK. Int J Climatol 37:722–740

Boudevillain B, Delrieu G, Wijbrans A, Confoland A (2016) A high-resolution rainfall re-analysis based on radar–raingauge merging in the Cévennes-Vivarais region, France. J Hydrol 541:14–23

Boyle DP, Gupta HV, Sorooshian S, Koren V, Zhang Y, Smith M (2001) Toward improved streamflow forecasts: value of semidistributed modeling. Water Resour Res 37(11):2749–2759

Cecinati F, de Niet AC, Sawicka K, Rico-Ramirez MA (2017) Optimal temporal resolution of rainfall for urban applications and uncertainty propagation. Water (Switzerland). https://doi.org/10.3390/w9100762

Cole SJ, Moore RJ (2008) Hydrological modelling using raingauge and radar-based estimators of areal rainfall. J Hydrol 358(3–4):159–181

Dirks KN, Hay JE, Stow CD, Harris D (1998) High-resolution studies of rainfall on Norfolk Island. Part II: interpolation of rainfall data. J Hydrol 208:187–193

Eischeid JK, Pasteris PA, Diaz HF, Plantico MS, Lott NJ (2000) Creating a serially complete, national daily time series of temperature and precipitation for the western United States. J Appl Meteorol 39(9):1580–1591

Fatichi S, Vivoni ER, Ogden FL, Ivanov VY, Mirus B, Gochis D, Downer CHW, Camporese M, Davison JH, Ebel B, Jones N, Kim J, Mascaro G, Niswonger R, Restrepo P, Rigon R, Shen CH, Sulis M, Tarboton D (2016) An overview of current applications, challenges, and future trends in distributed process-based models in hydrology. J Hydrol 537:45–60

Ficchi A, Perrin CH, Andréassian V (2016) Impact of temporal resolution of inputs on hydrological model performance: An analysis based on 2400 flood events. J Hydrol 538:454–470

Foster SB, Allen DM (2015) Groundwater–surface water interactions in a mountain-to-coast watershed: effects of climate change and human stressors. Adv Meteorol 22:861805

Freeze RA, Harlan RL (1969) Blueprint for a physically-based, digitally-simulated hydrologic response model. J Hydrol 9:237–258

Heistermann M, Kneis D (2011) Benchmarking quantitative precipitation estimation by conceptual rainfall–runoff modeling. Water Resour Res 47(6):1–23

Hughes RA (1996) 1:63,360/1:50,000 geological map series. Sheet number: 24E. Sheet title: Peebles. 1: 50,000. I.G.S. Geological Survey of Scotland, Edinburgh

Huisman JA, Breuer L, Bormann H, Bronstert A, Croke BFW, Frede H-G, Graff T, Hubrechts L, Jakeman AJ, Kite G, Leavesley G, Lanini J, Lettenmaier DP, Lindstrom G, Seibert J, Sivapalan MG, Viney NR, Willems P (2009) Assessing the impact of land use change on hydrology by ensemble modelling (LUCHEM) III: scenario analysis. Adv Water Resour 32:159–170

JHI (James Hutton Institute) (2014) Soil map (National Soil Map). 1:250,000. Vector data

Kim JW, Pachepsky YA (2010) Reconstructing missing daily precipitation data using regression trees and artificial neural networks for SWAT streamflow simulation. J Hydrol 394(3–4):305–314

Krajewski WF, Ciach GJ, Habib E (2003) An analysis of small-scale rainfall variability in different climatic regimes. Hydrol Sci J 48(2):151–162

Krause P, Boyle DP, Base F (2005) Comparison of different efficiency criteria for hydrological model assessment. Adv Geosci 5:89–97

Kuczera G, Williams BJ (1992) Effect of rainfall errors on accuracy of design flood estimates. Water Resour 28(4):1145–1153

Lewis E, Quinn N, Blenkinsop S, Fowler HJ, Freer J, Tanguy M, Hitt O, Coxon G, Bates P, Woods R (2018) A rule based quality control method for hourly rainfall data and a 1 km resolution gridded hourly rainfall dataset for Great Britain: CEH-GEAR1hr. J Hydrol 564:930–943

Lo Presti R, Barca E, Passarella G (2010) A methodology for treating missing data applied to daily rainfall data in the Candelaro River Basin (Italy). Environ Monit Assess 160(1–4):1–22

MacDonald AM, Maurice L, Dobbs MR, Reeves HJ, Auton CA (2012) Relating in situ hydraulic conductivity, particle size and relative density of superficial deposits in a heterogeneous catchment. J Hydrol 434–435:130–141

Maidment DR (2002) Arc Hydro: GIS for water resources. ESRI, Sacramento, p 203

Moriasi DN, Arnold JG, Van Liew MW, Bingner RL, Harmel RD, Veith TL (2007) Model evaluation guidelines for systematic quantification of accuracy in watershed simulations. Trans ASABE 50(3):885–900

Morris DA, Johnson AI (1967) Summary of hydrologic and physical properties of rock and soil materials as analyzed by the Hydrologic Laboratory of the U.S. Geological Survey. U.S. Geological Survey Water-Supply Paper 1839-D, p 42

Moulin L, Gaume E, Obled C (2008) Uncertainties on mean areal precipitation: assessment and impact on streamflow simulations. Hydrol Earth Syst Sci Discuss 5(4):2067–2110

O'Dochartaigh BE, MacDonald AM, Merritt JE, Auton CA, Archer N, Bonell M, Kuras O, Raines MG, Bonsor HC, Dobbs M (2012) Eddleston water floodplain project: data report. Nottingham, p 95

Pearce D, Rea BR, Bradwell T, McDougall D (2014) Glacial geomorphology of the Tweedsmuir Hills, Central Southern Uplands, Scotland. J Maps 10(3):457–465

Pauthier B, Bois B, Castel T, Thévenin D, Chateau Smith C, Richard Y (2016) Mesoscale and local scale evaluations of quantitative precipitation estimates by weather radar products during a heavy rainfall event. Adv Meteorol 2016:9

Ritter A, Muñoz-Carpena R (2013) Performance evaluation of hydrological models: statistical significance for reducing subjectivity in goodness-of-fit assessments. J Hydrol 480:33–45

Reusser DE, Blume T, Schaefli B, Zehe E (2009) Analysing the temporal dynamics of model performance for hydrological models. Hydrol Earth Syst Sci 13:999–1018

Sahoo GB, Ray C, De Carlo EH (2006) Calibration and validation of a physically distributed hydrological model, MIKE SHE, to predict streamflow at high frequency in a flashy mountainous Hawaii stream. J Hydrol 327(1–2):94–109

Singh VP (1997) Effect of spatial and temporal variability in rainfall and watershed characteristics on stream flow hydrograph. Hydrol Process 11(12):1649–1669

Singh CR, Thompson JR, Kingston DG, French JR (2011) Modelling water-level options for ecosystem services and assessment of climate change: Loktak Lake, northeast India. Hydrol Sci J 56(8):1518–1542

Song Y, Han D, Rico-Ramirez MA (2017) High temporal resolution rainfall rate estimation from rain gauge measurements. J Hydroinf 19:930–941

Sun X, Mein RG, Keenan TD, Elliott JF (2000) Flood estimation using radar and raingauge data. J Hydrol 239(1–4):4–18

Teegavarapu RSG, Nayak A (2017) Evaluation of long-term trends in extreme precipitation: implications of in-filled historical data use for analysis. J Hydrol 550:616–634

Thompson JR (2012) Modelling the impacts of climate change on upland catchments in southwest Scotland using MIKE SHE and the UKCP09 probabilistic projections. Hydrol Res 43(4):507

Thompson JR, Green AJ, Kingston DG, Gosling SN (2013) Assessment of uncertainty in river flow projections for the Mekong River using multiple GCMs and hydrological models. J Hydrol 486:1–30

Thompson JR, Green AJ, Kingston DG (2014) Potential evapotranspiration-related uncertainty in climate change impacts on river flow: An assessment for the Mekong River basin. J Hydrol 510:259–279

Tweed Forum (2016) The Eddleston Water Project Report (online). www.tweedforum.org. Accessed 20 Oct 19

Vaze J, Jordan P, Beecham R, Frost A, Summerell G (2012) Towards best practice model application. eWater Cooperative Research Centre, Australia, Bruce, p 46.

Vázquez RF, Hample H (2014) Prediction limits of a catchment hydrological model using different estimates of ET. J Hydrol 513:216–228

Vicente-Serrano SM, Beguería S, López-Moreno JI, García-Vera MA, Stepanek P (2010) A complete daily precipitation database for northeast Spain: reconstruction, quality control, and homogeneity. Int J Climatol 30:1146–1163

Villarini G, Mandapaka PV, Krajewski WF, Moore RJ (2008) Rainfall and sampling uncertainties: a rain gauge perspective. J Geophys Res 113:D11102

Walker WE, Harremoes P, Rotmans J, Van der Sluijs JP, Van Asselt MBA, Janssen P, Krayer von Krauss MP (2003) Defining uncertainty a conceptual basis for uncertainty management in model-based decision support. Integr Assess 4(1):5–17

Weisberg S (2005) Applied linear regression, 3rd edn. Wiley, Minneapolis, p 336

Acta Geophysica (2020) 68:577–596
https://doi.org/10.1007/s11600-019-00397-w

RESEARCH ARTICLE - ATMOSPHERIC & SPACE SCIENCES

Moon's subsurface heat flow mapping

Weijia Zhang[1,2] · Ben Zhao[3] · Xinyu Lou[4]

Received: 27 January 2019 / Accepted: 26 December 2019 / Published online: 10 February 2020

Abstract
This paper investigates the lunar subsurface heat flow using data from the recent Chinese lunar orbiting spacecrafts Chang'e 1 and 2 to explore variations in the subsurface temperature of the Moon. These variations include heat flow information of the subsurface and the interior of the Moon. This research aims to develop a radiative transfer forward model for an airless body and then utilize microwave radiometer (MRM) data to study an observed anomaly of elevated 2-m-deep TB measurements in the Oceanus Procellarum region on the lunar subsurface. After initial comparison of the data from MRM with that from instruments and modelling of the lunar regolith parameters, a multi-layer radiative transfer forward model has been derived using the fluctuation dissipation theorem. The forward model was then used to invert the MRM-measured TB data to generate temperature profiles of 2-m-deep subsurface. The provisional results show that, as expected, the temperature of 2-m subsurface is potentially correlated with the distribution of radioactive elements such as uranium and thorium in the lunar crust. The temperature map of 2-m subsurface was then converted to a lunar heat flow map, which was validated by the Apollo 15 and 17 measurements. Inspecting this heat flow map, abnormal high heat flow in the Oceanus Procellarum KREEP Terrain (PKT) region was noticed. The PKT is enriched with a high abundance of radioactive elements such as uranium and thorium. Hence, a heat flow model based on radioactive elements as well as internal cooling was built to investigate such a finding.

Keywords Lunar subsurface · Heat float mapping, radiative transfer forward model · MRM

Introduction

Importance of studying lunar subsurface temperature and heat flow

Missions exploring the lunar surface have greatly improved our understanding of the Moon's composition, origin and evolution. However, information about the properties of the lunar subsurface, deep structural features and thermal environment is hard to determine, except for measurements obtained at the Apollo and Luna landing sites and returned lunar samples (Heiken et al. 1991) and a number of gravity experiments in missions subsequent (Andrews-Hanna et al. 2014). Geochemical surveys of returned lunar samples cannot provide direct information on the global composition and physical properties of the subsurface. As a result, knowledge of the Moon's basic geophysical properties including its internal structure which can help in constraining theories about its formation and evolution remains lacking, and our understanding of the lunar origin and evolution is still limited (Hartmann et al. 1986). Due to these limitations, the lunar subsurface, deep structural features and thermal environment are still not fully understood. For example, the Moon that once thought to be cold and dead may have experienced recent volcanic eruptions in the last tens of millions of years (Braden et al. 2014) and hence some parts of the Moon may be warmer than previously thought (Braden et al. 2014).

The thermal evolution and current thermal state of the Moon is a very important active area of research. By measuring the internal heat flow and the deep subsurface temperature profile (1–5 m) of the Moon, this paper can trace back and estimate the lunar core's thermal flow. The results are important for developing theories about the Moon's crust and any residual activity in its core. Specifically:

✉ Weijia Zhang
east25220@126.com

[1] Department of Mathematics and Physics, Shaoxing University, Shaoxing, China

[2] Department of AOP Physics, University of Oxford, Oxford, UK

[3] Zhejiang Gongshang University, No. 149, J Road, Hangzhou 310000, China

[4] Department of the Environmental and Resource Science, Zhejiang University, No. 866, Yuhangtang Road, Hangzhou 310000, China

(a) Modelling the heat flow of the Moon as part of diagnostic tests for thermal evolution models.
(b) Using the distribution of radioactive elements to constrain the evolution of the lunar crust and its connection to differentiation processes during the Moon's formation. This can help us understand the quantity and distribution of radioactive elements between the crust and mantle, part of its differentiation story (Warren and Rasmussen 1987).
(c) To understand the nature of the Procellarum KREEP Terrane (PKT).[1]

Geochemical surveys have shown (Haskin 1998) that KREEP mainly occurs in the north-west quadrant of the Moon (Haskin 1998). The thermal modelling by Wieczorek and Phillips (2000) showed that the high radioactivity of PKT could contribute as much as 20 mW/m^2 of heat flow at the centre of PKT, so it is a significant energy source that needs to be quantified. By comparing the heat flow at the centre of the PKT with the average heat flow of the Moon, the overall abundance of radioactive materials can be estimated. The Apollo measurements were made at only two locations, so the available samples may not reasonably represent the concentration of radioactive elements in KREEP (Korotev 1998).

(d) Understanding the lunar subsurface temperature distribution is also critical in studying the timing and evolution of lunar volcanism (Andrews-Hanna et al. 2014). The detection of any anomalous hot spots not correlated with KREEP terrain needs to be investigated.

The advantages of microwave remote sensing measurements for determining lunar heat flow

Global measurements of lunar heat flow are required for understanding the Moon. Subsurface heat flow can generally be estimated in two ways, in situ measurements and by remote sensing. In situ measurements involve drilling a hole in the lunar surface and determining the temperature at specific depths.

Measurements at the Apollo 15 and 17 sites are complicated to interpret because of experimental difficulties, including making sure the regolith was not compacted prior to inserting the heat probe (Heiken et al. 1991). In addition, both the Apollo 15 and 17 heat measurement sites were in Maria regions near the lunar equator and thus cannot be easily compared with other areas. More importantly, the Apollo 15 and 17 sites are in or nearby KREEP rich terrain. Therefore, they cannot represent the lunar crust as whole (Hagermann and Tanaka 2006).

The second way to measure temperature profiles is by remote sensing. Since September 2009, the Diviner Lunar Radiometer Experiment (Diviner) on the Lunar Reconnaissance Orbiter (LRO) (Paige et al. 2010) has been acquiring an extensive set of thermal emission measurements from the lunar surface at infrared wavelengths generating global bolometric maps of the temperatures of the top 2 mm surface. Remote sensing techniques such as Diviner that use thermal infrared or visible wavelengths can only provide compositional and temperature information to a depth of a few millimetres. As a result, data on the global, deep (50 cm or more) lunar subsurface temperature structure, mineralogy and heat flow are limited.

Longer electromagnetic wavelengths in microwave region of the spectrum (> 1 mm) have much greater penetration depths and so can potentially probe at greater depths than infrared techniques alone, thereby revealing the lunar regolith's deeper (> 50 cm) temperature structure. In addition to regolith temperature, microwave remote sensing measurements can also potentially give information about other properties such as dielectric constant and density.

Microwave remote sensing aims to look into the shape and structure of an object by detecting radiation reflected or emitted at wavelengths that are typically > 1 mm. Microwave remote sensing techniques developed for Earth measurements in the late twentieth century can also be applied to other planets and extraterrestrial bodies, including the Moon. Using these longer wavelengths, temperatures at depths of several metres can then be estimated. Therefore, microwave remote sounding can compensate for the shortcomings of other remote sensing techniques (which can only penetrate < 2 cm), providing additional data. However, the modelling of microwave remote sensing is challenging because there is a dependence on many parameters including mineralogy, density, heat capacity, dielectric constant, etc.

Both CE-1 and CE-2 lunar orbiters were equipped with a passive microwave radiometer (MRM) to measure the brightness temperature of the lunar surface (Li et al. 2010). The measured lunar brightness temperature (TB) can then be used to determine the lunar subsurface temperature after taking into account certain lunar regolith properties (e.g. density, heat capacity, mineralogy, dielectric constants, etc.). Data in the microwave region of the electromagnetic spectrum measured by instruments, such as the MRM on CE-1 and CE-2, can penetrate deeper (up to 5 m) into the lunar subsurface than visible or thermal infrared instruments (~ 2 mm). This opens a window into deep lunar subsurface temperature and heat flow, which presents a 'microwave moon'.

[1] KREEP is an acronym built from the letters K (potassium), REE (rare Earth elements) and P (phosphorus).

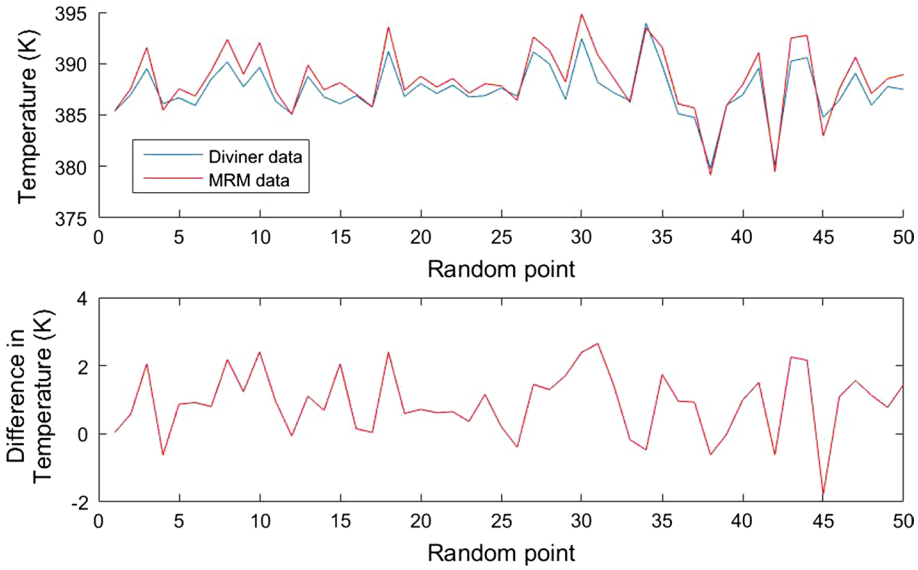

Fig. 1 Temperature measured by Diviner at 50 random equatorial lat/lon points was compared against the MRM data

MRM data validation

Both CE-1 and CE-2 MRMs have been used to detect the brightness temperature (TB) of lunar surface and retrieve lunar regolith thickness, temperature, dielectric constant and other related properties (Wang et al. 2008). Details of the instrument and ground calibrations are described by Wang et al. (2010).

The temperature variations in all operational orbits were between 12 and 23 K, with no more than 0.5 K temperature variation for each detected orbit period receiver (Wang et al. 2010). The performance was then acceptable to meet the radiometric accuracy requirement of < 0.5 K.

Assuming a nominal lunar regolith mineral content of $S = 10\%$ (S is defined as $S = \mathrm{Ti}\% + \mathrm{Fe}\%$ by mass fraction) and density of 1.9 g/cm^3, predicted penetrating depths are $< 0.5, < 1.0, < 2.0$ and ≥ 5 m at 37.0, 19.35, 7.8 and 3 GHz, respectively (Wang et al. 2008; Li et al. 2010).

The 3.0 GHz channel of the MRM can sense temperatures from depths of approximately 5 m below the lunar surface. Therefore, comparing data obtained from MRM with those gathered from instruments, such as the Diviner radiometer (which can sense temperatures to depths of 2 mm) of the LRO, is of great interest (Paige et al. 2010).

The Diviner Lunar Radiometer Experiment is a multichannel solar reflectance and infrared radiometer with high-frequency channels of the microwave instrument, of which three spectral filters are near 8 μm wavelengths and four filters cover approximately 13–23, 25–41, 50–100 and 100–400 μm wavelengths (Paige et al. 2010). Data are collected in a push-broom configuration across the surface of the Moon. The radiometer charts the temperature of entire lunar surface at approximately 500 m horizontal scales. To identify potential ice deposits, Diviner has been mapping the global thermal state of the Moon since July 2009.

The data from the high-frequency channel characterize the surface and can be compared with the Diviner data. Overlaps between CE-1 and Diviner data at specific local times were checked to verify the validity of both the Diviner and CE-1 MRM data as an independent inter-comparison of both data sets. CE-1 data were checked against the Diviner results when sampled on a similar spatial grid (Fig. 1). The effects of topography and local time were minimized by extracting Diviner data with local times and latitude/longitude coordinates within the region with the most CE-1 flyby times, e.g. 0° to 5° N and 40°–35° W for midday (11 a.m. to 1 p.m. local time) and 0° to 5° N and 140° to 145° E for midnight (11 p.m. to 1 a.m.). Data of two spacecraft were consistent, as their TBs matched within expected variation (± 5 K) (Fig. 1).

Numerical model of lunar regolith and lunar soil

Given that, to a first order at least, the MRM instruments are measuring the thermal–physical properties of the lunar regolith. It is important to define the controlling physical parameters such as density, permittivity and specific heat capacity as well as the sources of input energy. By combining these sources of information, it is then possible to start modelling the expected lunar subsurface temperature structure using thermal transfer models appropriate for the analysis of microwave remote sensing data.

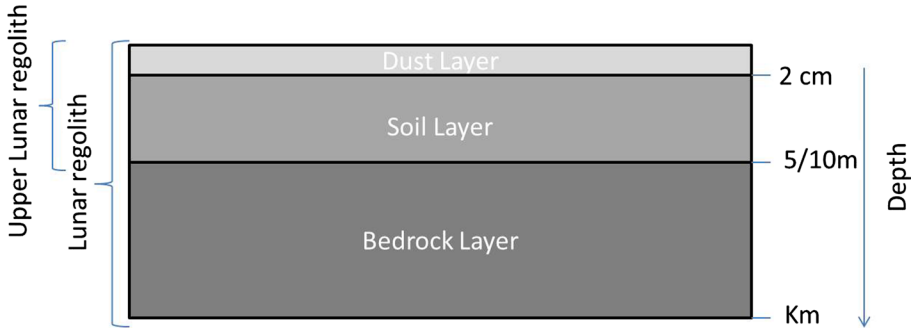

Fig. 2 Depth profile of the lunar surface and subsurface

Bulk density

The depth profile of the lunar surface and subsurface can be divided into three parts (Heiken et al. 1991) (Fig. 2):

1. A 2-cm dust layer on the surface;
2. A 5–10-m soil layer just below the dust layer;
3. A thick lunar bedrock layer below the soil layer (Fa and Jin 2007);

The top two parts of the lunar regolith are referred to as the upper lunar regolith.

Due to the lack of atmosphere and erosion processes on the lunar surface, individual grains that make up the upper lunar regolith layers have a 'pointy' structure. This combined with the low gravity of the Moon (1/6 that of Earth's) results in the upper lunar regolith layers being highly porous with large spaces between individual grains or agglomerates of grains. The bulk densities of the upper lunar regolith layers are defined as the mass per unit volume of the lunar regolith including these spaces.

Vasavada et al. (1999) assumed that the bulk density of the top 2-cm lunar dust layer is 1.3 g/cm^3 and of lunar soil layer is 1.6–2.1 g/cm^3 (Heiken et al. 1991). The relationship of the lunar soil layer bulk density profile with depth can be described as follows (Heiken et al. 1991):

$$\rho = 1.92\frac{z+12.2}{z+18}, \tag{1}$$

where 'z' is the lunar regolith depth, in centimetres.

Measurements of the Apollo core samples show that the average density of the upper lunar regolith layer increases with depth (Cartier et al. 1973). Knowledge of the density profile allows the study of another important factor, the dielectric permittivity.

Dielectric permittivity

The dielectric permittivity constant is important for modelling the MRM data because it determines from what depth the received radiance was emitted. The results of measurements on lunar samples from the Apollo and Luna missions (Heiken et al. 1991) show that when the frequency is greater than 1 MHz, the real part of the permittivity (dielectric constant) of the lunar regolith is dependent on the density of the lunar regolith assuming a nominal chemical composition (Heiken et al. 1991). Hence, the permittivity ε_r' can be estimated using an empirical relationship:

$$\varepsilon_r' = 1.919^{\rho}. \tag{2}$$

The imaginary part ε_r' of permittivity of the lunar soil is the product of the real part of the permittivity and the loss angle tangent[2] of lunar soil (Heiken et al. 1991; Olhoeft and Strangway 1975),

$$\varepsilon_r'' = \varepsilon_r' \times \tan\delta, \tag{3}$$

where $\tan\delta$ is the dielectric loss angle tangent of the lunar soil.

The current well-accepted theory (Olhoeft and Strangway 1975) is that the loss tangent is not only a function of the density of the lunar soil, but also related to the TiO_2 and FeO abundance (expressed by S). This can be modelled using a three-dimensional regression equation with mass fraction, which was derived from the lunar soil samples (Olhoeft and Strangway 1975):

$$\tan\delta = 10^{0.038\cdot(\%TiO_2+\%FeO)+0.312\rho-3.260}, \tag{4}$$

where $\%TiO_2$ and %FeO are TiO_2 and FeO abundances in the lunar soil, respectively.

We define S as sum of TiO_2 and FeO content present in minerals found in lunar soil.

Thermal conductivity

According to the Heiken et al. (1991), the upper 2-cm layer of lunar regolith (dust layer) has an extremely low thermal

[2] Dielectric loss angle tangent: dielectric loss measures a dielectric material's inherent dissipation of electromagnetic energy into heat, usually parameterized in loss angle tangent tan δ.

conductivity (1.5×10^{-5} W/cm^2 measured at the Apollo 15 Landing Site). Below the dust layer, the soil layer has a much larger thermal conductivity (7.5×10^{-5} W/cm^2 ~ 10.5×10^{-5} W/cm^2). This is because thermal conductivity is dependent on density and lunar dust layer has a much lower density of 1.3 g/cm^3 compared to the soil layer density of 2.1 g/cm^3. The variation with depth of thermal conductivity of lunar soil can be expressed as (Mitchell and Pater 1994) follows:

$$k = k_c\left[1+\chi\left(\frac{T}{T_{350}}\right)^3\right], \tag{5}$$

where k_c is the phonon conductivity, χ is the ratio of 'radiative conductivity' to phonon conductivity at 350 K, T is the subsurface temperature in kelvin which varies with the lunar regolith depth 'z', and T_{350} is 350 K. Vasavada et al. (1999) gave the coefficients of k_c and χ for lunar dust and soil layers as: $k_c=9.22\times10^{-4}$ W m^{-1} K^{-1}, $\chi=1.48$ for the dust layer, and $k_c=9.3\times10^{-3}$ W m^{-1} K^{-1}, $\chi=0.073$ for the soil layers.

Specific heat capacity

Horai and Fujii (1972) found that the specific heat (C) of the lunar regolith varies with temperature. Later, Jones et al. (1975) provided an empirical third-degree polynomial formula (determined by the least-squares technique based upon Apollo 11 regolith sample data) that determined its dependence on temperature (70–400 K):

$$C(T) = c_1T^3 + c_2T^2 + c_3T + c_4, \tag{6}$$

where C is in units of J g^{-1} K^{-1}. Urquhart and Jacksky (1997) found that $c_1=5.19\times10^{-9}$ J g^{-1} K^{-4}, $c_2=-8.20\times10^{-6}$ J g^{-1} K^{-3}, $c_3=4.98\times10^{-3}$ J g^{-1} K^{-2}, $c_4=-15.48\times10^{-2}$ J g^{-1} K^{-1}.

Vertical distribution of lunar subsurface temperature as the first estimate

Previous thermal diffusion modelling work

There are currently no conclusive data on the Moon's vertical temperature distribution. The subsurface heat flow has been measured at only two landing sites (Apollo 15 and Apollo 17), and these results show that the temperature fluctuations due to the diurnal wave decrease with depth until at about ~ 0.8 m below the lunar surface where they become negligible (Heiken et al. 1991; Horai and Fujii 1972).

One-dimensional thermal diffusion models such as Vasavada et al. (1999) predict the surface and subsurface profile of the lunar soil. The predicted surface and subsurface temperature structure can then be used in a microwave radiative transfer forward model to predict the TB observed by the MRM instrument.

Microwave radiative transfer in lunar surface layers can generally be modelled with the use of multi-layer models (Shrestha 2007). A detailed multi-layer model can more accurately reflect the change in the parameters with depth (e.g. density, permittivity, conductivity) and obtain good results. However, the computing complexity will increase proportional to the number of layers, which will complicate the inversion of lunar subsurface temperature. Therefore, we should consider the instrument details and number of available microwave channels to make a compromise before the construction of a model.

Six-layer thermal diffusion simulation model

All four MRM channels should be included to invert the MRM data effectively, and therefore this model should be a multi-layer model (assuming that each channel has a different maximum penetration depth). However, a trade-off exists with complexity. Hence, a total of six layers are considered in the model, as follows: the top 2-cm lunar dust layer, followed by four layers between 2 cm and 5 m (with a greater number of layers in the top 20 cm where the temperature changes most rapidly) and a deepest layer at 5 m (bedrock layer). The depth of four layers between 2 cm and 5 m was set by taking into account the predicted penetration depth of each of the four MRM channels using a nominal lunar soil composition. Hence, the following stratification is used:

$$\text{Zarr} = \begin{cases} 2,\ \text{lunar dust } d_1 \\ 3,\ \text{lunar soil } d_2 \\ 5,\ \text{lunar soil } d_3 \\ 10,\ \text{lunar soil } d_4 \\ 480,\ \text{lunar soil } d_5 \\ \text{Infinity},\ \text{lunar regolith } d_6 \end{cases}. \tag{7}$$

In the model, Zarr is the array of depths from the surface to base of each layer (not layer thicknesses) in centimetres and z is the symbol representing the depth in this work. An illustration is plotted in Fig. 3.

Subsurface microwave radiative transfer model

Although some preliminary results were derived, these only represent a qualitative first-order analysis of the Chang'e MRM data, for lunar subsurface temperature sounding. To exploit fully the measurements made by the MRM instrument and future microwave radiometers, the establishment of a lunar regolith microwave radiative transfer forward

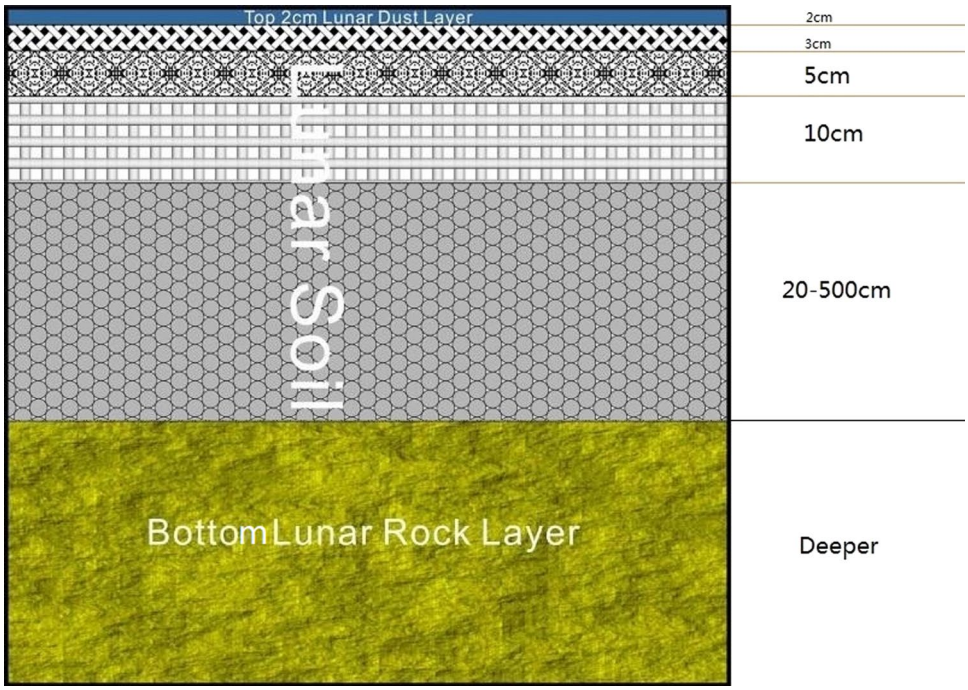

Fig. 3 Lunar soil layers for the thermal simulation model (which will also be used in the microwave radiative transfer model, Sect. 3.2)

model is required. This will allow quantitative insights into the subsurface temperature and compositional structure to be included when interpreting the MRM data. In turn, this is the key to exploiting the information on subsurface heat flow and its possible connection to the large-scale evolution of the lunar crust.

By considering the main factors affecting the measured brightness temperature with depth within the lunar regolith, we have developed a non-uniform multi-layer lunar soil radiative transfer model. This new model is entirely different to the models of Spencer et al. (1989) or Vasavada et al. (1999), because it is not an energy balance (thermal diffusion) model, but a microwave radiative transfer model using input data from the MRM measurements, effectively modelling the global subsurface radiative transfer for the time of the remote sensing observation. According to microwave radiative transfer theory (Jin 1993; Ulaby et al. 1981), the Chang'e MRM measurements of lunar regolith contain TB contributions from different layers within a certain depth of the subsurface. Physical properties of different depths of lunar soil, such as different temperature, dielectric constant, density, thermal conductivity and specific heat parameters, will be reflected in the microwave radiation transport model and thus the TB measured by the instrument.

The radiative transfer forward model is used to calculate contributions from different depths to the TB measured by the MRM radiometer's four channels. This can then be compared with other models and methods such as Keihm's model (1973) or Spencer et al. (1989), assuming a known vertical temperature distribution. Furthermore, to try and understand if there is correlation with the Fe/Ti content and the effective emission depth for the different MRM channels, a sequence of more complex models investigating radiative and conductive heating measured by each of the MRM channels has been developed.

Radiative transfer forward model derivation

The first step in developing the thermal transfer model is determining the contributions from each layer to the subsurface microwave propagation that is then received by the instrument. In this initial analysis, a six-layer model has been used for the reasons listed below.

The rationale for using a total of six layers is described in part 3, but to a first order is due to the number of available channels (4) of MRM data, assuming that each channel is sounding to a different depth. The number of required layers is equal to the number of channels plus a top layer and a bottom layer. The top layer is constrained by the surface temperature data from the Diviner instrument on the Lunar Reconnaissance Orbiter (Paige et al. 2010) (i.e. layer 1), the four MRM channels potentially provide measurements at four different depths (i.e. layers 2–5), and the bedrock temperature can be considered as a constant (i.e. layer 6). This allows the number of unknowns to equal the number of equations, making the problem pseudo-exact due to the presence of measurement and modelling error.

Existing microwave propagation models developed for the Earth's subsurface are not appropriate. The microwave propagation in the Earth's subsurface is heavily attenuated

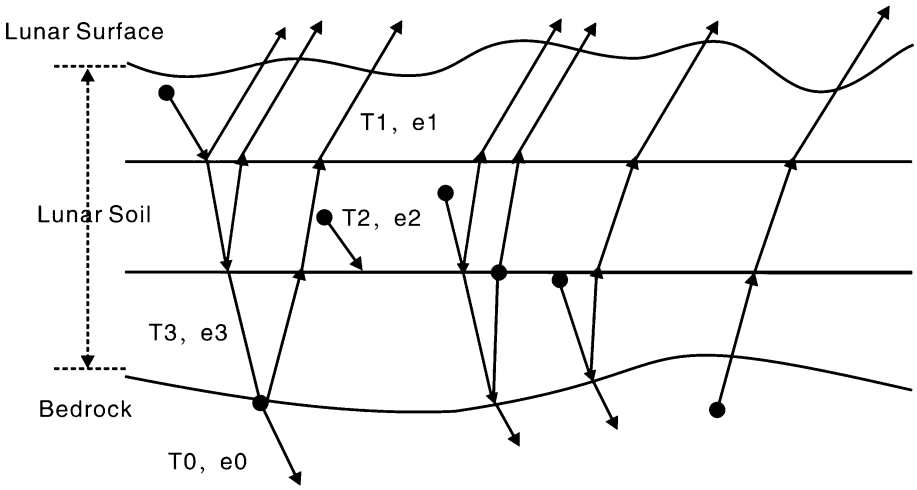

Fig. 4 Schematic diagram of microwave radiation emitted from a three-layer lunar regolith and bedrock structure. The T_B received by the MRM contains direct emission from each layer, as well as reflected beams at layer interfaces, although multiple reflections will not be considered in this model

by the presence of moisture (Jin 1993; Zhang et al. 2008), so existing terrestrial models are not applicable for the analysis of data from desiccated airless bodies such as the Moon. Therefore, we have constructed our own model using underlying principles of microwave radiative transfer theory. This approach will be summarized below, with references to the individual model components cited as required unless it is an original derivation.

Any substance with a temperature above absolute zero has a large number of charged particles that constantly collide with one another, causing the charged particles to be in a state of motion. Such changes in motion (i.e. acceleration) generate electromagnetic radiation, and different wavelengths of non-correlated wave components constitute emission of electromagnetic wave radiation. In electromagnetic terminology, the frequency range from 1000 MHz to 300 GHz is called microwave radiation. (This will be Planck radiation modified by the material if it is not transparent to its own radiation.)

A microwave radiometer is a high-sensitivity receiver designed to receive and record low-emission random microwave noise[3] radiation from a material. Objects in thermodynamic equilibrium have an emission power (in radio frequency microwave language this is referred to as the transmission power) P, which is a function of their physical temperature T. In the microwave range, P is proportional to T (the long-wave limit of the Planck function) (Ulaby et al. 1981). This is expressed as

$$P = \sigma e T \Delta\nu, \tag{8}$$

where σ is the Boltzmann constant, T is the thermodynamic temperature of the object, e is the emissivity of the material and $\Delta\nu$ is the radiometer bandwidth. This relationship between power and temperature defines the brightness temperature (T_B), which is characterized by the power received in a real scene:

$$T_B = eT = \frac{P}{\sigma\Delta\nu}. \tag{9}$$

Since e (the emissivity of the material) is dependent on the dielectric constant, it is also dependent on density, elemental composition, etc. The observed microwave TB is thus dependent on these characteristics (e.g. density, elemental composition, etc.), so we could, in principle, derive these lunar subsurface parameters, based on the MRM remote measurements of lunar surface brightness temperature using Eq. 9.

Figure 4 is a schematic diagram of the microwave radiation from a typical three-layer lunar regolith and bedrock structure (after Li et al. 2010). In addition to the microwaves being attenuated by medium during their propagation through the lunar surface, they will also be affected by changes in the medium. For example, if the lunar regolith comprises three layers with different dielectric properties and temperatures (T0, T1, T2, T3), then the emitted microwave radiation from each layer will be affected by reflection and transmission at every interface.

The total amount of radiation received by the microwave detector from the lunar surface is expressed by (Ulaby et al. 1981) as Eq. 10:

$$T_B = T_S e_s = T_s(1 - r_s), \tag{10}$$

where T_s is the thermodynamic temperature of the surface, e_s is the emissivity of the surface and r_s is the surface

[3] 'Noise' in this case implies that the radiation is not coherent, in contrast, for example, to a microwave receiver as used in communications or similar.

reflectivity. r_s can be calculated according to Fresnel's law of reflection:

$$r_s = \left| \frac{\varepsilon_{rs}\cos\theta - \sqrt{\varepsilon_{rs} - \sin^2\theta}}{\varepsilon_{rs}\cos\theta + \sqrt{\varepsilon_{rs} - \sin^2\theta}} \right|^2, \tag{11}$$

where ε_{rs} is the relative permittivity of the surface.

In the case of normal incidence, the reflectivity then becomes

$$r_s = \left| \frac{1 - \sqrt{\varepsilon_{rs}}}{1 + \sqrt{\varepsilon_{rs}}} \right|^2. \tag{12}$$

The subsurface temperature profile is given by $T(z)$, the absorption coefficient profile is $\alpha(z)$, and the permittivity profile is $\varepsilon(z)$, all are functions of the depth z. The depth profile of the layer dielectric constant $\varepsilon(z)$ is given by Tsang et al. (1975), and the absorption coefficient profile of the electric field intensity $\alpha(z)$ is expressed as

$$\alpha(z) = \frac{2\pi}{\lambda}\left\{ \frac{\mu_r(z)\varepsilon'_r(z)}{2}\left[\sqrt{1 + \left(\frac{\varepsilon''_r(z)}{\varepsilon'_r(z)} \right)^2} - 1 \right] \right\}^{1/2}, \tag{13}$$

where λ is the wavelength, ε'_r is the real part of the relative permittivity, while ε''_r is the imaginary part and μ_r is the real part of the magnetic permittivity. The power absorption coefficient $\kappa(z)$ is twice that of $\alpha(z)$, as expressed by

$$\kappa(z) = 2\alpha(z) \tag{14}$$

where $\kappa(z)$ and $\alpha(z)$ units are both in nepers (Np) per metre. (Neper is defined as 1 Np/m = 8.686 dB/m.) If the dielectric of each layer is the same and $\mu_r(z) = 1$, then the absorption coefficient $\kappa(z)$ can be expressed as

$$\kappa(z) = 2\mathrm{Im}\left\{ \frac{2\pi\sqrt{\varepsilon_r(z) - \sin^2\theta}}{\lambda} \right\}. \tag{15}$$

We need to define the difference between real temperature, effective temperature and brightness temperature:

1. *Real temperature* is the thermodynamic temperature of the regolith. This is the temperature that would be measured by an in situ temperature probe. In this model, it is assumed that each layer is isothermal at one real temperature.
2. The lunar surface has many areas of different temperatures, i.e. across a horizontal 2-cm space on the lunar surface the temperature can vary by up to 100 K. The temperature in the subsurface of the moon can vary by 150 K to depths of 5 m. The MRM instrument can sound to depths of 5 m, and its footprint is 18 km at its best resolution, so it contains a scene composed of many different temperatures both vertically and horizontally. The *effective temperature* can be thought of as the average temperature in such a scene.
3. *Brightness temperature* is the effective temperature multiplied by the effective emissivity of lunar regolith as measured by a microwave radiometer.

The model calculates the real temperatures of each layer. The real temperature from each layer is then multiplied by a weighting which is the power coefficient and the exponential of the negative power coefficient (Eq. 16). The real temperature multiplied by the weighing coefficient for each layer is then added together to give the effective temperature (Eq. 16). This effective temperature is then multiplied by the effective emissivity to give the TB that is measured by the MRM instrument. Then, Eq. 9 transforms into Eq. 16:

$$T_B = eT = e_{eff}T_{eff} = e_{eff}\int_{-\infty}^{0} T(z)\kappa(z)e^{-\kappa(z)}\mathrm{d}z, \tag{16}$$

where T_{eff} is the effective temperature, e_{eff} is the effective emissivity and represents the ratio of T_{eff} to T_B measured by MRM. Here, the $\kappa(z)e^{-\kappa(z)}$ weighting term comes from the derivative of $\exp(-\kappa(z))$.

Microwave radiation in the media can be simulated using two methods. The first is the coherent method based on Maxwell's equations and the fluctuation dissipation theorem (FDT). The coherent method considers the effects of reflection on both the amplitude and phase. The coherent method must be solved using Maxwell's equations to calculate electromagnetic field vectors and obtain radiation intensity. This approach requires that the medium is uniform as the scattering within each layer is ignored. The dielectric constant of each layer is also considered to be constant (Jin 1993).

The second method is the incoherent approach based on the vector radiative transfer theory, which only considers the amplitude and not the phase. This approach requires a large amount of scattering bodies whose dimensions are comparable to the wavelength of radiation (Ulaby et al. 1981). The random distribution of such scattering bodies generates random phase functions in wave transmission between two points, thus making the transmission an incoherent process.

Considering the nature of the lunar soil (e.g. the layers are almost level and uniform and each layer has a constant

dielectric constant) and the wavelengths measured by the MRM, the coherent method was chosen for this work. In coherent methods, the microwave radiation of the medium is caused by charged particles' fluctuating in the microscopic scale, that is, the fluctuant electromagnetic radiation. The expected relationship between the value of the electric current source (generated by the movement of charged particles) and TB is described by the fluctuation dissipation theorem (FDT). Details of this theorem are explained in Jin (1993) and are summarized below.

The fluctuation–dissipation theorem relies on the assumption that the response of a system in thermodynamic equilibrium to a small applied force is the same as its response to a spontaneous fluctuation.[4] Therefore, the theorem connects the linear response relaxation of a system from a prepared non-equilibrium state to its statistical fluctuation properties in equilibrium. According to FDT,

$$(\bar{J}_l(\bar{r},\omega) * \bar{J}_l(\bar{r}',\omega')) = \frac{4}{\pi}\omega\varepsilon_l''(z)\sigma T_l(z)\cdot\bar{I}\delta(\omega-\omega')\delta(r-r'), \tag{17}$$

where $\bar{J}_l(\bar{r},\omega)$ is the heat source of layer l among all N layers, ω is the heat radiation's angular frequency, r is the displacement vector, σ is the Boltzmann constant, and $T_l(z)$ is the real temperature distribution of layer l and $\varepsilon_l''(z)$ is the imaginary part of permittivity (dielectric constant); the term I in Eq. 17 is defined as follows:

$$\bar{I} = \hat{x}\hat{x} + \hat{y}\hat{y} + \hat{z}\hat{z} \tag{18}$$

Therefore, by the definition of TB and Eqs. 16–18, the polarized radiation TB can be written as Eq. 19:

$$\begin{aligned} T_B^p(\hat{k},\omega) = {} & \frac{(2\pi)^3}{B}\left(\frac{c}{\omega}\right)\frac{1}{2}c\varepsilon_0\int_0^\infty \mathrm{d}\omega'\int_0^\infty k^2\mathrm{d}k\int \mathrm{d}k' \\ & \times\left\{\hat{p}\cdot\left(\bar{E}(k,\omega)\bar{E}'(k',\omega')\right)\cdot\hat{p}\exp[i(\bar{k}-\bar{k}')\right. \\ & \left.\cdot\left(r-i(\omega-\omega')t\right)]\right\}, \end{aligned} \tag{19}$$

where $\hat{p}$ is the polarization sense, $\hat{p}=(\hat{v},\hat{h})$, $\hat{h}$ is the horizontal polarization vector, $\hat{v}$ is the vertical polarization vector, c is the light speed, ω is the frequency, r is the distance vector and ε_0 is the vacuum permittivity. Also, by using the parallel-layered media dyadic Green's function (Jin 1993) the electric field intensity (E) can be written as follows:

$$\vec{E}(\vec{r},\omega) = \sum_{l=1}^{N+1}\int_{-\infty}^{\infty} d\vec{\rho}'\int_{-d_l}^{-d_{l-1}} \mathrm{d}z'\overline{\overline{G}}_{0l}(\vec{r},\vec{r}')\cdot J_l(\vec{r}')\omega'. \tag{20}$$

In Eq. 20, J_l is the heat source and ρ is the x–y plane of the lth layer, representing the longitudinal coordinates of the lth layer; dyadic Green function in the region l can be written as

$$\begin{aligned} \overline{\overline{G_{0l}}}(\bar{r},\bar{r}') = {} & -\frac{\omega\mu}{8\pi^2}\int d\bar{k}\delta\left[k_z-\sqrt{\omega^2\mu\varepsilon_0-k_\rho^2}\right]\frac{1}{k_z}e^{i\bar{k}\cdot\bar{r}} \\ & \times\left\{\hat{h}(k_z)\left[A_l\hat{h}(-k_{lz})e^{-i\bar{k}\cdot\bar{r}}+B_l\hat{h}(k_{lz})e^{-i\bar{k}\cdot\bar{r}}\right]\right. \\ & \left.+\hat{v}(k_z)\left[C_l\hat{v}(-k_{lz})e^{-i\bar{k}\cdot\bar{r}}+D_l\hat{v}(k_{lz})e^{-i\bar{k}\cdot\bar{r}}\right]\right\}, \end{aligned} \tag{21}$$

where subscript 0 l indicates that the observation point $\bar{r}$ is in area 0 and the microwave emission source is located in area l. k_ρ is the wavenumber on the x/y plane, k_x is the wavenumber projected into the x-axis, and k_y is the wavenumber projected into the y-axis, $k_\rho^2 = k_x^2 + k_y^2$. μ is the vacuum magnetic permittivity; A_l, B_l, C_l and D_l can be derived by tangential continuous boundary constraints at layer interfaces. For an N-layer unevenly paralleled dissipation medium, when the observation angle is θ, the zero-order p-polarization TB of layered lunar soil medium measured by MRM can be transformed into Eq. 22:

$$\begin{aligned} T_{\mathrm{B}}^p(\theta) = {} & \frac{k_0}{\cos\theta}\sum_{i=1}^{n}\left\{\frac{\varepsilon_{\mathrm{ri}}''}{2k_{iz}''}\left|\beta_i^p\right|^2\cdot\left(1-e^{-2k_{iz}''d_i}\right)\right. \\ & \left.\cdot\left(1+\left|R_{i(i+1)}^p\right|^2e^{-2k_{iz}''d_i}\right)T_i\prod_{j=0}^{i=1}\left(\left|Q_{j(j+1)}^p\right|^2\cdot\left(e^{-2k_{jz}''d_j}\right)\right)\right\} \\ & +\frac{k_0\varepsilon_{\mathrm{r}(n+1)}''\left|\beta_{n+1}^p\right|^2}{\cos\theta\cdot 2k_{(n+1)z}''}\cdot\prod_{j=0}^{n}\left(\left|Q_{j(j+1)}^p\right|^2\cdot\left(e^{-2k_{jz}''d_j}\right)\right)T_r, \end{aligned} \tag{22}$$

where k is the wavenumber, k_{iz} is the projection on z direction of the i layer's wavenumber, d_i is the thickness of the i layer, T_r is the temperature of the lunar rock layer and the superscript $''$ means the imaginary part. The transmission coefficient (Q_{ij}) is

$$Q_{ij} = 1 + R_{ij}. \tag{23}$$

And the reflection coefficient is

$$R_{ij} = \frac{k_{iz}-k_{jz}}{k_{iz}+k_{jz}}. \tag{24}$$

Therefore, for a six-layer non-uniform parallel-layered dissipative media, when the observation angle is zero, as in the CE MRM data, based on Eq. 22, the layered medium polarized radiation brightness temperature measured by the microwave radiation detector can be deduced as

[4] Another example is Einstein's model of Brownian motion, also the use of fluctuation/dissipation theorem and derivation of refractive index.

$$
\begin{aligned}
T_B = {} & \frac{k_0\varepsilon_1''}{2\varepsilon_0 k_1''}\left|Q_{01}\right|^2(1-e^{-2k_1''d_1})(1+\left|R_{12}\right|^2e^{-2k_1''d_1})T_1 \\
& + \frac{k_0\varepsilon_2''}{2\varepsilon_0 k_2''}\left|Q_{01}Q_{12}\right|^2(1-e^{-2k_2''d_2})(1+\left|R_{23}\right|^2e^{-2k_2''d_2})e^{-2k_1''d_1}T_2 \\
& + \frac{k_0\varepsilon_3''}{2\varepsilon_0 k_3''}\left|Q_{01}Q_{12}Q_{23}\right|^2(1-e^{-2k_3''d_3})(1+\left|R_{34}\right|^2e^{-2k_3''d_3})e^{-2k_1''d_1}e^{-2k_2''d_2}T_3 \\
& + \frac{k_0\varepsilon_4''}{2\varepsilon_0 k_4''}\left|Q_{01}Q_{12}Q_{23}Q_{34}\right|^2(1-e^{-2k_4''d_4})(1+\left|R_{45}\right|^2e^{-2k_4''d_4})e^{-2k_1''d_1}e^{-2k_2''d_2}e^{-2k_3''d_3}T_4 \\
& + \frac{k_0\varepsilon_5''}{2\varepsilon_0 k_5''}\left|Q_{01}Q_{12}Q_{23}Q_{34}Q_{45}\right|^2(1-e^{-2k_5''d_5})(1+\left|R_{56}\right|^2e^{-2k_5''d_5})e^{-2k_1''d_1}e^{-2k_2''d_2}e^{-2k_3''d_3}e^{-2k_4''d_4}T_5 \\
& + \frac{k_0\varepsilon_6''}{2\varepsilon_0 k_6''}\left|Q_{01}Q_{12}Q_{23}Q_{34}Q_{45}Q_{56}\right|^2e^{-2k_1''d_1}e^{-2k_2''d_2}e^{-2k_3''d_3}e^{-2k_4''d_4}e^{-2k_5''d_5}T_6.
\end{aligned}
\tag{25}
$$

Equation 25 is the core of the model. Each term in this equation corresponds to a layer's contribution to the received TB (of specific wavelength) and is calculated based on Eq. 22. The first term corresponds to the lunar dust layer's radiation, and the last term corresponds to the lunar bedrock layer's radiation, while the other four terms correspond to each layer of the lunar soil. Except for the last term, all the other five terms contain both upwards radiation and downwards-reflected radiation. Equation 25 calculates the zero-order radiation TB, e.g. the effect of scattering is not considered. Other assumptions include: $T_6 = 250$ K (bedrock temperature), the vacuum permittivity is unity, and the bedrock layer permittivity is $8.0 + 0.5$i (Heiken et al. 1991). To determine the wavenumber k, we can write

$$k = \frac{\omega}{c}(\beta + i\alpha). \tag{26}$$

Then, according to Burke et al. (1979), the dispersion relation gives:

$$\beta = \left\{\frac{1}{2}(\varepsilon_{RJ} - \sin^2\theta_0)\left[1 + \left(1 + \frac{\varepsilon_{Ij}^2}{(\varepsilon_{RJ} - \sin^2\theta_0)^2}\right)^{1/2}\right]\right\}^{\frac{1}{2}} \tag{27}$$

$$\alpha = \frac{\varepsilon_I}{2\beta}. \tag{28}$$

Equations 23–24 are widely used in microwave remote sounding, including moisture estimation of terrestrial soil (Zhang et al. 2008). Equations 26–28 are also used in the inversion model developed in paper to allow estimation of k.

Inverting vertical subsurface temperatures of the equatorial region from MRM data and using the microwave forward model

The lunar subsurface is not isothermal, so the microwave radiation of the lunar surface is also affected by the actual temperature distribution of the subsurface of the Moon. By solving the radiation transmission equations (Eqs. 8–28), this paper will establish a lunar subsurface temperature inversion model, using the CE MRM measurements. To study the typical vertical distribution of the lunar subsurface temperature, this work will use the analytical microwave radiative transfer model to attempt an inversion of the equatorial region subsurface temperatures at different depths, based on the MRM data (Sect. 4.1).

What MRM 'measured' is then numerically studied: using the inverse method to retrieve the subsurface temperatures (T_2–T_5), defined as the unknown matrix x in the following discussion. To set up the basic equations for the inversion, the measurement vector should be the four MRM-measured brightness temperatures in each channel, e.g. TB1 (3 GHz), TB2 (7.8 GHz), TB3 (19.35 GHz) and TB4 (37 GHz), each with a measurement error of ± 0.5 K, respectively. The unknown vector x should be made of the real subsurface temperatures, T_2 (5 cm), T_3 (10 cm), T_4 (20 cm) and T_5 (2 m).

According to the inverse method (e.g. Rodgers 2000), the measurement vector (y) is equal to the vector of unknowns (x) multiplied by the weighting function matrix (K) plus the error matrix ($y = Kx + \text{error}$). The matrix of unknowns is defined by $x = [T_2, T_3, T_4, T_5]$ and y is defined in Eq. 29 derived from Eq. 25, which is the net TB contribution of each lunar soil layer excluding the contribution of dust and rock layer to TB. The dust and rock layer are excluded due to the fact that values of T_1 (Diviner data) and T_6 are known

(250 K, Apollo measurement, Lunar Sourcebook 1991), making the contribution from these two layers calculable.

$$y=\begin{bmatrix}\mathrm{TB}_1-\mathrm{CTB}_{3\,\mathrm{GHz}}\\ \mathrm{TB}_2-\mathrm{CTB}_{7.8\,\mathrm{GHz}}\\ \mathrm{TB}_3-\mathrm{CTB}_{19\,\mathrm{GHz}}\\ \mathrm{TB}_4-\mathrm{CTB}_{37\,\mathrm{GHz}}\end{bmatrix}=\begin{bmatrix}TB_1-\left(\frac{k_0\varepsilon_1''}{2\varepsilon_0 k_1''}\left|Q_{01}\right|^2(1-e^{-2k_1''d_1})(1+\left|R_{12}\right|^2e^{-2k_1''d_1})T_1\right.\\ \left.-\frac{k_0\varepsilon_6''}{2\varepsilon_0 k_6''}\left|Q_{01}Q_{12}Q_{23}Q_{34}Q_{45}Q_{56}\right|^2e^{-2k_1''d_1}e^{-2k_2''d_2}e^{-2k_3''d_3}e^{-2k_4''d_4}e^{-2k_5''d_5}T_6\right)_{3.0\,\mathrm{GHz}}\\ TB_2-\left(\frac{k_0\varepsilon_1''}{2\varepsilon_0 k_1''}\left|Q_{01}\right|^2(1-e^{-2k_1''d_1})(1+\left|R_{12}\right|^2e^{-2k_1''d_1})T_1\right.\\ \left.-\frac{k_0\varepsilon_6''}{2\varepsilon_0 k_6''}\left|Q_{01}Q_{12}Q_{23}Q_{34}Q_{45}Q_{56}\right|^2e^{-2k_1''d_1}e^{-2k_2''d_2}e^{-2k_3''d_3}e^{-2k_4''d_4}e^{-2k_5''d_5}T_6\right)_{7.8\,\mathrm{GHz}}\\ TB_3-\left(\frac{k_0\varepsilon_1''}{2\varepsilon_0 k_1''}\left|Q_{01}\right|^2(1-e^{-2k_1''d_1})(1+\left|R_{12}\right|^2e^{-2k_1''d_1})T_1\right.\\ \left.-\frac{k_0\varepsilon_6''}{2\varepsilon_0 k_6''}\left|Q_{01}Q_{12}Q_{23}Q_{34}Q_{45}Q_{56}\right|^2e^{-2k_1''d_1}e^{-2k_2''d_2}e^{-2k_3''d_3}e^{-2k_4''d_4}e^{-2k_5''d_5}T_6\right)_{19.0\,\mathrm{GHz}}\\ TB_4-\left(\frac{k_0\varepsilon_1''}{2\varepsilon_0 k_1''}\left|Q_{01}\right|^2(1-e^{-2k_1''d_1})(1+\left|R_{12}\right|^2e^{-2k_1''d_1})T_1\right.\\ \left.-\frac{k_0\varepsilon_6''}{2\varepsilon_0 k_6''}\left|Q_{01}Q_{12}Q_{23}Q_{34}Q_{45}Q_{56}\right|^2e^{-2k_1''d_1}e^{-2k_2''d_2}e^{-2k_3''d_3}e^{-2k_4''d_4}e^{-2k_5''d_5}T_6\right)_{37.0\,\mathrm{GHz}}\end{bmatrix}. \tag{29}$$

where CTB is the contribution of dust and rock layer to the TB measured by the MRM instrument. Note that the CTB is a known quantity as it is set by Diviner and Apollo measurements. Q is the transmission coefficient (Eq. 23), and R is the reflection coefficient (Eq. 24).

According to the temperature uncertainty of the MRM instrument (± 0.5 K), the measurement uncertainty covariance matrix is then:

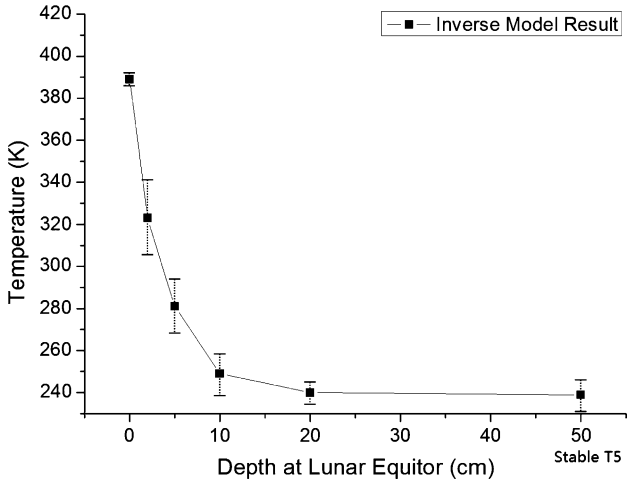

Fig. 5 Based on Chang'e 1 MRM data and our radiative transfer model, the 'measured' mean vertical temperature profile beneath the lunar equatorial surface, at the lunar midday, was inverted

$$S_\varepsilon=\begin{bmatrix}0.25 & 0 & 0 & 0\\ 0 & 0.25 & 0 & 0\\ 0 & 0 & 0.25 & 0\\ 0 & 0 & 0 & 0.25\end{bmatrix}, \tag{30}$$

where the diagonal elements are given as the square of the error of the MRM instrument. And according to Eq. 25, the weighting function matrix is

$$K=\begin{bmatrix}C^{\mathrm{Second}}_{3.0\times10^9\,\mathrm{GHz}} & C^{\mathrm{Third}}_{3.0\times10^9\,\mathrm{GHz}} & C^{\mathrm{Fourth}}_{3.0\times10^9\,\mathrm{GHz}} & C^{\mathrm{Fifth}}_{3.0\times10^9\,\mathrm{GHz}}\\ C^{\mathrm{Second}}_{7.8\times10^9\,\mathrm{GHz}} & C^{\mathrm{Third}}_{7.8\times10^9\,\mathrm{GHz}} & C^{\mathrm{Fourth}}_{7.8\times10^9\,\mathrm{GHz}} & C^{\mathrm{Fifth}}_{7.8\times10^9\,\mathrm{GHz}}\\ C^{\mathrm{Second}}_{19.0\times10^9\,\mathrm{GHz}} & C^{\mathrm{Third}}_{19.0\times10\,\mathrm{GHz}} & C^{\mathrm{Fourth}}_{19.0\times10^9\,\mathrm{GHz}} & C^{\mathrm{Fifth}}_{19.0\times10^9\,\mathrm{GHz}}\\ C^{\mathrm{Second}}_{37.0\times10^9\,\mathrm{GHz}} & C^{\mathrm{Third}}_{37.0\times10^9\,\mathrm{GHz}} & C^{\mathrm{Fourth}}_{37.0\times10^9\,\mathrm{GHz}} & C^{\mathrm{Fifth}}_{37.0\times10^9\,\mathrm{GHz}}\end{bmatrix}, \tag{31}$$

where

$$C^{\mathrm{Second}}=\frac{k_0\varepsilon_2''}{2\varepsilon_0 k_2''}\left|Q_{01}Q_{12}\right|^2(1-e^{-2k_2''d_2})(1+\left|R_{23}\right|^2e^{-2k_2''d_2})e^{-2k_1''d_1} \tag{32}$$

$$C^{\mathrm{Third}}=\frac{k_0\varepsilon_3''}{2\varepsilon_0 k_3''}\left|Q_{01}Q_{12}Q_{23}\right|^2(1-e^{-2k_3''d_3})\times(1+\left|R_{34}\right|^2e^{-2k_3''d_3})e^{-2k_1''d_1}e^{-2k_2''d_2} \tag{33}$$

$$C^{\mathrm{Forth}}=\frac{k_0\varepsilon_4''}{2\varepsilon_0 k_4''}\left|Q_{01}Q_{12}Q_{23}Q_{34}\right|^2(1-e^{-2k_4''d_4})\times(1+\left|R_{45}\right|^2e^{-2k_4''d_4})e^{-2k_1''d_1}e^{-2k_2''d_2}e^{-2k_3''d_3} \tag{34}$$

Table 1 Data used in forward model calculation are an average of CE-1 and CE-2; details are given in this table

	CE-1 microwave brightness temperature data set	CE-2 microwave brightness temperature data set
Size details (MB)	346	992
Time span	2007.11.27–2008.06.30	2010.10.15–2011.05.20
Space resolution	3 GHz channel space resolution is 50 km. All other channels had a spatial resolution of ~ 35 km	3 GHz channel space resolution is 25 km. All other channels had a spatial resolution of ~ 17.5 km

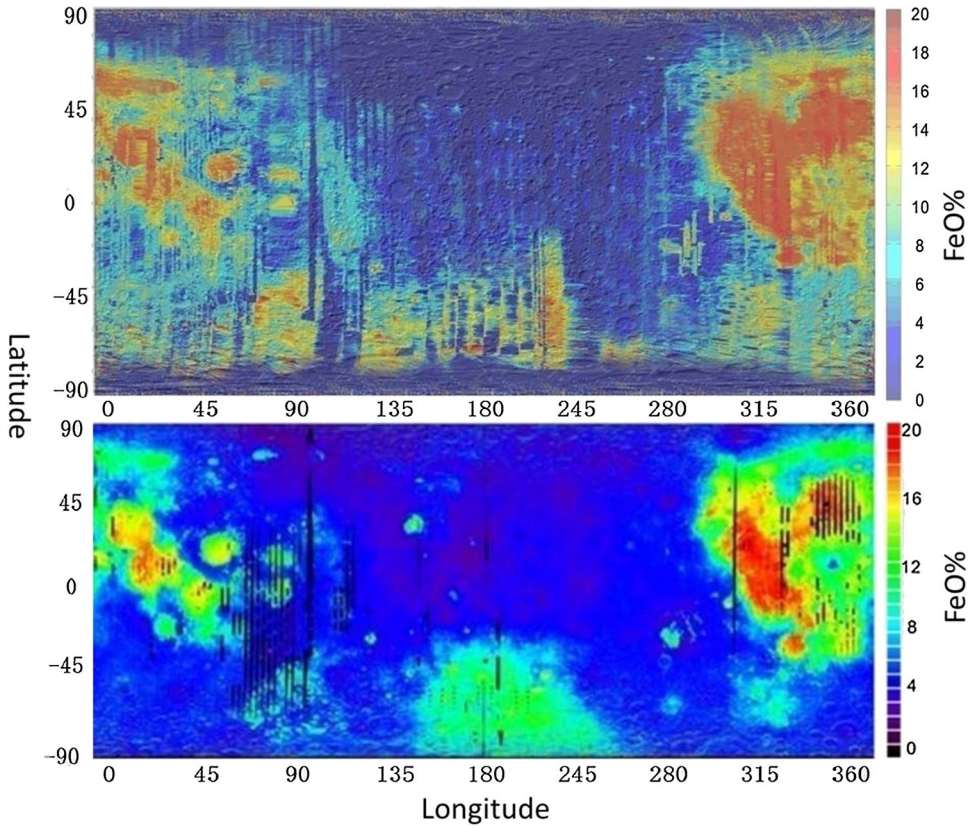

Fig. 6 (Top) Retrieved FeO content from M^3 over plotted on a Clementine base map. Fe content is between 0 and 20% in this map. Several artefacts remain in this plot; they come from the M^3 optical period. (Bottom) Clementine FeO map

$$C^{\text{Fifth}} = \frac{k_0 \varepsilon_5''}{2\varepsilon_0 k_5''} \left| Q_{01} Q_{12} Q_{23} Q_{34} Q_{45} \right|^2 (1 - e^{-2k_5'' d_5}) \times (1 + \left| R_{56} \right|^2 e^{-2k_5'' d_5}) e^{-2k_1'' d_1} e^{-2k_2'' d_2} e^{-2k_3'' d_3} e^{-2k_4'' d_4}. \quad (35)$$

According to the inverse theory (Rodgers 2000),

$$x = (K^T S_\varepsilon^{-1} K)^{-1} K^T S_\varepsilon^{-1} y \quad (36)$$

and the expression for the error covariance of the state x vector is

$$S_x = (K^T S_\varepsilon^{-1} K)^{-1}. \quad (37)$$

The vector of unknowns (x) and its associated error covariance (S_x) can therefore be estimated. However, this S_x is the model calculation error, without the parameter modelling error included.

A simple test of Eq. 36 was done to generate a vertical temperature profile for the lunar equator. When assuming a value of $S = 15$ (typical for the lunar equatorial region—according to Heiken et al. 1991), a rough average subsurface temperature curve for the Moon's equatorial region can be generated using the radiative transfer model and inverting the equatorial MRM data (Fig. 5). The surface temperature points are constrained by Diviner measurements (Paige et al. 2010). The stated error of the Diviner data is within ± 2 K (Paige et al. 2010). The bedrock temperature is taken from the Apollo experiment with ± 10 K error (Heiken et al. 1991), and the other points have been derived from the Chang'e MRM measurements. The error is within ± 6 K. The model shows that the lunar soil temperature changes significantly within the top 2 cm and becomes stable below 20 cm. Comparing it with the theoretical thermal simulations, we notice that they agree to within the stated uncertainties. The

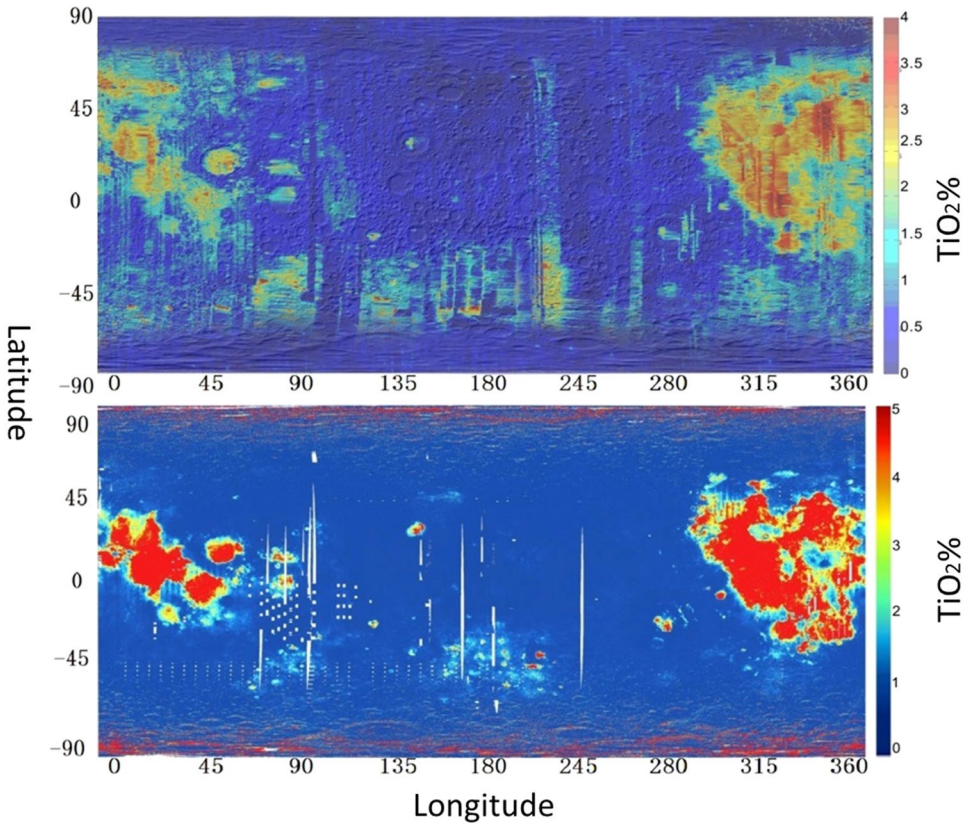

Fig. 7 (Top) Retrieval result of TiO_2 content derived using the Shkuratov model from the M^3 FeO map, over plotted on a Clementine base map; (Bottom) Clementine titanium map (Korokhin et al. 2008)

data used for this forward model calculation are summarized in Table 1.

Both the thermal simulation and the MRM data (Fig. 5) show that the surface temperature at the lunar equator at noon is ~ 390 K and drops significantly within 20 cm and then is almost stable at ~ 240 K at depths below 20 cm to 50 cm. This is also described in the lunar source book ($220 < T < 255$ K (Heiken et al. 1991)).

In the model covariance matrix, it was noticed that the first three off-diagonal elements are quite large (e.g. ± 20 K), but the fourth off-diagonal element (T_5 error) was below 2–10 K. The MRM signal mainly comes from the lunar soil at a depth of > 50 cm (Figs. 6, 7).

Preliminary subsurface temperature maps

Mineralogy data sources for inclusion in the improved forward model

Mineralogy can significantly change the penetration depth of microwave signals. The sensitivity analysis in the previous section indicates that knowledge of the Fe/Ti abundance (particularly Ti) and bulk density is particularly important to the proposed forward model.

Based on data in Zhang (2014), mineralogical and bulk density information is added to the thermal transfer model, including the effects of varying Fe/Ti composition and varying density profiles across the Moon.

The Zhang (2014)'s paper is concerned with the development of a method for deriving FeO and TiO_2 content from the data measured by the Moon Mineralogy Mapper (M^3) instrument on the Chandrayaan-1 mission.

Zhang (2014) analysed the FeO content based on M^3 data and Lucey et al. (1995, 1998)'s approach.

The derived Fe distribution from the M^3 data has also been compared with the Lunar Prospector Fe mapping results, and they have been found to agree within ± 6%. Such consistency validates the methods used. Several small features that are noticeable on the M^3 are not seen on the Clementine or Lunar Prospector results, as the M^3 has a much higher spatial resolution than the other two data sets.

For the TiO_2 content retrieval, Lucey's method (1998) also introduces a simple relation between the UV/VIS ratio (415/750 nm) and TiO_2 content. However, an alternative method is required because the M^3 does not include a 415-nm band. The 256 channels that are available in the M^3 data allowed for investigation of other approaches that were inaccessible from the Clementine data, which were more spectrally limited. Two different TiO_2 analysis techniques were applied to the data and are described in Zhang (2014).

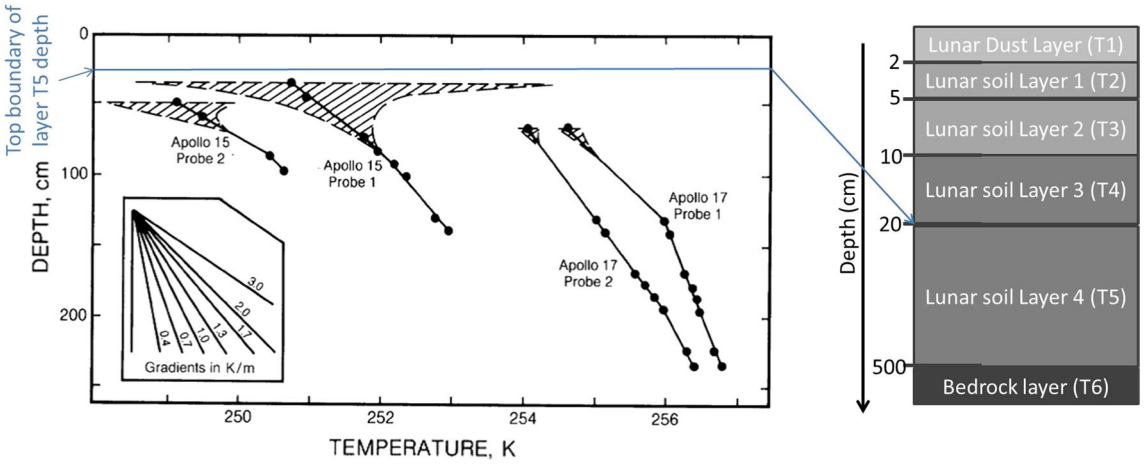

Fig. 8 (Left) Temperature fluctuations in the lunar regolith as a function of depth (from Langseth et al. 1976). Note that the small temperature scale at the bottom of the diagram does not permit the extreme temperature fluctuation at depths less than ~ 30 cm to be plotted; this region is left blank. Hatched areas show day–night temperature fluctuations below ~ 30–70 cm. Below the blue line is the T_5 layer. (Right) Layer stratification used in the microwave radiative transfer forward model described in Sect. 4

The content of surface TiO_2 based on M^3 data according to Zhang (2014) is given as follows:

The result is then used in this section to model spatial variations in lunar subsurface temperatures. We conduct two procedures before the inversion. First, abnormal MRM data are eliminated. Even in the gridded-level 2C microwave radiometer data used in this research, problematic measurements still exist, such as negative and unphysically large values. To remove them, we set threshold values for the brightness temperature in the equatorial region (14° S to 14° B) at local noon time. A brightness temperature greater than 360 K or less than 40 K is judged as abnormal and is excluded in the inversion.

Second, as we are retrieving the base regolith temperature value, the depth value for this inverted temperature needs to be determined. The lunar regolith was divided into six layers (i.e. lunar dust layer, lunar soil layer 1, lunar soil layer 2, lunar soil layer 3, lunar soil layer 4, and lunar rock layer) in Sect. 3. The temperature (T_5, note that in this scheme the lunar dust layer is layer 1; therefore, lunar soil layer 4 is actually the fifth layer) of the lowest soil layer during lunar midday (representing a depth of 0.2–5 m) is derived because it represents a stable temperature that does not vary with insolation. In addition, according to error analysis, the error covariance suggests that the inverse error of T_5 is the smallest among $T_2 - T_5$. Due to the above reasons, this section will solely focus on T_5, 0.2 to 5 m temperature inversion.

In addition, temperature T_5 should be interpreted as a temperature value at the median depth of the fifth layer rather than a temperature for all soils ranging from 0.2 to 5 m. Although the temperature is almost stable below 20 cm, it still slightly increases with depth (Fig. 8). The representative depth of this inversion result can be estimated by the following method: within the fifth layer (ranging from 0.2 to 5 m), the stable temperature slightly increases with depth, but the temperature gradient becomes shallower after 2 m (Fig. 8), probably due to more compact soils which could conduct heat easier; hence, as we can notice from Fig. 8, 2 m is an approximate median value of the fifth layer (0.2–5 m); here, we use a depth of 2 m to interpret the inverted temperature T_5.

Inversion result

We selected midday local observation times (0° < solar angle < 14°), and we inverted the MRM data to reveal the 2 m depth temperature (T_5) from 0° to ± 14° N for the lunar nearside (Fig. 9b).

This research did not invert data from the lunar farside because the farside region dielectric constant and density depth profiles have not been studied and may have added complications. By putting the lunar regolith (Sect. 3), mineralogy S-parameter and density values (Sect. 5) into the forward model (Sect. 4) equations, i.e. Eqs. 29 and 36, it is possible to get an estimate of the fifth layer's temperature (T_5) at midday. However, the addition of extra a priori information and the quantification of its associated error into the inversion modify the approach in Sect. 3, so Eq. 3.29 will be replaced as described below.

First, we calculated T_5 without a priori for a small sample region. We improved the density profile with geographical information from Sect. 5 (e.g. highland, Maria, etc.). We then calculated T_5 again with a priori error covariance included to account for the forward model uncertainty. Then, with a priori, Eq. 36 becomes Eq. 38:

$$x_{\text{improved}} = (K^T S_\varepsilon^{-1} K + S_a^{-1})^{-1} (K^T S_\varepsilon^{-1} y + S_a^{-1} X_a), \tag{38}$$

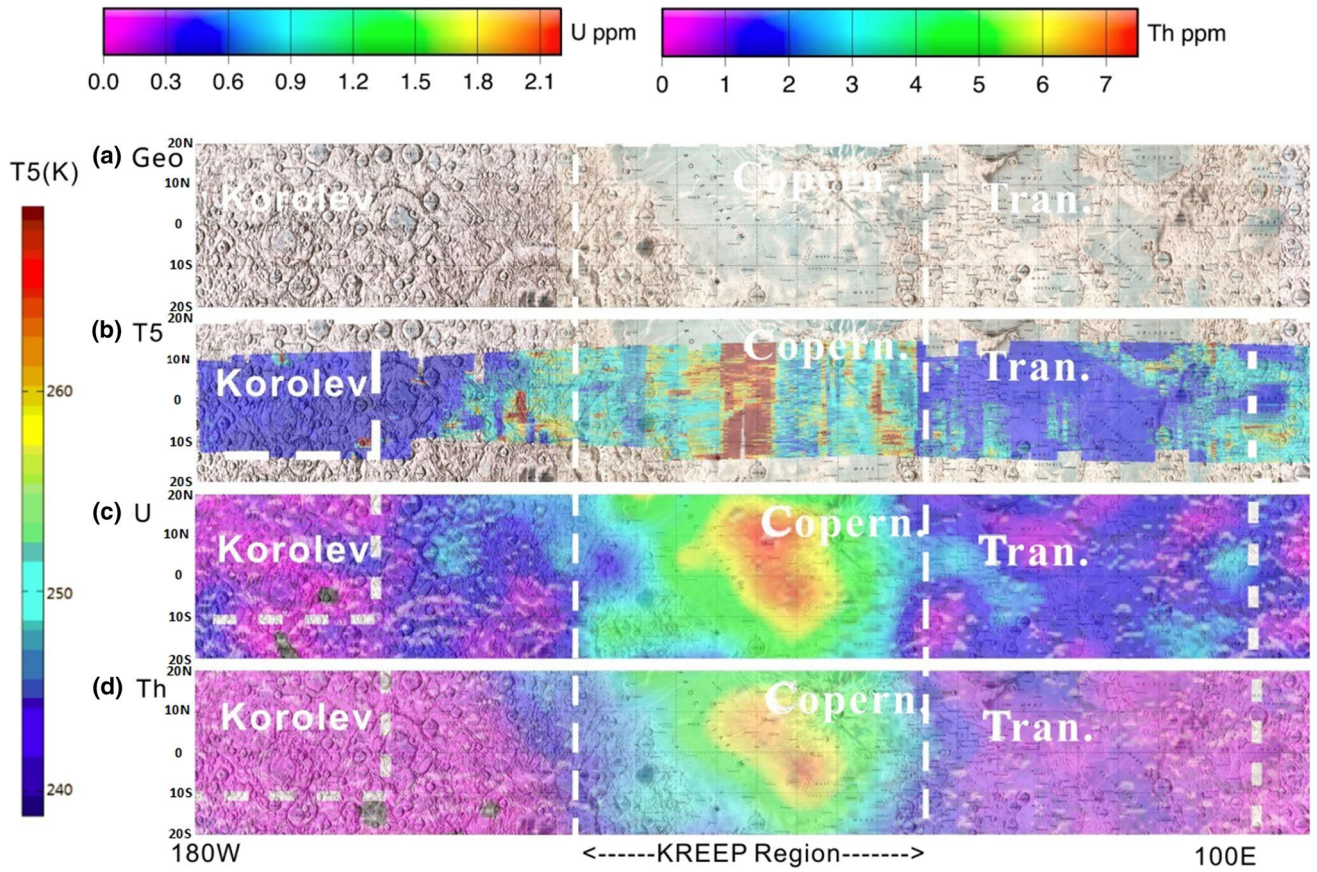

Fig. 9 Map of the inversion result of the 2-m-subsurface temperature (layer 5) (**b**) with relevant lunar surface properties (**a**, **c**, **d**) for comparison. **a** Shaded relief map of the corresponding area; **b** T_5: subsurface temperature at a 2 m depth from the inverted CE MRM data. This figure is the direct output of our work. T_5 is the median temperature of the fifth layer (2 m). 'Stripy' artefacts can be seen in the T_5 map because it is derived from the FeO/TiO_2 maps from M^3 data; **c** lunar uranium (U) concentration levels on the lunar surface as measured by the Kaguya mission (Adapted from Yamashita et al. 2010); **d** lunar thorium (Th) distribution. Adapted from Yamashita et al. 2010. Abbreviations: Copern is the short form for Copernicus crater; Korolev, for Korolev Crater; and Tran, for Mare Tranquillitatis

where the newly added S_a is the error covariance matrix of our a priori guess.

By combining the a priori information with the lunar regolith parameters derived in Sect. 3 (dielectric constant, specific heat and thermal conductivity) and Sect. 5 (mineralogy and bulk density) with the model outlined in Sect. 4 (Eqs. 29 and 38), we can get an inversion result for the lunar soil layer 5 temperature at midday as shown in Fig. 9b. The inversion result Fig. 9b is shown with (a) a geographic map, (c) a uranium distribution map and (d) a thorium distribution map for comparison.

The above results indicate a strong connection between the subsurface temperature and the U/Th distribution. U and Th are both radioactive elements that produce heat in the lunar mantle (Hagerty et al. 2009). Both elements are found in the KREEP regions, and the KREEP regions have the highest subsurface temperature across the Moon. (The average temperature across the KREEP region is ~ 260 ± 6 K.) The regions with the lowest U/Th distribution, such as Mare Tranquillitatis (and all purple regions on map c), have the lowest 2-m-subsurface temperature (~ 240 ± 4 K), which agrees with Keihm et al.'s (1973) and Keihm (1984) model. Outside the KREEP region, the average 2-m-subsurface temperature is 246 ± 4 K, so there is a significant subsurface temperature elevation of 14 ± 10 K inside the KREEP region.

It is possible that the elevated temperature in the KREEP region is caused by factors other than the heating from radiogenic elements. Two other possible factors are geographic, i.e. differences between the highland and Maria regions and differences between the input mineralogy parameter, S. Geographic factors were excluded because in our inversion result Maria regions show both very high subsurface temperature (KREEP region—260 K) and very low subsurface temperatures (Maria outside of KREEP region—240 K).

The influence of the input mineralogy parameter can also be excluded. The two Maria regions, namely the West (Oceanus Procellarum) and East parts (Mare Tranquillitatis,

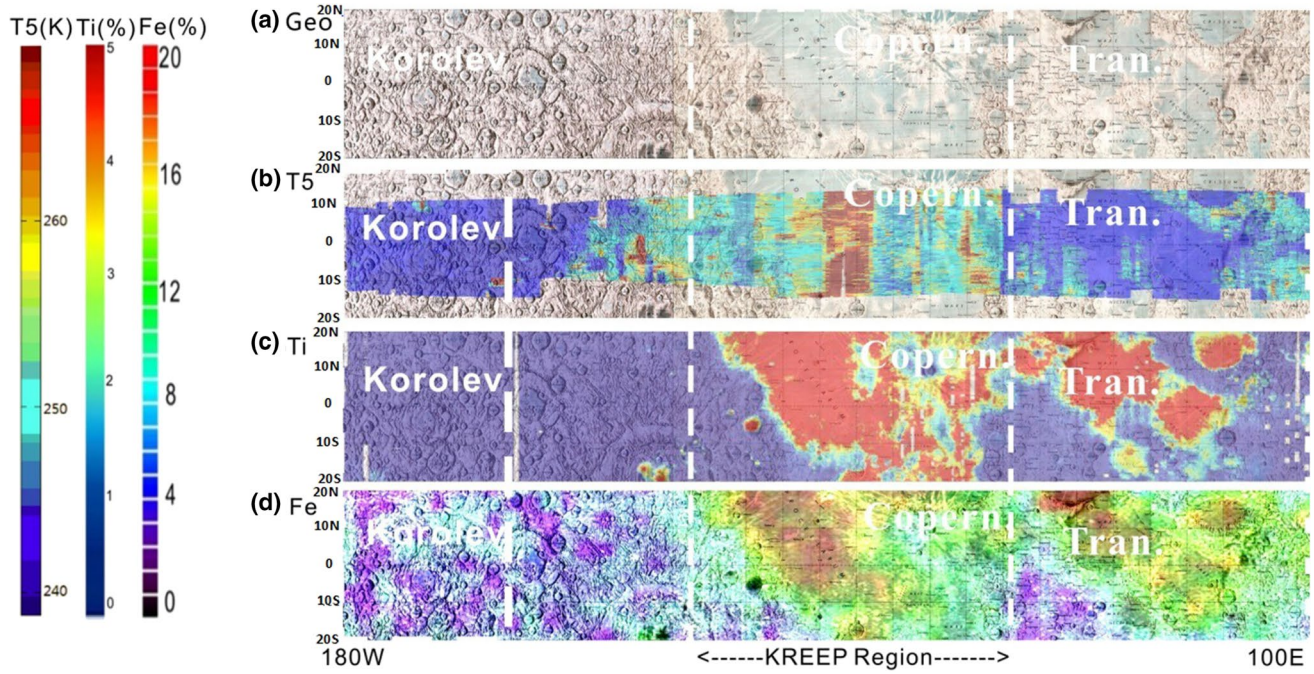

Fig. 10 **a** Corresponding area's shaded relief map; **b** T_5—subsurface temperature inverted at 2 m depth from CE MRM data; **c** lunar titanium distribution from the Clementine data (Korokhin et al. 2008); **d** lunar iron distribution from the Lunar Prospector data (Lawrence et al. 2002)

Mare Serenitatis, Mare Nectaris and Mare Crisium), exhibited extremely different subsurface temperatures although they have highly similar FeO and TiO_2 distributions (Shkuratov et al. 1999; Korokhin et al. 2008). Overall, no obvious connections are evident in the derived temperature at 2 m depth when it is compared with the Fe or Ti distribution map (Fig. 10c, d).

As shown in Figs. 9 and 10, the KREEP region has a considerably higher subsurface temperature than other mare regions, indicating an additional source of heat. The 1 sigma error in the inversion is ± 6 K inside the equatorial KREEP region and is ± 4 K across the global lunar subsurface.

For the non-KREEP regions, our result agrees with the Keihm et al.'s (1973) and Keihm (1984) model. Keihm et al. (1973) and Keihm (1984) predicted the central lunar equatorial subsurface temperature at a 2 m depth to be 250 ± 7 K, assuming that the only heating source was solar radiation. Our derived temperature is in agreement with Keihm's model, providing a non-KREEP average result of 246 ± 4 K.

Inversion of lunar heat flow

Introduction and background to the heat sources of the Moon

Lunar heat flow is defined as the heat released from the lunar interior per unit area per unit time. Through an evolution spanning 4.6 billion years, most of the internal heat of the Moon has been dissipated; however, residual heat of formation is still present, thereby providing information on the origin and evolution of the Moon.

Lunar heat flow contains two endogenic sources, radiogenic heat flow and lunar mantle cooling heat flow. Neither the tenuous (10^{-14} atm) lunar atmosphere nor the static lithosphere contribute to heat redistribution. Consequently, the Moon is in a steady state, and the internal lunar heat flow should be approximately equal to the sum of heat produced by radioactive elements, mainly uranium (U), thorium (Th) and potassium (K), as well as lunar mantle heat flow, which comes from the long-term cooling process of the interior (Korotev 1998).

According to Langseth et al. (1976), the heat flow of the long-term cooling process is approximately 4 mW/m^2. The ratio of lunar interior cooling heat to overall heat is called the Urey coefficient. Spohn and Breuer (2002) reported that about 50% of Moon's heat comes from the decay of radioactive elements, and the remaining 50% is caused by the cooling process inside the Moon, which corresponds to a Urey coefficient of 0.5. A Urey coefficient of 0.5 can be applied to the Earth and Earth-like planets. A coefficient of 0.5 is consistent with the estimate based on geochemical data measured for the Earth. The Earth's bulk heat flow is 44.2 ± 1.0 TW in total, and 24.0 ± 8.8 TW is estimated to be contributed by the radiogenic heat production (The KamLAND Collaboration, 2011). Unlike heat released by

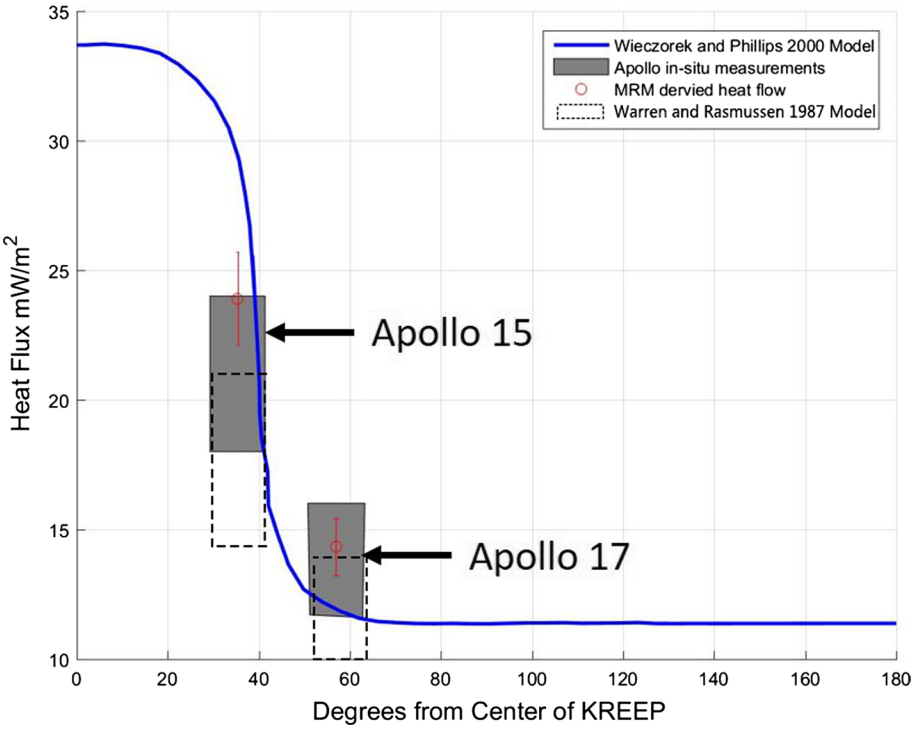

Fig. 11 Plot of the modelled present-day surface heat flow as a function of distance from the approximate centre of the Procellarum KREEP Terrane (solid line). Also shown are the Apollo heat flow measurements, grey boxes show the measurements after correction by Langseth et al. (1972), while the dotted boxes are after correction for any enhancement due to their location at a mare/highlands boundary (Warren and Rasmussen 1987). Figure cited from Wieczorek and Phillips (2000)

cooling from the interior, radiogenic heat production varies as a result of local geology.

On the lunar surface, the distribution of radioactive elements, including uranium, thorium and potassium, is concentrated in the Procellarum KREEP Terrane (PKT). The PKT is the distinct geochemical crustal province formed by the Procellarum and Imbrium regions. According to geochemical studies (Spudis and Schultz 1985), a large portion of the lunar crust in this locale consists of a material that is similar in composition to Apollo 15 KREEP basalt. KREEP basalt consists of about 300-fold more uranium and thorium than highland material, implying that a large portion of the heat-producing elements of the Moon are located within this single crustal province.

To date, the only lunar surface heat flow experiments were conducted at the Apollo 15 and 17 landing sites. Drilling experiments measured the thermal conductivity and heat flow. After correcting for the influence of the astronauts on modifying the top layers of regolith, Langseth et al. (1972) found heat flow of 21 mW/m^2 and 14 mW/m^2 for the Apollo 15 and 17 sites, respectively.

Despite a lack of other in situ measurements, some studies have made early attempts to model the average lunar heat flow. For example, Krotikov and Troitski (1964) used ground-based radio astronomy observations and estimated the average heat flow value to be 54.4 mW/m^2; however, this value is higher than the Apollo measurements (Langseth et al. 1972). According to ground observations of microwave brightness temperature and reanalysis of Apollo 17 data, Langseth et al. (1976), this value was later reduced to give an estimate of the approximate average heat flow of the nearside of 30 mW/m^2.

Heat flow based on MRM-derived temperature

Lunar heat flow may be calculated using the subsurface temperatures from the CE MRM data, as derived in Sect. 5. By definition, lunar heat flow can be represented as the product of conductivity and temperature gradient given by

$$Q = -k\frac{\mathrm{d}T}{\mathrm{d}z}, \tag{39}$$

where Q is the heat flow, T is the temperature, z is the depth and k is the thermal conductivity.

Using the previously derived 2-m-subsurface temperature, Eq. 5 is used to obtain the thermal conductivity k values. The derived k value and temperature gradient are then substituted into Eq. 39, to calculate the heat flow.

Before applying this method to all the data, it may be tested by comparison with the in situ measurements made at the Apollo 15 and 17 landing sites. The subsurface temperatures of the Apollo 15 and 17 sites are not directly obtained, because they are on the edge of the MRM-derived temperature map (Fig. 11). Therefore, their derived subsurface temperatures are derived by elongation interpolation. The interpolated values for the Apollo 15 and 17 landing sites are 255 and 256 K, respectively. The surface temperature at

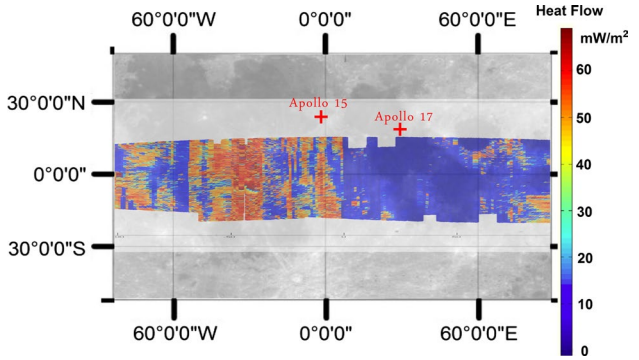

Fig. 12 CE and M^3 measurement heat flow map of the lunar nearside overlaid on Clementine shaded relief map

the Apollo 15 and 17 landing sites was obtained from the Diviner measurements and is 250 and 253 K, respectively.

Thus, the derived heat flow at the Apollo 15 site (HF_{A15}) by this thesis is given by:

$$HF_{A15} = -k\frac{dT}{dz} = -K_c\left[1 + \chi\left(\frac{T}{T_{350}}\right)^3\right]\cdot\frac{dT}{dz}. \quad (40)$$

Similarly, the heat flow at the Apollo 17 landing site (HF_{A17}) is estimated as

$$HF_{A17} = -k\frac{dT}{dz} = -K_c\left[1 + \chi\left(\frac{T}{T_{350}}\right)^3\right]\cdot\frac{dT}{dz}. \quad (41)$$

The calculated heat flow at the Apollo 15 site is 23.9 ± 1.8 mW/m^2 and the heat flow at the Apollo 17 landing site is 14.3 ± 1.1 mW/m^2. These estimates of the heat flow are based on the derived subsurface temperature and temperature gradients from Chang-E, M^3 and Diviner measurements.

Figure 11 shows the theoretical model by Wieczorek and Phillips (2000) of the lunar heat flow in the KREEP Terrane compared with direct measurements from the Apollo heat flow experiments. The heat flow model by Wieczorek and Phillips (2000) indicates that KREEP regions have a significantly higher heat flux (34 mW/m^2) than non-KREEP regions (11 mW/m^2) in the Moon. As shown in Fig. 11, the calculated heat flow at the Apollo 15 and 17 landing sites estimated in this thesis agrees with the previous model by Wieczorek and Phillips (2000) and with the Apollo measurements.

After performing the validation using the Apollo 15 and 17 site data, this method can be applied to the rest of the Moon. However, the farside value of dz (T_5 depth) in Eq. 39 cannot be estimated; hence, we only calculated the nearside heat flow. A heat flow map of the nearside (latitude 14° S to 14° B) from the CE data and using M^3 measurements for mineralogy is overlaid on the Clementine shaded relief map, as shown in Fig. 12.

The inverted 2-m lunar subsurface heat flow ranges from 2 to 68 mW/m^2, which is in the same order of magnitude as earlier ground-based remote sensing measurements, as well as the estimates based on radioactive elements (Little et al. 2003). This also compares well in non-KREEP regions with the model by Wieczorek and Phillips (2000) which predicts a heat flow of 11 mW/m^2, in agreement with this thesis which predicts a heat flow of 11 ± 4 mW/m^2. However, in the KREEP region this work predicts a heat flow of 45 ± 6 mW/m^2 compared to the Wieczorek and Phillips (2000) prediction of 34 mW/m^2. Although there is a slight difference in the two values, this difference is small and can be explained by a small error (± 5 mW/m^2) in Wieczorek and Phillips (2000) model. Unfortunately, no error analysis was provided (Wieczorek and Phillips 2000).

Results of this section provide clues to the lunar geologic history. First, as shown in Fig. 12 in which MRM shows the inverse subsurface heat flow result, we can see that although there is a large error range of ± 6 mW/m^2, it is still clear that the KREEP regions, especially the Oceanus Procellarum region, have particularly high subsurface heat flow (45 ± 6 mW/m^2), while for the non-KREEP terrain the average is only 11 ± 4 mW/m^2. Even in KREEP regions, the subsurface heat flow seems to rise towards the centre of the region. For instance, the Apollo 15 site, which is closer to KREEP centre areas, has a subsurface heat flow of 24 ± 1.8 mW/m^2, while the Apollo 17 site, further from the centre of the KREEP region, has a lower subsurface heat flow of 14.34 ± 1.1 mW/m^2. These values are in accordance with the Apollo in situ measurements, which suggest 22 mW/m^2 for Apollo 17 and 14 mW/m^2 for Apollo 15.

This result is important to our understanding of the KREEP terrain. Because if the centre of KREEP has higher subsurface heat flow than neighbouring KREEP regions around it, and the entire KREEP terrain as a whole has a much higher average subsurface heat flow than other non-KREEP lunar regions, then this would imply that the potential origin of the PKT is a large-scale volcanic event, such as a mantle plume (Campbell 2005). Mantle plumes are believed to start at the core–mantle boundary and rise through the lunar mantle, pushing KREEP materials upwards and forming the distinct region of KREEP terrain that we observe on the Moon today.

Evidence for a volcanic rather impact-driven process to form the PKT can be found in deep surface gravity anomalies measured by recent GRAIL gravity gradient mapping mission. GRAIL also found a polygon-like formation resembling a system of rift valleys surrounding the region beneath the lava plains, suggesting that the basin was formed by heating and cooling of the lunar surface by internal processes rather than by an impact, which would have left deep structures more typical of a large impact basin (Andrews-Hanna et al. 2014).

Secondly, another implication of this result is that the Moon may still be geologically active. Based on the CE MRM inverted subsurface heat flow results, average non-KREEP region subsurface temperature is 11 ± 4 mW/m^2. However, if we only consider the cooling process due to a completely geologically inactive solid core, then this value should be ~ 4 mW/m^2 (Langseth et al. 1976). This also explains some recent finding that some parts of the Moon may be warmer than previously thought (Braden et al. 2014). Volcano activity at Ina ended about 33 million years ago, and at another irregular mare patch, Sosigenes, it stopped only about 18 million years ago.

The lunar surface temperature has been measured using the Diviner lunar radiometer; however the subsurface temperature had only been measured directly at the Apollo 15 and 17 landing sites before the launch of Chang'e 1 (CE-1) and Chang'e 2 (CE-2).

In this paper, firstly, using the parameters derived in the previous step for the one-dimensional thermal diffusion model, a microwave radiative transfer model was established to interpret the MRM data according to the coherent approach of microwave transmission theory and fluctuation–dissipation theorem. To test the forward model, the subsurface variation of the lunar temperature with depth at a single point in the equatorial region was derived and compared with the theoretical predictions of the one-dimensional thermal diffusion model.

The global subsurface temperature at 2 m depth was derived by inverting the MRM brightness temperatures using the newly developed thermal transfer model with new mineralogy and density inputs from Zhang (2014). Comparisons of uranium, thorium and potassium abundance maps show that there is spatial correlation between the temperature of 2 m depth subsurface and the distribution of the abundances of these elements. These radioactive elements would provide a local radiogenic heating source that would elevate the temperature at a depth of 2 m. The regions with the lowest heating source (i.e. the lowest abundance of uranium, thorium and potassium) have the lowest temperature of 2-m subsurface (approximately 240 ± 4 K). This finding is in agreement (to within 3%) with the model used by Keihm et al. (1973), which did not consider radiogenic heating. By contrast, the region with the highest heating source (KREEP) has the highest temperature of 2-m subsurface (approximately 260 ± 6 K). The KREEP region on the lunar surface contains the greatest abundance of uranium, thorium and potassium. The average temperature of 2-m subsurface in non-KREEP regions is 246 ± 4 K. The difference between the KREEP region and the non-KREEP is supported by Wieczorek's KREEP heat flow model (Wieczorek and Phillips 2000), which predicts a 10 K difference between the KREEP centre and non-KREEP regions.

Finally, the lunar heat flow was calculated based on the subsurface temperature result obtained from the MRM data inversion. According to the inversion result, the heat flow at the Apollo 15 landing site was 23.9 ± 4 mW/m^2 and the heat flow at the Apollo 17 landing site was 14.3 ± 4 mW/m^2. Such values are in good agreement (< 10% deviation) with Apollo heat flow measurement results (Warren and Rasmussen 1987). A heat flow map of 2-m-deep lunar subsurface was also derived from the MRM data. The heat flow of 2-m subsurface was found to range from 2 to 68 mW/m^2 and was found to have a strong correlation with the radioactive elements distribution.

References

Andrews-Hanna JC, Besserer J, Head JW III et al (2014) Structure and evolution of the lunar Procellarum region as revealed by GRAIL gravity data. Nature 514(7520):68–71

Braden SE, Stopar JD, Robinson MS et al (2014) Evidence for basaltic volcanism on the Moon within the past 100 million years. Nat Geosci 7(11):787

Burke WJ, Schmugge T, Paris JF (1979) Comparison of 2.8- and 21-cm microwave radiometer observations over soils with emission model calculations. J Geophys Res 84:287–294

Campbell IH (2005) Large igneous provinces and the mantle plume hypothesis. Elements 1(5):265–269

Cartier WDIII, Mitchell JK, Mahmood A (1973) The nature of lunar soil. NASA STI/Recon Tech Rep A 99:813–832

Fa WZ, Jin YQ (2007) Simulation of brightness temperature from lunar surface and inversion of regolith-layer thickness. J Geophys Res 112:E05003

Hagermann A, Tanaka S (2006) Ejecta deposit thickness, heat flow, and a critical ambiguity on the Moon. Geophys Res Lett 33(19):277–305

Hagerty J, Lawrence D, Hawke B, Gaddis L (2009) Thorium abundances on the Aristarchus plateau: insights into the composition of the Aristarchus pyroclastic glass deposits. J Geophy Res. https://doi.org/10.1029/2008JE003262

Hartmann WK, Phillips RJ, Taylor GJ (1986) Origin of the Moon. Lunar & Planetary Institute, Houston, p 1

Haskin LA (1998) The Imbrium impact event and the thorium distribution at the lunar highlands surface. J Geophys Res 103:1679–1689

Heiken GH, Vaniman DT, French BM (1991) Lunar source book: a user's guide to the Moon. Cambridge University Press, Cambridge

Horai K, Fujii N (1972) Thermophysical properties of lunar material returned by Apollo missions. Moon 4(3):447–475

Jin YQ (1993) Electromagnetic scattering modelling for quantitative remote sensing. World Scientific Publishing, Singapore

Jones WP, Watkins JR, Calvert TA (1975) Temperatures and thermophysical properties of the lunar outmost layer. Moon 13:475–494

Keihm SJ (1984) Interpretation of the lunar microwave brightness temperature spectrum: feasibility of orbital heat flow mapping. Icarus 60(3):568–589

Keihm SJ, Peters K, Langseth MG (1973) Apollo 15 measurement of lunar surface brightness temperatures thermal conductivity of the upper 1 and 1/2 metres of regolith. Earth Planet Sci Lett 19:337–351

Korokhin VV, Kaydash VG, Shkuratov YG, Stankevich DG, Urs M (2008) Prognosis of TiO_2 abundance in lunar soil using a non-linear analysis of Clementine and LSCC data. Planet Space Sci 56:1063–1078

Korotev RL (1998) Concentrations of radioactive elements in lunar materials. J Geophys Res Planets 103(E1):1691–1701
Krotikov VD, Troitski UIVS (1964) Radio emission and nature of the Moon. Phys Usp 6(6):841–871
Langseth MG Jr, Keihm SJ, Chute JL Jr (1972) Heat-flow experiment. Moon 4:390–410
Langseth MG, Keihm SJ, Peters K (1976) Revised lunar heat flow values. Lunar Planet Sci Conf Proc 7:3143–3317
Lawrence DJ, Feldman WC, Elphic RC et al (2002) Iron abundances on the lunar surface as measured by the lunar prospector gamma-ray and neutron spectrometers. J Geophys Res 107:5130
Li Y, Wang ZZ, Jiang JS (2010) Simulations on the influence of lunar surface temperature profiles on CE-1 lunar microwave sounder brightness temperature. Sci China Earth Sci 53(9):1379–1391
Little RC, Feldman WC, Maurice S et al (2003) Latitude variation of the subsurface lunar temperature: lunar Prospector thermal neutrons. J Geophys Res Planets 108(E5):5046
Lucey PG, Taylor GJ, Malaret E (1995) Abundance and distribution of iron on the Moon. Science 268(5214):1150–1153
Lucey PG, Blewett DT, Hawke BR (1998) Mapping the FeO and TiO_2 content of the lunar surface multispectral imagery. J Geophys Res 103:3679–3699
Mitchell DL, Pater ID (1994) Microwave imaging of Mercury's thermal emission at wavelengths from 0.3 to 20.5 cm. Icarus 110:2–32
Olhoeft GR, Strangway DW (1975) Dielectric properties of the first 100 metres of the Moon. Earth Planet Sci Lett 24:394–404
Paige DA, Foote MC, Greenhagen BT et al (2010) The lunar reconnaissance orbiter diviner lunar radiometer experiment. Space Sci Rev 150(1–4):125–160
Rodgers CD (2000) Inverse methods for atmospheric sounding: theory and practice. World Scientific, Singapore
Shkuratov YG, Kaydash VG, Opanasenko NV (1999) Iron and titanium abundance and maturity degree distribution on lunar nearside. Icarus 137(2):222–234
Shrestha D (2007) An emission model for lunar regolith surfaces based on matrix doubling method. Electrical Engineering, pp 1–85
Spencer JR, Lebofskyf LA, Sykes MV (1989) Systematic biases in radiometric diameter determinations. Icarus 78(2):337–354
Spohn T, Breuer D (2002) Surface heat flow, radiogenic heating, and the evolution of the Moon. In: EGS General Assembly Conference Abstracts, p 27
Spudis PD, Schultz PH (1985) The proposed lunar procellarum basin: some geochemical inconsistencies. In: Lunar and planetary science conference, vol 16, pp 809–810
The Kam LAND Collaboration (2011) Partial radiogenic heat model for Earth revealed by geoneutrino measurements. Nat Geosci 4:647–651
Tsang L, Njoku E, Kong JA (1975) Microwave thermal emission from a stratified medium with non uniform temperature distribution. J Appl Phys 46(12):5127–5133
Ulaby FT, Moore RK, Fung AK (1981) Microwave remote sensing: active and passive. Volume 1-microwave remote sensing fundamentals and radiometry. Taylor & Francis, Routledge
Urquhart ML, Jacksky BM (1997) Lunar thermal emission and remote determination of surface properties. J Geophys Res 102:10959–10969
Vasavada AR, Paige DA, Wood SE (1999) Near-surface temperatures on Mercury and the Moon and the stability of polar ice deposits. Icarus 141:179–193
Wang ZZ, Li Y, Jiang JS, et al (2008) Microwave transfer models and brightness temperature simulations of MWS for remote sensing lunar surface on CE-1 Satellite. In: 2008 International conference on microwave and millimeter wave technology, pp 21–24
Wang ZZ, Li Y, Zhang XH et al (2010) Calibration and brightness temperature algorithm of CE-1 lunar microwave sounder (CELMS). Sci China Earth Sci 53:1392–1406
Warren PH, Rasmussen KL (1987) Megaregolith insulation, internal temperatures, and bulk uranium content of the Moon. J Geophys Res Solid Earth 92(B5):3453–3465
Wieczorek MA, Phillips RJ (2000) The "Procellarum KREEP Terrane": implications for mare volcanism and lunar evolution. J Geophys Res 105(E8):20417–20430
Yamashita N et al (2010) Uranium on the Moon: global distribution and U/Th ratio. Geophys Res Lett 37:L10201
Zhang WJ (2014) Estimate of lunar TiO_2 and FeO with M cube data. Encyclopedia of lunar science. Springer, Cham
Zhang WJ, Zhang XJ, Li F (2008) Backscattering from multilayer soil and its application to deep soil moisture estimation. J Electr Inf Technol 30(9):2107–2110

11600

Acta Geophysica

Volume 68
Number 2
2020

ACTA GEOPHYSICA
Vol. 68 • No. 2 • 2020 • pp. 289–596

(Contents continued on inside back cover)